The Effect of Thermomechanical Process Parameters on the Microstructure and Crystallographic Texture Evolution of Near-α Aerospace Alloy Timetal®834.

Matthew James Thomas

Department of Engineering Materials

The University of Sheffield

Thesis submitted for the degree of
Doctor of Philosophy
June 2007

SUMMARY

Understanding the effects of thermomechanical process parameters on the microstructure evolution and subsequent mechanical properties of near-alpha titanium alloy Timetal®834 is a key step in optimising the performance of the alloy particularly for operation in the high temperature compressor section of a gas turbine engine. This work investigates the effect of variables typical of the industrial forging process on the microstructure and the crystallographic texture of this alloy.

The state of the art thermomechanical compression apparatus at the University of Sheffield was used in order to carry out a detailed schedule of heat treatments and axisymmetric compression tests. Optical metallography and image analysis techniques were used in order to investigate the test specimens microstructure after deformation. The microstructural analysis completed allowed process parameter related microstructural features to be identified. Furthermore, established texture determination techniques and state of the art scanning electron microscopy were used to analyse the crystallographic texture evolution through the schedule of thermomechanical compression tests.

Through the axisymmetric compression testing results the flow behaviour of this alloy was analysed and a friction coefficient of $\mu = 0.197$ and a value for Q_{def} of 958.70 kJ/mol were determined. Equiaxed α_p are believed to strain harden during deformation and there is a suggestion that if transformed lamellar or widmanstätten α_s is present it will flow soften due to bending or kinking of the lamellae. The deformation mechanisms apparent in the α_p have been identified using trace analysis and local misorientation information.

The results prove the benefits of obtaining both micrographs and EBSD OIM's of areas of interest and detail the difficulties in assessing the morphologies of the hexagonal α phase through EBSD analysis. As such, a method developed for determining the texture of each phase separately using both images is detailed and the texture evolution of each phase with increasing strain has been determined.

TABLE OF CONTENTS

NOMENCLATURE

a	Lattice parameter
A	Cross-sectional area
A	Equation constant
A_0	Original cross-sectional area
A_1	Equation constant
A_2	Equation constant
α	Alpha phase of Titanium
α	Equation constant
α_p	Primary alpha grain morphology
α_s	Secondary (transformed) alpha morphology
α_t	Thermal expansion coefficient
α'	Martensitic alpha morphology
b	Positive driving force
B	Basal texture component
B_ϵ	Equation constant at defined strain
β	Beta phase of Titanium
β	Equation constant
BCC	Body centred cubic crystal
c	Lattice parameter
d	Diameter
d_p	Crosshead displacement
ΔG	Difference in free enthalpy
ΔF	Helmholtz free energy
ΔW	Work done
δ	Displacement of upper tool
ϵ	Strain
$\dot{\varepsilon}$	Strain rate
ϵ_p	Strain at peak stress
ϵ_{ss}	Strain at steady-state stress
ϵ_r	Transient strain constant

ϵ_1	Strain component
ϵ_2	Strain component
ϵ_3	Strain component
F	Force
FCC	Face centred cubic crystal
H	Height
HCP	Hexagonal close packed crystal
h	Height
h_0	Initial height
h_c	Height at room temperature
hkl	Miller indices of crystal plane
ID	Inner diameter
IMI	Acronym for Imperial Metal Industries
L	Mean linear intercept
MPa	Megapascal, Unit of stress
μ	Coefficient of friction
ND	Normal Direction
N_L	Number of boundaries pre unit length
OD	Outer diameter
P	Mean Pressure
P	Stress at a given time
P	Stress at a gi
P_p	Number of counts per phase
Pr	Prismatic plane of hexagonal crystal
Py	Pyramidal plane of hexagonal crystal
Q	Activation energy
Q_{def}	Activation energy of deformation
r	Direction vector
R	True stress
R	Universal gas constant
RD	Rolling direction
ρ	Stress normal to the shearing stress
S_1	Stated phase volume fraction
S_n	Alternative phase volume fraction

σ	Stress
σ_ϵ	Stress at defined strain
σ_0	Initial stress
$\sigma_{0.1}$	Stress at a strain of 0.1
σ_p	Peak stress
σ_{ss}	Steady-state stress
T	Transverse texture component
T	Temperature
T_0	Initial temperature
TD	Transverse direction
T_β	Beta transus temperature
τ	Shearing stress
Φ	Euler angle of rotation about the X axis
ϕ_1	First Euler angle of rotation about the Y axis
ϕ_2	Second Euler angle of rotation about the Y axis
uvw	Miller indices of crystal direction
V	Volume
V_v	Volume fraction of single phase
WD	Working distance
Z	Zener-Hollomon parameter
Z	Atomic number
Z_{SSD}	Distance from specimen to sample in the electron microscope

ACKNOWLEDGEMENTS

There have been many people who have helped me during the completion of this thesis and I would like to acknowledge everyone who has been involved. I would like to begin by thanking my first supervisor Brad Wynne, as his support has not only aided this academic achievement but also my personal development. I would also like to thank my second supervisor Mark Rainforth for his interest and advice, the encouragement of both my supervisors has assisted me throughout this work.

I have received a great deal of support from the Sheffield Materials Forum and Dr M Frolish for which I am extremely grateful, also the help received from my many industrial supervisors from Firth Rixson PLC including Dr A Partridge, Dr K Wrigley, Dr A Davidson, Mr J Cason and Dr Lee Shaw has been beneficial. I would like to acknowledge the EPSRC (Engineering and Physical Sciences Research Council) for their financial support.

I thank my many friends in D1 and throughout IMMPETUS and wish you all success in your own work... whenever you choose to complete it.

I am extremely grateful to all the technical staff that have enabled me to carry out my experimental work; Dr P Korgul for his wealth of knowledge and experience in all things, Dr H. Bagshaw and Dr P Cizek for SEM guidance, Mr I watts, Mr P Staton, Mr S Bates, Mr A Lacey and Mr D Manvell.

I would like to thank all my family and friends, especially my Father, with whom I have discussed all aspects of this work, and found all answers and suggestions returned extremely beneficial. Finally, I would like to thank Amy, for her constant presence and for helping with every word on every page

For my Mum...

1. INTRODUCTION

1.1 The Role of titanium in the Aeroengine

The complexities of powered flight including non linear loading sequences and strict needs of safety in conjunction with economic and environmental restrictions mean aircraft engines need to satisfy numerous competing engineering requirements to sustain a prolonged service life (Boyer, 1996). For example, these engines must be:

- *lightweight*, as a heavy engine decreases the amount of excess power available;
- *small* and *easily streamlined*, large engines with substantial surface area create too much drag, wasting fuel and reducing power output;
- *powerful*, to overcome the weight and drag of the aircraft;
- *reliable*, as losing power in an aeroplane is a substantially greater problem than an automobile engine seizing. Aircraft engines operate at temperature, pressure, and speed extremes, and therefore need to operate reliably and safely under all these conditions; and
- *repairable*, to keep the cost of replacement down. Minor repairs need to be relatively inexpensive.

In most modern jet turbine engines, high strength titanium based alloy parts make up to 20% to 30% of the dry weight, primarily in the region from the turbine blades through to the high pressure compressor section, i.e. in the region of the aeroengine operating up to temperature of approximately 600°C. Traditionally, the higher temperatures experienced towards the rear of the engine have forced materials selection to veer towards nickel-based superalloys though more recently developed titanium alloys have been optimised to operate further towards the back of the engine, where operating temperatures approach 650°C. Temperature, however, is not the only design consideration as aeroengine components experience complex dynamic loading conditions, therefore the materials used must also possess good creep and fatigue resistance. Timetal®834 is one such titanium alloy believed to possess the optimum balance of these properties at temperatures up to 600°C, and in fact has gained significant interest from the industry as a viable alternative material for compressor discs.

1.2 Timetal®834

Timetal®834 (previously known as IMI 834) was developed by IMI Titanium in the United Kingdom, in the mid-1980's and is currently finding use in European military jet engines and within the compressor sections of variations of Rolls Royce and General Electric engines. Perhaps rather unfortunately, one major disadvantage of Timetal®834 is its susceptibility to low temperature dwell fatigue, a phenomenon where rest periods in the fatigue cycle substantially reduce the number of cycles to failure of the component. It is believed that the materials microstructure and local crystallographic orientation are the reason for this susceptibility and consequently, there is a major drive to understand the effects of the industrial process parameters on the resulting microstructure and subsequent mechanical properties. Furthermore, a concern with the current manufacturing route is that it often produces variations in the extent of crystallographic texture within the material, which is a possible cause for the materials dwell fatigue susceptability. Thus this work, with the support of Firth Rixson PLC, investigates the effect of manufacturing process variables on the substructure and crystallographic texture development of Timetal®834.

1.3 Project Aim

To investigate the microstructure and crystallographic texture evolution of Timetal®834 under deformation conditions typical of the hot forging process route.

1.4 Project Objectives

- Using the state of the art thermomechanical compression (TMC) apparatus at the University of Sheffield the work will investigate the industrial process route. Controlling variable parameters such as temperature, applied strain and strain rate will allow for determination of processing effects.
- Using optical metallography and image analysis techniques the microstructures of the thermomechanical compression test materials will be analysed such that any process parameter related microstructural features can be identified and assessed.

- Using established texture determination techniques and state of the art scanning electron microscopy, the crystallographic texture evolution through the schedule of thermomechanical compression tests will be investigated.

1.5 Thesis Outline

The following thesis will document the achievement of said aim using said objectives and shall be structured in the following way;

- **Chapter 2** will include the relevant theoretical background behind the major issues of this work (titanium alloys, mechanical testing, electron backscatter diffraction (EBSD) analysis) with the aim of identifying the state of the art as well as gaining an understanding and appreciation of the field. Methodologies utilised in this work will be introduced and their use in previous works will be reviewed.
- In **Chapter 3** the production of Timetal®834 from the point of sourcing raw materials through to the supplying of the billet to the component manufacturer will be detailed. This is necessary as the process history of what is labelled 'starting material' may have an effect on results gained.
- In **Chapter 4** the experimental techniques used in this work will be described in detail. This chapter will initially describe beta approach curve determination work of the as-received Timetal®834 as this was the first set of experiments completed as part of this thesis. This work is a suitable introduction to the effect of thermal treatment on this alloy and material preparation techniques for optical analysis which were used subsequently in further work completed. The chapter will then continue to describe axisymmetric compression testing, metallographic preparation for optical and electron microscopy and finally texture determination techniques used, concentrating on electron back scatter diffraction techniques.
- **Chapter 5** includes an extension of the experimental procedures and the axisymmetric compression testing results. This chapter is a key part of this thesis as these results are used in the development of constitutive equations and then discussed in the analysis of this materials flow behaviour under the thermomechanical compression conditions investigated in this work.

- **Chapter 6** presents the metallographic results gained from the axisymmetric compression testing detailed in Chapter 5 and further thermomechanical testing completed. The EBSD results gained are seen in this chapter as Euler colouring Orientation Image maps (OIM's) and {0002} and $\{10\bar{1}0\}$ pole figures in order to systematically present each map obtained.
- During the completion of this work a novel technique to separate the orientations of primary alpha from those of the transformed beta grains in the EBSD data set was developed. **Chapter 7** will document the development of this technique, some of the results gained and a comparison with other techniques used.
- The EBSD results seen in Chapter 6 are then analysed using a number of post-mapping processing methods available. This analysis is detailed in **Chapter 8** and combined with the optical metallographic results seen in Chapter 6 the microstructural and crystallographic texture evolution of this alloy is investigated.
- **Chapter 9** summarises the principal observations and draws some conclusions from this work.
- By taking into consideration the work completed through Chapters 5, 6, 7 and 8 and the conclusions made in Chapter 9, **Chapter 10** suggests some key areas that would be usefully investigated if any future work was undertaken.

2. LITERATURE REVIEW

2.1 Introduction:

In order to understand the effect of thermomechanical processing on the microstructure of titanium alloys (e.g. grain size, grain shape, crystallographic texture, phase morphology and phase volume fraction and distribution) a first requirement is to fully comprehend the fundamentals involved in producing that microstructure, which includes crystallography, fundamental physical metallurgy, deformation mechanics and flow behaviour. Thus, the following literature review will include the relevant theoretical background of these issues with the aim of gaining an understanding and appreciation of all these fields as well as identifying the state of the art.

The chapter will initially investigate alloy development and microstructure tailoring, paying great attention to the importance of manipulation of duplex microstructures and subsequent effects on the resulting mechanical properties. This will also include an overview of the image analysis techniques needed in order to quantify the volume fraction of each phase. Secondly, the deformation mechanics of titanium will be reviewed with particular attention paid to hot uniaxial compression in order to gain an appreciation of the calculation of strain and its variation within an axisymmetric compression sample. Finally and perhaps most importantly, the microstructures, crystallography and textures of titanium alloys will be investigated and studied in order to be able to consider the effect of the varying deformation parameters on them and their subsequent effect on mechanical properties, particularly low temperature dwell fatigue.

2.2 Titanium

2.2.1 Introduction

Titanium (symbol Ti and atomic number 22) is a light, strong and corrosion-resistant metal. One of titanium's most notable characteristics is that its alloys can be as strong as steel but have only 60% of its density; thus the combination of high strength-to-weight ratio, excellent mechanical properties, and corrosion resistance makes

titanium and its alloys an excellent material choice for many critical applications particularly for the aerospace (Figure 2.1), energy, and chemical industries.

Figure 2.1 The turbine engine of an Airbus A380 containing large amounts of Titanium and an example of a,titanium compressor section taken from a Solar T-62T-32 engine (www.technologie-entwicklung.de /Gasturbines.html, 2005).

2.2.2 Crystallography.

Titanium is a transition metal with a melting temperature of 1678°C. At 882.5°C it undergoes an allotropic transformation from a hexagonal close-packed (HCP) structure, referred to as the alpha (α) phase, to a body centre cubic (BCC) structure known as the beta (β) phase.

2.2.2.1 The Hexagonal Close-Packed Crystal Structure.

The hexagonal close packed unit cell is one of three common metallic crystal structures (the other two being face centre cubic (FCC) and BCC). The top and bottom faces of the unit cell consist of six atoms that form regular hexagons which surround a single atom in the centre of the plane. In addition another plane provides three extra atoms to the unit cell which is situated between the top and bottom planes (Callister, 2003). Consequently, there is the equivalent of six atoms contained in one unit cell: one-sixth of each of the 12 top and bottom face corner atoms, one half of each of the 2 centre face atoms and all 3 mid plane atoms.

A schematic diagram of the unit cell for α titanium can be seen in Figure 2.2. This figure also highlights the two lattice parameters required to define the unit cell; **a,** the distance from the centre to the corner of the hexagon plane and **c,** the distance between the two hexagon planes. For α titanium the values of **a** and **c** are 0.295nm and 0.468nm, respectively resulting in a **c/a** value of 1.587 which, in turn, produces a packing density of 56.70 atoms/nm^3. The figure also illustrates the three most close packed planes of the hexagonal unit cell, the (0002) plane, also called the basal plane, one of the three $\{10\bar{1}0\}$ planes, known as prismatic planes and one of the six $\{10\bar{1}1\}$ planes, known as pyramidal planes.

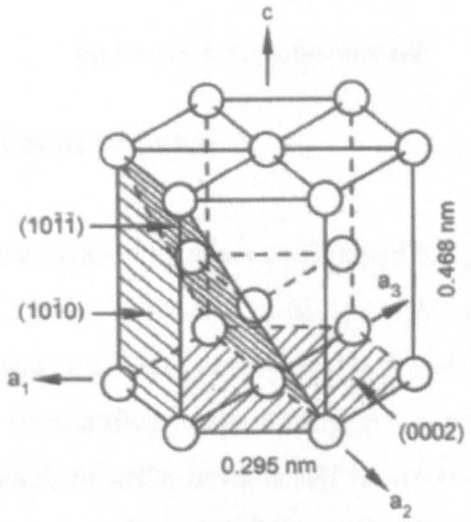

Figure 2.2, α Titanium unit cell (Leyens and Peters, 2003).

2.2.2.2 The Body Centred Cubic Crystal Structure.

The BCC unit cell consists of a cube with atoms located on each of the corners and a single atom at the cube centre. Thus, there is the equivalent of two atoms in one unit cell: one-eighth of each of the corner atoms and the centre atom. To completely define the unit cell only one lattice parameter, **a**, is required as shown in Figure 2.3. For β-titanium the value of **a** is 0.332 nm, which results in a packing density of 54.65 atoms/nm^3. Thus on transformation from α to β phase there is a 3.75% increase in volume. Figure 2.3 also shows the six most densely packed lattice planes of the BCC structure which are the {110} planes and the close packed directions which are the four <111> directions (Donachie, 1998 and Leyens and Peters, 2003).

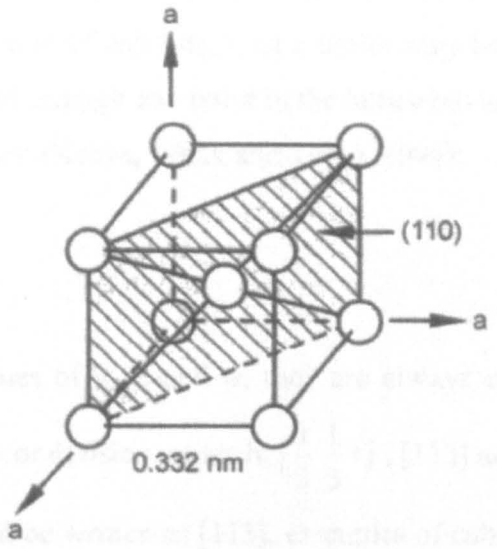

Figure 2.3, β Titanium unit cell

2.2.3 Miller and Miller-Bravais Notation

In thinking about crystals it is often convenient to ignore actual atoms, ions or molecules and to focus on the geometry of the periodic arrays. The crystal is then represented as a lattice, that is a three dimensional array of points (lattice points), each of which has identical surroundings; see Figure 2.4 (Cullity and Stock, 2001). In crystals of cubic, tetragonal, or orthorhombic lattice structures a Cartesian coordinate frame is tied to the lattice, x, y, z aligned with the unit cell vectors a, b and c.

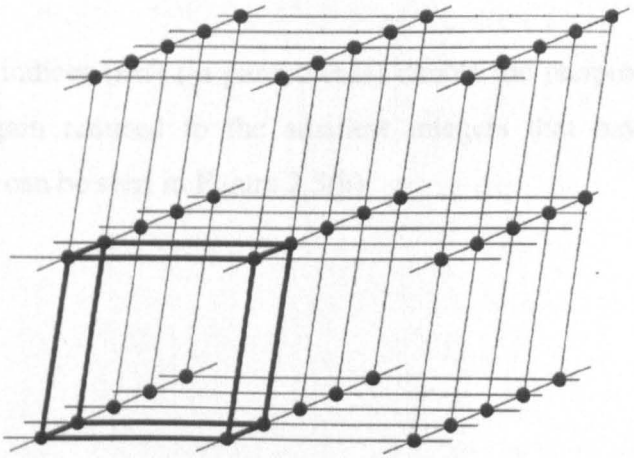

Figure 2.4 Three dimensional lattice with a primitive unit cell highlighted in bold. Lattice points are represented by solid circles/spheres (Cullity and Stock, 2001).

Within a crystal frame, it is common to describe lattice directions and planes by integer indices. The direction of any line, r, in a lattice may be described by drawing a line through the origin and through any point in the lattice having coordinates *u, v and w* according to the vector sum (Kocks, Wenk and Tome, 1998);

$$r = ua + vb + wc \tag{2.1}$$

Whatever the values of *u, v,* and *w*, they are always converted to the smallest integers by multiplication or division, as such, $[\frac{1}{3}\ \frac{1}{3}\ 1]$, [113] and [226] all represent the same direction and should be written as [113], examples of cubic directions can be seen in Figure 2.5(a).

The orientation of a surface or a crystal plane may be defined by considering how the lattice plane (or indeed any parallel plane) intersects the main crystallographic axes of the solid. The orientation of planes in a lattice may be represented symbolically according to a system popularised by Miller, where the orientation of the plane is described by expressing the point where the plane intercepts one of the three axes as a fraction of the axial length. A set of parallel lattice planes is described according to the equation;

$$h\frac{x}{a} + k\frac{y}{b} + l\frac{z}{c} = 1 \tag{2.2}$$

The miller indices (*hkl*) (in parentheses) denote the reciprocal multiples of the axis intercepts, again reduced to the smallest integers that have the same ratios, examples of which can be seen in Figure 2.5(b)

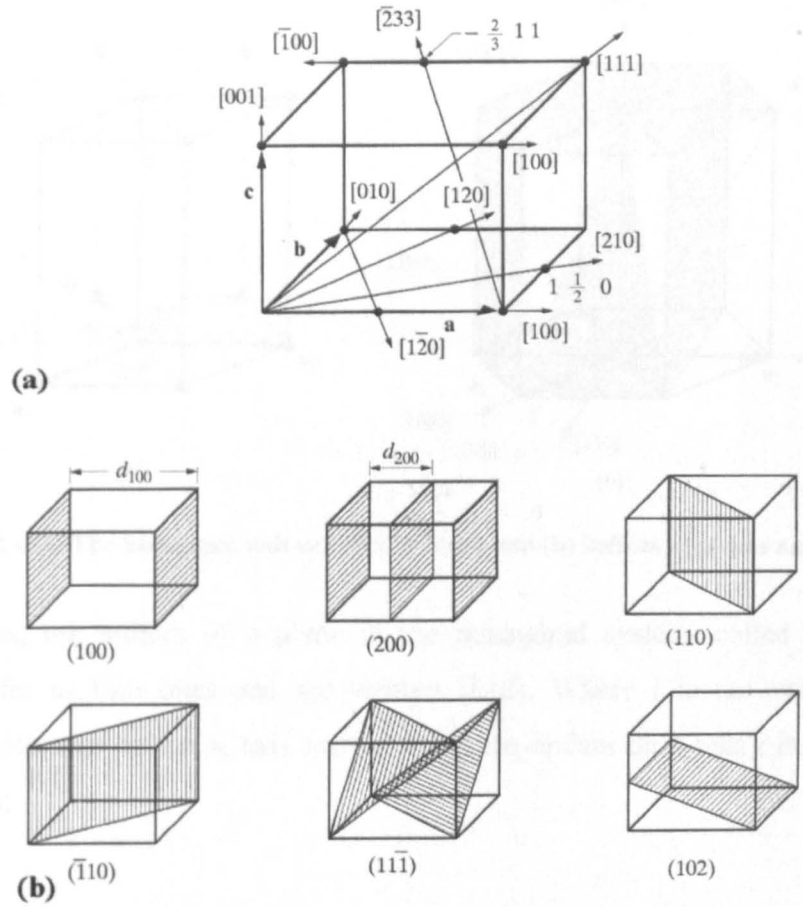

Figure 2.5 Examples of (a) indices of directions and (b) Miller indices of lattice planes. The distance *d* is the plane spacing.

For the hexagonal crystal system a slightly different system of plane indexing is used, defined by two equal and coplanar vectors $\mathbf{a}_1$ and $\mathbf{a}_2$ at 120° to another , and a third axis **c** at right angles. When repeated translations of the points at the unit cell corners are constructed the hexagonal symmetry of the lattice is seen in Figure 2.6, and a third axis, $\mathbf{a}_3$, lying in the basal plane, symmetrically related to $\mathbf{a}_1$ and $\mathbf{a}_2$ is used.

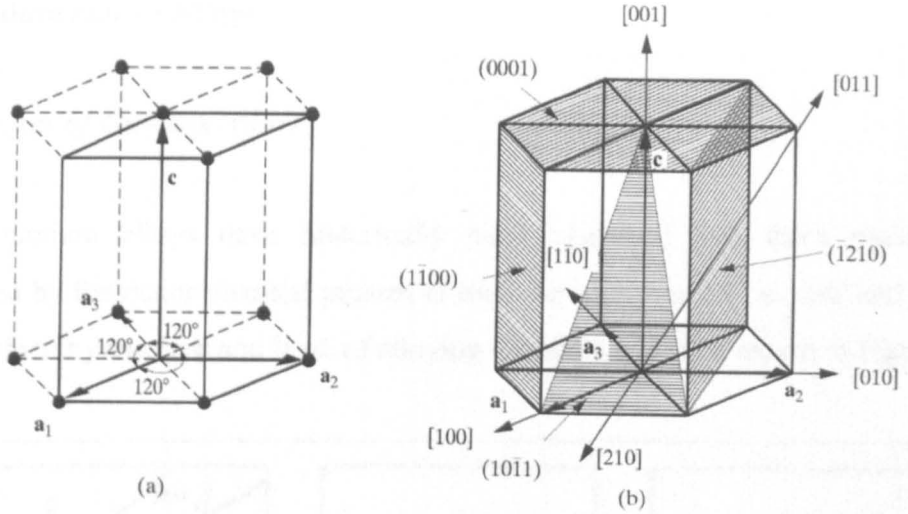

Figure 2.6 (a) The hexagonal unit cell (heavy lines) and (b) indices of planes and directions.

Thus, the indices of a plane in the hexagonal system, called Miller-Bravais indices, refer to four axes and are written (*hkil*). Where *i* is the reciprocal of the fractional intercept on the a_3 axis and its value, dependant on h and k is determined by the relation;

$$h + k = -i \tag{2.3}$$

Directions in the hexagonal system can also be described using four indices, each index relating to a component vector parallel to a_1, a_2, a_3 and c. As such, [uvtw] are the four axis indices and are related to [UVW] as follows.

$$U = u - t \qquad u = \left(\frac{2U - V}{3}\right)$$

$$V = v - t \qquad v = \left(\frac{2V - U}{3}\right)$$

$$W = w \qquad t = -(u + v) = \left(\frac{-(U + V)}{3}\right)$$

$$w = W \tag{2.4}$$

Thus, [100] becomes [2110] and [210] becomes [1010], etc.

2.3 Titanium and its Alloys

2.3.1 Classes of Titanium Alloys

Titanium alloys have historically been classified into three main groups designated by the major phase(s) present at room temperature, i.e. α , α/β and β, which is determined by the type and level of alloying elements added as shown in Figure 2.7.

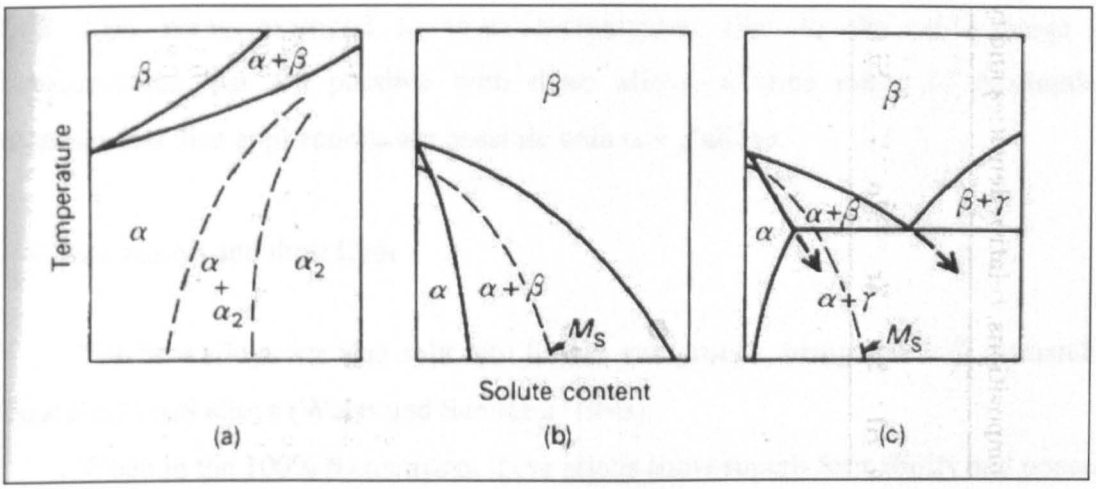

Figure 2.7 Basic types of phase diagrams for titanium alloys. The dotted phase boundaries in (a) refer specifically to the Ti-Al system. Alloying elements favouring the different types of phase diagram are (a) alpha stabilisers Al, O, C, Ga, N; (b) beta stabilisers Mo, W, V, Ta; (c) Cu, Mn, Cr, Fe, Ni, Co, H (Polmear, 1995)

2.3.2 Alpha Alloys and their Uses.

Alpha titanium alloys commonly contain aluminium (Al) and oxygen (O) as well as possible additions of nitrogen (N) and carbon (C). This class of titanium alloy is further sectioned into unalloyed titanium, α alloys and near-α alloys (Weiss and Semiatin, 1999). Unalloyed and fully α alloys are single phase alloys with relatively low tensile strength but good creep properties. Due to the hexagonal structure of the alpha phase these alloys have limited formability due to a reduction in number of available slip systems compared to cubic structures.

Near-α alloys are sometimes referred to as super-α alloys as, although they retain some beta phase (approx. 2%), they consist primarily of α and behave in a similar fashion to that of conventional α alloys. These alloys possess higher room temperature tensile strength than full-α alloys and the greatest creep resistance of all Ti alloys at

temperatures above 400°C and thus are often used in applications with higher operating temperatures such as the compressor section of gas turbines.

2.3.3 Alpha + Beta Alloys and their Uses

Alpha + beta alloys usually possess a number of both α and β stabilising elements, such as vanadium (V), molybdenum (Mo), niobium (Nb), silicon (Si) and iron (Fe), and they retain more beta phase on cooling than near α alloys due to the $\alpha + \beta$ phase field being extended to room temperature. Due to the wide range of microstructures that are possible with these alloys, a wide range of mechanical properties and thus applications are possible with $\alpha + \beta$ alloys.

2.3.4 Beta Alloys and their Uses

The beta alloys are also split into further sub groups, being stable β, metastable β, and β rich α/β alloys (Weiss and Semiatin, 1998).

When in the 100% β condition, these alloys show superb formability and possess good toughness and ductility. Thus, it is clear to see, that by appropriate alloying a broad range of properties can be developed in titanium alloys which are shown schematically as a function of microstructure in Figure 2.8.

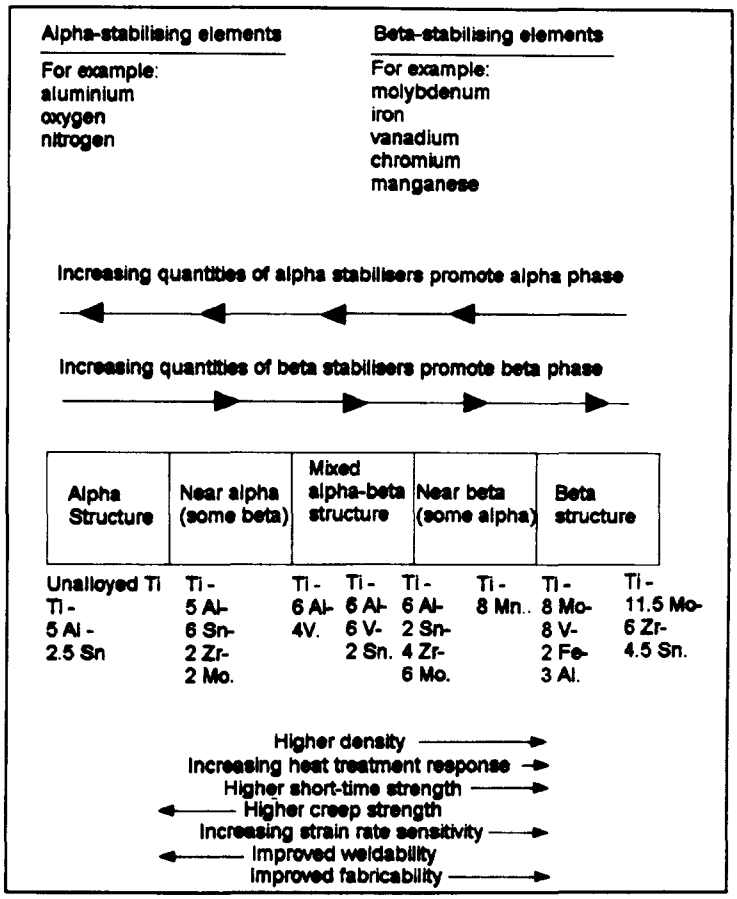

Figure 2.8 Schematic relationships: titanium alloying effects on structure; selected alloy characteristics (Donachie 1988).

2.4 High Temperature Titanium Alloys

The development of titanium alloys in the last 50 years, in the most part, has been driven by the aerospace industry. With a specific gravity of 4.54 and some alloys exhibiting room temperature tensile strengths of more than 1500 MPa and others being useable at temperatures as high as 650°C titanium based alloys are seen to have great potential to meet the needs of the industry (Naka 1996, Polmear 1995), particularly where higher strength to weight ratios at elevated temperatures are needed to improve fuel efficiencies.

The $\alpha + \beta$ alloy IMI315 (Ti-2Al-2Mn), developed in 1953 for use in the Rolls Royce Avon engine (Polmear, 1995), initiated the progression of high temperature titanium alloy development. This was closely followed by the $\alpha + \beta$ alloy IMI550 (Ti-4al-2Sn-4Mo-0.5Si) based on the discovery of the effect of a small addition of silicon significantly improved high temperature creep performance by the precipitation of silicides, Ti-6242S and Ti-10-2-3 (Brewer et al, 1998). The first commercial high

temperature capable near α alloy was IMI 679 (Ti-6Al-5Zr-0.5Mo-0.25Si) but this alloy had a narrow α + β phase field making α + β processing difficult to control on the industrial scale. However, in the 1960's and 1970's it was found that higher temperature capabilities could be achieved in near α alloys by processing in the β phase field to produce a microstructure consisting of fully transformed β microstructure, i.e. fully lath alpha as used with IMI685 (Ti-6Al-5Zr-0.5Mo-0.25Si) and IMI829 (Ti-5.5Al-3.5Sn-3Zr-1Nb-0.25Mo-0.3Si). The most recent development in near α alloys is the addition of carbon in order to change the shape of the beta approach curve so that the alloy can be successfully industrially α + β processed and heat-treated. This development culminated in the production of Timetal®834 (Ti-5.8Al-4sn-3.5Zr-0.7Nb-0.5Mo-0.35Si-0.06C) which is a near α alloy with a fine-grained α + β structure and a creep capability up to 600°C (Blenkinsop and Neal, 1994.)

2.5 Morphology of Transformed β

Part of the versatility of titanium alloys is the tailoring of microstructure made possible by controlling the transformation of the β phase on cooling to the α phase. This microstructure development is dependant on various factors. At very slow cooling rates the α forms as continuous layers on the prior β grain boundaries and as colonies of lamellar structures inside of which are solute enriched platelets of retained β as seen in Figure 2.9(a) (Flower, 1990). The width of the α lamellae and the extent of the continuous α layer are also a function of cooling rate (Lutjering, 1998). As the cooling rate increases the number of lamellar colonies per prior beta grain increases as shown in Figure 2.9(b). This eventually produces the well-known basketweave structure with regularly interleaved colonies of plates on a number of crystallographically distinct planes as seen in Figure 2.9(c). Each of these colonies act as a large microstructural unit with easy slip transfer across the plate interfaces (even with a thin layer of β between them, as is usually the case in near-α or α+ β alloys). Slower cooling rates promote larger colonies particularly after limited working in the β phase field. Large colonies are also favoured by decreasing β stabilisation, increasing solution treatment temperature or increased time at temperature (i.e. increased β grain size). For example in the near- α alloy IMI-685 colonies have been observed to vary in size from 10 to 250μm depending on processing conditions. At even faster cooling rates more α variants are nucleated and

the scale of precipitation becomes finer, resulting in a true Widmanstätten morphology being developed which greatly reduces the microstructural unit size as shown in figure 2.9(d). At extreme cooling rates (525°Cs^{-1} in Ti-6Al-4V as detailed in Ahmed and Rack, (1998)), i.e. quenching, diffusion assisted reactions are significantly inhibited and hexagonal α' martensitic structures result as shown in Figure 2.9(e). The amount of β present at room temperature in the structures described above depends on the balance and absolute levels of α and β stabilising solute present in the alloy (Flower, 1990).

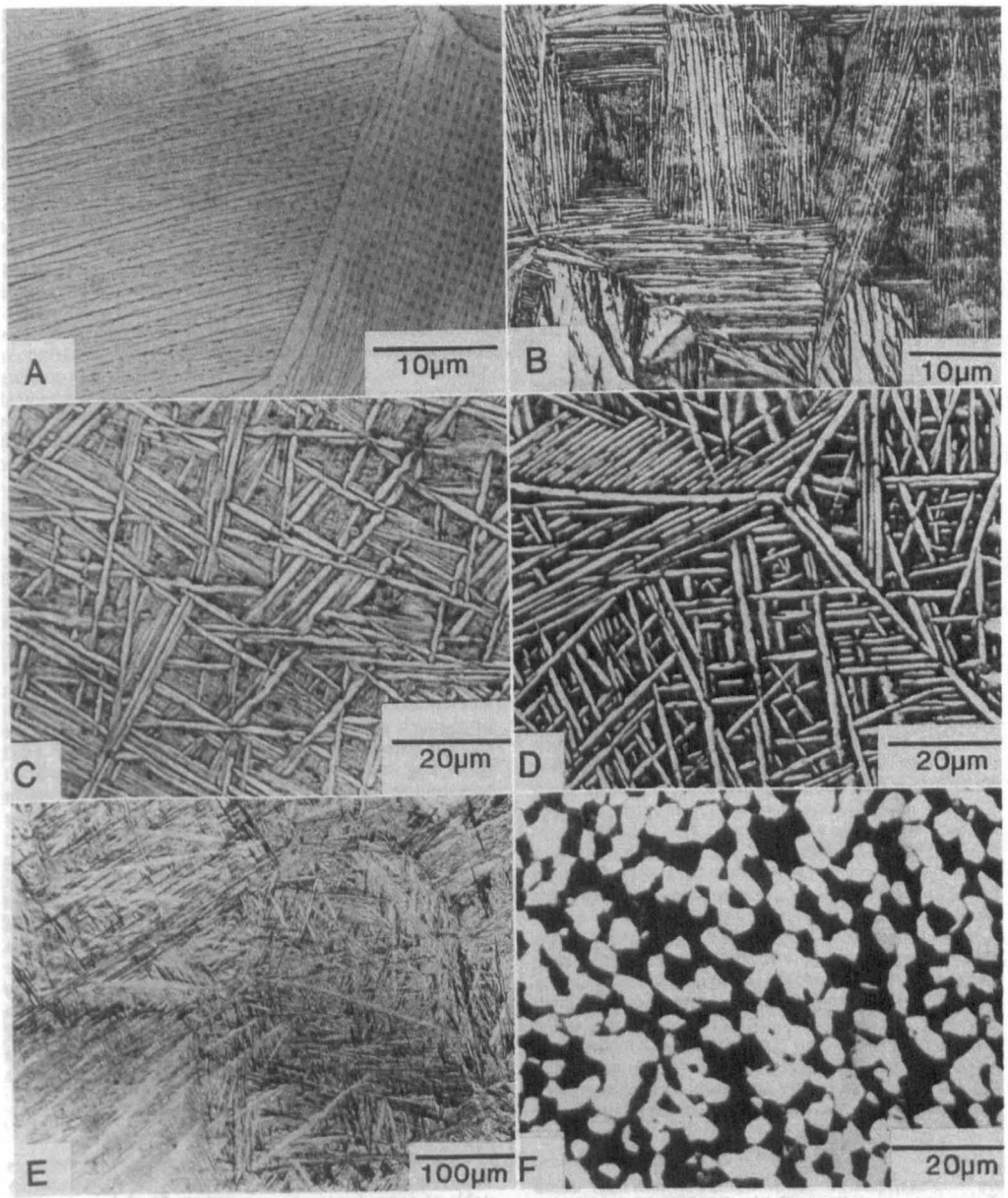

Figure 2.9 Range of Ti microstructures produced by varying cooling rates from (a) slow furnace cooled Ti-1Mo, through (b) slow air cooled Ti-1Mo, (c) air cooled IMI 550, (d) forged and air cooled IMI 550 and (e) water quenched IMI 829. (e) shows forged and annealed IMI 550 with equiaxed microstructure (Flower, 1990).

Stanford and Bate (2004) offer further insight into the transformation with particular concentration on the orientation relationship between the two phases. They say "The transformation from β to α is known to begin by the formation of grain boundary α. Once this grain boundary α is formed, the interior of the grain is isolated from the effects of the adjacent β orientation. The critical event in the selection process (for the lath orientations) must be the precipitation of α at the grain boundary". In the work completed by Stanford and Bate (2004), samples were heat treated in the fully β phase field at 1020°C, removed from the furnace and held for 7s before quenching in water. It was found through SEM analysis that approximately 1/3 of the grain boundaries were found to have diffusional transformation product (i.e. grain boundary α), with the remaining boundaries having a complete Widmanstätten morphology on either side. The grain interiors showed no evidence of diffusional transformation. SEM-EBSD analysis showed that the Widmanstätten colonies that dominated the microstructure had orientations determined by the orientations in the grain boundary α. This grain boundary α was shown to nucleate first, and had an orientation dependence on the adjoining β orientations, specifically the alignment of <110> directions suggesting there was a complicated relationship between the processing history and the microstructure morphology.

Work completed by Filip et al (2003) reported on the influence of the possible α_s morphologies on the tensile properties and fracture toughness of Ti-6Al-4V and Ti-6Al-2Mo-2Cr. The work concluded that tensile elongation is at a maximum at intermediate cooling rates, 7 $^{o}Ks^{-1}$ and fracture toughness increases with a decrease in lamellar width associated with faster cooling rates. Lutjering et al (1996) gained less extensive but similar results on IMI834, also concluding an increase in the yield stress at the highest cooling rates.

2.6 Orientation Relationships in Phase Transformations

2.7.1 Introduction

Orientation relationships (OR) have most commonly been researched involving steels and the BCC-FCC transformation of austenite to ferrite. When a phase transformation takes place in steel, an orientation relationship exists between the lattices

of the parent and the child crystals. The most frequently cited relationships are known as the Bain, the Kurdjumov-Sachs-Taylor (priv comm. B Hutchinson, 2006) (K-S-T), and the Nishiyama–Wassermann (N-W) relationships. The BCC β to HCP α phase transformation in titanium alloys has also been well studied (Burger, 1934) and is described by an OR known as the Burgers Relationship.

2.7.2 Burgers relationship

The Burgers relationship states that the (110) plane of β lies parallel to the basal plane of α and within those planes the $[1\,\bar{1}\,1]$ direction of β is parallel to $[11\bar{2}0]$ direction of α and is generally shown as:

$$(110)\beta \parallel (0002)\alpha$$
$$[1\,\bar{1}\,1]\beta \parallel [11\bar{2}\,0]\alpha$$

According to this relationship, the high temperature BCC can transform to 12 distinct hexagonal variants, having different orientations with regard to the parent β crystal. This burgers relationship is closely obeyed for both the martensite transformation and the conventional nucleation and growth process (Lutjering & Williams, 2003).

2.7 Oxygen and Alpha case

Oxygen and nitrogen react with titanium at the surface of the metal. Oxygen (or nitrogen) pickup during heat treatment results in a surface structure composed predominantly of α phase (oxygen and nitrogen are alpha stabilisers). The interstitial-enriched layer is commonly called "alpha case". Alpha case is detrimental because of the brittle nature of the oxygen-enriched alpha structure. This layer must be removed before service to avoid stress concentration points (Donachie, 1998).

2.8 Thermomechanical Processing of Titanium

2.8.1 Introduction

The thermomechanical processing route of any industrial titanium produced will generally have two goals; the first is providing the customer with an amount of material the size and shape that they require and secondly the material must have the microstructural and mechanical properties desired by the customer. As mentioned previously in section 2.3 the control of alpha α and β phases through alloying additions and thermomechanical processing is the basis for the titanium alloys used by industry today and it is also the primary method for classifying titanium alloys.

2.8.2 Forging and Forming

The typical hot working approach for processing α alloys comprises a primary ingot breakdown in the β phase field and secondary working (forging, rolling, etc.) to produce a specific shape, either below or above the β transus (T_β) (Weiss and Semiatin, 1999)). An example of T_β and recommended hot working temperatures for α and near – α alloys including Timetal 834 can be seen in Table 2.1.

Table 2.1 T_β and recommended hot working temperatures for alpha and near –alpha titanium alloys. (Weiss and Semiatin, 1999)

Alloy type	Alloy composition	Beta transus temperature T_β (°C)	Hot working temperature range (°C)	
			Ingot breakdown	Secondary working
Alpha	Ti–0.25Fe–0.08C–0.2O–0.03N–0.15H (CP grade 2)	915	975–1100	825–875
Alpha	Ti–5Al–2.5Sn (Ti–5–2.5)	1040	1120–1175	900–1000
Near alpha	Ti–8Al–Mo–1V (Ti–8–1–1)	1040	1120–1175	930–1010
Near alpha	Ti–6Al–5Zr–0.5Mo–0.25Si (IMI 685)	1020	1125–1175	1025–1075
Near alpha	Ti–5.8Al–4Sn–4Zr–1Nb–0.5Mo–0.35Si (IMI 834)	1040	1130–1185	1010–1075
Near alpha	Ti–6Al–2.75Sn–4Zr–0.4Mo–0.45Si (Ti–1100)	1015	1145–1195	1025–1125

The cast ingot structure is generally broken down in the β phase field in order to generate a uniform recrystallised structure. Any further processing is conditioned by the requirements of producing the desired shape change with the minimum energy input, and producing the required microstructure in the shaped item. These conditions are often mutually incompatible. Accuracy of shape requires low working temperatures, but

minimum energy input requires high temperatures while, depending on the desired microstructure beta field or alpha beta field working may be required.

2.8.3 Heat Treatments

Titanium and titanium alloys are heat treated for a number of reasons, namely;

- To produce the most acceptable combination of ductility, machinability, and stability in the final product, especially in α/β alloys.
- To reduce residual stresses developed during fabrication.
- To increase strength by solution treatment and ageing.

By working (forging) and/or heat treating alloys below or above the β transus, substantial microstructural changes can occur. In some near-α and α/β alloys solution treatment plus aging is used to produce maximum strength. Heating a near-α or α/β alloy to the solution treating temperature generally produces a higher ratio of β phase to α phase. Selection of a solution treatment is made after considerations of mechanical properties desired from the aging treatment. Solution treatment above the β transus provides optimum creep resistance at the expense of reduced ductility and fatigue strength. The optimum combination of creep and fatigue strength is achieved with the near- α alloy Timetal®834 and will be discussed in further detail later.

The cooling rate from the solution treating temperature has an important effect on strength of α/β titanium alloys. Appreciable diffusion can occur during cooling if the rate is too slow. This diffusion will change the phase chemistry and/or ratios as subsequent decomposition of the altered β phase during aging may not provide effective strengthening (Neal, 2001).

2.8.3.1 Processing Assessment

Work by Flower 1990, examined some general characteristics of the thermomechanical process in titanium alloys with the following conclusions; the most important distinction to be made between the α and β phases is that diffusion is much faster in β at any given temperature. In pure titanium, at the allotropic transition from α to β at 883°C the diffusivity increases by nearly three orders of magnitude, and in alloys

diffusion is a hundred or more times as fast in β as in α. Consequently processes of diffusional deformation and of recovery and recrystallisation occur at lower temperatures and higher strain rates in the β phase than in the alpha. Thus although both α and β show a high temperature sensitivity of the flow stress at temperatures at which diffusion is slow, and a low sensitivity when diffusion is fast enough to contribute to the deformation process, the transition in behaviour occurs at much lower absolute temperatures for the β phase. Hence, β shows a much lower temperature dependence of the flow stress than does the α phase at practical α/β hot working temperatures. In consequence, even α/β working shows a strong stress-temperature relationship when α is the major phase. At temperatures at which β becomes the continuous phase, the flow stress reflects the character of this phase rather than the isolated α particles which behave like hard inclusions in the soft β matrix. Frictional heating during deformation, which is important since the thermal conductivity of titanium is low, can thus lead to substantial reductions in the flow stress in the $\alpha+\beta$ field and, at low temperature, can lead to localised shear band formation. The practical limits of working temperatures are set by excessive grain growth and surface contamination by absorption of oxygen and nitrogen at high temperatures and by excessive deformation loads and the onset of shear banding at low working temperatures. Transformed β structures are more susceptible to shear banding over a larger temperature and strain rate range than are equiaxed α/β microstructures.

2.9.4 Deformation Mechanisms

The von Mises Criterion (1913), also known as the maximum distortion energy criterion, octahedral shear stress theory, or Maxwell-Huber-Hencky-von Mises theory, is often used to estimate the yield of ductile materials under complex loading conditions. The von Mises criterion states that yielding occurs when the energy of distortion reaches the same energy for yielding in uniaxial tension. Mathematically, this is expressed as,

$$\frac{1}{2}\left[(\sigma_1-\sigma_2)^2+(\sigma_2-\sigma_3)^2+(\sigma_3-\sigma_1)^2\right]\leq\sigma_y{}^2 \tag{2.5}$$

In the cases of plane stress, $\sigma_3 = 0$. The von Mises criterion reduces to,

$$\sigma_1^2 - \sigma_1\sigma_2 + \sigma_2^2 \leq \sigma_y^2 \tag{2.6}$$

This equation represents a principal stress ellipse in the 2D stress space as illustrated in Figure 2.10,

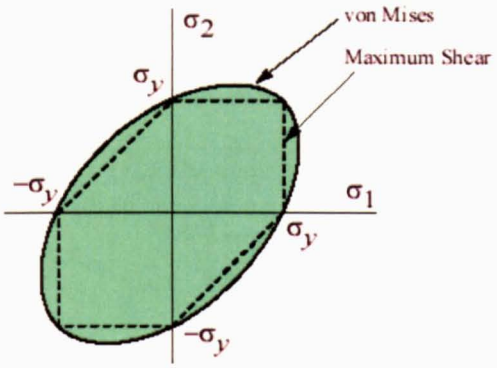

Figure 2.10 von Mises stress for yielding in two dimensions

Also shown in Figure 2.10 is the maximum shear stress criterion (dashed line). This theory is more conservative than the von Mises criterion since it lies inside the von Mises ellipse. In addition to bounding the principal stresses to prevent ductile failure, the von Mises criterion also gives a reasonable estimation of fatigue failure, especially in cases of repeated tensile and tensile-shear loading.

During deformation material must make compensations for the shape change brought about by deformation. In uniaxial loading, as in a tension or compression test, macroscopic plastic flow begins at the yield stress, σ_0. On a microscopic scale, plastic deformation corresponds to the net movement of large numbers of atoms in response to an applied stress. During the process, inter-atomic bonds must be ruptured and then reformed. In crystalline solids, plastic deformation most often involves the motion of dislocations. Dislocations do not move with the same degree of ease on all crystallographic planes of atoms and in all crystallographic directions. Ordinarily there is a preferred plane, and in that plane there are specific directions along which dislocation motion occurs. This slip plane and associated slip directions are known as slip systems and vary from material to material.

The principal deformation mechanisms in pure α titanium are basal (0001) and first order prismatic $\{10\bar{1}0\}$ slip with a $<11\bar{2}0>$ slip vector, i.e. <a> type slip (Lütjering & Williams, 2003; Leyens & Peters, 2003). However, these slip systems produce only 4 independent slip systems which is insufficient to satisfy the von Mises

criteria for homogeneous plastic deformation which requires 5 independent slip systems. Hence for polycrystal deformation further slip system activity and/or deformation twinning is required to accommodate an arbitrary shape change. Extensive research over a number of years has suggested that there are up to 6 possible slip systems and 6 twinning modes that can operate within the α titanium, which are shown in Tables 2.2 and 2.3.

Table 2.2 Possible titanium slip systems

Slip Type	Slip Direction	Slip plane
<a>b	$<11\bar{2}0>$	(0001)
<a>Pr	$<11\bar{2}0>$	$\{01\bar{1}0\}$
<a>Py	$<11\bar{2}0>$	$\{01\bar{1}1\}$
<c+a>Pr	$<11\bar{2}3>$	$\{01\bar{1}0\}$
<c+a>Py1	$<11\bar{2}3>$	$\{01\bar{1}1\}$
<c+a>Py2	$<11\bar{2}3>$	$\{11\bar{2}2\}$

Table 2.3 Possible titanium twinning systems

Twin Type	Shear Direction	Shear Plane
$\{10\bar{1}2\}$ Twin	$<\bar{1}011>$	$\{10\bar{1}2\}$
$\{11\bar{1}1\}$ Twin	$<11\bar{2}6>$	$\{11\bar{2}1\}$
$\{11\bar{2}3\}$ Twin	$<33\bar{3}2>$	$\{11\bar{2}3\}$
$\{11\bar{2}2\}$ Twin	$<11\bar{2}3>$	$\{11\bar{2}2\}$
$\{10\bar{1}1\}$ Twin	$<10\bar{1}2>$	$\{10\bar{1}1\}$
$\{11\bar{2}4\}$ Twin	$<22\bar{4}3>$	$\{11\bar{2}4\}$

The type of deformation mode activated is then sensitive to crystal orientation, temperature and chemical composition (Partridge, 1967; Paton. & Backofen, 1970; Williams et al., 2002). With increasing Al content, Timetal®834 has 5.8wt% Al, it has been reported that there is an increase in the propensity of <c+a> slip and a suppression of twinning (Williams et al, 2002). This, in conjunction with a reduction in critical resolved shear stress of non-basal planes with respect to the basal plane with increased

deformation temperature (Williams et al, 2002) suggests we should see significant <c+a> slip within α deformed under industrial forging conditions.

Bridier et al (2005) analysed the evolution of activated slip systems during a tensile test on Ti-6Al-4V using EBSD. The approach applied to a large number of grains allowed a statistical analysis of the nature (basal, prismatic, pyramidal) and distribution of the slip systems according to the crystallographic texture, as seen in Figure 2.11.

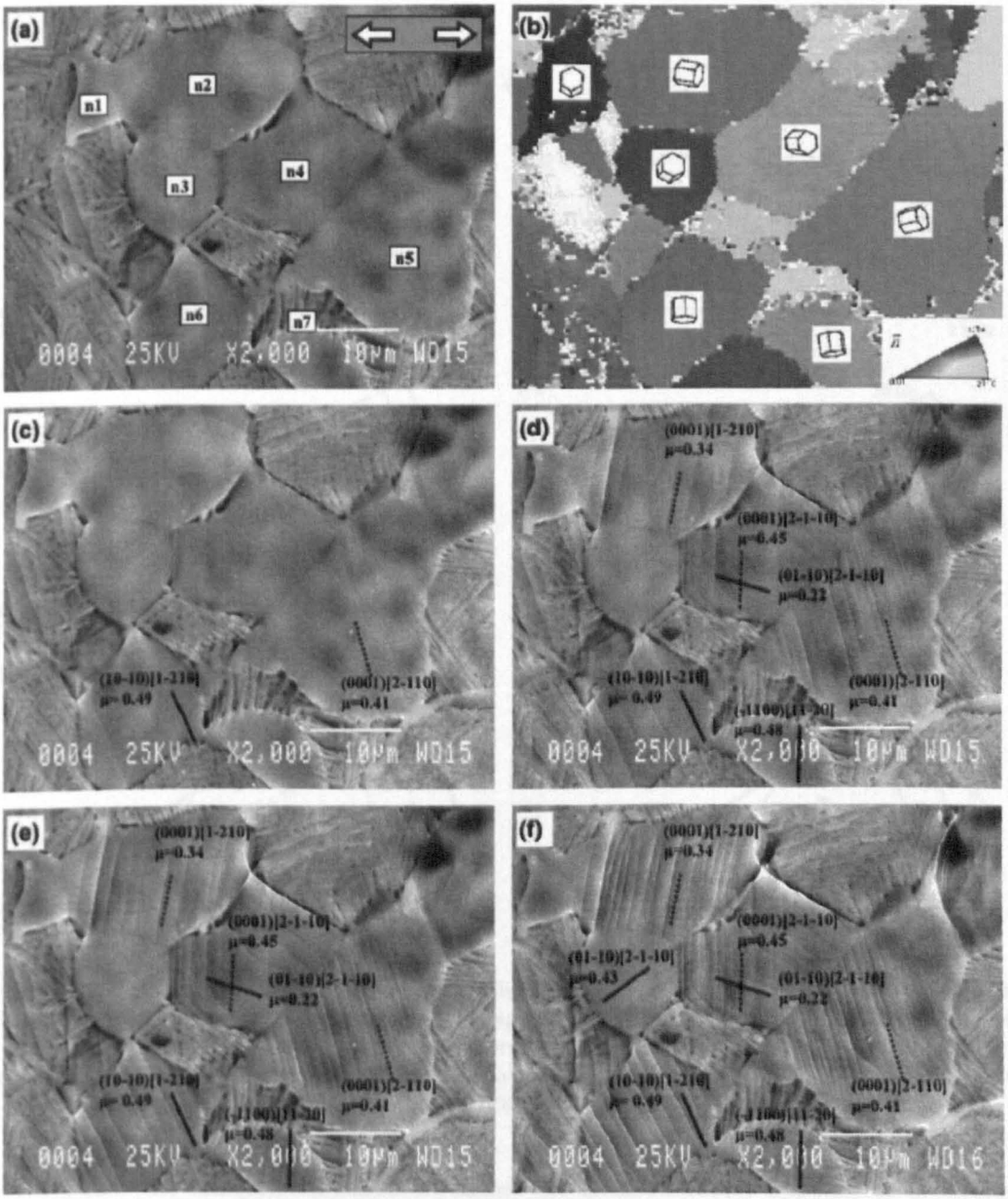

Figure 2.11 Examples of identification of activated slip systems on α_p nodules: (a) SEM image of the microstructure before the tensile test. Arrows indicate the tensile direction. (b) Corresponding EBSD map. (c–f) SEM images at different steps of the tensile test and slip lines identification. Continuous and dotted black lines represent calculated traces of prismatic and basal slip systems, respectively, from Bridier, 2005.

A discussion concerning the pertinence of Schmid's law to explain the occurrence and succession of slip events is then proposed. The domain in favor of each type of slip system is finally presented by using inverse pole figures mapped with Schmid's factor iso-curves as seen in Figure 2.12(a) and then compared with previous data from the literature, Figure 2.12(b) (Tan 1998, Akhtar 1975, Naka 1991 and Chan 1981). The coexistence of basal, prismatic and first-order pyramidal slip modes has thus been proved.

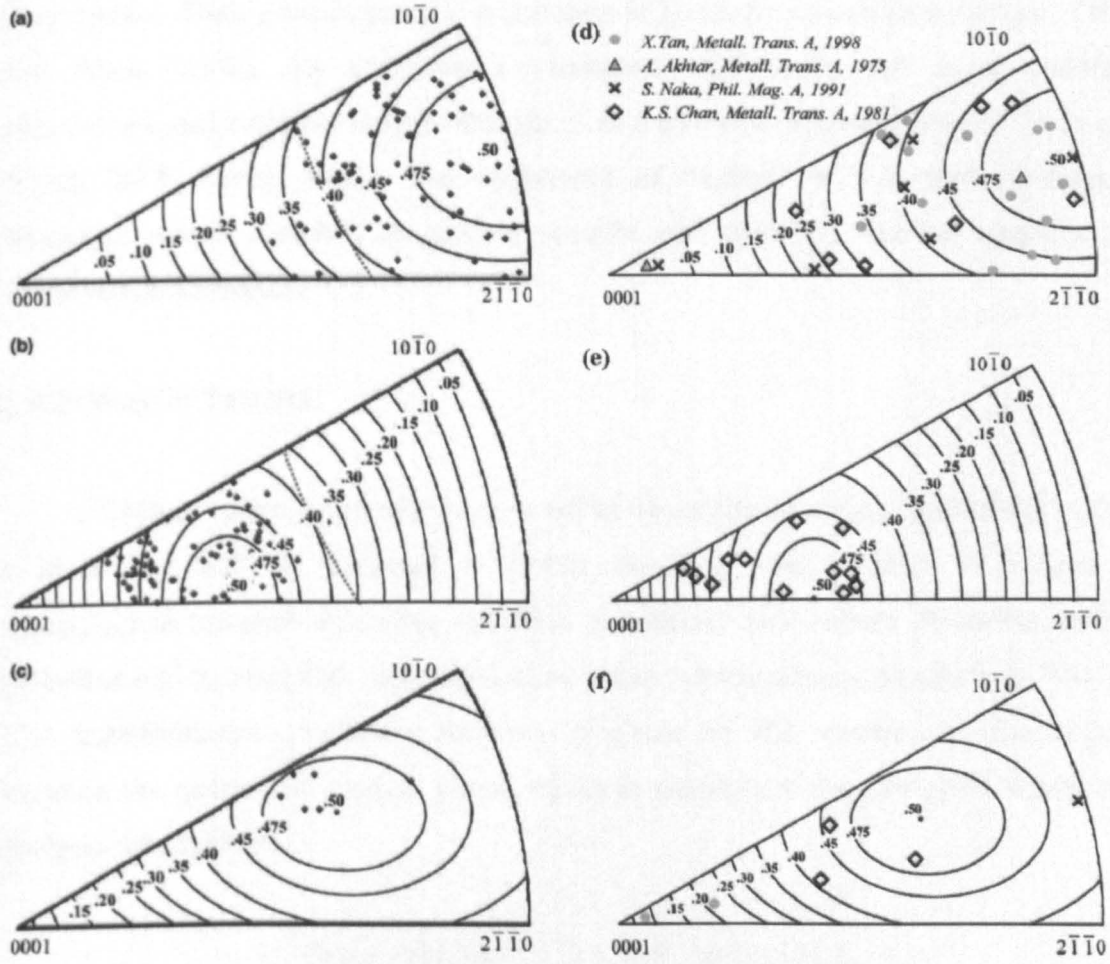

Figure 2.12 Unit triangle with iso-curves of Schmid's factor for (a) prismatic, (b) basal and (c) first-order pyramidal gliding with in superposition experimental data. For prismatic (d), basal (e) and first-order pyramidal (f) slip systems, poles corresponding to experiments from literature are reported on the unit triangle mapped with Schmid's factor contour lines, compiled from Bridier et al (2005).

From the analysis of these domains, the Schmid factor appears as a relevant parameter to predict the nature of the slip systems (basal, prismatic, pyramidal, etc.) if they are activated. However, it is not sufficient to anticipate their activation or no-activation.

2.9 Textures in Titanium

2.9.1 Introduction

Texture refers to the distribution of the orientations of individual grains within a metal. Texture development is a complex function of mechanical and thermal treatments as well as the material itself (Hatherly and Hutchinson, 1979). Most commonly used materials, either manmade or naturally occurring, are aggregates of crystals or polycrystals. Their crystallographic orientation is generally non-random (Kocks, Tome and Wenk, 2000). All non-random orientation distributions are called preferred orientations, and therefore may be thought of as a statistical tendency (Kocks Tome and Wenk, 2000. Dieter, 1988). The importance of 'texture' is that most mechanical properties within materials are texture specific and, therefore, can be exploited for improved performance.

2.9.2 Origin of Textures

Texture refers to the distributions of the orientations of individual grains within a metal and will be discussed in further detail in later chapters. A natural or technological material will often exhibit a completely new texture following certain processes e.g. deformation, recrystallisation, phase transformation (Randle et al, 2000). The transformation textures commonly originate in the orientation relationships between the parent and product phase, which in titanium is the previously mentioned Burgers relationship;

$$(0001)\,\alpha \parallel (110)\,\beta \quad : \quad [1120]\,\alpha \parallel [111]\,\beta$$

These relationships demonstrate that where a specific texture existed originally, a different texture is created by the transformation.

Textures created during deformation depend on the crystal structure as well as the magnitude and nature of deformation. Factors including original texture, thermal and mechanical history, temperature and rate of deformation all act as variables influencing the final texture (Hatherly and Hutchinson, 1979).

2.9.3 Deformation Textures

Textures created during deformation depend on the crystal structure as well as the nature and severity of the working process (Hatherly and Hutchinson, 1979). Rolling textures are relatively common, especially in BCC metals and textures developed from specific forging routines and extrusion processes are also regularly observed.

2.10.4 Deformation Textures in Titanium.

Texture development in titanium alloys is most pronounced as a result of working the elastically and plastically anisotropic hexagonal α phase. In hot α/β worked structures the texture diminishes as the temperature is increased and the volume fraction of α is decreased. However, fully β worked structures can develop a texture if the precipitated α on cooling produces only a limited number of crystallographically possible α variants in the β grains (Flower 1990).

In Ti-6Al-4V plate products textures are known to be fairly intense although cross rolling reduces the intensity of texture and the texture symmetry in the final product. This intense texture is addressed in Lütjering et al (2003) and describes the axisymmetric compression textures of α/β processed alloys (Ti-6Al-4V) to consist of two major components: i) basal, where the (0002) plane lies perpendicular to the compression direction, and ii) transverse, where the (0002) plane lies parallel with the compression direction in any radial direction. At processing temperatures high in the α/β phase field, close to the β transus, where the β volume fraction is high, Lütjering et al (2003), Leyens and Peters (2003) and Williams and Starke, Jr. (2002) point out that the transverse texture dominates. In contrast, the basal texture dominates when deformation takes place at relatively low temperatures and, thus, with a very high α volume fraction. The origins of the tranverse texture are in the transformation of the β deformation texture, where only one of the six possible variants of the burgers relationship is selected.

2.9.5 Transformation Textures

The effect of phase transformations on the texture of a material is simple in principle but complex in practice (Cahn, 1991). In most materials there is a certain relationship between the parent and product phases, e.g. Kurjimov-Sachs in steels and the Burgers relationship in titanium. These orientation relationships predict that each volume element of the new phase will have a definite relationship to the corresponding volume element of the parent phase but more than one variant is possible. The number of variants depends on the extent of coincidence between the alignment elements and the crystal structures. The {111} plane in the Kujimov-Sachs relationship, for example, means that there are four variants of the transformed texture volume element, just based on choice of plane alone. Therefore one key conclusion is that a transformation texture is likely to be significantly weaker than the parent phase texture (Kochs, Wenk and Tome, 2000)

A large amount of work has been carried out on billet texture, variant selection, and preferred transformation textures in titanium alloys, (Humbert, 2005; Germain 2005; Stanford and Bate, 2004; and Zhu et al 2000) and electron backscattered diffraction (EBSD) texture measurements showed that the α texture is in most cases markedly sharper than that calculated on a basis of equal variant probability, indicating that significant variant selection occurs during diffusional transformation.

2.9.6 Effect of Texture on Mechanical Properties

Alpha and near-α titanium alloys containing substantial amounts of the hexagonal α phase show marked elastic and plastic anisotropy when having a strong texture (Polmear, 1995). Some important mechanical properties of crystals such as elastic modulus, strength, ductility and fatigue performance (Shih et al, 1995) all depend on their orientation or texture.

The plastic yielding of a material requires a shear stress to act on one or more of its crystallographic slip systems for each single grain (Hatherly and Hutchinson, 1979). If a component under stress, consisting of a number of crystals, has no preferred orientation then the slip planes will be randomly orientated. However, if the preferred orientation, across the component, of these slip systems is aligned with the acting stress

then the constraint is lost and slip will take place. In $\alpha + \beta$ alloys the effect of crystallographic texture on the mechanical properties has been described in detail in Lutjering et al (2003) and is as stated as being pronounced for both bi-modal and equiaxed structures.

The mechanical properties for the two textures described in section 2.10.4, namely the tranverse (T) and the Basal textures. The tensile properties of the two textures as a function of test direction can be seen in Figure 2.11, for a fine equiaxed Ti-6Al-4V alloy, taken from Lutjering et al (2003).

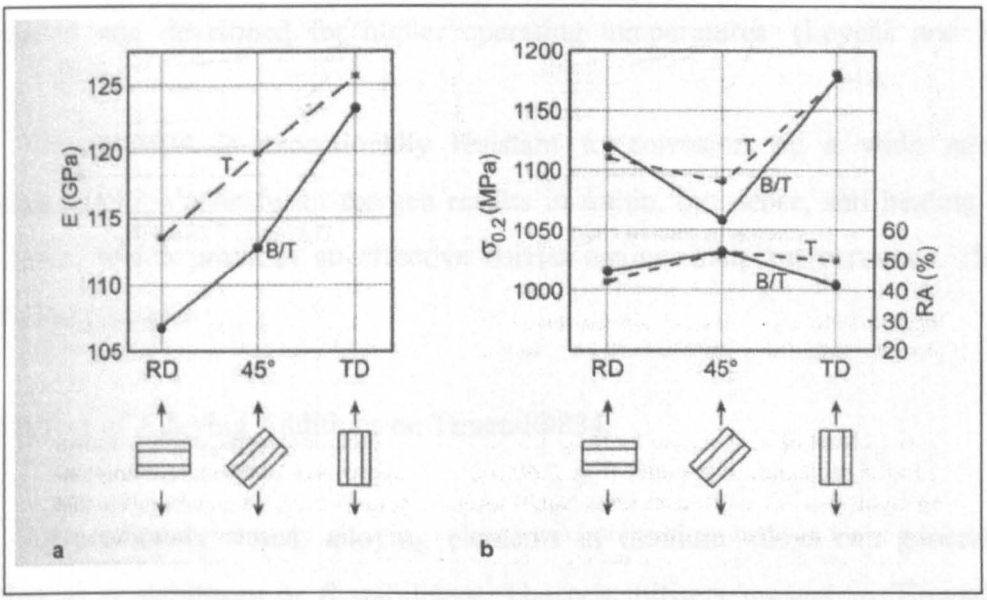

Figure 213 Influence of loading direction on tensile properties of fully equiaxed microstructures with B/T and T textures, Ti-6Al-4V: (a) Modulus of elasticity E (b) Yield stress $\sigma_{0.2}$ and ductility RA, Lutjering (2003)

For an easier visualisation of the angle between the basal planes and the test direction, the position of the hexagonal unit cell for the T texture is illustrated in the lower part of Figure 2.13. The B/T texture has lower E values than the T texture because of the contribution from the Basal (b) component having a low E value for all test directions. The E value for a random texture is about 119 GPa.

2.10 Timetal®834

2.10.1 Introduction

Timetal®834 is a state of the art near-α class of high temperature titanium alloy, with a potential operating temperature of 600°C. As such, Timetal®834 is currently finding use in European military jet engines and within the compressor sections of variations of Rolls Royce Trent engines. Timetal®834 is believed to be the pinnacle of high temperature alloy development and, as such, titanium aluminides are being investigated and developed for higher operating temperatures. (Leyens and Peters, 2003)

Timetal®834 is exceptionally resistant to corrosion by a wide range of chemicals. Its high affinity for oxygen results in a thin, but dense, self healing stable oxide layer, which provides an effective barrier against incipient corrosion. (Struers Application Notes)

2.10.2 Effect of Alloying Additions on Timetal®834,

As previously stated, alloying elements in titanium alloys can generally be classified as α stabilisers or β stabilisers. The α stabilisers present in Timetal®834 increase the a α to α+β transus temperature and therefore increase the size of the α phase field though oxygen and nitrogen which are strong alpha stabilisers with strengthening properties at lower temperatures are kept to relatively low levels as they reduce stability and ductility. Aluminium is also beneficial as it reduces the density of the alloy further as well as increasing tensile and creep strengths. Aluminium, however, can also form an ordered intermetallic compound with titanium known as α-2 (Ti_3Al).

Small amounts of β stabilisers such as, molybdenum and niobium are also present in Timetal®834, however in order to keep creep resistance high these are limited. The main reason for the addition of molybdenum is to promote increased strength and increased hardenability at elevated temperatures. Niobium is included as it improves the high temperature oxidation resistance of the alloy. Molybdenum and niobium also have the effect of mitigating against ordering, by occupying some of the lattice sites normally occupied by aluminium or tin. This consequently allows an

increase in the amount aluminium that can be added and an increase in creep performance. When selecting alloy compositions there is always the need to control the aluminium equivalent, which has a detrimental effect on ductility and deformation capability. The aluminium effect is calculated with the following equation;

$$\text{Al eq.} = \text{wt.\%Al} + 1/3\text{wt.\%Sn} + 1/6\ \text{wt.\%Zr} + 10\text{wt.\%O} \qquad (2.7)$$

Nominally, an Al eq > 9 wt.% leads to the precipitation of the alloy-embrittling intermetallic compound Ti_3Al (Polmear, 1995).

Carbon increases strength by solid solution hardening and increases the β transformation temperature. By increasing the β transformation temperature it expands the $\alpha+\beta$ phase field allowing a greater control of volume fractions of α and β phase during heat treatment. Tin and Zirconium are neither α or β stabilisers possessing high solubility in the both the α and β phases, however, both increase hot strength (Neal, 2001) and retard the rates of transformation (Donachie, 1988). Silicon is also present in Timetal®834 as it has a major influence on the creep resistance forming the compound Ti_3Si_3 as well as giving considerable static strength.

2.10.3 Processing Philosophy

Near-α titanium aerospace alloys have been conventionally divided into two types depending on their heat-treatment and resulting mechanical properties. An approximately equal proportioned α/β heat treatment produces a relatively fine grained equi-proportioned primary alpha (α_p)/ transformed beta (α_s) microstructure leading to increased fatigue resistance, ductility and defect tolerance whereas a β heat treatment produces a large grained fully α_s microstructure which has improved creep resistance and fracture toughness. In order to gain an optimum balance between strength, fatigue and creep more recent near-α alloys, have been developed to be heat treated just below the β transus to retain a small amount of α_p limiting β grain growth, which upon cooling produces a bimodal microstructure of α_p in a matrix of fine grained α_s (Neal, 1988).

The most advanced near-α alloy to be thermomechanically processed sub β transus is Timetal®834. When processed to produce a bimodal microstructure consisting of approximately 15% α_p in a fine α_s matrix, the alloy possesses an excellent

combination of properties for operating in a high temperature environment, such as the compressor section of a jet engine. This can be achieved without the requirement of unrealistic temperature control during thermomechanical processing, as the small addition of carbon gives the alloy a relatively shallow β approach curve, leading to accurate control of the α_p volume fraction (Neal, 1988). It is important to note that Timetal®834 is highly regarded for its excellent combination of properties resulting from its well engineered fine grained microstructure. The effect of the processing route on the resulting texture and its effect on mechanical properties is a much less researched area which will be addressed further later.

The heat treatment of Timetal®834 has seen a number of developments due to the work of D Neal, (1988 and 2001) and the preferred heat treatment developed can be seen in Figure 2.14. The secondary deformation step in the $\alpha+\beta$ phase represents a ring rolling process included in the initial process route for compressor rings. However, in the production of current compressor discs the open die forging and ring rolling steps are replaced by a closed die forging routine.

The important aspects of the $\alpha+\beta$ phase field solution treatment are highlighted in Neal (2001) as;

a) alpha/beta proportion (temperature)
b) grain size (time and forging practice)
c) transfer time to quench medium (if used)
d) cooling rate
e) transfer time to stress relief

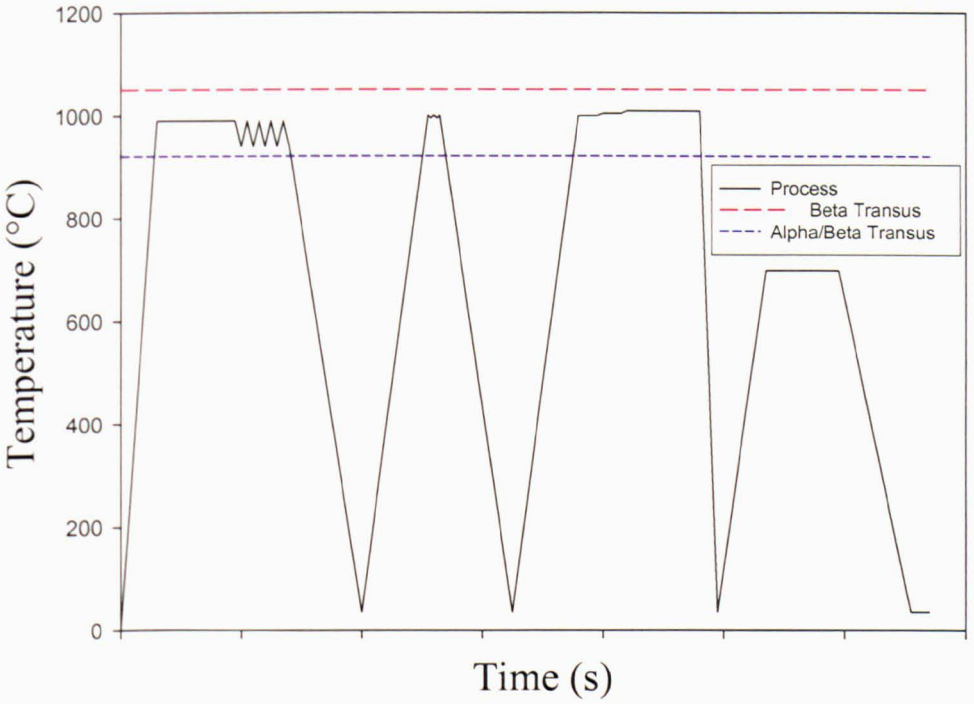

Figure 2.14 Preferred process route for Ti 834 compressor discs

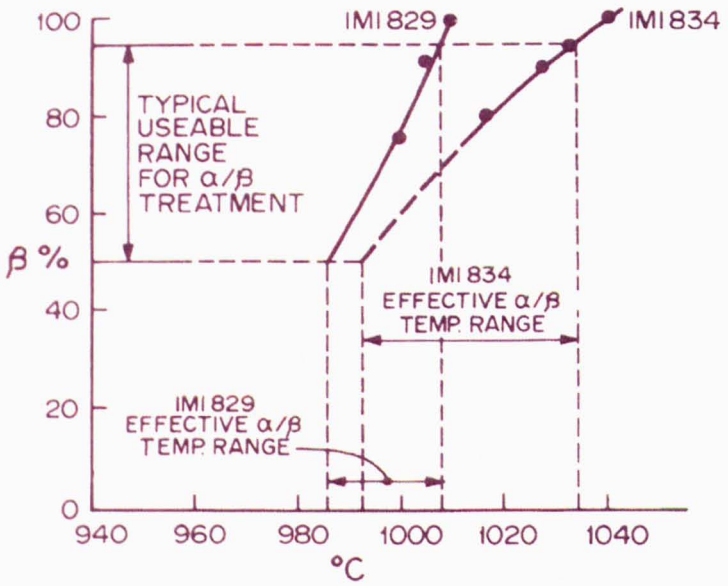

Figure 2.15 Beta transus approach curves for Ti 829 and Ti 834 (Polmear, 1995)

Although it is clear that the temperature does affect the volume fraction of the two phases, there seems to be some confusion as to the exact nature of this effect (Polmear 1995, Neal 1984, 1988 and 2001, and Ridley 1995). One of the major advantages of Timetal®834 is that theoretically it possesses a wide heat treatment 'window' meaning that the control of the volume fraction of both phases can be controlled accurately, see Figure 2.13. However, a number of sources (Neal, 1984,1988

and 2001, Flower, 1990 and Ridley, 1995) show different gradients and trends for this heat treatment window, also known as the beta approach curve, see Figure 2.16. Particularly worrying is the gradient of the Flower data, seen independently in Figure 2.17, as the heat treatment window is not nearly as wide as the other literature states and the alloy suppliers would suggest. The volume fraction of the α_p grains is important as it pins the β boundaries upon reheating, therefore controlling the β grain size (Lutjering, 1998) and subsequent mechanical properties, see Figure 2.18.

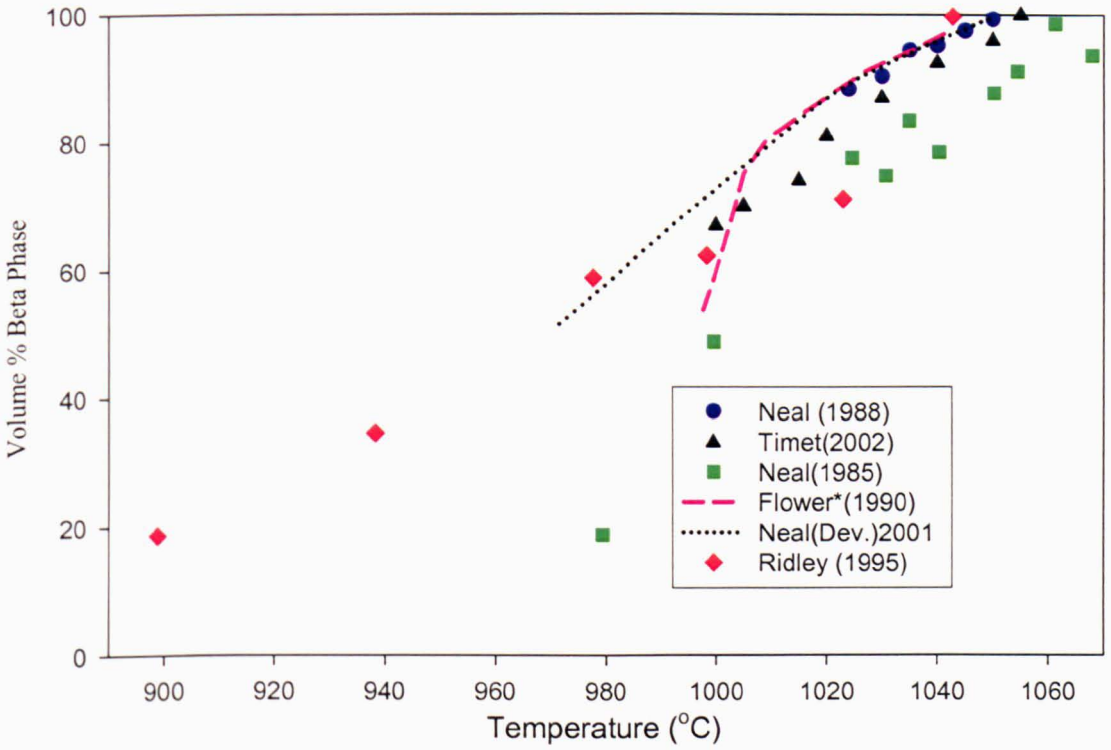

Figure 2.16 Showing the variation in Beta approach curve data from various sources.

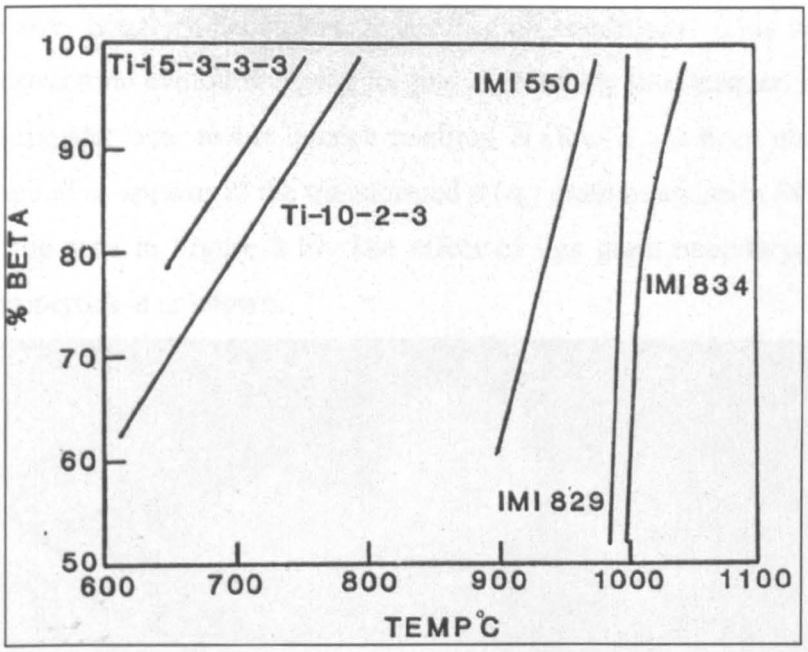

Figure 2.17 Beta transus approach curves for various Ti alloys (Flower 1990)

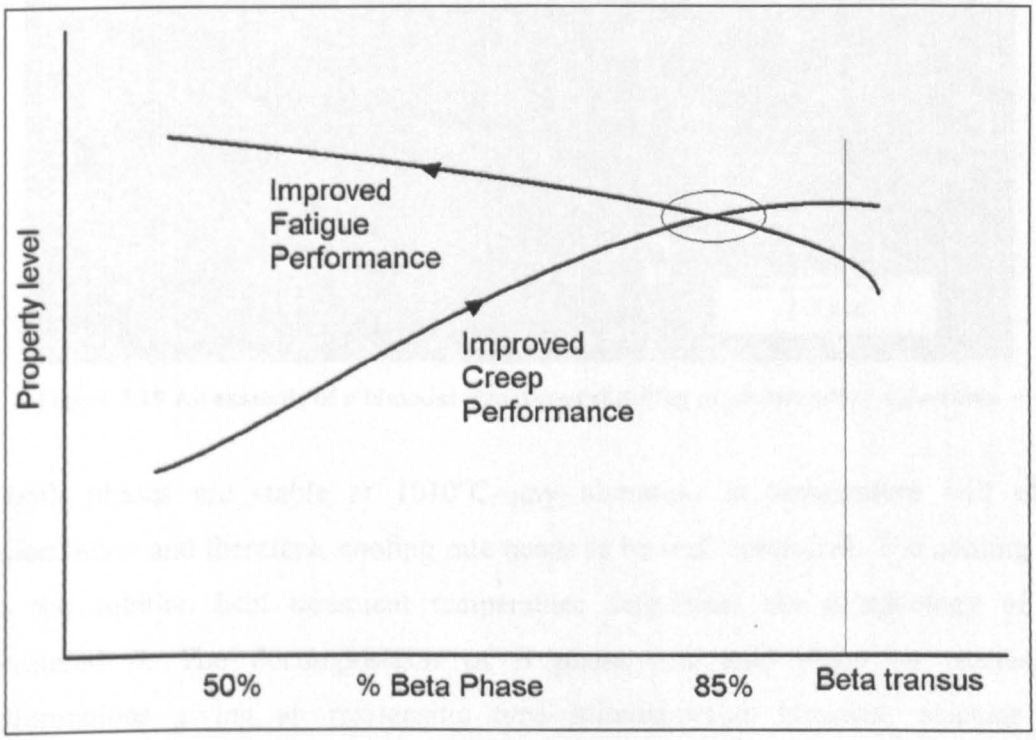

Figure 2.18 Effect of alpha/beta phase proportions on creep and fatigue properties (schematic), (Daubler, Neal, 1990)

The effect of forging on grain size, refers to both the forging temperature and the effect this has on pinning the grain boundaries and the size of the β grain size and the strains and strain rates experienced and there effect on sub-grain development. However, the work of Kestler et al, (1995) concludes that 'Solution heat treatments lead to a very homogeneous distributions of the α_p content, α grain size and transformed β

(α_s) lamellae size, largely independent of the forging conditions'. This would suggest that the microstructural evolution during forging is relatively inconsequential.

If the transfer time to the quench medium is slow it has been observed that a high percentage of α_p appears at the transformed β (α_s) grain boundaries (Nishikori et al, 1995) as can be seen in Figure 2.19. The effect of this grain boundary alpha on the mechanical properties is unknown.

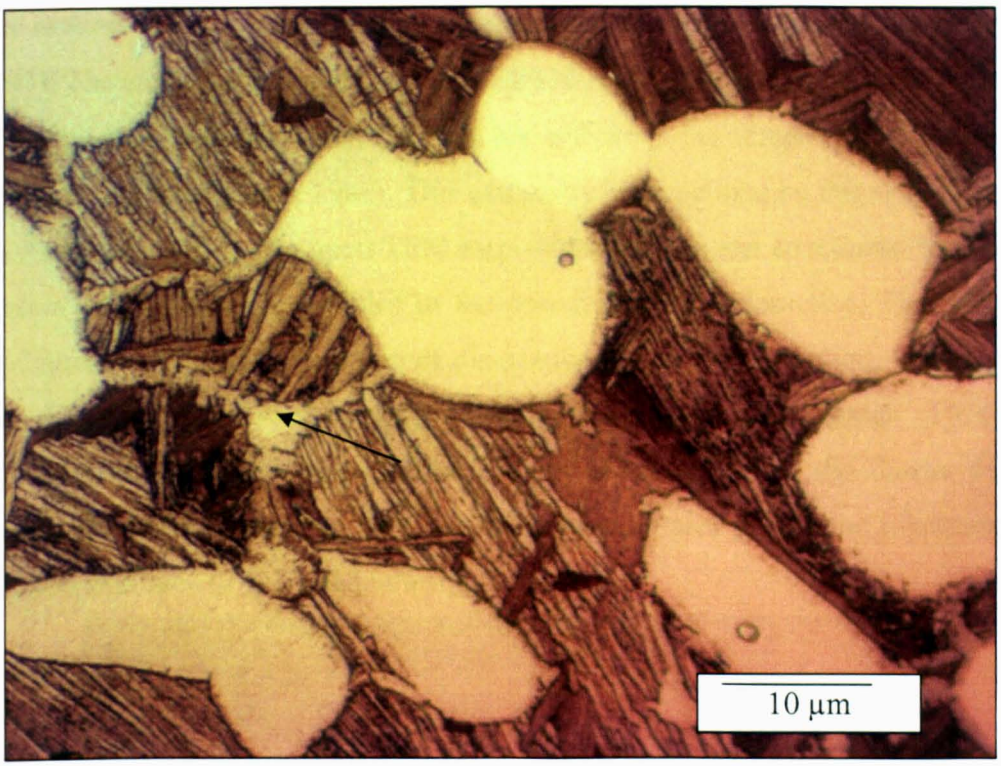

Figure 2.19 An example of a bimodal structure exhibiting grain boundary α_p(arrow).

As both phases are stable at 1010°C any alteration in temperature will effect transformation and therefore, cooling rate needs to be well controlled. The cooling rate from the solution heat treatment temperature determines the morphology of the transformed β. The decomposition of β phase can take place by martensitic transformations giving an martensitic type microstructure however, acicular and lenticular plate like structures can also appear without the formation of martensite. Figure 2.9 in section 2.5 shows the effect of cooling rate on the resultant morphology of the transformed β and has been discussed previously.

2.11 Mechanical Properties

2.11.1 Creep Resistance

Timetal®834 is available for service for long times at 550-625°C (Polmear, 1995 and Es-souni, 2001). The creep deformation in Timetal®834 in the temperature regime around 600°C is controlled by dislocation movement in the α phase (Andres et al, 1997). The creep performance of Timetal®834 is seen to improve when solution heat treatment time is increased from 0.5 to 4 hrs and when the temperature of the ageing treatment is increased (Neal, 1988). This can partly be explained by the work completed by Kestler *et al.,* 1995, who upon TEM inspection of creep test specimens found a fine dispersion of (Ti, Zr)$_6$ Si$_3$ silicides in the transformed beta lamellae. These silicides precipitate out of the solid solution at dislocations during deformation, hindering any further deformation and can be seen in Figure 2.18 taken from Baxter, (1994). The amount of precipitation is dependant on the preceding ageing, as the shorter the time and lower the temp of ageing the more silicon precipitates during the treatment, thus less silicon available to precipitate during deformation.

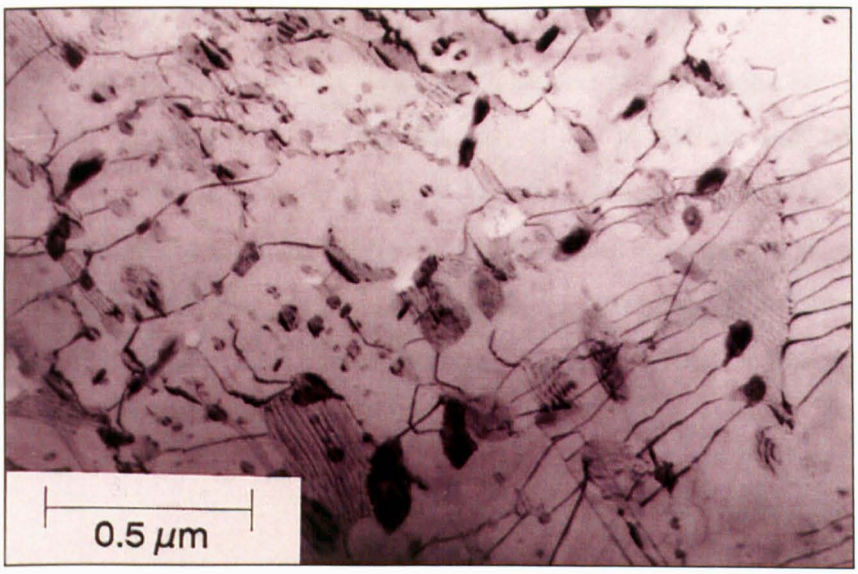

Figure 2.20 TEM Micrograph showing the precipitation of silicides at dislocations in IMI 834 (Baxter, 1994).

2.11.2 Ductility

The ductility of an aerospace component is important, as it will affect the impact resistance of the material, which, needs to be sufficient to prevent failure from

erroneous debris and bird strikes. The $\alpha+\beta$ titanium alloys are known to have an excellent combination of strength and ductility, however, this will all depend on an optimum heat treatment and the preferred orientation of the crystallographic structure (Donachie, 1988).

2.11.3 Ultimate Tensile Strength

The minimum tensile strength of titanium alloys varies from 240 MPa in commercial grades to 1400 MPa in an alloy known as Transage 129 (Ti-2%Al-2%Sn-11%Zr-11%V). The minimum tensile strength of Timetal®834 is stated in the Timet Data Sheets as 1030 MPa; however, higher tensile strengths are possible after sufficient heat treatment. When solution heat-treated, oil quenched and aged the tensile strength of the alloy has been recorded at 1050 MPa.

2.12 Fatigue Performance and Low Temperature Dwell Fatigue

2.12.1 Introduction

Compressor discs are under severe operating conditions during service. In these high cyclic loads conditions such as, fatigue, creep oxidation and corrosion are important factors in determining the life of the component. Generally, resistance to fatigue crack initiation for titanium alloys is reduced as the microstructure coarsens, i.e., fine equiaxed microstructures have higher fatigue strength than coarse lamellar microstructures and Figure 2.21 shows Wöhler diagrams of differently processed Ti-6Al-4V specimens (Polmear, 1995).

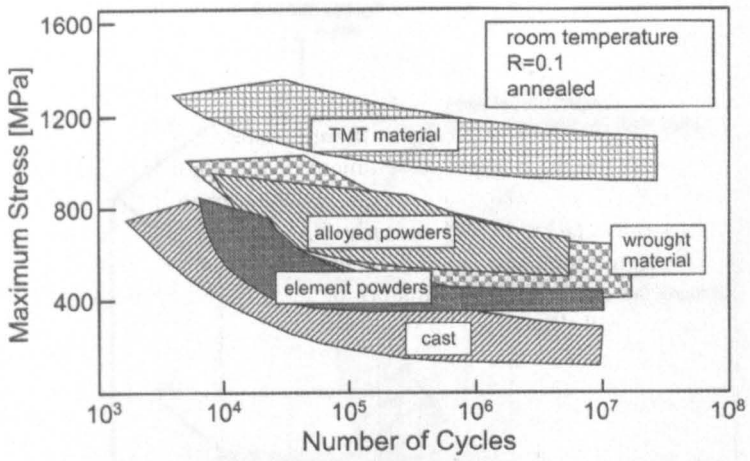

Figure 2.21 High-cycle fatigue of Ti-6Al-4V at room temperature for different alloy conditions.

The loading cycle of a Timetal®834 compressor disc during service will include a number of fatigue cycles as well as a number of periods where the operation requires the loads to be held at near steady state conditions (Pang and Reed, 2001).

This period of time is known as a dwell time. Low temperature dwell fatigue refers to the reduction in cyclic life of components when subjected to loads for a dwell time at low temperatures. Fatigue lives measured under dwell conditions in the disc material were significantly reduced, (Bache, Cope, Davies, Evans and Harrison, 1997 and Thomsen and Hoeppner, 1998)

2.12.2 Quasi-cleavage Facets

Facets with basal plane {0002} orientation are a natural feature of cyclic or time dependant fractures in α/β titanium alloys in air or aggressive environments. As basal slip is a significant deformation mode for this alloy the facets are believed to be caused by the separation of the slip bands under the action of a tensile stress normal to the slip plane. The basal slip plane can be seen in Figure 2.22 along with the other slip planes in alpha titanium. Evidence would suggest that their formation is due to the stress distribution brought about by the inhomogeneous distribution of slip systems and microstructure, which results in the weaker regions off loading onto the stronger features, illustrated in Figure 2.23.

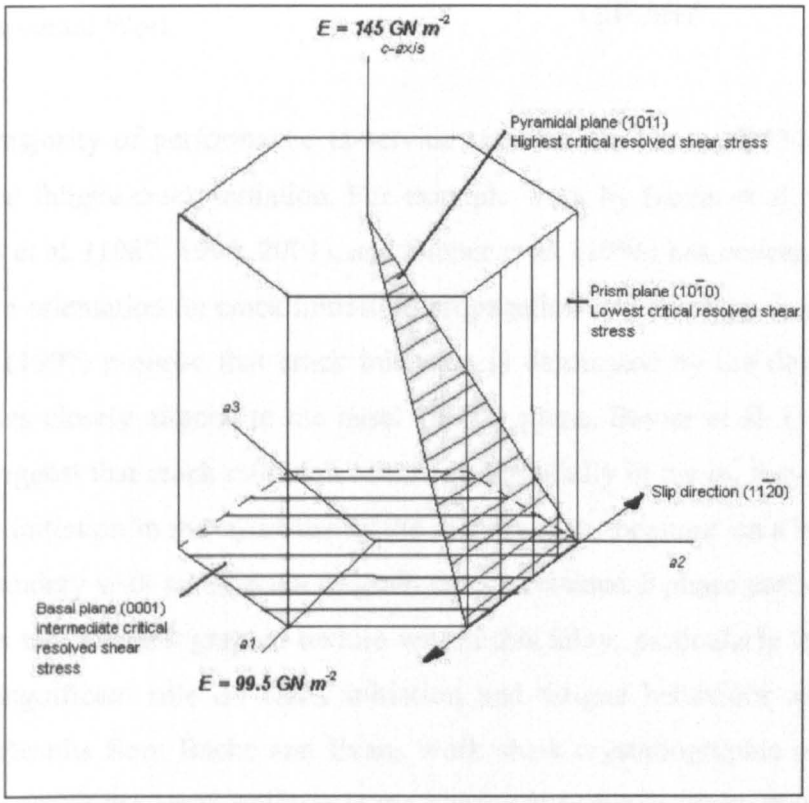

Figure 2.22 Slip planes in alpha titanium (Polmear, 1995)

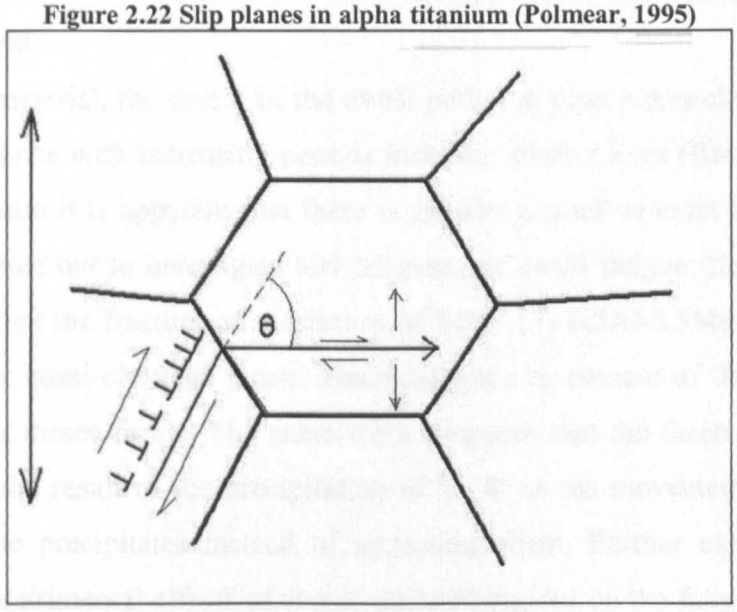

Figure 2.23 The stress redistribution process in the formation of facets (Evans, 1998)

This redistribution process is said to be directly responsible for low temperature dwell sensitivity (Evans, 1998).

UNIVERSITY
OF SHEFFIELD
LIBRARY

2.12.3 Experimental Work

The majority of performance in-service research on Timetal®834 has focused on fatigue and fatigue crack initiation. For example work by Bache et al. (1997, 1998, 2001). Evans et al. (1987, 1995, 2001), and Baxter et al. (1996) has concentrated on the effect of grain orientation on crack initiation, propagation and cleavage facet formation. Bache et al. (1997) propose that crack initiation is dominated by the development of cleavage facets closely aligned to the basal {0002} plane. Baxter et al. (1996) expand further and suggest that crack initiation occurs preferentially in the α_p; they propose that fatigue crack initiation in the α_p occurs by the pile-up of dislocations on a basal plane at either the boundary with an adjacent α_s grain or at a retained β phase particle in the α_p. This suggests that crystallographic texture within this alloy, particularly that of the α_p, will play a significant role on crack initiation and fatigue behaviour and therefore, service life. Results from Bache and Evans work show crystallographic orientation of the colony in which the crack initiates is the dominant factor in controlling fatigue life (Bache et al. 1998).

In disc material, the extent of the dwell period at peak stress clearly affects the fatigue performance with increasing periods inducing shorter lives (Bache et al. 1997). From the literature it is apparent that there is already a small amount of experimental work being carried out to investigate low temperature dwell fatigue. Zeng et al (2000) has concluded that the fracture of specimens of TC11 (Ti-6.5Al-3.5Mo-1.5Zr-0.3Si) is characterised by quasi-cleavage facets. Decreasing the α_p content of the alloy reduces the incidence of theses facets. The same work proposes that the facets and associated planar slip are the result of the precipitation of Ti_3Al as the movement of dislocation cuts through the precipitates instead of bypassing them. Further experimental data concerning the detrimental effects of coarse textured regions on the fatigue performance of Ti alloy Ti-6Al-7Nb was produced by Lindeman and Wagner (1999)

Bache et al (1997) have also used EBSD to investigate the quasi cleavage facets of IMI 685 and IMI 834 (now Timetal 834) produced by fatigue failures generated in the laboratory, the results of which are seen in Figure2.24

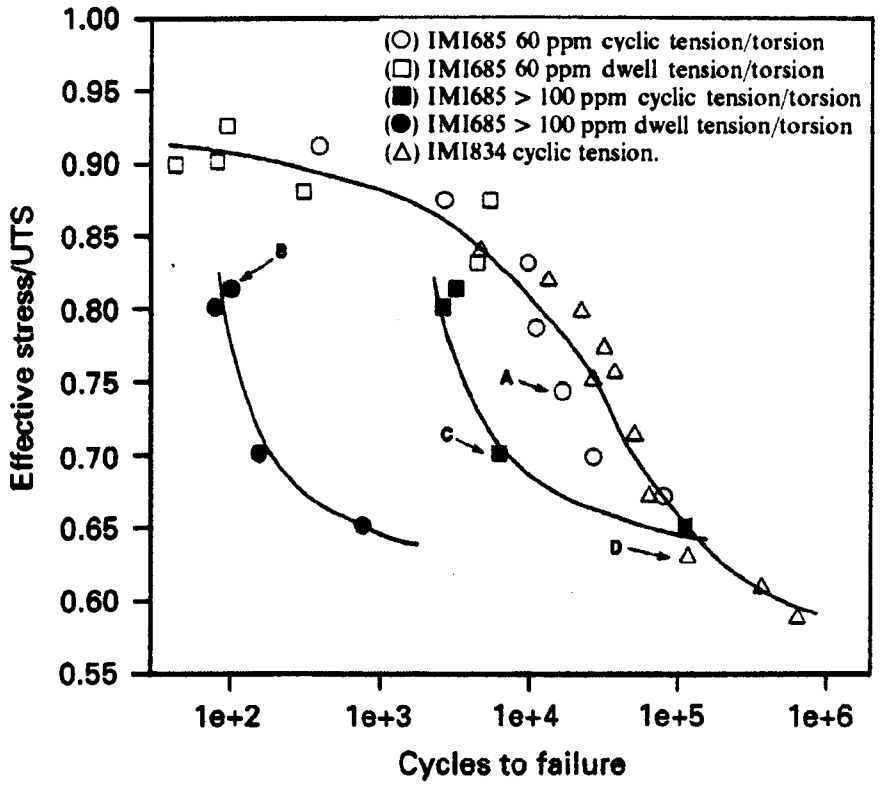

Figure 2.24 Low cycle fatigue data for IMI685 and IMI834 (Bache et al, 1997)

Facets occurring in the material in the IMI 834 were described as similar in appearance to those occurring in IMI 685 but were much finer and therefore more numerous, Figure 2.25(a). EBSD analysis of the facets resulted in the observation of a near-basal orientation of the facet as illustrated by the inverse pole figure produced, shown in Figure 2.25(b).

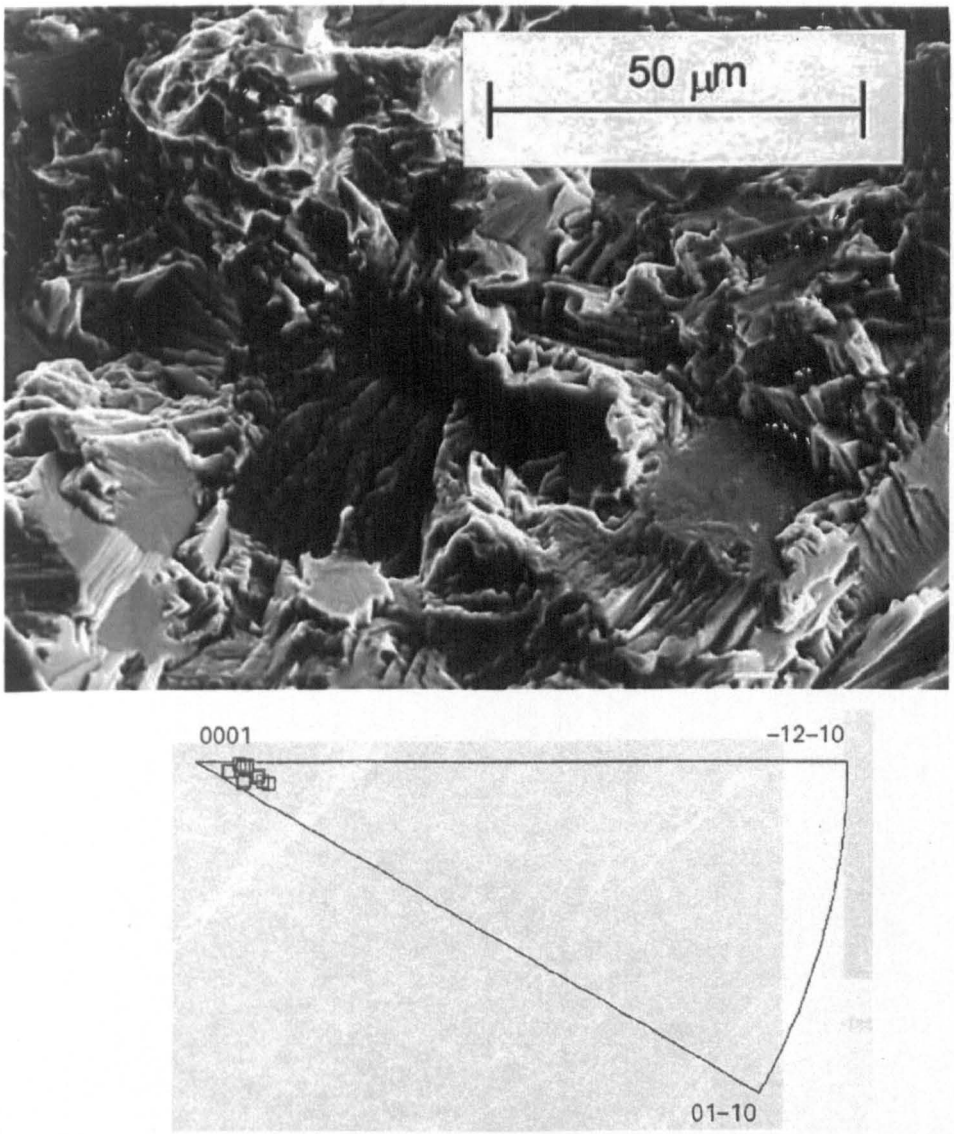

Figure 2.25 (a) Facets at the sub-surface failure initiation site and (b) inverse pole figure representing EBSD readings taken directly from facets on a fracture surface. (Bache 1997)

The work completed by Bache et al. and Evans et al. has proved the importance of the orientation of the basal plane and its effect on the materials performance. As such, one of the major aspects of this work will be the analysis of the basal orientation of the α_p grains.

2.13 Electron Backscattered Diffraction and Texture Determination Techniques

2.13.1 Introduction to Texture Determination

The determination and analysis of the texture of materials has developed over the years and currently can be accomplished using the more classical approach of X-ray

diffraction and TEM or the more recently developed modern approaches such as EBSD and neutron diffraction.

Texture can be divided into macro texture and micro texture. In macro texture, the grains are regarded as a statistical population, while micro texture is a more complete analysis where the spatial locations of individual grains are related to their orientations, with the current techniques involved allowing an orientation accuracy of about 1°. The classical approach refers to the use of X-ray diffraction in order to determine the macrotexture grain orientations in polycrystals which, on some occasions may be random or as in most cases possess a pattern in the orientations and a propensity for the occurrence of certain orientations produced firstly during solidification or recrystallisation and subsequently by further thermomechanical processing.

The modern approach to texture determination and analysis is attempting to discern a materials microtexture using a higher resolution technique such as EBSD to investigate the orientation grain by grain or even sub grain misorientations.

2.13.2 Texture Determination Techniques

The texture of a specimen can be determined by a number of methods, see Figure 2.26. As described previously, X-ray diffraction is often used for macro texture determination and electron back-scattered diffraction is used to obtain higher resolution micro textures.

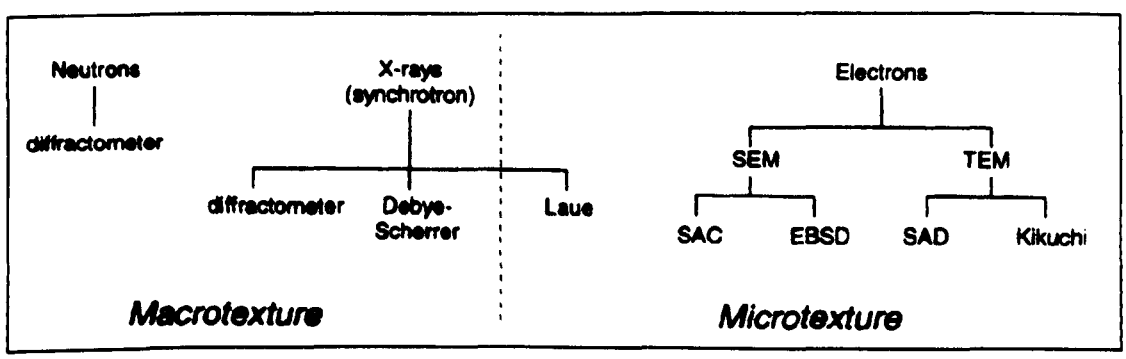

Figure 2.26 Mainstream techniques for texture determination (Randle, 2000)

X-ray goniometery is the most established method and optimises the Schultz reflection method and the standard goniometry apparatus can be seen in Figure 2.27.

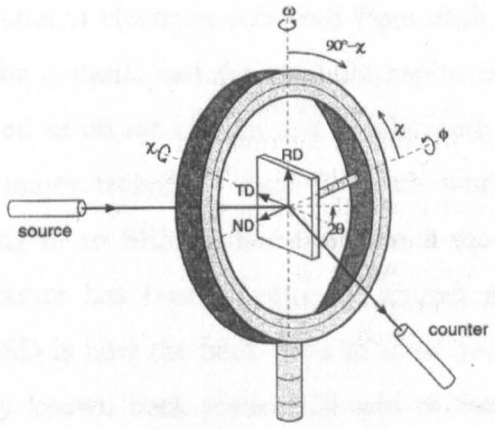

Figure 2.27 Standard geometry of an x-ray goniometer.

A specimen of desired history and orientation can be placed into the goniometer, the apparatus is capable of translating the specimen through three types of movement;

1) A simple to and fro oscillation allowing greater statistical averaging of the texture measurement due the grater number of grains sampled.
2) Rotation about an axis perpendicular to the specimen surface (angle chi)
3) Rotation about an orthogonal axis through the angle phi (Hatherly et al, 1979).

At each desired position a count is taken of reflected x-rays rebounding off planes satisfying the Bragg angle. Theses counts are tabulated and can be used with the related angles positions to calculate preferred orientations. This operation must first be carried out on an untextured, random sample so that, as with many other texture analysis methods, further results can then be described in terms of "multiples of a random distribution" (MRD) (Vaudin, 2001).

In order to obtain microtextural information it is important that the probe size formed by the exploring radiation (i.e. x-rays, neutrons or electrons) is smaller than the features for which information is needed (Randle et al, 2000). It is for this reason that X-ray diffraction is not suitable for micro texture determination and electron back scattered diffraction (EBSD) techniques are optimised instead.

2.13.3 Electron Back-Scattered Diffraction

Electrons are ideal for combined microstructural/crystallographic studies and back scattered electrons (BSE) are emitted when an electron beam incises on a sample.

The number of back scattered electrons collected from each point is dependant on the atomic number (Z) of the material and the crystallographic orientation in the case of a crystalline sample as well as on the current and accelerating voltage applied. Until the 1980's TEM was the major technique used for such work, with some input from selected area channelling in an SEM. Since that time a more convenient SEM-based technique for micro-texture has been developed, known as electron back-scattered diffraction, EBSD. EBSD is now the back-bone of most microtexture research. EBSD or, as it is equivalently known back-scatter Kikuchi diffraction, BKD, is an add-on package to an SEM.

EBSD measurements consist of the following steps;

- Specimen production
- EBSP production
- Calibration
- EBSP analysis
- Automation

Specimen preparation for EBSD analysis is very much material dependant and will usually consist of a combination of any of the following methods; Mechanical grinding using silicon carbide papers or equivalent, mechanical polishing using diamond paste on the appropriate pads, and a mechanical/chemical polish using colloidal silica. For some materials electro-polishing is required as a well prepared sample is a prerequisite to obtaining a good diffraction pattern. Surfaces must be sufficiently smooth to avoid forming shadows on the diffraction pattern from other parts of the sample and all surface damage should be removed. In order to utilise the SEM beam for EBSD applications an appropriate detector is needed. An EBSD camera consists of a phosphor screen integrated with an intensified CCD camera. The NordLYs camera used at The University of Sheffield has a rectangular phosphor which is matched to the size of the CCD. The detector has a vacuum tight tube that can be inserted into the SEM chamber via an electric motor. The most attractive feature of EBSD is its unique capability to perform concurrently rapid, usually automatic diffraction analysis to give crystallographic data and imaging with a spatial resolution of less than 0.5μm, combined with regular capabilities of an SEM such as capacity for

large specimens, option of chemical analysis, and the ability to image rough surfaces (Randle et al, 2001). Within the SEM the sample must me tilted to an angle greater than 65° in order to minimise the distance the back scattered electrons have to travel through the specimen and increasing the chances of getting a good pattern, see Figure 2.28

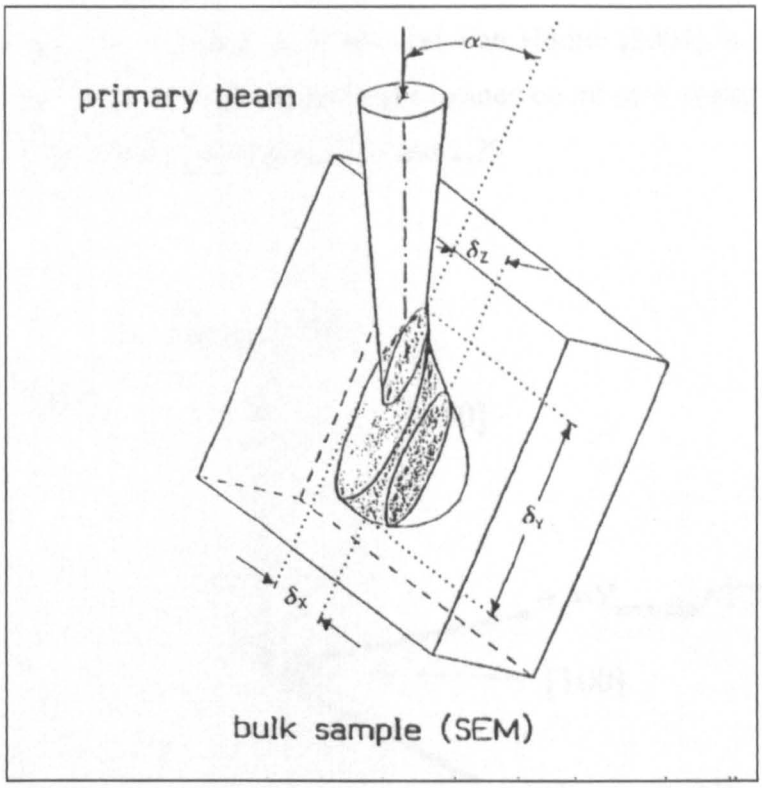

Figure 2.28 Diagram showing the specimen-beam interaction in a tilted specimen. (Randle, 2000)

The scan coils of the SEM are turned off in order to obtain a stationary beam and an electron detection camera is inserted in front of the tilted specimen to capture the kikuchi diffraction pattern. The number of back scattered electrons collected from each point is dependant on the atomic number (Z) of the material and the crystallographic orientation in the case of a crystalline sample as well as on the current and accelerating voltage applied.

The Kikuchi patterns recorded are interfaced to a closed circuit camera and in turn processed by a computer so that each Kikuchi pattern is indexed and the orientation of the crystal determined. Using standard EBSD analysis software packages mapping of a required area can be carried out, the stationary electron beam can be moved and a Kikuchi pattern obtained for each of a number of steps within a matrix, the orientation of each of these steps can spatially related producing an EBSD map.

2.13.4 Euler Space and Bunge Notation.

In quantitative texture analysis the coordinate systems of the sample and of the crystal need to be related (Wenk and Van Houtte, 2004). In other words a relationship is needed between the grain and material in order to define the orientation of the grain within the material. As described in Wenk and Van Houtte (2004), this requires three quantities that will relate two orthogonal right-handed coordinate systems through three rotations, as described through Figures 2.26 and 2.29.

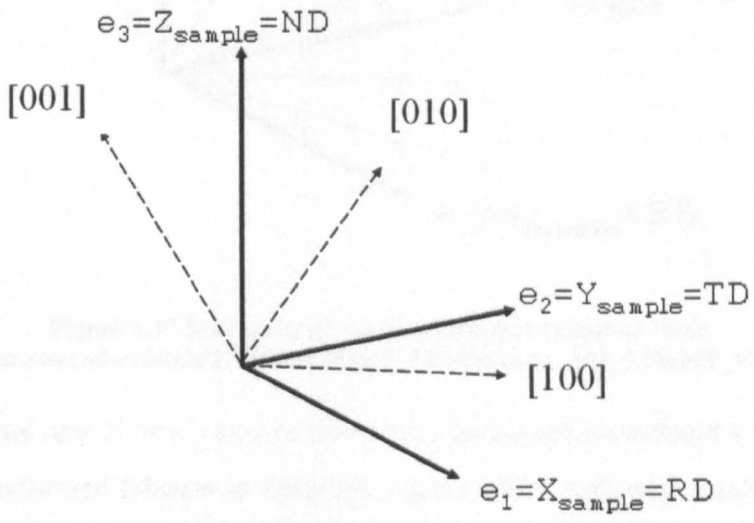

Figure 2.29 Initial schematic of sample (black) and crystal (blue) co-ordinates (adapted from http://neon.mems.cmu.edu/rollett/27750.old. Spg05/Components _pt2_13Jan05_v2.ppt., 04/06/06).

Figure 2.26 shows the orientation of a cubic crystal (blue dotted lines) as well as the coordinate system (solid black lines) of the material. The crystal orientation can be defined using Euler angles described in the Bunge notation.

A triplet of Euler angles is useful to describe rotations or relative orientations of orthogonal coordinate systems. Unfortunately, their definition is not unique and in the literature there are as many different conventions as authors. The convention employed in this work is one of the more common ones and utilises the Bunge notation (ϕ_1, φ,ϕ_2). All rotations are in a counter-clockwise fashion.

The Euler angles (ϕ_1, φ, ϕ_2) relate two orthogonal coordinate systems having a common origin. The transition from one coordinate system to the other is achieved by a series of two-dimensional rotations. The rotations are performed about coordinate

system axes generated by the previous rotation step. The convention used here is that ϕ_1 is a rotation (shown in RED) about the Z axis or e'$_3$ of the initial coordinate system, seen in Figure 2.27.

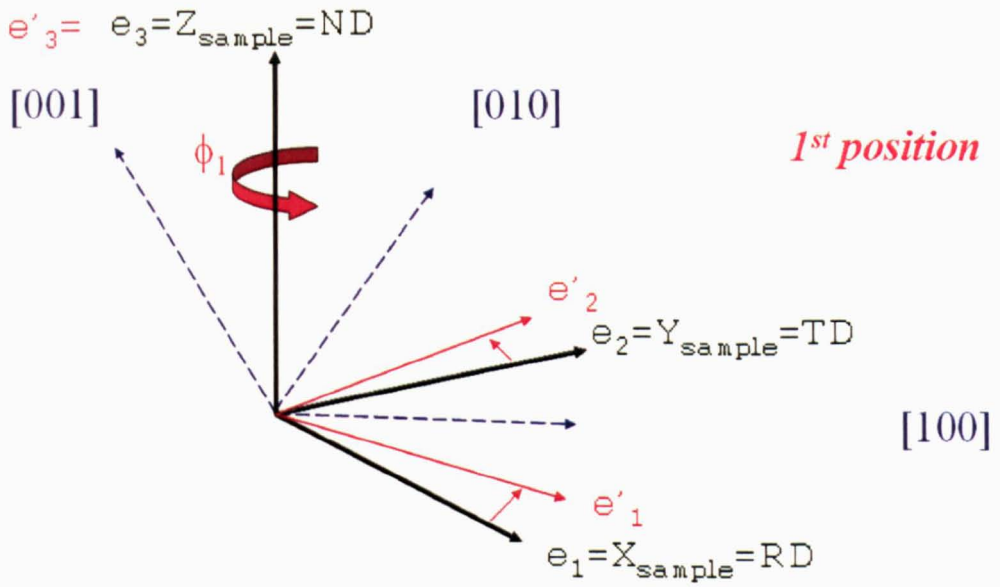

Figure 2.30 Schematic of initial ϕ_1 rotation (adapted from http://neon.mems.cmu.edu/rollett/27750.old. Spg05/Components _pt2_13Jan05_v2.ppt., 04/06/06).

About the new X or e'$_1$ axis of this newly generated coordinate system a rotation by φ is then performed (shown in GREEN, Figure 2.28), followed finally by a rotation by ϕ_2 about the new Z axis (Shown in Blue, Figure 2.28).

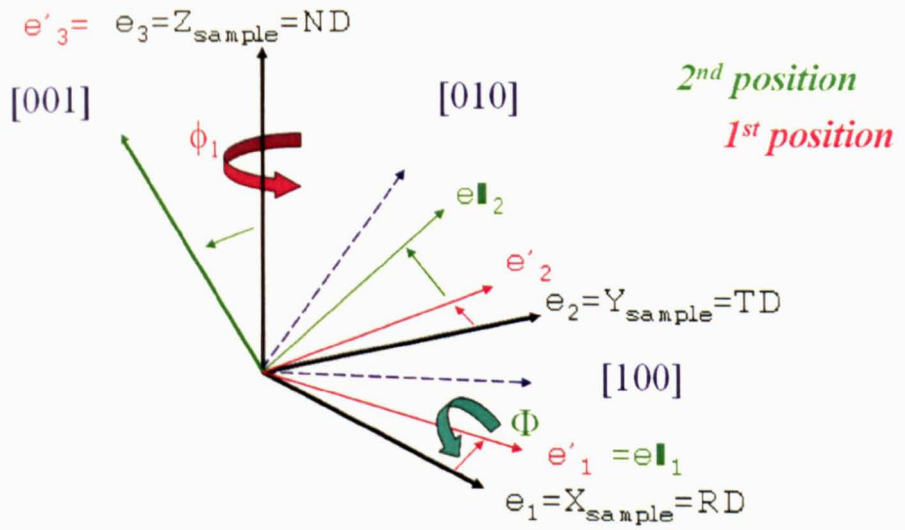

Figure 2.31 Schematic of φ rotation (adapted from http://neon.mems.cmu.edu/rollett/27750.old. Spg05/Components _pt2_13Jan05_v2.ppt., 04/06/06).

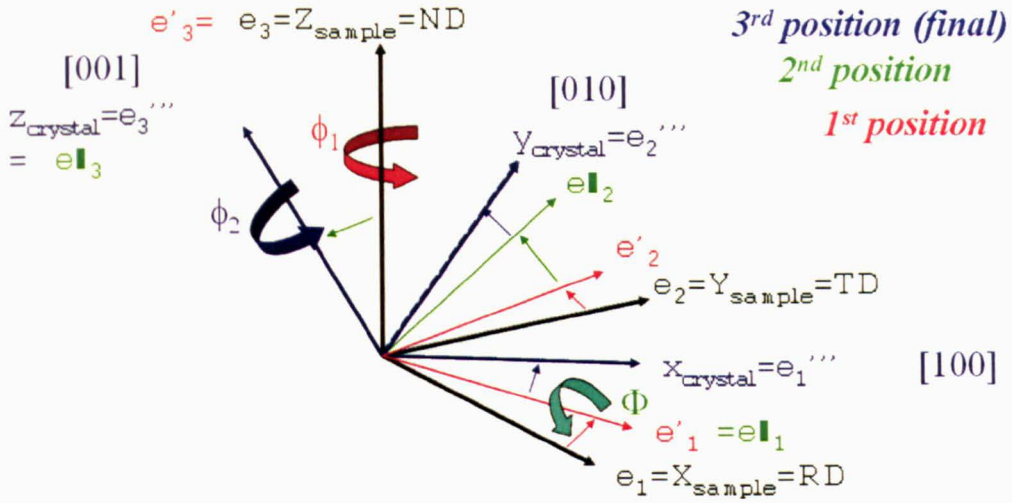

Figure 2.32 Schematic of ϕ_2 rotation (adapted from http://neon.mems.cmu.edu/rollett/27750.old. Spg05/Components _pt2_13Jan05_v2.ppt., 04/06/06).

When using Euler angles to describe metalworking textures it is common to relate the sample coordinate system X,Y, and Z to directions defined by the forming process such as rolling direction (RD), Transverse direction (TD), Extrusion direction (ED) and normal direction (ND).

2.13.5 Orientation Image Maps

The orientation image map (OIM), is a spatial representation of the orientation information obtained during EBSD mapping. An OIM colours the point or pixel in the mapped area based upon their orientation, so grains which share the same orientation appear as the same colour. There are a number of components that can be highlighted with an OIM, orientations can be shown with respect to their Euler angles or to an inverse pole figure. The variation in band contrast, grain boundaries substructure can also be illustrated.

There are a number of key factors to obtaining a statistically relevant OIM by EBSD, these are; the specification of grid size, mechanisms to locate the sampling point and Data storage, display and retrieval. In order to obtain an OIM in a reasonable time and to posses a large enough dataset to make statements about the materials texture a trade-off is needed. The specification of grid size is one area where compromises are often made and the step size chosen will depend very much on the nature of the inquiry (Randle and Englar, 2001). A texture determination run can be carried out with a much

larger step size than a run intending to determine sub-grain dislocations and grain boundary characteristics.

There is a choice of two basic approaches for location of sampling points on a specimen surface; The specimen is moved under the stationary incident beam, or, the beam itself is deflected across the stationary sample, similar to conventional SEM. Each sampling point is stored with its orientation, spatial coordinates and often a pattern quality index. These data then allow the output of user defied map formats.

2.13.6 Pole Figures

Pole figures have commonly been employed to represent the relation between the orientation of the crystallographic axes of a crystal of arbitrary lattice structure with respect to the coordinate system of a sample of arbitrary symmetry, or vice versa (Kocks, Tome and Wenk, 2000). A pole figure is a two-dimensional projection of this three-dimensional distribution and represents the probability of finding a pole to lattice plane (hkl) in a certain sample direction. Pole figures are normalised to express this probability in multiples of a random distribution (MRD). Depending on the application stereographic or equal angle projection of the spherical pole density distribution is used (Wenk and Van Houtte, 2004). An example of the construction of a pole figure can be seen in Figure 2.30 taken from Hatherly and Hutchinson, (1979).

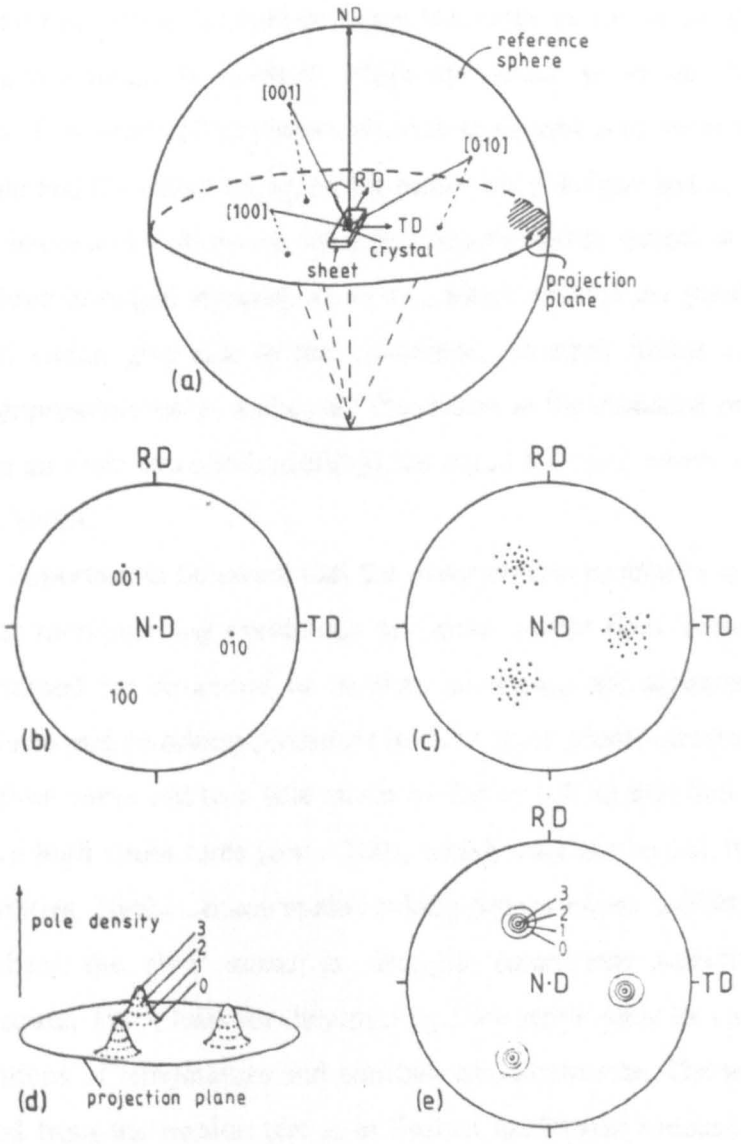

Figure 2.33 (a) projection sphere and reference direction, (b) projection of poles for a single grain, (c) projection of poles from textured grains (d) pole density distribution and (e) contour map of pole density, Hatherly and Hutchinson, (1979).

2.14 Thermomechanical Testing

2.14.1 Introduction

In order to use laboratory testing to simulate thermomechanical processing, it is important to be able to fully comprehend the state of stress and strain rate of a given test piece under a stated load. Determination of the state of stress is necessary for the analysis of plastic deformation in metals. The state of stress at a point may be determined by calculating the stresses acting on three mutually perpendicular orientated

planes passing through a point. When determining the complete state of stress at a point, it is found that on one plane the normal stress increases as the angle of the plane is increased until a maximum is reached, whilst the shear stress on the same plane decreases to zero. This plane of maximum normal stress and zero shear stress is called the principal plane and the stress acting on the plane, the principal stress. There are also principal strains associated with theses stresses. Thus the stress system at a point can be represented by three principal stresses, σ_1 σ_2 σ_3 , which control the yielding behaviour of the metal and which give rise to the associated principal strains ϵ_1 ϵ_2 ϵ_3. In the axisymmetric compression test ϵ_1 and ϵ_2 are the strains in the direction perpendicular to the length and in an ideal test (no barrelling) are equal to - $\epsilon_3/2$ where ϵ_3 is the length strain (Roebuck, 2002).

It is also important to be aware that the experimental problems in measuring the flow curve under metalworking conditions are more severe than in the usual stress-strain test determined for structural or mechanical design applications, as stated by Dieter (1988). Since metalworking processes involve large plastic strains, it is desirable to measure the flow curve out to a true strain of 2.0 to 4.0. In addition many of these processes involve high strain rates (e/s ~ 100), which may not be obtained easily with ordinary test facilities. Further, many metalworking processes are carried out at elevated temperatures where the flow stress is strongly strain rate sensitive but nearly independent of strain. Thus, tests for determining flow stress must be carried out under controlled conditions of temperature and constant true strain rate. The true stress-strain curve determined from the tension test is of limited usefulness because necking limits uniform deformation to true strains less than 0.5.(Dieter, 1998)

2.14.2 Axisymmetric compression testing.

Since the majority of metal forming processes involve compression there have been a number of compression tests developed to elucidate metal behaviour in compression. The compression of a short cylinder between anvils is a better test than the tensile test for measuring the flow stressing metal working applications. There is no problem with necking and the test can be carried out at strains in excess of 2.0 if the material is ductile. However, the friction between the specimen and the anvils can lead to difficulties unless it is controlled. (Dieter, 1998)

2.14.3 Friction and Lubrication.

The friction forces developed between the workpiece and the forming tools are an important consideration in metalworking. The frictional conditions on the top and bottom faces of the disk are described by a constant coefficient of coulomb friction.

$$\mu = \frac{\tau}{p} \qquad [2.8]$$

Where τ = the shearing stress at the interface

p = the stress normal to the interface

Lateral flow of the metal outward as it is being compressed leads to shearing stresses at the die contact surfaces. This surface shear is directed toward the centre of the disk, opposing the outward radial flow. These frictional shear stresses lead to lateral pressure in the material, which is zero at the edges of the disk and builds up in the centre (Dieter, 1988) and this will need to be determined in order for the flow behaviour of Timetal®834 to be determined by axisymmetric compression testing.

One of the most established tests proven to study the friction conditions is the ring compression test (Bowden and Tabor, 1967). The test was initially developed by Kunogi (1954) and further developed by Male and Cockcroft (1964). The principles of the ring compression test are well understood and the test has been completed previously on the apparatus at The University of Sheffield (Jupp, 2005). For given conditions of temperature, strain rate, strain and initial specimen geometry according to the ratio of outer diameter to inner diameter to ring height (OD:ID:H) the deformation of the inner diameter of the specimen may be calculated as a unique function of the interfacial friction coefficient. Determining the friction is done by comparing the reduction in height and the change in the inner diameter to the calibration chart for the initial ring geometry.

It has been found in this literature that the friction conditions are strongly affected by a large number of parameters. Jupp (2005) states that conflicting experimental results regarding the influence of temperature and strain rate and lubrication have been reported (Bowden and Tabor 1967, Ford and Alexander 1963,

Lundberg, 1986) indicating that direct comparison of results is difficult because of the large number of variables.

2.15 Summary

Within this literature review the fundamentals behind the proposed work including crystallography, metallurgy, deformation mechanics and flow behaviour of itanium alloys and specifically Timetal®834 have been introduced and discussed. From the literature review a number of complications and contradictions have arisen. One of the most pressing issues is the lack of conformity in the beta approach work completed on Timetal®834 and this will be addressed initially. Secondly, the current industrial models will be analysed in order to assess the common industrial parameters. The flow behaviour of this alloy has been reviewed previously by Wanjara, (2005) and Stanford and Bate, (2004), however the material used in these investigations had already been solution treated and as such the starting condition is different from industry. As such in order to investigate the microstructure and crystallographic texture evolution of Timetal 834 through the *typical* hot forging process route the starting material and parameters previously investigated need to be altered.

Consequently, the crux of this work will be to investigate the effect of industrial process parameters, obtained from current industrial models, on the crystallographic texture and microstructural development of the as-received billet material, whilst setting precedents and good practices with regards to thermomechanical processing and analysis of titanium, specifically Timetal®834, at the University of Sheffield.

3 TIMETAL®834 PRODUCTION ROUTE

3.1 Introduction

Having addressed the current literature the following chapter will detail the production of Timetal®834 prior to the point of interest of this work. This chapter will detail the production of the Timetal®834 billet from the point of sourcing the raw materials through to the supplying of the billet to the component manufacturer. The chapter is deemed necessary as it gives an account of the history of the component material before component manufacture. From the literature review it is clear that all steps in the processing from the first melt onwards have an effect on the texture evolution.

3.2 Production route

3.2.1 Mixing

The billet manufacturing process begins with the mixing stage, the raw materials, in the form of pellets and powders of Ti sponge, master alloys and elementals, are thoroughly mixed together in a series of hoppers and spinners in batches of 3 Tonnes. This mix is further separated into six half Tonne batches which are then broken down into 14 equal 43kg lots via a spinning hopper.

In order to create greater handleability each 43kg lot is compacted into D-shaped solids known as compacts which are then used to build up the electrode that will be used in the Vacuum Arc Remelt (VAR) furnace later in the process. In total 84 compacts are used to piece together a 19 inch (483mm) diameter electrode. At this point it should be noted that extreme care is taken during assembly as many of the elementals and master alloy powders within the mix have a significantly smaller diameter than the Ti sponge which, if not handled correctly could lead to fallout and incorrect alloy content. Once placed together the compacts are plasma welded together in a plasma chamber, eight seam welds travelling the length of the electrode hold the compacts together ready for the first melt, this can be seen schematically in Figure 3.1. Care is taken to keep the electrode off the floor as they can pick up contaminants which will also affect the chemistry of the product if carried into the furnace.

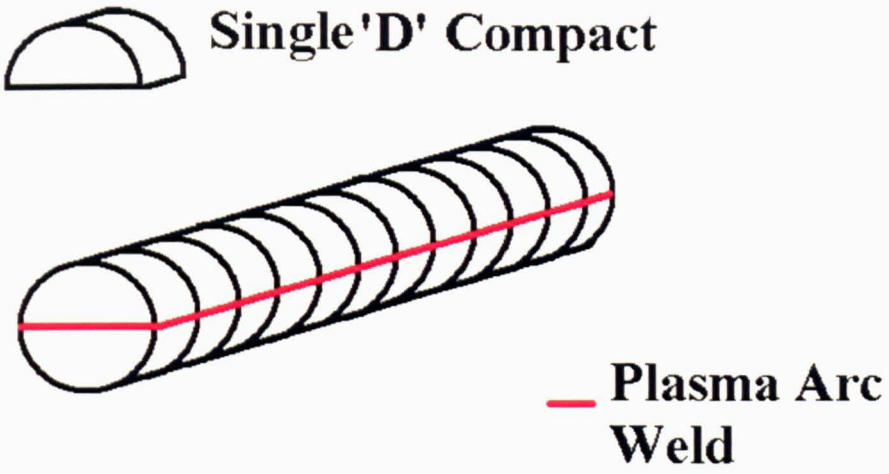

Figure 3.1 Schematic of the VAR electrode lay-up of 'D' compacts.

3.2.2 Vacuum Arc Re-melt Furnace

Once an electrode is prepared it is ready for vacuum arc re-melting (VAR) in one of the many furnaces at Timet UK. The electrode is placed within a copper crucible and a stub is used to spark an initial contact causing a small melt pool on the top of the electrode. The stub, held by a ram, is then plunged into the melt pool which subsequently solidifies creating a join between the stub and the electrode. The ram is then raised and the electrode is lifted off the ground, using the ram as a control parameter a spark is then initiated between the electrode and the copper crucible causing the electrode to melt. As the melt continues the spark is maintained between the top of the melt pool and the electrode and the process continues until the electrode is consumed.

Control of the melt pool is gained within the VAR furnace by varying the following parameters;

- Melt schedule, there is a close relationship between the macrostructure and the temperature profile (Hyun et al, 2003).
- Arc Coil,
- Stirring
- KA V
- Vacuum
- Profile

After the initial melt process the electrode is machined with a floating tool to remove scale followed by a fixed tool for shaping. A further two melts are carried out in a different furnace to the first melt in order to isolate any impurities to the first step of the process. After each melt the electrode is inverted so that any solidification induced segregation is distributed and broken up slightly. As the melts progress the diameter of the electrode increases, for the fist melt the ingot diameter is approximately 23", it is then increased to 26" and finally finishes at 30" (760 mm) diameter.

3.2.3 Forging

Following ingot production, hot forging is required to breakdown the microstructure and create the desired shape of billet (round or square). The process can be seen schematically in Figure 3.2, based on private communications with Timet, UK. Using an 1800T Davy Forge hydraulic press, the 3 tonne 760 mm diameter cylindrical billet is initially high temperature β worked well above the β transus for shaping to a rectangle followed by a low temperature α/β forge just below the β transus in order to control the beta grain size. The α/β forging is followed by sectioning and then forging well within the α/β phase field, all based on the customers requirements. The exact temperatures of the forging steps and the reductions made are determined by the customers requirements for specific sizes and microstructures, however the final α/β forge generally involveds a further shape change from a rectangular to cylindrical cross-section.

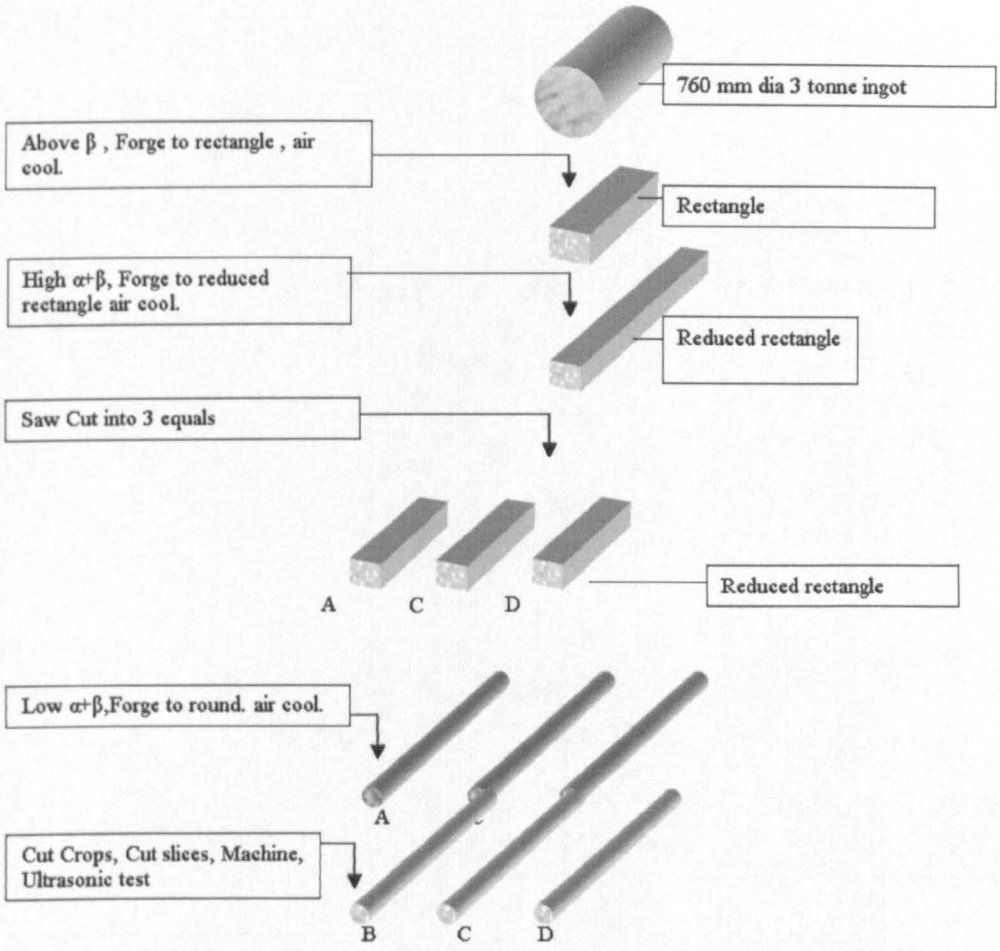

Figure 3.2 Schematic of Timetal 834 billet process route.

3.2.4 Routine Testing on the Billet

After machining to remove oxides and other surface defects the billet is tested for quality control purposes via various destructive and no destructive testing methods. Initially the whole billet is tested ultrasonically for inclusions or large microstructural anomolies that may lead to failure in service.

Once the billet has been ultrasonically tested, a slice is removed, sectioned and tested for macro and micro-structure using optical microscopy, from this analysis a beta approach curve is produced. The remaining slice material is used to machine mechanical testing samples used to determine tensile strength, creep and fatigue resistance.

4. EXPERIMENTAL PROCEDURE

4.1. As-received Material

The Timetal®834, composition shown in Table 4.1, was supplied in the form of hot forged billet (200 mm diameter) by Firth Rixson Ltd, Darley Dale, UK. The material, itself, was purchased by Firth Rixson PLC from Timet, UK and was produced as described in Chapter 3; the full data sheet supplied with the material can be seen in Appendix A. The as-received microstructure consisted of approximately 70% equiaxed primary alpha (α_p) grains with an average grain size of 30μm, in a matrix of coarse secondary alpha (α_s) lamellar as seen in Figure 4.1.

Table 4.1. Chemical composition of as-received Timetal®834 [wt%] (Taken from the Timet data sheet for the as-received material from Timet UK)

Al	Sn	Zr	Nb	Mo	Si	C	Fe	O	N	Ti
5.74	3.99	3.47	0.72	0.50	0.30	0.06	0.008	0.1050	0.0025	Bal

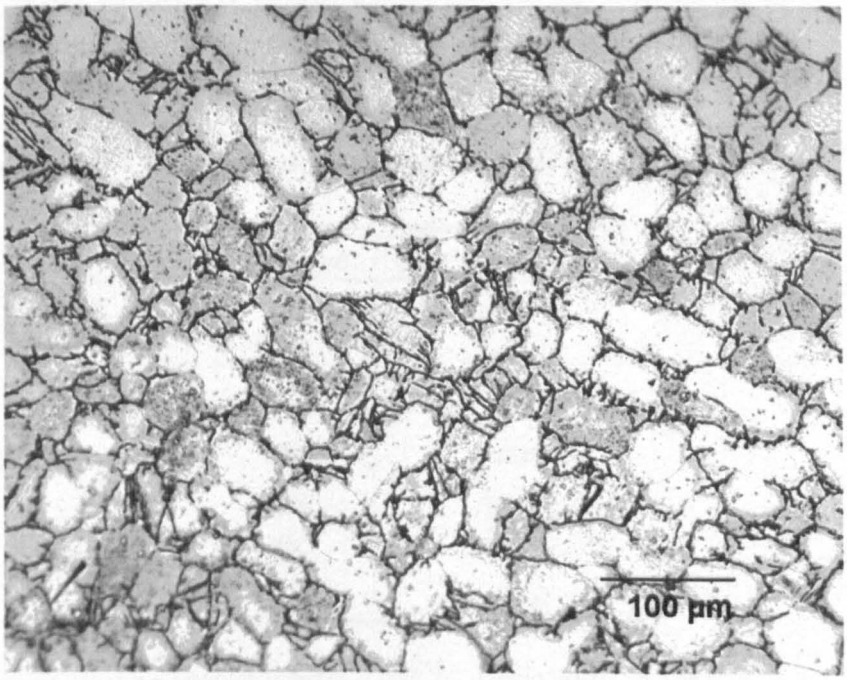

Figure 4.1 The as-received microstructure of Timetal 834. The plane of observation is the Billet cross-sectional plane.

The slice was taken from the top end of the billet and as such small segregation effects could be inherent, however, this is an area from which components are manufactured and the billet production route utilises 3 VAR routines in order to minimise segregation.

4.2 Introduction

A number of laboratory simulations, material preparation techniques and analytical procedures were utilised during this work. In order for the results to be reliable and the tests repeatable, detailed good practice guides were followed and established techniques repeated. The remainder of this chapter details these procedures and techniques.

4.3 Beta Approach Curve Determination.

The β approach curve for the as-received material was determined using heat treatment and optical microscopy. Samples were sectioned into approximately 150x150x150 mm samples with a 1.5mm diameter hole drilled into the middle for which a K-type thermocouple was inserted to ensure that sample temperature was being measured and not the furnace temperature. The samples were then heated to a number of temperatures in a muffle furnace which are detailed in Table 4.2

Table 4.2 Temperatures used for beta approach curve determination.

Specimen	*Temperature (°C)*
B1	950
B2	980
B3	990
B4	1000
B5	1010
B6	1020
B7	1030

For each test the furnace was heated to 10°C below the desired temperature and once the furnace was stable the sample with inserted thermocouple was placed in the centre of the furnace. Once the sample temperature had stabilised the temperature of the furnace was increased gradually until the temperature of the sample was at the desired

level. The sample was then held at this temperature for 30 minutes and then immediately quenched in water to room temperature. This resulted in a microstructure of equiaxed α_p in a matrix of very fine needle like α_s which was assumed to have previously been high temperature β. Each sample was then sectioned in the billet plane at a depth well beyond the effect of oxygen pick up, which, is a well known α stabiliser. In this instance etching was performed using a 2% Ammonium Hydrogen Diflouride (NH_4F:HF) solution. Volume fraction analysis of the α_p and α_s was then performed using the image analysis software KS 400 using reflected light threshold. Figure 4.2(a) shows a micrograph of a Timetal®834 sample etched with NH_4F:HF for a few seconds and illustrates the good contrast between the equiaxed α_p grains and the transformed α_s grains. Figure 4.2(b) shows the associated greyscale intensity of the micrograph in (a) clearly depicting the difference in reflected light intensity of the two phases. This variation in reflected light intensity allowed the software to allocate the areas to various data sets based on the user defined light threshold intensity, therefore allowing quantification of the two phases.

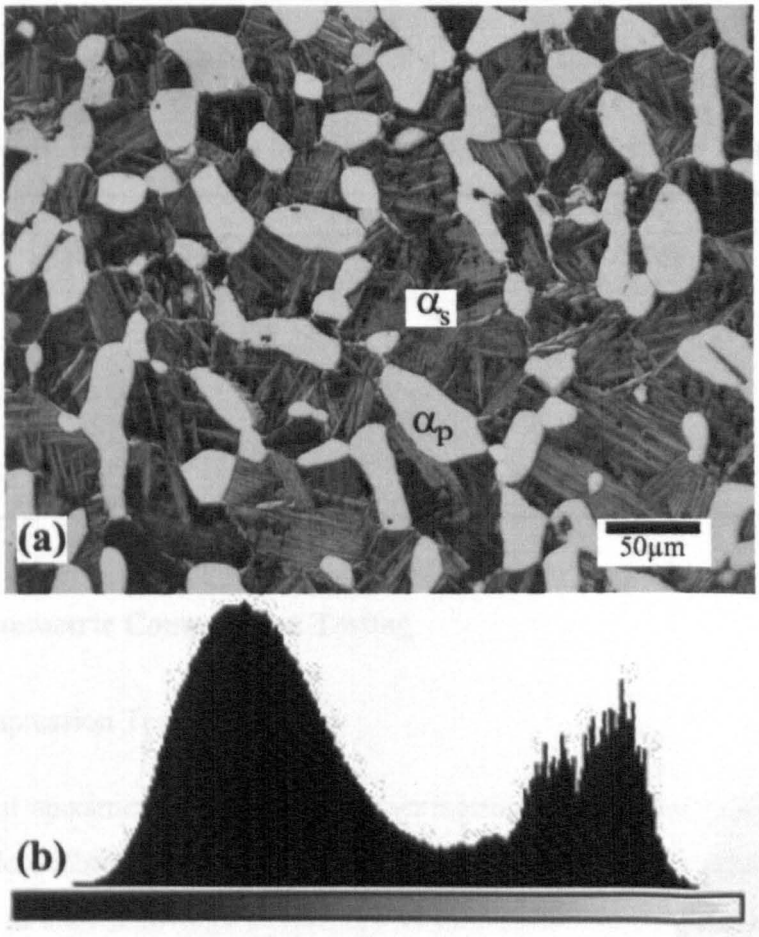

Figure 4.2 (a) Micrograph of Timetal®834 etched with 2% NH_4F:HF with (b) showing the associated greyscale intensities for the image.

In cases where the volume fraction of the α_s was low the software had difficulty in discriminating between α_p and α_s making it difficult to get a quantifiable volume fraction. In theses cases point counting methods were used which involved a 40 x 40 point grid being superimposed on x300 and x600 magnification images and the points falling within an alpha grain counted (P_p). These counts (P_p) were then represented as a percentage of the total number of points of the grid (P) and all results were tabulated and the graphs can be seen in the results section. Using this method, as described in Sellars and Higginson, 2003, the volume fraction can then be defined as;

$$V_v = \bar{P} \tag{4.1}$$

And the expected relative standard error in the value V_v for a minor phase can be estimated from the relationship

$$\left(\frac{S(V_v)}{V_V}\right)^2 = \frac{(1-V_v)}{PV_v} \approx \frac{\left(1-\bar{P}_p\right)}{P\bar{P}_p} \tag{4.2}$$

Substitution in equation 4.2 leads to the values given in Table 4.3

Table 4.3 Relative errors of volume fraction by point counting (Sellars and Higginson, 2003)

(1)	*(2)*	*(3)*		
Relative Error, $\frac{S(V_v)}{V_v}$	Relative 95% C.L.	Number of Points P $V_v = 0.01$	0.1	0.5
0.01	± 2%	990000	90000	10000
0.025	± 5%	158400	14400	1600
0.050	± 10%	39600	3600	400
0.100	± 20%	9900	900	100

4.4 Hot Axisymmetric Compression Testing

4.4.1 The Compression Test

The test specimens for the hot axisymmetric compression testing were in the form of cylinders 12mm in diameter and 15mm in height. A schematic diagram of the test specimen is shown in Figure 4.3. To ensure sufficient lubrication was retained during the heating cycle of the test a small lip was added to the top and bottom of the

test specimen as can be seen in Figure 4.3. All test specimens were machined such that the long axis of the cylinder corresponded to the longitudinal axis of the as-received billet. This meant the compression plane of the tests was perpendicular to the longitudinal axis of the billet which corresponds to the practice used by Firth Rixson PLC. in their forging operations of Timetal®834. To ensure homogeneity of starting microstructure and crystallographic texture test specimens were only taken from billet material at a radius of 125mm or less as shown schematically in Figure 4.4. In order to control temperature during the test a thermocouple hole 1.1mm in diameter was drilled into the specimen at the mid-height of the specimen to a depth of 6mm.

To ensure good practice was maintained during test specimen manufacture and the tests themselves the UK National Physical Laboratory Good Practice Guide for Hot Axisymmetric Testing (Roebuck et al. 2002) was followed. This included machining specimens to minimise residual stresses and changes in microstructure close to the surface and ensuring that each test piece dimensions were measured such that accurate comparisons between the initial and final tested dimensions were made. Furthermore, the good practice guide required all measurements and readings from each test to be recorded on a data sheet.

The tests were performed using The University of Sheffield's thermomechanical compression machine (TMC). The TMC apparatus was developed by Servotest, Feltham and was built specifically for the University of Sheffield. The apparatus consists of three furnaces, a preheat furnace, an annealing furnace and a test furnace. Enclosed within the test furnace are the forging platens consisting of a fixed bottom platen and a ram driven upper platen. The maximum achievable force for the ram being 500 kN with a working stroke 100 mm. The ram operates with a minimum velocity 0.01 mm/s and a maximum velocity 2.9m/s (when applying a force of 100kN). As well as high achievable loads the ram also possesses a stopping point accuracy less than +/- 0.1mm at low speeds allowing excellent control of applied strains.

Another important aspect of the TMC apparatus can be seen in Figure 4.5 and 4.6, the fast thermal treatment unit (FTTU) located directly in front of the test furnace consists of an induction coil and cooling unit allowing the simulation of complex industrial heating and cooling/quenching routines.

The transfer of the test specimen from FTTU to testing furnace and vice versa was controlled by a robotic arm powered by hydraulics, allowing rapid transfer ensuring desired testing parameters are maintained.

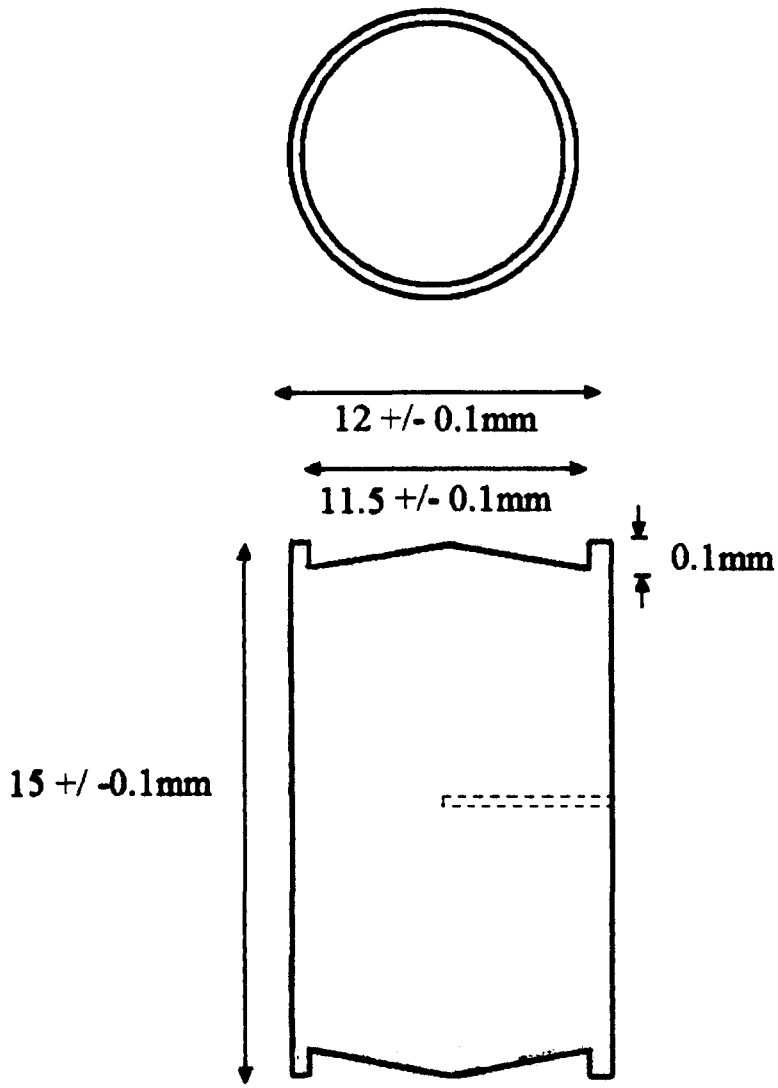

Figure 4.3 Schematic diagram of the axisymmetric compression sample, the diagram shows the lip profile used to maintain lubricant and the location of the thermocouple hole.

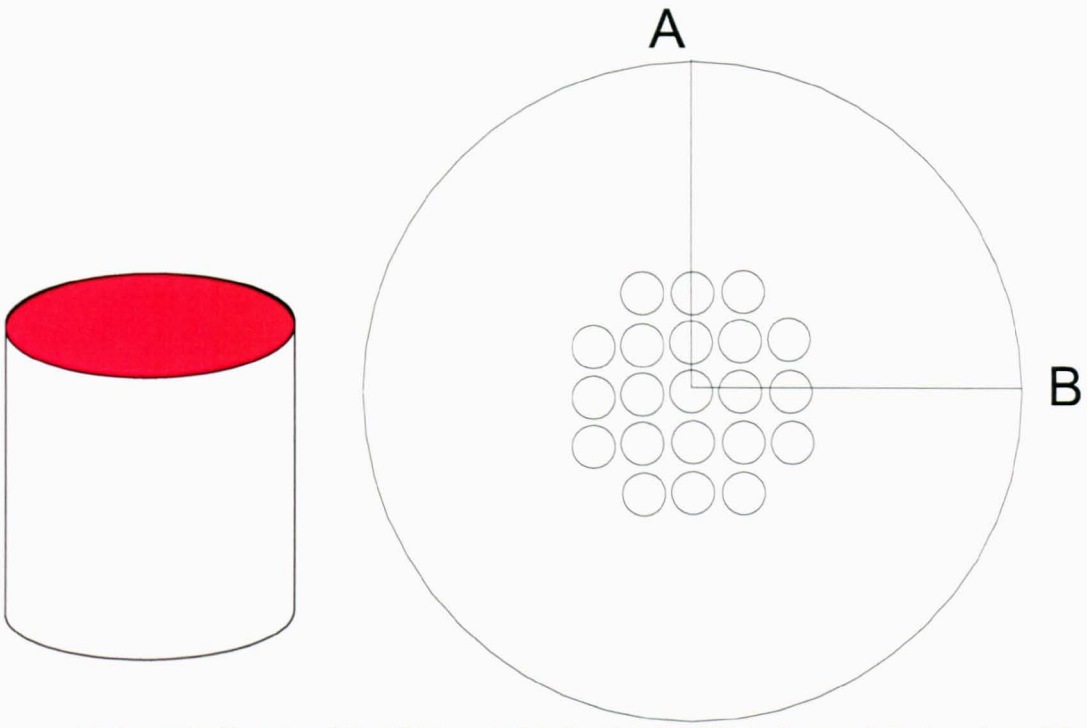

Figure 4.4 Schematic diagram of the billet material showing the billet plane and the location of the axisymmetric compression samples produced.

The test piece is placed in the jaws of the computer controlled thermomechanical compression machine (TMC) showed in Figure 4.6. Temperature is controlled via an N-type thermocouple, calibrated to +/- 1°C. If lubrication is required it is applied at this point to avoid further handling and disruption of lubricant coverage. The relevant instructions including test temperature, heating profile, strain and strain rate are input into the computer prior to testing. The testing apparatus in Figure 4.5 is shown schematically in Figure 4.6.

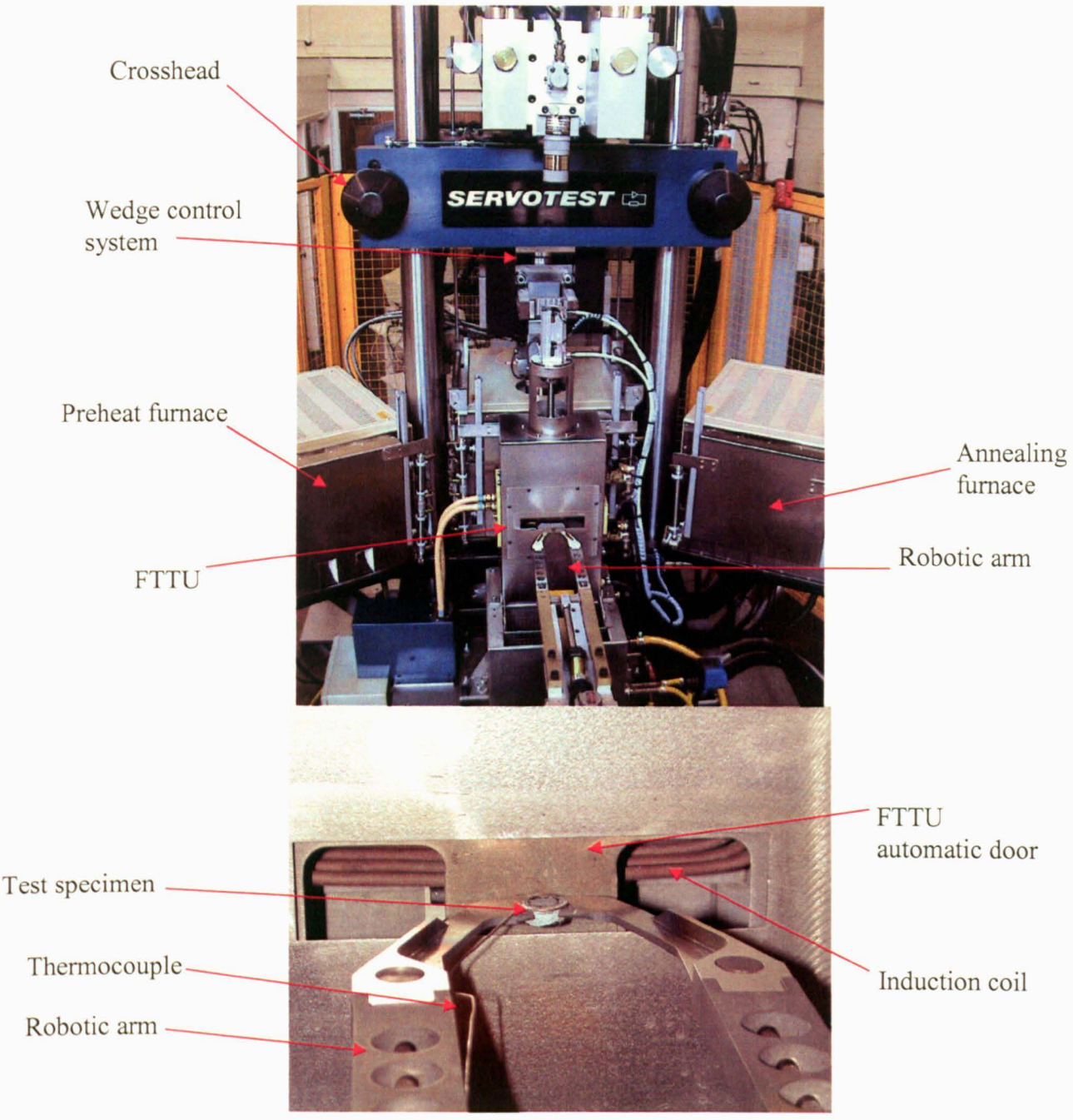

Figure 4.5 TMC apparatus at The University of Sheffield

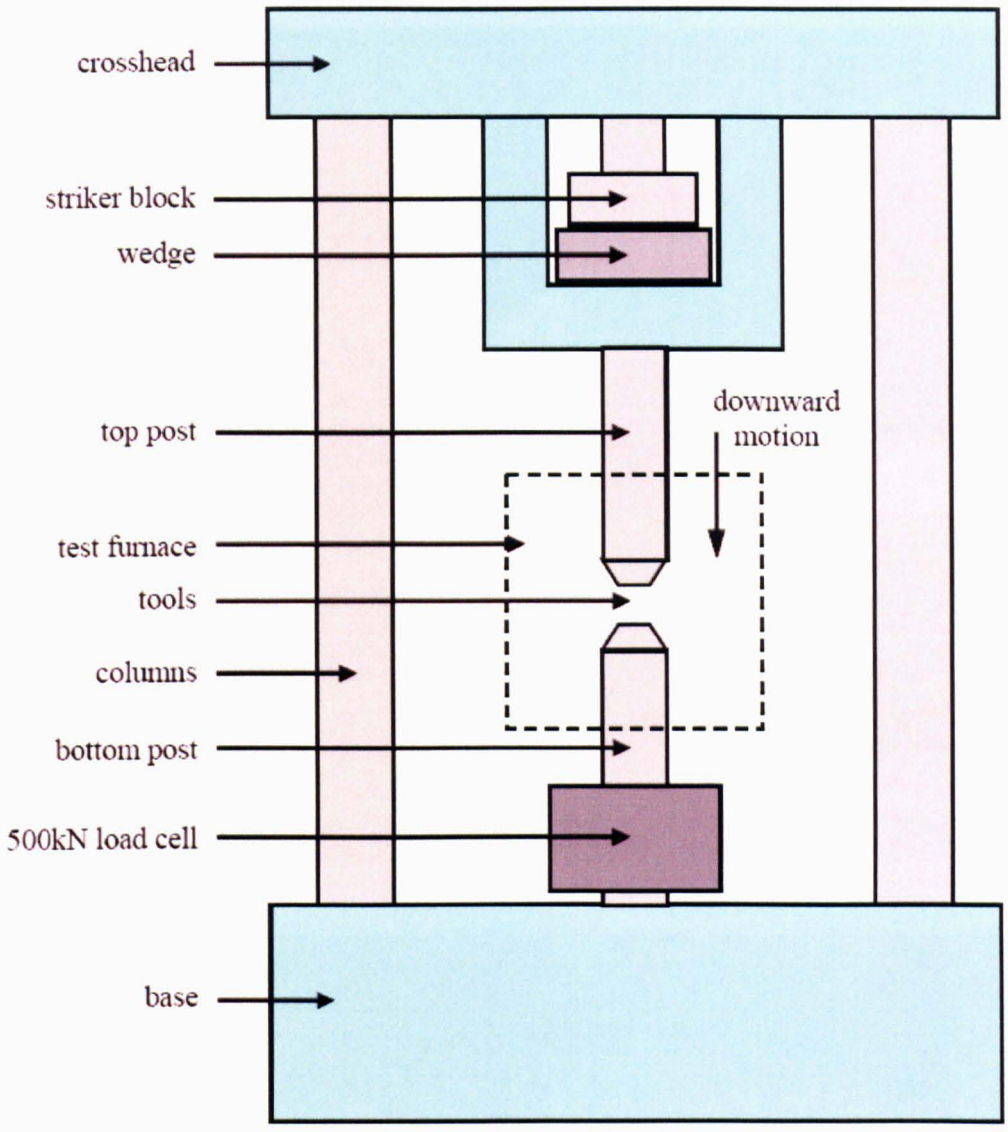

Figure 4.6 A schematic showing the location of the induction coil and tools within the testing furnace (Hinton, 2006).

The uniaxial compression test is split into 4 segments; heating, pre-treatment, deformation and cooling. The heating profile is carried out within the fast thermal treatment unit (FTTU) after which the sample is rapidly transferred to the deformation furnace for deformation. The forging platens are manufactured from M22 tool steel.

After deformation the test piece is transferred to the quenching unit and subjected to cooling at the desired rate. Once the test has finished the data, including time, temperature, load, displacement and velocity are taken from the computer and analysed and the deformed test piece, Figure 4.7 and Figure 4.8, is retained for microstructural investigation.

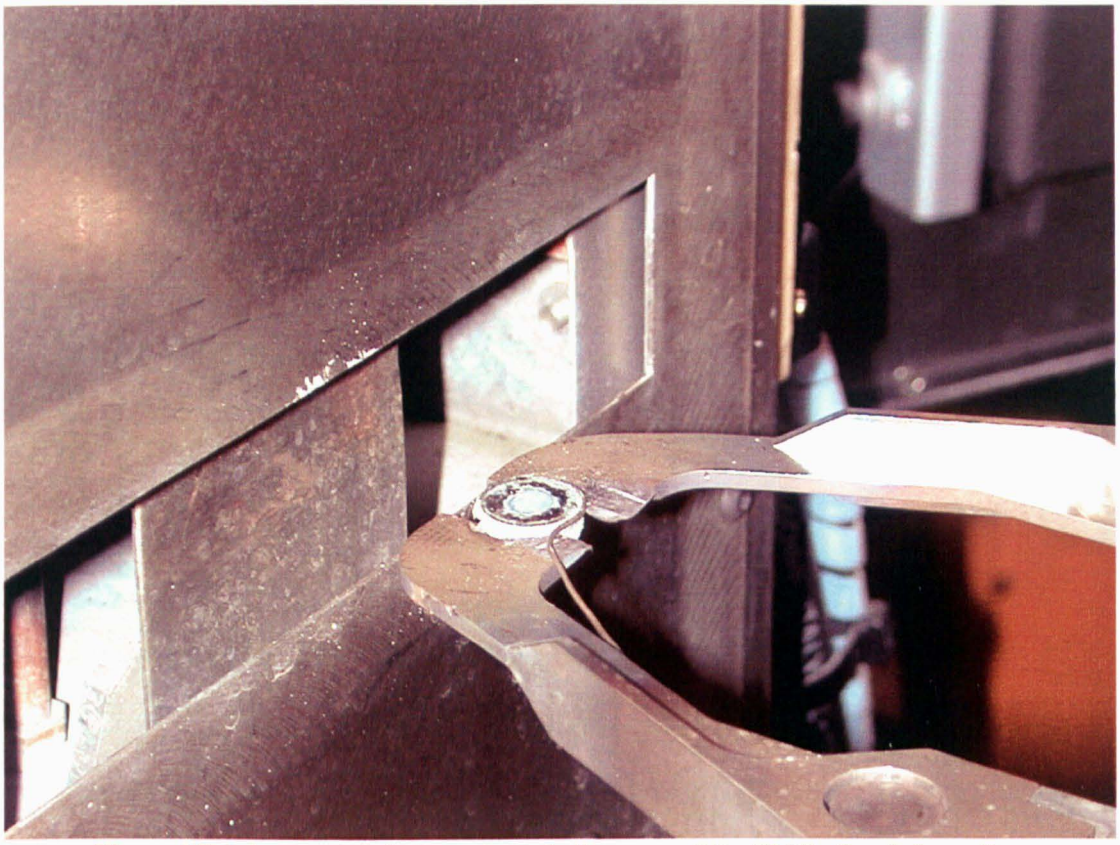

Figure 4.7 Axisymmetric test specimen in the arms of the TMC after deformation

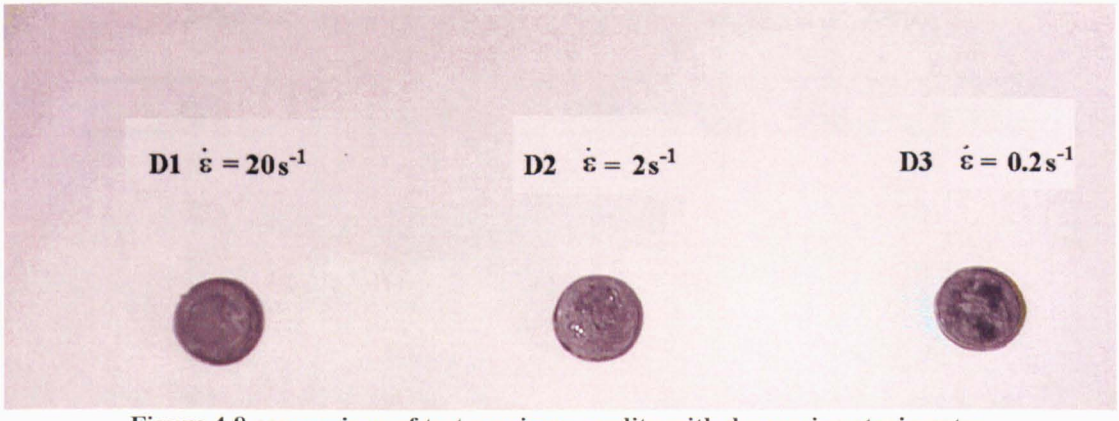

Figure 4.8 comparison of test specimen ovality with decreasing strain rates.

In order to carry out the aims of this work, a very simple simulation of the industrial forging routine was used, with the variable parameters being temperature, strain and strain Rate. In Figure 4.9 we can see the variable parameters schematically and Table 4.4 details each of the axisymmetric compression tests separately.

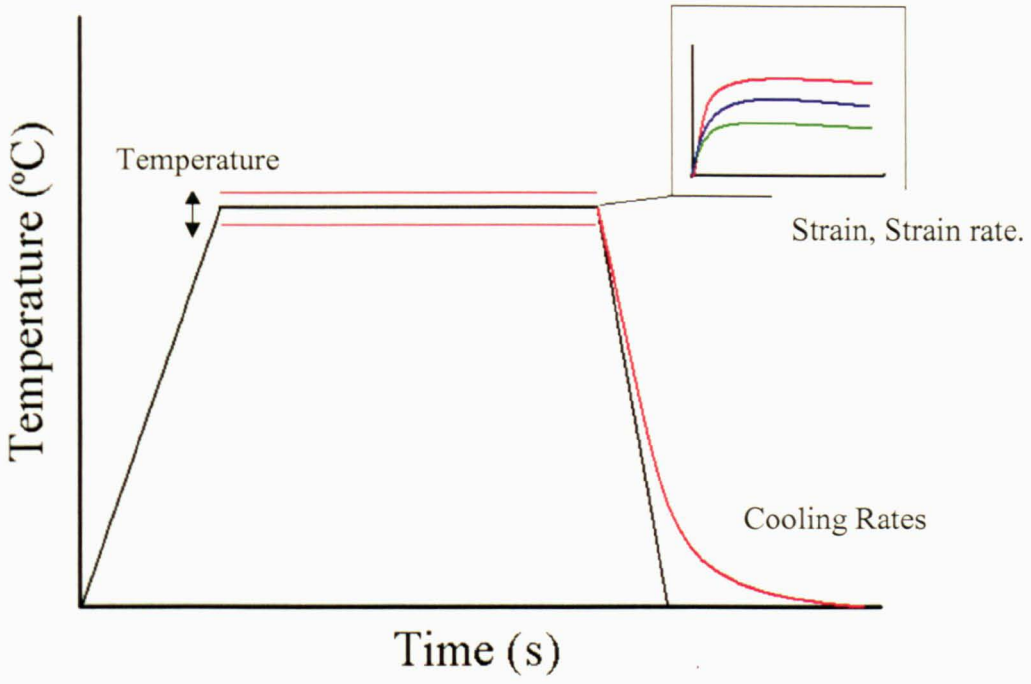

Figure 4.9 The Industrial forging simulation schematic, this diagram illustrates the variable parameters for this work.

Table 4.4 Testing Schedule for axisymmetric compression testing.

Test	*Strain*	*Strain Rate ($\dot{\varepsilon}$)*	*Temperature(°C)*
I1	0.3	2	1000
I2	1.5	2	1000
I3	0.15, 0.15	2	1000
I4	0.3	2	1000
T1	0.375	2	1000
T2	0.75	2	1000
T3	1.165	2	1000
T4	1.5	2	1000
T5	0.375	2	1010
T6	0.375	2	1010
T7	0.375	2	1010
T8	0.75	2	1010
T9	0.75	2	1010
T10	1.125	2	1010
T11	0.375	2	1010
T12	0.75	2	1010

T13	1.125	2	1010
T14	0.375	2	1010
T15	0.75	2	1010
T16	0.175	2	1010
T17	0.55	2	1010
IN1	0	0	1010
IN2	0	0	1010
IN3	0.375	2	1010
IN4	0.375	2	1010
IN5	0.375	2	1010
IN6	0.375	2	1010
IN7	0.375	2	1010
IN8	0.375	2	1010
D1	0.7	20	950
D2	0.7	2	950
D3	0.7	0.2	950
D4	0	0	990
D5	0.7	20	990
D6	0.7	2	990
D7	0.7	0.2	990
D8	0.7	20	1030
D9	0.7	2	1030
D10	0.7	0.2	1030

The schedule detailed in Table 4.4 allowed the investigation of the stated variable parameters within the time period and available material.

4.4.2 Compression test data analysis

The data obtained from the TMC is in the form of load (kN) and displacement (mm), which is converted into stress-strain curves using equations 4.3 and 4.4 (Roebuck et al, 2006).

Where, ϵ_c is the compressive strain, h is the instantaneous height of the sample and h_0 is the initial height of the sample

$$P = \frac{F}{A} \tag{4.3}$$

Where, P is the stress at a given time, F is the instantaneous load and A is the instantaneous cross sectional area of the sample, as calculated by equation 4.4.

$$A = A_0 \times \exp(\varepsilon) \tag{4.4}$$

Where, A is the instantaneous cross sectional area, A_0 is the original cross sectional area and ϵ is the instantaneous strain. There is an assumption being made here that there is no barrelling and the change in cross sectional area is linear during deformation. Further data analysis is documented later in this work in Chapter 5, where constitutive equations for the flow behaviour of this material are developed.

4.5 Metallographic Preparation and Examination

4.5.1 Introduction

For this research three types of material specimen were routinely investigated;

- Samples of the as-received billet,
- β approach curve determination samples, and
- axisymmetric compression test pieces.

The principles and techniques used for microstructural investigation remain the same whether the intention is to examine the test samples through optical or electron microscopy or whether they are to be used for EBSD analysis.

4.5.2 Sectioning

Sectioning of Timetal®834 was completed using a cutting disc with a low feed rate in order to reduce heat gained during machining. The specimens were sectioned in order to expose the area of interest using an Abrasimet, which is a hand operated abrasive rotating saw. Further cuts, where greater accuracy was required, were performed using an Accutom. This has a similar rotating wheel to the Abrasimet but is automated and can be programmed to cut to an accuracy of 0.1mm.

Due to flow behaviour and adiabatic heating illustrated in Figures 4.10(a) and (b) (courtesy of Michael Blackmore, The University of Sheffield) the axisymmetric compression samples were always sectioned at a quarter height in order to avoid the friction/geometry induced deadzone and the area of high deformation heating in the middle of the sample. This region also corresponded closest to the nominal deformation conditions imposed.

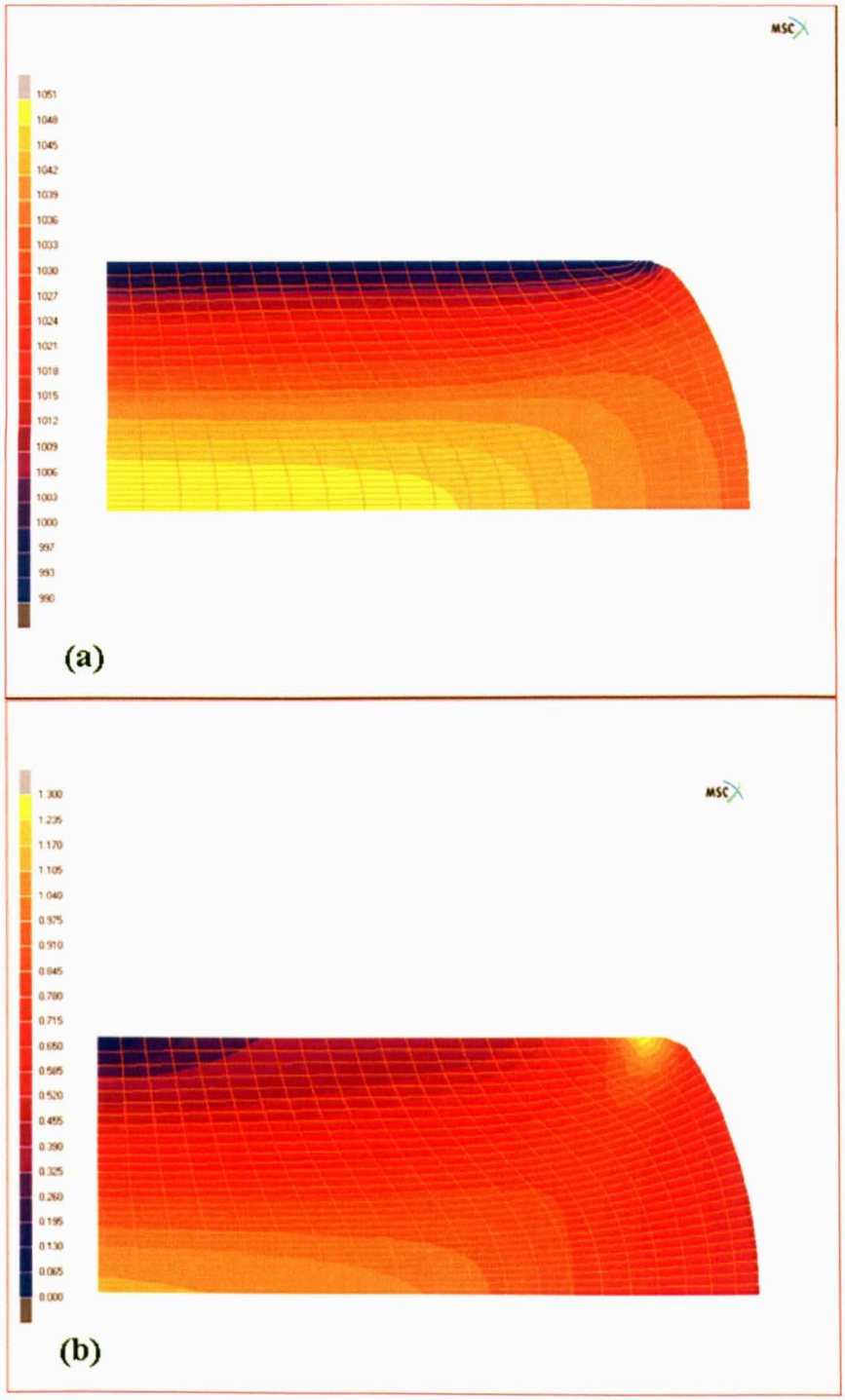

Figure 4.10 FEM of axisymmetric compression test showing (a) Temperature and (b) applied strain after a total applied strain of 0.7

4.5.3 Metallographic Preparation

The preparation of Timetal®834 for metallographic examination is made particularly difficult by the presence of the two microstructural morphologies and their different responses to mechanical grinding and polishing. Another problem of preparing titanium for microscopic observation is its high ductility, which makes titanium difficult to cut, grind and polish (Struers e-metalog guide, 2004).

The aim of specimen preparation was to create a flat, smooth clean surface ready for etching or EBSD. Each specimen was ground and polished using a Struers grinding system and a Struers Largo honeycomb pad with 9μm diamond suspension. Disc speeds of 150 rpm with loads of approximately 100N proved to give the best results. A final polish was achieved using colloidal silica (Silco of 0.05μm), a mechanical/chemical polish, which lead to an improved surface finish. To reduce the depth of the chemical polish associated with a Silco routine an addition of 10% H_2O_2 was added, this decreases the likelihood of shadowing during tilting in the SEM.

4.5.4 Etching

Once fully polished, before microstructural examination in an optical microscope was possible the specimen required chemical etching in order to show up the microstructure for analysis. Due to the high corrosion resistance of Timetal®834 standard chloride based etchants used on steels will not affect the surface of the specimen and, therefore, stronger fluoride based etchants such as Ammonium Hydrogen Di-fluoride or Hydrofluoric acid are needed. The etchants used in this work were;

Krolls Reagent;

- 1-3 ml HF
- 2-6 ml HNO_3
- 100 ml H_2O

And,

2% Ammonium Hydrogen Di-Fluoride;

- 2g Ammonium Hydrogen Di-fluoride (??)
- 100 ml De-ionised H_2O

Each etch involved submerging the specimen in the etchant for a period of 8-12 seconds followed by soaking in a lime solution for 30 seconds followed by holding in water for 60 seconds. The time of the submersion was dependant upon the microstructure of the specimen, it was observed that as the primary alpha volume fraction decreased the time for a good visible etched surface increased. Once fully etched the specimen's microstructure is immediately ready for optical examination using reflected light microscopy. It is important to analyse the sample immediately as the quality of the etched surface will decrease with time and therefore the specimen should be re-polished before re-etching to avoid pitting.

4.5.5 Optical Microscopy

Surfaces were observed under reflected light conditions at various magnifications. Images were captured digitally using an Image grabber and a Polyvar microscope with KSRun software. Graticules were also captured using the same microscopes under the same conditions. Optical microscopy was used for the samples throughout the process route and to provide qualitative and quantitative descriptions of microstructural changes. This allowed for inspection at macroscopic levels (low magnification), before proceeding to microscopic details at higher magnifications. Quantitative details that were of interest are grain size, grain shape, phase morphology and phase volume fraction and distribution.

4.5.5.1 Optical Grain Size Determination

Both computational and manual approaches were used to analyse the grain size of both morphologies present in the final microstructure. A commercial computer package, KSRun, was used to provide a number of measures from an optical image and the linear intercept method was used to determine the average grain size manually. The mean linear incept, $\bar{L}$, is the average distance between grain boundaries along lines placed at random on the plane of polish. The method of measurement involves counting the number of grain boundaries per unit length, $\overline{N_L}$ and defining $\bar{L}$ as;

$$\bar{L} = \frac{1}{\overline{N_L}} \tag{4.5}$$

Observations made on a plane section of an ideal material with grains of uniform size and shape would show a size variation from zero to a maximum tangent diameter of the grains in the volume. The frequency distributions of linear intercepts and of planar areas have been derived from this idealised structure, but for real metal, in which there is a distribution of grain sizes in the volume, the observed frequency distributions are wider than ideal.

4.5.5.2 Optical Volume Fraction Determination

Volume fraction analysis was used to determine the percentage of α_p in the microstructures. As with the beta approach determination work detailed in section 4.3, the polyvar microscope with KSRun software was used.

4.5.6 Scanning Electron Microscopy (SEM)

Initially the Camscam series 2 SEM and Jeol 6400 SEM were used for scanning electron microscopy, however as the work dictated the advanced Sirion field emission gun SEM (FEGSEM) was used as it possesses a much higher resolution capability and produces a much more consistent image quality. The SEM images were taken using Secondary and Back Scattered Electrons in order to obtain topographical and elemental information.

4.6 Texture Determination.

4.6.1 Introduction

As the texture evolution of the alloy is a major contribution of the work to be carried out, it has been critical to determine the texture of a number of test pieces after their various hot working and heat treatments. There are a number of ways to determine the texture of a specimen, three such ways have been chosen for this work, namely;

- X-ray goniometry
- EBSD (electron back-scattered diffraction) on the JEOL 6400

- EBSD on the Sirion FEGSEM (Field emission gun scanning electron microscope)

4.6.2 X-ray Goniometry

In order to use X-tray traces to determine the texture, it is necessary to first find the 2theta angles of the poles with the highest intensity using a standard 2theta scan of the specimen. Once this is done it is then possible to carry out an equal angle scan of each pole taking counts at all angles.

Initially a random sample of titanium powder bound together with a small amount of epoxy resin was scanned in order to have a random count so that proceeding results could be represented in terms of MRD. Once this was done it was possible to carry out counts on other specimens as desired, these were placed into the holder and held in place using plasticine. The specimens had to be flat and mounted flush with the holders face, ensuring no additional angle was imposed. Results from the scan were taken in terms of three datum angles, theses being theta, phi and chi. At each point counts were recorded for 2 seconds and tabulated, and these data files were then entered into a Visual Fortran program in order to convert them into an epf. file. The epf. files were then be entered into additional software developed at Los Alamos University called popLa in order to create an ODF diagram representing the texture distribution of the desired sample.

4.6.3 EBSD

Micro texture analysis on the JEOL 6400 involves good specimen preparation and a relatively easy microscope set-up procedure. As described in Section 2.14.3 the ease to which the back-scattered electrons can travel towards the camera the better the quality of the pattern. For this reason the surface finish of the sample is of high importance, grinding debris or a contaminated surface will affect the pattern quality, so together with standard metallographic preparation (Section 4.5) increased length of time for colloidal silica are required.

Once surface quality was sufficient the specimen was placed in the JEOL 6400 SEM using a tailored specimen holder measuring 8x10x5mm, aligned along an axis of interest and tilted to an angle of 70°. The angle reduces the depth of the interaction of

the specimen beam allowing the back-scattered electrons easier access to the detection camera. Area scans were then employed to examine a section of microstructure. The electron beam scans the area through a number of steps, and at each step the diffraction pattern is recorded and the orientation of the microstructure calculated. The step size is an important variable since it is the pixel size of the OIM image produced. For this reason the step size chosen should be considered based on the microstructural features under investigation and the time available on the microscope. Accuracy is increased with the decreasing step size, but this greatly increases the run `time. It is generally considered that for an accuracy of 5% in orientation determination, a minimum of 8 pixels per grain are required (Humphreys, 2001).

The EBSD acquisition software contains a number of variable parameters that will influence the acquisition time and quality of the kikuchi patterns produced. The quality of a kikuchi pattern can be improved through increasing the number of frames used for averaging and resolution of the frame taken. In general the more frames averaged, the better the quality of pattern produced, but this will increase the mapping duration as will increasing the resolution of the frame. From this averaged frame the background pattern (taken prior to the run) is subtracted and then the diffraction pattern is indexed and saved using the software.

The Sirion FEGSEM is much more powerful than the JEOL 6400, it uses a field emission gun (FEG) to achieve an electron beam with a smaller spot size. This leads to a much higher resolution than the JEOL 6400, because should the interaction volume fall over a number of grains they would not be singularly identified. However, if the beam were smaller it would be more likely that the interaction volume would fall within one grain. The same principal is applied when choosing the accelerating voltage during operation, as essentially there is a linear relationship between accelerating voltage and interaction volume for a specific element (Randle, 2000). If a high accelerating voltage is used then electron beam penetrates further and the interaction volume increases. An image of the internal chamber of the Sirion FEGSEM has been captured and can be seen in Figure 4.11. Once the sample has been tilted and the rarea of interest located, Figure 4.11(a), the HKL Nordlys EBSD camera is inserted, as seen in Figure 4.11(b).

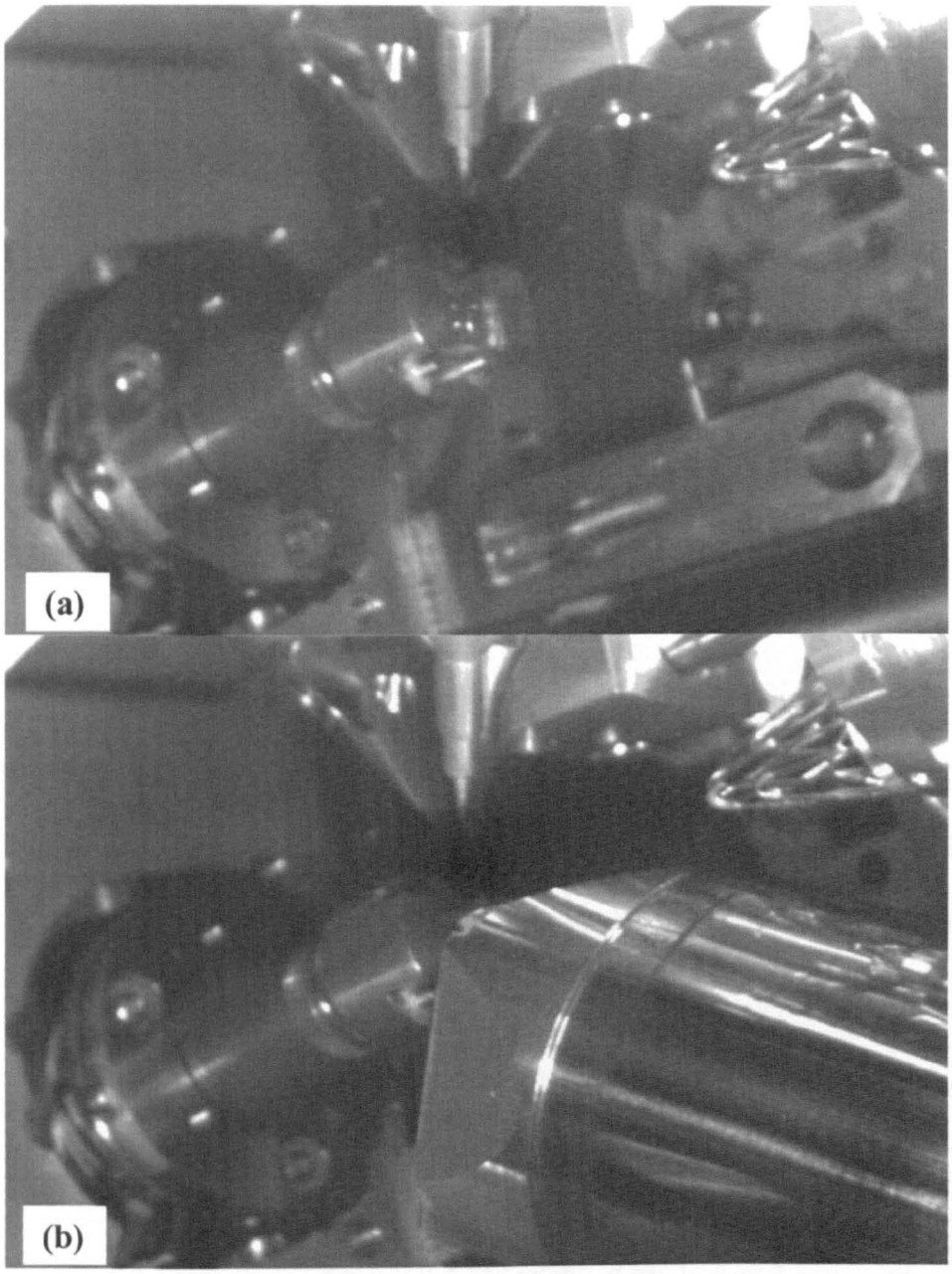

Figure 4.11 In-chamber CCD images from the FEI Sirion FEGSEM at the University of Sheffield showing (a) the specimen in the holder tilted to 70° and (b) with the HKL Nordlys EBSD camera inserted.

The Sirion FEGSEM has a unique in-lens detection system that allows ultra-high resolution imaging in both secondary and back-scattered modes at voltages down to 500V.

One of the major factors when using the FEGSEM for texture analysis is the time taken for mapping. There are a number of parameters that will affect the time taken to index a Kikuchi pattern. EBSD is based on the acquisition of diffraction patterns from bulk samples. This is known as orientation imaging microscopy (OIM) and area

scans of a sample surface can be obtained rapidly and automatically. Mapping Parameters used when using the FEI Sirion SEM for EBSD can be seen in Table 4.11.

Table 4.11 Mapping Parameters used in the Sirion FEGSEM

Parameter	*Values Used*
Magnification	200-400X
Beam Spot Size	3
Beam Voltage	15-20 keV
No of Background Frames	64
No of Averaged Frames	4-8
Timing per Frame	100-120
Step Size	0.25-3
Mapping Rate	0.8-1.2 s^{-1}
Camera Binning	4x4 or 8x8

4.6.3.1 Microscope Set-up

Figure 4.12 shows a schematic of the specimen and detector screen placement with the major reference axes illustrated.

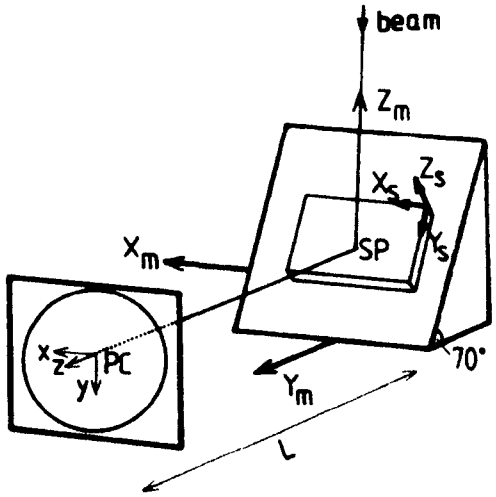

Figure 4.12 Microscope paramteres required for EBSD orientations measurements

The most important parameters in order to make orientation measurements from EBSD are; The co-ordinates of the pattern centre PC, the point on the phosphor which is closest to the excitation volume, the specimen-to-screen distance Z_{SSD} or L, the relationship between reference directions in the microscope X_m, Y_m, Z_m, specimen X_s,

Y_s, Z_s and screen pattern xyz. In this work the L value was set at 25mm, however, this was not an absolute value and calibration was completed before every run, the reference directions were as in Figure 4.14.

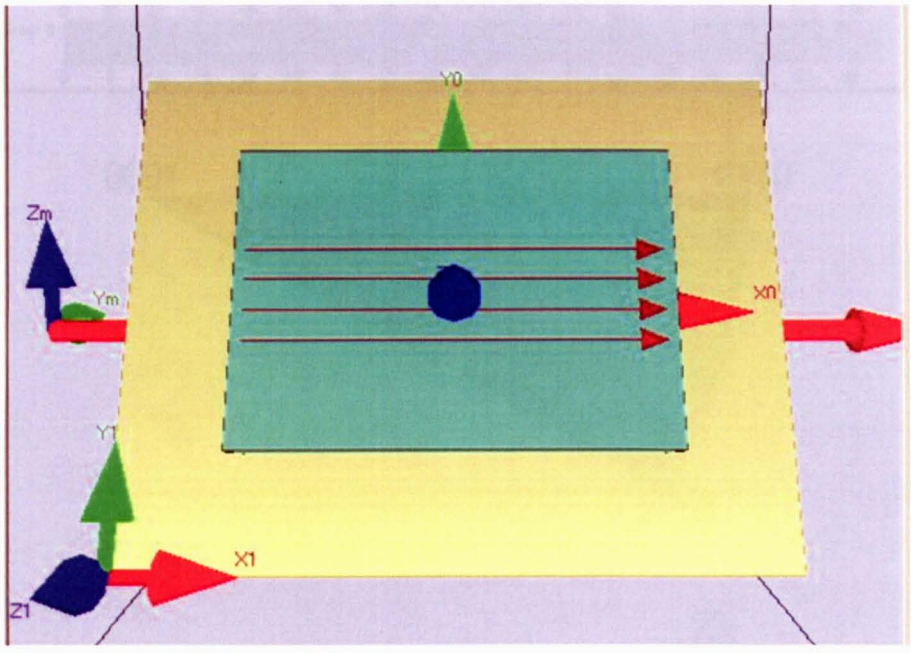

Figure 4.13 A schematic of the virtual chamber with the major reference axes illustrated

Another parameter important for EBSP acquisition is the working distance (WD) which is usually defined as the distance the specimen and the bottom of the pole piece. Within the Sirion FEGSEM the WD is calibrated at 14mm and this is maintained after tilting.

4.6.3.2 Presentation of EBSD data

EBSD data can be visualised in several different ways and this section will briefly explain the major representation techniques used in this work, this will be discussed further in Chapter 6. In this study, the most common methods of data presentation were a orientation image maps (OIM's) using both Euler and Inverse Pole colouring colouring based on the legends in Figure 4.14(a) and (b) and (0002) and $\{10\bar{1}0\}$pole figures. In Euler colouring maps, each pixel is a blend of the 3 colours in Figure 4.14(a) depending on the magnitude of each Euler angle. In IPF colouring, each pixel is coloured relating to the plane parallel with the stated plane, as illustrade in Figure 4.14(b)

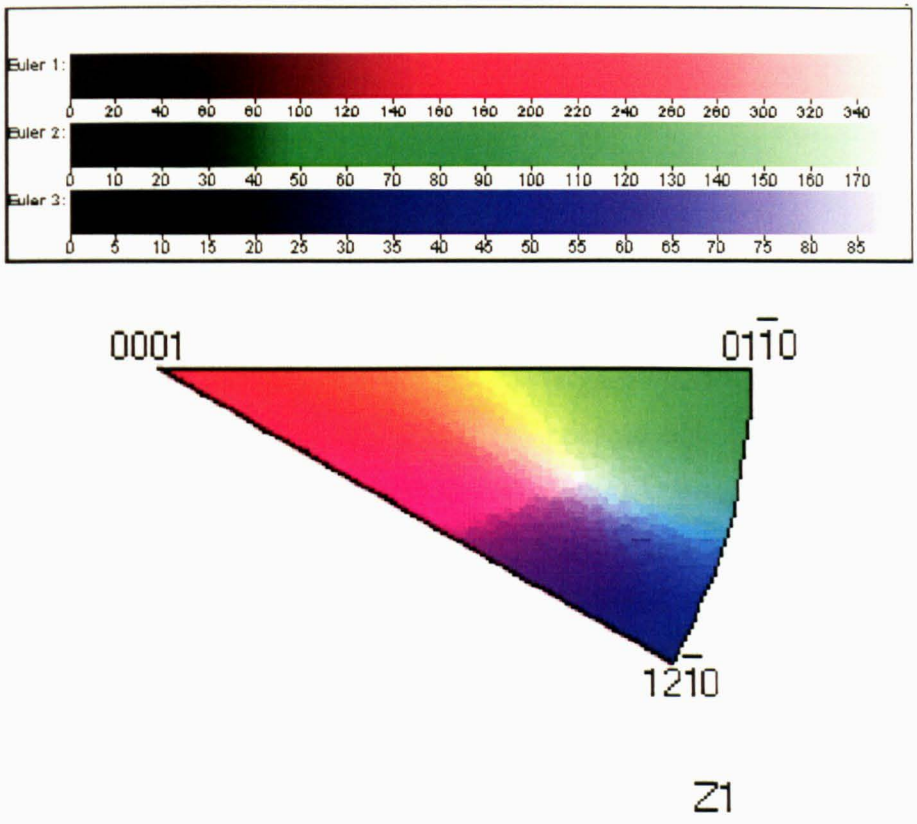

Figure 4.14 Legends illustrating the colour schemes in both(a) Euler colouring and (b) IPF colouring

In terms of the orientation information, IPF colouring was employed to initially present the results. This was because this technique allowed the crystallographic orientation in the specimen to be quickly interpreted in terms of the sample coordinate system. However, IPF colouring does not describe the texture completely as the method illustrates the pole parallel with the identified direction and as such does not give any idea of rotation about the direction of interest.

4.7 Summary

This chapter has provided a chronological guide through the experimental techniques used in this research, ranging from optical to electron microscopy procedures and axisymmetric compression testing. The following chapters illustrate and discuss how these methods were employed to investigate the microstructure and crystallographic texture evolution of Timetal®834 through the typical hot forging process route.

5. FLOW BEHAVIOUR ANALYSIS AND RESULTS

5.1 Introduction

The following chapter describes the axisymmetric compression testing and associated thermomechanical processing investigations completed during this work. The chapter begins with an analysis of the industrial forging operation using data received from Firth Rixson PLC with the aim being the determination of the processing range (e.g. strain, strain rate and temperature) occurring within a typical industrial forging operation. This would then determine the testing parameters used in subsequent uniaxial compression tests. Once these parameters were obtained initial compression testing began in order to assess the suitability of the TMC apparatus as the compression testing of Timetal®834 detailed in this work was the first of its kind using the TMC. Thus it was essential to prove the TMC was capable of carrying out testing of this type as well as maintaining the desired temperature profile via the FTTU. The ability to achieve repeatable results and the achievement of a uniform strain rate during deformation was also yet to be tested. Having determined the integrity of the TMC, testing was then undertaken to examine the flow behaviour as a function of the test variables. This data was then subsequently used to determine a value for the activation energy for deformation, Q_{def}, and to develop constitutive equations for the determination of flow stress as a function of strain, strain rate and temperature.

5.2 Industrial Data

The industrial data received from Firth Rixson PLC was taken from a Q-FORM finite element model, used at the Darley Dale works in order to understand the internal strain, strain rate and temperature gradients within a closed die forging. The data received was in the form of graphs showing the accumulation of strain at certain points within the forging during each blow, see Figure 5.1, as well as schematic diagrams showing the strain variation within the forging after each blow, see Figure 5.2. Using this information a graph accumulating the 5 heats and 17 blows over the entire closed die forging operation was constructed showing the total applied strain for each blow as well as average strain rates achieved. This information was then used to determine strain

and strain rate range for this work. The tracked point from which the data was obtained from the model was identified as the area in the final machined component which most susceptible to low temperature dwell fatigue determined by tests completed by Firth Rixson PLC.

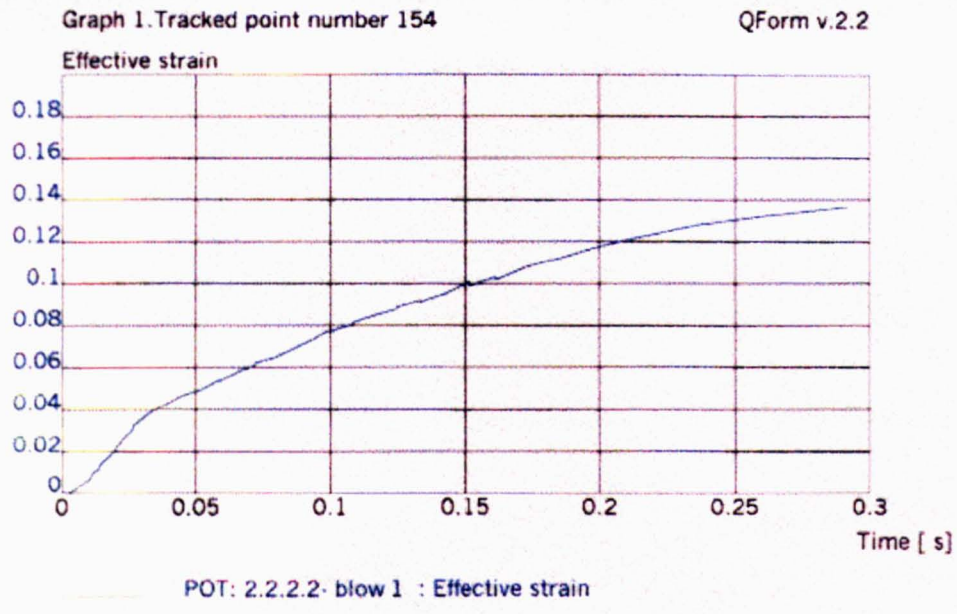

Figure 5.1 A graph showing the effective strain applied to point 154 during blow 1 taken from Q-Form model.

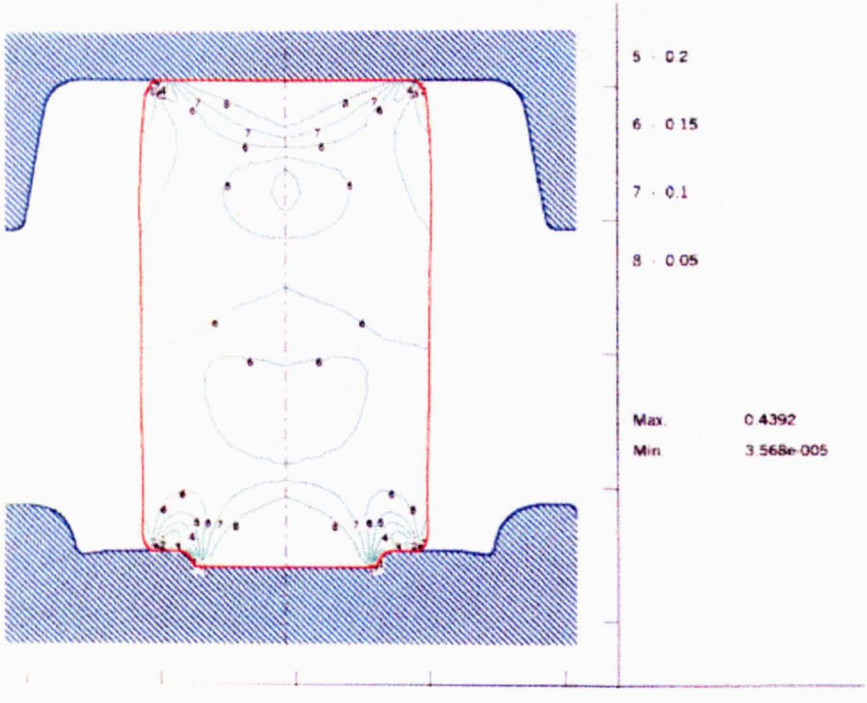

Figure 5.2 A schematic showing the effective strain gradients applied across a forging after blow 1 taken from Q-Form model.

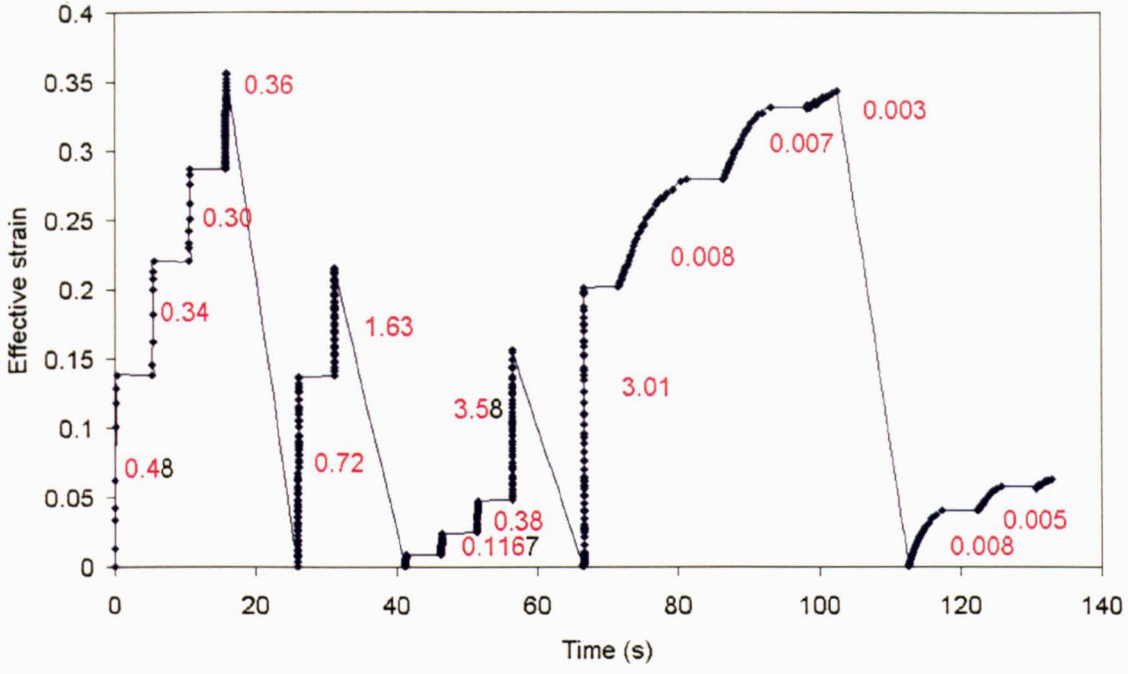

Figure 5.3 Graph showing the effective strain and strain rate (red) per blow during forging.

From Figure 5.3 it can be clearly seen that strain rates ranged between 0.002 and $30s^{-1}$ within the forging operation. Thus, in conjunction with the knowledge that 3 strain rates of increasing orders of magnitude were needed for constitutive equation development (Davenport et al, 2000), strain rate values of 0.2, 2 and 20 s^{-1} were decided upon for the axisymmetric compression testing. Figure 5.3 also shows the total applied strain per blow ranges from 0.02 to 0.2, whereas the total applied strain value per stage ranges from approximately 0.05 to 0.35, furthermore the total accumulated applied strain value is 1.1326. The Q-form model assumes that the strain value returns to zero after each heat, however the possibility that this is not the case and some strain remains in the material may need to be considered. As such, the parameters for investigation have been chosen with the possibility of strain accumulation with applied strains ranging from 0.15 to 1.5. As mentioned previously, the optimum combination for creep and fatigue properties for this alloy are obtained with an α_p volume fraction of roughly 15% and as such industrial forging temperatures are set to achieve this. Running in parallel with the β approach curve determination work the temperatures selected for axisymmetric testing ranged from 950 -1030°C

Table 5.1 summarises the parameter limits chosen for further investigation.

Table 5.1, Variable parameter limits determined from industrial data

Parameter	*Industrial values*	*Parameter limit*
Temperature	1000-1010	950-1030
Applied Strain	0.02-2	0-1.5
Strain Rate	0.002-30	0.2-20

5.3 Initial Testing and Analysis

5.3.1 Introduction

The modelling of a metal's flow behaviour during industrial thermomechanical processing is necessary in order to improve the mechanical efficiency of the operation as well as improving our understanding of the dynamic microstructural changes taking place during deformation. The development of constitutive equations for modelling the hot working of metals has been well documented in work by Davenport et al (2000), Lin et al (2003), and Sellars et al. (1995) and is based on the assumption that the mechanical state of the material is solely a function of strain, strain rate and temperature. Constitutive equations are then derived in two stages;

1) First stage equations are derived from discrete points on the flow stress curve; these points relate the stress at these values to the calculated value of Z (a temperature compensated strain rate).
2) Second stage equations then describe the continuous flow stress curves and are derived from the first stage equations and additional information.

Thus, the key to developing confidence in constitutive equation development is ensuring that the experimental flow stresses being used in there formulation have been obtained under rigorous experimental conditions. In order to achieve this goal we needed to first assess that the TMC machine was capable of testing of this nature, i.e. uniaxial compression, and that the data was reliable and consistent. Secondly, tests were needed to determine the friction coefficient for Timetal®834 against the M22 tool steel

platens under the conditions of these tests to remove any friction contribution from the flow stress curves.

5.3.2 Integrity Tests

Initial compression tests to prove the integrity of the TMC testing apparatus are referred to in this work as the integrity tests. The tests I1-I4 are detailed in Table 5.2 and the results are shown in Figures 5.4-5.7. Note that test I3 was a double hit test.

Table 5.2 Initial testing parameters

Test	*Strain*	*Strain Rate*	*Temperature*
I1	0.3	2	1000
I2	1.5	2	1000
I3	0.15, 0.15	2	1000
I4	0.3	2	1000

The stress-strain curves were constructed by initially calculating strain, ϵ, using equation 5.1;

$$\varepsilon = \ln \frac{h_0}{h} \tag{5.1}$$

Where h_0 is the initial height of the test piece corrected for thermal expansion and h is the instantaneous height during deformation. The cold h_c measurements were used to calculate the hot height of the specimen using equation 5.2;

$$h_0 = h_c + \alpha_t h_c (T - T_0) \tag{5.2}$$

Where α_t, is the thermal expansion coefficient for Timetal® 834 at 10.9 x 10^{-6} which was assumed to be constant throughout the temperature range), T and To are the temperature of the test and temperature when the test piece was measured in Kelvin. Thus the instantaneous height, h, of the specimen during deformation can be calculated by equation 5.3;

$$h = d_p - h_0 \tag{5.3}$$

Where d_p is the cross head displacement.

The true stress, σ, is then calculated using equation 5.4;

$$\sigma = \frac{F}{A} \tag{5.4}$$

Where F, is the measured load and A is the instantaneous cross sectional area and is determined from the instantaneous height assuming a constant volume and no sample barrelling.

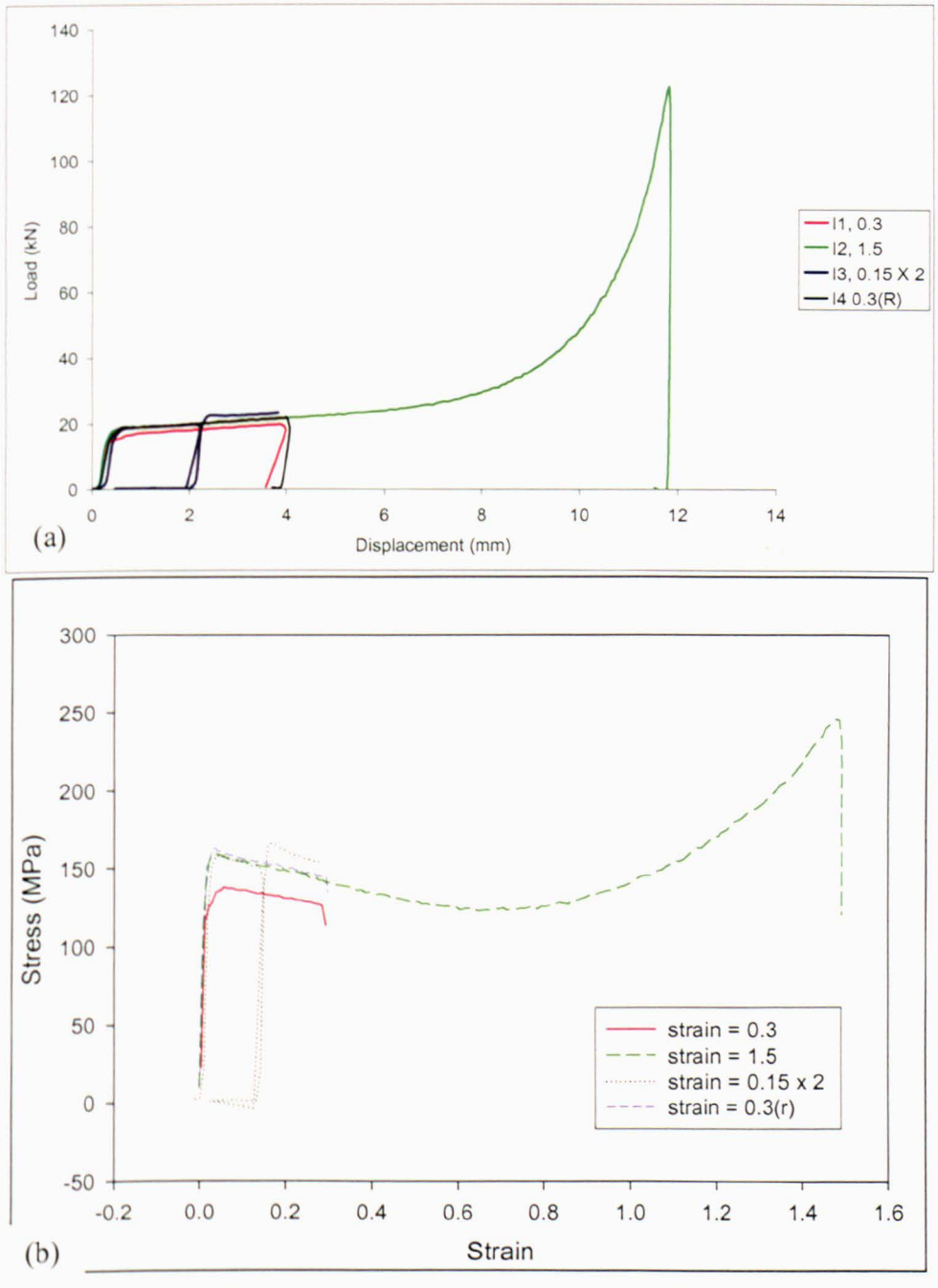

Figure 5.4(a) Load vs Displacement and (b) Stress-strain curves for the initial axisymmetric compression tests completed.

Figure 5.4(a) shows the raw load displacement curves and Figure 5.4(b) shows the stress-strain curves without any corrections for temperate rise, friction or test piece barrelling. Figures 5.5(a) and (b) show the temperature at the centre of each test specimen during heat up and deformation. The velocity of the deformation actuator and the temperature rise due to deformation as a function of strain are shown in Figures 5.6 and 5.7 respectively.

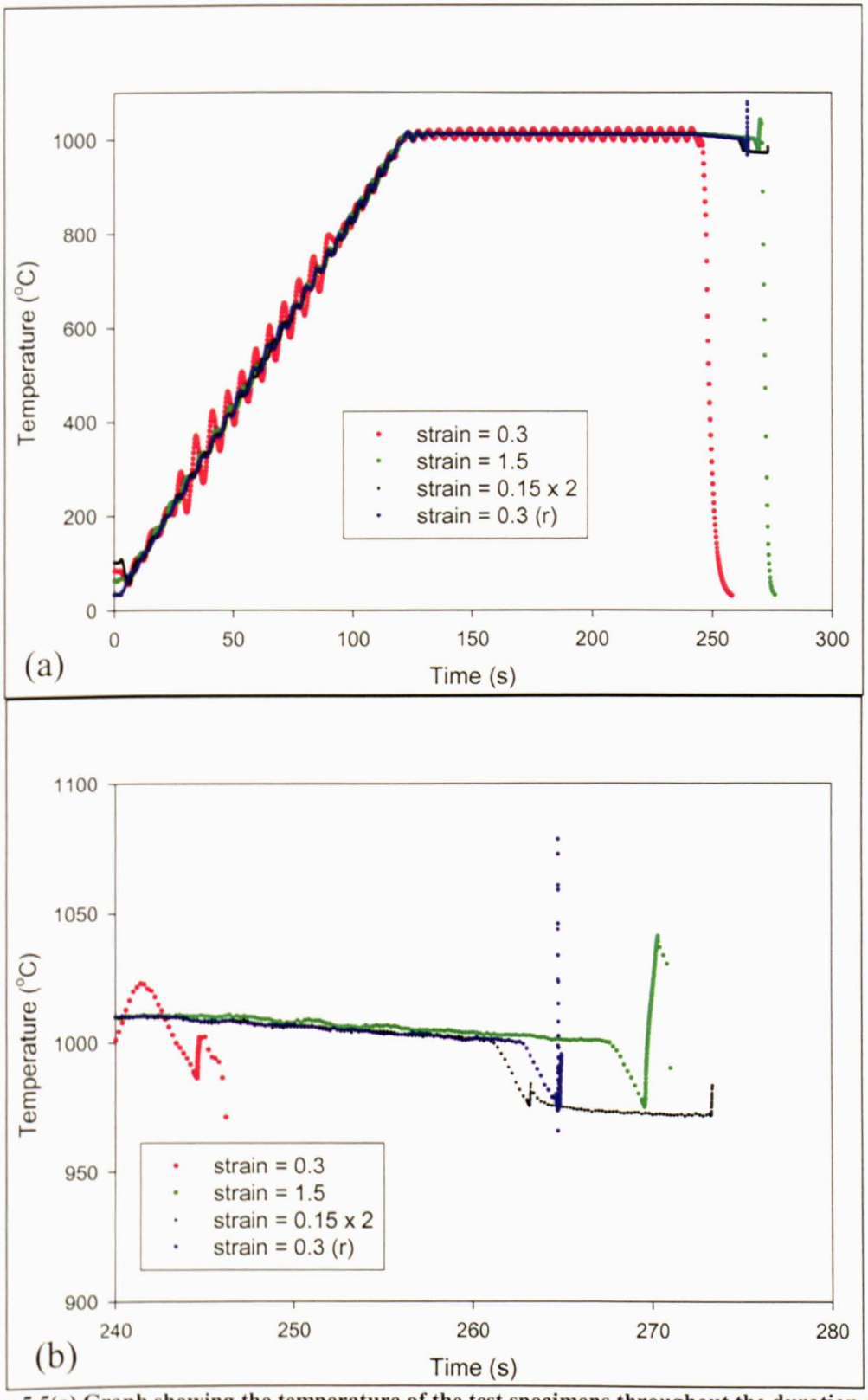

Figure 5.5(a) Graph showing the temperature of the test specimens throughout the duration of the test and (b) a more detailed view of the deformation only.

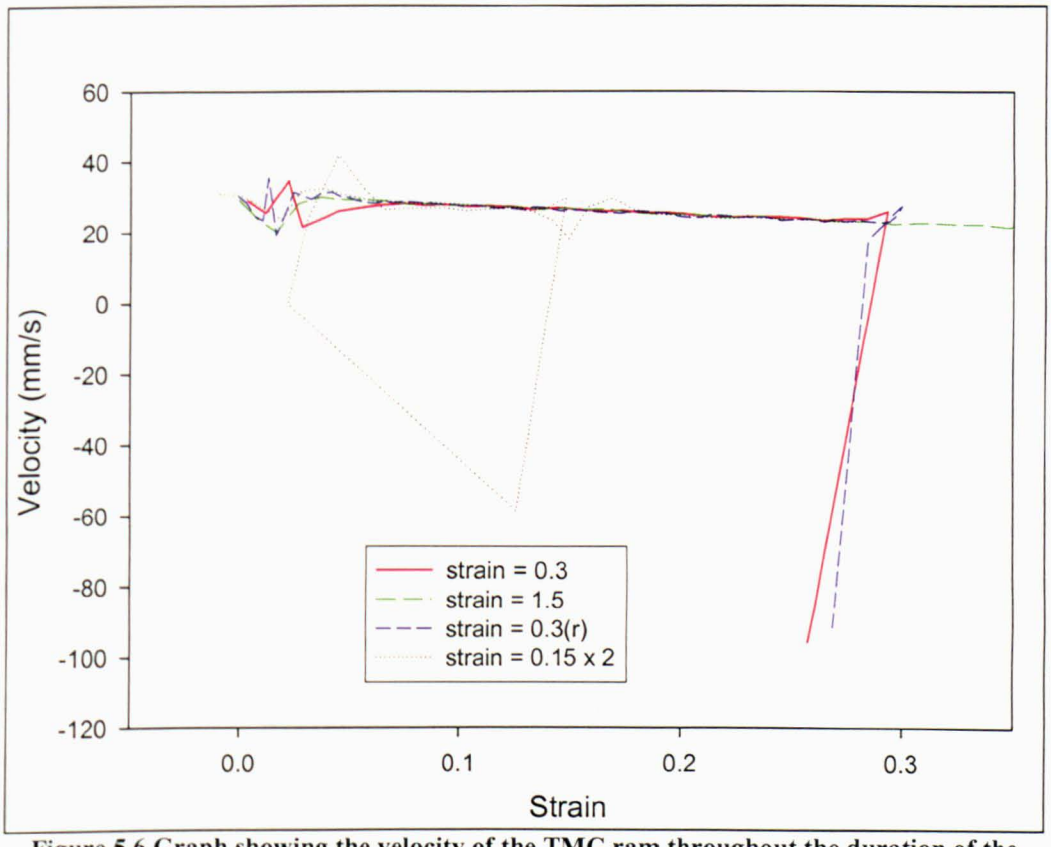

Figure 5.6 Graph showing the velocity of the TMC ram throughout the duration of the deformation.

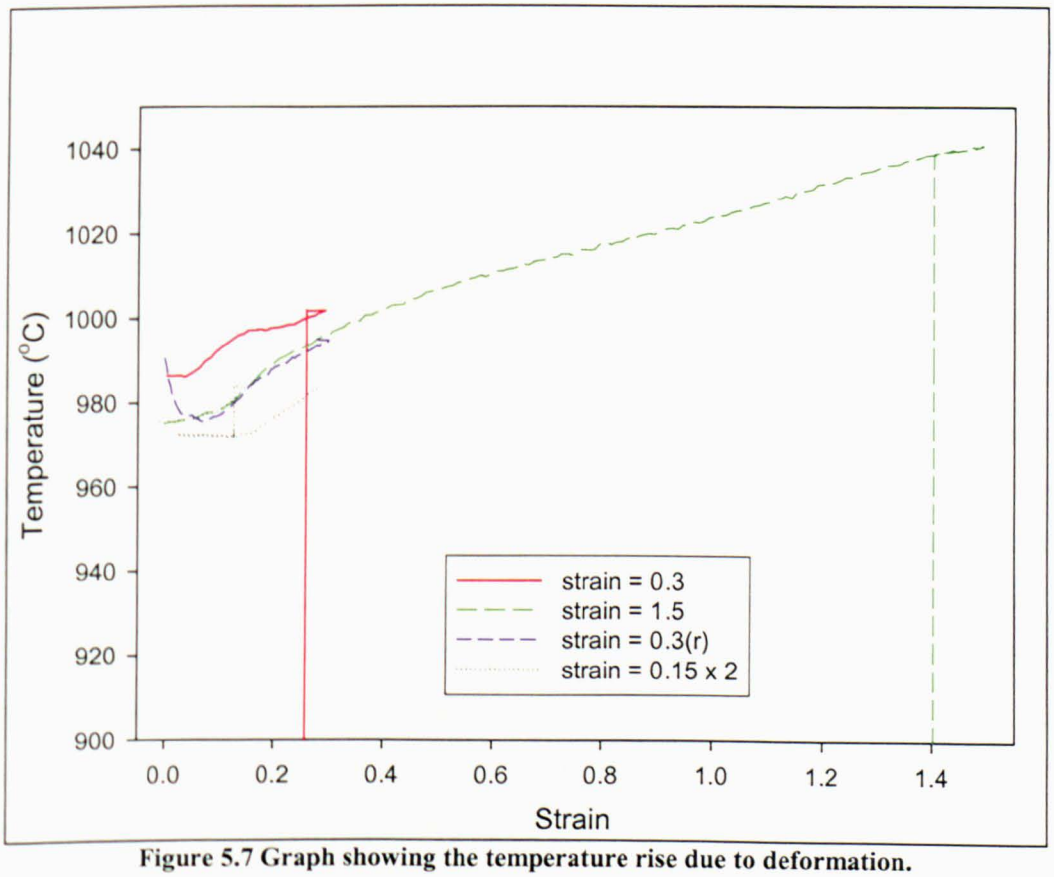

Figure 5.7 Graph showing the temperature rise due to deformation.

5.3.2.1 Summary of integrity testing

The raw load-displacement curves of the integrity tests I1-I4 (Figure 5.4(a)) should have, at least theoretically, shown 4 curves which follow the same trend but it is clear that this is not the case. Converting this information into stress-strain curves, as in Figure 5.4(b) yields the same conclusion. Only the curves for I2, I4 and the initial blow of I3 overlap closely whilst the second I3 blow and I1 record higher and lower strength, respectively. This could suggest non-repeatability in the test itself but closer analysis of the data in Figure 5.5(b) indicates that the samples were not deformed under the exact same test conditions. For example, the difference in peak stresses can be explained by looking at the temperature at the start of each of the tests in Figure 5.5(b) which have up to a 20°C difference. This is also the most likely reason that flow behaviour of the second blow of I3 does not continue the trend as seen in the first blow. There are also a number of other issues highlighted by Figure 5.5(b) that need be discussed here, most notably the oscillation in temperature during the pre-treatment. This is believed to be caused by poor coupling between the thermocouple and the test piece leading to uncertainty in the control. This phenomenon was eliminated in all subsequent tests by ensuring the thermocouple was inserted fully in to the test piece and secured tightly. Secondly, there is clearly a difference in the time delay from the end of the pre-treatment after 245 seconds and the onset of deformation. This is due to the position of the test specimen in the robotic arms and the final height dimension of the test piece. As the test specimen sits in the robot arms, the curvature of the grips ensure that the specimen is held laterally central, however, because there is no vertical restraint the specimen can sit high or low by as much as ±1mm. This difference leads to a difference in the gap required between the tools allowing the specimen smooth access prior to deformation. An increase in the gap between the tools leads to a difference in the time taken from the end of the pre-treatment to the contact of tools with the test specimen

It is a direct result of these issues and the thermal conductivity of this alloy that the temperature at the start of each test is not constant. The variation in the test temperature and its effect on the load experienced can be seen in Table 5.3 and Figure 5.8. The almost linear nature of the graph in Figure 5.8 would suggest that the variation in load experienced is a direct result of the start temperature of deformation. It was,

therefore, concluded that testing could continue with confidence but accurate knowledge of the true start temperature was required.

Table 5.3 Effect of temperature of yield value

Test	*Yield*	*Temperature*
I1	16.39	986.4066
I2	18.41	974.7335
I3	17.67	990.4693
I4	19.031	975.5637

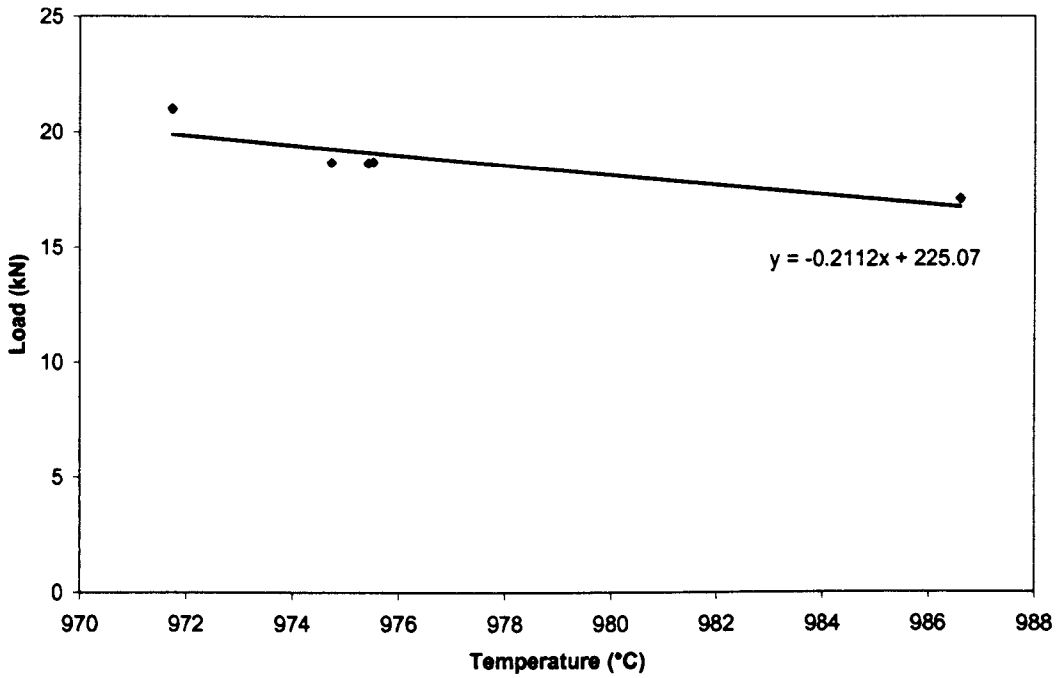

Figure 5.8 Show the temperature sensitivity of this alloy, the peak load is represented against the temperature at the start of deformation

5.3.3 Testing

As described previously for the purpose of determining the discrete points for the development of the constitutive equations the following tests, detailed in Table 5.4, were completed.

Table 5.4 Testing schedule for constitutive equation development

Test	*Temperature*	*Applied Strain*	*Strain rate*
D1	950	0.7	0.2
D2	950	0.7	2
D3	950	0.7	20
D4	990	0.7	0.2
D5	990	0.7	2
D6	990	0.7	20
D7	1030	0.7	0.2
D8	1030	0.7	2
D9	1030	0.7	20

The stress strain curves for tests D1-D9 without any correction factors are shown in Figures 5.9-5.11. As expected the flow curves show the standard response to changes in strain rate and temperature with the highest flow stress observed for the highest strain rate and lowest temperature and the lowest flow stress observed for the lowest strain rate and highest temperature combination.

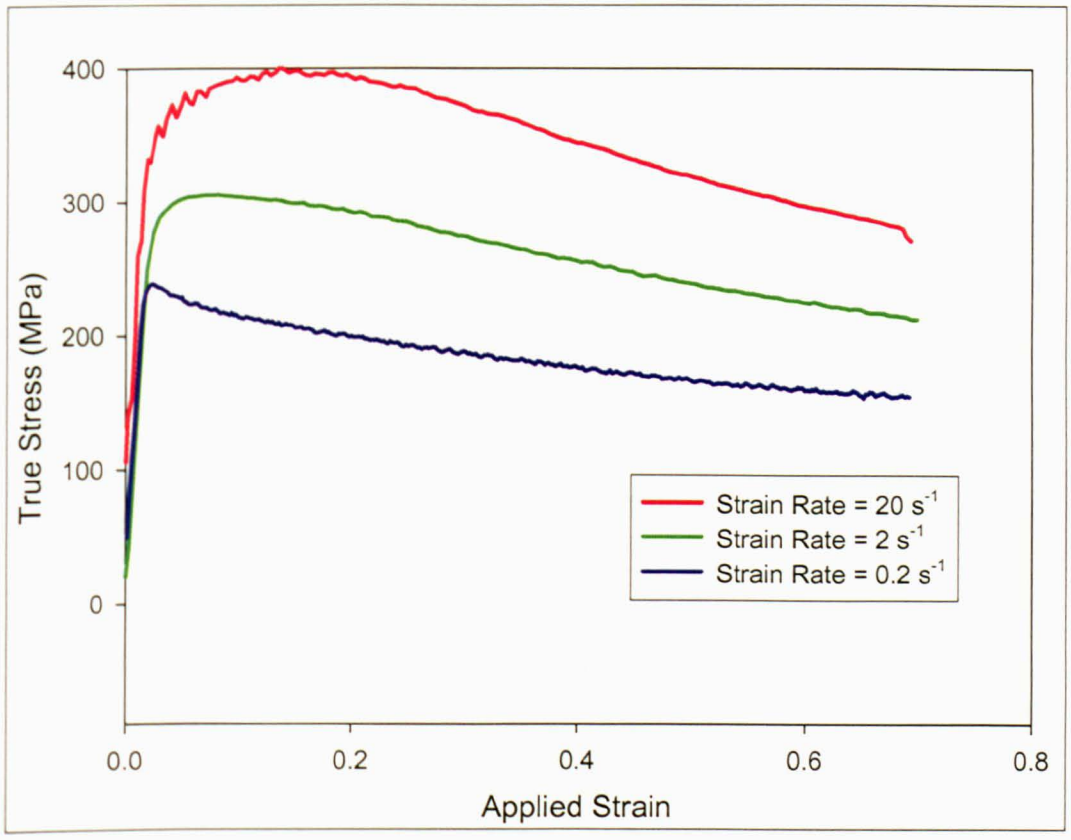

Figure 5.9 Initial stress-strain curves at 950°C.

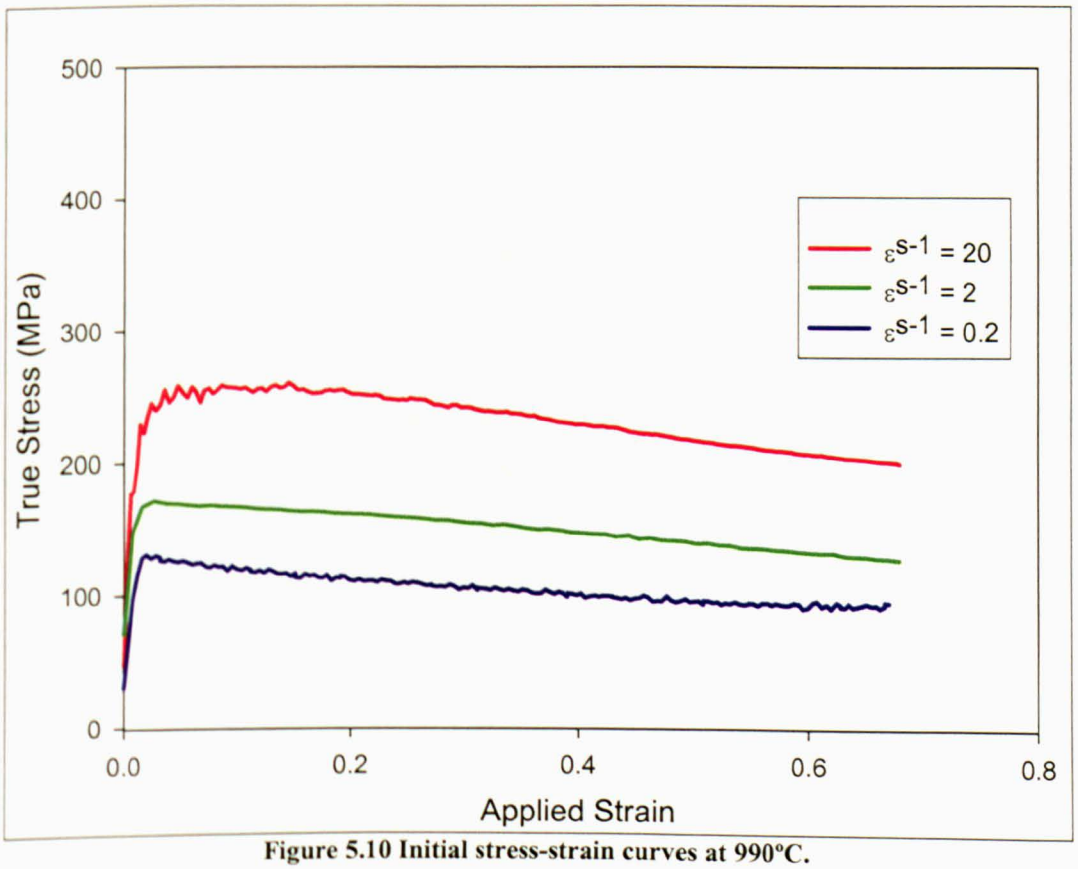

Figure 5.10 Initial stress-strain curves at 990°C.

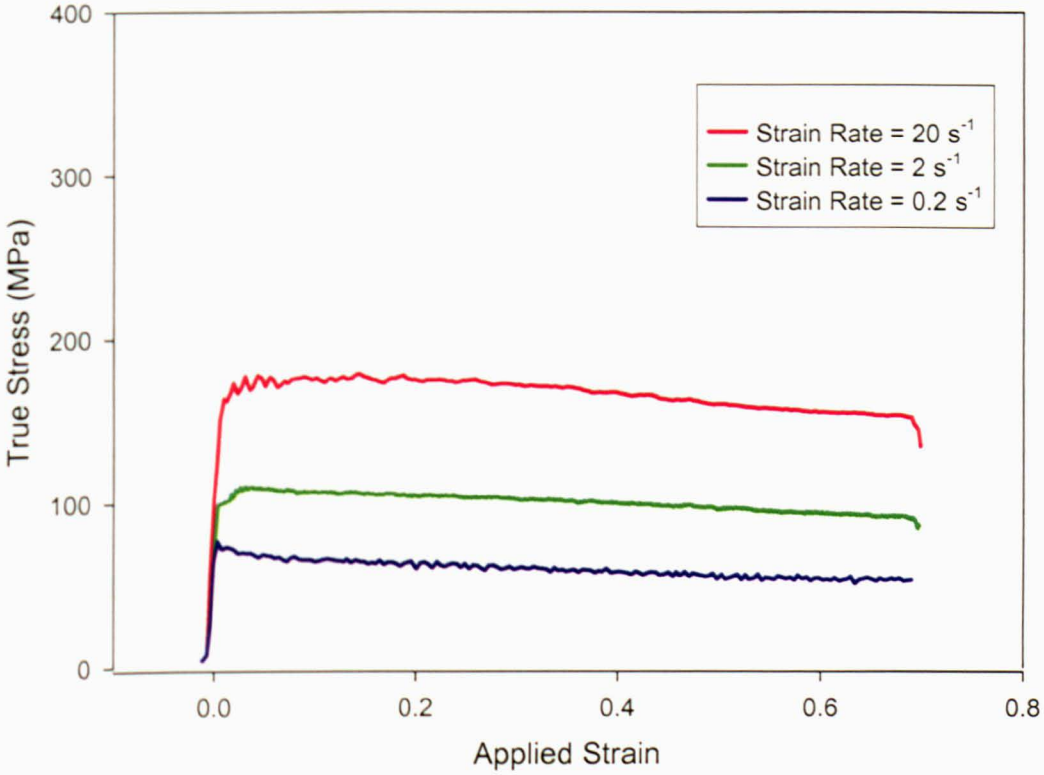

Figure 5.11 Initial stress-strain curves at 1030°C.

In order to characterise the discrete points in the first stage equations the above curves were first required to be corrected for friction and adiabatic heating, this procedure is outlined in the following section, Section 5.3.4.

5.3.4 Friction Coefficient Determination

Two methods were used to calculate the friction coefficient, μ: 1) the variation in dimension test and 2) the ring compression test. For the variation in dimension tests the sample diameters were kept constant and the heights were varied as shown in table 5.5 and the initial stress-strain curves for tests deformed to an applied strain of 0.7 at strain rates of $2s^{-1}$ can be seen in Figures 5.12-5.14.

Table 5.5 Test Specimen Geometry

Sample	*Before test*	
	Height/mm	Diameter/mm
Friction 1	12.05	12.01
	12.05	12.02
	12.06	12.01
	12.05	12.00
Mean	12.05	12.01

Sample	*Before test*	
	Height/mm	Diameter/mm
Friction 2	13.45	12.04
	13.42	12.04
	13.42	12.05
	13.48	12.05
Mean	13.44	12.05

Sample	*Before test*	
	Height/mm	Diameter/mm
Friction 3	15.11	12.13
	15.11	12.12
	15.11	12.12
	15.11	12.11
Mean	15.11	12.12

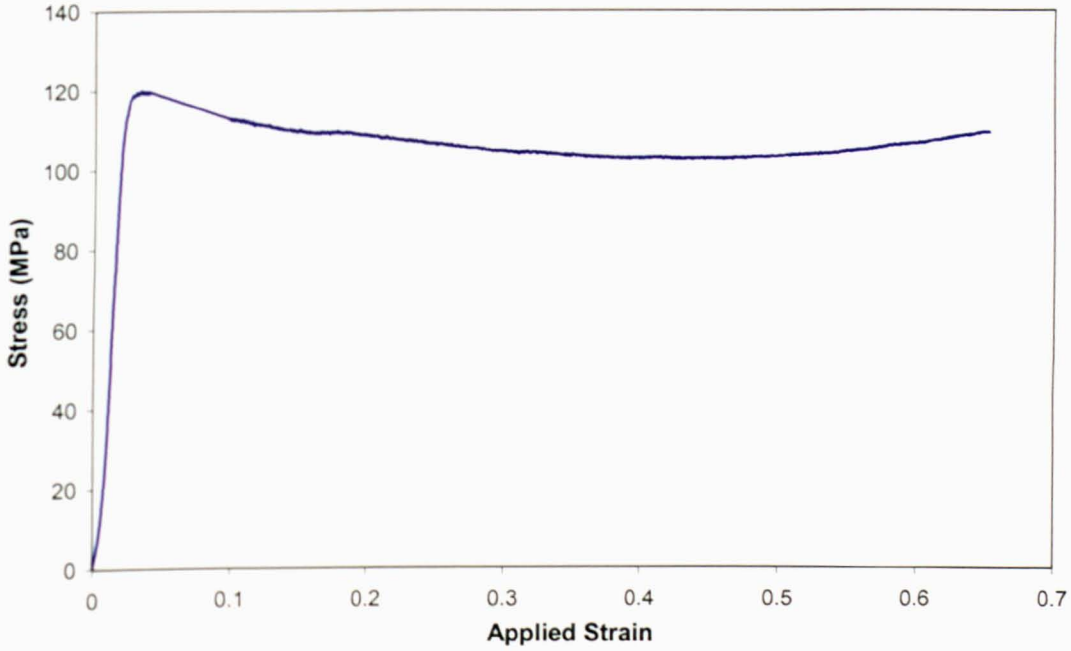

Figure 5.12 The stress-strain curve for geometry with aspect ratio 1

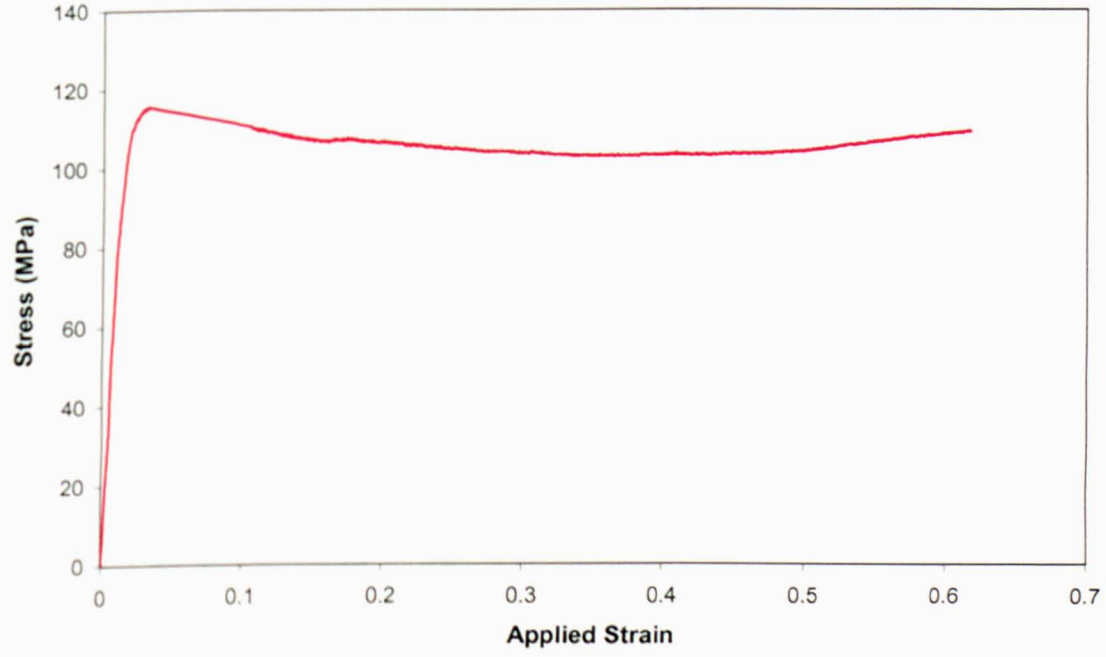

Figure 5.13 The stress-strain curve for geometry with aspect ratio 1.125

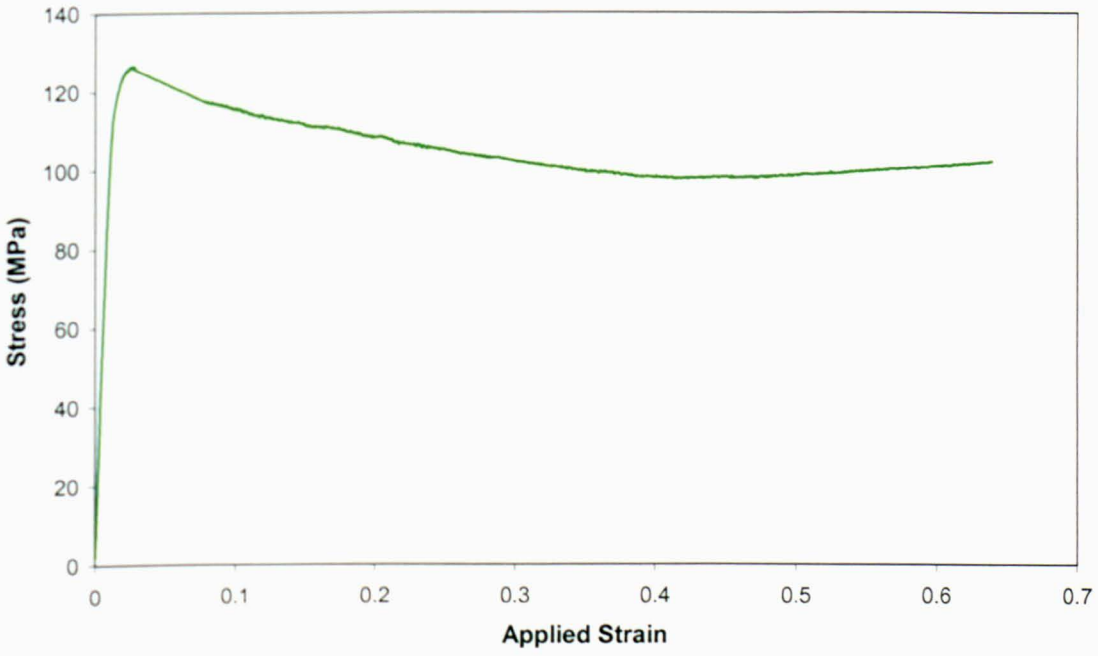

Figure 5.14 The stress-strain curve for geometry with aspect ratio 1.25

Using the curves the friction coefficient μ, can be calculated by applying a friction correction equation to the measured stress, which results in a value of true stress being obtained. If the value of μ used in the equation is equal to the true friction occurring during deformation, then the flow behaviour will be similar for each of the tests completed as the effect on the flow behaviour caused by friction (affected by geometry) will have been removed, i.e., we can calculate an equivalent von Mises (or tensile) stress for the more complicated deformations that have been generated by the interfacial friction.

The friction correction Equation 5.5 is applied as below;

$$P = \frac{R}{2}\left[\frac{h}{\mu d}\right]^2\left[\exp\left[\frac{\mu d}{h}\right] - \frac{\mu d}{h} - 1\right] \tag{5.5}$$

Where P is the mean pressure, R is the true stress, h is the sample height, d is the sample diameter and μ is the coefficient of friction. As we know the mean pressure P, by rearranging Equation 5.5 into the form of Equation 5.6 we can obtain a value of friction corrected true stress and curves can be plotted.

$$R = \frac{2P}{\left[\frac{h}{\mu d}\right]^2\left[\exp\left[\frac{\mu d}{h}\right] - \frac{\mu d}{h} - 1\right]} \tag{5.6}$$

Figures 5.15 -5.19 show the friction corrected stress-strain curves using various values for μ.

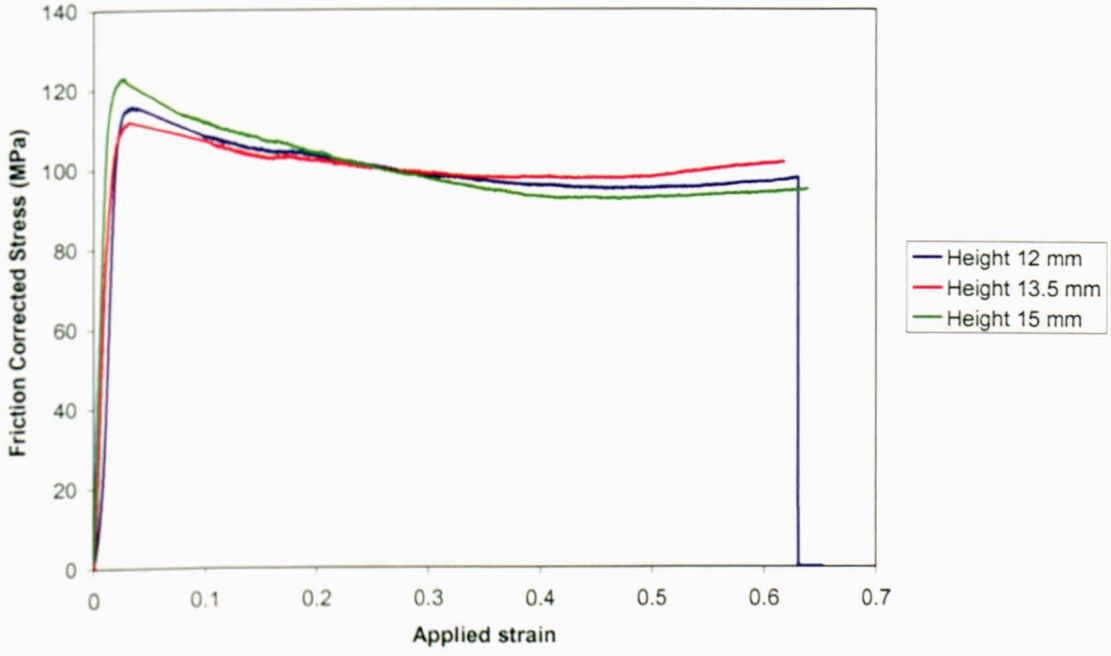

Figure 5.15 Corrected stress-strain curves using a μ value of 0.1

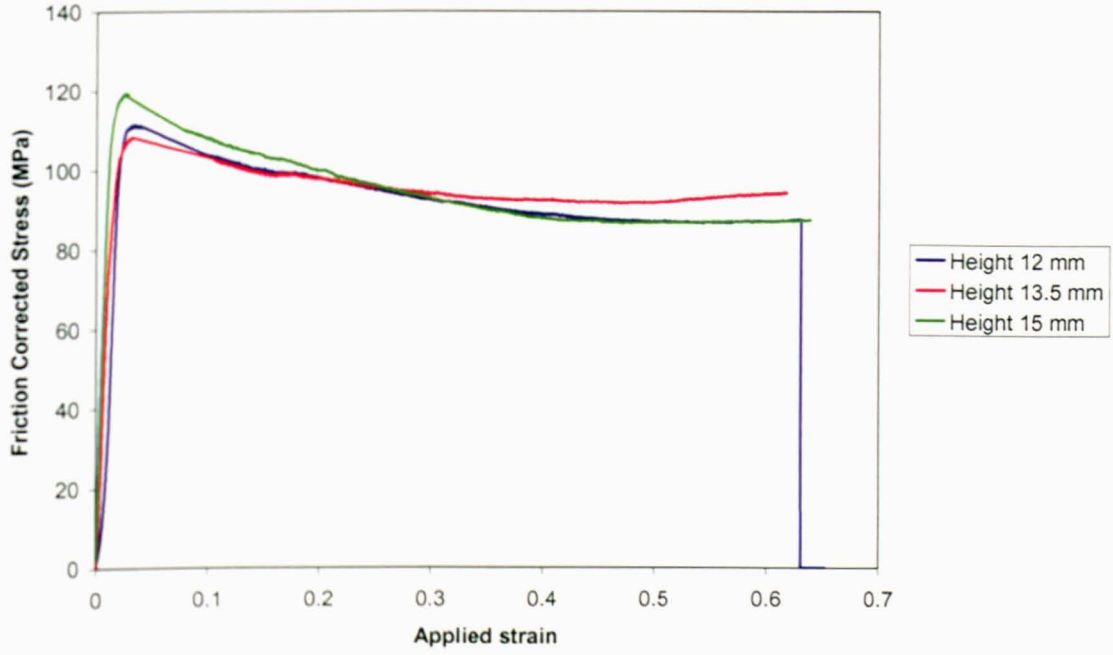

Figure 5.16 Corrected stress-strain curves using a μ value of 0.2

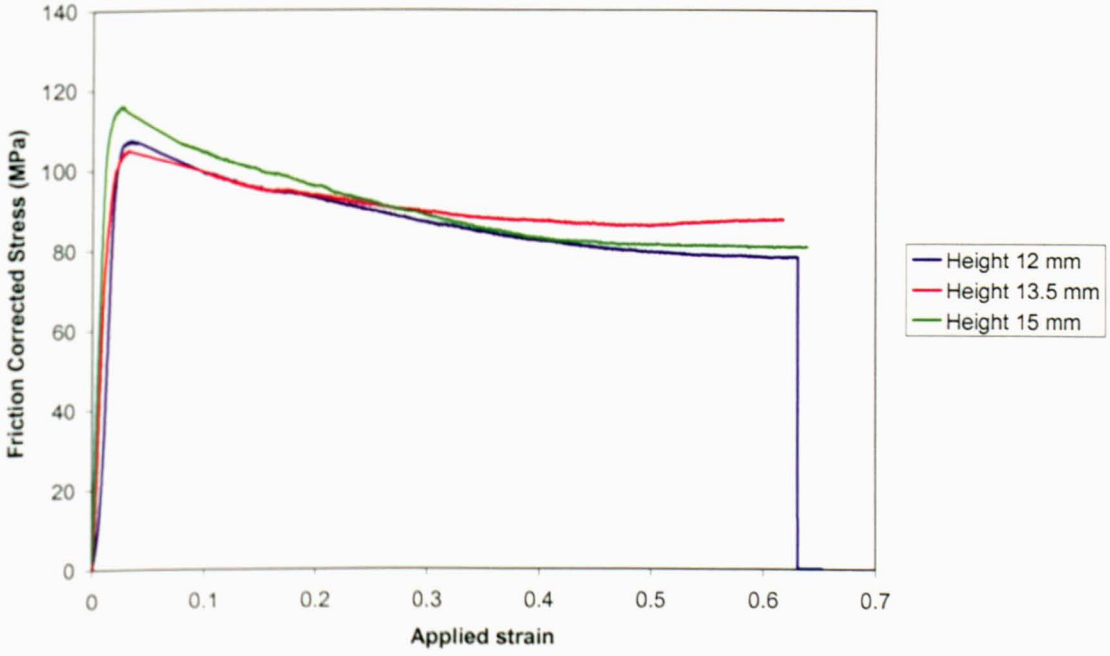

Figure 5.17 Corrected stress-strain curves using a μ value of 0.3

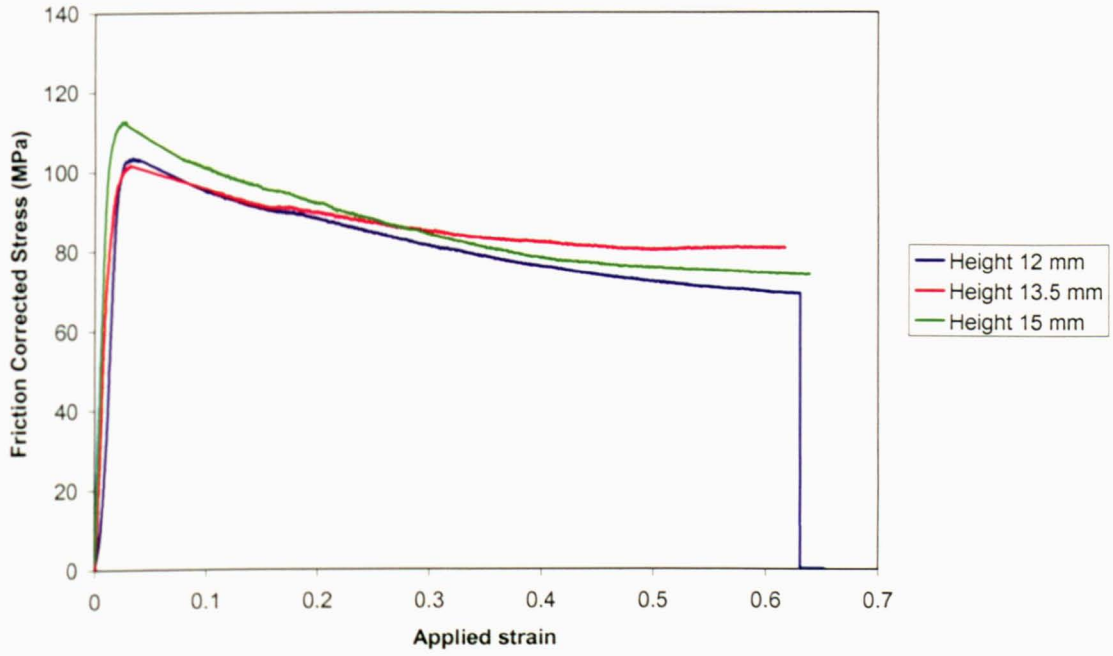

Figure 5.18 Corrected stress-strain curves using a μ value of 0.4

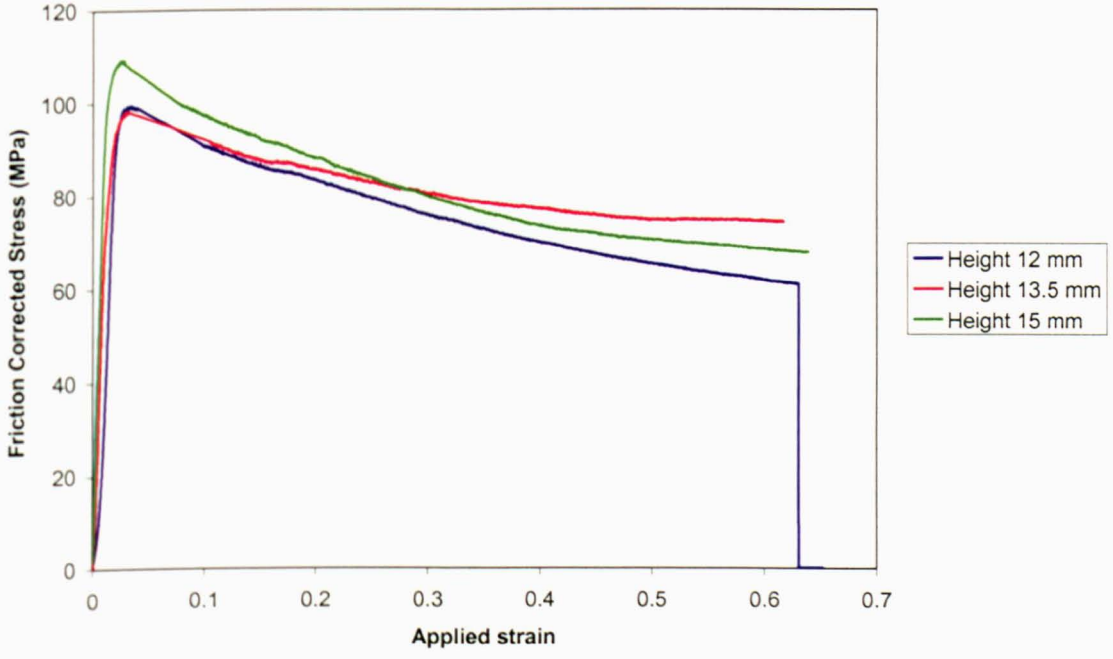

Figure 5.19 Corrected stress-strain curves using a μ value of 0.5

From the graphs it would appear that the greatest similarity between curves is seen in Figure 5.16, investigating values in this area lead to the closest similarity seen using a value for μ of 0.22, as seen in Figure 5.20.

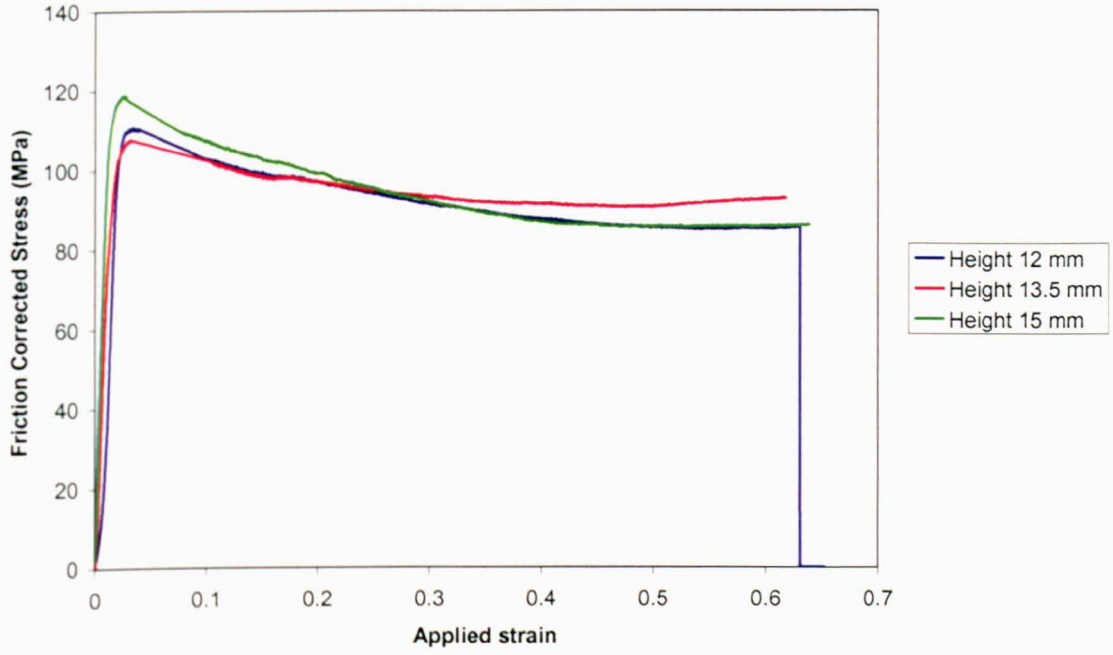

Figure 5.20 Corrected stress-strain curves using a μ value of 0.22

5.3.5 The Ring Compression Test.

The ring compression technique has gained wide acceptance to measure the coefficient of friction of the frictional shear factor at the platen/specimen interface. It was originated by Kunogi (1956) and later improved and presented in a usable way by Male and Cockroft (1965). This technique relates dimensional changes of a test specimen to the coefficient of friction. When a flat ring specimen is plastically compressed between two flat platens, increasing levels of friction result in an inward flow of material. Whereas decreasing levels of friction results in an outward flow of material. The measurement of the internal diameter of a compressed ring specimen gives a particular knowledge about the coefficient of friction at the platen/specimen interface, since the internal diameter increases when the friction is low and decreases when the friction is high. As recommended in the literature, once the change in internal diameter and the height of the ring are known, both μ and the frictional shear factor m can be found from the charts seen in Figures 5.21 and 5.22 regardless of material being deformed and test conditions.

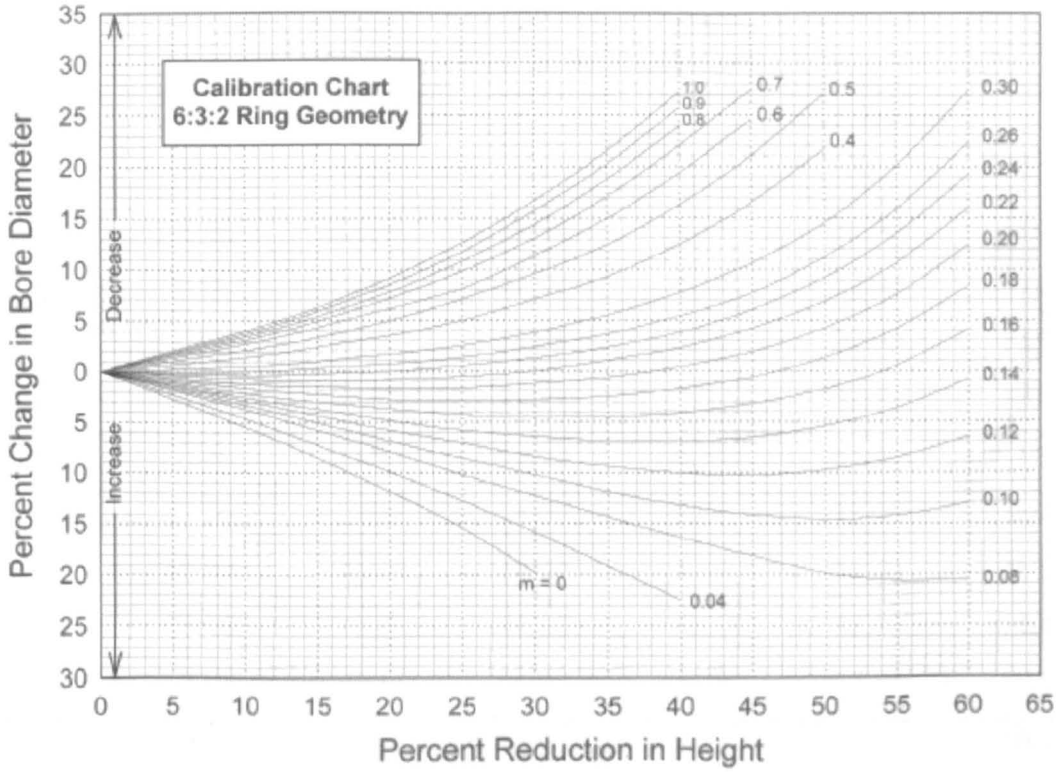

Figure 5.21 Calibration chart for calculating m

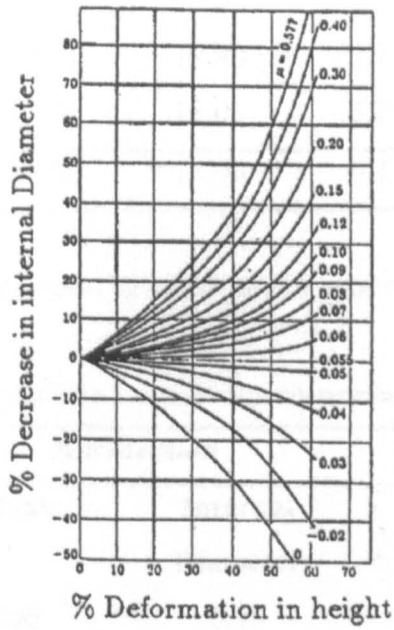

Figure 5.22 Calibration chart for calculating μ (Sufogulu et al, 2002)

For this work 3 separate ring geometries were used, always maintaining the OD:ID:H ratio of 6:3:2. Ring compression tests were again completed in the TMC using AML1000 lubrication. Rings were deformed to an applied strain of 0.7 at a strain rate of 2 s^{-1}. The dimensions of the ring test samples can be seen in Table 5.5.

Table 5.5 Ring test specimen geometries

Sample	*Before Testing*			*After Testing*		
	H	OD	ID	H	OD	ID
Ring 1	7.98	23.95	11.94	4.15	31.00	12.11
	7.98	23.97	11.97	4.10	32.07	10.62
	7.99	23.96	11.98	4.18	29.93	12.04
	7.99	23.98	11.98	4.13	32.97	10.63
Average	7.99	23.97	11.97	4.14	31.49	11.35
Ring 2	10.06	30.02	14.99	5.21	38.97	9.92
	10.05	30.02	14.97	5.17	38.48	9.84
	10.05	30.03	14.98	5.11	38.20	11.42
	10.04	30.02	14.98	5.28	37.81	10.61
Average	10.05	30.02	14.98	5.19	38.37	10.45
Ring 3	11.84	36.12	18.1	6.14	48.25	14.11
	11.83	35.95	18.03	6.17	45.74	13.70
	11.82	36.22	17.90	6.73	47.93	13.83
	11.86	35.73	18.06	6.26	45.58	14.66
Average	11.84	36.01	18.00	6.33	46.88	14.08

The ring compression tests detailed above produced the following values, as seen in Table 5.6;

Table 5.6 Friction values determined

	% Reduction			
Sample	**Height**	**Internal Diameter**	**M**	**μ**
1	48.06	5.18	0.21	0.07
2	47.46	30.24	0.65	0.20
3	46.54	21.78	0.45	0.17

As Table 5.6 shows, the ring compression tests result in an average friction shear factor of 0.436 and an average coefficient of friction of 0.147.

5.3.6 Summary of Friction Coefficient Determination Work

The effect of friction on the raw load displacement curve is to gradually increase the load experienced. If there was no effect of friction, i.e. perfect sliding conditions, once the compression test had reached steady state flow conditions the load would be uniform. However, when no zero friction is experienced the load required to deform the sample must also overcome the sticking experienced due to friction, as described previously in Chapter 2, and the load would gradually rise as the specimen area in contact with the tools increases.

When using the shape of the load-displacement curve to indicate effects of friction, consideration should also be paid to the levels of deformation heating experienced as a rise in the samples temperature will decrease the load needed for deformation. Furthermore, microstructural phenomenon such as dynamic recrystallisation will also reduce the load required for deformation, where at critical temperatures and strain rates new strain free grains originate at the old boundaries. As such, the work completed here in order to determine the friction coefficients experienced in testing of this type was critical in order to investigate the flow properties of this material.

The results gained in this work show the difficulty in determining a single value for the friction coefficient under deformation at "known" lubrication conditions. From this work alone the friction coefficients are seen to vary from 0.07 to 0.22, with an average of 0.165 achieved. If the 0.07 is assumed erroneous then an average of 0.197 is achieved.

The reasons for theses difficulties are believed to have their origins in the coverage of lubricant as the test progresses due to the variations in surface area. It is not unlikely that as the test progresses and the area of the specimen in contact with the platen tools increases, the presence on lubricant between the test specimen surface and the platen tool may become intermittent and as this cannot be controlled the coefficients determined although similar will not be the same. The graph in Figure 5.23 shows the effect of friction on the stress-strain curve.

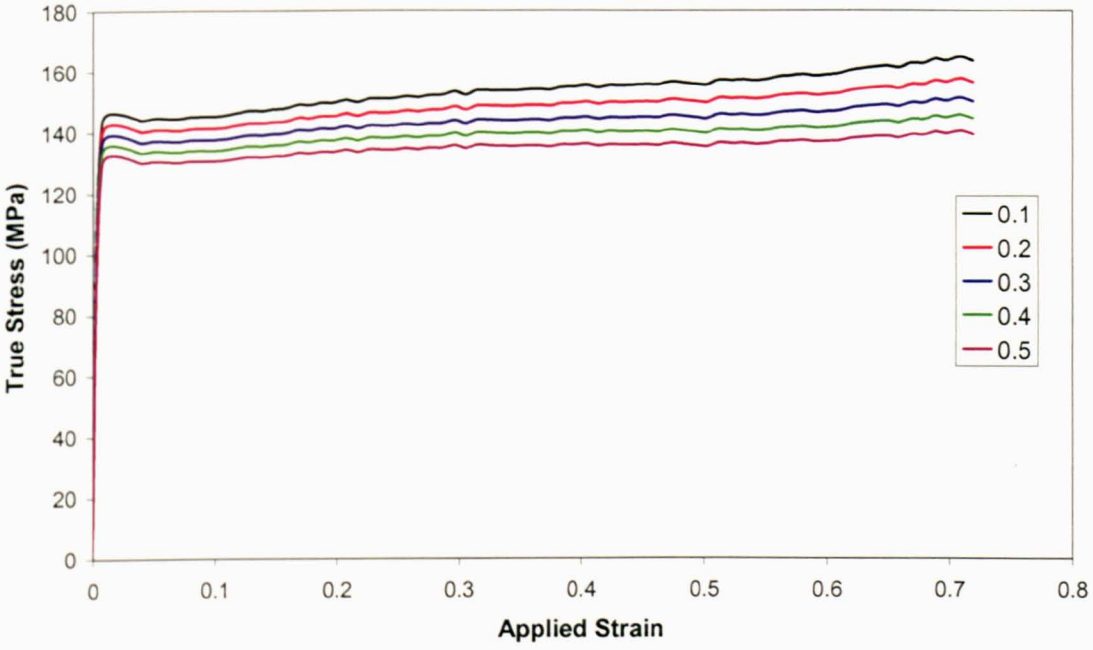

Figure 5.23 Effect of friction correction on stress-strain curves.

To address the issue of non-consistent lubrication, further work could be completed looking at alternative non-liquid lubricants such as foils or applying the lubricant to the tools rather than the test-piece.

5.3.7 Curve Correction

Using a value for $\mu = 0.2$, determined from both the coefficients of friction determination work we can correct the initial stress strain curves for friction effects using equation [5.2] in section 5.4. The corrected stress strain curves can be seen in Figures 5.23 to 5.25.

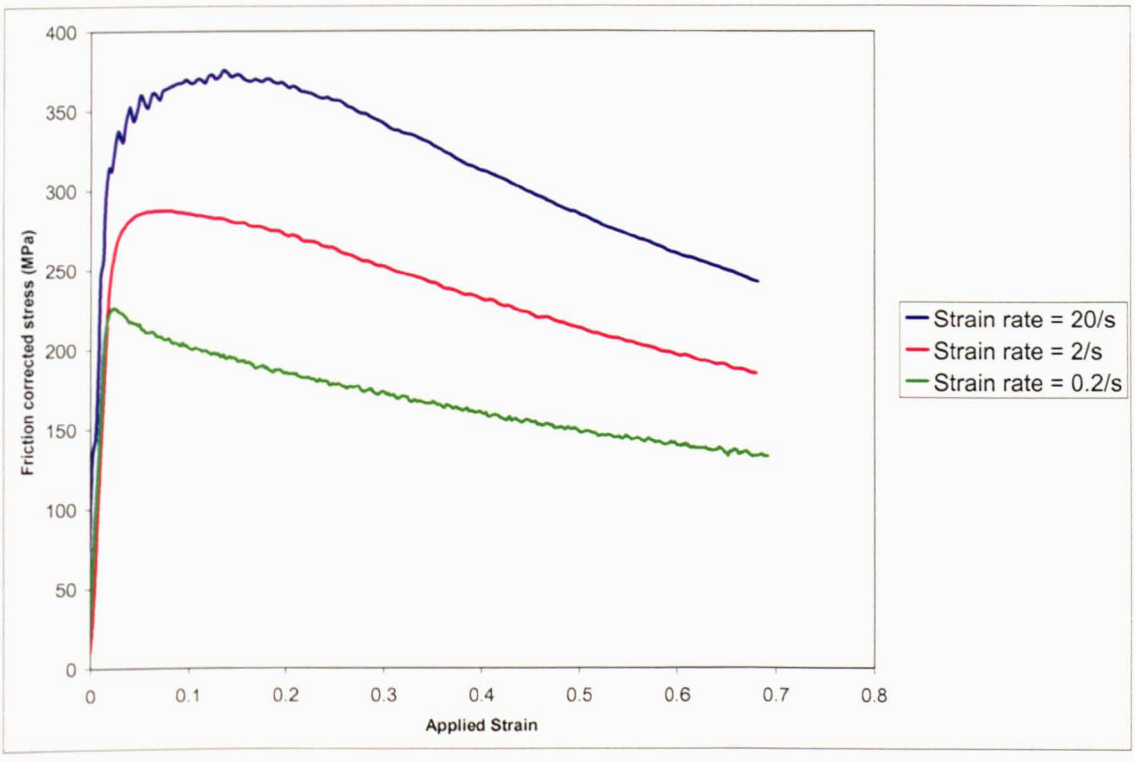

Figure 5.24 Friction Corrected stress-strain curves at 950°C

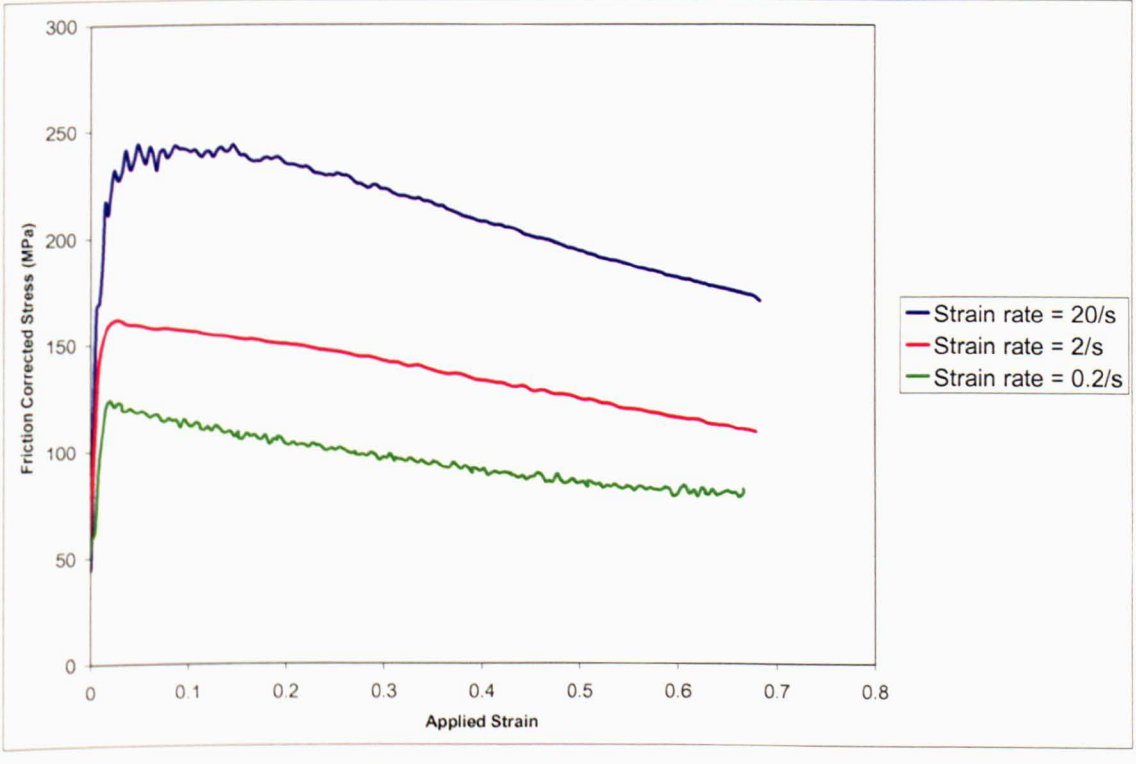

Figure 5.25 Friction Corrected stress-strain curves at 990°C

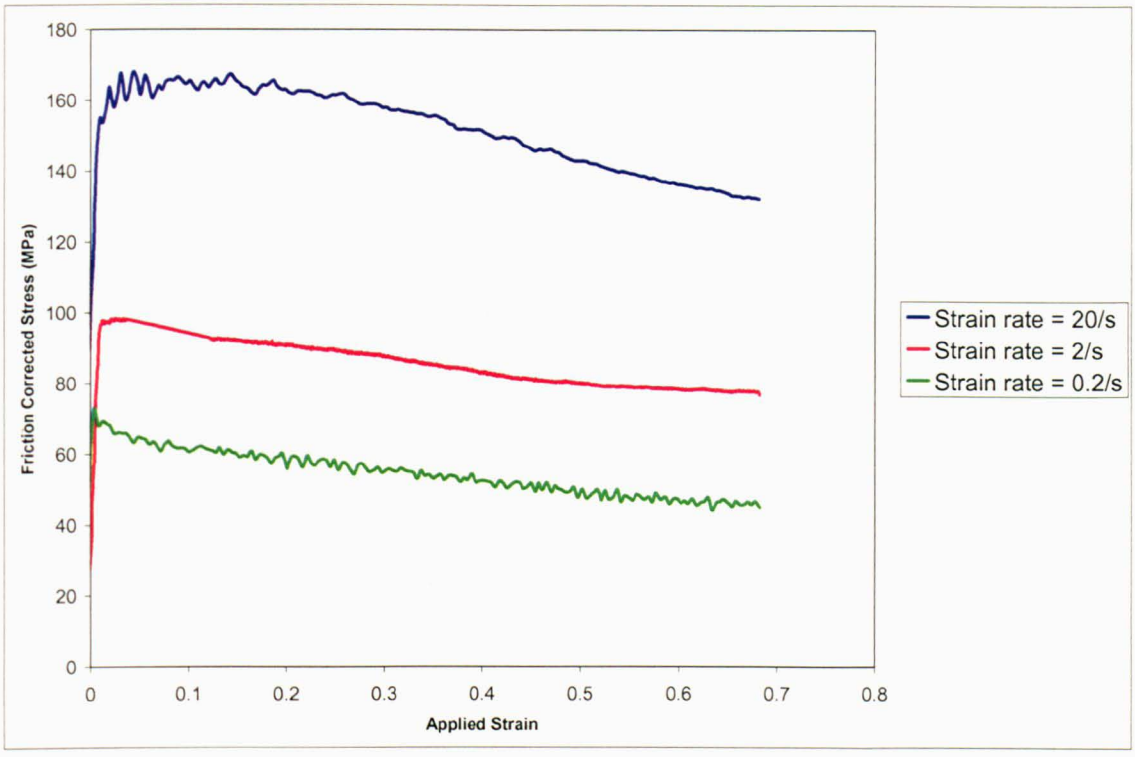

Figure 5.26 Friction Corrected stress-strain curves at 1030°C

5.3.8 Constitutive equation development

Development of second stage equations depends on subjective assessment of several 'characteristic points' on the flow stress curve, such as the strain at which steady state is achieved. Material softening arising from adiabatic heating can lead to poor estimates of these characteristic points. Consequently, for consistency in the analysis, all flow stress curves should be isothermally corrected (Davenport et al, 2000). The sensitivity of the flow curves to strain rate and temperature can be described by the following equation, 5.7;

$$\sigma_{\varepsilon} = B_{\varepsilon} f\left(\dot{\varepsilon} \exp\left(\frac{Q_{def}}{RT}\right)\right) \tag{5.7}$$

where $\dot{\varepsilon} \exp\left(\frac{Q_{def}}{RT}\right)$ is known as the Zener Hollomon parameter (Z) and, therefore equation 5.7 can be described as;

$$\sigma_{\varepsilon} = B_{\varepsilon} f(Z) \tag{5.8}$$

In order to calculate Q_{def} and thus Z, equation [5.8] needs to be re-written taking a fixed strain value so that we know σ_{ϵ} , we also know that B_{ϵ} is a constant and we can therefore plot the log of $\dot{\varepsilon}$ s^{-1} against the inverse temperature (1/T). The slope of such a plot will then be equal to $(-1/R\ln 10)Q_{def}$ allowing us to determine Q_{def}.

Initially, however, we must plot $\ln(\epsilon/s)$ vs σ in order to be able to extract the data for a constant stress as seen in Figure 5.27.

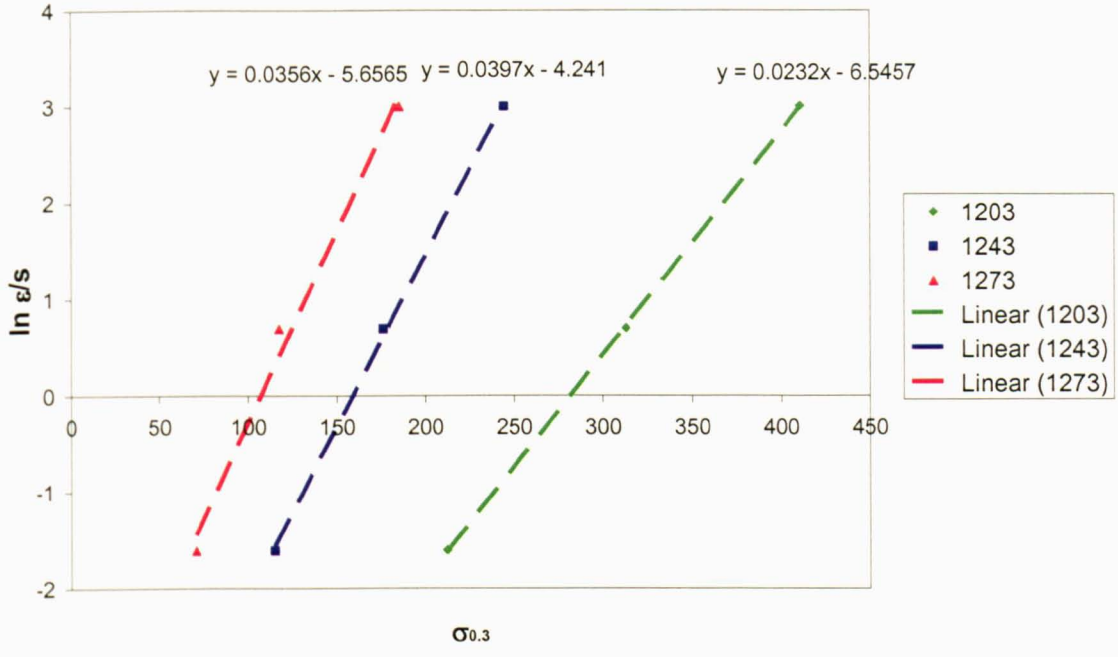

Figure 5.27 Graph illustrating the relationship between strain rate and stress at fixed strains.

Next we determine the strain rate to give the same flow stress at different temperatures, Table 5.7;

Table 5.7 Strain rates giving the same flow stress at different temperatures

T(K)	Ln(ϵ/s) at σ value of					
	100	**125**	**150**	**175**	**200**	**225**
1203					-1.9057	-1.3257
1243	-2.0965	-1.2065	-0.3165	0.5735	1.4635	2.3535
1273	-0.271	0.7215	1.714	2.7065		

Plotting these $\ln(\epsilon/s)$ values against 1/T gives us a graph as seen in Figure 5.27 showing 6 lines, which are not parallel suggesting that Q_{def} is not constant over the data range analysed. For the purposes of this work, but with the knowledge that it is

insufficient for accurate modelling we will average the gradients and assume a constant Q_{def}.

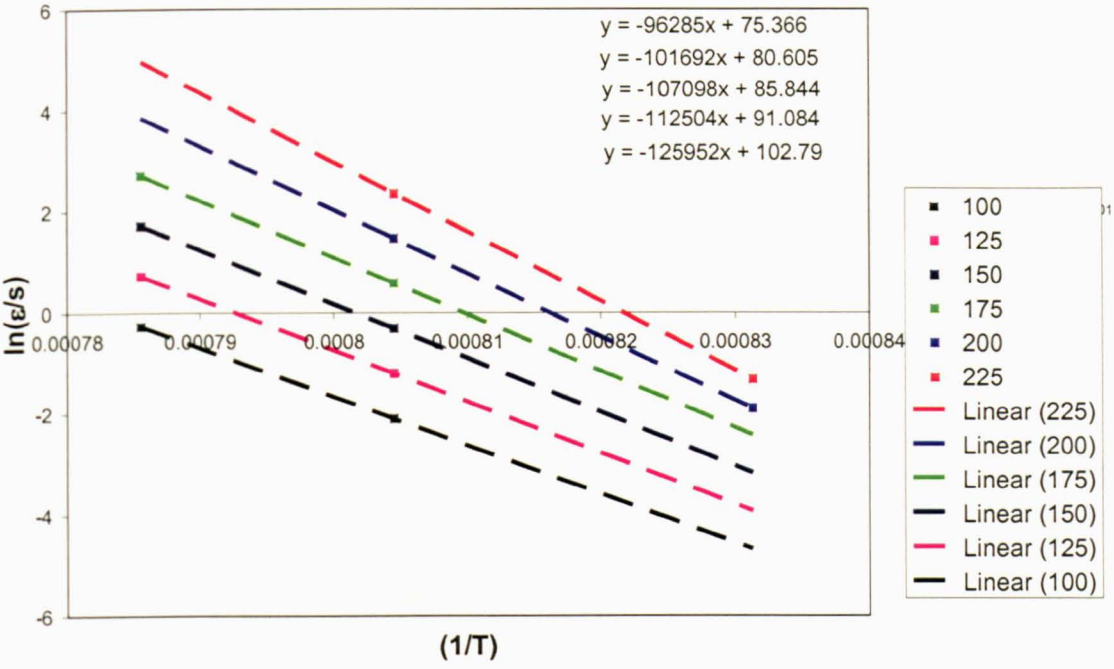

Figure 5.28 Graph to determine Q_{def} at varying stresses.

From Figure 5.28 we can calculate an average gradient of 113511.8333 which, is equal to;

$$Gradient = \frac{-Q_{def}}{R}$$

Therefore, measuring the gradients of the data in Figure 5.27, we can determine Q_{def} equals 943737.382 J/mol or as it is more commonly expressed 943.737 kJ/mol.

This routine was repeated at various strain values in order to obtain a more accurate result and the results are tabulated below;

Table 5.8 Q_{def} values determined at increasing strain values.

Strain Value	*Qdef determined*
0.1	939.505
0.2	935.065
0.3	943.737
0.4	965.786
0.5	1,009.426

Again the Qdef value is seen to vary at progressive strain values, the average value is calculated as **958.70 kJ/mol** and it is this value that is used in further analysis.

5.3.8.1 First stage constitutive equations

First stage constitutive equations were developed so that the appropriate material parameters were defined to temperature correct the flow curves. The dependence of Z on the flow stress may be expressed empirically by power, exponential and hyperbolic functions, as shown below.

$$Z = \dot{\varepsilon} \exp\left(\frac{Q_{def}}{RT}\right) = A_1 \sigma^n \tag{5.9}$$

$$Z = \dot{\varepsilon} \exp\left(\frac{Q_{def}}{RT}\right) = A_2 \exp(\beta\sigma) \tag{5.10}$$

$$Z = \dot{\varepsilon} \exp\left(\frac{Q_{def}}{RT}\right) = A(\sinh \alpha\sigma)^n \tag{5.11}$$

where A_1, A_2, A, n, α and β are constants. The value of Q_{def} used in the above equations was determined using the method described in section 5.34 and the values in Table 5.8 were used. The constants may be resolved directly from each of the graphs that were constructed using the equations. Equation 5.11 is a general form that reduces to Equation 5.9 at low stresses (where $\alpha\sigma << 1$) and to Equation 5.10 at higher stresses.

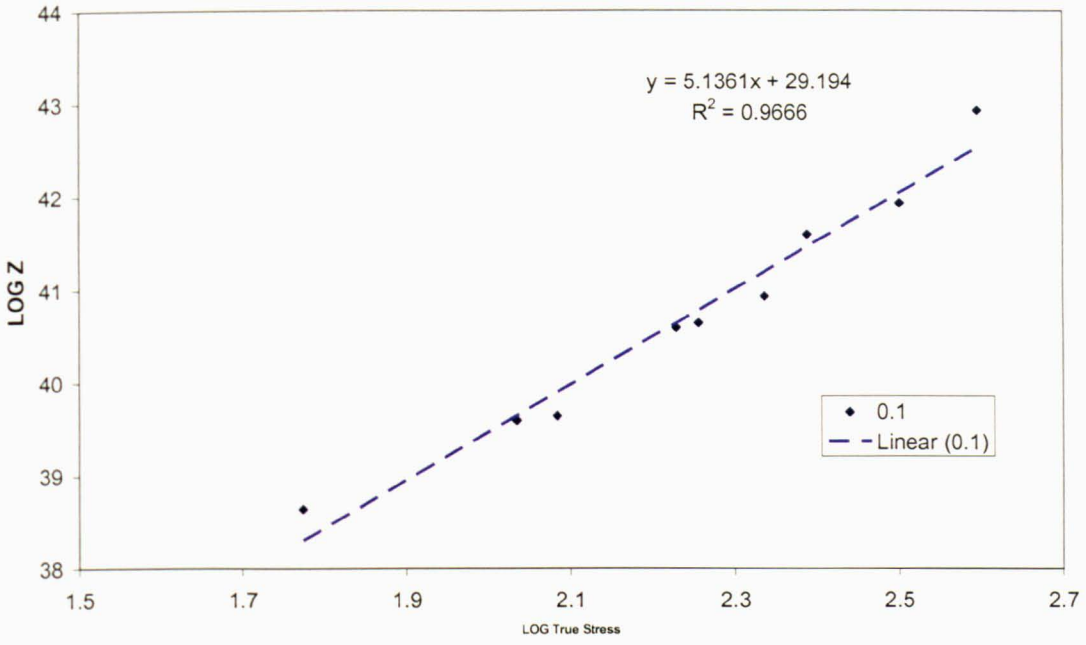

Figure 5.29 LOG Z vs LOG stress graph constructed for Equation 5.9

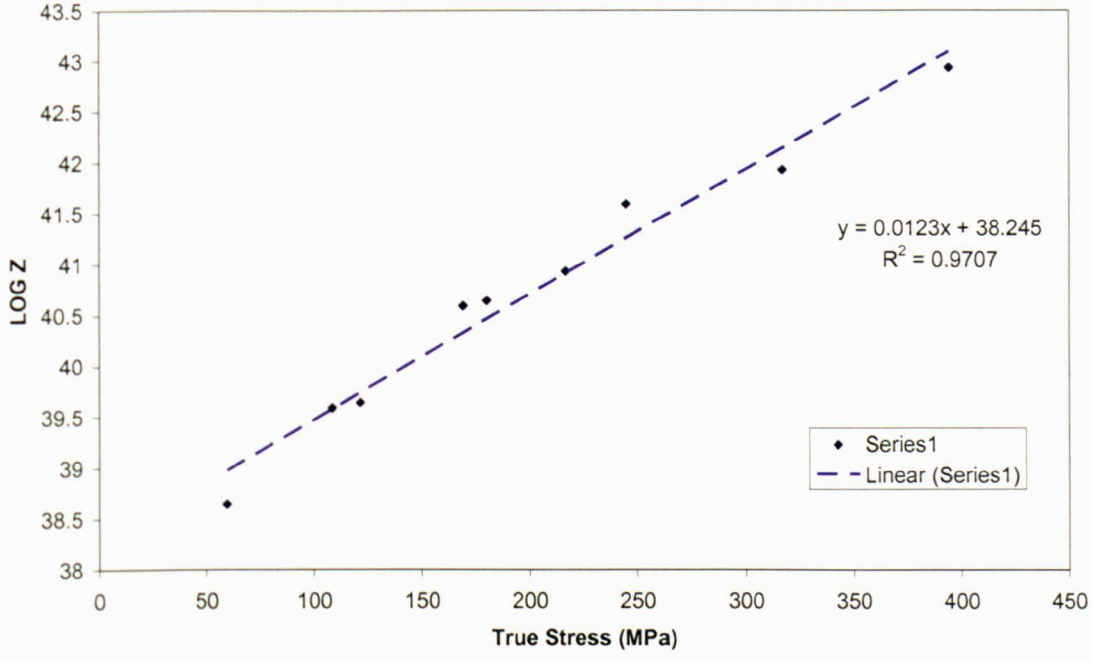

Figure 5.30 LOG Z vs LOG stress graph constructed for Equation 5.10

The constants were determined from the graphs, from Equation 5.12

$$\log Z = n \log \sigma + C_1 \qquad \text{where } A_1 = 10^{C_1} \tag{5.12}$$

and from Equation 5.13

$$\log Z = (2.303\beta)\sigma + C_2 \qquad \text{where } A_2 = \exp(2.303C_2) \tag{5.13}$$

The sinh function in Equation 5.14 was then applied across the entire stress range, with α given by the approximation

$$\alpha = \frac{\beta}{n} \tag{5.14}$$

Therefore a plot of log Z vs log (sinh $\alpha\sigma$) will determine A in equation 5.11. Figure 5.21 illustrates this with a plot for the entire stress range at a strain increment of 0.1.

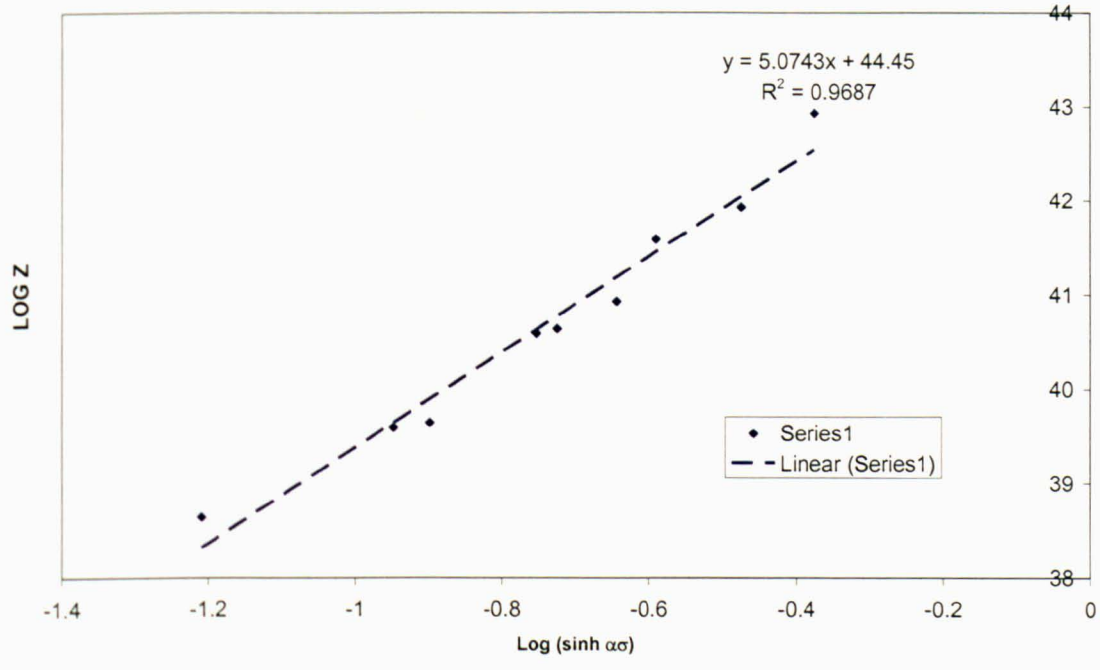

Figure 5.31 log Z vs log (sinh $\alpha\sigma$) graph plooted to determine A.

At this point it is important to state a large assumption made in this work in order to achieve our goal. The constitutive equation development, Q_{def} determination and equations for calculating Z are all combined to describe the relation between stress and strain in terms of the variables of strain rate and temperature. However, in this alloy a further variable in the form of phase volume fraction will be present in each test. The assumption made here is that this effect is negligible and thus not considered, however

the effect on the results will be discussed later in this chapter as further in depth analysis may require this assumption to be removed.

5.3.8.2 Deformation Heating Correction

To present the test isothermally the following equation is used;

$$\sigma_{iso} = \sigma_1 + \frac{Q_{def}}{\beta R}\left(\frac{1}{T_1} - \frac{1}{T_2}\right) \tag{5.15}$$

where, σ_{iso} is the isothermally calculated stress, σ_1 is the uncorrected stress value, R is the universal gas constant, T_1 and T_2 are the instantaneous and desired isothermal temperatures respectively and Q_{def} and β material constants calculated from initial analysis.

It is important to note that these isothermal curves, seen in Figures 5.32, still do not incorporate any effect of any strain rate fluctuation, however, this is minimal in the apparatus used for these tests.

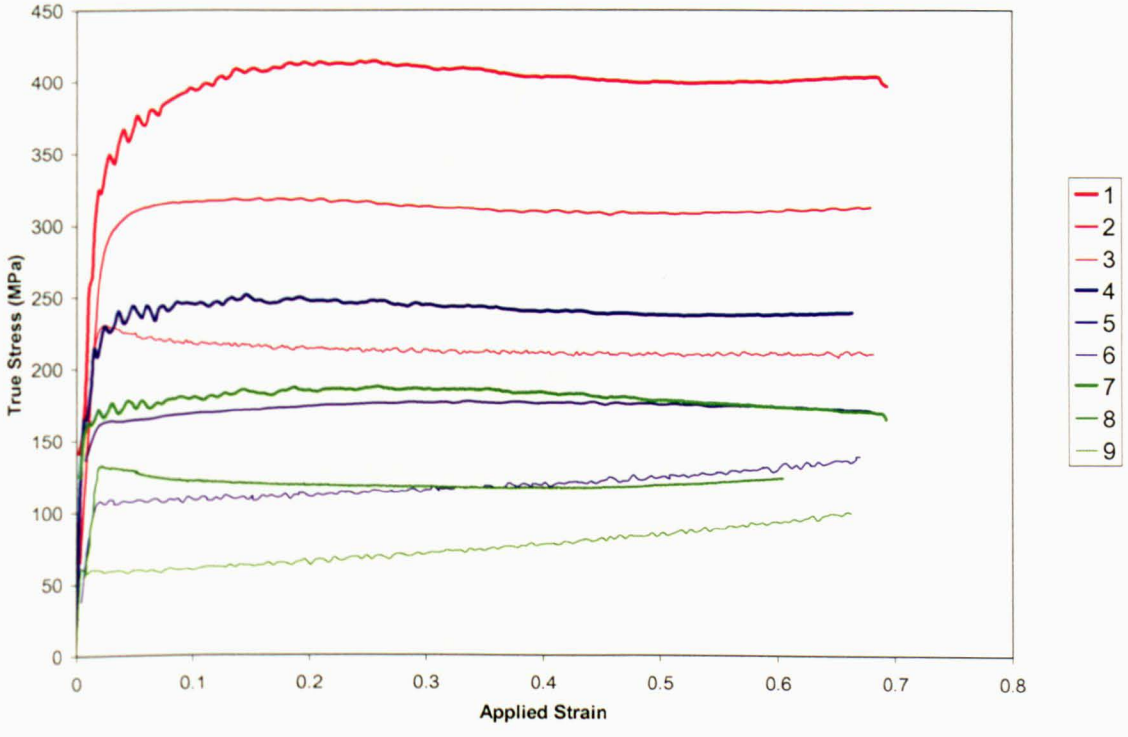

Figure 5.32 True Stress-strain curves for tests D1-9

5.3.8.3 Second Stage Constitutive Equation Development

Once an isothermal stress-strain curve has been produced it is then possible to begin the second stage of analysis. To begin, the following characteristic points upon the stress-strain curve need to be identified;

1) σ_0, the maximum stress when plastic strain = 0

2) $\sigma_{0.1}$, the stress when = 0.1

3) σ_p and ϵ_p, the peak stress, and

4) σ_{ss} and ϵ_{ss}, the steady state stress

Once identified for each test these points can be plotted against the Zener-Hollomon parameter for that test as seen in Figures 5.33-5.35.

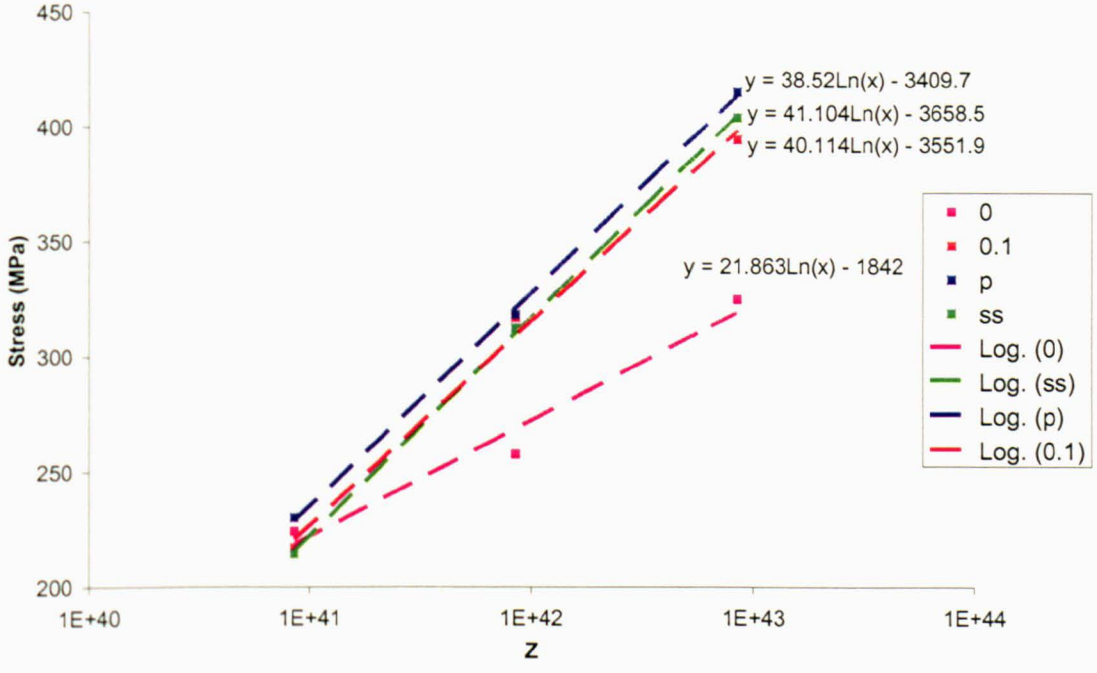

Figure 5.33 The relationship between Z and chosen discrete points at 1203K

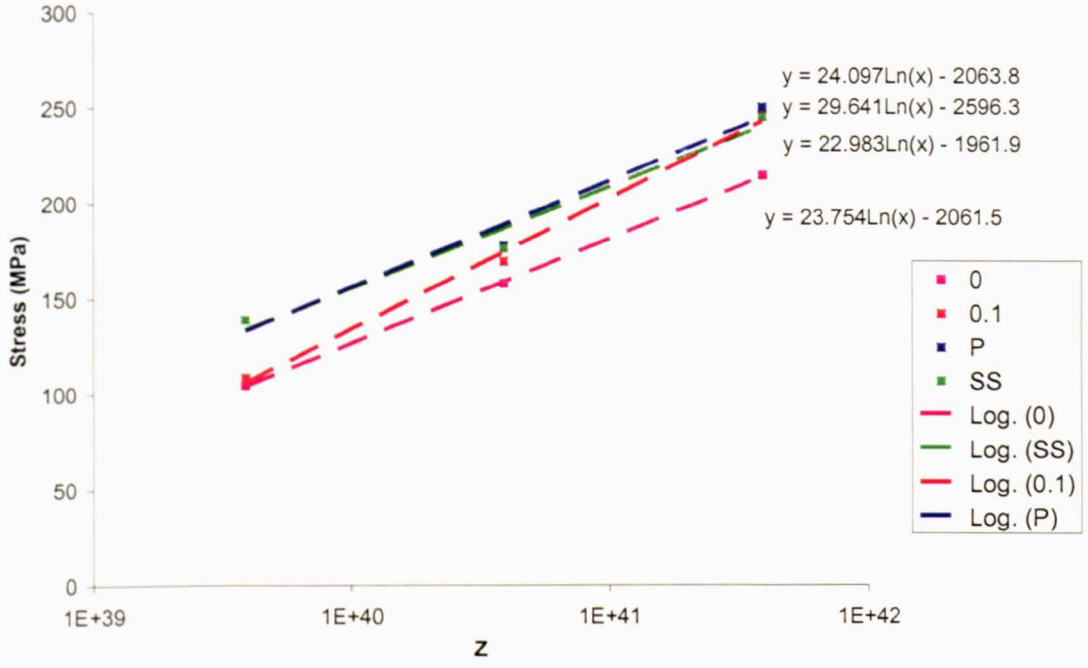

Figure 5.34 The relationship between Z and chosen discrete points at 1243K

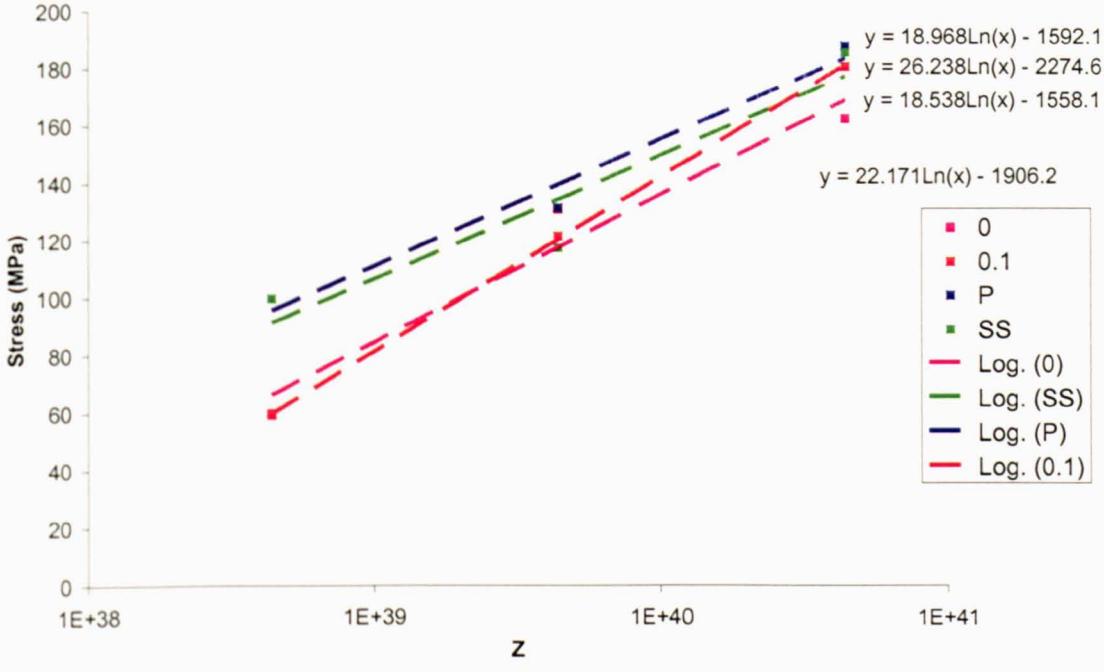

Figure 5.35 The relationship between Z and chosen discrete points at 1273K

Finally the equations representing the characteristic points as a function of Z can be collated into a final equation of the type developed by Davenport et al (2000);

$$\sigma = \sigma_0 + (\sigma_{ss(\varepsilon)} - \sigma_0)\left[\left(1 - \exp\left(\frac{-\varepsilon}{\varepsilon_r}\right)\right)\right]^{\frac{1}{2}} \tag{5.16}$$

Where, ϵ_r is stated in Davenport et al (2000) as 'the transient strain constant' and can be calculated from the equation;

$$\varepsilon_r = -0.1\left(\ln\left\{1 - [(\sigma_{0.1} - \sigma_0)/(\sigma_s - \sigma_0)]^{\frac{1}{m}}\right\}\right) \tag{5.17}$$

Where the constant m = 0.5 according to Davenport et al. (2000).

Using Equations 5.16 and 5.17 a spreadsheet was assembled and the results are summarised in Table 5.9. In Figures 5.36-5.38 the actual curves are seen as a solid line and the equation fitted can be seen as a dotted line.

Table 5.9

Temperature	***Relationship between Z and;***			
(°K)	**σ=0**	**σ=0.1**	**σ=Peak**	**σ=SS**
1203	21.869ln(Z)-1842	38.52ln(Z)-3406.7	40.114ln(Z)-3551.9	41.104ln(Z)-3651.5
1243	23.754ln(Z)-2061.5	29.641ln(Z)-2596.3	24.097ln(Z)-2063.8	22.983ln(Z)-1961.9
1273	22.171ln(Z)-1906.2	26.238ln(Z)-2274.6	18.968ln(Z)-1592.1	18.538ln(Z)-1558.1

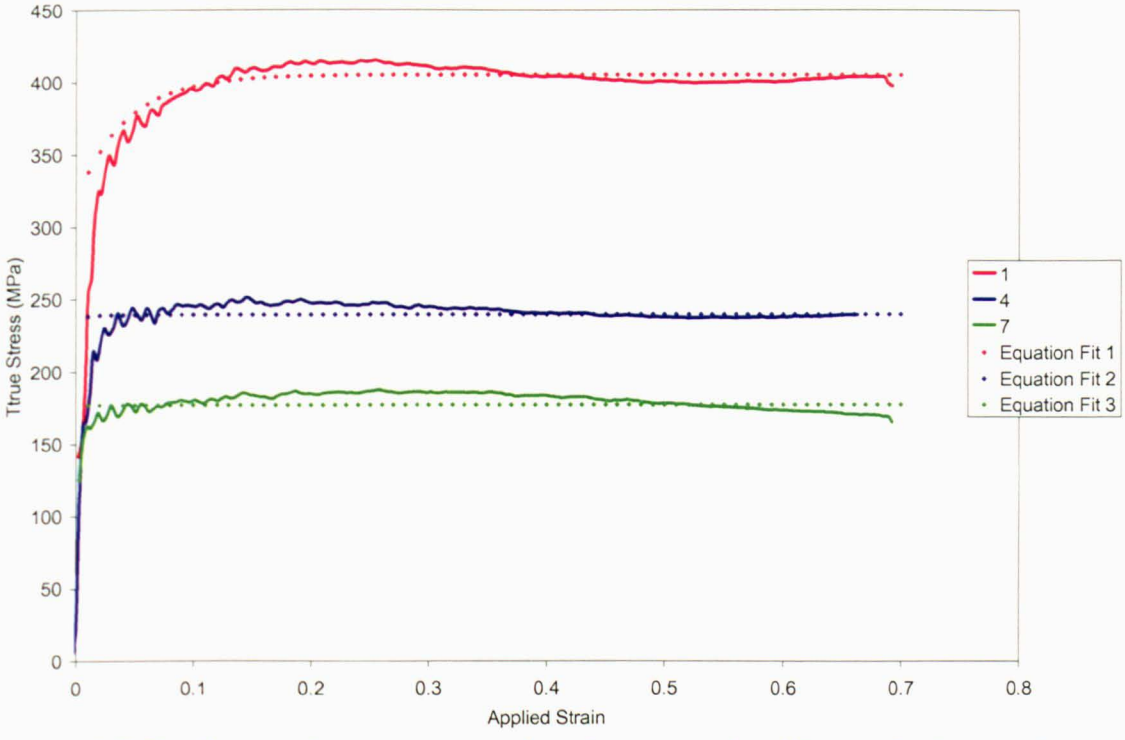

Figure 5.36 Graph comparing true stress-strain and curves produced by constitutive equations at 1203K

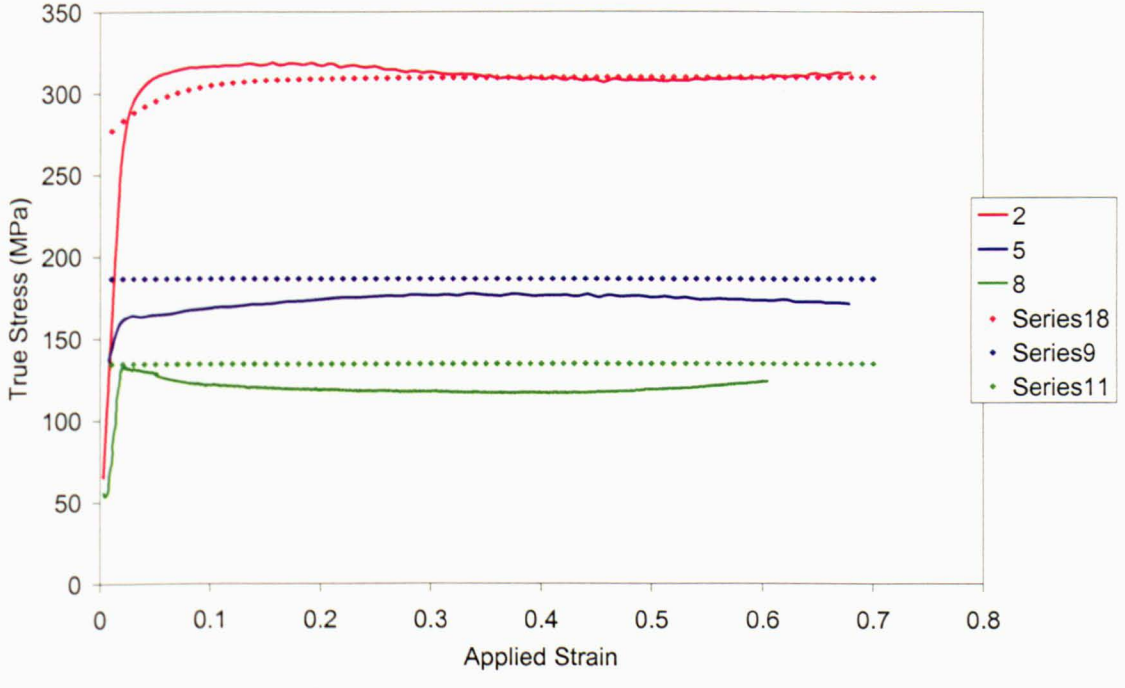

Figure 5.37 Graph comparing true stress-strain and curves produced by constitutive equations at 1243K

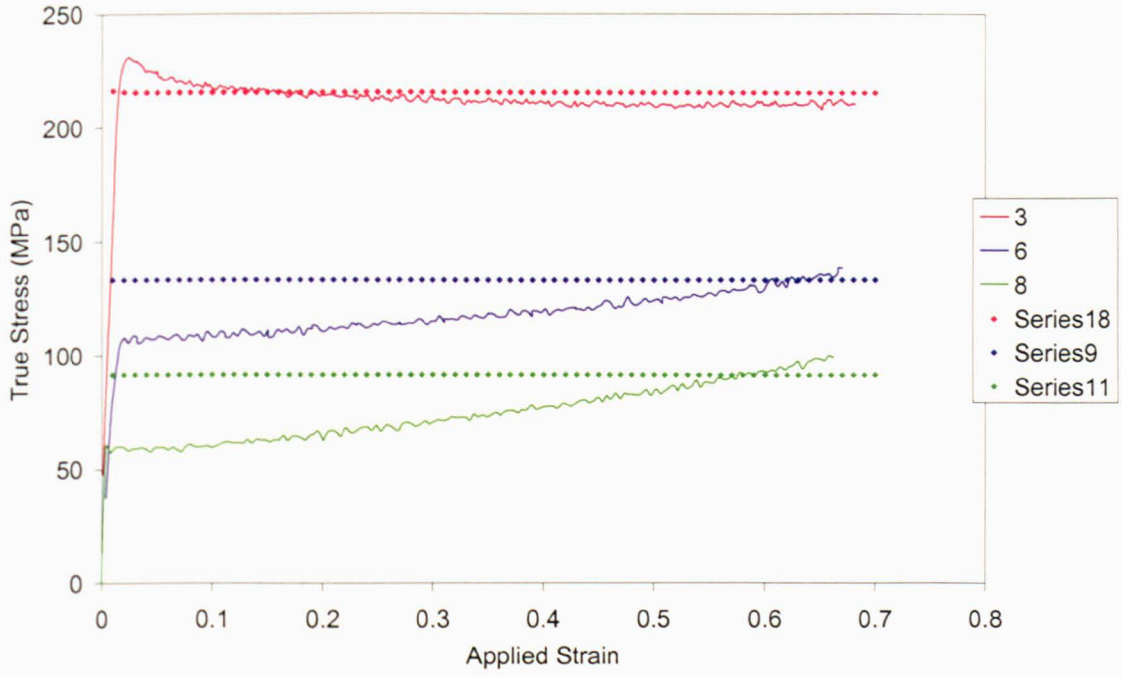

Figure 5.38 Graph comparing true stress-strain and curves produced by constitutive equations at 1273K

5.3.9 Summary of constitutive equation development

This chapter has detailed the completion of axisymmetric compression tests scheduled in order to assess the integrity of the testing apparatus and to develop constitutive equations for the modelling of this materials flow behaviour. It is believed by the author that the integrity of the testing apparatus are sound and the constitutive equation development achieved, although unconventional when compared with similar work done on steels and aluminium, is sufficient for this work. Further work, developing the approach is suggested in Section 5.6.

5.4 Axisymmetric Compression Testing and Flow Behaviour Analysis

After the integrity of the testing apparatus was proved and the constitutive equations had been determined, the tests scheduled to investigate variable forging parameters were undertaken and the results and analysis are detailed in this section.

5.4.1 Post Processing TMC Data

The initial load and displacement data for T1 can be seen in Figure 5.39 and the 3 plots represent the raw data, an initial zero correction based on the undeformed

specimens hot thickness and a correction based on the deformed specimens measured thickness.

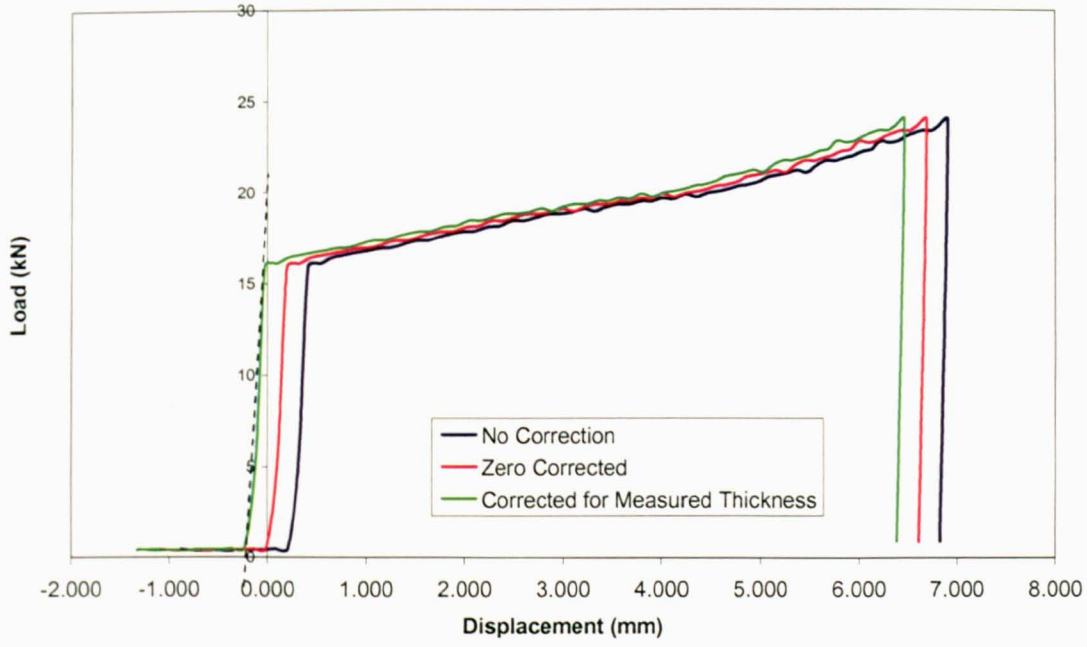

Figure 5.39 Zero correction of Load vs Displacement curves.

The initial origin correction was applied to the raw data for errors in the zero position. This is shown in the Figure 5.39 where the red data has been corrected from the raw blue data by means of a simple addition (or subtraction) from the displacement data. The aim of this was to correct for slight drift in the machine and align the slope which arises from machine compliance with the origin, as shown in Figure. 5.39. The second origin correction, shown by the green line in Figure 5.39 was applied for errors that arise from the maximum displacement recorded by the displacement transducers on the ram. This was done by measuring the mean thickness of the specimen after the deformation. The value was again corrected for the thermal expansion of the specimen. From the initial and final hot thickness, the maximum displacement of the upper tool $\delta^{\max}_{\text{measured}}$ was derived. This figure was then compared to the maximum value recorded by the displacement transducer $\delta^{\max}_{\text{nominal}}$. Any discrepancy between the values was corrected for by shifting the load displacement curve in such a way that the maximum actuator displacement was equal to the maximum measured displacement. Thus

$$\delta'_{\text{corr}} = \delta_{\text{nominal}} - \left(\delta^{\max}_{\text{nominal}} - \delta^{\max}_{\text{measured}}\right) \tag{5.17}$$

$$\delta'_{corr} = \delta_{nominal} - \delta_{\sigma_c} \tag{5.18}$$

Lacey et al.(2002) and Silk et al.(1999) have described a load elongation compensation (LEC), which accounts for the elastic tool deformation when using maximum load. The TMC machine has a machine stiffness of approximately 410kNmm^{-1} which implies that at maximum load, the machine frame and tooling will deform elastically by more than 1 mm.

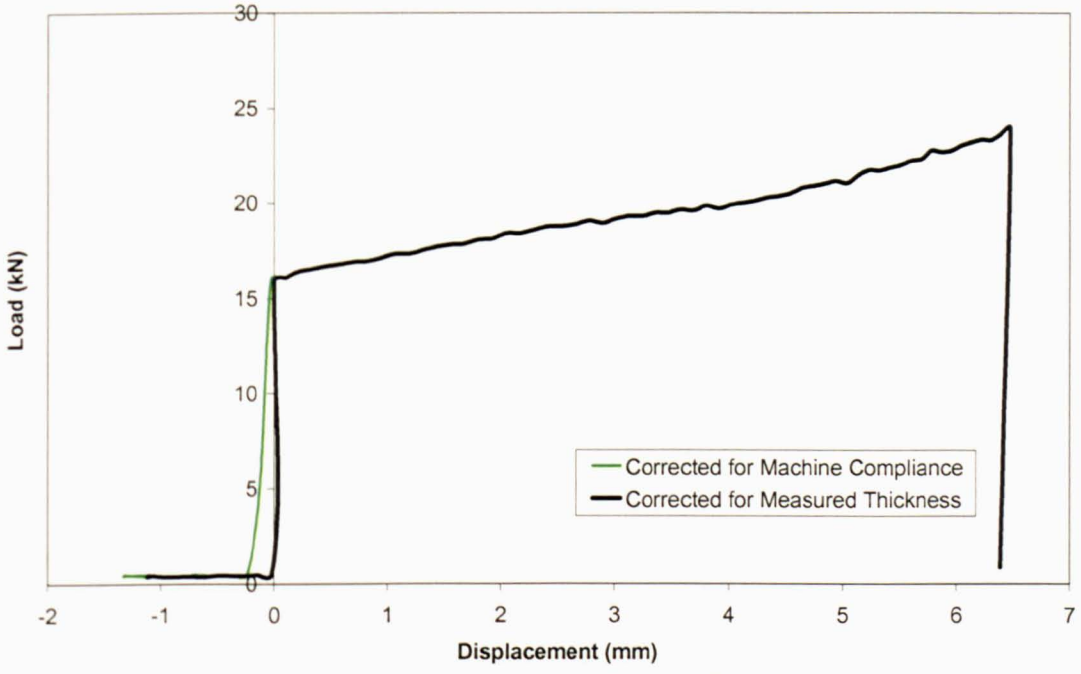

Figure 5.40 Load vs Displacement curve showing machine compliance correction

The machine compliance (slope of the load/displacement curve as shown by the dashed line in Figure 5.39) was measured for each test. Thus, this technique was used to correct the displacement data at the beginning of the deformation. This is shown in Figure 5.39, with the data followed on from Figure 5.38. This method produced a corrected data set of load and displacement values. When combined with the temperature, time and velocity data, the equivalent stress and strain and strain rate could then be determined with a high level of confidence.

5.4.2 Strain Variation Test

The stress-strain curves for tests T1-T4, developed from the load displacement data seen in Figure 5.41, are shown in Figure 5.42.

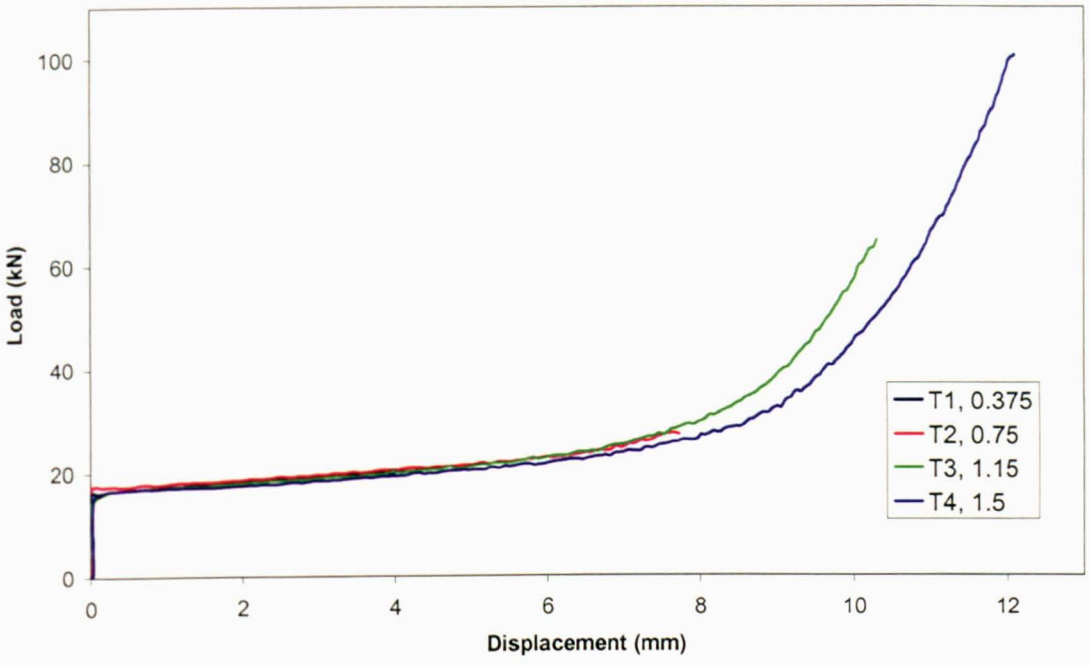

Figure 5.41 Load vs. displacement curves for test T1-T4

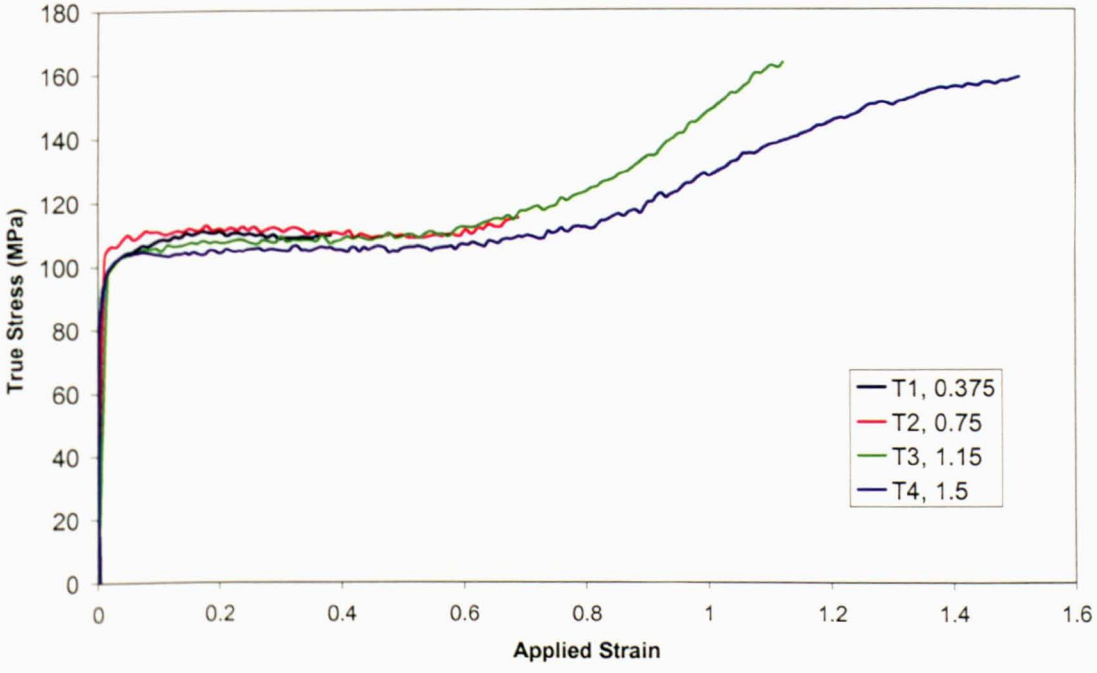

Figure 5.42 Stress-Strain Curves for tests T1-T4

The stress-strain curves show the flow properties of the alloy when deformed to strains of 0.375, 0.75, 1.165 and 1.5 without lubrication, for these tests a pre-

deformation hold time of 30 minutes was used. These were the initial strain values chosen for investigation based on review of the Q-form model from Firth Rixson UK.

For these curves a friction coefficient of 0.4 was used as this was believed to be a suitable value for sliding friction between Steel and Titanium (Qu et al, 2005). As well as friction corrected, theses curves have also been corrected for deformation heating. From the stress–strain curves it is clear that the magnitude of friction correction after an applied strain of approximately 0.7 is insufficient. The gradient on the curves increases after this value and the differences between curves also increases. The success of these tests is tabulated in Table 5.3 and the platen temperatures during each test are tabulated in Table 5.4. The strain rate during deformation can be seen in Figures 5.35.

Table 5.10 Results of Secondary Compression Tests

Test	*Applied Strain*	*Strain Rate*	*Heat Treatment*	*Quench*	*Notes*
Test 8-T1	0.375	2	Heat to 1010°C in 120s, hold for 30 mins, drop to 1000°C then forge	Water	Good
Test 9	0.75	2	As above	Water	Failed
Test 10-T2	0.75	2	As above	Water	Good
Test 11-T3	1.165	2	As above	Water	Good
Test 12-T4	1.5	2	As above	Water	No Quench

Table 5.11 Furnace and Platen temperatures during tests in the TMTS apparatus

Test	*Furnace Temp (°C)*	*Top Platen Temperature (°C)*	*Bottom Platen Temperature (°C)*
T1	1040	990	1010
T2	1040	990	1005
T3	1040	998	1010
T4	1040	998	1010

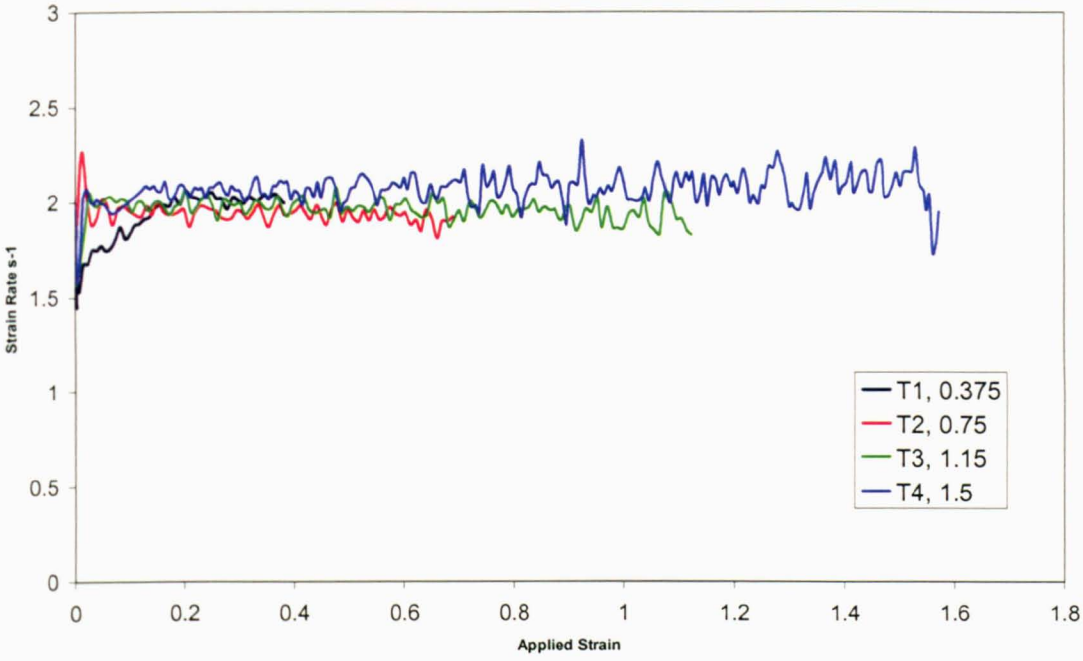

Figure 5.43 A graph showing the strain rate during deformation for tests T1-T4

The data shows that the testing conditions and the strain rates used are comparable, this is fortunate as the only variable parameter was intended to be total applied strain. As mentioned earlier these tests were completed without lubrication and, as such, the barrelling co-efficient described in Section 2.14 was outside allowable values. However, some initial microstructure and texture analysis was carried out on samples and can be seen in Chapter 8.

Having concluded that an unlubricated test was inappropriate for this work, lubricants for hot working of titanium were investigated and the glass based lubricant AML 1000 was chosen as the most promising. The tests T1-3 were repeated with lubrication, however, T4 was omitted as the final test piece dimensions after a strain of 1.5 lead to difficulty with transferring the test piece from between the tools to the FTTU.

The stress-strain curves for tests T5-10 can be seen in Figures 5.36-5.38. The stress-strain curves show the effect of using AML 1000 lubrication and friction correction using a coefficient of 0.2, determined previously in section 5.3.4.

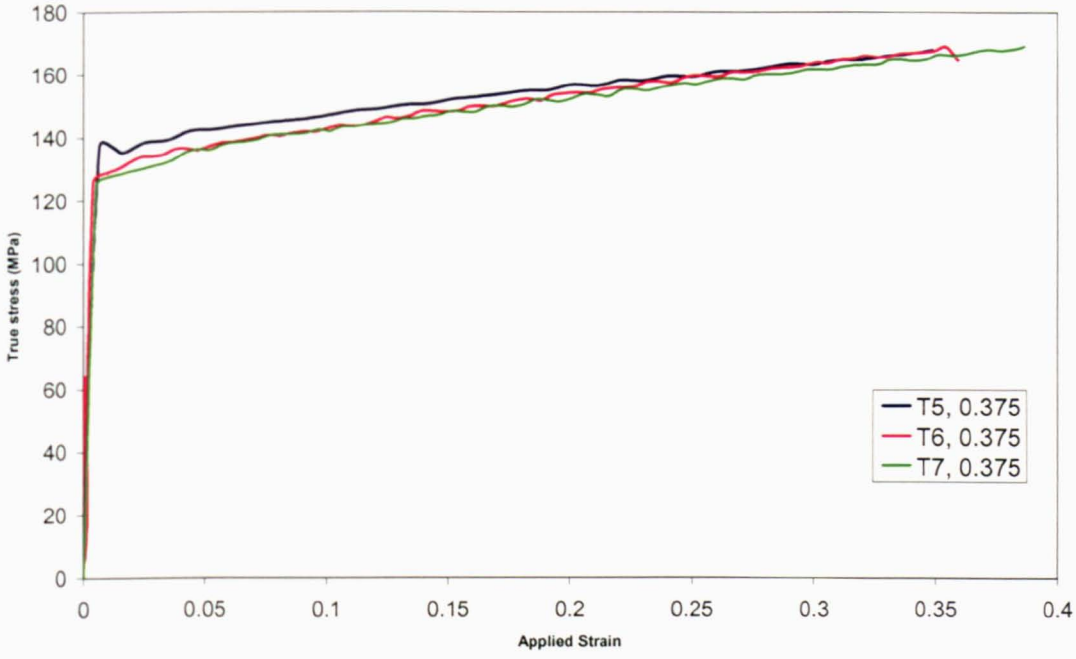

Figure 5.44 Stress-strain curves for T5-T7

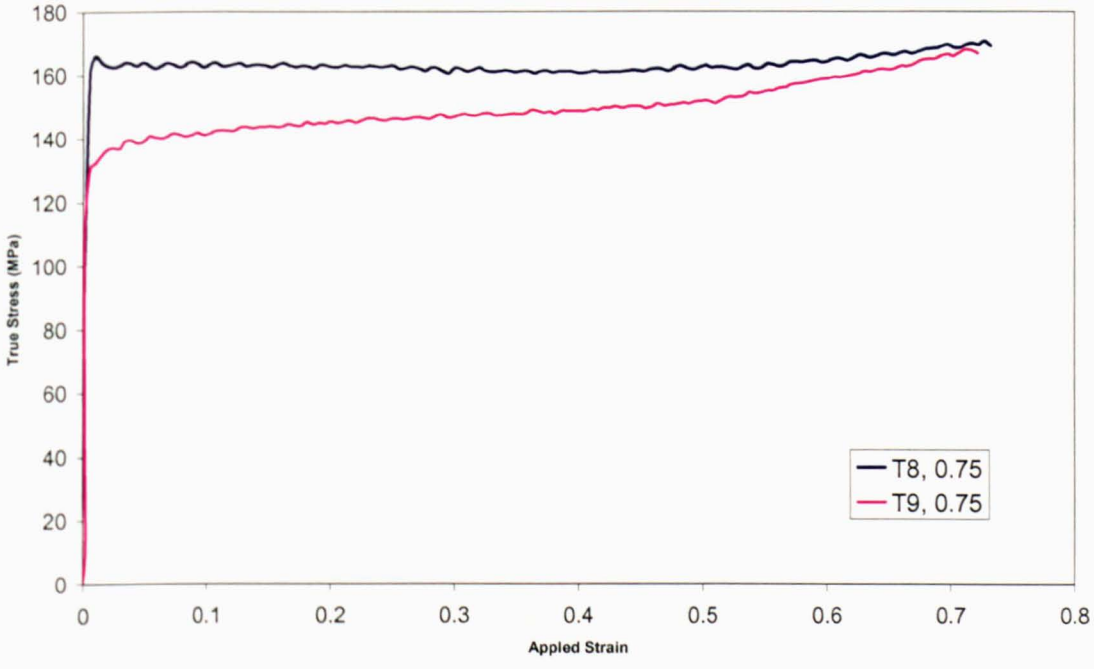

Figure 5.45 Stress-strain curves for T8 and T9

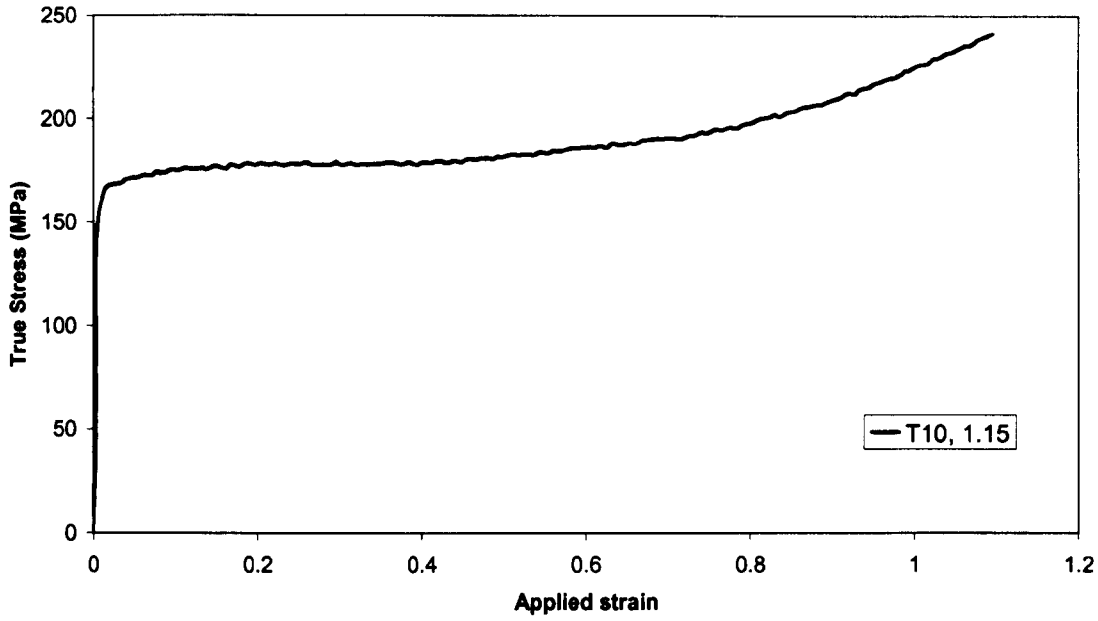

Figure 5.46 Stress-strain curves for T10

As with tests T1-4 there is still evidence from the friction correction being insufficient by the gradient of the curves in the latter stages of deformation and the variation in the curves for tests T8 and T9. These anomalies are believed to have there origins in the decomposition of the lubricant due to the length of the hold time at 1010°C. As the lubricant decays the surface of the axisymmetric compression sample becomes exposed and as such the test cannot be classed as lubricated. The lack of lubrication also led to the loss of a number of test specimens.

As a result of the decomposition of the lubricant the hold time was reduced to 5 minutes and strain values of 0.15, 0.375, 0.55 and 0.75 were chosen to reduce deformation times and the contact time with the tools. It was then hoped that this would reduce the decomposition of the lubricant whilst still allowing sufficient time for the equilibrium volume fraction of α and β phases at the pre-deformation temperature. The stress-strain curves for these tests can be seen in Figure 5.39.

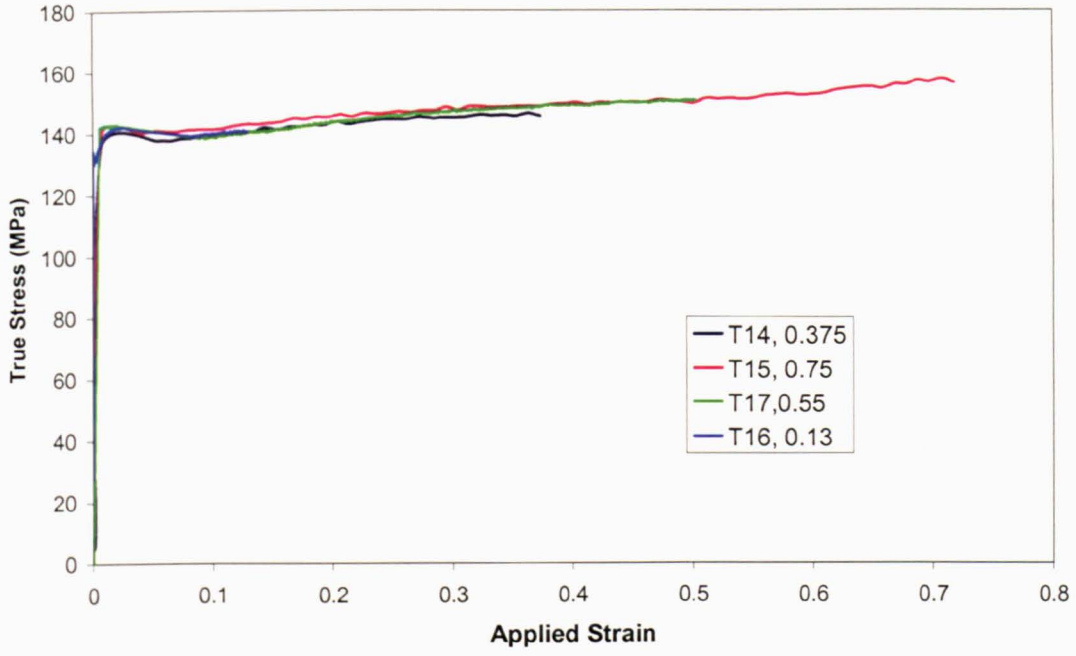

Figure 5.47 Stress-strain curves for T14-T17

5.5 Discussion of Flow Behaviour Results and Analysis

5.5.1 Initial testing and constitutive equation development.

The axisymmetric compression testing of tests D1-D9 were used in calculations to determine a value for Q_{def} and for developing constitutive equations. In this work a value for Q_{def} of 958.70 kJ/mol was determined which varies from previous work taken from other sources as shown in table 5.12.

Table 5.12 Comparisons of Q_{def} values from literature.

Authors	*Alloy*	*Al*	*Sn*	*Zr*	*Nb*	*Mo*	*Si*	*C*	*Fe*	*O*	*Ti*	Q_{def}	*Year*
Thomas et al	Timetal 834	5.74	3.99	3.47	0.72	0.50	0.30	0.06	0.008	0.1	Bal	959	2005
Bate et al	Timetal 834	5.82	4.46	3.96	0.72	0.54	0.35	0.05	0.02	-	Bal	803	1988
Wanjara et al	Timetal 834	5.8	4.0	3.5	0.7	0.5	0.35	0.06				703	2005
Semiatin et al	6242	6.0	2.2	4.1	-	2.0	0.09	-	-	-	Bal	624	2004

From the other authors, various analyses of the Q_{def} determination are given. Bate et al. suggests the higher values obtained for Q_{def} in the alpha + beta field results from recystallisation and some other diffusion dependant process. Wanjara et al.

explains that for deformation in the two phase region activation energies reported for titanium alloys are usually much higher than that for self diffusion which is consistent with the results produced in that work.

An explanation as to why the results from the various sources are different is needed and in order to address this issue a more comprehensive explanation of Q_{def} is needed, which is given in the following section.

5.5.1.1 Importance of Q_{def}

Figure 5.48 (Kocks, Argon, Ashby; Thermodynamics and Kinetics of slip, Pergamon Press,1975) shows a glide resistance diagram and an applied stress σb that is lower than the magnitude of the barrier. A dislocation traveling from left to right in the direction "a" is under a positive driving force b in some regions, but would be in (static) equilibrium at position S. A finite increment of area further on would be a second equilibrium position, U. The first position (S) is stable, the second position (U) is unstable. If thermal fluctuations transferred the dislocation from the stable to the unstable equilibrium position, it would then again be under positive driving force.

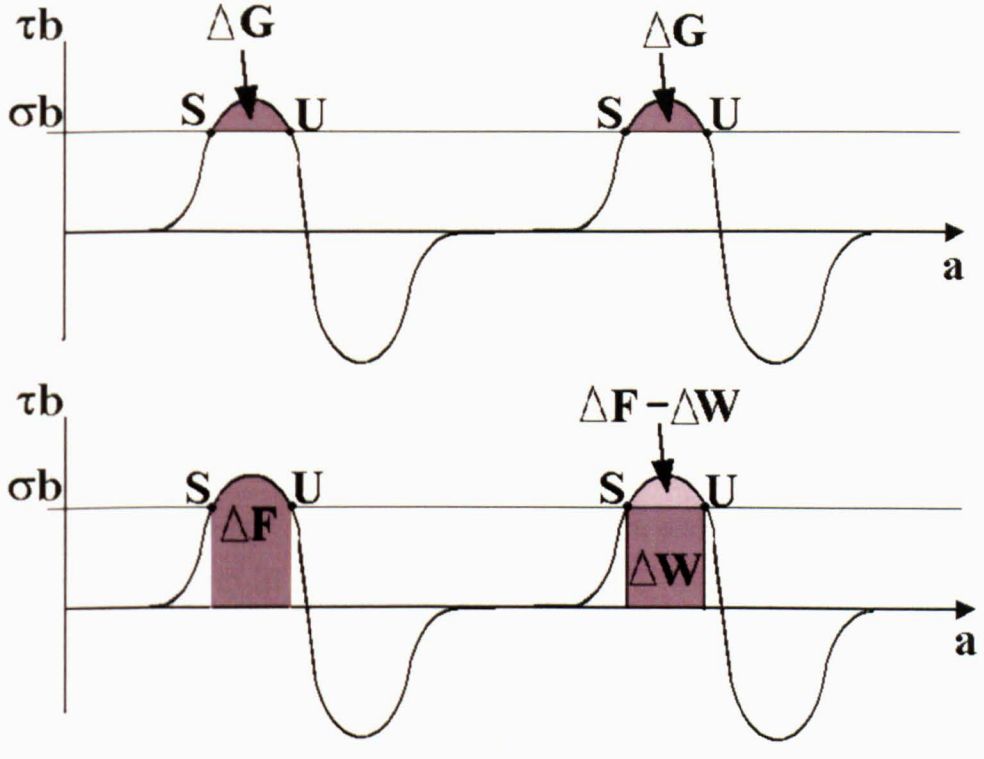

Figure 5.48 (a,b) A glide resistance diagram illustrating the quantities ΔG, ΔF, ΔW and Δa

The difference in energy between the stable and unstable equilibrium states, at a given stress and temperature, is the shaded area in Figure 5.48(a) and is given by Equation 5.19.

$$\Delta G = \int_{as}^{au} (\tau_{line} - \sigma) b da \tag{5.19}$$

This energy has been identified as a difference in free enthalpy ΔG .

Figure 5.48(b) shows a different illustration of the same process. During slip, this motion known as the Helmholtz free energy of the crystal may locally provide a resistance to motion this energy is represented in Figure 5.48(b) by the grey area labeled ΔF, and given by Equation 5.20.

$$\Delta F = \int_{as(a)}^{au(a)} (\tau_{line}) b da \tag{5.20}$$

Not all of this energy must be applied by thermal fluctuations, since at constant applied stress, some work ΔW would be done during activation. By subtracting the work done by the applied stress during activation from the (Helmholtz) free energy necessary for such an activation to take place, we obtain the energy that must be supplied by thermal fluctuations at constant temperature and stress.

$$\Delta G = \Delta F - \Delta W \tag{5.21}$$

The contributing proportions of stress and thermal fluctuations are altered depending on strain rate and temperature of the deformation. For a constant temperature condition the thermal energy in the system remains constant. The stress would have increased if the strain was increased. So, visualizing a dislocation moving along a line with glide resistance to its motion, at increased strain rates more dislocations have to overcome these obstacles in a given period of time. Therefore, the required stress would be higher and as such, at lower strain rates the required stress is lower as the rate of deformation and required dislocation motion is slower.

Hinton (2006) summarises, Q_{def} is described as an important material constant, and when combined with temperature and strain rate in the Zener Hollomon parameter

describes the flow stress during hot deformation. The value for Q_{def} must take into account the individual activation energies for all the active mechanisms during deformation. For example in materials that readily undergo dynamic recovery, the macroscopic activation energy may initially correspond to that of dislocation motion but may come to characterise that of subgrain formation towards the end of the deformation. Therefore Q_{def} may be considered to be an empirical material constant for the apparent activation energy of a combination of these physical processes during deformation.

Timetal 834, investigated in this work is a dual phase material at the deformation temperatures used here. As such, extra considerations should be taken into account when calculating Q_{def}. Material properties such as phase volume proportions and deformation behaviour in the dual-phase condition will affect the Q_{def} value but are not classically included in the calculation. Figure 5.49 illustrates the possibility that the energy barriers to dislocation motion will be different for the two different phases present. As such, the Helmholtz energy for each phase will vary and as such the Gibbs free energy will also vary.

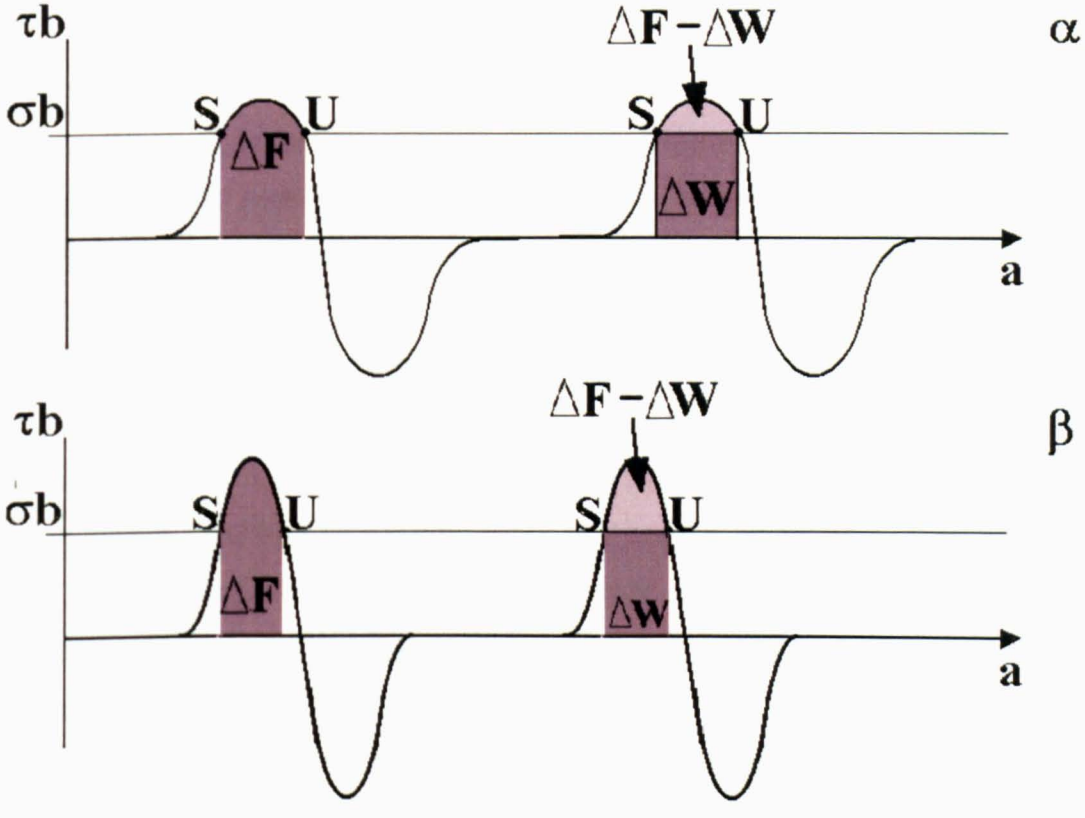

Figure 5.49 A schematic diagram illustrating the suggestion that the glide resistance in the (a) alpha phase and (b) beta phase will be different.

Furthermore, whilst the exact deformation behavior is unknown it would not be unreasonable to expect one phase to deform more readily than the other and therefore the σb value may not be the same for each phase.

Where as the modeling philosophy used in this work has been well established for single phase steels it does not consider the effect of phase volume fractions in dual phase materials. The modeling philosophy developed by Sellars (for example, Sellars, 1995) is based on the following function;

$$\sigma = f(\varepsilon, \dot{\varepsilon}, T) \tag{5.22}$$

Therefore, assuming that the flow behaviour is solely a mechanical function of the three parameters stated. For this alloy there would have to be an allowance within the model for the effect of a microstructural change and its effect on the activation energy;

$$\sigma = f(\varepsilon, \dot{\varepsilon}, T, S_1 - S_n) \tag{5.23}$$

Where S_1, is the effect of one defined microstructure (volume fraction), through to S_n referring to another defined microstructure. Throughout the constitutive equation development there was always the effect of the phase volume fraction on the value for Q_{def} and the relationship between Z and the discrete points that would ultimately need quantifying or at least addressing for the purposes of this work.

It was decided that rather than increase the work to be completed for this project the issues involved with the effect on phase volume fraction on constitutive equation development should be acknowledged but examined in future work. From figures 4.27-4.29 it can be seen that the fit at 950°C is quite close, certainly close enough for an industrial prediction. However, as the temperature increases the accuracy of the fit decreases and at 1030°C the fit is quite poor.

It is suggested that the reason for this decline of accuracy is due to the variation in phase proportion that this alloy incurs as temperature increases.

5.5.2 General flow behavior.

Figures 5.31, 5.41 and 5.43-5.46 show all the stress strain curves produced for this work, as detailed in Chapter 4 after friction and deformation heating correction. Figures 5.31 and 5.46 show the flow behavior of the successful axisymmetric compression tests where the obtained deformed test pieces have been sectioned and used for metallographic examination. The flow behavior of the compression tests consists of an initial rapid rise in the flow stress reaching a peak, followed by behavior very close to steady-state where the behavior is almost perfectly plastic, i.e., the stress is uniform with increasing strain. The flow curves are seen to vary in magnitude with varied temperature and strain rate, and the trends associated with each parameter can be seen best in Figure 5.31 and Figure 5.50.

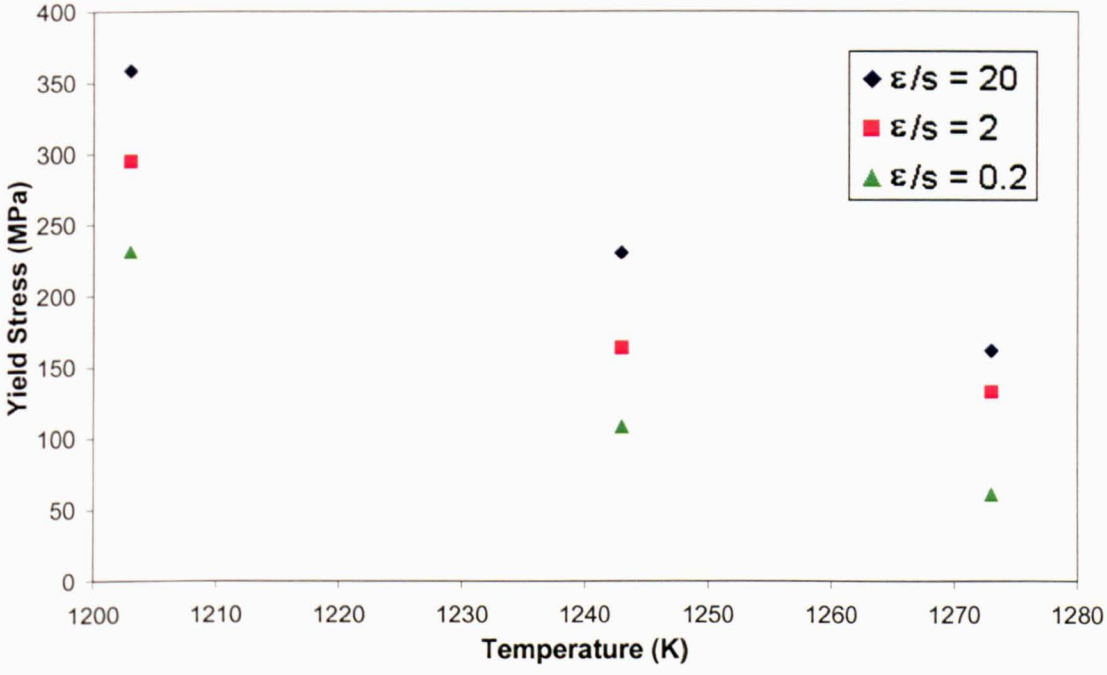

Figure 5.50 A graph showing the trends in yield stress associated with temperature and strain rate of deformation.

As expected as the temperature at which deformation increases the strength of the material decreases and as the strain rate at which deformation increases so does the flow stress experienced. The flow curve labeled 1 shows the axisymmetric compression test completed at 950°C with a strain rate $20s^{-1}$, the flow curve rapidly rises to reach a yield point at the peak stress, this stress is then maintained with increasing strain. The flow curve labeled 9 shows the axisymmetric compression test completed at 1030°C

with a strain rate of $0.2s^{-1}$. In this curve the flow stress is again seen to rise initially very quickly until the yield at which point the flow stress gradient changes and a steady increase in flow stress is seen with increasing strain. In the curves labeled 6,8 and 9 the flow stress does not reach steady-state up to a strain of 0.7.

Figure 5.51 shows the flow curves seen previously in Figure 5.31, however, the Zener Hollomon parameter for each test is identified and labeled alongside. It can be seen in this figure that a change in flow behavior is apparent between a Zener Hollomon of $8.95x10^{38}$ and $5.43x10^{39}$.

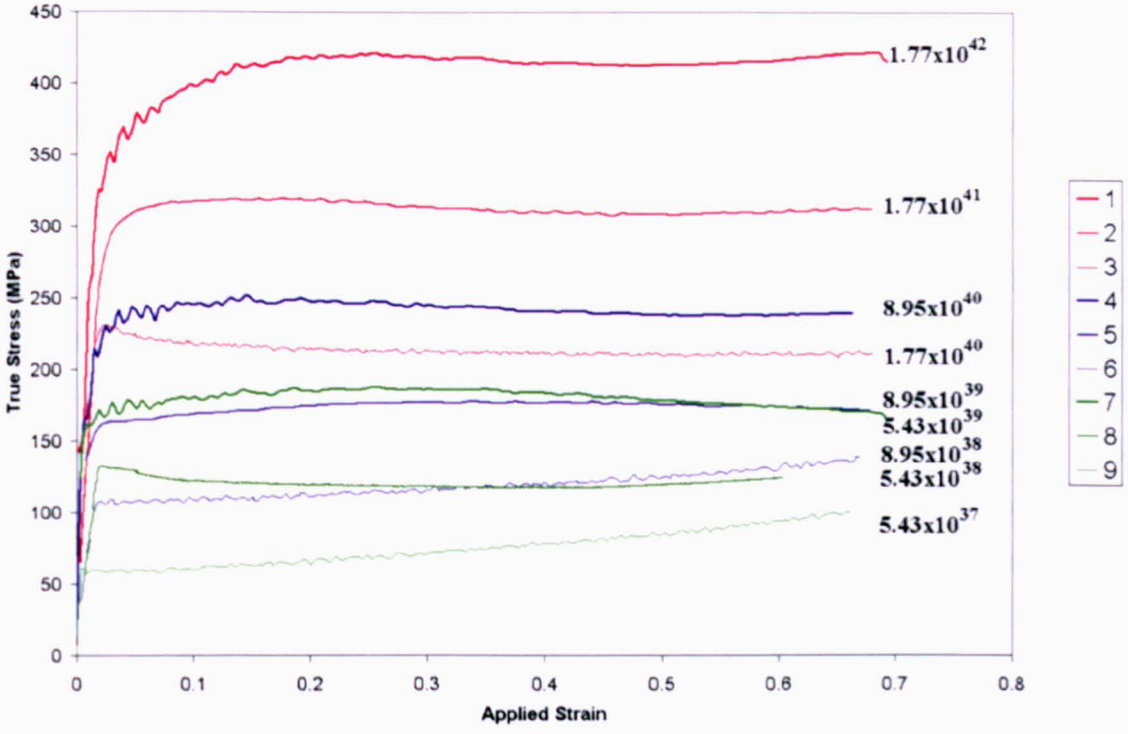

Figure 5.51 Stress-strain curves of axisymmetric compression test including Zener-Hollomon parameters.

5.5.2.1 Comparisons with previous work

These results and flow behavior seen are contradictory to previous work completed by Bate et al (1998) using strain rates of $3x10^{-2}$-$3x10^{-4}$ s^{-1}. Bate et al's (1998) results show significant flow softening at 1000°C with up to 15% drop in the flow stress observed, see figure 5.52. Bate et al. (1998) summarise 'the overall deformation behavior was characteristic of material deforming by a combination of recovery and recrystallisation and it is likely that the flow softening that occurred at

high strain rates ($3x10^{-2}$ s^{-1}) was caused by enhanced dynamic recrystallisation associated with the rapid deformation'.

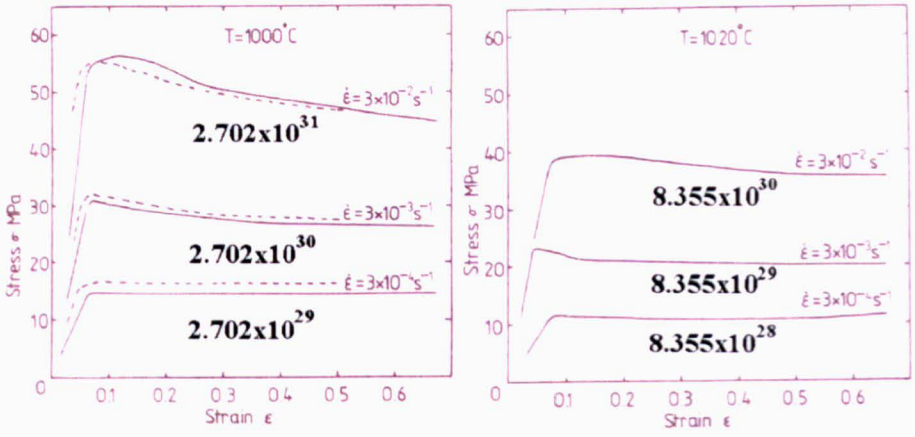

Figure 5.52 Flow stress behaviour of Timetal 834 at 1000°C and 1020°C, taken from Bate et al, 1988.

Further work has also been completed by Wanjara et al. (2005) with various similarities and differences to the results of this work. In the work of Wanjara et al. (2005) the flow behaviour Timetal®834 was investigated by compression tests at temperatures 950-1125°C, strain rates 0.001-$1s^{-1}$ to a true strain of 0.8, see figure 5.53. The flow curves from this work exhibit flow softening behaviour and are described by the authors 'after an initial peak stress is reached the flow stress decreases with increased strain and steady-state stresses were not observed even up to a strain of 0.8'. The flow softening behaviour in Wanjara et al's (2005) work is attributed to deformation heating, which is identified in the text and further attributed to the physical manifestation of shear bands illustrated in the work and shown in Figure 5.54. However no correction for this heat rise is apparent in the paper regarding calculation of the flow stress, the effect of which is known from this work to be substantial as seen in Figure 5.55.

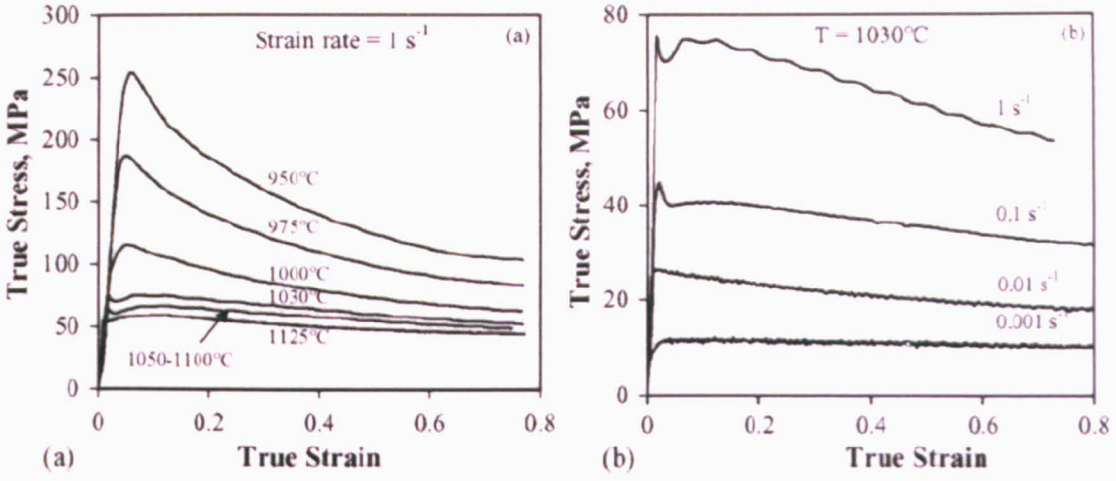

Figure 5.53 Flow behaviour of Timetal 834 showing (a) the effect of forging temperature and (b) strain rate, taken from Wanjara et al, 2005.

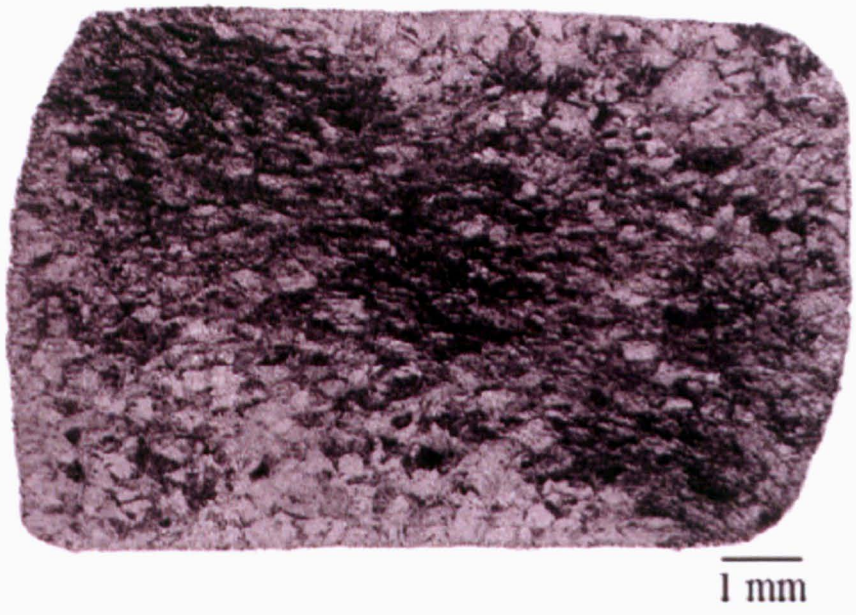

Figure 5.54 Micrographs of (a) Wanjara et al's axisymmetric compression sample and(b) a quartile of a specimen taken from this work

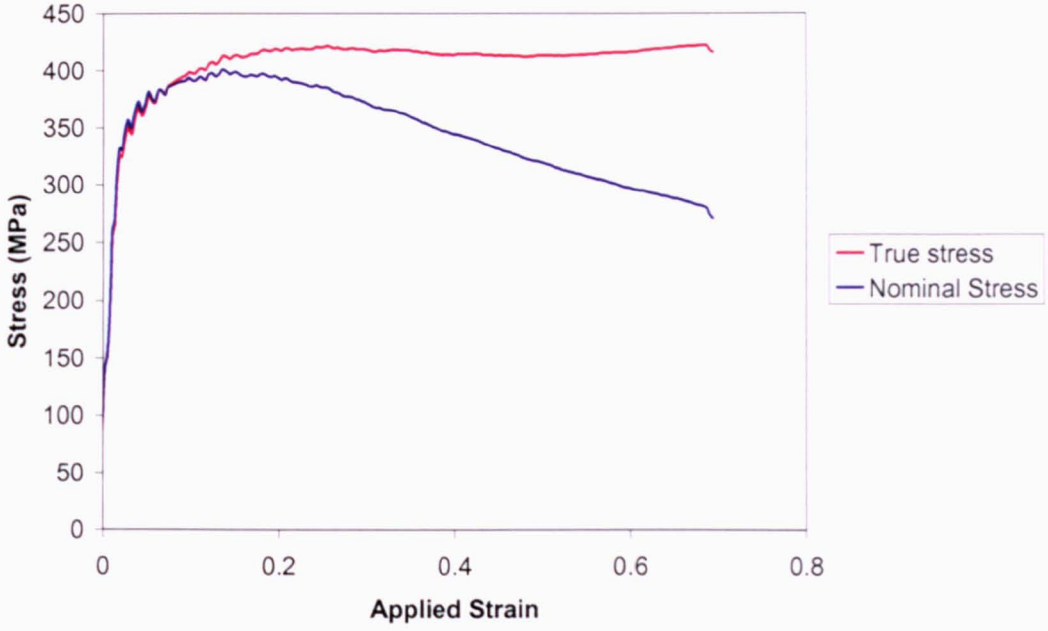

Figure 5.55 A direct comparison of the flow softening exhibited in this work compared with Wanjara et al's results can be seen in Figure 5.53

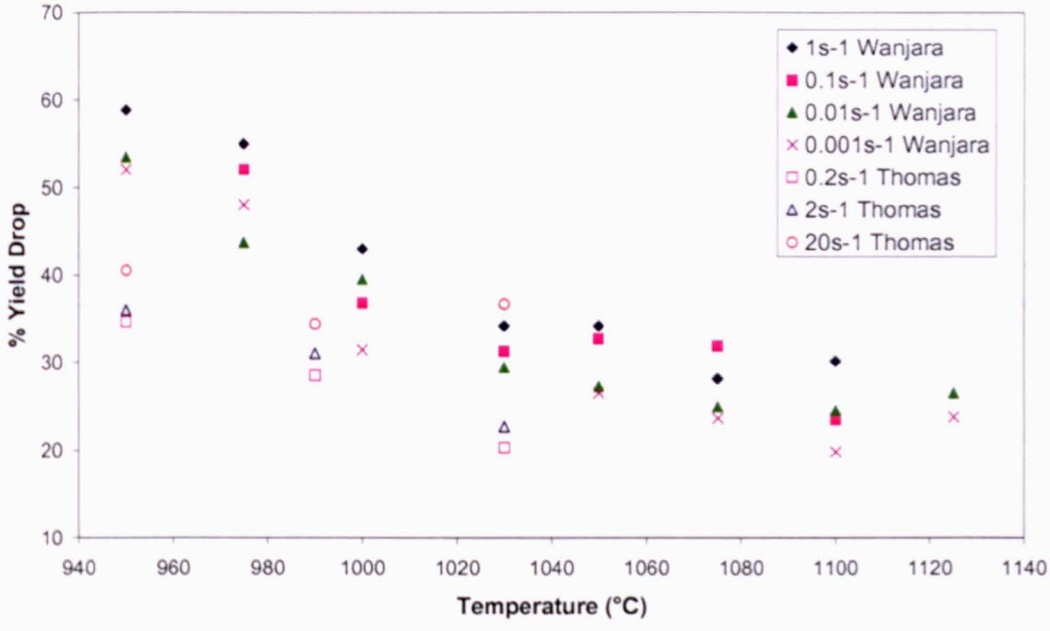

Figure 5.56 Comparison of flow softening behaviour of axisymmetric compression tests.

Table 5.13 details the parameters of tests completed and the Zener Hollomon parameters for those tests based on the values of Q_{def} used.

Table 5.13 Zener Hollomon values of tests completed based on activation energies (Q_{def}) used.

Author	*Temp (°K)*	*ϵ/s*	*Z (Thomas)*	*Z(Bate)*	*Z(Wanjara)*
Thomas	1223	20	$1.77x10^{42}$	$4.00x10^{35}$	$2.13x10^{31}$
Thomas	1223	2	$1.77x10^{41}$	$4.00x10^{34}$	$2.13x10^{30}$
Thomas	1223	0.2	$1.77x10^{40}$	$4.00x10^{33}$	$2.13x10^{29}$
Thomas	1263	20	$8.95x10^{40}$	$3.28x10^{34}$	$2.38x10^{30}$
Thomas	1263	2	$8.95x10^{39}$	$3.28x10^{33}$	$2.38x10^{29}$
Thomas	1263	0.2	$8.95x10^{38}$	$3.28x10^{32}$	$2.38x10^{28}$
Thomas	1303	20	$5.43x10^{39}$	$3.14x10^{33}$	$3.05x10^{29}$
Thomas	1303	2	$5.43x10^{38}$	$3.14x10^{32}$	$3.05x10^{28}$
Thomas	1303	0.2	$5.43x10^{37}$	$3.14x10^{31}$	$3.05x10^{27}$
Bate	1273	0.03	$6.56x10^{37}$	$2.70x10^{31}$	$1.06x10^{30}$
Bate	1273	0.003	$6.56x10^{36}$	$2.70x10^{31}$	$2.66x10^{29}$
Bate	1273	0.0003	$6.56x10^{35}$	$2.70x10^{31}$	$7.03x10^{28}$
Bate	1293	0.03	$1.61x10^{37}$	$8.35x10^{30}$	$1.52x10^{25}$
Bate	1293	0.003	$1.61x10^{36}$	$8.35x10^{29}$	$1.52x10^{26}$
Bate	1293	0.0003	$1.61x10^{35}$	$8.35x10^{28}$	1.52E+27
Wanjara	1223	1	$8.87x10^{40}$	$2.00x10^{34}$	1.52E+28
Wanjara	1248	1	$1.34x10^{40}$	$4.12x10^{33}$	1.85E+26
Wanjara	1273	1	$2.19x10^{39}$	$9.00x10^{32}$	2.11E+27
Wanjara	1303	0.001	$2.71x10^{35}$	$1.57x10^{29}$	2.11E+26
Wanjara	1303	0.01	$2.71x10^{36}$	$1.57x10^{30}$	2.11E+25
Wanjara	1303	0.1	$2.71x10^{37}$	$1.57x10^{31}$	7.55E+26
Wanjara	1303	1	$2.71x10^{38}$	$1.57x10^{32}$	7.55E+25
Wanjara	1398	1	$6.64x10^{35}$	$1.02x10^{30}$	7.55E+24

5.5.3 Evaluation of Differences

Through analysis and critical assessment of the three pieces of work compared in Section 5.5.3.1, it was determined that there a numerous reasons why the data compared is, in many cases, not directly similar. The most notable difference was the flow hardening behavior of the material used in this work compared with flow softening behavior experienced in the other sources. Once the flow behavior data gained through axisymmetric compression are corrected for deformation heating and friction effects all signs of flow softening disappear, see Figure 5.55, leading us to ask the question on whether dynamic recrystallisation takes place and the deformation heating correction is eradicating the flow stress behavior associated with the phenomenon.

The stress-strain curve of a dynamically recrystallising material may be characterized by a single peak or several oscillations; this is not evident in the corrected curves seen in Figure 5.51 as it is in curves from Bate et al. (1998) and Wanjara et al. (2005) Figures 5.52 and 5.53.

If a material was to dynamically recrystallise then at a critical strain value new grains would nucleate and grow free of dislocations and replace the deformed material leading to flow softening. Dependant of the degree of recrystallisation the microstructure would consist of a number of equiaxed strain free grains.

Strain hardening is the phenomenon whereby a ductile metal becomes harder and stronger as it is plastically deformed. The strain-hardening phenomenon is explained on the basis of dislocation-dislocation strain field interactions. The dislocation density in a metal increases with deformation, due to dislocation multiplication or the formation of new dislocations. Consequently, the average distance of separation between dislocations decreases. On the average, dislocation-dislocation strain interactions are repulsive. The net result is that the motion of a dislocation is hindered by the presence of other dislocations. As the dislocation density increases, this resistance to dislocation motion by other dislocations becomes more pronounced. Thus the imposed stress necessary to deform a metal increases with increasing cold work. The microstructure of a strain hardened material would include deformed, possibly 'pancaked' grains with a high dislocation density. In order to further discuss and confirm the assumptions on strain hardening made in this chapter and dismiss the suggestion that recrystallisation takes place within this alloy the microstructure of both phases present in the test specimens need to be examined. This will be documented in Chapter 6 and discussed further in Chapter 8.

It would be an oversight to assume that the differences in flow behaviour are solely due to deformation heating correction. The comparisons of this work and the previous work completed by Bate et al and Wanjara et al, has allowed us to acknowledge the effect of starting microstructures on the flow behaviour of this alloy. The as-received microstructure of the material used in this work consists of 70% α_p with the remaining 30%, a coarse α_s microstructure present at tri-points. In Bate et al the as-received microstructure consisted of 40% α_p surrounded by 60% lamellar α_s. Finally, Wanjara et al.'s as-received microstructure, initially, is very similar to Bate et al's.

The differences in as-received microstructures prior to testing will lead to variations in the microstructures at deformation temperatures as the α morphologies present will vary.

If we consider a test where deformation takes place at 990°C, the high temperature microstructure, determined from the beta approach curve seen in figure 5.57, of the as-received material used in this work will consist of approximately 50% α_p in a matrix of 50% β whilst Bate et al's high temperature microstructure will consists 40% α_p, 10% α_s and 50% β. The major difference will be in Wanjara et al's microstructure as prior to deformation the testpieces are heated to 1050°C, i.e. almost fully β, the testpiece is then cooled to the deformation temperature and as such the microstructure consists of 50% α_s and 50% β.

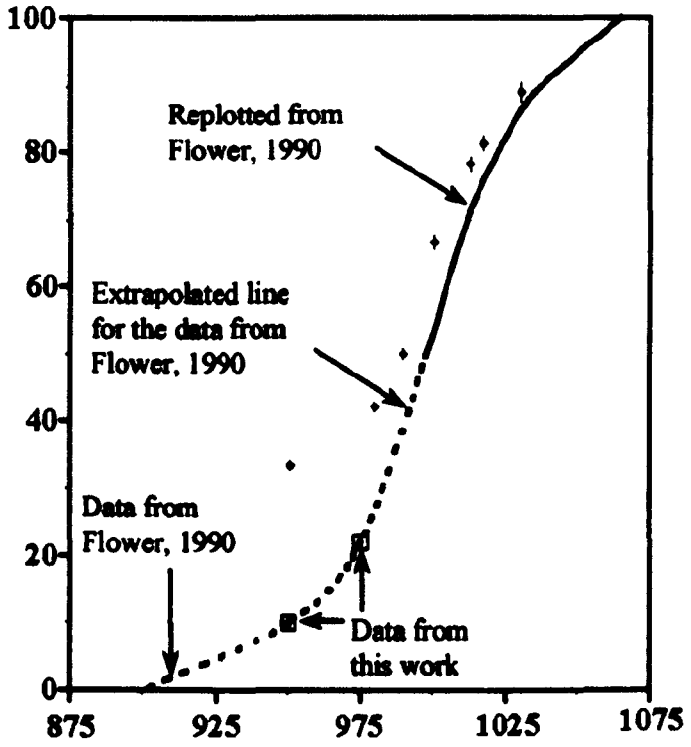

Figure 5.57 Beta Approach curve detailed in Wanjara (2005)

The flow behaviour of the various morphologies is known to differ and therefore differences in microstructure will lead to differences in flow behaviour (Ding et al, 2002). Weiss and Semiatin 1999, discuss deformation in single phase α_p alloys and state that stress-strain curves show an initial work hardening period followed by a regime of near steady-state flow. Higher peak stresses are observed at higher strain rates and lower temperatures.

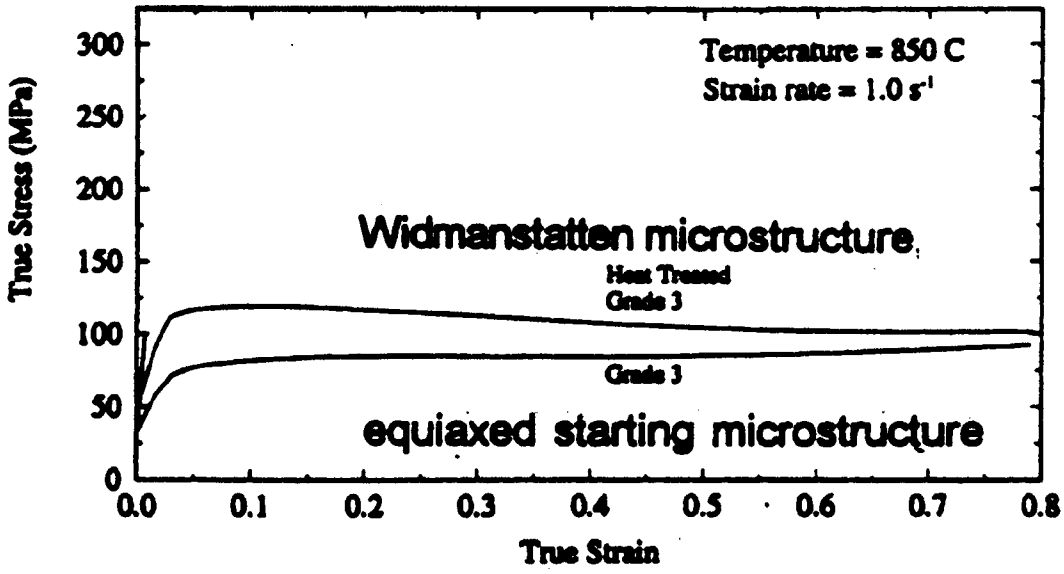

Figure 5.58 Effect of starting microstructure on flow behaviour (Weiss and Semiatin, 1999)

Figure 5.58 shows stress strain curves for CP titanium grade 3 (0.28O, 0.2Fe) taken from where variations in starting microstructure were investigated. The results show that material with an equiaxed starting microstructure shows lower flow stresses and work hardening during deformation, thus leading to homogeneous flow under most deformation conditions. When CP titanium grade 3 with an equiaxed microstructure is heat treated to produce a Widmanstatten microstructure, the flow stress increases and slight flow softening is detected. Similar effects have been observed in alpha zirconium where the level of fineness of the acicular microstructure controls the flow stress and the extent of flow softening during high temperature deformation (Abson, Jonas, 1977). The flow softening experienced in the flow curve with a Widmanstatten microstructure is believed to be due to spheroidisation (or globularistaion) of the α_s laths (priv comm., Prof Peter Bate, 2007).

Breakdown of the transformed microstructure during hot working at temperatures below the beta transus plays a key role in the development of the equiaxed alpha microstructure frequently desired for final shaping or service. Because of its great technological importance, the process of globularisation of the transformed microstructure to obtain an equiaxed one has received considerable attention from the viewpoint of both phase transformation kinetics and mechanisms.

Globularisation behavior was studied by Semiatin et al.(1999) and quantified using moderate magnification optical photographs with selected observation at high (SEM) magnifications. SEM micrographs and optical micrographs for compression tests

at 0.1 s^{-1} and test temperatures of 815 and 955°C showed microstructures comprising bent and kinked lamellae and an absence of globularisation at low strains (0.96) and almost fully globularised microstructures at large strains (2.56). The nucleation sites for globularisation occurred at kinks in the lamellae as well as some of the prior-beta grain boundaries.

5.6 Summary

The results of the chapter can be summarised as follows:

- A friction coefficient of μ = 0.197 was determined when deforming Timetal®834 using AML 1000 lubrication.
- A value for Q_{def} of 958.70 kJ/mol has been determined.
- Variations in flow behaviour with previous work are caused by the variation in morphology of the α phase in the dual phase field at deformation temperatures.
- Equiaxed α_p are believed to strain harden during deformation and transformed lamellar or widmanstatten α_s flow soften due to bending and kinking of the lamellae.

In the following chapters the microstructural analysis of the axisymmetric compression tests will be used to further explain the flow behaviour of Timetal 834.

6. METALLOGRAPHIC RESULTS

6.1 Introduction

The following chapter contains the optical and electron microscopy results produced during the project. In order to present the results in a clear and succinct way they have been separated in terms of there purpose and have been sectioned as follows:

- Beta approach curve determination; and
- Metallographic and texture examination and OIM acquisition.

6.2 Beta Approach Curve Determination

The volume fraction analysis results for the beta approach curve determination can be seen in Table 6.1 and are plotted in a Figure 6.1.

Table 6.1. Summary of Beta Approach Determination Work (* determined by point counting)

Test ID	*Temperature ± 0.05 (°C)*	*Average Beta vol.%*	*Standard Deviation*
B1	950	33.54	
B2	980	42.21	
B3	990	49.98	1.012
B4	1000	66.80	1.210
B5	1013.5	78.34	1.317
B6	1017.5	81.50	1.120
B7	1030.5	89.15	1.733

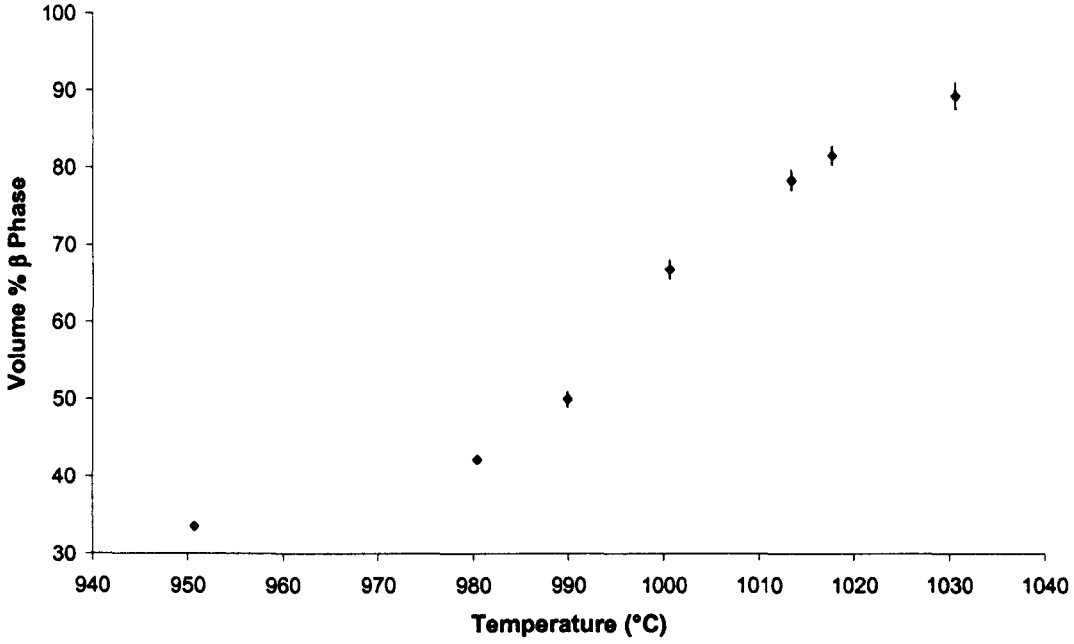

Figure 6.1 Beta approach curve of as-received material produced at The University of Sheffield.

An example of the micrographs used and the resulting analysed image produced can be seen in Figure 6.2(a) and (b) on the following page. The colours used to identify α_p grains are randomly determined by the software.

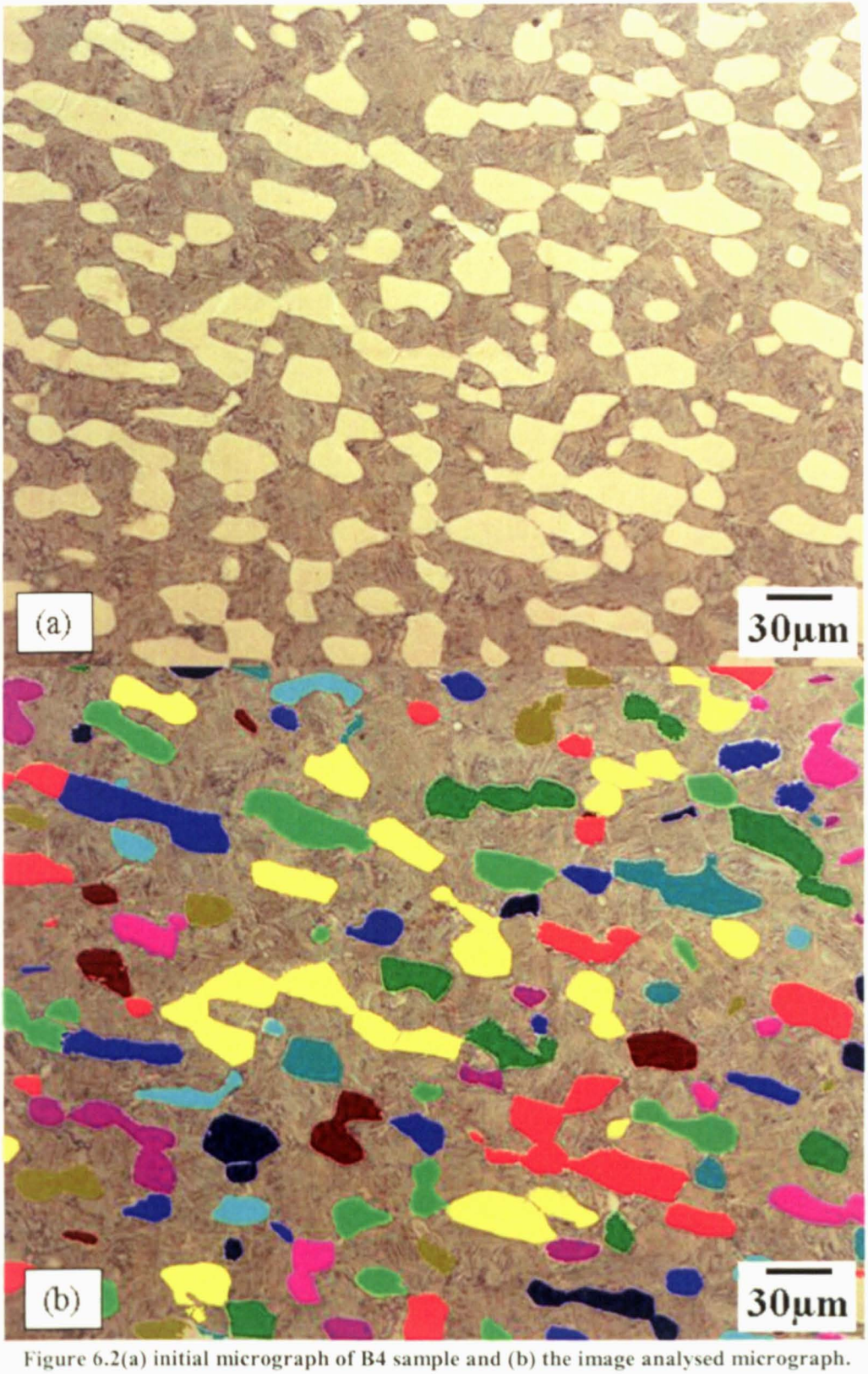

Figure 6.2(a) initial micrograph of B4 sample and (b) the image analysed micrograph.

At low heat treatment temperatures the software has difficulty calculating the volume fraction of both phases, for example Figure 6.3(a) shows a micrograph of a Timetal®834 sample heat treated to 950°C and (b) the associated analysed image. The

software cannot distinguish one grain from the next and, as such, over estimates the α_p volume fraction.

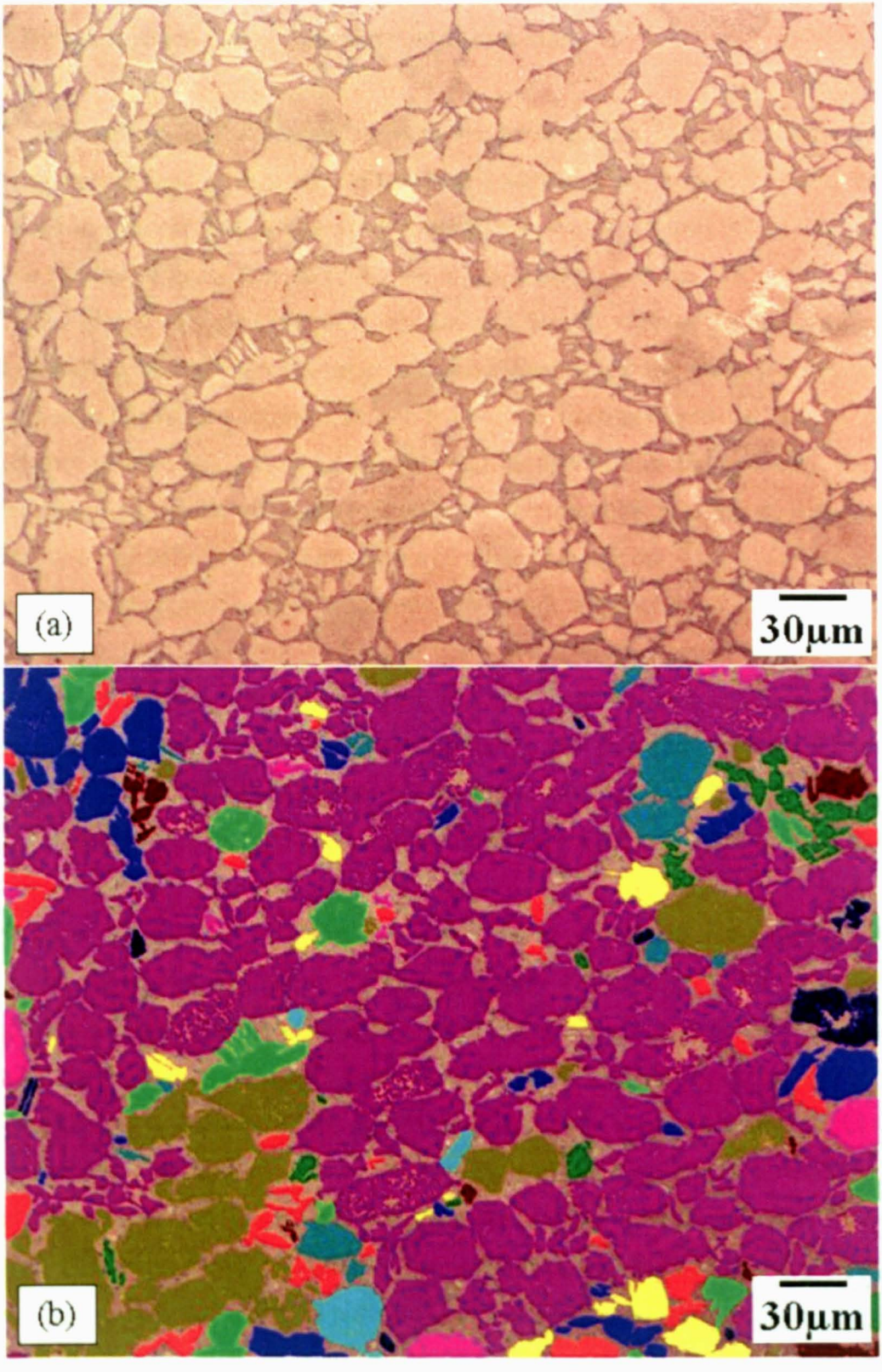

Figure 6.3(a) initial micrograph of a B1 sample and (b) the image analysed micrograph.

In these cases point counting was used as detailed in Sellars & Higginson (2003) to determine to volume fraction of the α_p.

6.2.1 Beta Approach Curve Summary and Discussion.

The aim of the beta approach work was to identify a β approach curve for the material received and to elucidate the trends that were contradictory in the previous data discussed in Chapter 2.10.3. From the micrographs seen in Figures 6.3(a) and (b) it is easy to see the difficulty the software had in calculating a low α_s volume percentage; firstly, the high volume fraction of α_p appears to affect the stain of the etch, as such the contrast difference is not as obvious as with the higher temperature tests (see Figure 6.2) and although this has a minimal effect on the volume fraction calculated, it does lead to uncertainty in terms of grain size analysis and its distribution and secondly, the high percentage of α_p is believed to have an effect on the morphology of the α_s and decrease the ability of the software to determine the α_p phase from the α_s.

The beta approach curve produced in this work, Figure 6.1, shows a small 'knee' at just below 1000°C, i.e. the gradient of the curve is much steeper between 990 and 1000°C than anywhere else on the curve. Though as can be seen in Figure 6.4(a) the curve produced from this work is very similar to the data published by Timet UK produced at Timet UK, Birmingham for the same cast material used, suggesting the methods used and the temperature control in-house are similar to those used by the cast provider.

It is important to note that the reason the beta approach curve determination work was undertaken was due to the steep gradient of the Flower (1990) data and the consequence this would have on the volume fraction control during heat treatment. Fortunately, the results from the work undertaken show a shallower curve, nothing like the gradient of the Flower (1990) data, and consequently a good working window for heat treatment. Figure 6.4(b) shows a comparison of the beta approach results gained from this work against the Flower data over the volume fraction region of industrial interest. This graph shows the ability to control the volume fraction of this alloy in the area of interest as 0.869% β/°C. This result agrees with the philosophy that this alloy has good tailoring ability and allowed us to complete our testing schedule with confidence of the microstructure of the material at temperature.

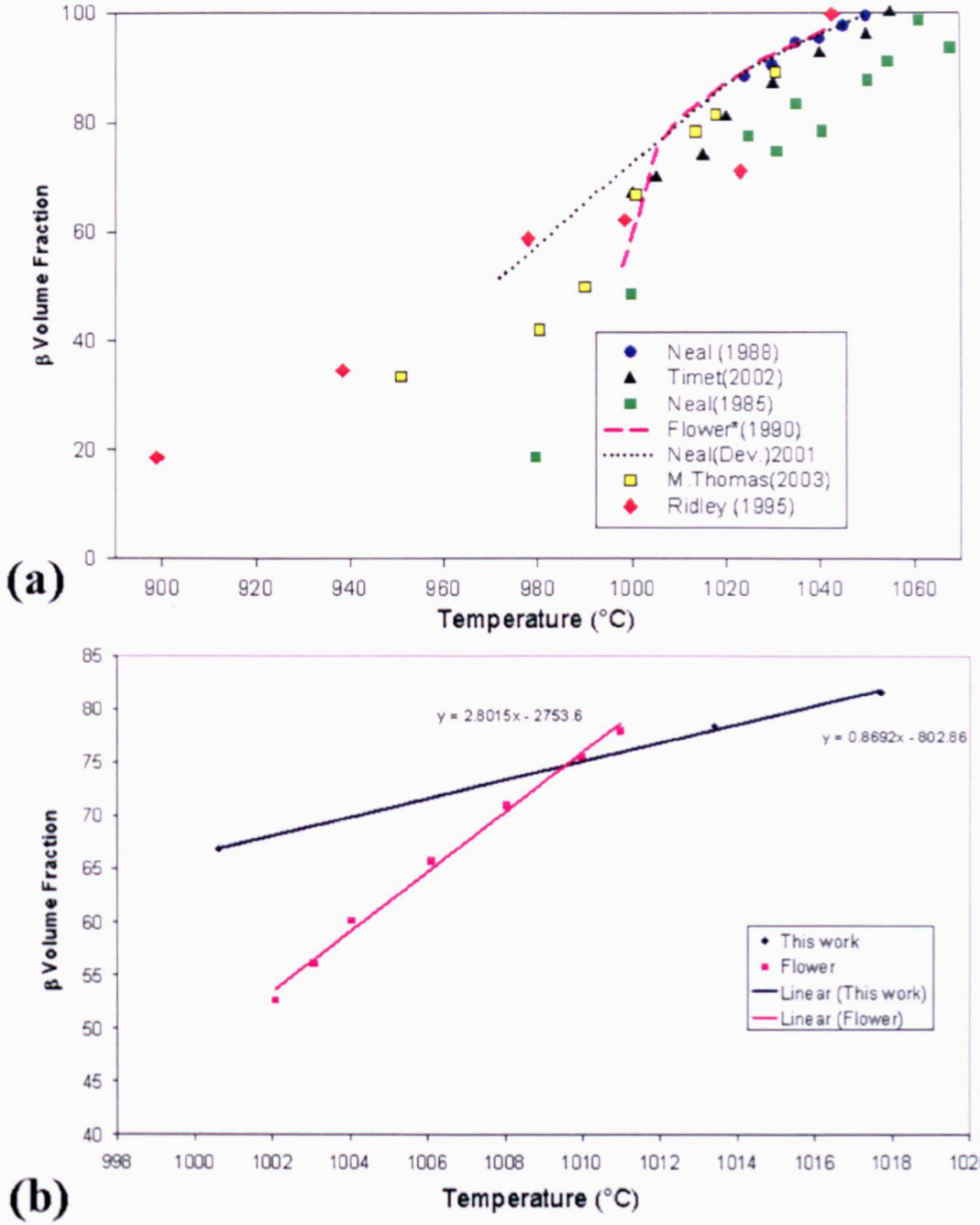

Figure 6.4(a) Beta Approach results gained in this work with previous data and (b) difference in gradients in area of interest.

6.3 Metallographic Examination and OIM Acquisition

6.3.1 Introduction

Metallographic examination of the billet material and subsequent thermomechanically processed axisymmetric compression tests were carried out both optically and through SEM and EBSD analysis. This section will present the optical and electron micrographs as well as OIM's, collected through EBSD, of the deformed

samples. Due to the nature of crystallographic orientation data acquisition and the subsequent analysis involved, the results in this section will only consist of a single Euler colouring OIM of the entire dataset obtained; this effectively allows the OIM image to be viewed in a similar way to a micrograph. In Chapter 8, entitled 'EBSD Analysis and Interpretation', the OIM's have again been considered but in this case in terms of there orientation information and they have been analysed in combination with the pole figures which will be presented in the next section. Where EBSD datasets have been obtained they will be shown in this chapter in the form of Euler colouring OIM's with black lines representing 10° misorientations between neighbouring grains.

Initially the as-received material was mapped to assess the starting material. This was followed by the thermo-mechanically processed axisymmetric compression test samples. The latter maps were obtained using both large step sizes for statistical texture determination and small step sizes (<0.5μm) for high resolution microstructural analysis. The process of OIM production was mentioned in Chapter 4 and is explained in detail in the following section.

6.3.1.1 OIM production

As detailed in Chapter 2 the back scattered electron produced Kikuchi pattern is used to determine the materials orientation at the point directly under the electron beam. Having mapped an area the software initially presents the operator with a dataset of co-ordinates and Euler angles, an example of which can be seen in Table 6.2

Table 6.2, Information included in EBSD dataset

Phase	*X*	*Y*	*Bands*	*Error*	*Euler1*	*Euler2*	*Euler3*	*MAD*	*BC*	*BS*
1	0.0000	0.0000	6	0	70.443	108.82	33.291	0.6000	139	0
1	0.2000	0.0000	6	0	70.443	108.82	33.291	0.4000	117	0
	1.0000	0.0000	6	0	70.489	108.86	33.920	0.6000	135	0
1	0.6000	0.0000	6	0	70.515	108.81	33.910	0.6000	101	0
1	1.8000	0.0000	6	0	70.358	109.97	31.516	0.6000	121	0
1	2.0000	0.0000	6	0	67.215	145.91	26.676	0.5000	139	0
1	2.2000	0.0000	6	0	67.215	145.91	26.676	0.2000	121	0

The table shows;

- Both the x and y coordinates of the pixel with reference to the start position
- The number of kikuchi bands indexed
- The 3 Euler angles
- The mean angular deviation (MAD)
- The band contrast
- And the band slope

All but 3 of these sources of information can be used to produce an OIM. The calculation of Euler colouring, IPF colouring and the other major mapping characteristics used in this work will be detailed in the following chapters.

6.3.1.2 Noise Reduction

Whilst constructing an OIM it is important to remove the 'noise' or indexing errors from the dataset. Using a collected dataset an OIM is produced as seen in Figure 6.5(a), showing the initial OIM obtained from T1, Figure 6.5(b) shows the noise reduced image.

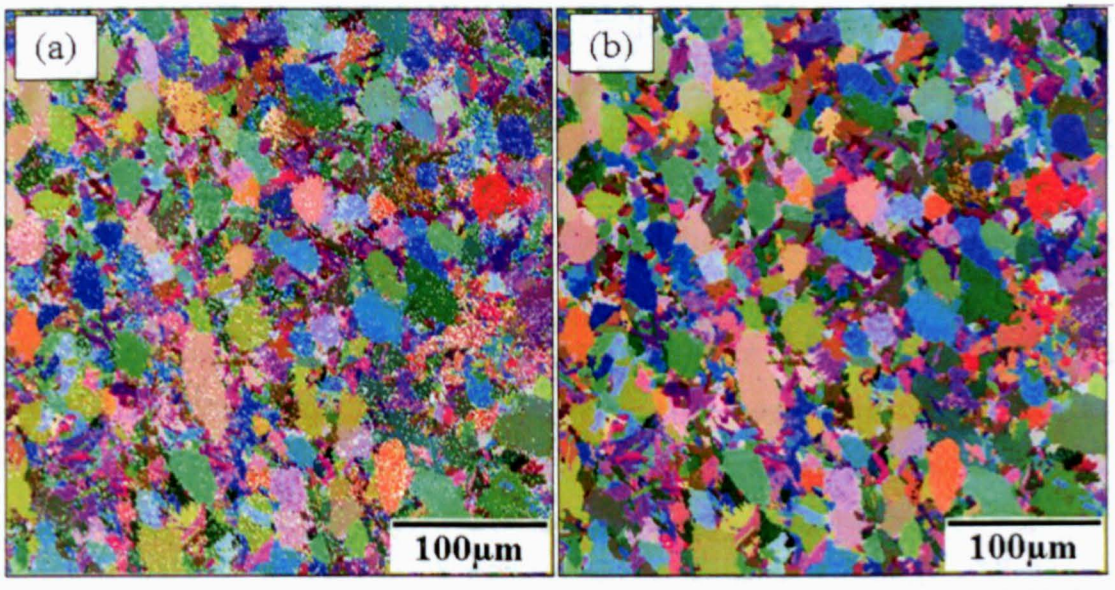

Figure 6.5(a) OIM produced from raw data showing non indexed points and (b) the OIM after noise reduction.

Figure 6.5(a) contains a number of white areas, these white pixels represent a point in the map where the kikuchi pattern remains un-indexed. A non indexed point can appear for a number of reasons;

- Contamination of sample leading to no kikuchi pattern or a kikuchi pattern resulting from the contaminant which the software has not been instructed to index.
- The sample preparation is insufficient, such that the kikuchi pattern produced is poor due to sub-surface deformation or a non-uniform surface.
- The interaction volume of the electron beam impedes a number of grains and as such more than one kikuchi pattern is produced and as such indexing is complicated.

The non indexed points can be removed through noise reduction techniques included in the Channel 5 software, seen in greater detail in Figure 6.6(a) and (b).

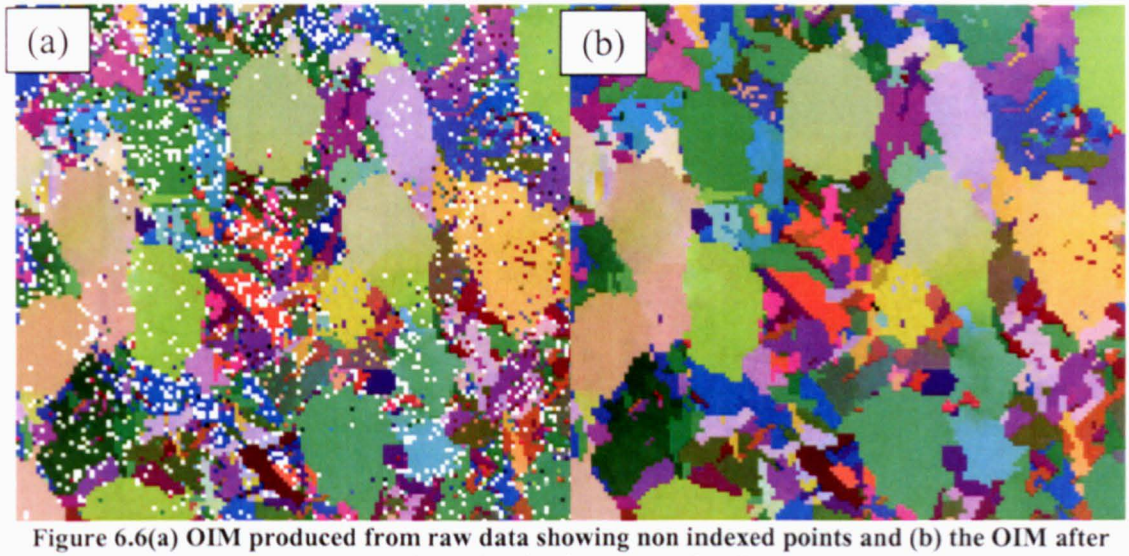

Figure 6.6(a) OIM produced from raw data showing non indexed points and (b) the OIM after noise reduction in greater detail.

The process of noise reduction involves the reduction of 'Wild Spikes' followed by general noise reduction of zero indexed points. Spikes are measurement points with a wrong indexing solution; spikes may occur where no or only very poor quality back scattered electron signals are generated, i.e. at grain boundaries, cracks, dislocation clusters, voids, inclusions or around damages on the sample surface. Zero indexed points are allocated the same orientation as their neighbouring pixels, the magnitude of noise reduction is determined by the number of neighbouring pixels with the same orientation used to noise reduce and in this work was set to 4. The standard noise reduction should be used with caution as large regions of zero solutions could indicate the presence of unknown phases or surface contamination (Channel 5, service pack 7 Help File, 2006).

6.3.1.3 Grain boundary determination

The Channel 5 software uses local misorientations to construct grain boundaries, which allow comparisons with micrographs. The levels of misorientation can be specified as in Figure 6.7 where the red lines are misorientations between 2-10° and the black lines are misorientations greater than 10°.

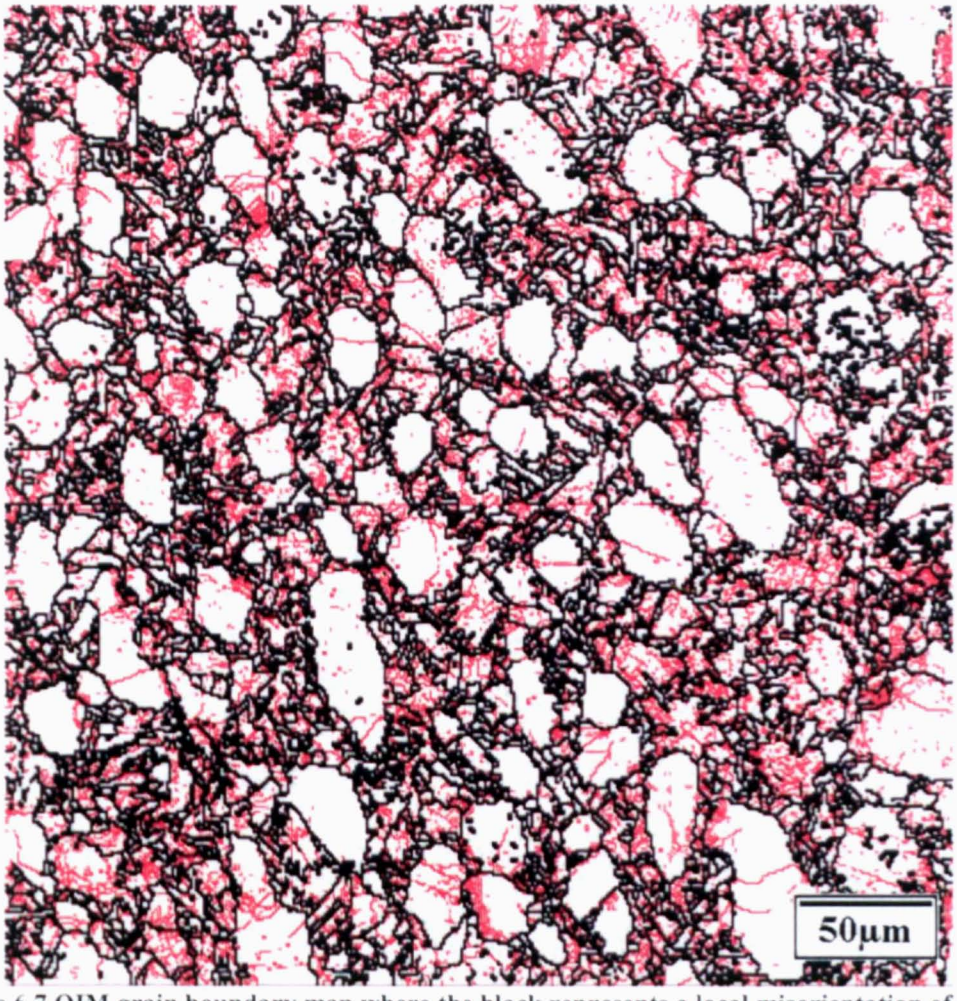

Figure 6.7 OIM grain boundary map where the black represents a local misorientation of 10° or higher and the red lines show misorientation between 2-10°

6.3.1.4 Phase identification

Another aspect of the software is to illustrate the OIM using phase colouring as seen in Figure 6.8(a), where the red pixels are HCP titanium α and the blue represents the BCC β phase. It is clear from Figure 6.8(b) that this type of OIM can be more useful when combined with grain boundaries.

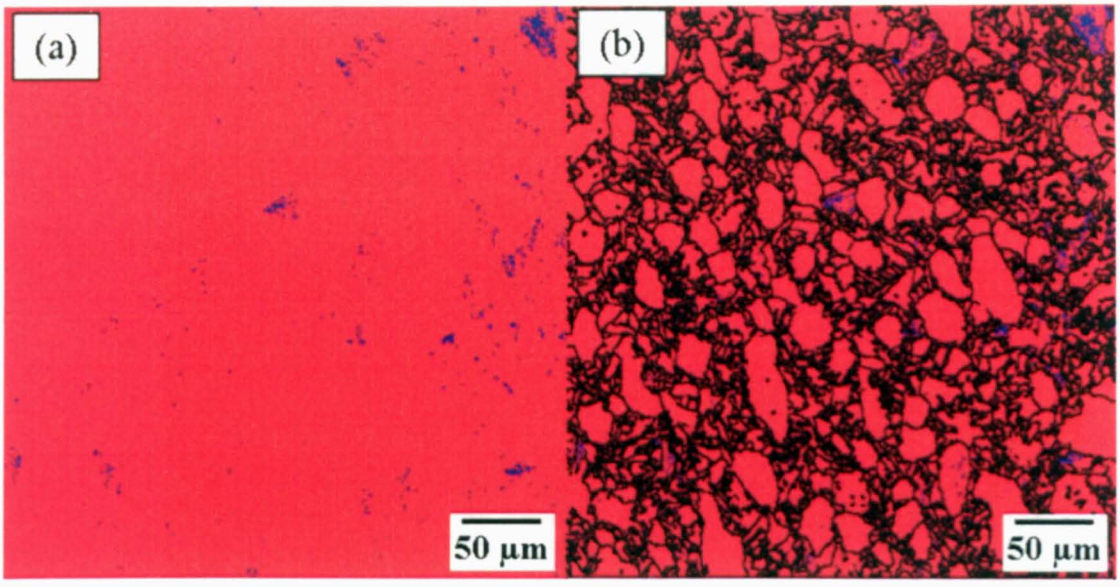

Figure 6.8(a) OIM using phase colouring, (b) and then combined with grain boundaries.

6.3.2 Initial Texture Determination and Micrographs of billet material

6.3.2.1 X-ray analysis

Initially the billet material was analysed using X-ray goniometry techniques, as described in Chapter 2.13. The results from the goniometry can be seen in Figures 6.9-6.11 in the form of $\{10\bar{1}0\}$ and $\{0002\}$ pole figures taken from central, position A and outer diameters, Position B and C as detailed previously in Chapter 4.6.2.

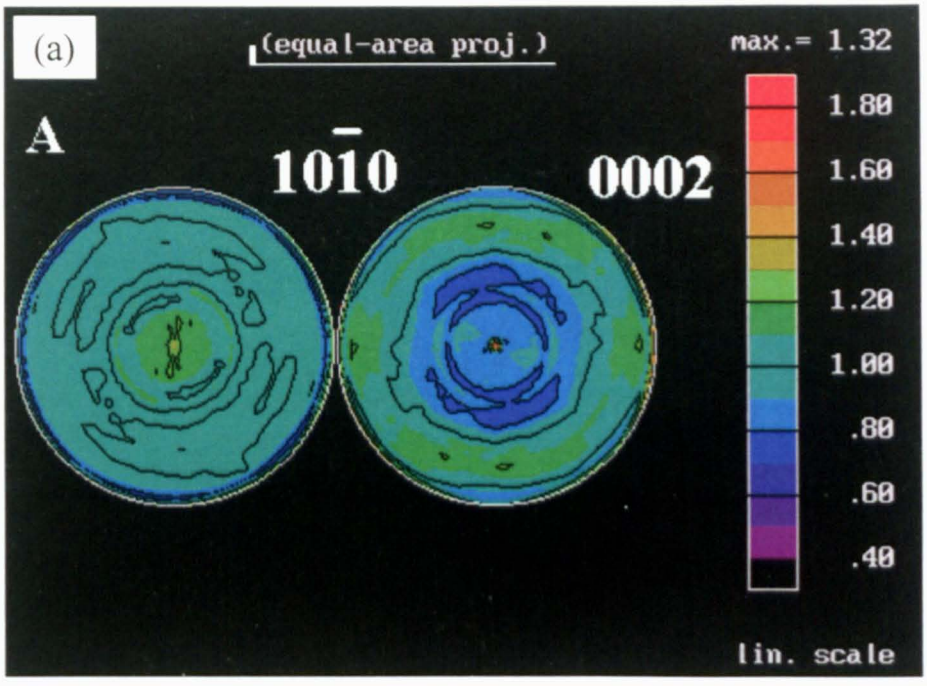

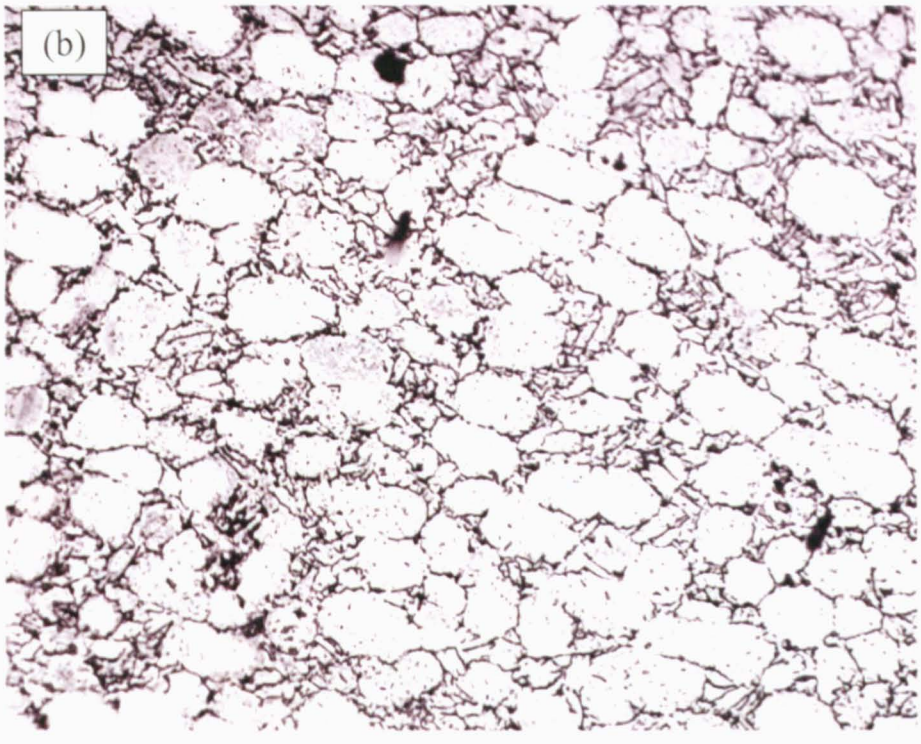

Figure 6.9(a $\{10\bar{1}0\}$ and (0002) pole figures for sample A of the billet material and (b) the corresponding optical micrograph

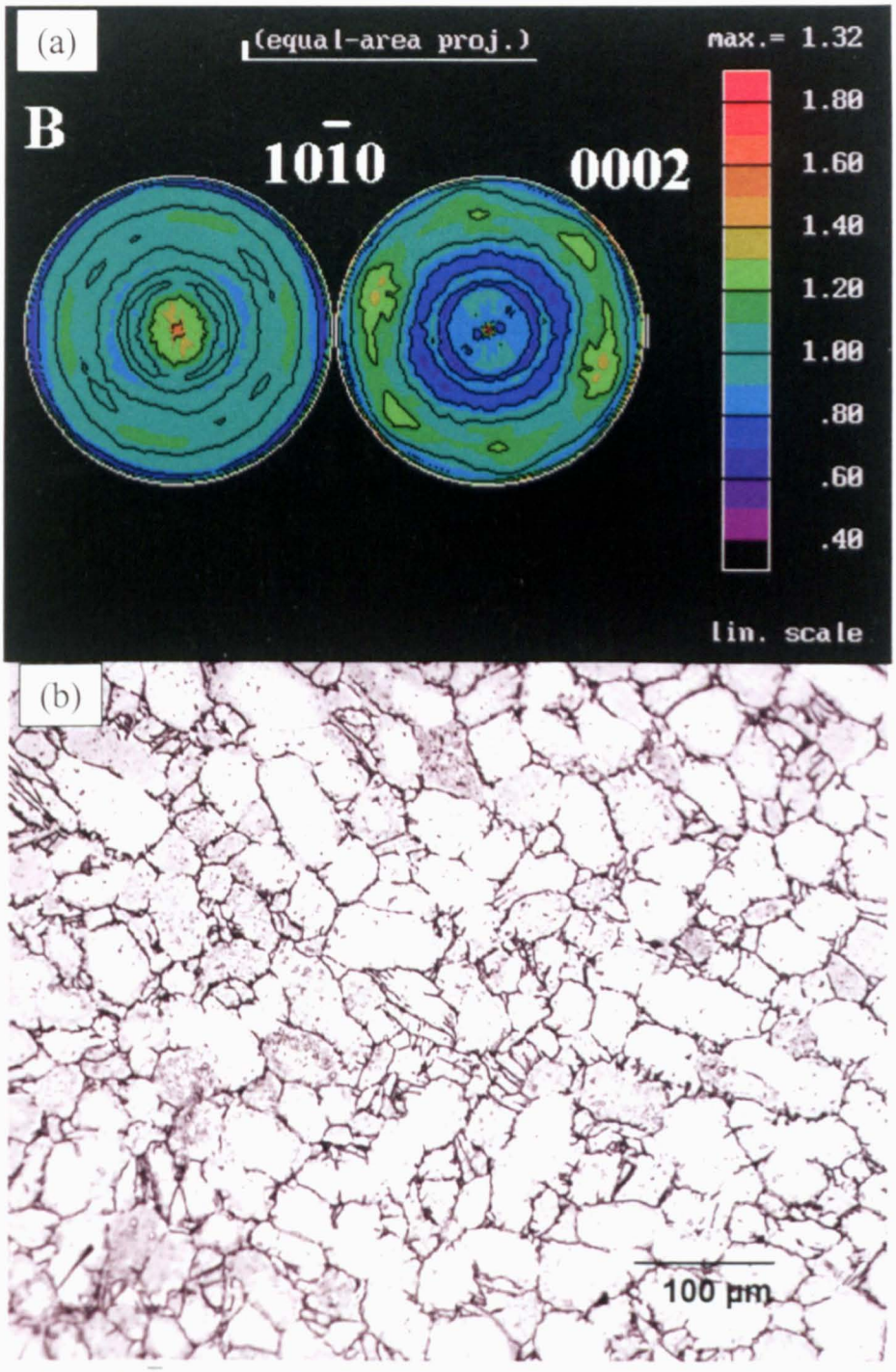

Figure 6.10 (a) $\{10\bar{1}0\}$ and (0002) pole figures for sample B of the billet material and (b) the corresponding optical micrograph

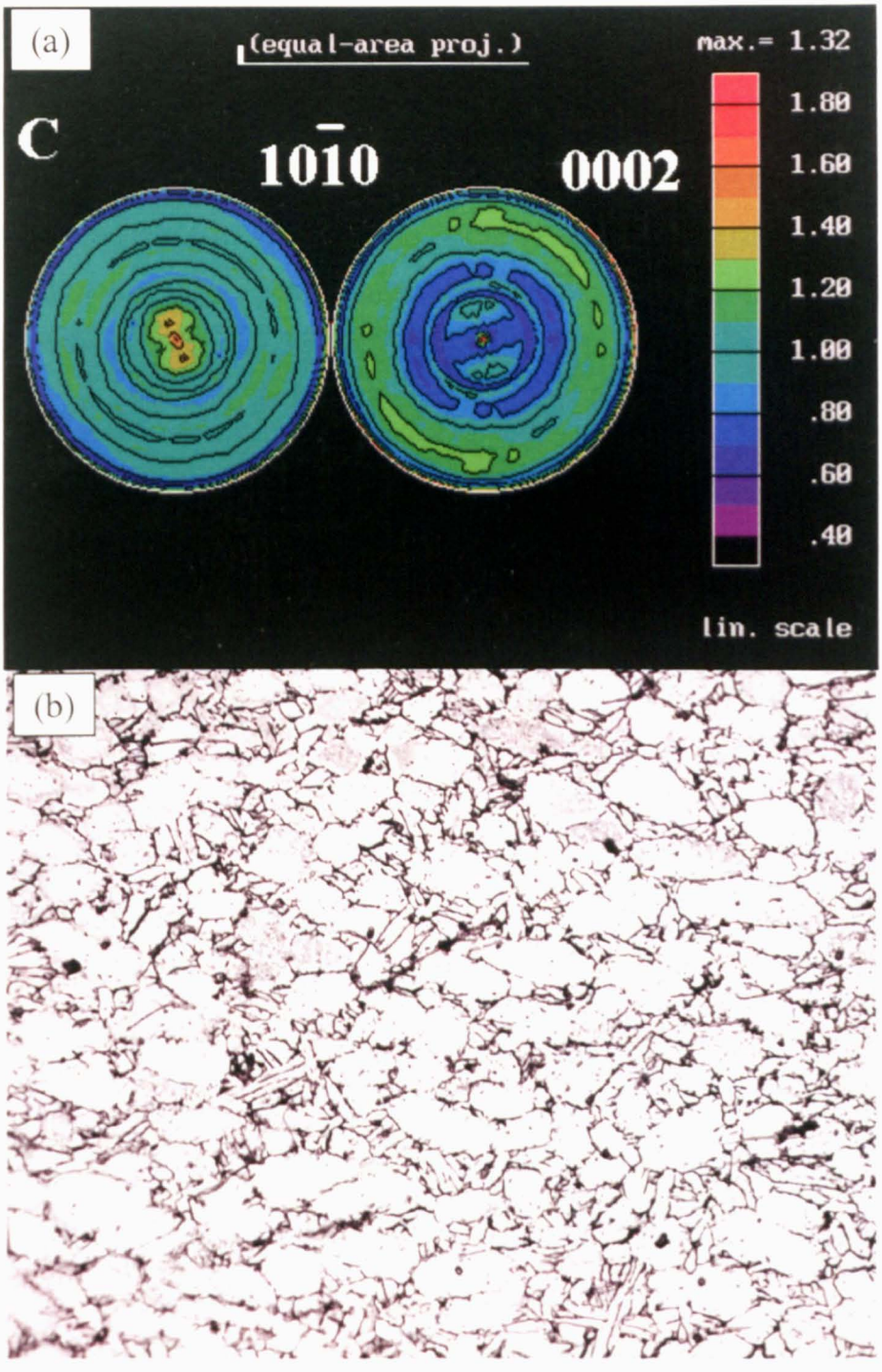

Figure 6.11 (a) {10 $\bar{1}$ 0} and (0002) pole figures for sample C of the billet material and (b) the corresponding optical micrograph

6.3.2.2 EBSD analysis

An OIM taken from the centre radius of the billet can be seen in Euler colouring with grain boundaries specified as misorientations greater than 10° in Figure 6.12. The OIM was obtained using a step size of 3μm over an area on 1mm^2 and the software was asked

to index both the α titanium HCP crystal and the β titanium BCC crystal. The mapping of billet material was made slightly easier as the Channel 5 software found it easier to index the undeformed equiaxed microstructures, mapping speeds averaged 3 points/s. As such the average map could be obtained within a few days. Figure 6.13 shows the alpha crystal $\{0002\}$ and $\{10\bar{1}0\}$ pole figure produced from this dataset and an associated SEM micrograph from a similar area can be seen in Figure 6.14(a) and (b).

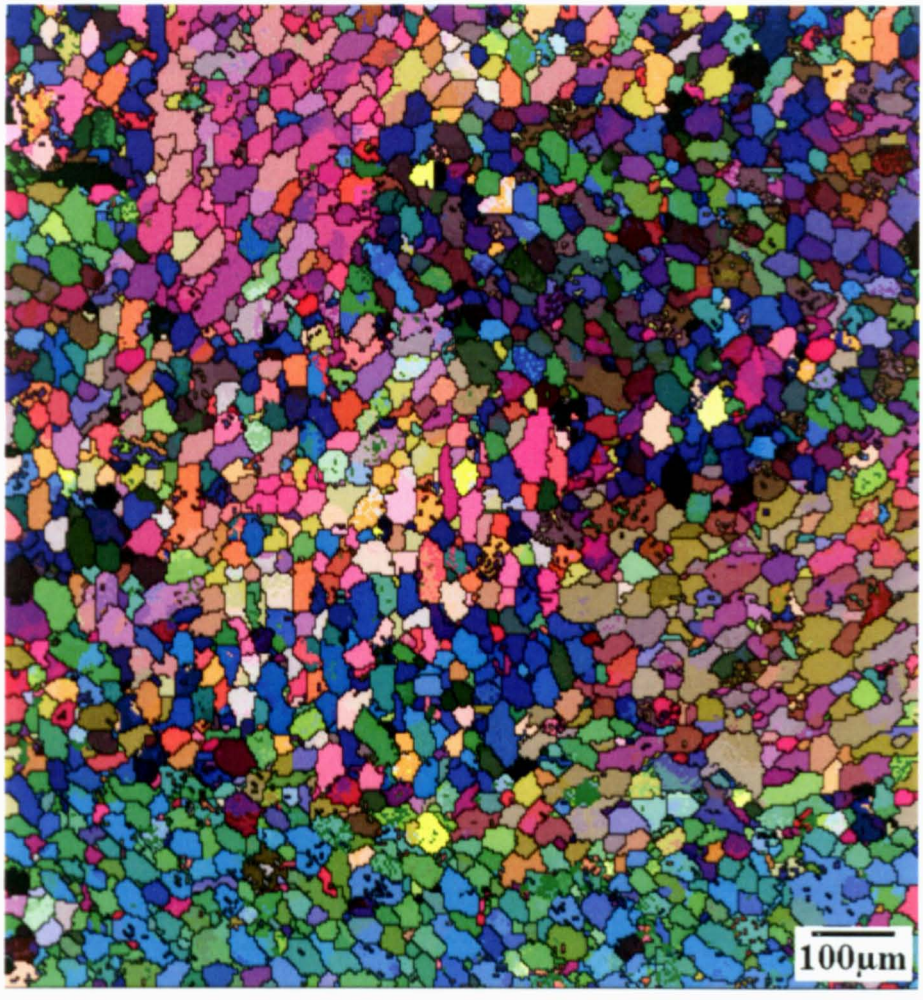

Figure 6.12 Initial scan of Billet material shown in Euler colouring.

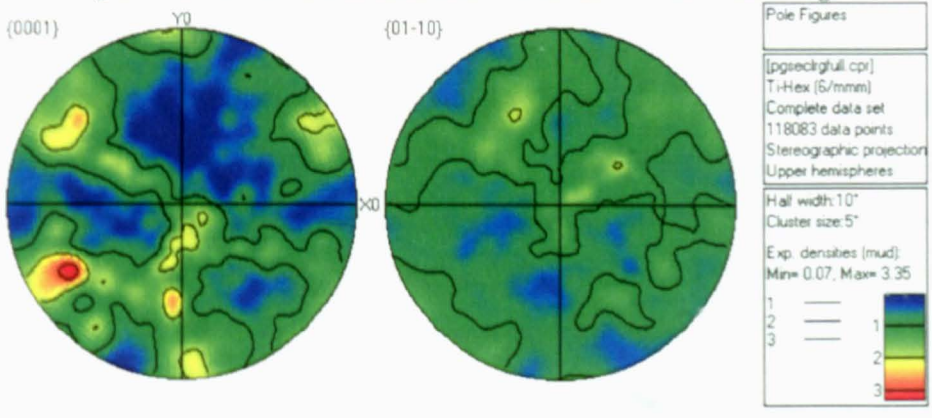

Figure 6.13 $\{0002\}$ and $\{10\bar{1}0\}$ pole figures of Billet material produced from initial scan

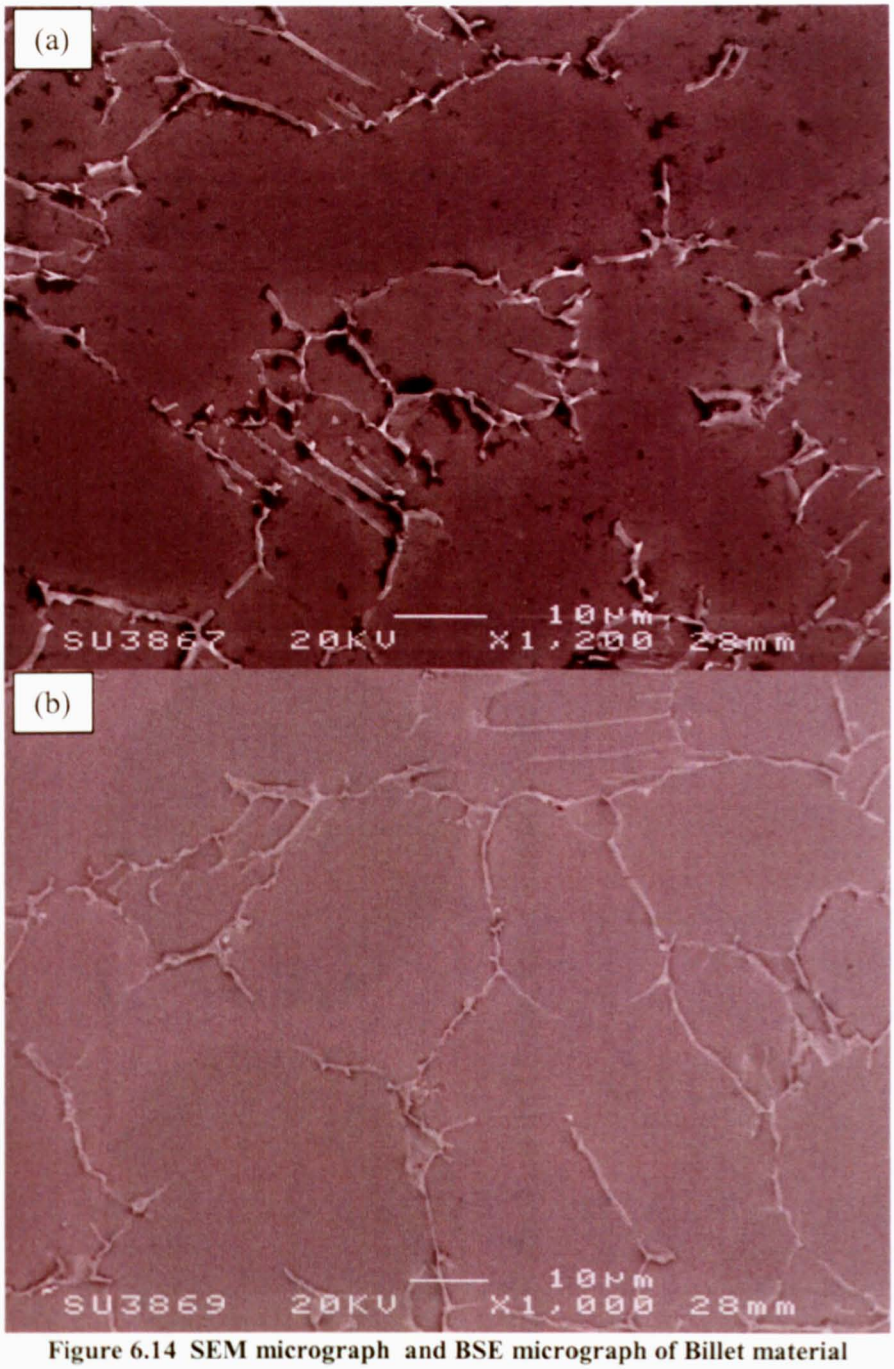

Figure 6.14 SEM micrograph and BSE micrograph of Billet material

Figures 6.12 and 6.14 show a billet microstructure consisting of approximately 70% α_p, with 30% of coarse α_s. The SEM image also shows the, approximately 2%, metastable beta visible (thin white plates) at the grain boundaries. An α_p grain size of approximately 25-30 µm can be determined from these and similar images. Due to the clustered appearance of the OIM in Figure 6.12 and the lack of fibres in the pole figures in Figure 6.13, to be discussed later, a second and ultimately third map was obtained over larger areas.

Figure 6.15 Scan of billet material over a larger area

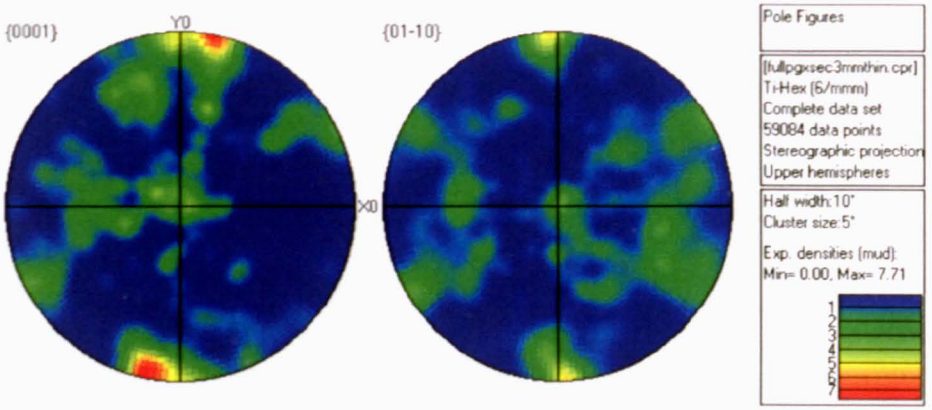

Figure 6.16 {0002} and {10 $\bar{1}$ 0} pole figures of Billet material produced 2nd scan

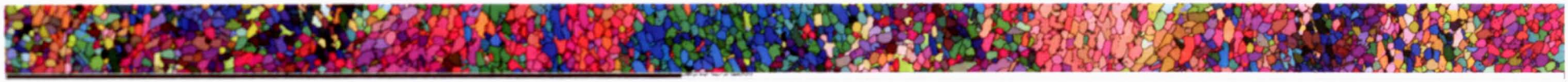

Figure 6.17 Another large scan of billet material over a larger area

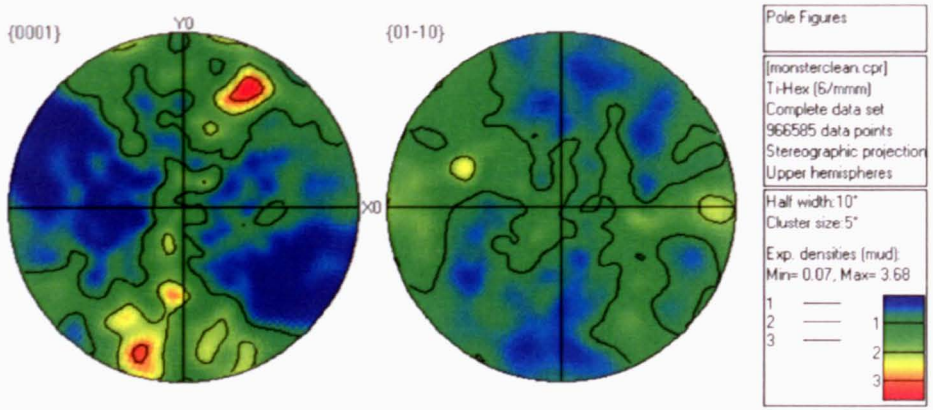

Figure 6.18 {0002} and $\{10\bar{1}0\}$ pole figures of billet material produced by Figure 6.17

These subsequent OIM's can be seen in Euler colouring with their associated pole figures in Figures 6.15-18. Figure 6.15 was produced using a step size of 1.5μm over an area of 1.5mm x 200μm whilst Figure 6.17 was obtained over a period of 13 days using a step size of 1μm over an area of 4.6mm x 250μm. The pole figures again show a lack of any radial fibre about the Z direction which is aligned with the billet elongation axis.These larger maps were the first of this size obtained on the FEGSEM at the University of Sheffield, proving the ability of the FEGSEM and the acquisition software to run over a period of 13 days.

6.3.3 Thermomechanical Test Results

Figure 6.19 shows an OIM of a sample heated to 1010°C and air cooled, the OIM and optical micrographs give a good indication of the high temperature microstructure prior to deformation, the OIM was obtained again using a step size of 3μm over an area of approximately $1mm^2$. Figure 6.20 shows the associated pole figures from this dataset. Optical micrographs can be seen in Figures 6.21 & 6.22. The OIM resembles that in Figure 6.8 of the as-received material, however there are distinct differences in the grain shape in certain areas of the OIM. The optical micrographs are quite different from the microstructure in Figures 6.9, 6.10, 6.11 and 6.14 showing the as received material. The optical micrographs show a microstructure of approximately 22% α_p in a matrix of lamellar transformed β, α_s. From the higher magnification micrograph in Figure 6.22 the lamellar nature of the undeformed α_s can be seen as each lath appears to travel parallel for the entire width of the grain.

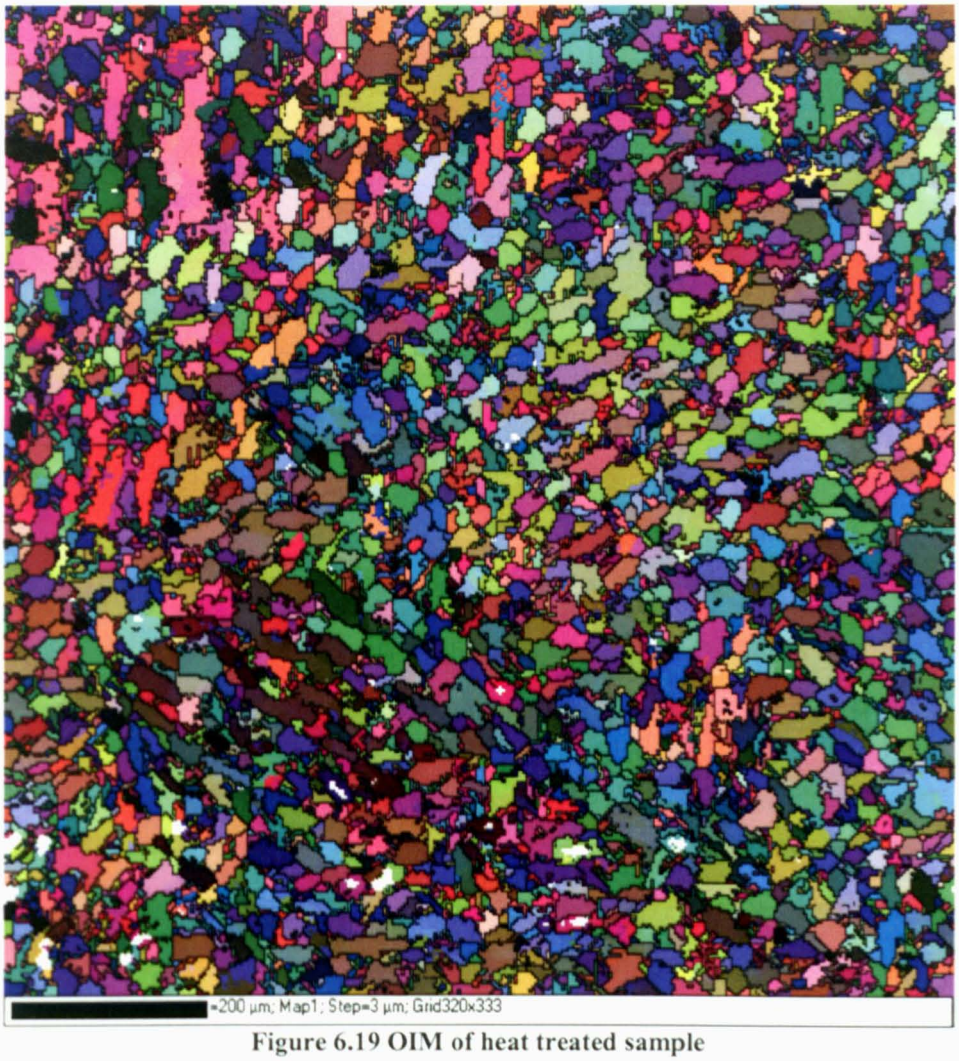

Figure 6.19 OIM of heat treated sample

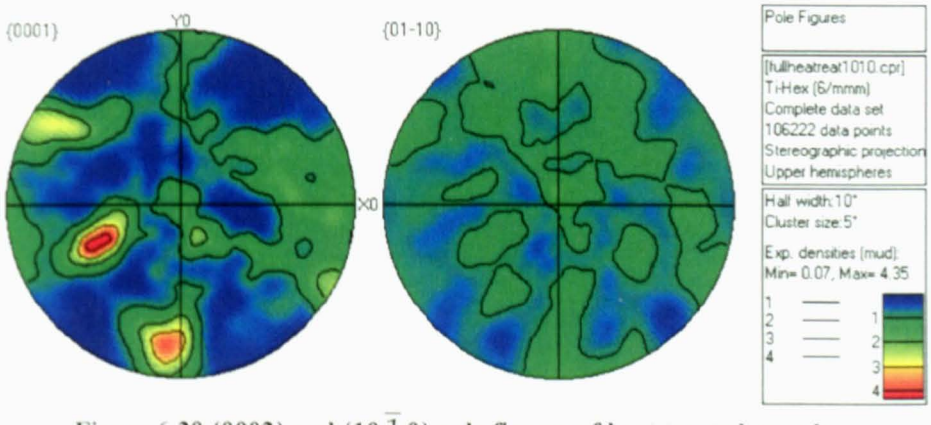

Figure 6.20 {0002} and {10 $\bar{1}$ 0} pole figures of heat treated sample

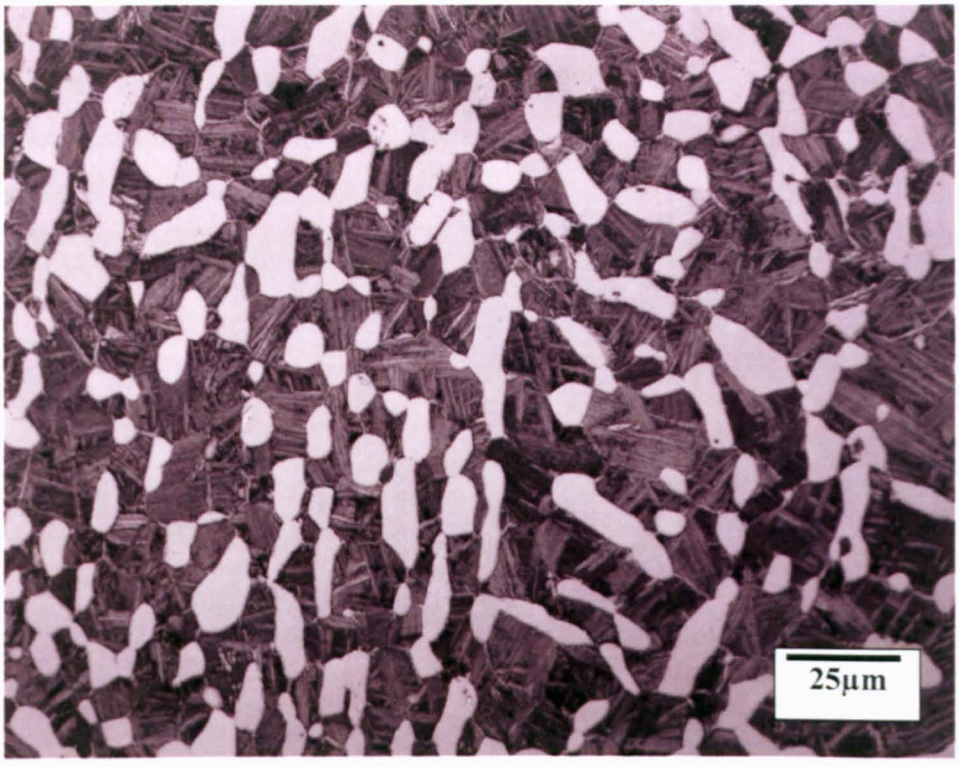

Figure 6.21 Optical micrograph of the heat treated sample

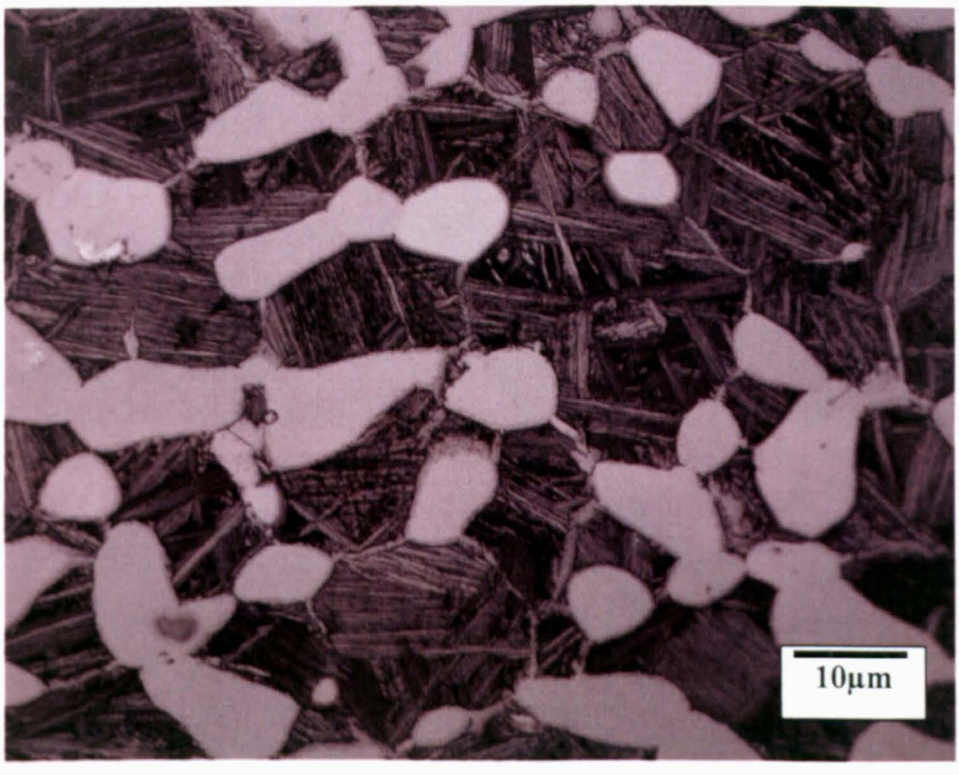

Figure 6.22 Optical micrograph of the heat treated sample at higher magnification

Figure 6.23 shows the OIM in Euler colouring of an axisymmetric compression test sample T16 having been heated to 1010°C and deformed to a strain

of 0.175 at a strain rate of $2s^{-1}$. The OIM was obtained using a step size of 1.5μm over an area of approximately $1mm^2$ and the related pole figures can be seen in Figure 6.24. Figures 6.25 to 6.35 show comparative OIM's, optical micrographs and Pole figures for the axisymmetric compression test samples having received strains 0.375, 0.55 and 0.75 respectively at a strain rate of $2s^{-1}$.

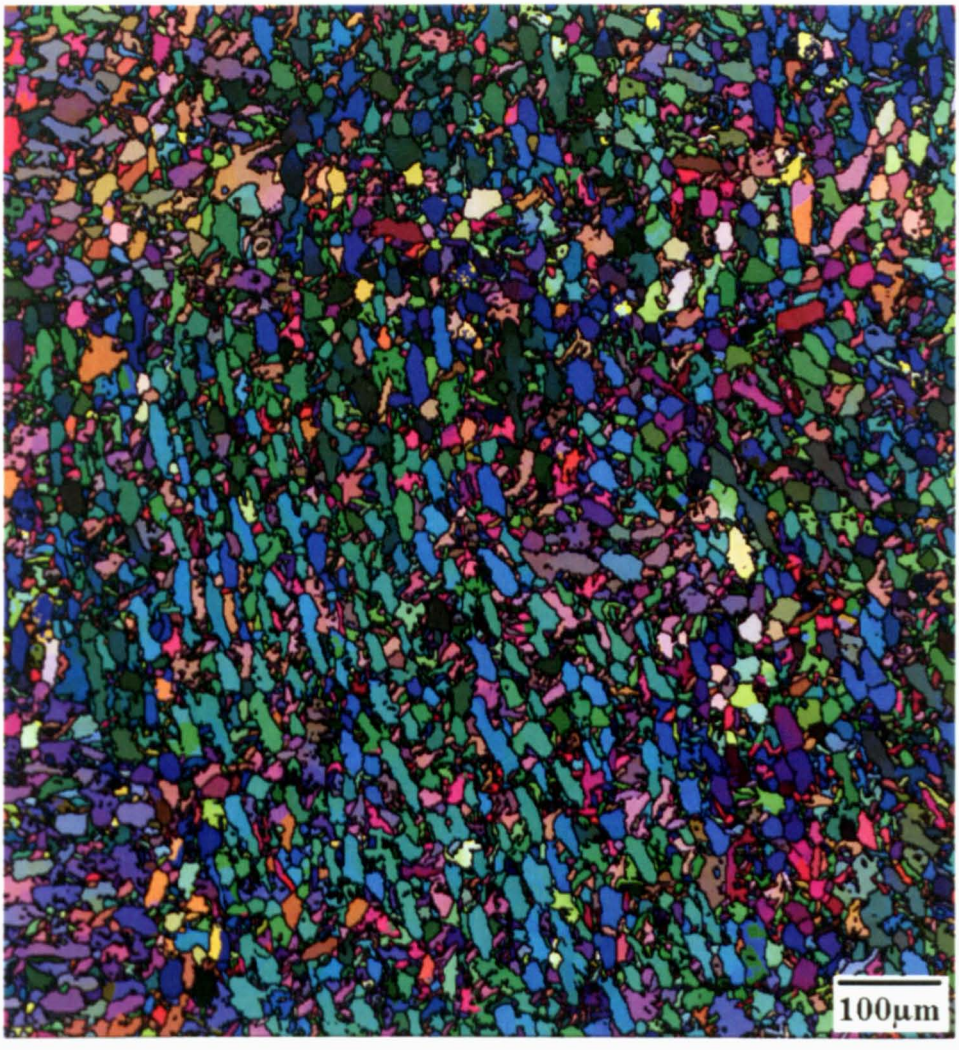

Figure 6.23 Euler colouring OIM of specimen T16 having received ϵ=0.175

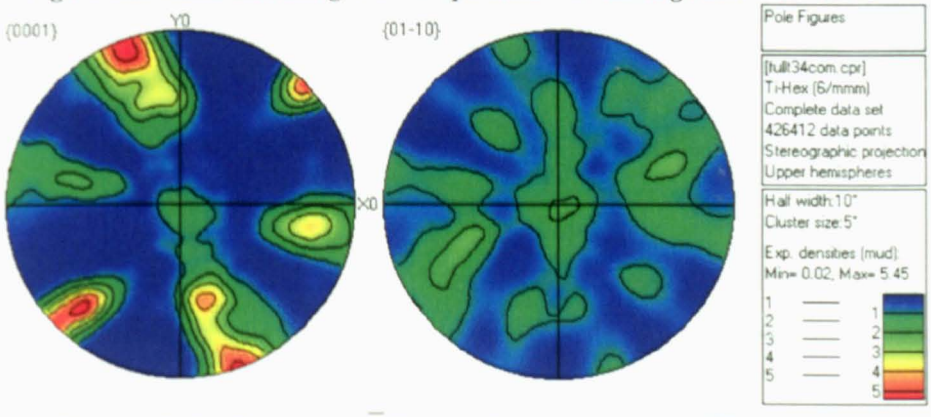

Figure 6.24 {0002} and {10 $\bar{1}$ 0} pole figures produced by Figure 6.23

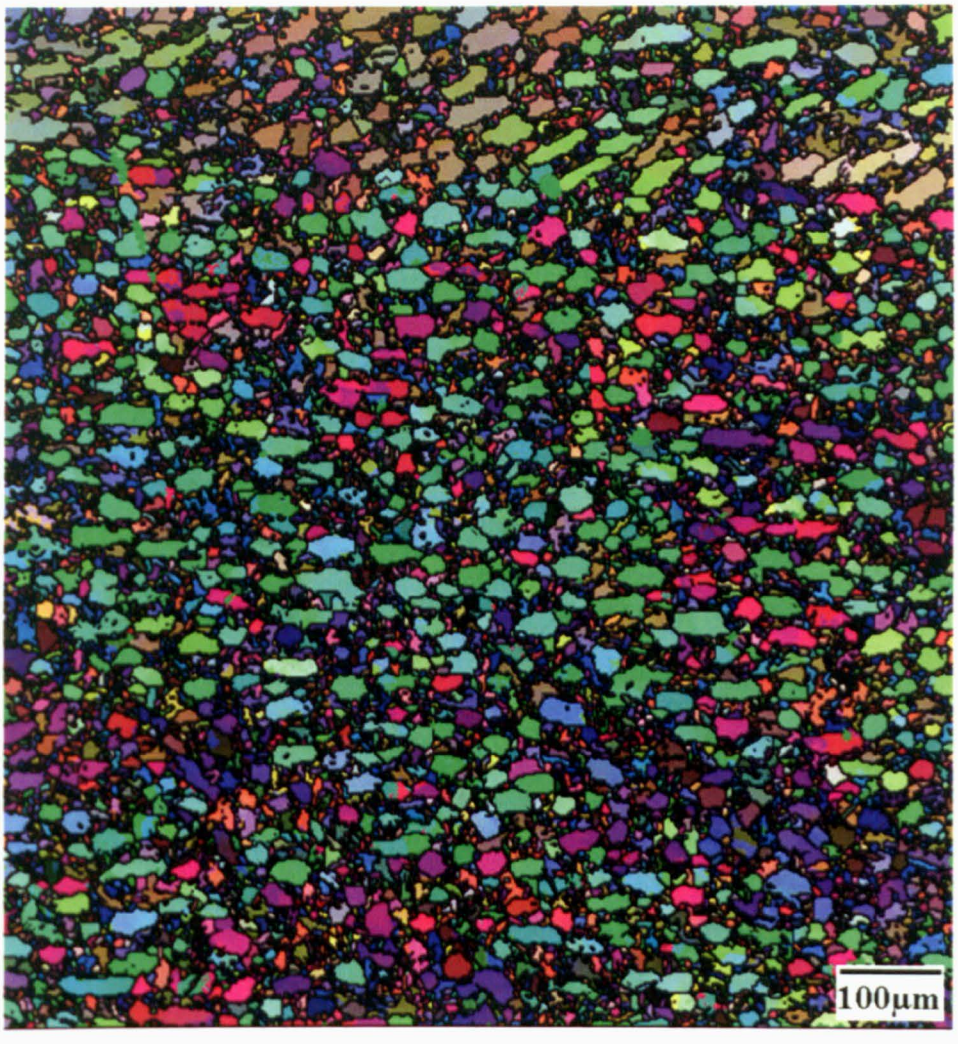

Figure 6.25 Euler colouring OIM of specimen T14 having received ϵ=0.375

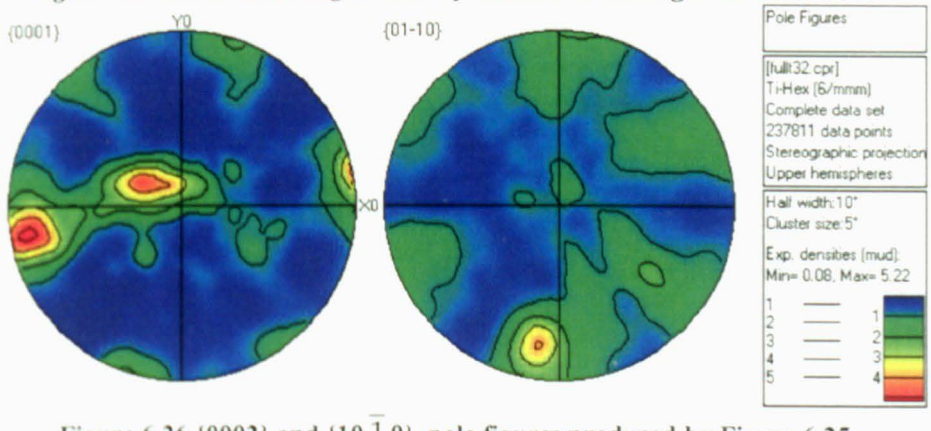

Figure 6.26 {0002} and $\{10\bar{1}0\}$ pole figures produced by Figure 6.25

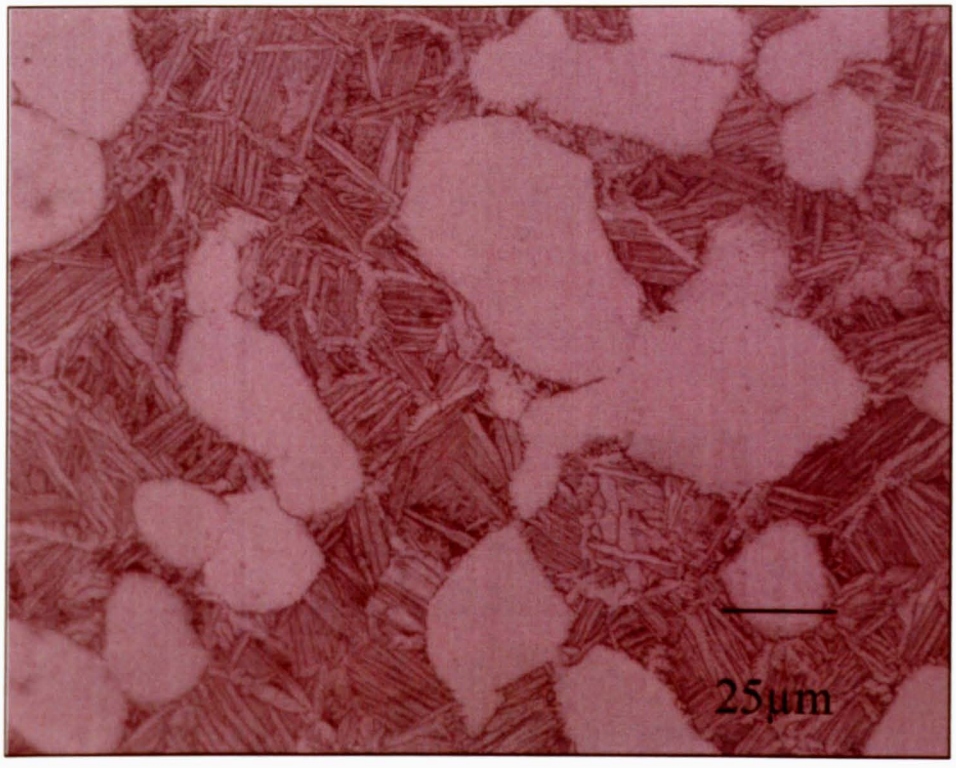

Figure 6.27 Optical micrograph of specimen T14 having received ϵ=0.375

A larger map was obtained from the T14 sample and can be seen in Figure 6.28, along with the associated {0002} and $\{10\bar{1}0\}$ pole figures. The map shows a degree of homogeneity throughout and with Figure 6.25, however there are clear inhomogeneities in the Euler colouring across the width of the map.

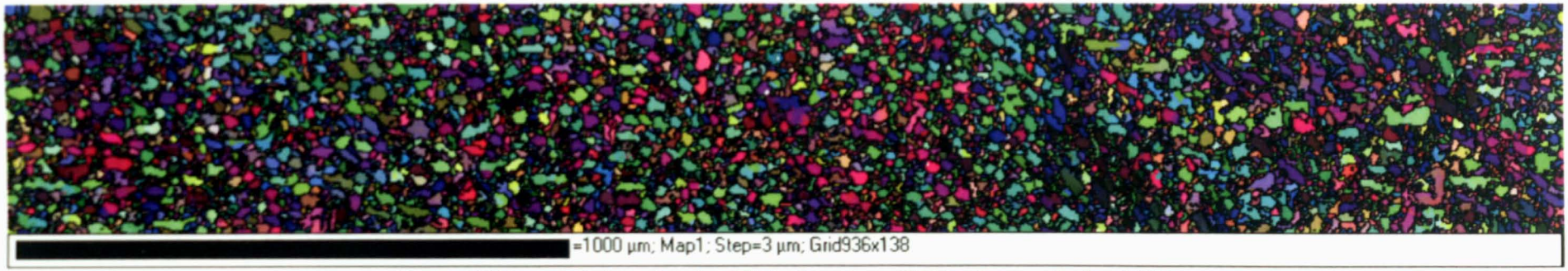

Figure 6.28 Larger Euler colouring OIM of specimen T14 having received ϵ=0.375

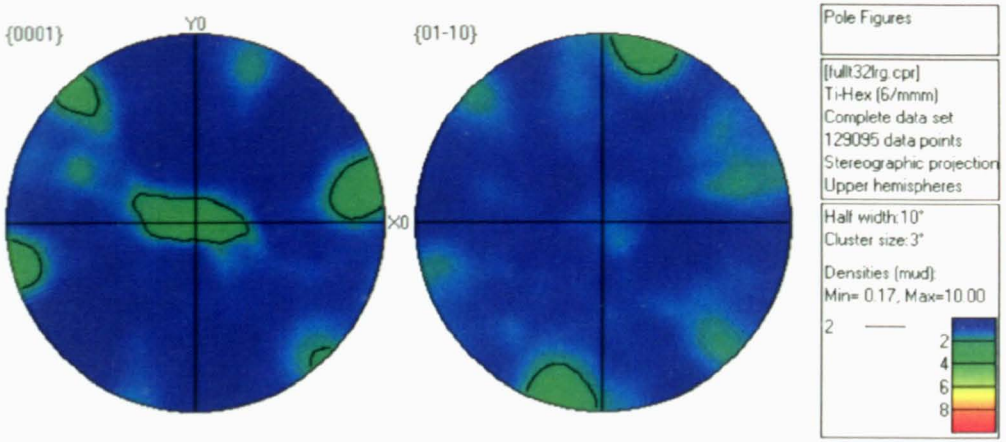

Figure 6.29 {0002} and {10 $\bar{1}$ 0} pole figures produced by Figure 6.28

Figure 6.30 Euler colouring OIM of specimen T17 having received ϵ=0.55

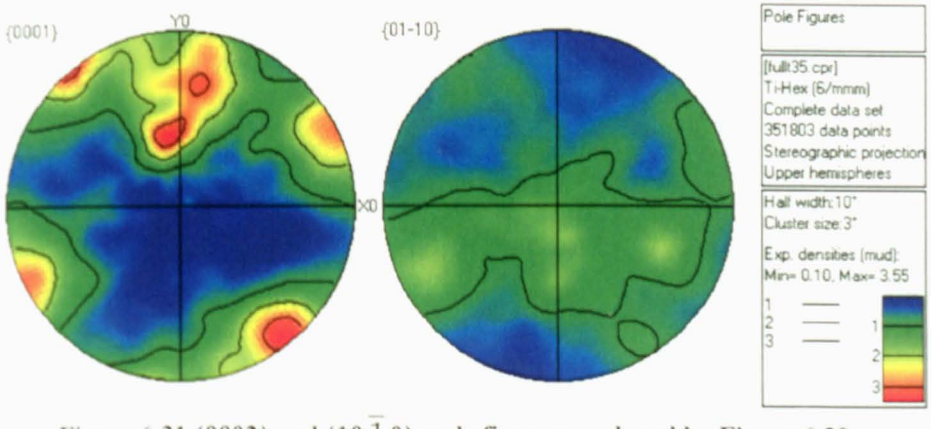

Figure 6.31 {0002} and {10 $\bar{1}$ 0} pole figures produced by Figure 6.30

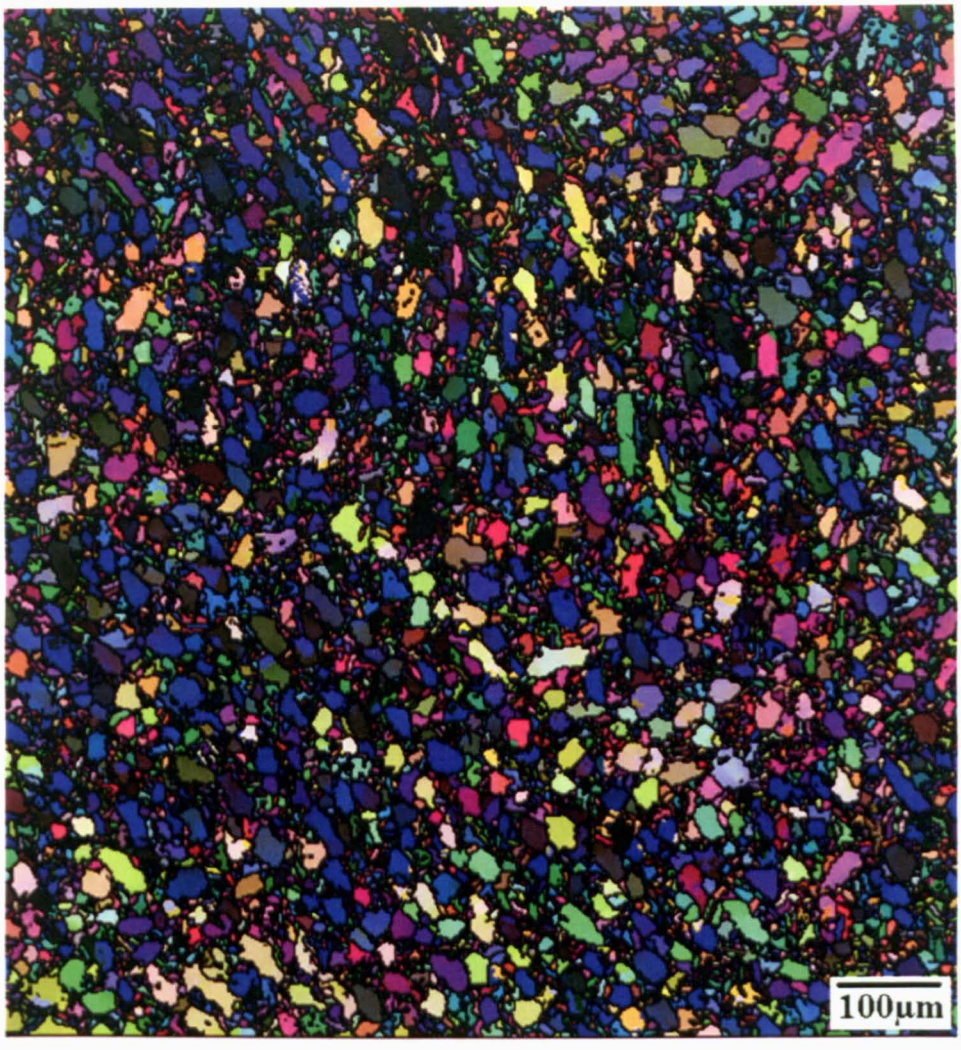

Figure 6.32 Euler colouring OIM of specimen T15 having received ϵ=0.75

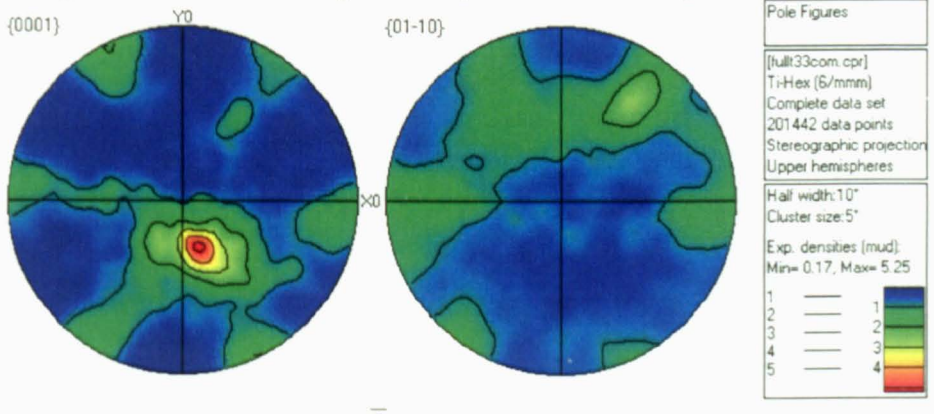

Figure 6.33 {0002} and {10 $\bar{1}$ 0} pole figures produced by Figure 6.28

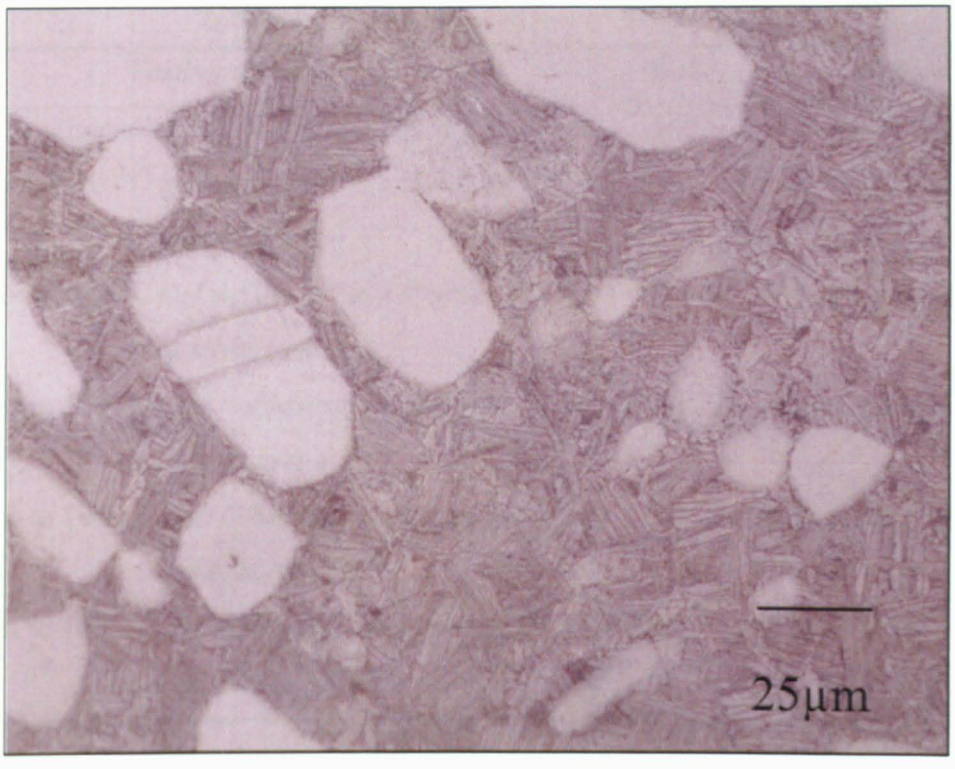

Figure 6.34 Optical micrograph of specimen T15 having received ϵ=0.75

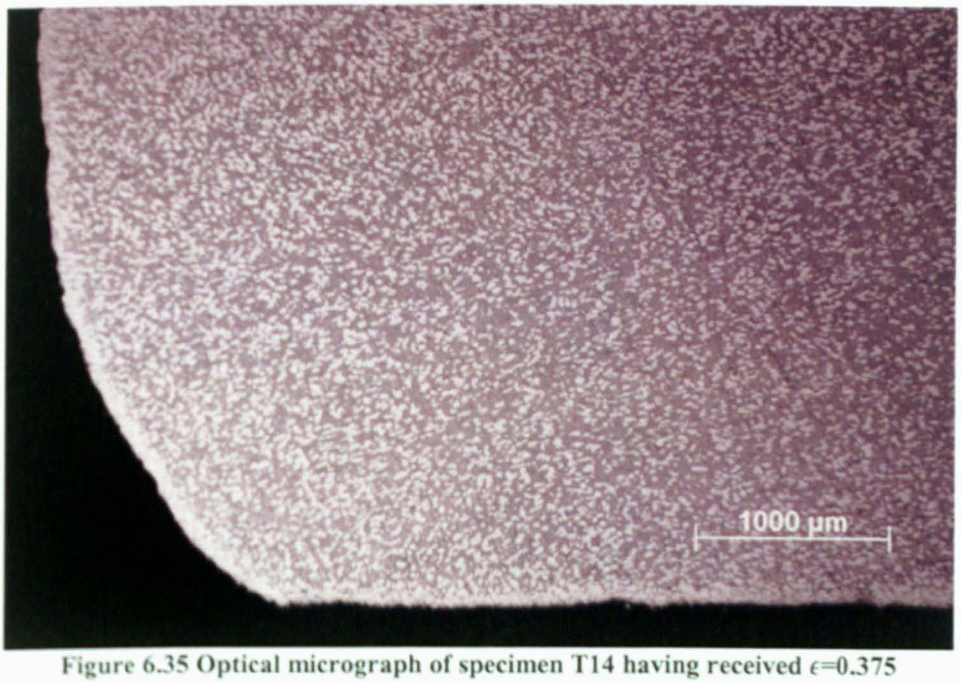

Figure 6.35 Optical micrograph of specimen T14 having received ϵ=0.375

The OIM's in Figures 6.23, 6.25, 6.28, 6.30 and 6.32 show the deformed microstructures of Timetal®834 under given processing parameters, it is clear from these OIM's that the α_p remains a similar size to that of the billet and heat treated samples. Figures 6.36-6.47 show the OIM's and associated pole figures of the matrix of axisymmetric compression tests detailed in Table 6.3.

Table 6.3 Test parameters of further EBSD maps.

Testing Parameters	*Test*	*Figure*
Heated to 990°C and air-cooled	D4	Figures 6.29 & 6.30
Heated to 990°C and deformed to a strain of 0.75 at a strain rate of 20	D5	Figures 6.31 & 6.32
Heated to 990°C and deformed to a strain of 0.75 at a strain rate of 2	D6	Figures 6.33 & 6.34
Heated to 1030°C and deformed to a strain of 0.75 at a strain rate of 20	D8	Figures 6.35 & 6.36
Heated to 1030°C and deformed to a strain of 0.75 at a strain rate of 2	D8	Figures 6.37 & 6.38
Heated to 1030°C and deformed to a strain of 0.75 at a strain rate of 0.2	D10	Figures 6.39 & 6.40

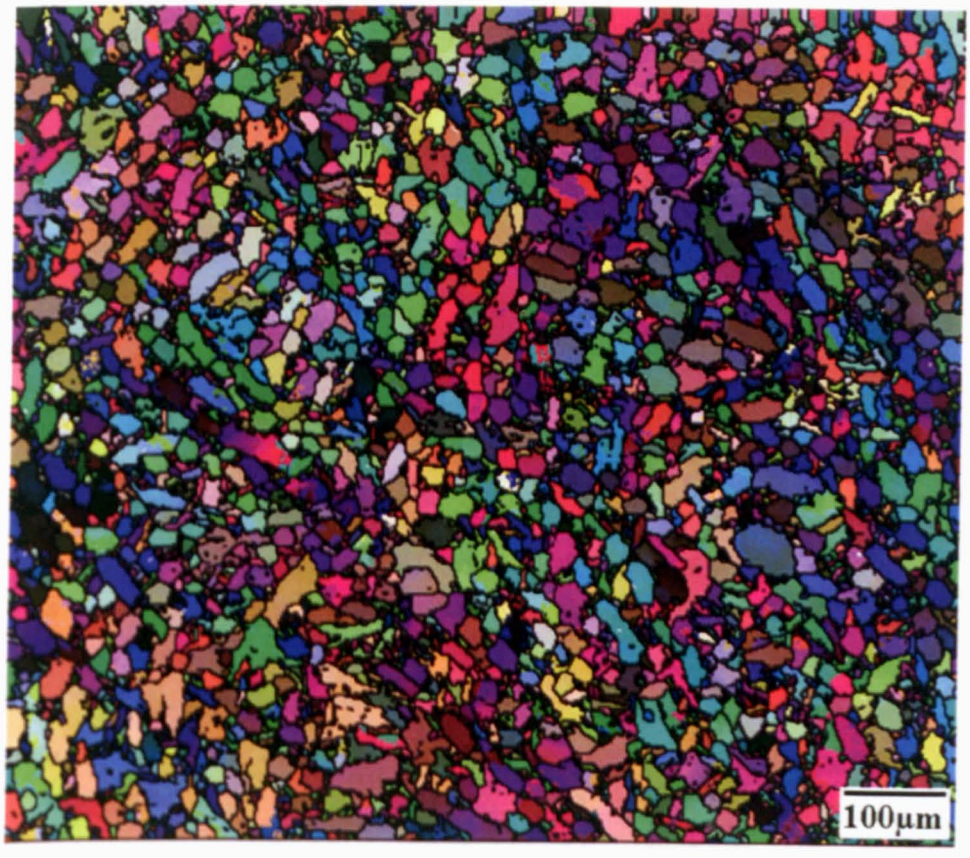

Figure 6.36 A4 Euler colouring OIM of specimen D4

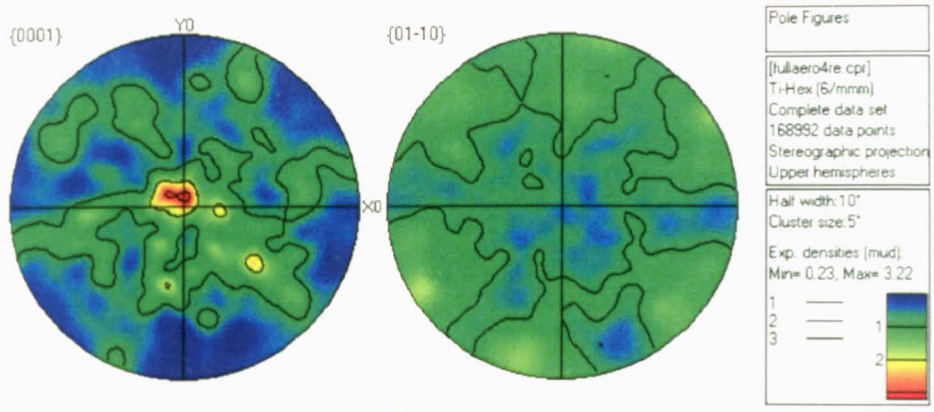

Figure 6.37 A4 {0002} and $\{10\bar{1}0\}$ pole figures produced by Figure 6.36

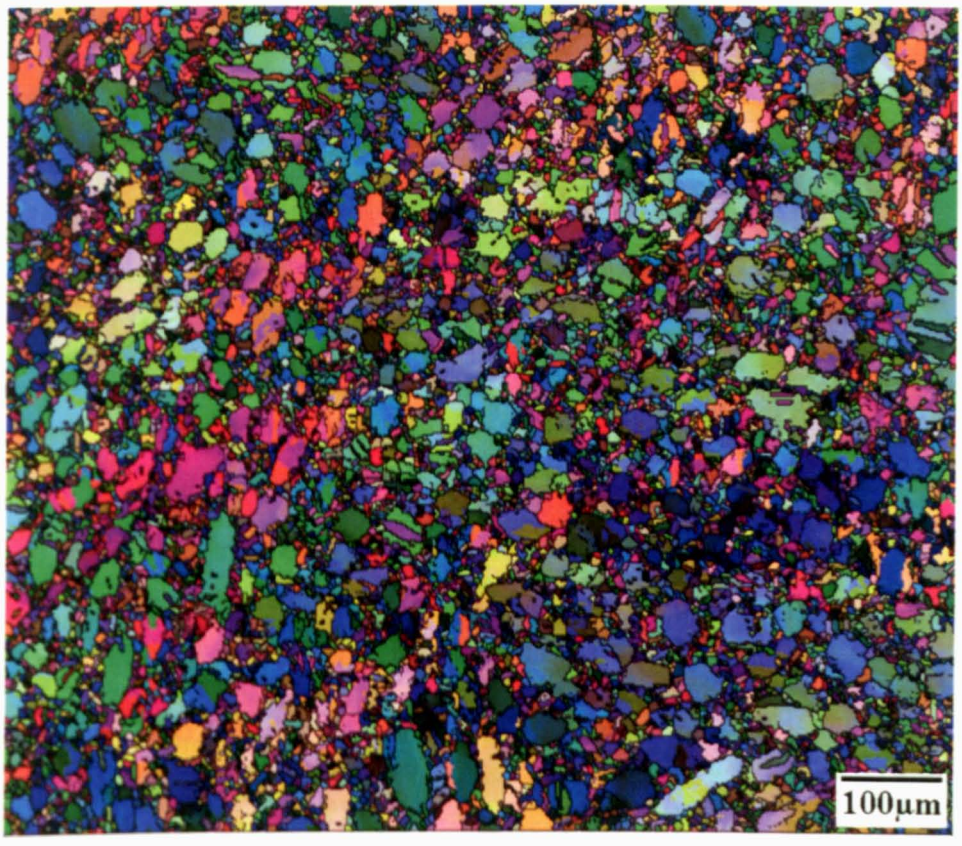

Figure 6.38 A5 Euler colouring OIM of specimen D5

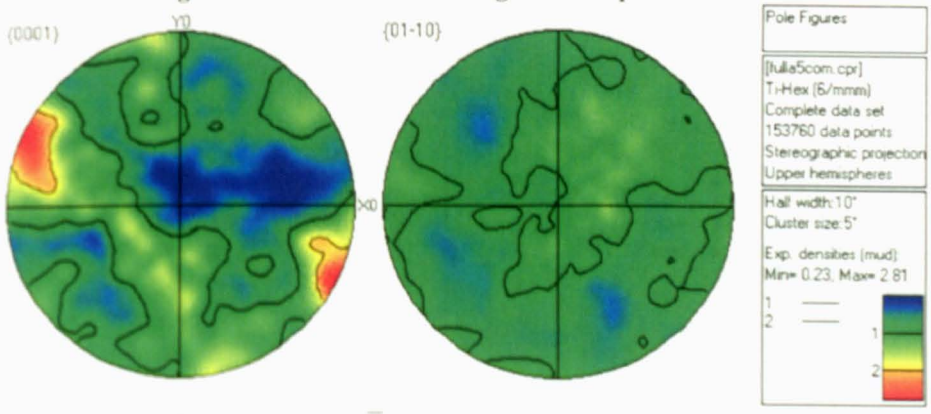

Figure 6.39 {0002} and $\{10\bar{1}0\}$ pole figures produced by Figure 6.38

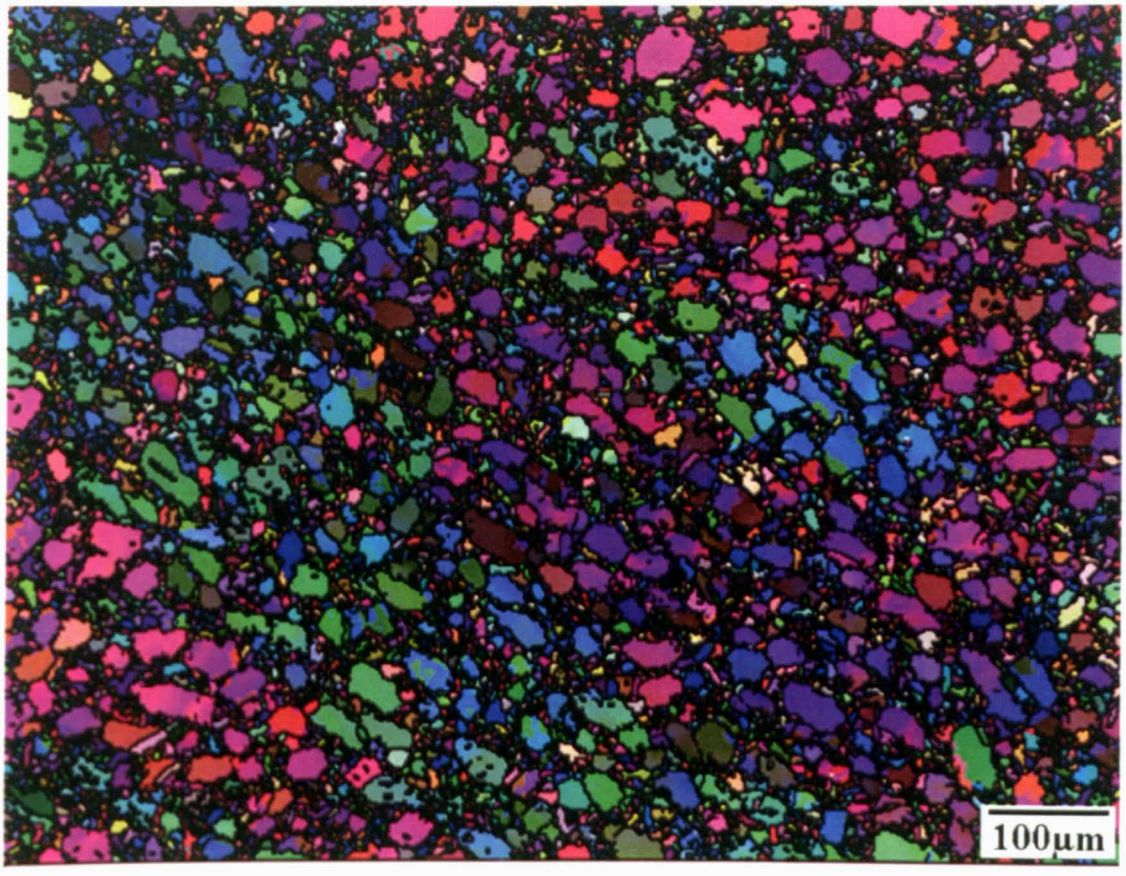

Figure 6.40 A6 Euler colouring OIM of specimen D6

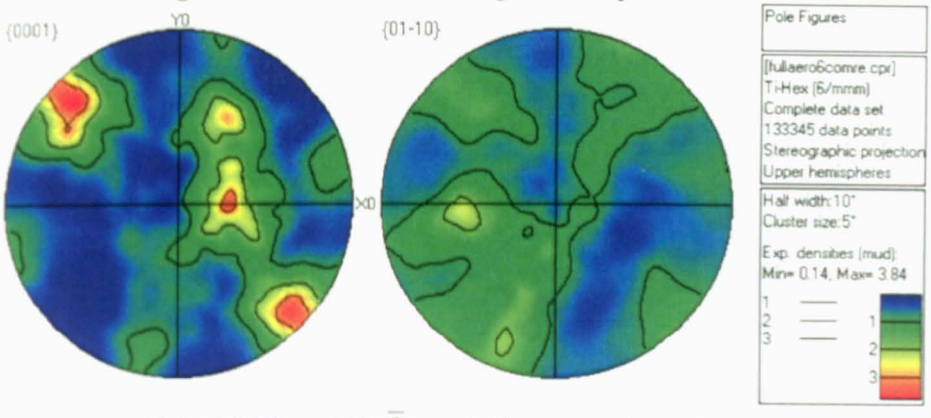

Figure 6.41 A6 {0002} and {10 $\bar{1}$ 0} pole figures produced by Figure 6.40

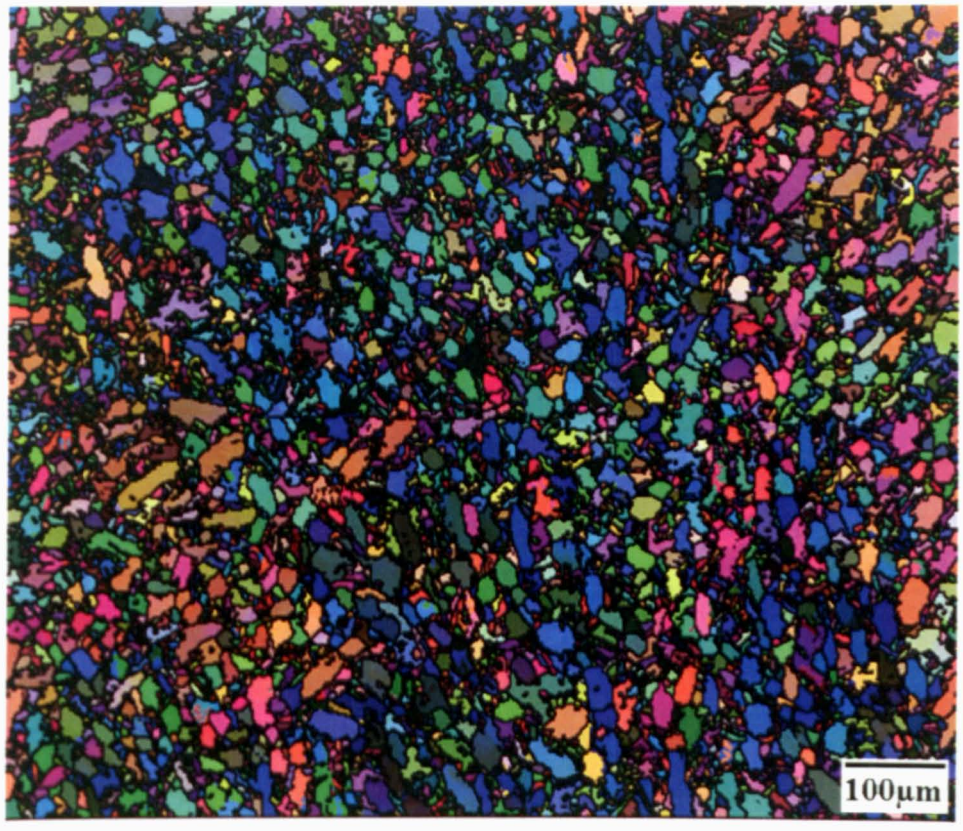

Figure 6.42 A8 Euler colouring OIM of specimen D8

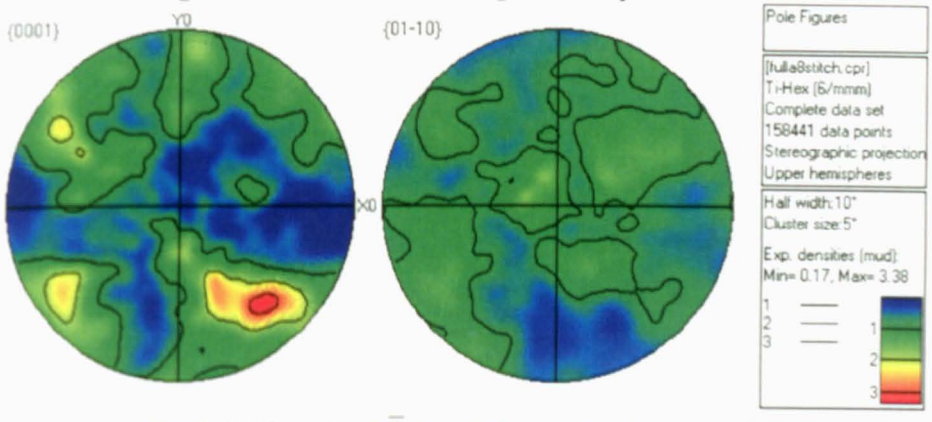

Figure 6.43 A8 {0002} and $\{10\bar{1}0\}$ pole figures produced by Figure 6.42

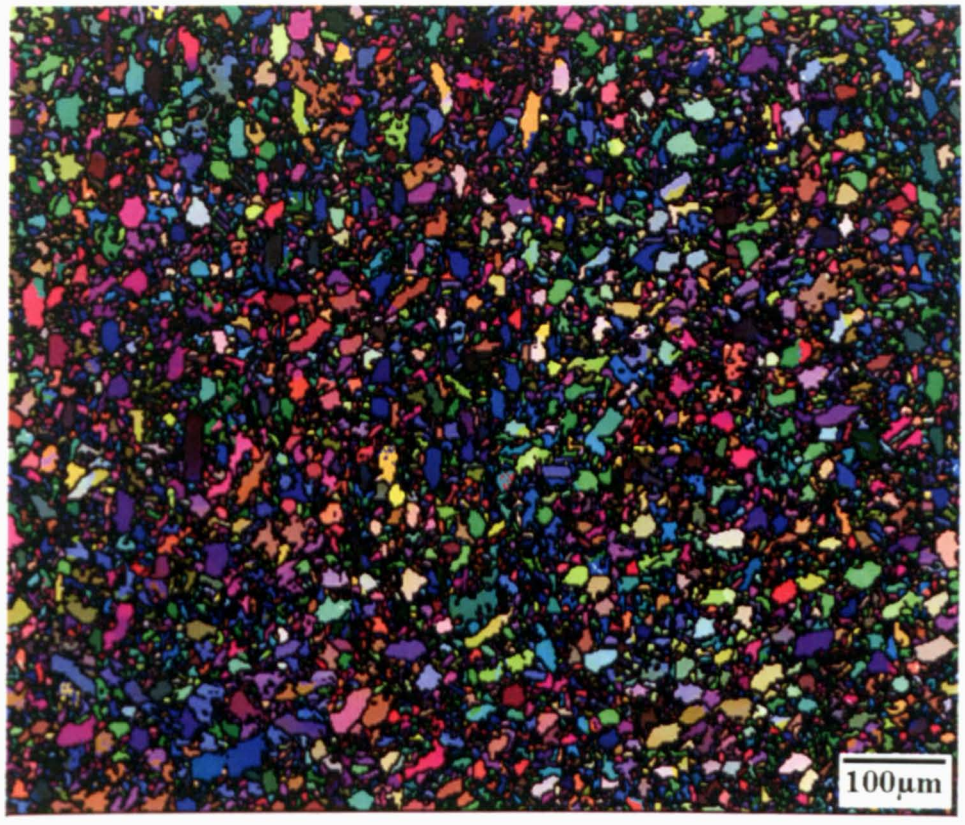

Figure 6.44 A9 Euler colouring OIM of specimen D9

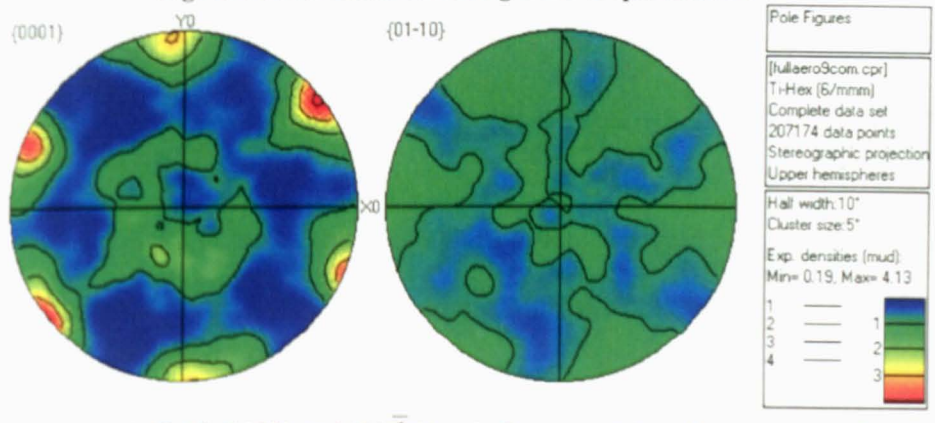

Figure 6.45 A9 {0002} and {10 $\bar{1}$ 0} pole figures produced by Figure 6.45

Figure 6.46 A10 Euler colouring OIM of specimen D10

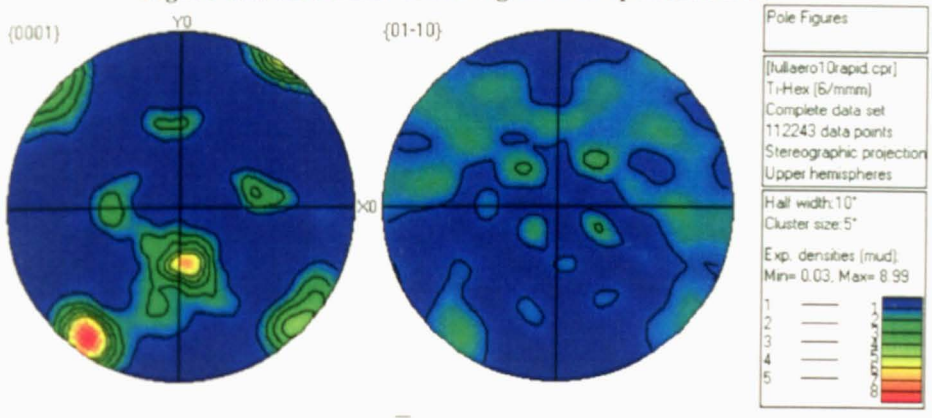

Figure 6.47 A10 {0002} and {10 $\bar{1}$ 0} pole figures produced by Figure 6.46

The complete pole figures of the thermomechanically deformed samples rarely show textures higher than 4 MRD.

6.3.4 High Resolution Microstructure Runs

The OIM's seen in the section were obtained based on a different philosophy than the "texture" runs that have been shown previously. The OIM's shown in the following section were obtained using a much smaller step size which produces, effectively, a higher resolution OIM of the material, highlighting microstructural features such as twins, grain boundaries, grain substructure etc. The OIM's are presented in Euler colouring and IPF colouring, the IPF colouring system used to highlight smaller misorientations with a greater contrast. The black lines illustrated in

the following OIM's represent a misorientation between neighbouring pixels of greater than 15°. The

The bi-modal microstructures illustrated by the OIM's show the difficulty in the determination of what is α_p and α_s. The reason for this is due to the similar orientations seen in parallel laths in the α_s which share habit planes and will be discussed in greater detail in Chapters 7 and 8.

(a)

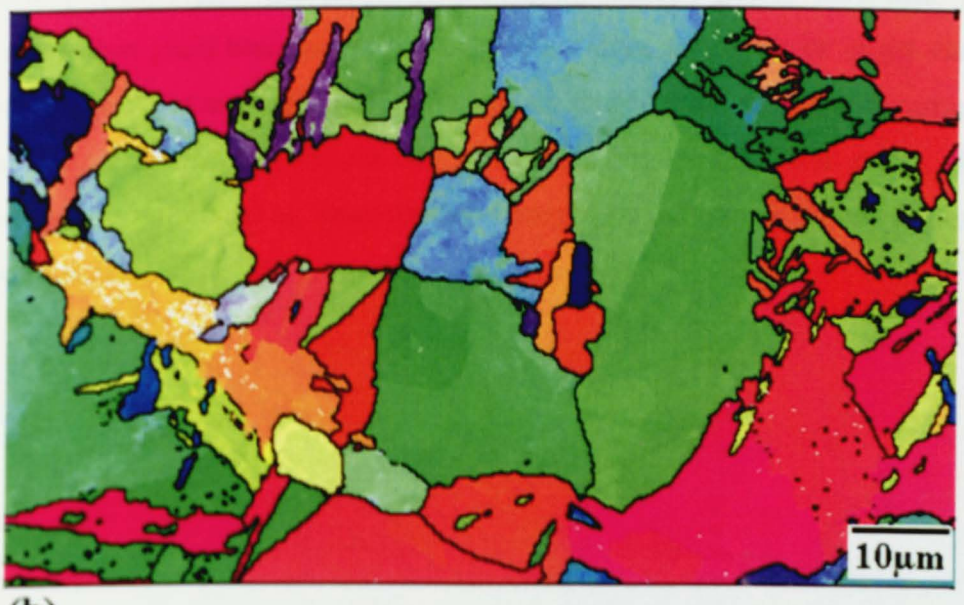

(b)

Figure 6.48 High resolution OIM's of the heat treated sample in (a) Euler colouring and (b) IPF colouring

Figure 6.48(a) shows an OIM of the heat treated sample, 100μm x 60μm in size using a 0.2μm step size. The IPF OIM seen in Figure 6.48(b) shows very little

colour variation within grain boundaries suggesting little or no sub-grain deformation. Figure 6.49 shows an optical micrograph of the same specimen the lack of deformation is apparent in the large packet size in the α_s microstructure.

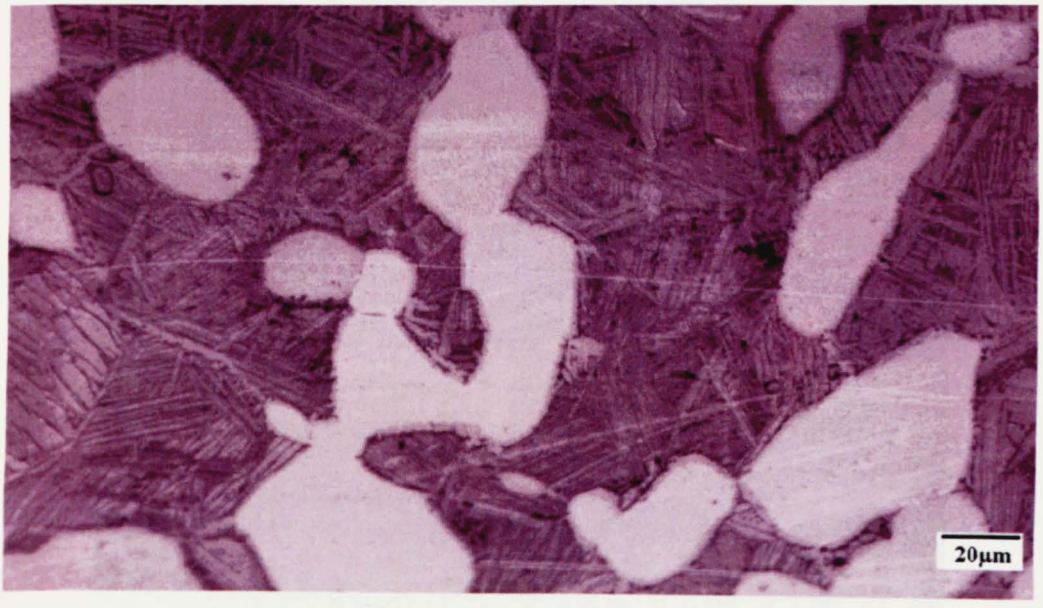

Figure 6.49 Optical micrograph of heat treated specimen

Figure 6.50(a) and (b) show OIM's of the axisymmetric compression sample having received a strain of 0.175, an area of 200μm x 200μm is mapped using a 0.3μm step size. Again the IPF OIM in Figure 6.50(b) shows very little colour variation within grain boundaries, however, there does appear to be slight variation towards grain edges suggesting slight sub-grain deformation or grain curvature. An optical micrograph of the sample can be seen in Figure 6.51 and shows slightly smaller packets within the α_s, however the micrographs in Figure 6.49 and Figure 6.61 are very similar.

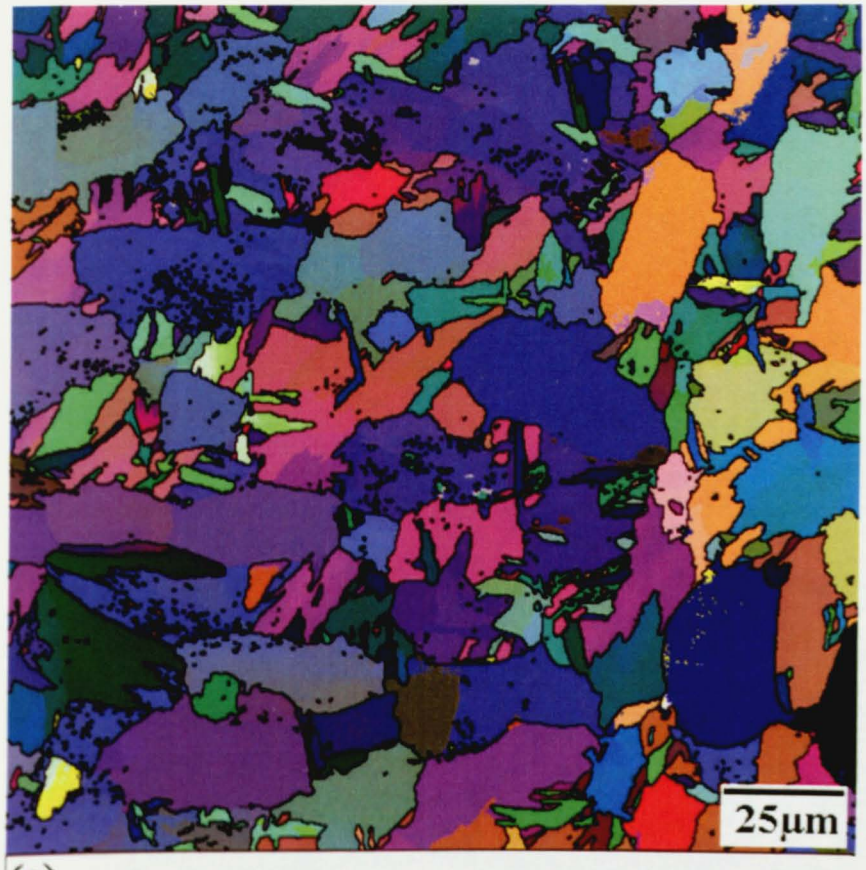

(a)

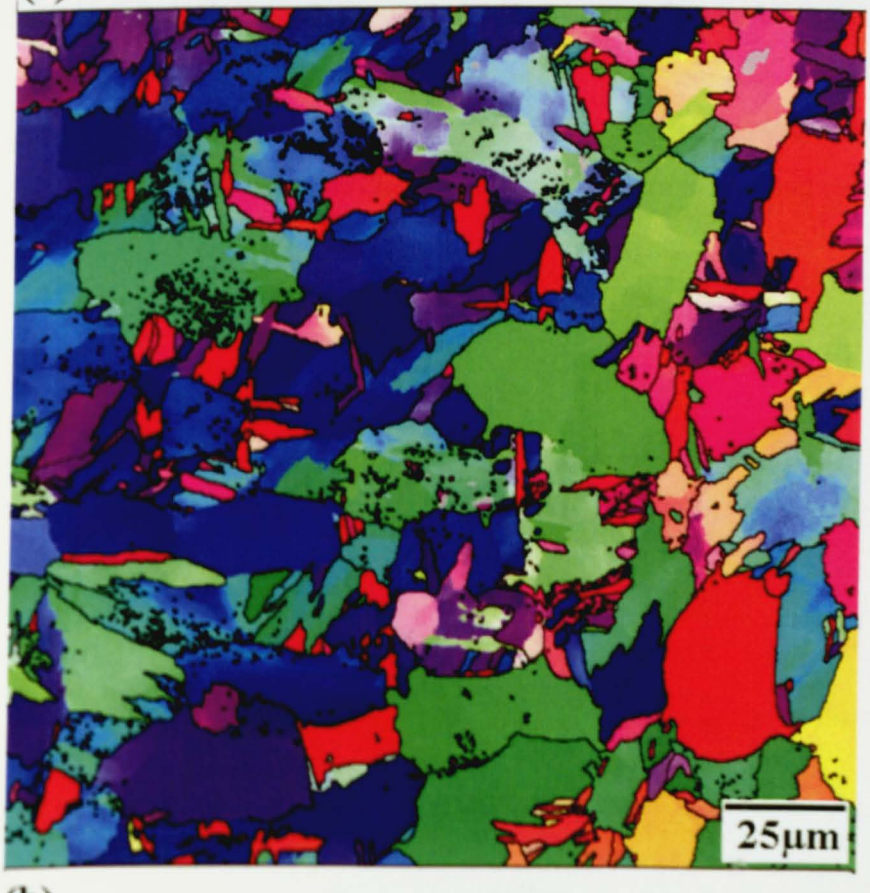

(b)

Figure 6.50 High Resolution OIM of sample T16 in (a) Euler colouring and (b) IPF colouring

Figure 6.51 Optical micrograph of T16

Figure 6.52(a) and (b) show OIM's of the axisymmetric compression sample having received a strain of 0.375, an area of 250μm x 150μm is mapped using a 0.2μm step size.

(a)

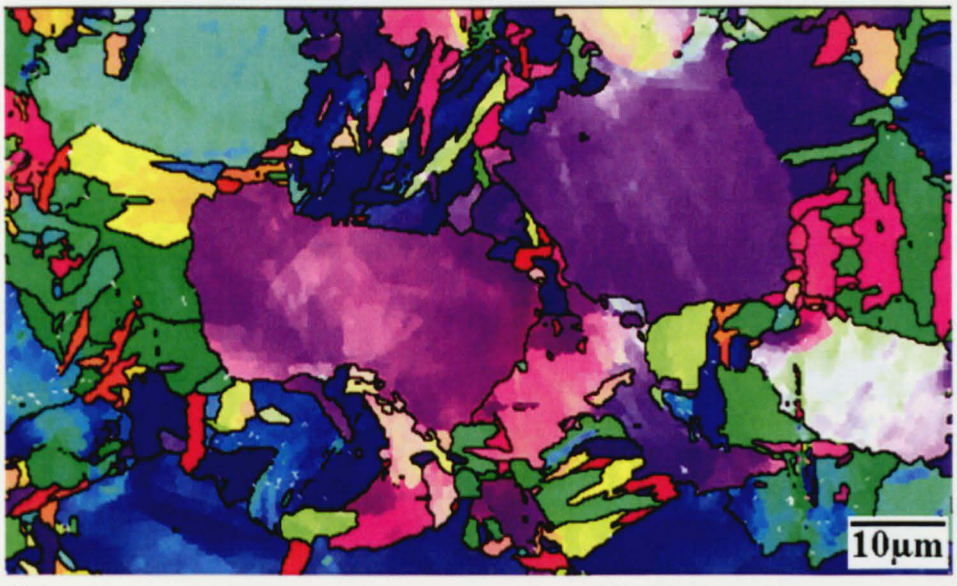

(b)

Figure 6.52 High Resolution OIM of sample T14 in (a) Euler colouring and (b) IPF colouring

The IPF OIM in Figure 6.52(b) shows a high degree of contrast within enclosed grain boundaries, suggesting sub-grain deformation. An optical micrograph of the microstructure of this specimen can be seen in Figure 6.53.

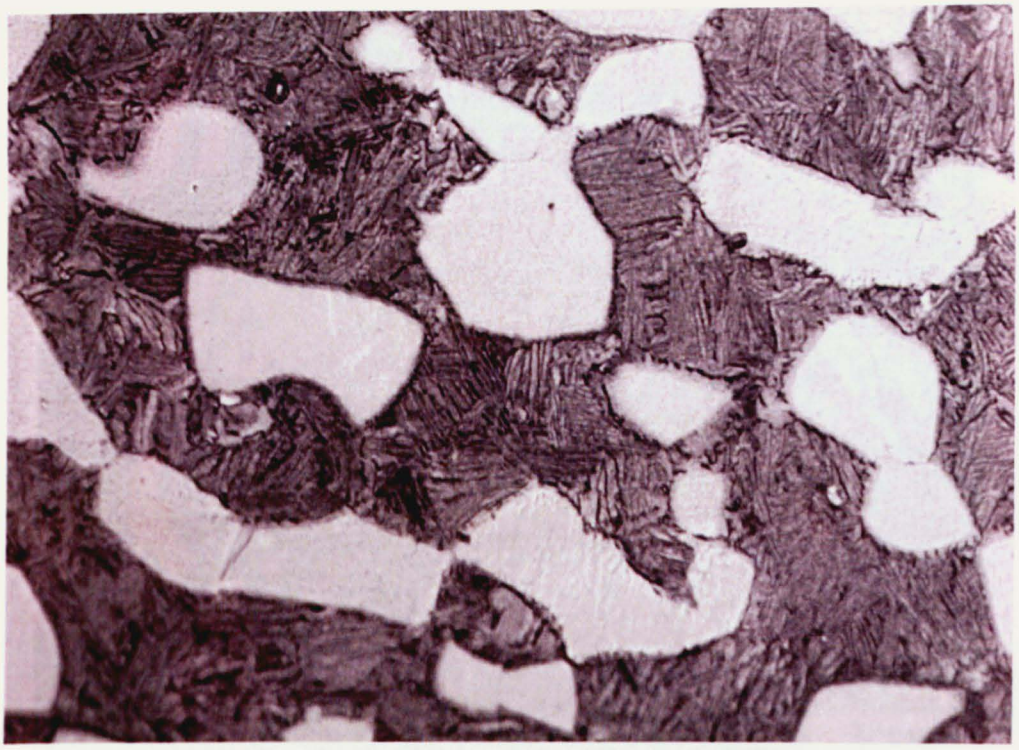

Figure 6.53 Optical micrograph of sample T14

The sub-grain misorientation visible in Figure 6.52(b) is again apparent in the OIM's representing the increased strain test pieces of 0.55 and 0.75, shown in Figures 6.54 and 6.55.

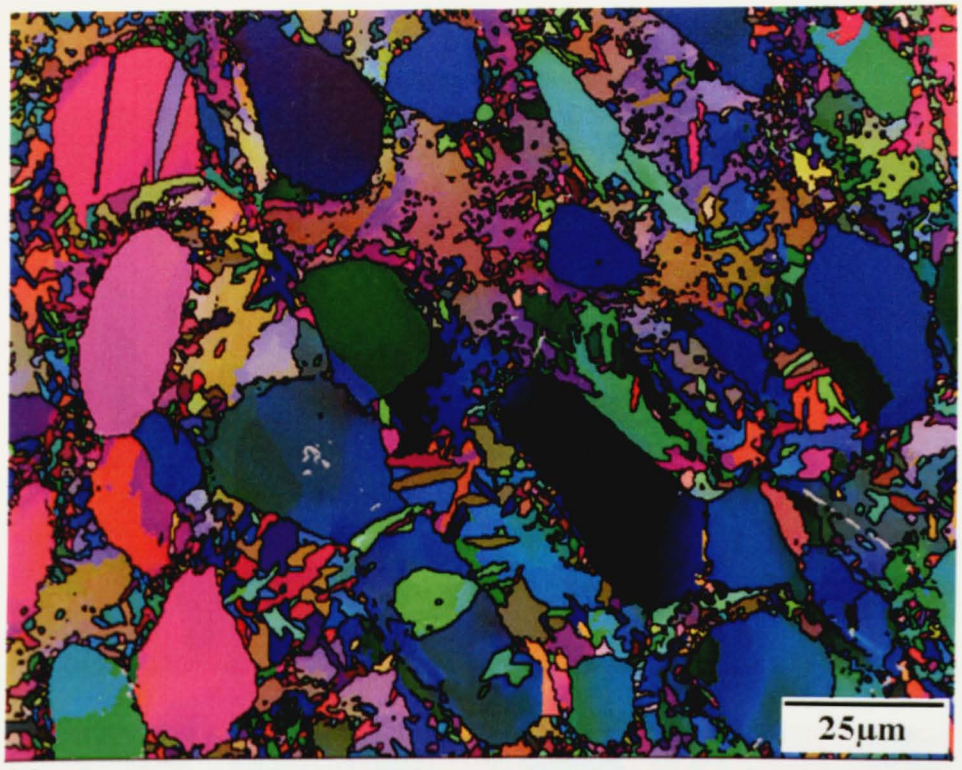

(a)

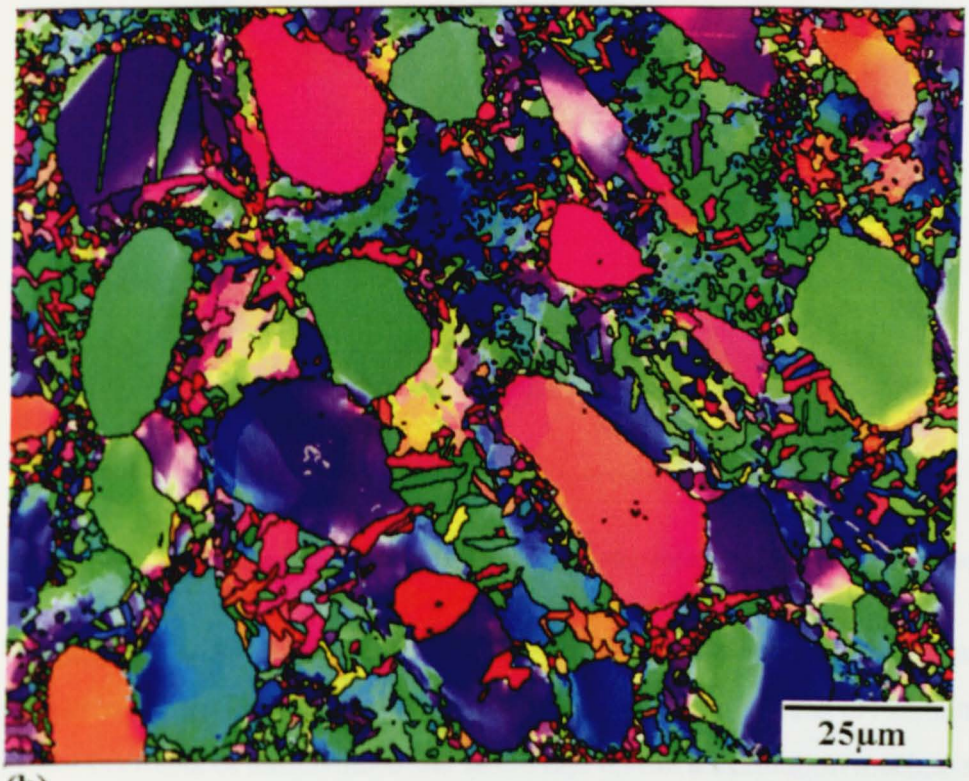

(b)

Figure 6.54 High Resolution OIM of sample T17 in (a) Euler colouring and (b) IPF colouring

04 Down With The Sickness.mp3

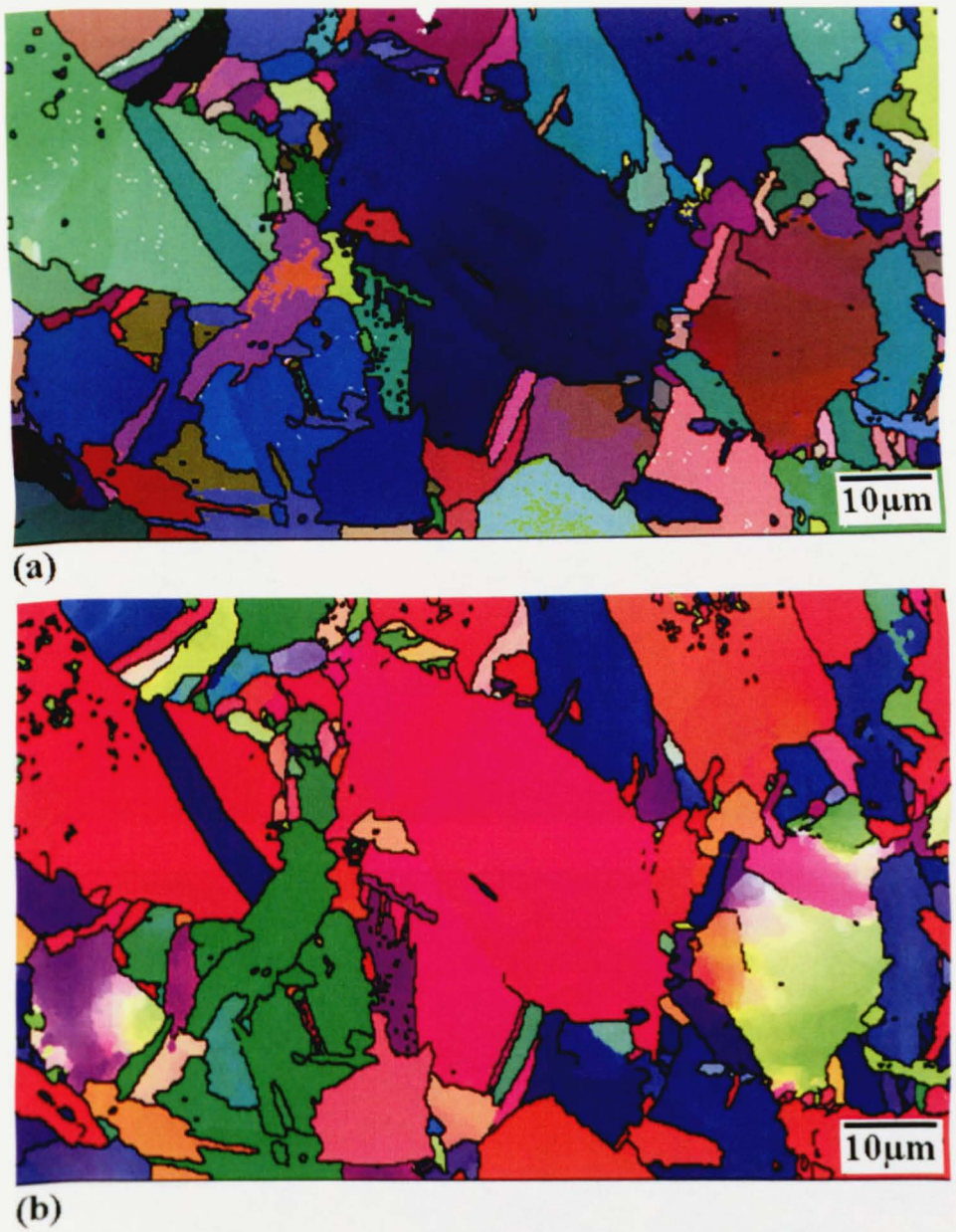

Figure 6.55 High Resolution OIM of sample T15 in (a) Euler colouring and (b) IPF colouring

Figures 6.56-58 show OIM's obtained from the constitutive equation development work having received a strain of 0.7 detailed in Table 6.4 obtained in order to assess effects of temperature and strain rate on the deformation mechanisms.

Table 6.3 Description of further EBSD analysis and OIM#s produced.

Testing Parameters	*Figure*
Heated to 990°C, deformed to a strain of 0.75 with a strain rate of 20 s^{-1}	Figure 6.56
Heated to 990°C, deformed to a strain of 0.75 with a strain rate of 0.2 s^{-1}	Figure 6.57

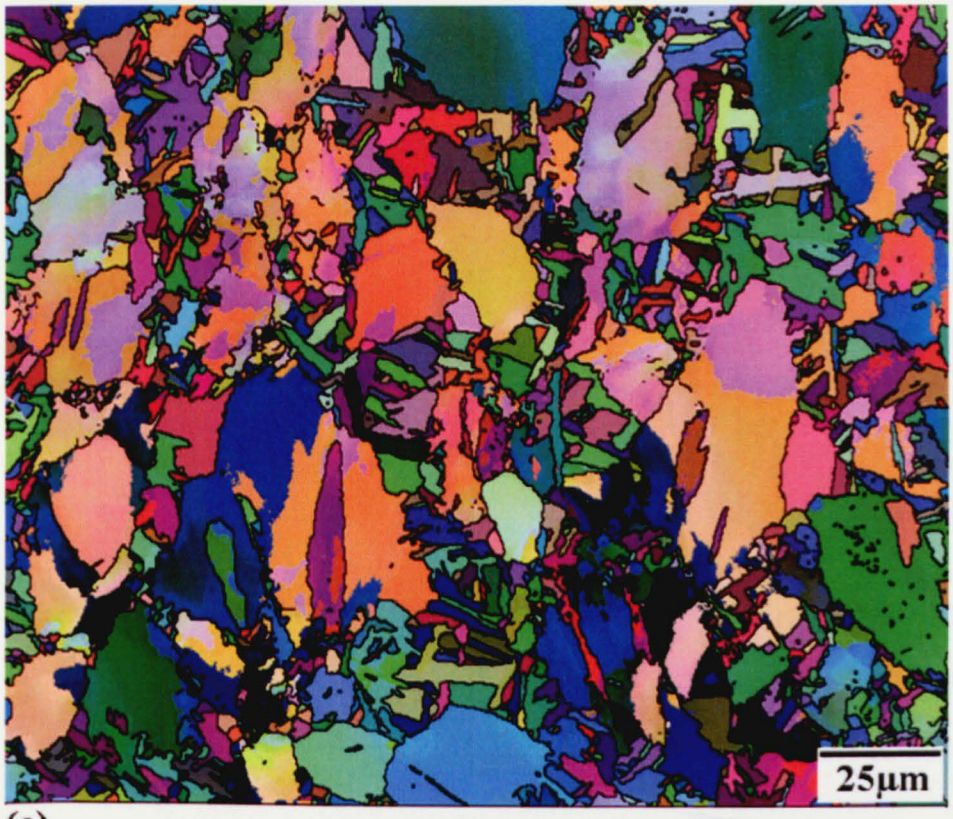

(a)

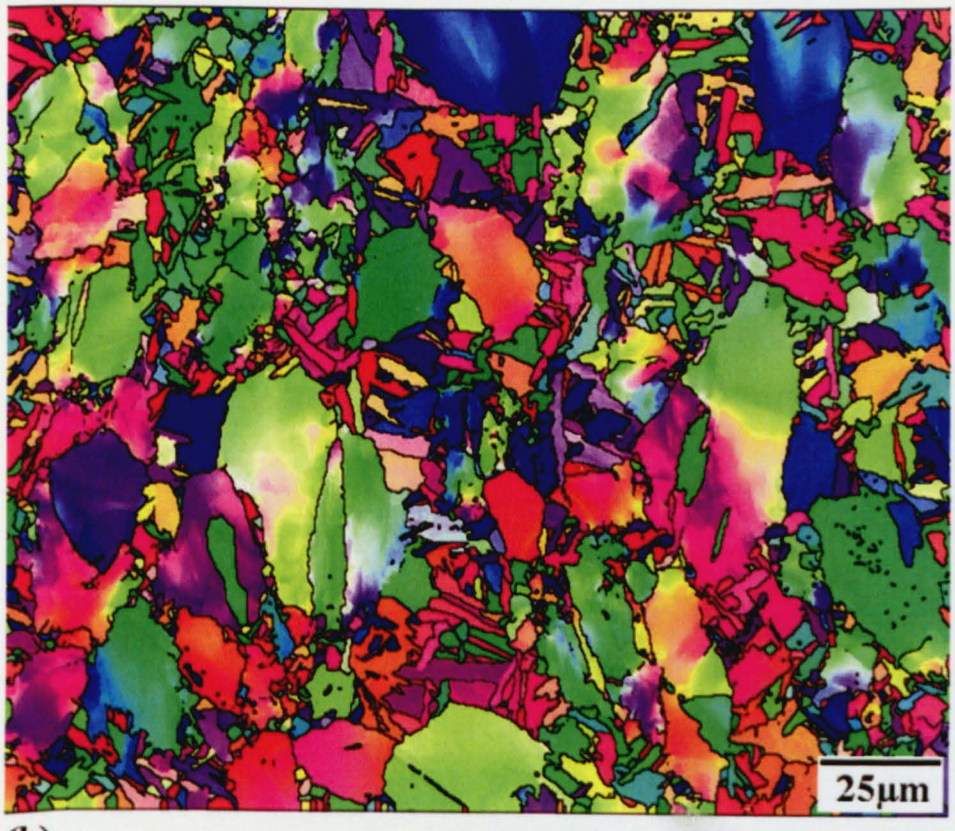

(b)

Figure 6.56 High Resolution OIM of sample D5 in (a) Euler colouring and (b) IPF colouring

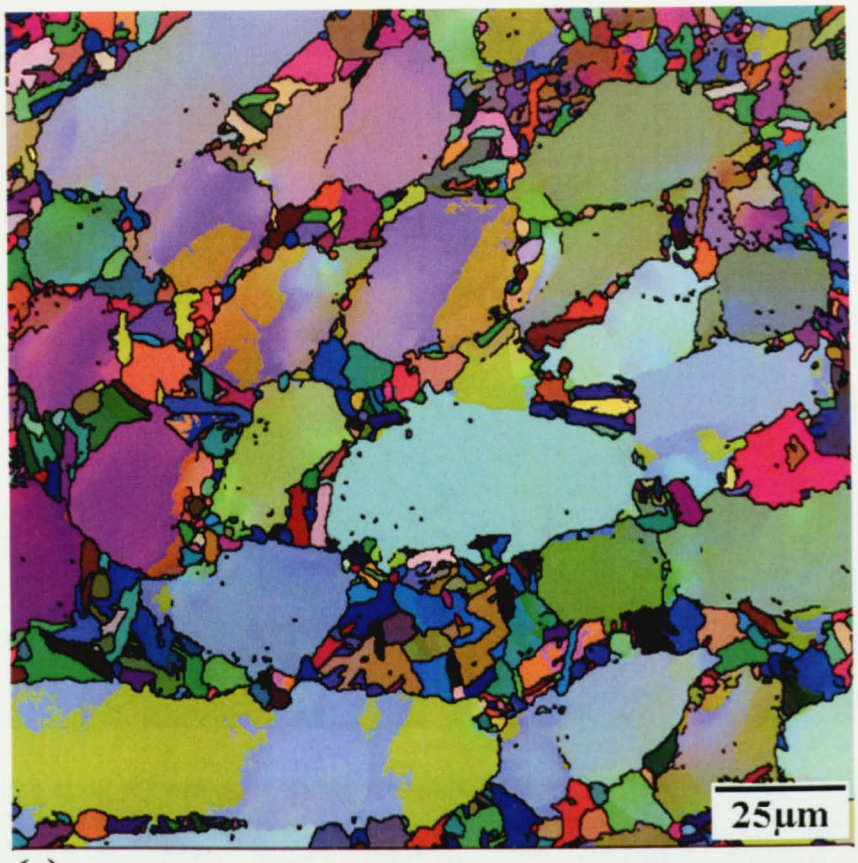

(a)

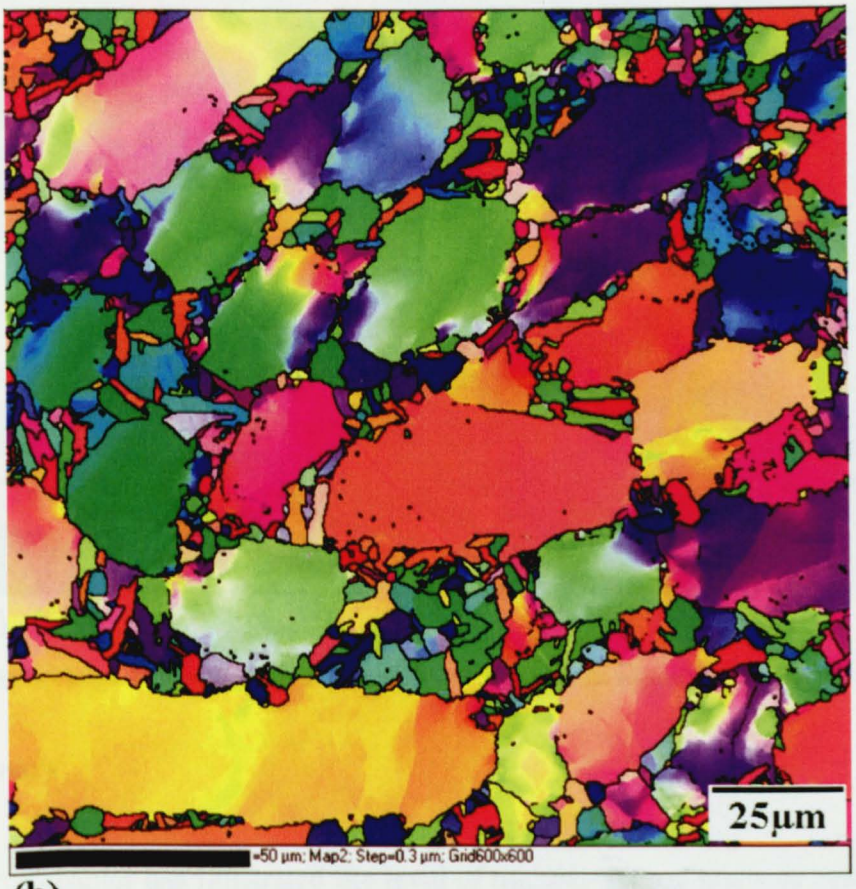

(b)

Figure 6.57 High Resolution OIM of sample D7 in (a) Euler colouring and (b) IPF colouring

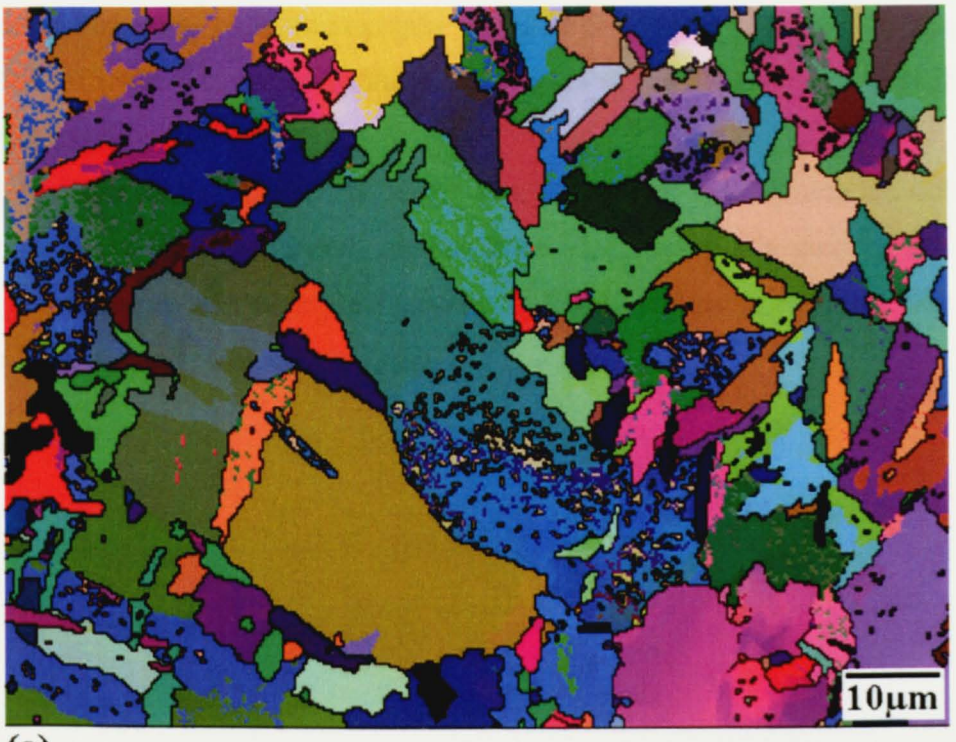

(a)

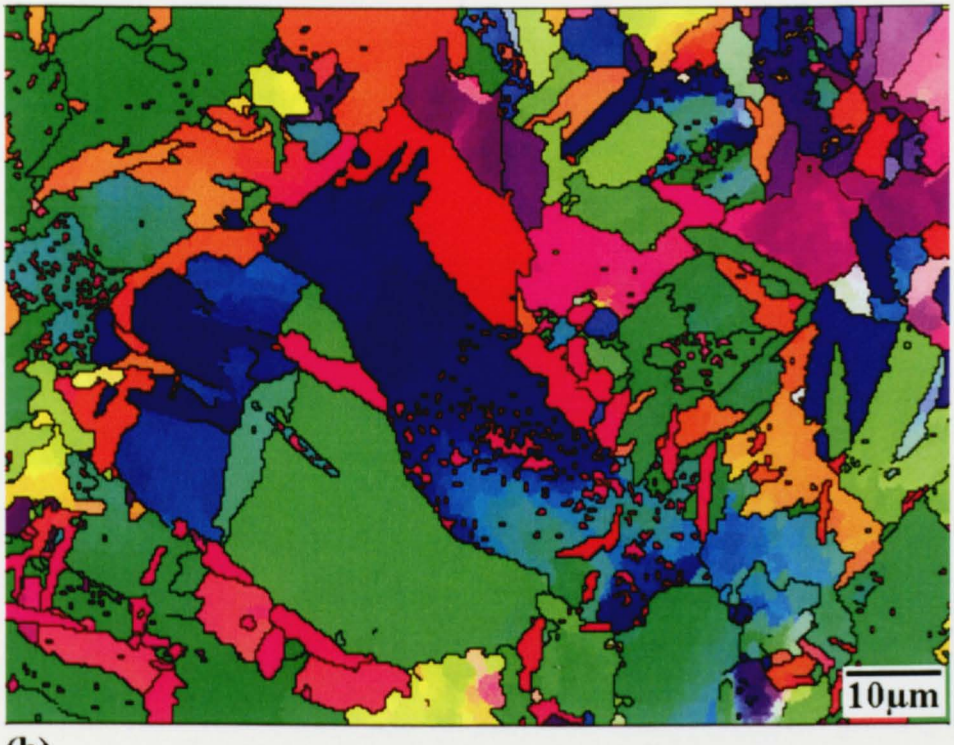

(b)

Figure 6.58 A9 High Resolution OIM of sample D9 in (a) Euler colouring and (b) IPF colouring

6.4 Summary

This chapter has illustrated the level of microstructural analysis carried out on billet material and thermomechanically processed samples. The results prove the

benefits of obtaining both micrographs and EBSD OIM's of areas of interest and detail the difficulties in assessing the morphologies of the hexagonal α phase through EBSD analysis.

In the following chapter (Chapter 7) a method for determining the texture of each phase separately using both images is detailed. Using this method as well as other post-mapping processing techniques the EBSD and metallographic results are further analysed and discussed in Chapter 8.

7 DATA SEPARATION TECHNIQUE

7.1 Introduction

As this work progressed, significant difficulty was found in analysing, specifying and interpreting the texture data produced by the bimodal nature of this alloy. The room temperature microstructure of this alloy (equiaxed α_p in a matrix of transformed α_s) meant that any global textures obtained using bulk X-ray analysis techniques and macrotexture EBSD maps were difficult to interpret as the data was a function of the volume fraction of each transformation product, i.e. the primary alpha grains (α_p) and the transformed secondary alpha grains (α_s). Moreover, since the α_p and α_s have the same α-HCP structure any texture determined will be dominated by the α hexagonal component with the highest volume fraction.

A number of methods have previously been suggested in order to overcome this difficulty for example by Germain et al (2005) and Glavicic (2005). These methods, however, were complicated, multi-stage techniques and in some cases the results produced were indirect and as such an alternative method was developed as part of this work. The following chapter describes the alternative technique developed which has been published Thomas et al, (2005) and shows the initial results which proved the method and allowed its subsequent use throughout the remaining work.

7.2 Description of the Method.

The procedure for obtaining separate orientation datasets for both α_p and α_s can be split into three steps;

- Acquisition of orientation data through EBSD to generate the OIM.
- Location of the mapped region using the optical microscope and subsequent image analysis (as used in the beta approach curve determination work), and
- Correlation of the OIM with the optical image and separation of the orientation datasets for each microstructural component.

The crucial issue in the successful application of the technique is the location of the orientation mapped region in the optical microscope. Although it is possible to achieve this by marking the sample or by measuring from the edge of the sample, this issue can be achieved relatively simply by taking advantage of an artefact of the specimen-electron beam interaction. By etching the specimen immediately after EBSD mapping a large un-etched area equivalent to that scanned during OIM acquisition is revealed, an example of which is shown in Figure 7.1

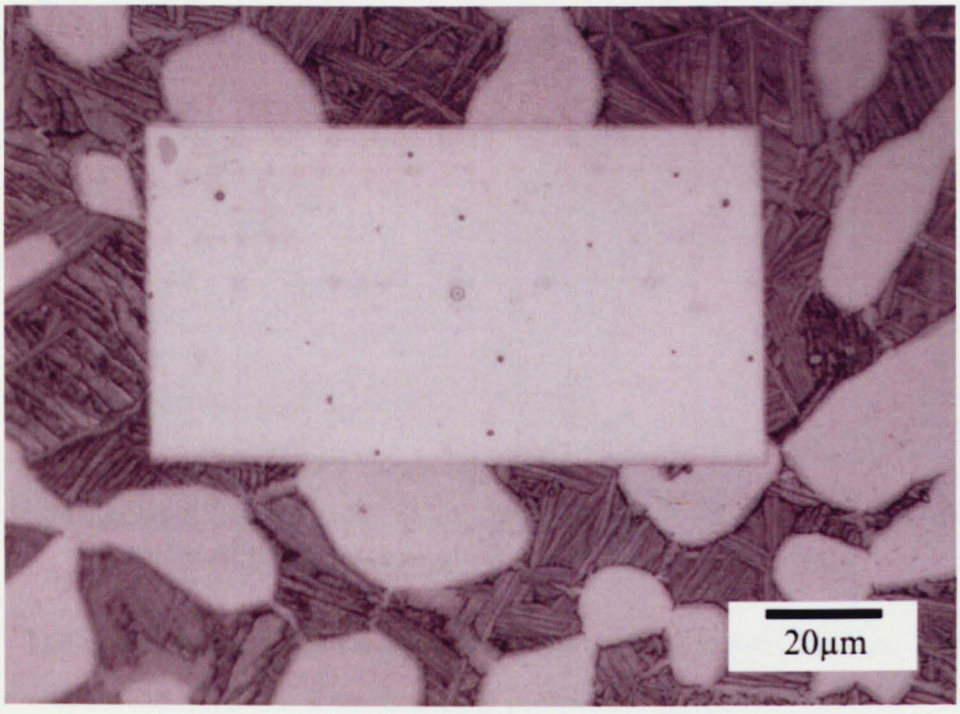

Figure 7.1 Optical micrograph of 'blanked' OIM area

This is believed to be due to carbon contamination, a well known phenomenon in electron microscopy (Williams, 1984), and from now on this area will be referred to as the 'blank'.

The appearance of the blank is directly related to the step size and the time taken per data point acquisition. When a small step size is used, $< 0.5\mu m$, with a long data acquisition time, > 0.5 sec, the blank is very strong and easily recognisable as in Figure 7.1. However, when a larger step size is used with increased data acquisition rates, typical of what would be used in a texture analysis map, the effect is reduced to such an extent that no sign of the blank can be found. For this reason, the blanks are used in two different ways. For high resolution EBSD maps used for microstructure analysis, the step size is small enough to form a blank over the entire area of the

EBSD map, therefore locating the mapped region directly. Whereas for texture acquisition runs, for which the EBSD data is obtained with a much larger step size, to locate the map at a later stage, a small step size map is performed in each corner of the larger run creating visible markers after etching as seen in figure7.2.

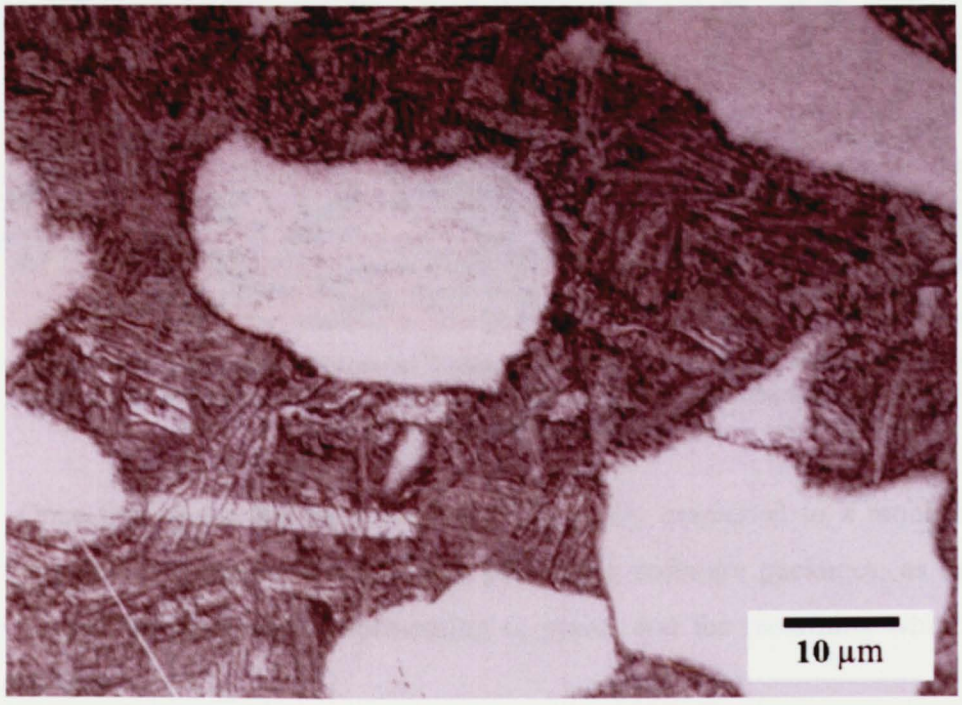

Figure 7.2 Blank produced at the start of a larger texture map.

The methodologies used to obtain the EBSD data, create the OIM, polishing and etching are standard and were described in detail in Chapters 3 and 6.

Once a successful etch and location of the orientation image mapped area are achieved the separate microstructural components, α_p and α_s, need identifying. This can be easily achieved using optical image analysis as was used previously in the β approach curve determination work detailed in Chapter 3. Figures 7.1 and 7.2 show optical micrographs of Timetal 834 etched with a 2% solution of Ammonium Hydrogen Di-fluoride (NH4F:HF), for which an excellent contrast between the α_p, the α_s and the blank can be seen. Of all the etchants tested NH4F:HF gave the greatest contrast between α_p and α_s. This in turn gives a bimodal grey level histogram with two distinct pixel intensities clustered around two well-separated peaks, the first corresponding to the dark pixels of the transformed β and the second, to the primary α. Image segmentation can then be performed using a simple thresholding procedure,

available in most image analysis software packages, with little or no image processing required, an example of which is shown in Figure 7.3(a).

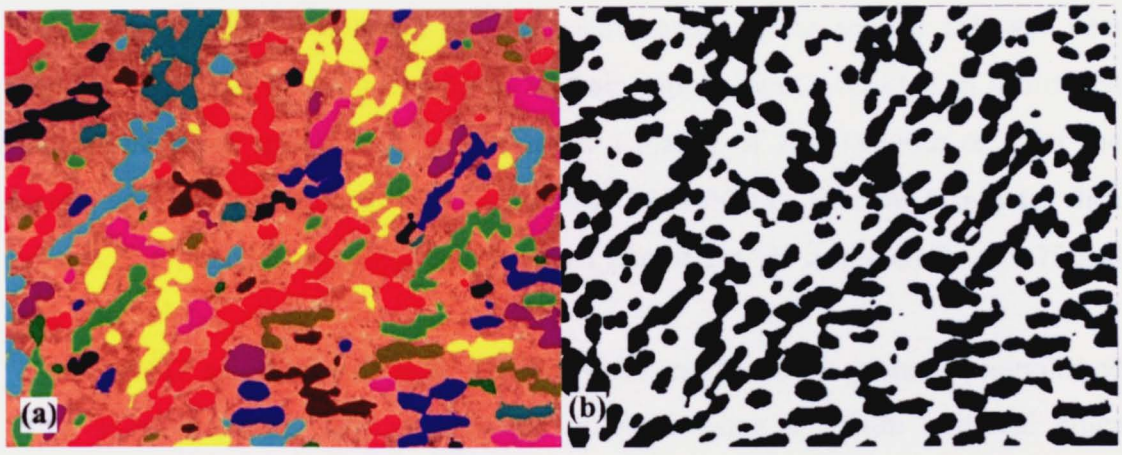

Figure 7.3(a) An optical image of bimodal Timetal 834 subjected to simple light thresholding to highlight the alpha p shown coloured, and (b) the associated monochromed image of (a) where black represents alpha p.

Once this image has been obtained it is easily converted to a monochrome bitmap image using one of many image processing software packages, as seen in Figure 7.3(b), the black areas representing α_p grains and the remaining white areas representing α_s.

The final step of the procedure is the correlation of the OIM with the monochromed image and extraction of the individual orientation datasets. As the blank or blanks define the exact location of the OIM in the optical image all that is required is rotation and resizing of the optical image to match that of the OIM; no image translation or shearing is necessary. A simple subroutine is then used to designate each pixel within the OIM as either α_p or α_s depending on if the corresponding bit in the monochromed bitmap image is a 0 (black) or 1 (white) respectively.

7.3 Applications: high resolution microstructure and microtexture analysis

In this section two examples of the application of the separation method proposed are presented. The first, an investigation of microstructure at high magnification, demonstrates that by combining EBSD and optical analysis gives a much clearer account of microstructure evolution, in particular that of the formation of feathery α. Whilst the second example highlights the efficiency of the method to extract accurate orientation datasets for both α_p and α_s.

7.3.1 Experimental

For the high resolution microstructure analysis, the sample D4 was heat treated to 1010°C, held for 5 minutes and air cooled, which resulted in a bimodal microstructure of approximately 20% α_p in a matrix of fine lamellar α_s. For the texture analysis a sample was heated to 990°C (≈44% α_p), held for 5 minutes then deformed in uniaxial compression at a strain rate of 2 s^{-1} to a true strain of 0.75 and then air-cooled.

EBSD specimens of both samples were mechanically ground, pre-polished using 9μm diamond paste and finally polished using a 0.5μm colloidal silica suspension. To ensure there was no polishing residue on the surface to be analysed the specimens were ultrasonically cleaned in isopropanol (C_3H_8O) just prior to EBSD analysis. Acquisition of EBSD data was done using the FEI Sirion FEGSEM, equipped with a fully automatic HKL Technology EBSD attachment, operated at 15 kV. Orientation mapping for the high resolution sample was performed on a rectangular grid with a step size of 0.2μm covering an area of 100 x 60 μm^2.

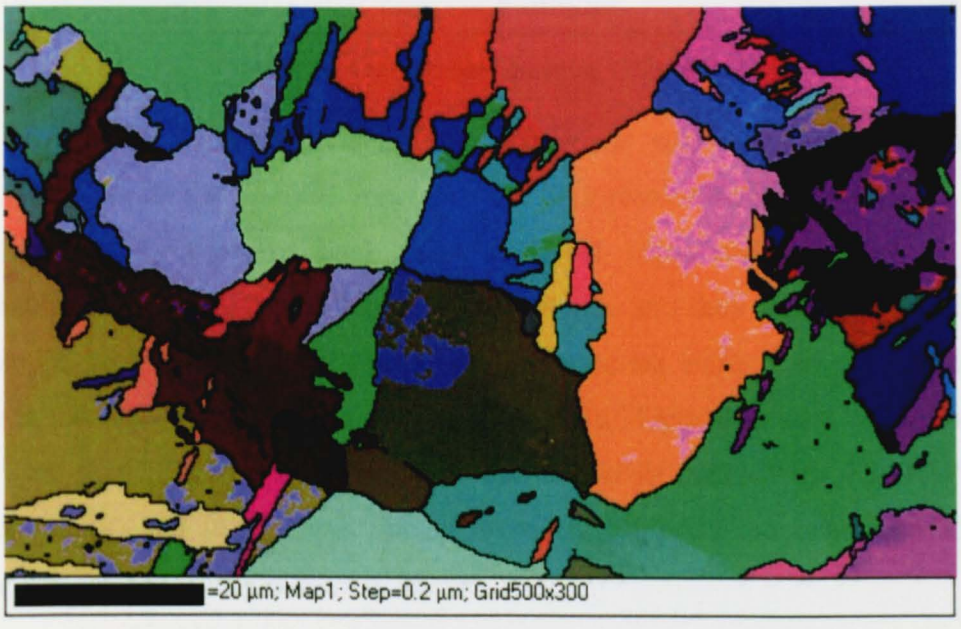

Figure 7.4 Euler colouring OIM of heat treated Timetal 834.

For the texture analysis a step size of 2 μm was used on beam scans of 200 x 200 μm^2 which were then stitched to together to cover an area of approximately 1 mm^2, seen in Figure 7.5. On completion of the texture map four 10 x 30 μm^2 maps

with a step size of 0.2 μm were performed on each corner of the map to be used as location markers for subsequent optical analysis. Pattern solving efficiencies were in the order of 85%.

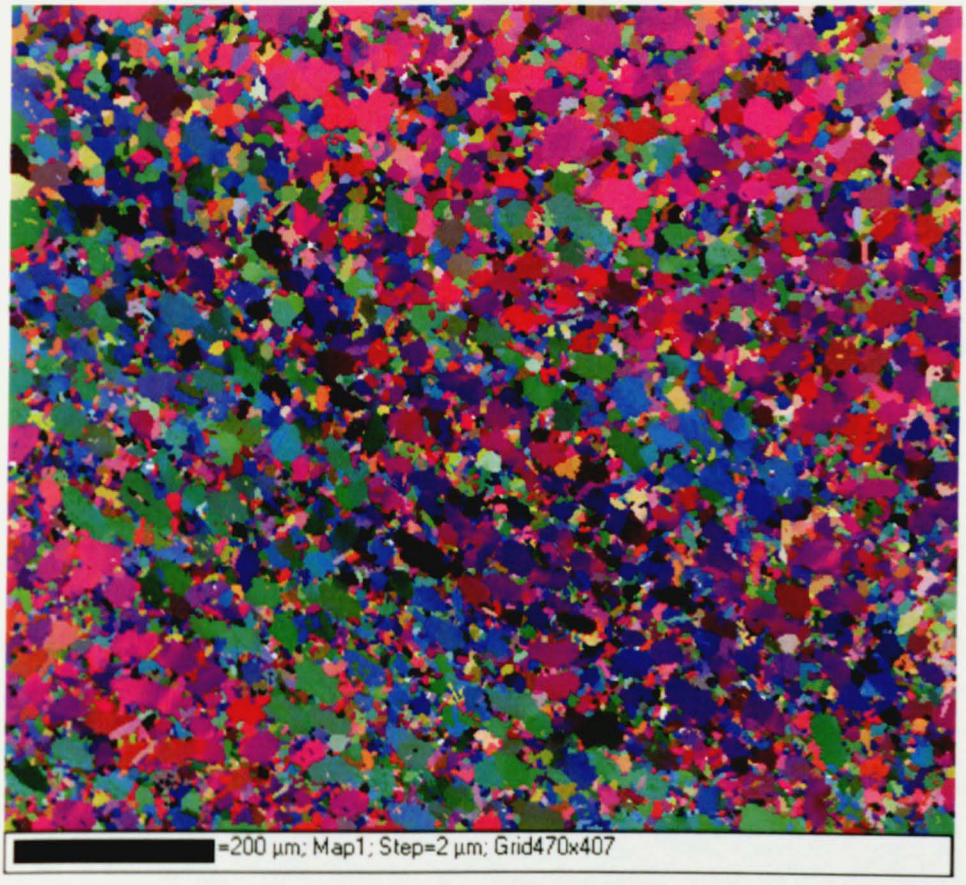

Figure 7.5 Large Euler colouring OIM of D6

After EBSD data acquisition the specimens were immediately etched in NH_4F:HF to reveal the blanked areas. For the high resolution EBSD map, the blank was then slightly polished back using colloidal silica and re-etched. In such circumstances the edges of the blank are still visible and they were used to relocate the mapped area. For the larger texture analysis runs the mapped area is not blanked so the initial etch was sufficient for image analysis. Optical images of the mapped areas were then rotated and resized to obtain a best fit match with the OIM's, see Figures 7.6 (a) and (b). These images were subsequently monochromed and the separate orientation datasets were extracted.

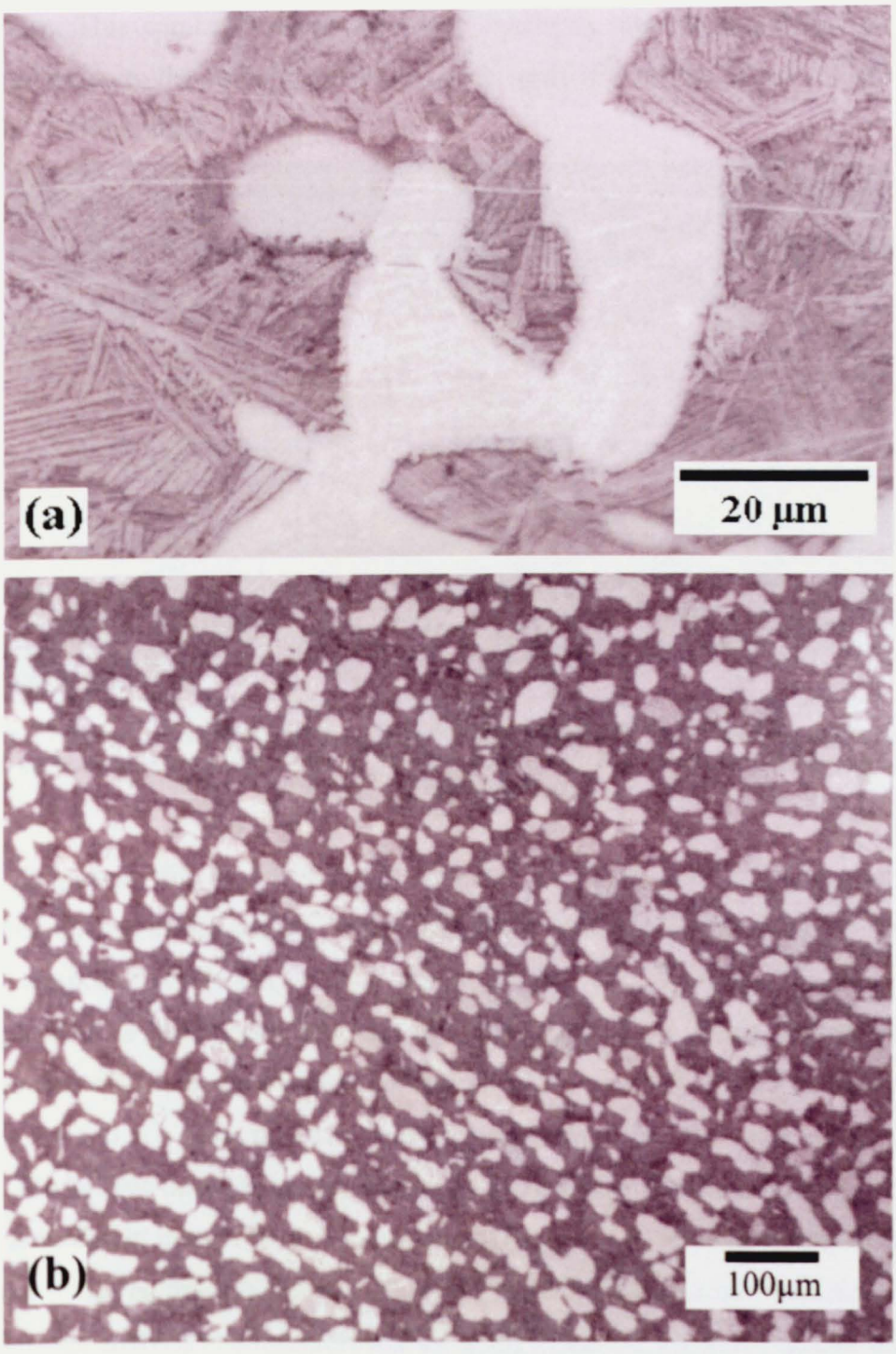

Figure 7.6 Optical micrographs of mapped areas (a) heat treated sample and (b) sample D6

7.3.2 Results and discussion

7.3.2.1 High Resolution Analysis

Figure 7.7 shows the OIM of the heat treated sample with high angle boundaries (>10°) shown as a black line, combined with the optical micrograph of the

same area. This combined image not only highlights the efficiency of fit but also draws attention to the complicated nature of α_p grain boundaries in a $\alpha + \beta$ processed bimodal titanium alloy.

Figure 7.7 Map associating the OIM and the optical micrograph; the black lines represent the high angle boundaries (>10°) from the EBSD dataset overlying the optical micrograph seen previously in Figure 7.6(a)

It appears, that on first viewing, that there is a difference in the location of α_p grain boundaries in the optical image compared with that of the OIM. In fact, the EBSD boundary is always located on or outside of that shown in the optical micrograph. It is our opinion that this not an artefact of the fitting procedure but a consequence of the thermomechanical history of the material. Closer comparison of Figures 7.4 and 7.7 show that the areas of discrepancy have the same orientation as the α_p. We believe that this has its origins during cooling where so-called feathery α, which is similar in morphology to transformed β, appears to be propagating epitaxially from the initial α_p grain boundary. As such, the feathery α is not identified during optical image analysis and therefore not included within the separated α_p data set.

This observation of similarly orientated feathery α may explain a major source of the incorrectly assigned 6% of pixels in the work of Germain et al (2005). It seems reasonable to suggest that the feathery α has been included in their manually obtained EBSD α_p data set whilst in their BSE image it would have been allocated as α_s. For this particular example the feathery α makes up 8.5% of the manually selected α_p dataset. The appearance of a common α_p/feathery α orientation may also explain Bache et al.'s (1997) observation that α_p cleavage facets in material subjected to

LCDF extended beyond the alpha phase boundaries into the surrounding transformed matrix material.

7.3.2.2 Microtexture Analysis

Figures 7.8(a) and (b) show the α_p separated optical image, and the combined OIM/separated image respectively for the area analysed. The excellent fit revealed in Figure 7.8(b) confirms, once again, the efficiency of the proposed separation technique.

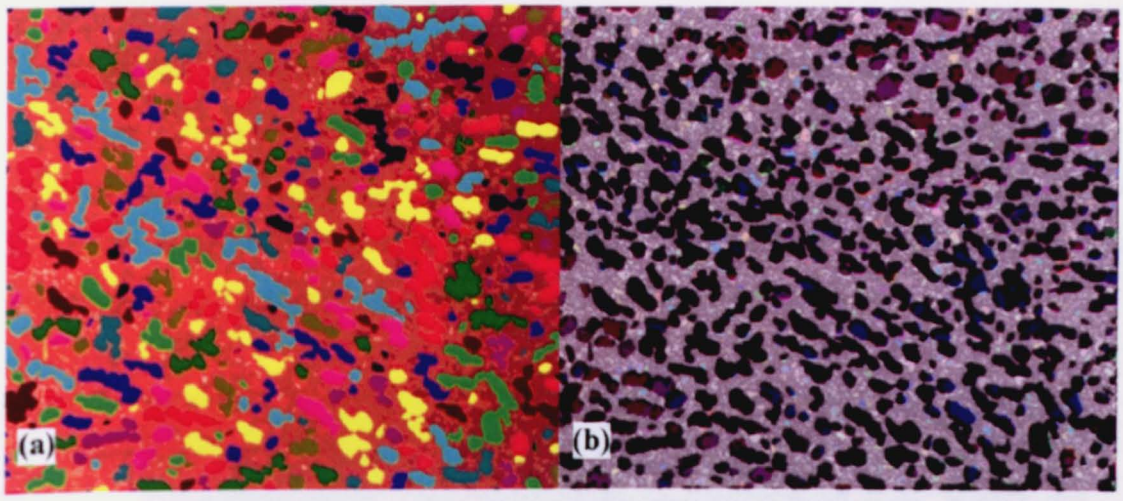

Figure 7.8 (a) Image analysed optical micrograph of sample D6 and (b) the associated OIM and transparent monochromed optical image where the black layer overlaps the detected α_p grains

In traditional X-ray analysis of axisymmetric compression of α/β processed alloys two major texture components are seen: i) basal, where the (0002) plane lies perpendicular to the compression direction, and ii) transverse, where the (0002) plane lies parallel with the compression direction in any radial direction. Lütjering (1998), by processing through the temperature range from high α to high β content concluded that the basal texture was a product of primary α deformation and the transverse texture was a consequence of deformation in the β and subsequent transformation to α. Figure 7.9 shows the $\{0002\}$ and $\{10\bar{1}0\}$ pole figures produced by the complete EBSD dataset for the analysed sample and if we had analysed this under the above guidelines we would have been drawn to the conclusion that the strong texture components had there origin from transformed β.

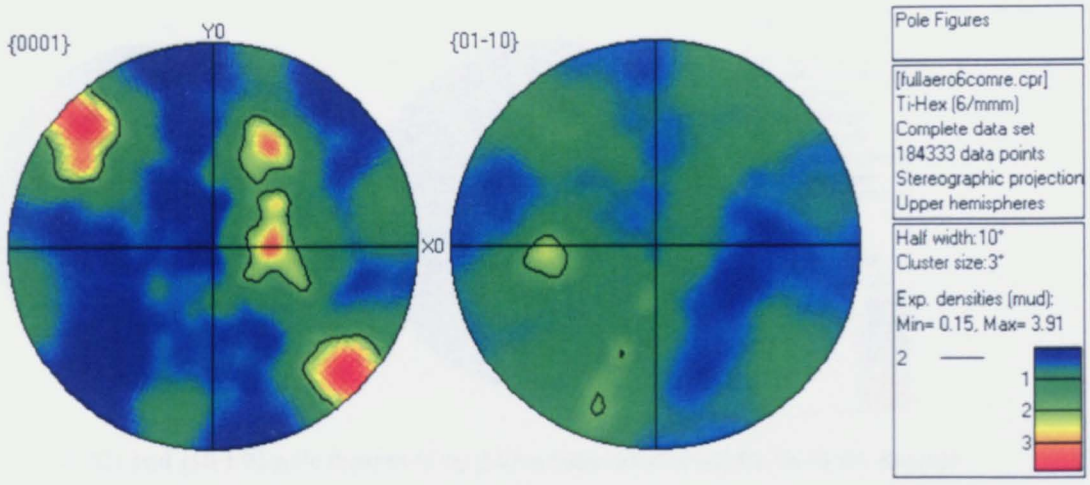

Figure 7.9 {0002) and {10 $\bar{1}$ 0} pole figures from complete D6 dataset

However, Figures 7.10 and 7.11 show the separated α_p dataset and the associated {0002) and {10 $\bar{1}$ 0} pole figures, which clearly show a major component of the α_p texture is transverse basal. This clearly shows the importance of using EBSD to analyse textures in bimodal titanium alloys and subsequent use of separation techniques to fully quantify texture development through the processing route.

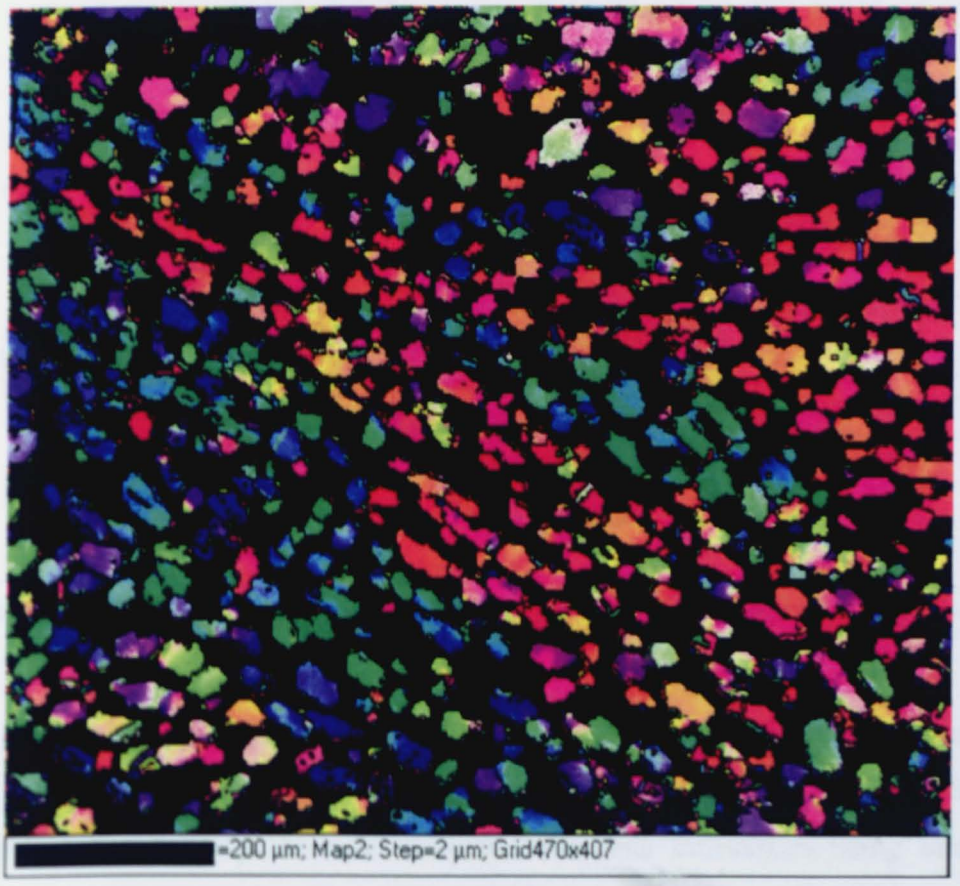

Figure 7.10 The α_p grains separated from D6 OIM

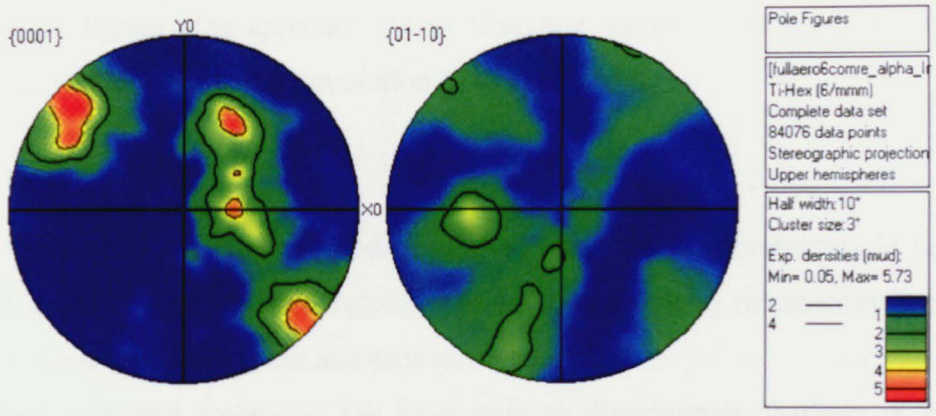

Figure 7.11 (0002) and {10 $\bar{1}$ 0} pole figures of α_p grains separated from D6 OIM D6 dataset

The textures revealed by the separated datasets show well defined macrozone textures, as have previously been described by Germain et al (2005) confirming that the proposed technique has a high level of efficiency. However, this technique, and that proposed by Germain et al. (2005) are still relatively time consuming. To investigate if this time investment was worthwhile we compared the results generated via the separation technique with results obtained directly from the OIM based on size distribution. It was assumed that the largest grains observed in the OIM were α_p and all small grains were associated with the α_s lamellar. The α_p and α_s could then be separated based on the known volume fraction of α_p, which in this case is 44%.

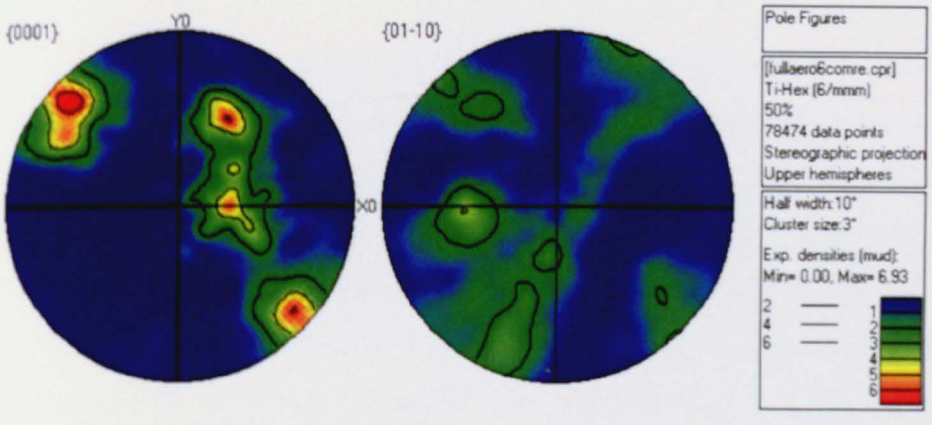

Figure 7.12 (0002) and {10 $\bar{1}$ 0} pole figures of α_p grains separated from D6 OIM D6 dataset using a size distribution method

Figure 7.12 shows the α_p and separated pole figures using the size distribution technique. The pole figures are almost identical to those presented in Figure 7.11, the pole figures produced using the new technique, the only differences being small variations in intensity but not position. This would suggest that in the first instance a

morphological/grain size approach direct from the EBSD dataset is sufficient for observing any trends in texture evolution of both α_p and α_s.

7.43 Summary

1) A method to separate α_p and α_s microstructures and microtexture in bimodal Timetal 834 using high resolution EBSD and optical microscopy has been proposed, demonstrated and proved successful.
2) The proposed technique has been able to discriminate feathery α, formed epitaxially on the α_p grain boundaries during cooling, from the initial α_p giving us a much greater insight into the microstructure effects that may influence in-service performance.
3) Data obtained in bulk X-ray analysis is insufficient to fully quantify textures formed during thermomechnical processing in bimodal titanium alloys. To fully quantify texture development in these alloys EBSD plus a α_p/α_s separation technique must be used.
4) If trends in texture development as a function of processing route are only required, texture data sets of α_p and α_s can be obtained using a morphological/grain size approach direct from the EBSD dataset, saving significant time with only a slight loss of accuracy.

8. EBSD ANALYSIS AND INTERPRETATION

8.1 Introduction

In Chapter 6, complete pole figures and Euler colouring OIM's of areas mapped during EBSD were shown. However, as explained in Chapter 6 the results produced by EBSD mapping are complex datasets containing a wealth of orientation information at defined points within a mapped area that can be analysed in many different ways. As such, this chapter includes further in-depth analysis of the texture data and microstructure information available within the datasets using post-mapping processing methodologies, available within the Channel 5 software and developed in-house. This has enabled a number of features to be highlighted including billet texture and α_p clustering, bimodal texture separation, the formation of feathery α and possible deformation mechanisms in the α_p.

8.2 Billet analysis

Initially the post OIM acquisition analysis was carried out on the EBSD datasets obtained from samples of the billet material. For example, Figure 6.8 shows the OIM and two pole figures, {0002} and $\{01\bar{1}0\}$ of the as-received material taken from the centre radius of the billet. The {0002} pole figure produced of this area shows two major components: i) an almost parallel basal orientation, where the {0002} plane is almost perpendicular with the longitudinal plane of the billet and ii) a set of transverse orientations, where the basal plane lies parallel to the longitudinal direction. The deformation history of the billet would suggest the only axis of deformation symmetry in the billet would be the longitudinal direction. It is, therefore, somewhat surprising that the transverse texture consists of only three distinct components and not a fibre of orientations about the longitudinal direction which is usually associated with such a deformation symmetry. The origin of this lack of a fibre appears to be an orientation clustering effect that can be seen in Figures 6.8, 6.11 and 6.13. The Euler orientation colouring used in Figures 6.8, 6.11 and 6.13 displays the clustering of similarly orientated α_p grains, creating an effective large clustered grain of approximately 300μm in diameter. This clustering was not expected and as such required further investigation.

8.2.1 Orientation Clustering

The clustering visible on the Euler colouring OIM shown in Figure 6.8, shows a number of clusters ($\approx$10) of approximately 110 α_p grains sharing very similar orientations. Using Channel 5 software it was possible to separate the clusters by selecting the similarly orientated grains within proximity of each other. These separated clusters can be seen in Figures 8.1-8.8 along with the associated {0002} and $\{01\bar{1}0\}$ pole figures. In general, the separated clusters identified show rotations of the transverse basal orientation, visible in the previously seen pole figures. The prism $\{01\bar{1}0\}$ plane is often located in the centre of the pole figure, showing the $\{01\bar{1}0\}$ planes to be parallel with the viewing plane, in this case, the cross sectional billet plane. This section will examine each cluster in greater detail in order to assess the billet microstructure and identify possible trends.

The cluster shown in Figure 8.1 is approximately 300μm in diameter and consists of approximately 60 grains with a strong transverse basal orientation. The {0002} and $\{01\bar{1}0\}$ pole figure (Figure 8.2) shows the prism planes to be orientated parallel with the billet cross section.

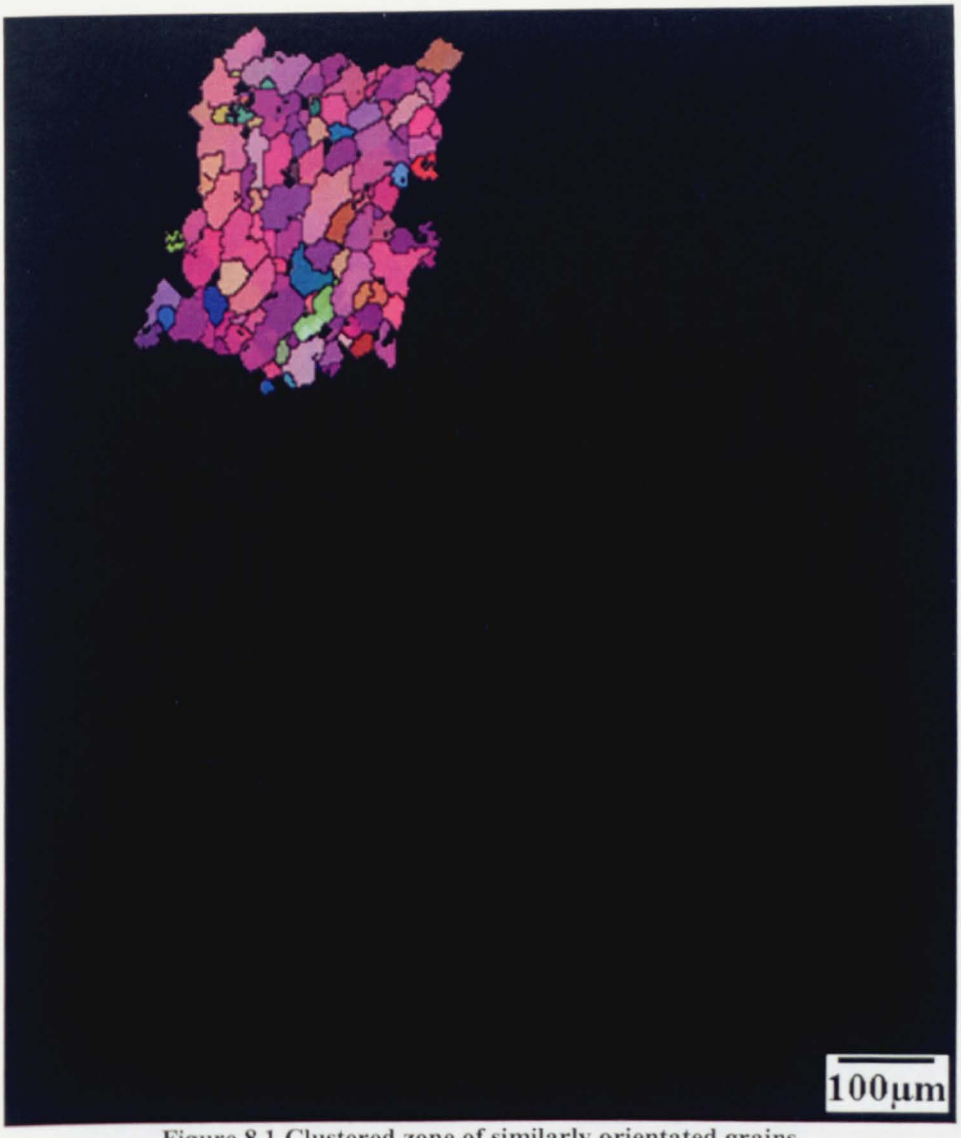

Figure 8.1 Clustered zone of similarly orientated grains

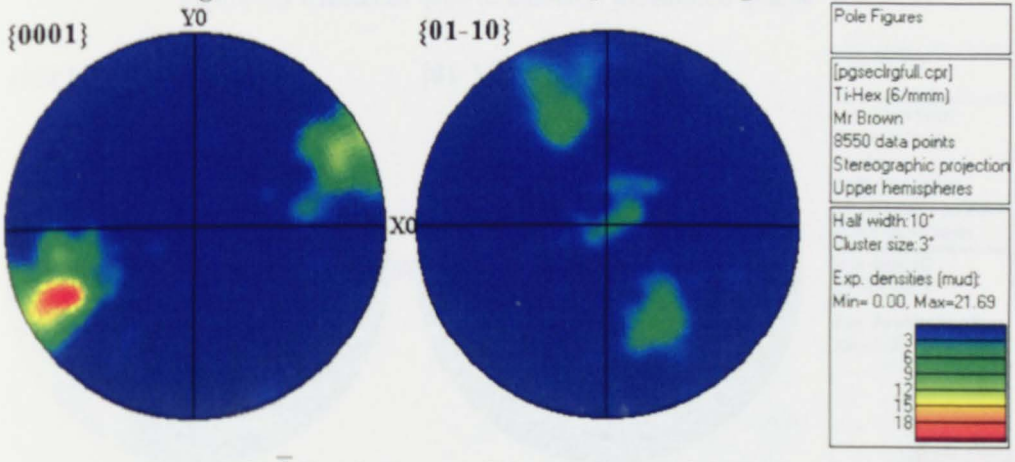

Figure 8.2 {0002} and {01 $\bar{1}$ 0} pole figures of clustered zone of similarly orientated grains

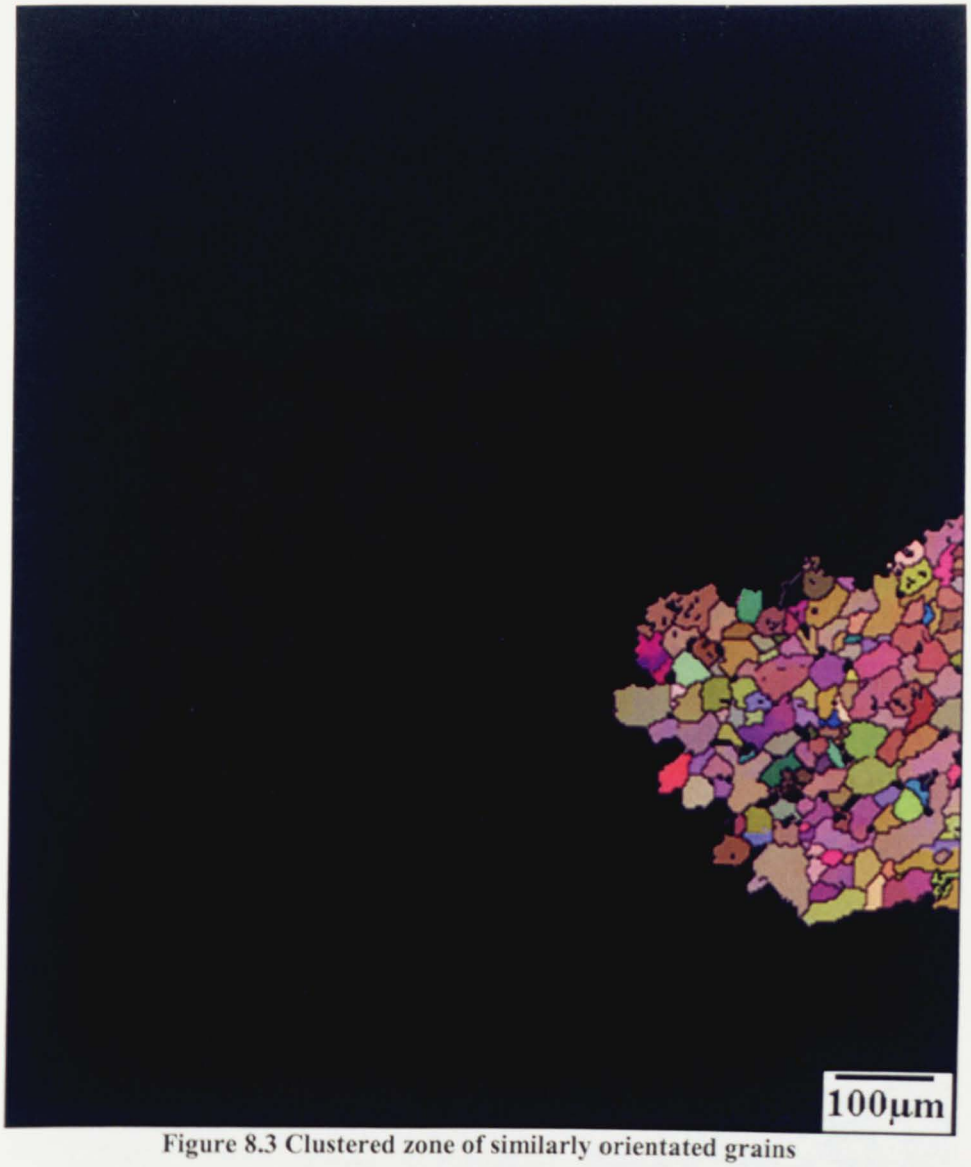

Figure 8.3 Clustered zone of similarly orientated grains

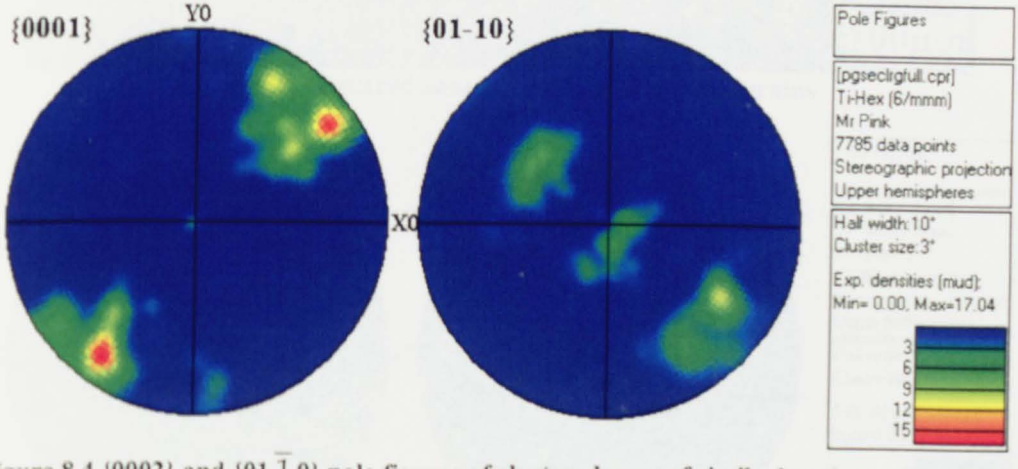

Figure 8.4 {0002} and {01 $\bar{1}$ 0} pole figures of clustered zone of similarly orientated grains

The cluster in Figure 8.3 is incomplete due to map size restrictions, however, it still measures approximately 400µm in diameter and shares a similar orientation to that

seen in Figure 8.1, as shown by the {0002} and {01 $\bar{1}$ 0}pole figures in Figure 8.4. Figure 8.5 shows the largest cluster seen in this OIM, occupying the full width of the mapped area this incomplete cluster is at least 1mm wide. Again, the {0002} and {01 $\bar{1}$ 0} pole figures show a transverse basal orientation, as seen in Figure 8.6.

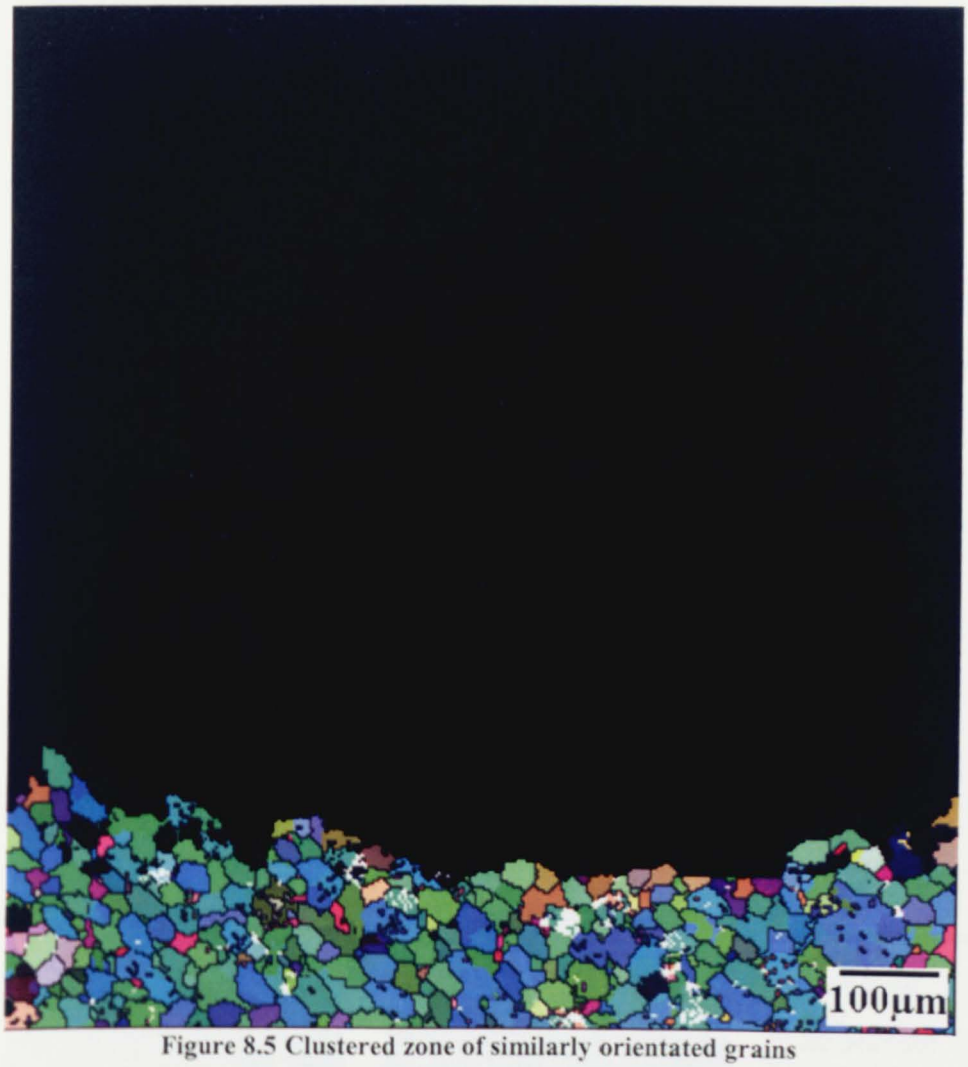

Figure 8.5 Clustered zone of similarly orientated grains

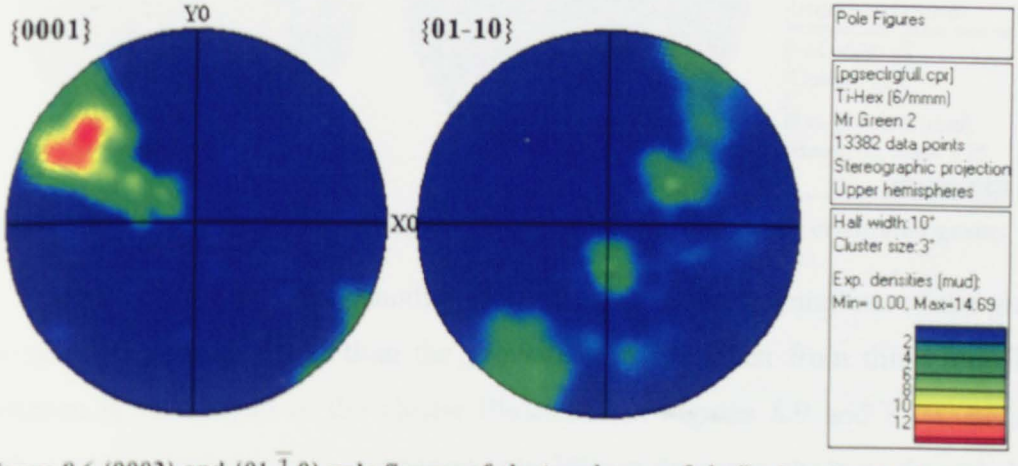

Figure 8.6 {0002} and {01 $\bar{1}$ 0} pole figures of clustered zone of similarly orientated grains

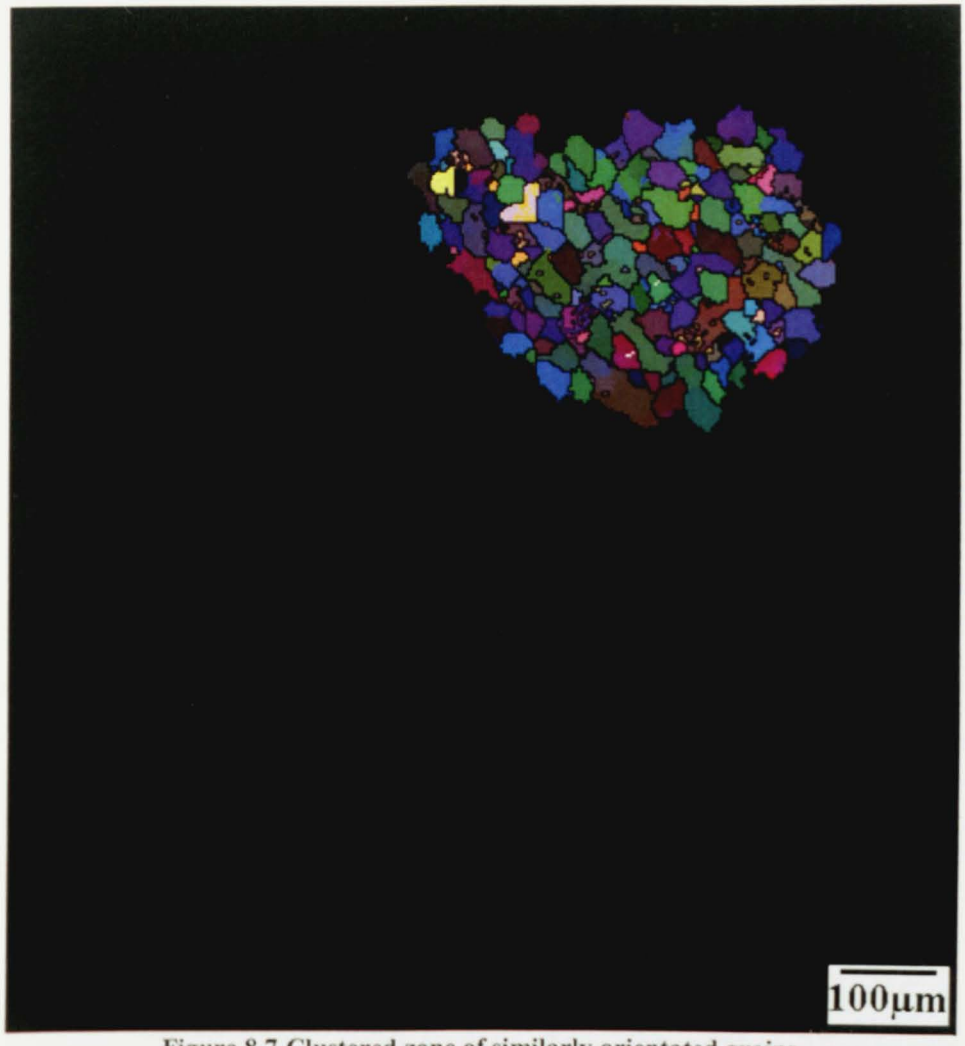

Figure 8.7 Clustered zone of similarly orientated grains

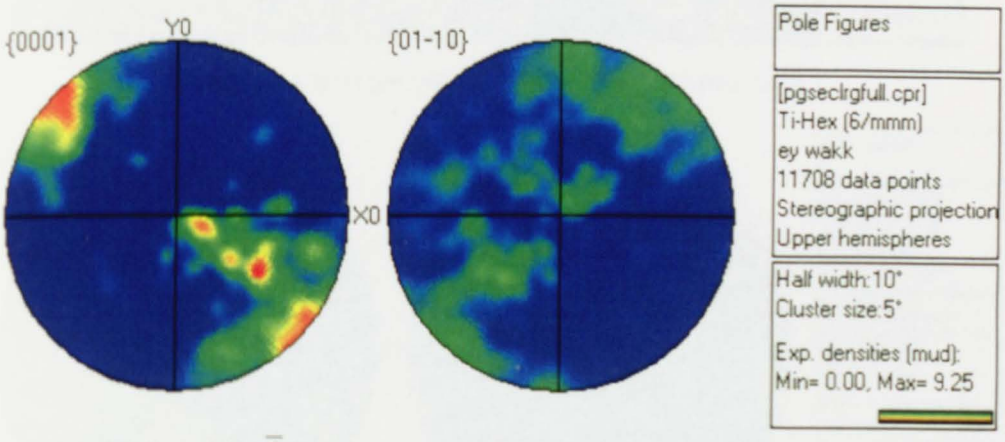

Figure 8.8 {0002} and {01 $\bar{1}$ 0} pole figures of clustered zone of similarly orientated grains

Figures 8.7 and 8.8 show another cluster however, the orientations of the grains are spread over a larger range than the previous clusters taken from this OIM. This phenomenon is seen again in the cluster illustrated in Figures 8.9 and 8.10. Both of these clusters are similar in size, approximately 350µm diameter, the pole figures show

a slight transverse basal rotating with added components of an almost parallel basal orientation.

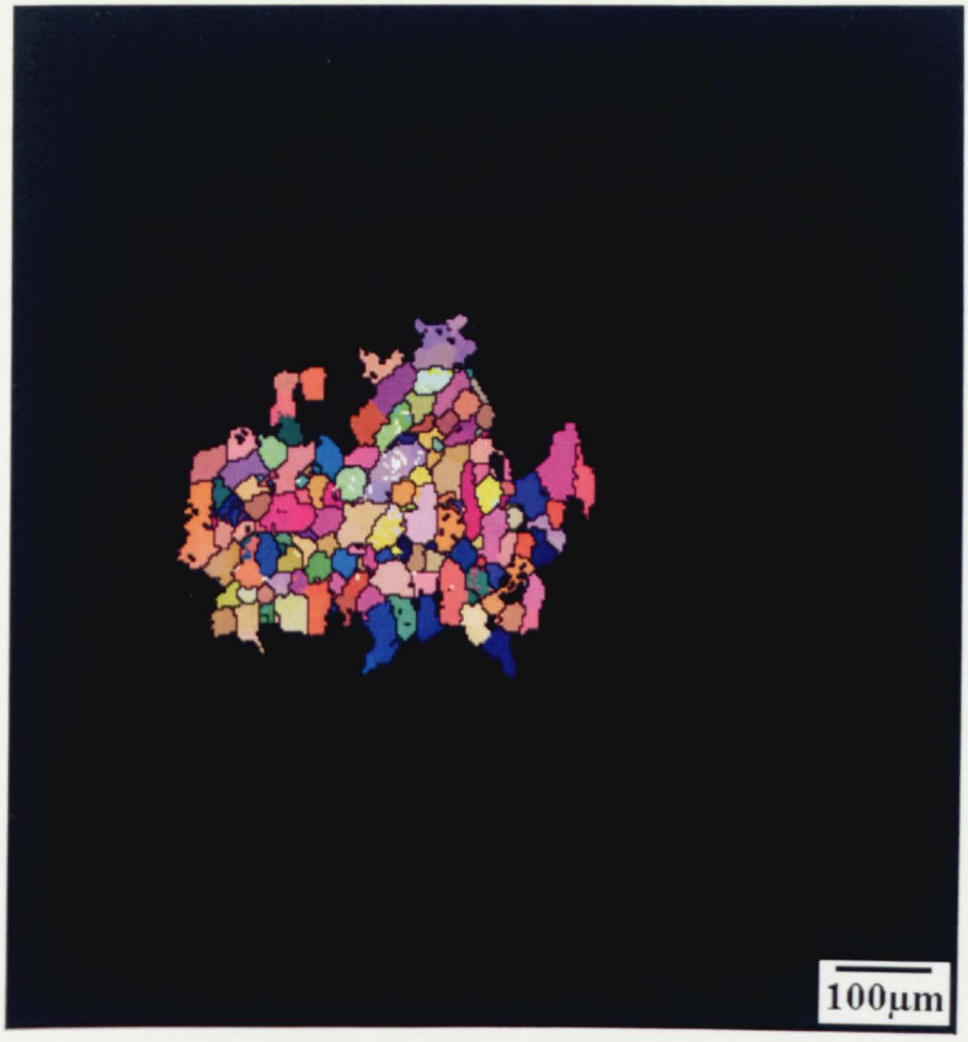

Figure 8.9 Clustered zone of similarly orientated grains

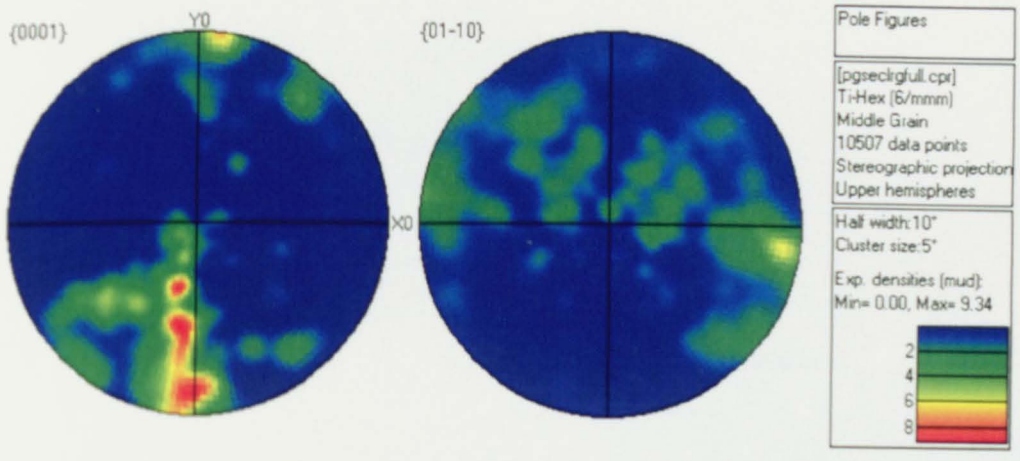

Figure 8.10 {0002} and {01 $\bar{1}$ 0} pole figures of clustered zone of similarly orientated grains

The clusters in Figures 8.1-8.10 led to further investigation of the billet material and the completion of larger OIM's in order to further examine and determine the

average size and the preferred orientations of the clusters. Two further OIM's were produced, shown in Figures 6.11 and 6.13 and again show a number clusters of similarly orientated α_p grains. Again, the pole figures show the clusters generally possess a transverse basal orientation. In total 12 clusters have been identified in Figures 8.1-8.24 and all but one show transverse basal textures with a prism plane almost parallel with the billet cross section. Figures 8.16 and 8.17 show an incomplete cluster approximately 550μm in diameter with pole figures suggesting a basal orientation. The basal plane is orientated parallel with the billet cross section and there is a distinct lack of fibre in the $\{01\bar{1}0\}$ pole figure.

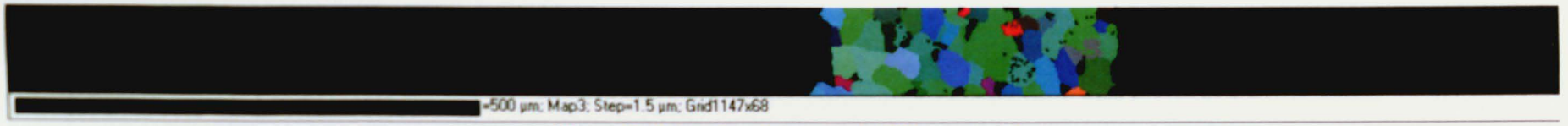

Figure 8.11 Further clustering in billet material

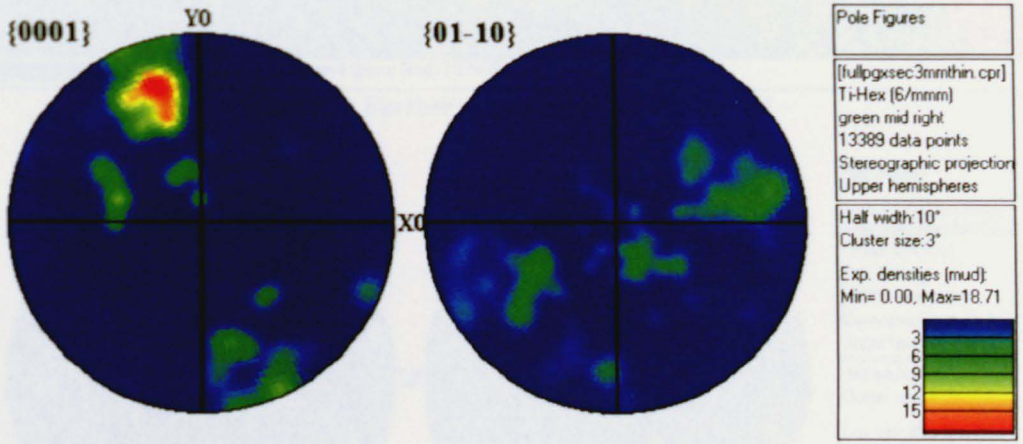

Figure 8.12 {0002} and {01 $\bar{1}$ 0} pole figures of clustered zone of similarly orientated grains

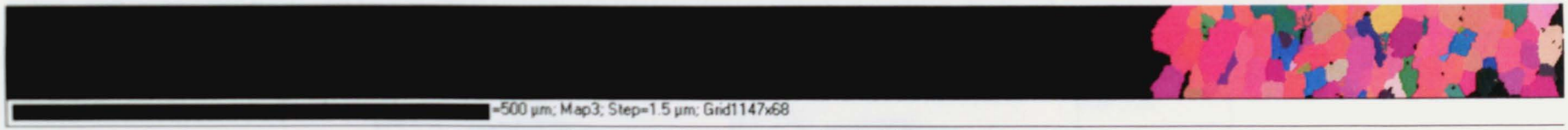

Figure 8.13 Further clustering in billet material

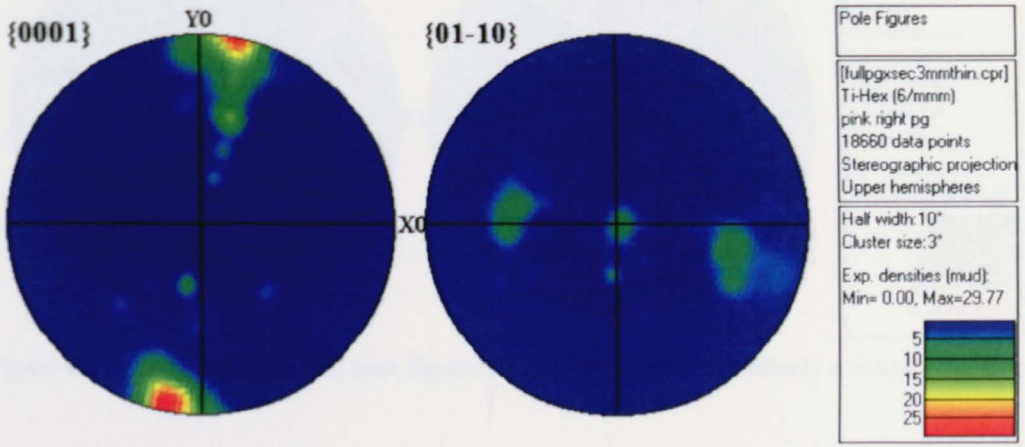

Figure 8.14 {0002} and {01 $\bar{1}$ 0} pole figures of clustered zone of similarly orientated grains

Figure 8.15 Further clustering in billet material

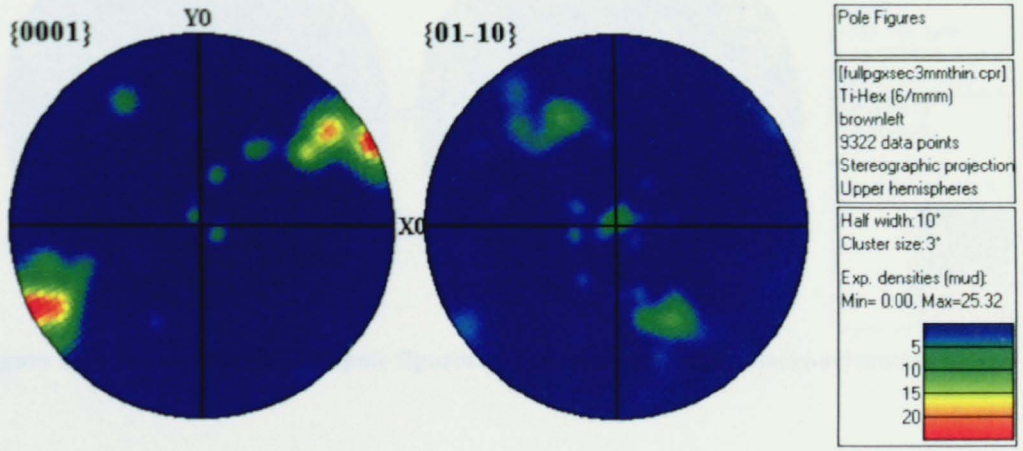

Figure 8.16 {0002} and {01 $\bar{1}$ 0} pole figures of clustered zone of similarly orientated grains

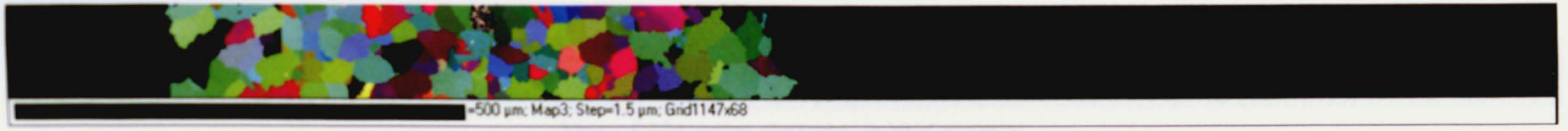

Figure 8.17 Further clustering in billet material

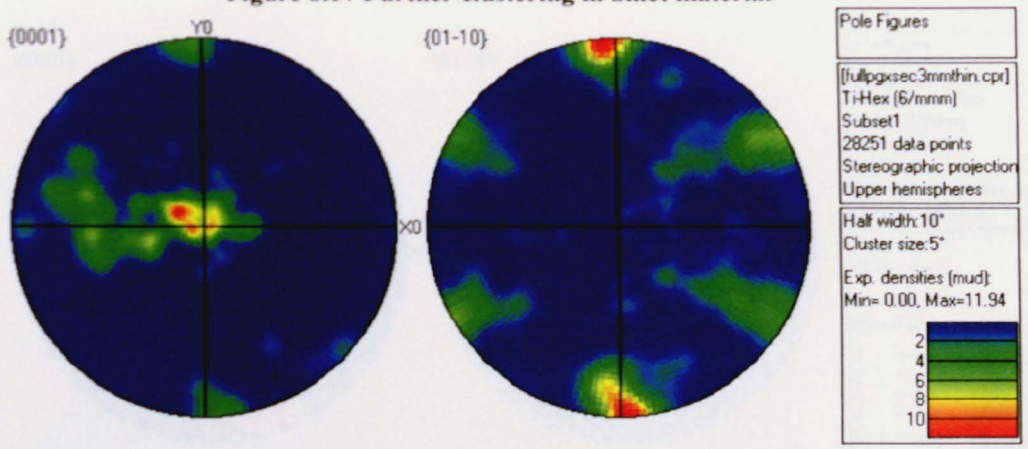

Figure 8.18 {0002} and {01 $\bar{1}$ 0} pole figures of clustered zone of similarly orientated grains

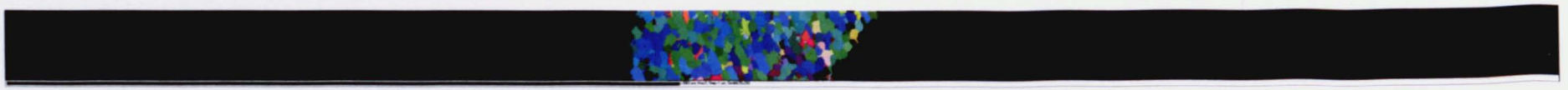

Figure 8.19 Further clustering in billet material

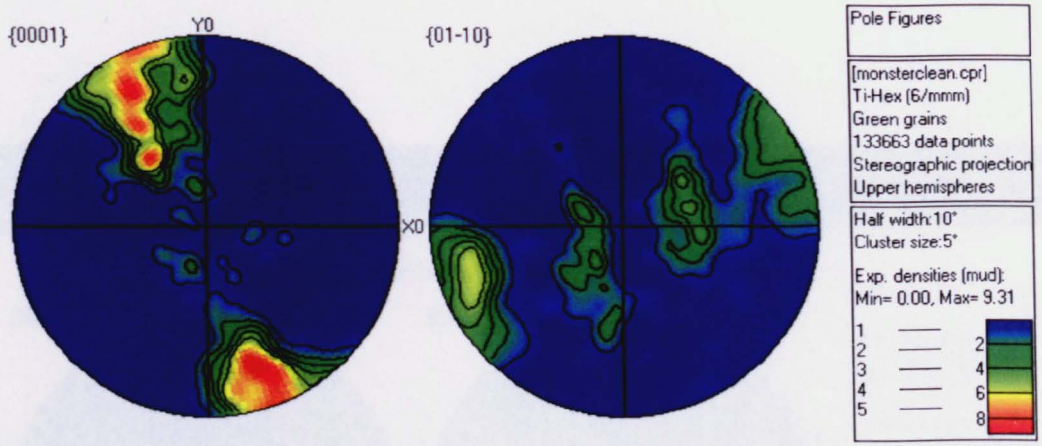

Figure 8.20 {0002} and {01 $\bar{1}$ 0} pole figures of clustered zone of similarly orientated grains

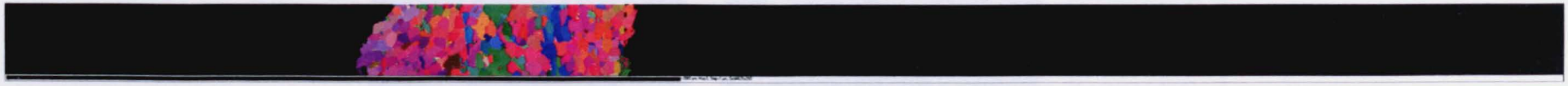

Figure 8.21 Further clustering in billet material

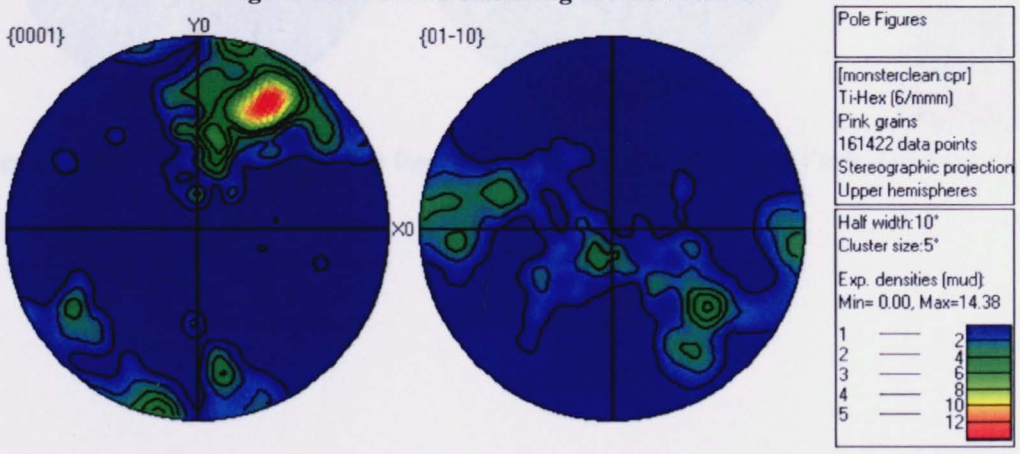

Figure 8.22 {0002} and {01 $\bar{1}$ 0} pole figures of clustered zone of similarly orientated grains

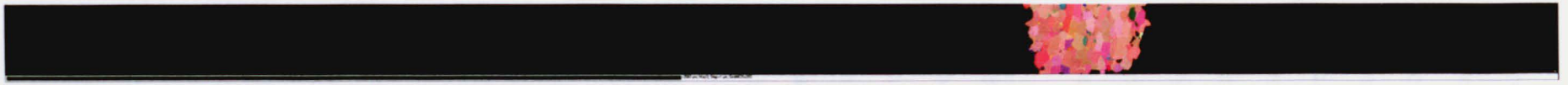

Figure 8.23 Further clustering in billet material

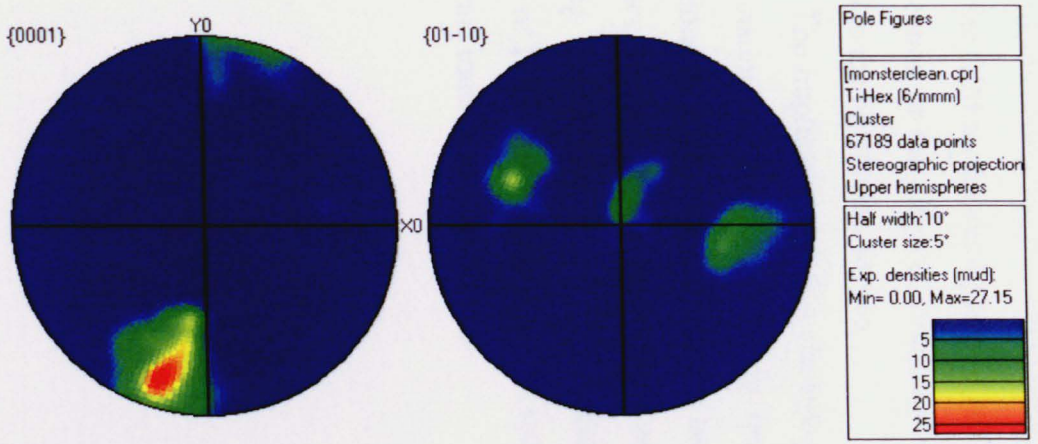

Figure 8.24 {0002} and {01 $\bar{1}$ 0} pole figures of clustered zone of similarly orientated grains

The pole figures in these results show each cluster to possess a transverse basal orientation with a varying degree of rotation around the <0002> direction, the longitudinal direction of the billet. It is interesting to see in the pole figures that in nearly all the identified clusters the $\{01\bar{1}0\}$ planes are parallel with the viewing plane, perpendicular to the forging direction. The {0002} pole figures are interesting also, Figure 8.25 shows the pole figures grouped based on the OIM they were obtained from. Of the 5 clusters identified in the first OIM, there are 2 occasions where 2 clusters share almost identical orientations. These results, therefore, imply that there is a strong texture within the OIM as the basal plane in each cluster always lies perpendicular to the billet cross section or the plane of examination as well as the prismatic plane always lying parallel to the billet cross section.

The implications of this clustering on the dataset size needed for global texture determination is that, where as in the OIM shown in Figure 6.9 in Chapter 6 approximately 1100 separate α_p grains are being analysed, the effect of these clusters is to reduce this to ~10 similarly orientated regions. Therefore, the pole figures are only showing the orientations of ~10 clustered groups and not the orientation of global dataset of 1100 separate grains and as such, we are only seeing the basal orientation and 3 separate transverse orientations.

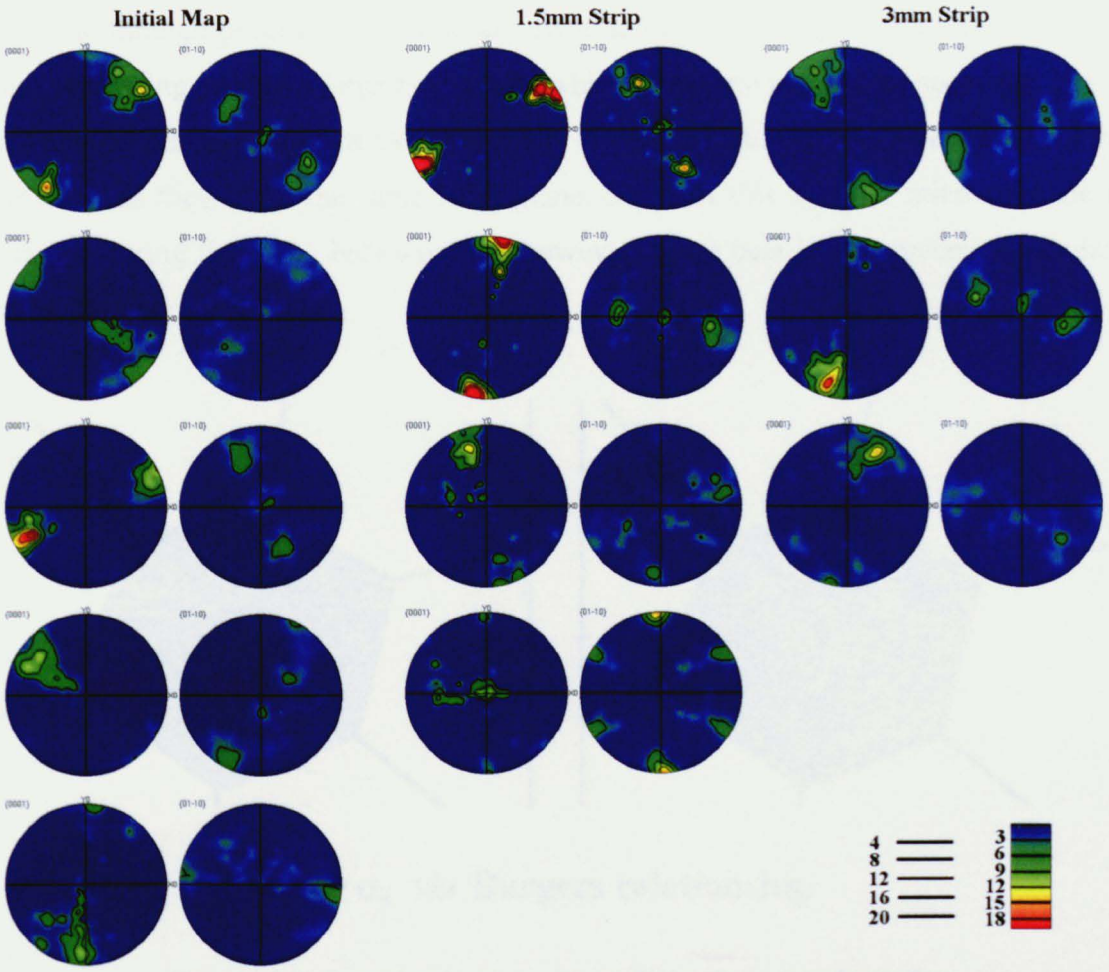

Figure 8.25 Complete clustering behaviour in billet OIM's

Having determined that the starting material is heavily clustered the implications on the thermo-mechanically processed specimens is that the assessment of the evolution of texture will be complicated. The results gained in this work have been restricted by time available on the microscope and the maximum area to be mapped due to the specimen holder. Further work should include a new larger specimen holder and using X-ray and neutron analysis as other methods to investigate size and distributions of these clustered areas.

8.2.2 Discussion of Clustering Behaviour.

The clustering of similarly orientated α_p grains is believed to have its origins in the billet processing and particularly in the globularisation of prior α_s laths as outlined in Bieler and Semiatin, 2002. As detailed in Chapter 3 the billet processing route involves an initial beta working followed by secondary working in the α/β field. As

such the through process microstructure evolution can be described as follows: Initial beta processing produces large beta grains which transform to lamellar secondary alpha (α_s) upon cooling as illustrated schematically in Figure 8.26, the lath orientations will be the same as they share the same habit plane. Some of this lamellar microstructure is retained during the alpha beta working; however, some beta is also present dependant on the forging temperature.

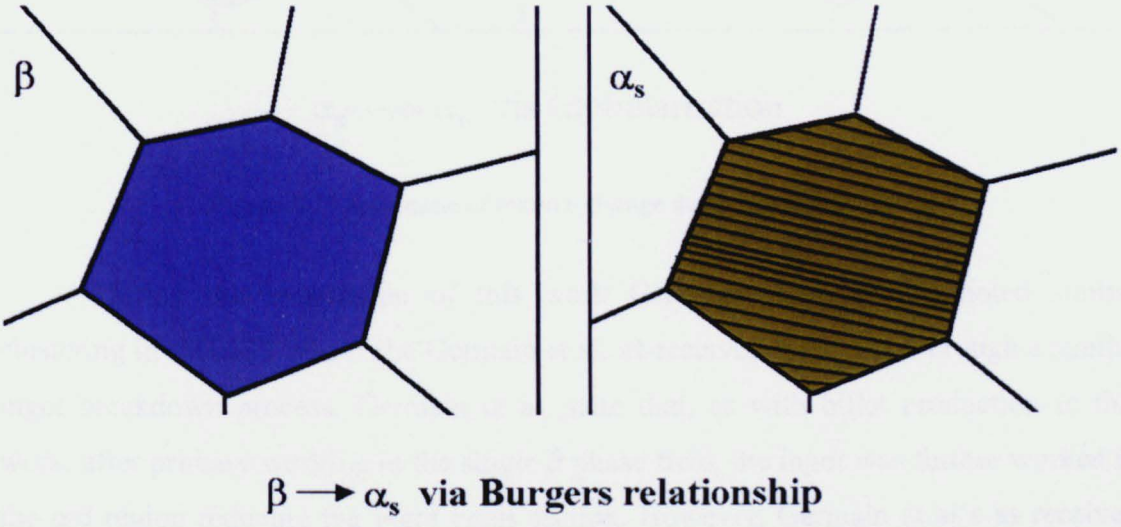

Figure 8.26 schematic of texture change during β→ α transformation

The application of strain at this point due to forging leads to the globularisation of the individual α_s lamellar, however the shared orientations of the lamellar and similar effects of the localised strain mean that the equiaxed alpha also share a very similar orientation leading to the clusters seen in Section 8.2.1.

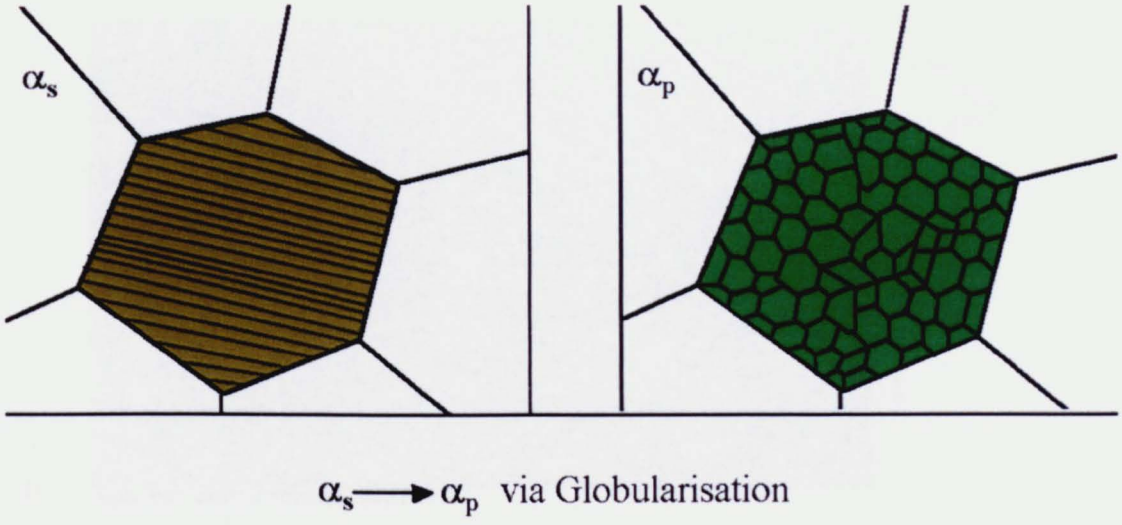

Figure 8.27 schematic of texture change during globularisation

During the completion of this work Germain et al. (2005) noted similar clustering in IMI 834 billet. The Germain et al. as-received billet went through a similar ingot breakdown process. Germain et al. state that, as with billet production in this work, after primary working in the single β phase field, the ingot was further worked in the α/β region reducing the ingot cross section. However, Germain et al's as received material was heat treated such that the starting microstructure consisted of approximately 30% α_p grains surrounded by α_s colonies. The α_p grain size was reported as approximately 25μm and the prior β grain size was calculated as 60μm.

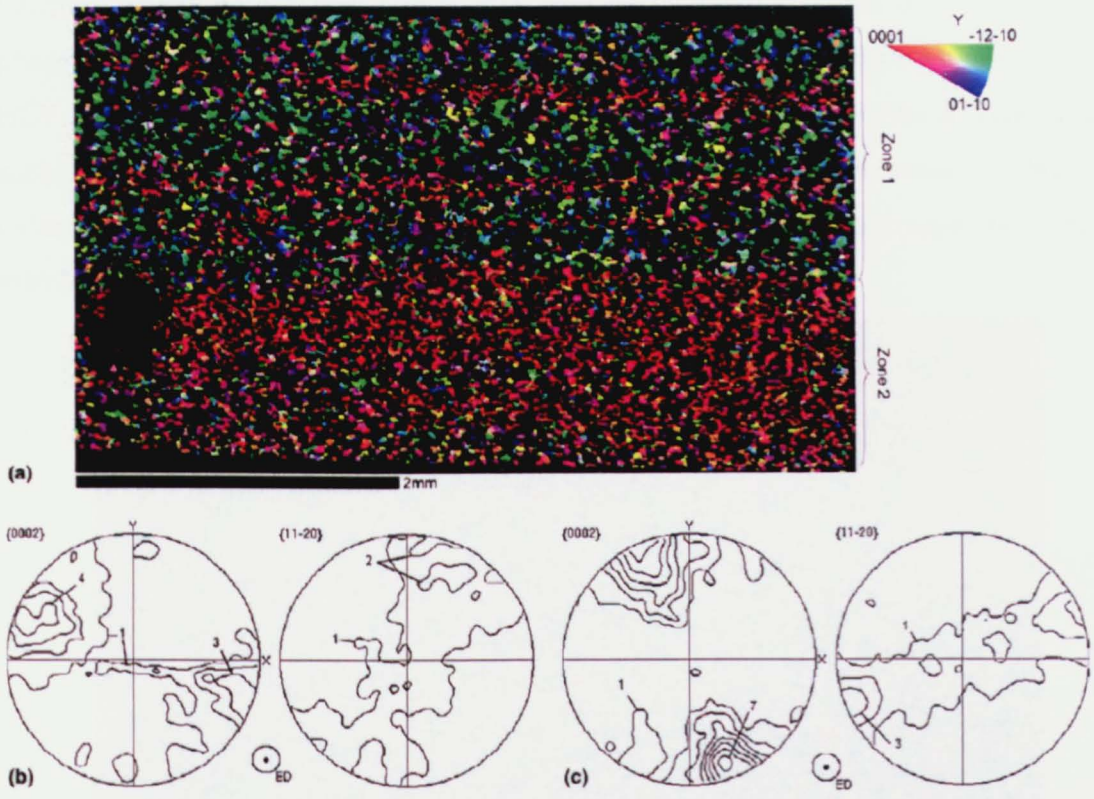

Figure 8.28 From Germain et al. α_p microtexture obtained from the local EBSD scan: (a) IPF map; (b) local α_p texture of zone 1; (c) local α_p texture of zone 2

The explanation of the α_p microtexture seen in the as-received material in Germain et al. includes the use of the term 'macrozone', defined as a group of α_p grains orientated around a single texture component with about 20° spread, and agrees with the findings of this work. Germain et al. go on to express that the α_p grains significantly contribute to the sharp texture of a macrozone, even if they represent only 30% of the volume.

8.2.3 Phase Identification.

The OIM in Figure 6.8 shows the distribution of α and β phases within the mapped area, it was hoped that the orientation of the metastable β phase would give an indication of the parent textures related to the clusters. However, it can be seen that the distribution of β in the OIM does not relate to the previous micrographs of billet material seen in Figures 6.10 (a) and (b). It is probable that this is due to the problem of there being only a very small chance of indexing the stable β phase consistently as it exists in the microstructure as very thin <1μm laths. As such anytime the electron

beams interacts with a beta lath it may also be interacting within the surrounding α phase which will distort the Kikuchi pattern. There is also a possibility that the certain HCP α orientations will produce a very similar Kikuchi pattern as the β phase and as such, some phase mis-indexing has occurred. Due to the occurrence of this mis-indexing and the worry that it would affect the success of subsequent maps, the β crystal match units were removed form the mapping parameters.

Figure 8.29 Phase Identification OIM of billet material

Figure 8.30 Phase Identification OIM of billet material

Figure 8.31 Phase Identification OIM of billet material

8.2.4 Summary of Billet Condition

The billet received from Firth Rixson PLC, produced by Timet UK consists of a microstructure of 70% equiaxed α_p surrounded by coarse α_s laths. The 2% metastable β present within the material is seen to reside at grain boundaries in the form of sub-micron laths, visible through SEM and BSE analysis. EBSD of the β phase as it exists in this microstructure proved difficult and the minimal results gained were disregarded.

The texture of the billet material was determined by EBSD analysis, showing heavily textured localised clusters. Although some clusters were seen to possess a near basal texture, the majority possessed a transverse basal texture with the basal and prism planes showing little rotation and a lack of a texture fibre. Clusters ranged in size from approximately 200μm to 800μm, with an average diameter of 380μm.

8.3 Thermomechanically Processed Samples

8.3.1 Introduction

Having assessed the billet condition and determined the textures present, the next step in the investigation of the microstructural evolution of this alloy was to analyse the datasets obtained from the thermomechanically tested specimens. This analysis has been completed in two ways, both of which will be detailed in the following sections. Firstly, on a crystallographic texture level as detailed in Section 8.3.2, the specimens have been assessed in terms of the global texture of the full dataset and of each morphology separately. Secondly, high resolution OIM's have been obtained from central areas of the larger OIM's in order to investigate micro-textures and sub-grain mis-orientations and can be seen in Section 8.3.3

8.3.2 Separate morphology orientation analysis

As discussed previously in Chapter 7, any textural analysis of thermomechanically processed Timetal 834 samples is confused by the presence of both the deformed α product (α_p) and the deformed and transformed α product (α_s). As such, by analysing each data set separately a clearer picture of the texture evolution can be developed. Using the morphology separation technique described in Chapter 7, as well as a size distribution technique which assumes the α_p grain to be largest, these two products were separated and the resulting OIM's and pole figures can be seen in the next section. The textural evolution of each α morphology after deformation can then be assessed.

8.3.2.1 Primary alpha analysis

Initially the α_p component of heat treated sample was separated from the full data set and is shown in Figure 8.32 in Euler and IPF colouring. The corresponding {0002} and $\{01\bar{1}0\}$ pole figures are included in Figure 8.33. The α_p texture illustrated by the pole figures is similar to that of the billet material shown in the previous section.

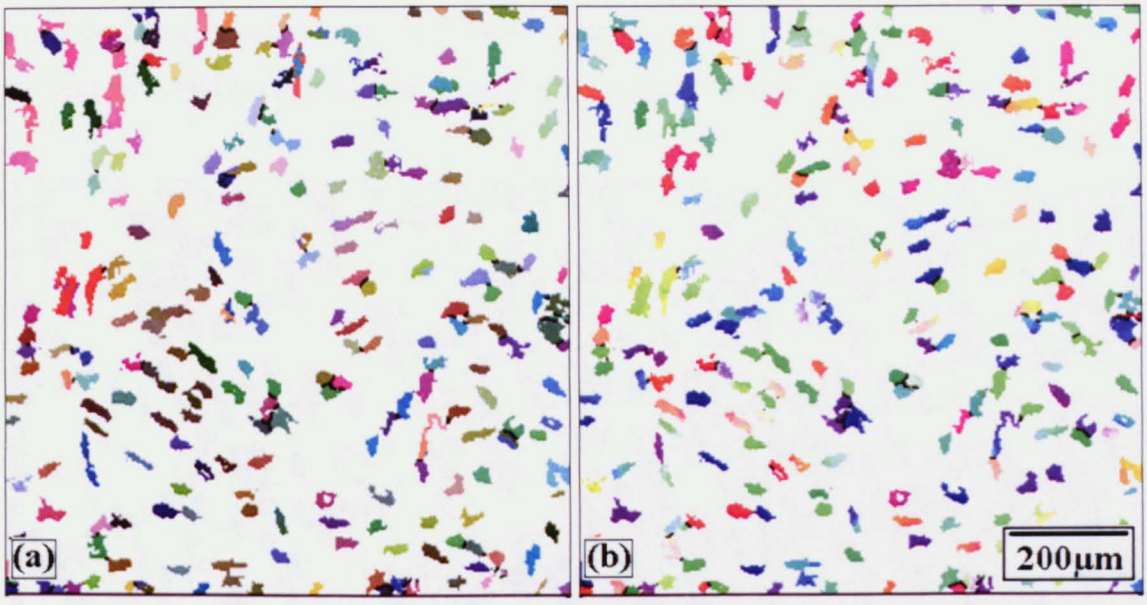

Figure 8.32 Separated α_p OIM's of the heat treated sample in (a) Euler and (b) IPF colouring.

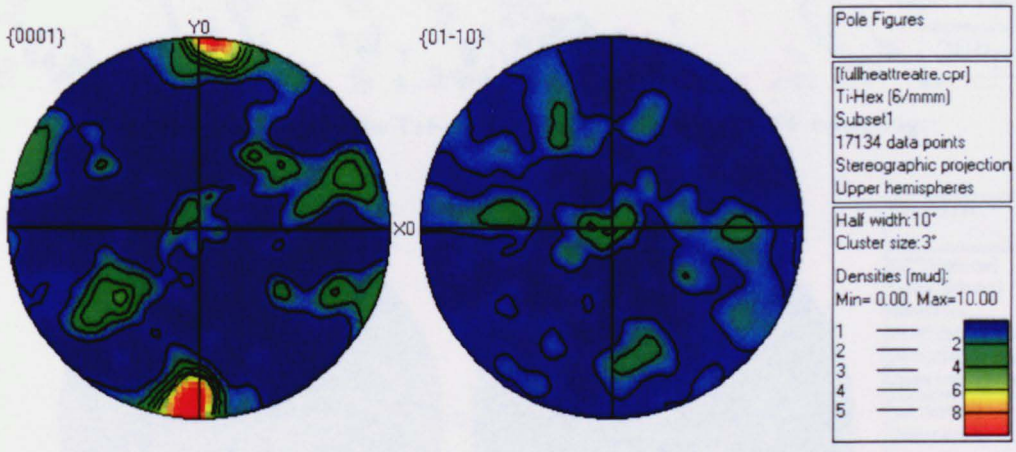

Figure 8.33 {0002} and {01 $\bar{1}$ 0} pole figures of clustered zone of similarly orientated grains

The preferred orientation of the basal plane in the heat-treated sample remains transverse, as would be expected as there has been no deformation. As the volume fraction of the α_p is only 22%, there are less data points for the EBSD dataset when compared with the billet data set so the appearance of the pole figure is more fragmented, when compared with the billet texture seen earlier in Figure 6.13.

The OIM's of the α_p component separated from the dataset of T16, having received a strain of 0.175, are shown in Euler and IPF colouring in Figure 8.34, again the corresponding pole figures are shown in Figure 8.35. This dataset was produced using the method described in Chapter 7, therefore, the associated analysed micrograph can be seen in Figure 8.36. The pole figures illustrate that the basal orientations present are again very similar to that seen in the billet and the heat treated specimen, previously

described as a transverse texture. There is a single preferred transverse basal orientation present with two smaller components at other rotations about the Z-axis.

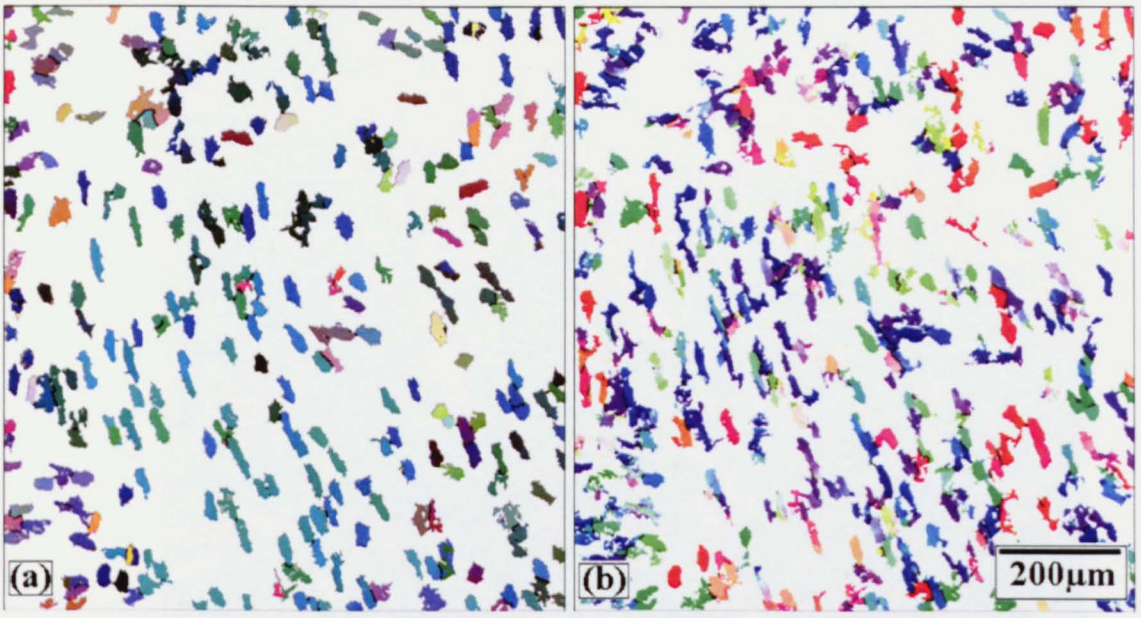

Figure 8.34 α_p OIM's of the T16 sample in (a) Euler and (b) IPF colouring.

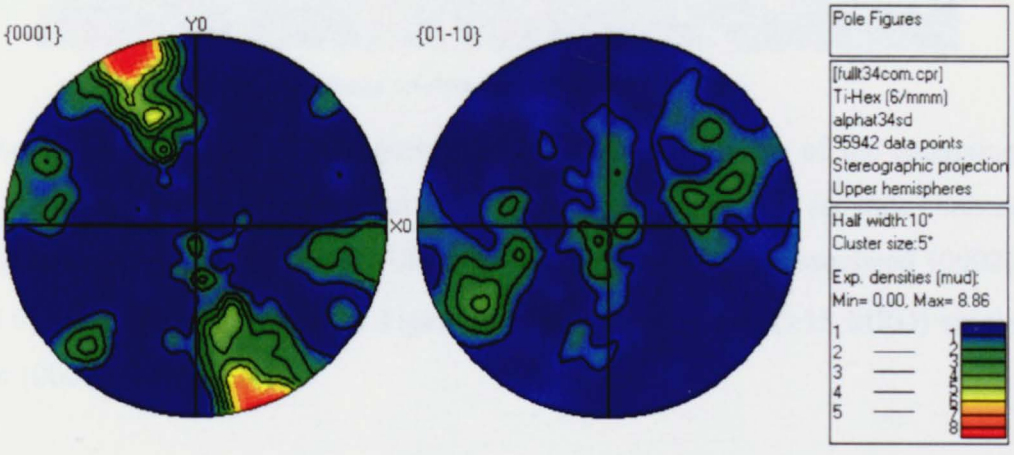

Figure 8.35 {0002} and {01 $\bar{1}$ 0} pole figures of clustered zone of similarly orientated grains

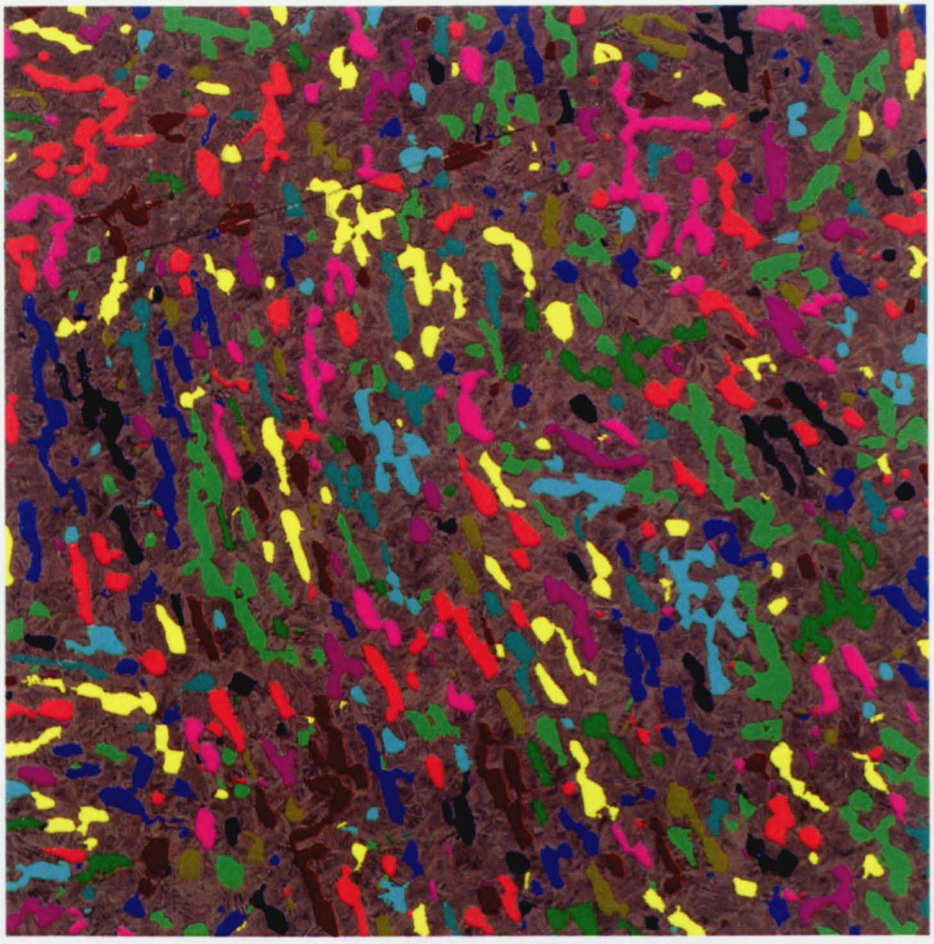

Figure 8.36 Image analysed optical micrograph

The Euler colouring OIM suggests that there are still aspects of the clustering observed previously in the billet material. In the 22% α_p remaining two separate clusters of the α_p grains were separated and are illustrated in Figure 8.37. The associated {0002} and $\{01\bar{1}0\}$ pole figures are seen in Figure 8.36 and show strong (>15 MRD) single transverse {0002} orientations.

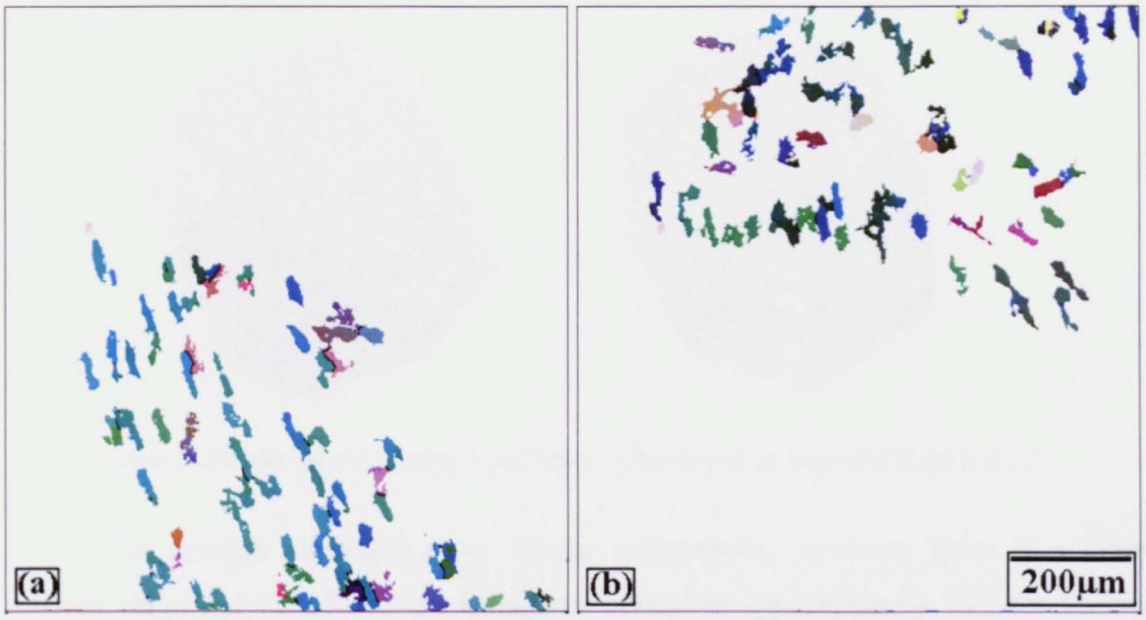

Figure 8.37 Clustering displayed in α_p OIM's of the T16.

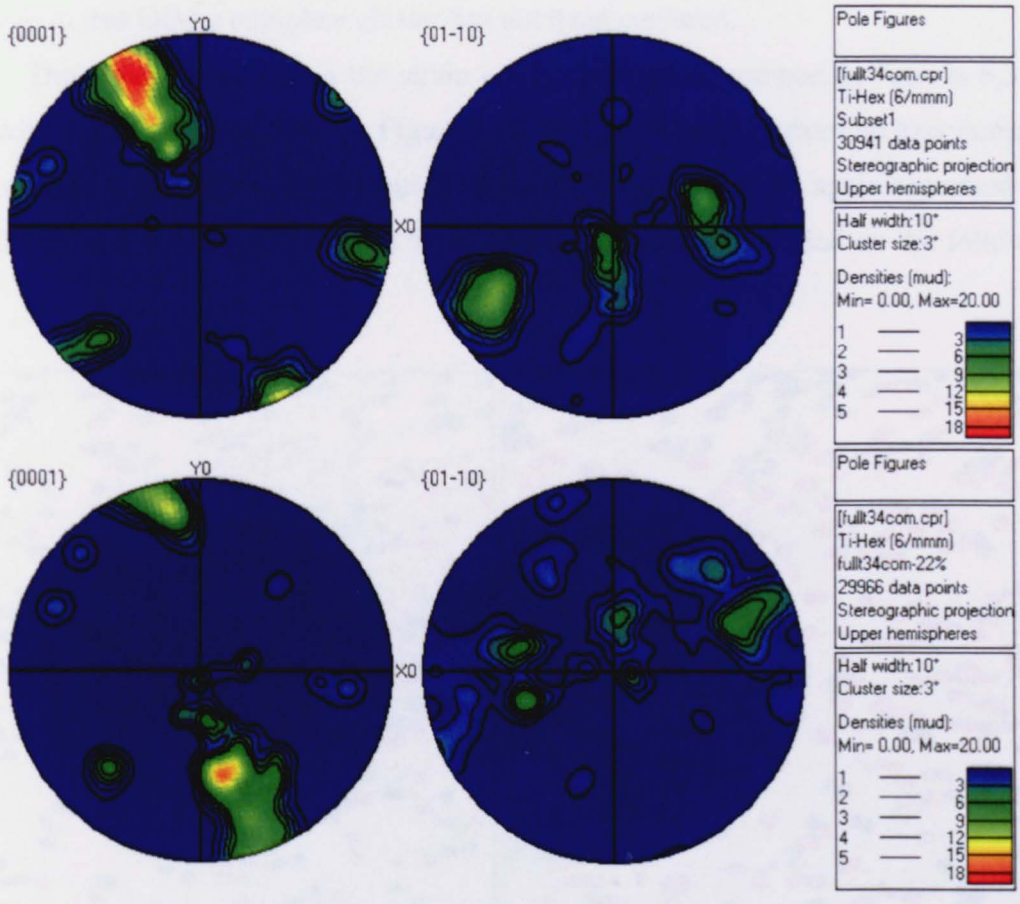

Figure 8.38 {0002} and {01 $\bar{1}$ 0} pole figures of clustered zone of similarly orientated grains

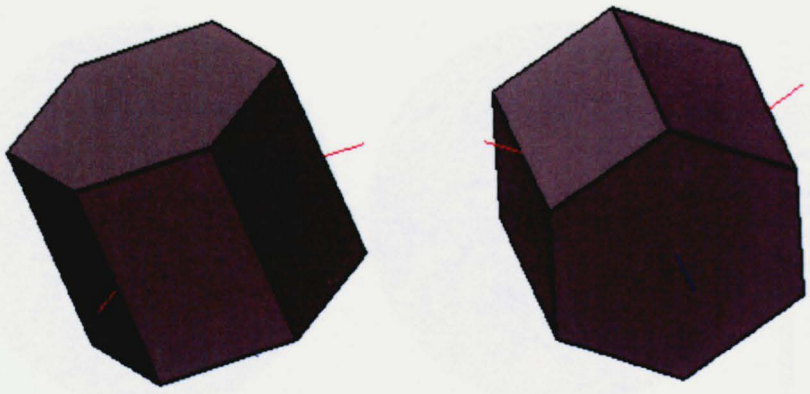

Figure 8.39 3-D crystal orientation of clusters illustrated in Figure 8.37 (a) and (b)

The clusters separated show similar orientations, however, there is a clear rotation about the **<1210>** of the hexagonal crystal of approximately 10°, see Figure 8.39. The two clusters separated here are approximately 400-500μm in diameter, although in this OIM a complete cluster has not been captured.

The effect of increasing the strain can be seen when comparing Figures 8.35 to 8.39 with Figures 8.40 to 8.44. In Figure 8.40 the OIM shown is from an axisymmetric specimen, T14, having received a strain of 0.375, the α_p grains are again separated and the {0002} and {0110} pole figures have been produced and included on the following page.

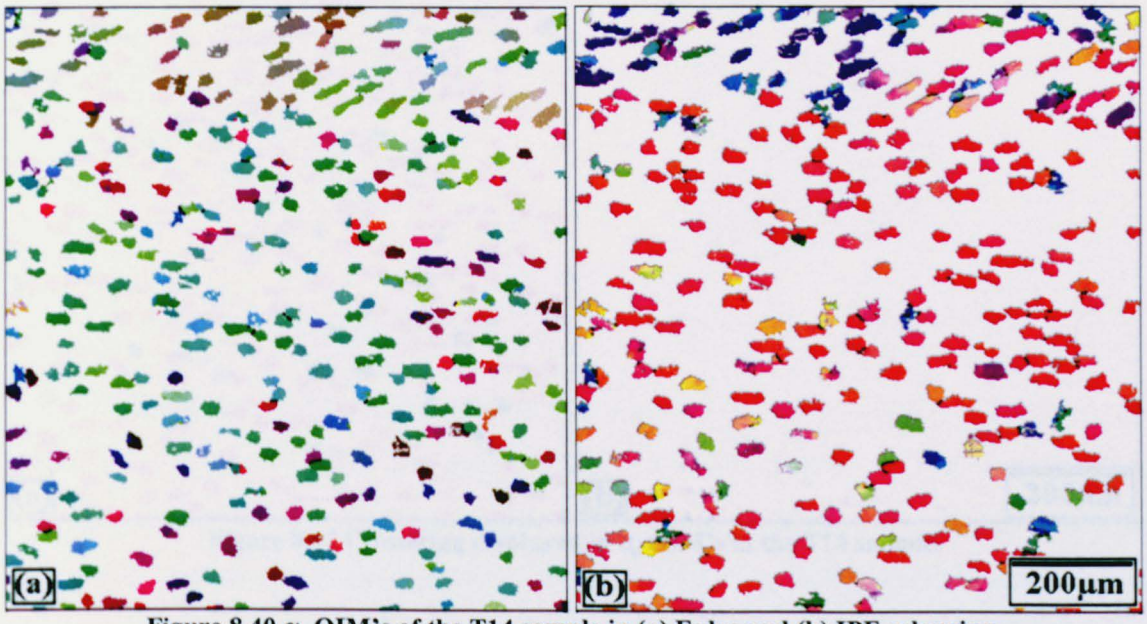

Figure 8.40 α_p OIM's of the T14 sample in (a) Euler and (b) IPF colouring.

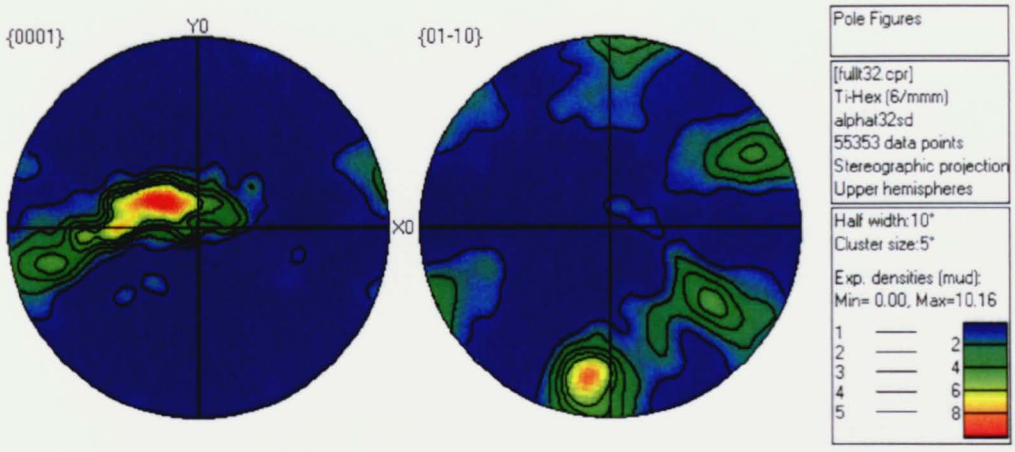

Figure 8.41 {0002} and {01 $\bar{1}$ 0} pole figures of clustered zone of similarly orientated grains

In this case, the {0002} pole figure suggests that the basal plane sits almost parallel with the viewing plane, this is a 90° rotation from the billet orientation and the orientations observed in T17. The {01 $\bar{1}$ 0} pole figure would, again, suggest that there is no rotation about the c-axis. Closer inspection of the α_p IPF colouring OIM for this specimen again shows clustering in the α_p, as illustrated in Figure 8.42 where the clusters have been separated, a transition from one cluster to another is clearly visible in the IPF OIM.

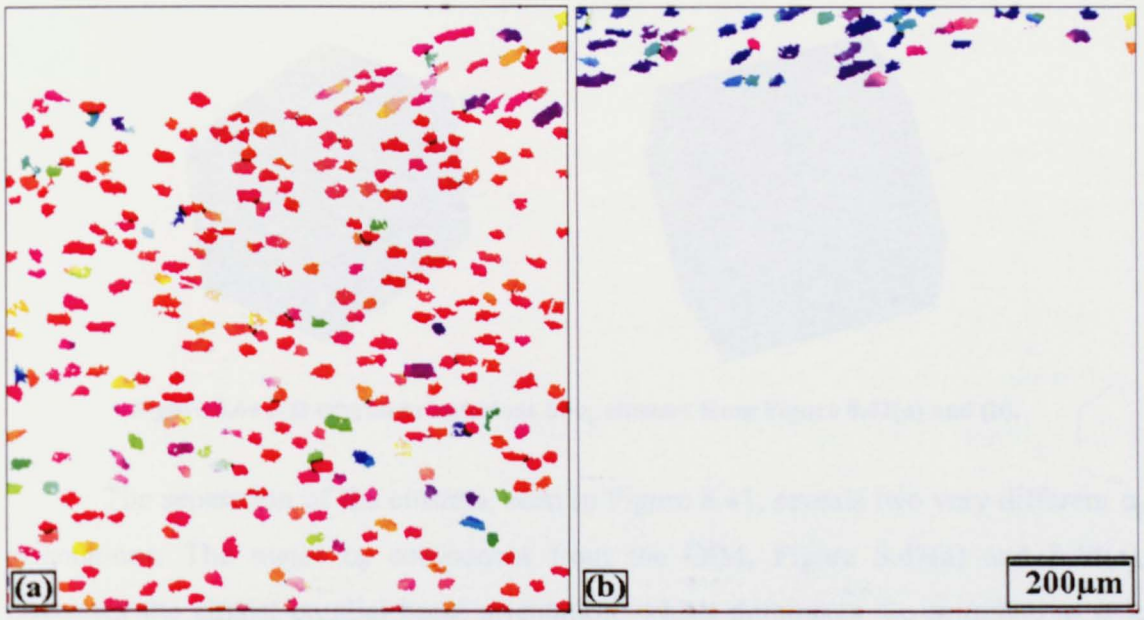

Figure 8.42 Clustering displayed in α_p OIM's of the T14 sample.

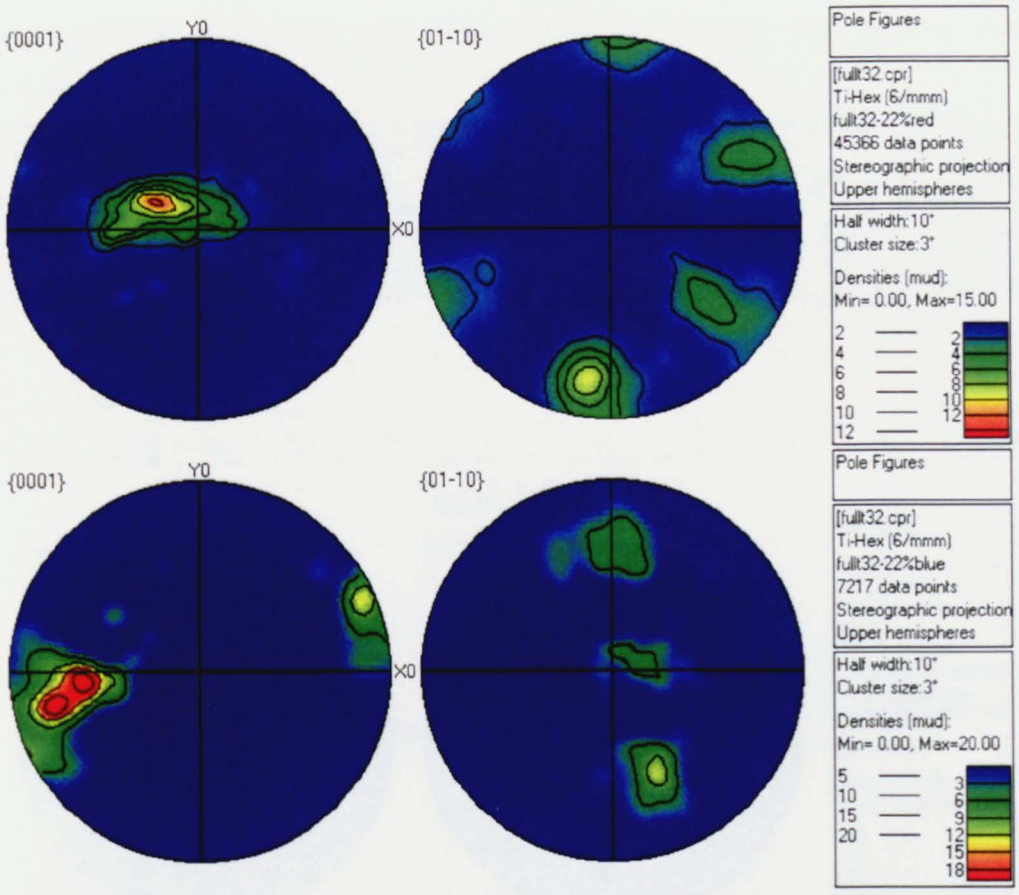

Figure 8.43 {0002} and {01 $\bar{1}$ 0} pole figures of clustered zone of similarly orientated grains

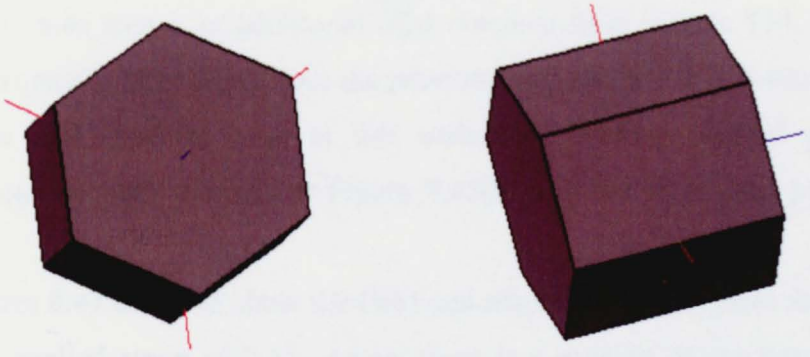

Figure 8.44 3-D crystal orientations of α_p clusters from Figure 8.42(a) and (b).

The separation of the clusters, seen in Figure 8.41, reveals two very different α_p orientations. The major α_p component from the OIM, Figure 8.43(a) and 8.44(a), possesses the almost parallel basal orientation, which dominates the complete α_p pole figure. The second component, Figure 8.43(b) and 8.44(b), possesses a transverse basal texture similar to those seen in the billet and heat treated samples. In this case, the cluster sizes are much larger than seen previously, measuring over 1mm in diameter, spanning the width of the OIM. A larger OIM of this sample was obtained and can be

seen in Figure 8.45 along with associated {0002} and $\{01\bar{1}0\}$ pole figures, seen in Figure 8.46.

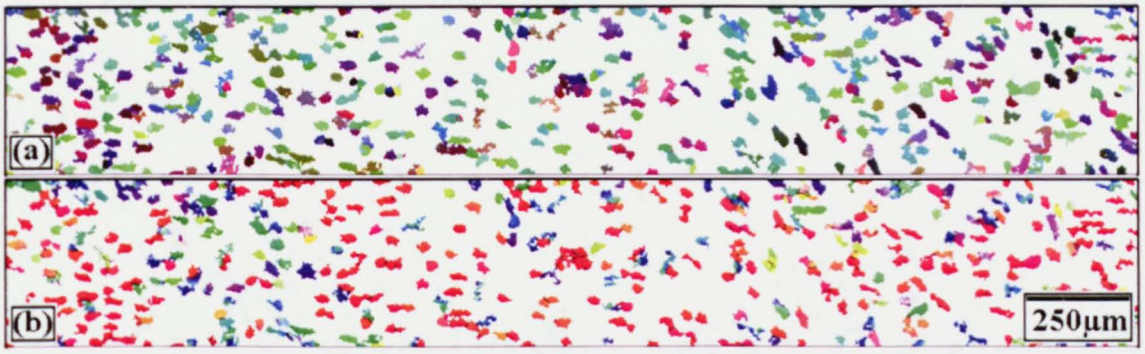

Figure 8.45

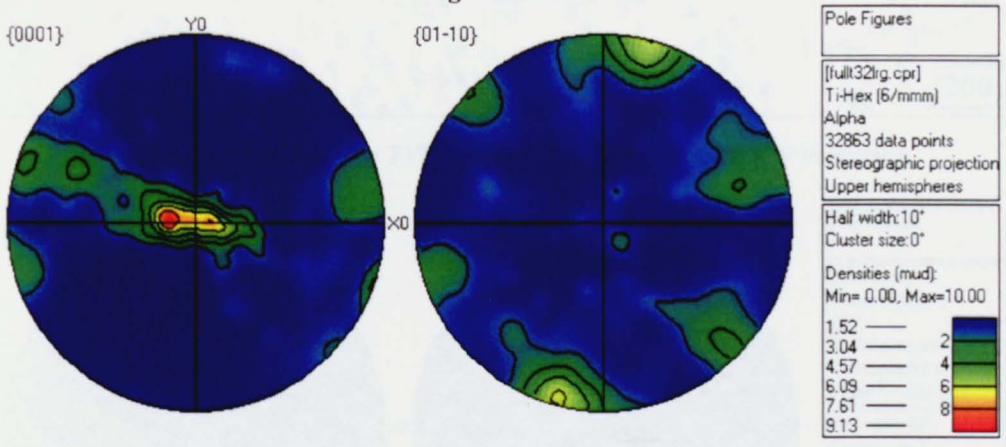

Figure 8.46

Figure 8.46 shows an additional OIM obtained from sample T14, this map was taken approximately 1mm away from the previous map and is 2.8 X 0.4mm in size. The clustering is still apparent even at this scale the dominant almost parallel basal orientation can be seen throughout Figure 8.45(b) and the associated pole figures in Figure 8.46.

Figures 8.47 and 8.48 show the OIM and associated pole figures for T17, having received an applied strain of 0.55. Again, there is a rotation of the basal plane away from the orientations seen in the billet (Figure 6.13) and the heat treated sample (Figure 8.33) towards an almost parallel basal orientation.

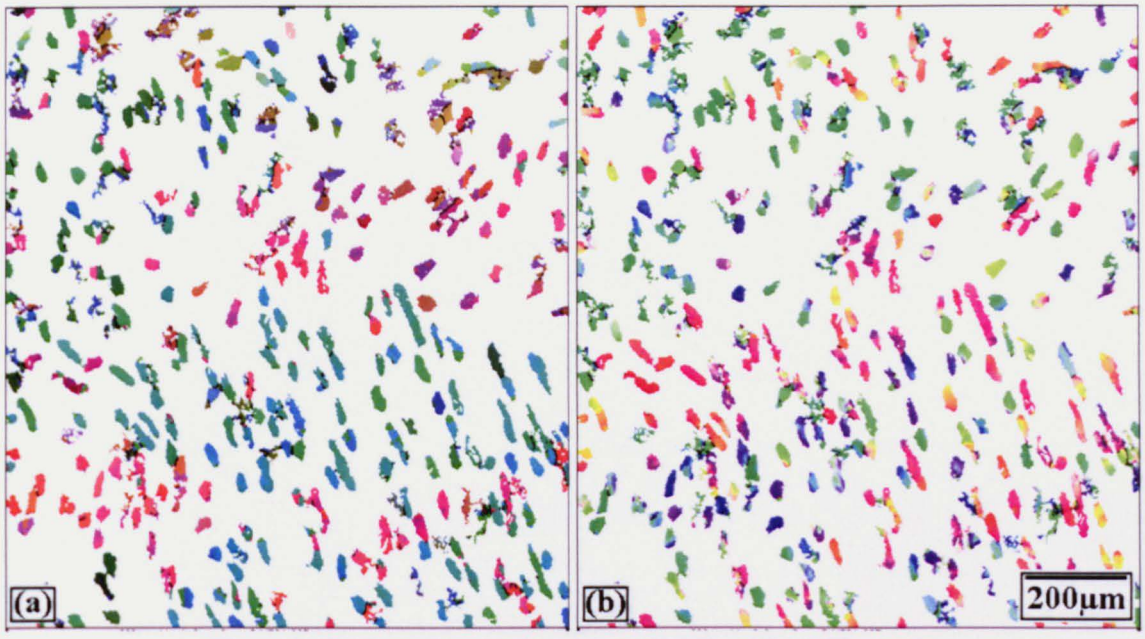

Figure 8.47 α_p OIM's of the T17 sample in (a) Euler and (b) IPF colouring.

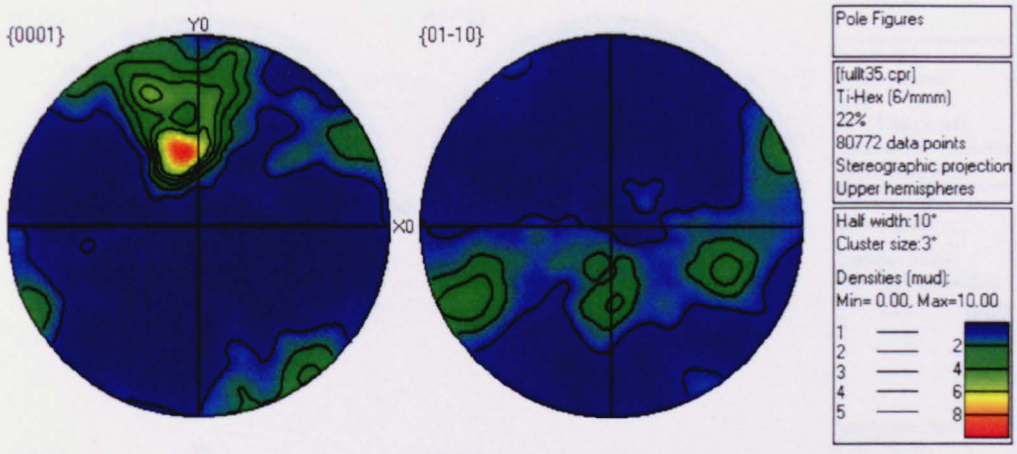

Figure 8.48 {0002} and {01 $\bar{1}$ 0} pole figures of clustered zone of similarly orientated grains

Furthermore, in this sample clustering is again seen, although it is not as clear to visualise as in Figure 8.42. Figure 8.49 illustrates the similarly orientated α_p grains in the T17 OIM and although certainly clustered the grain shape isn't as equiaxed as previously seen in this work.

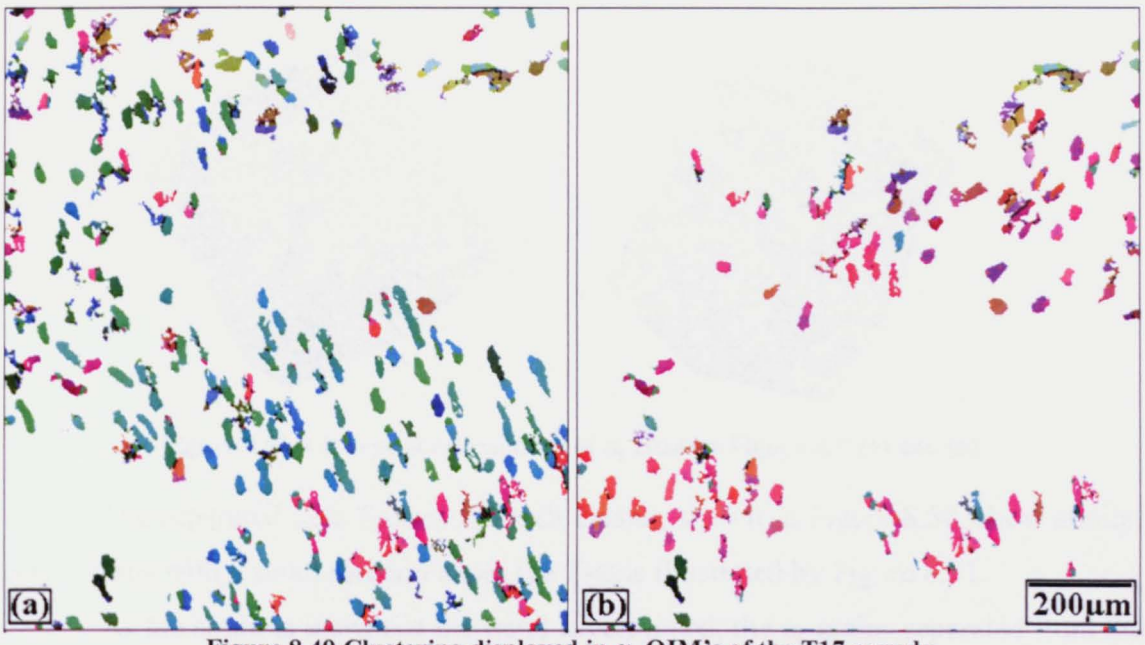

Figure 8.49 Clustering displayed in α_p OIM's of the T17 sample.

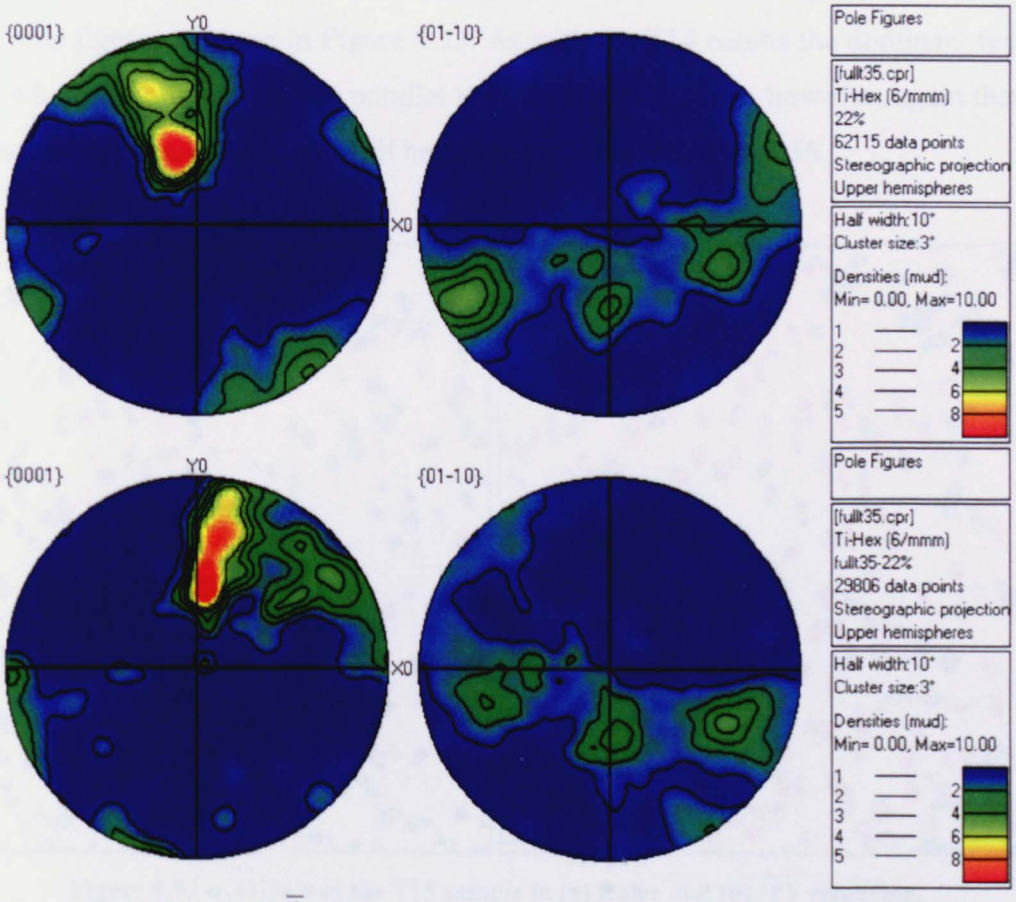

Figure 8.50 {0002} and {01 $\bar{1}$ 0} pole figures of clustered zone of similarly orientated grains

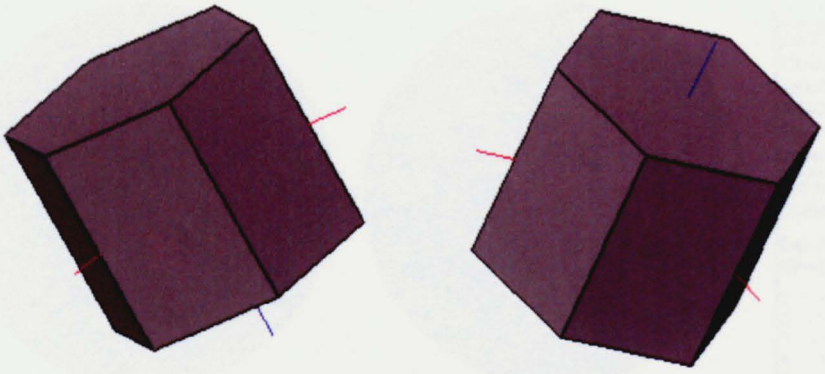

Figure 8.51 3-D crystal orientations of α_p clusters Figure 8.47(a) and (b).

The separated pole figures for each cluster, shown in Figure 8.50, show similar orientations with a small rotation about the Z-axis illustrated by Figure 8.51.

As the strain is increased the trend is continued, the α_p grains separated from the test sample T15, having received a strain of 0.75 can be seen in Figure 8.52 and again the α_p pole figures are seen in Figure 8.53. As with the T14 results the dominant texture is one where the basal plane lies parallel with the viewing plane, however, again there is evidence of the clustering effect still being present, Figures 8.54-8.56.

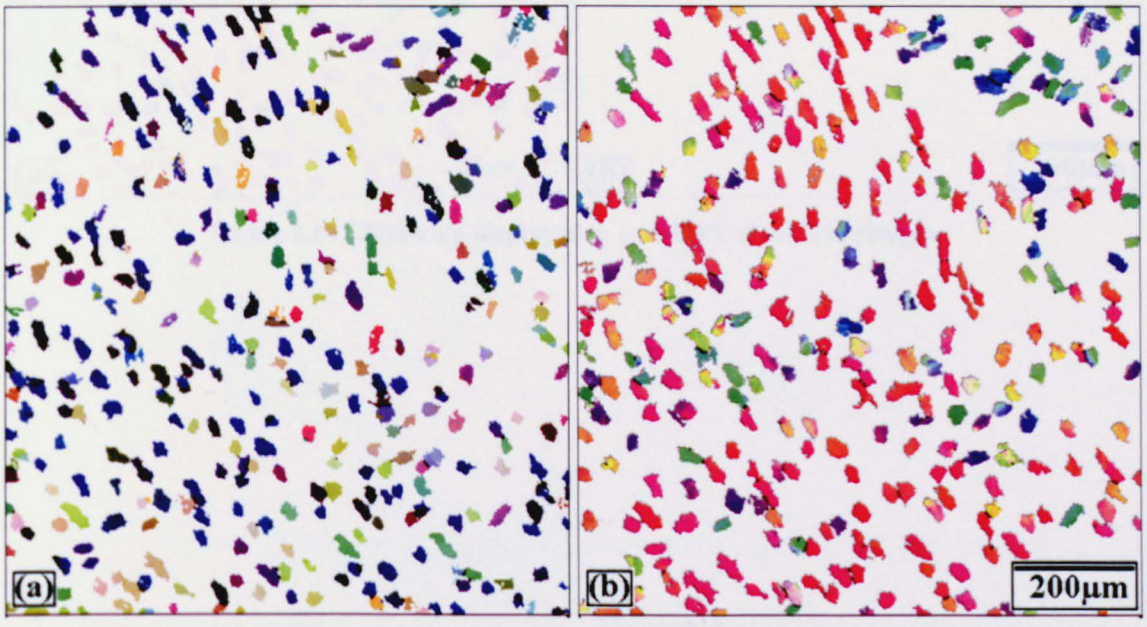

Figure 8.52 α_p OIM's of the T15 sample in (a) Euler and (b) IPF colouring.

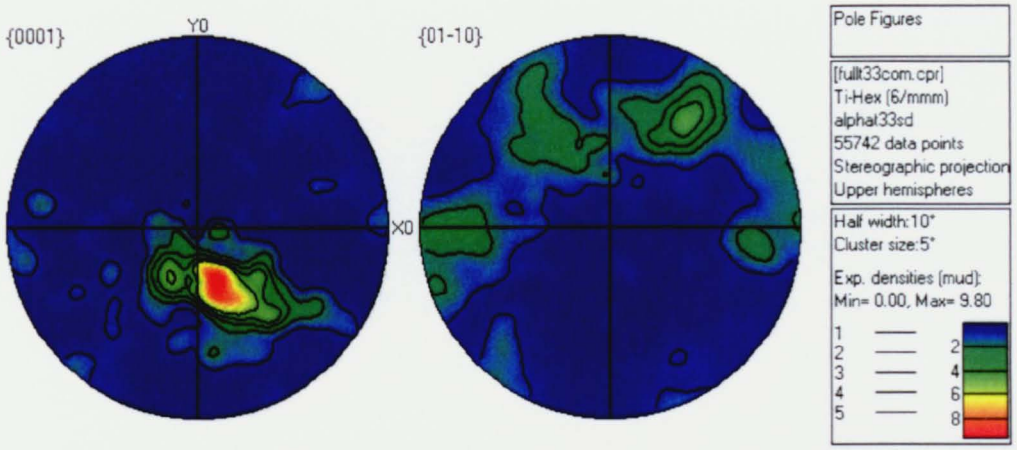

Figure 8.53 {0002} and {01 $\bar{1}$ 0} pole figures of clustered zone of similarly orientated grains

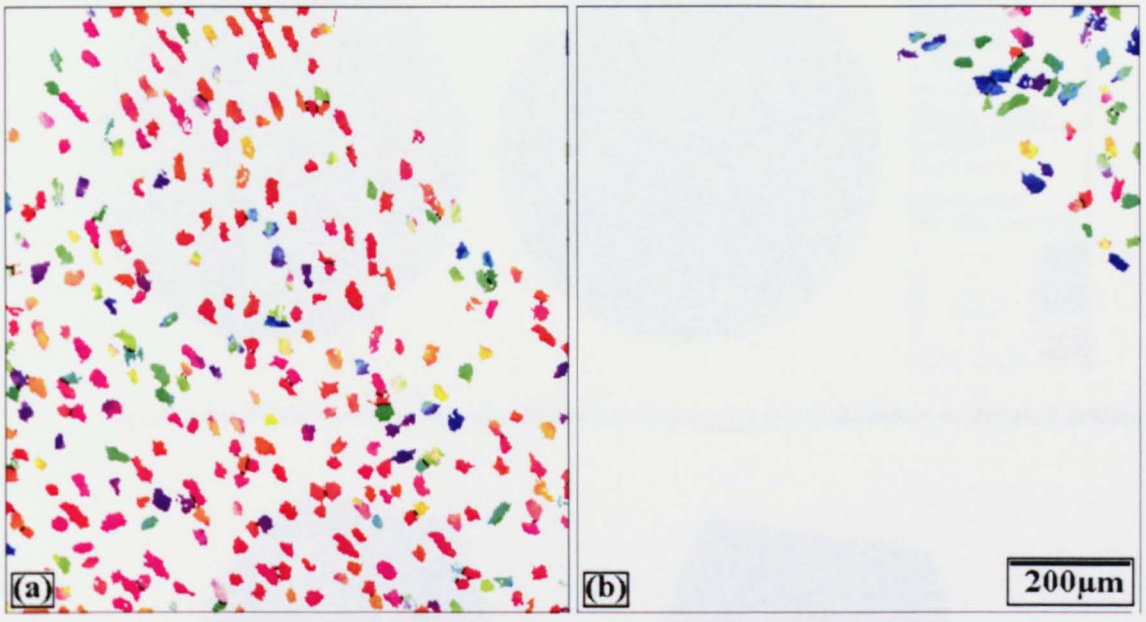

Figure 8.54 Clustering displayed in α_p OIM's of the T15 sample.

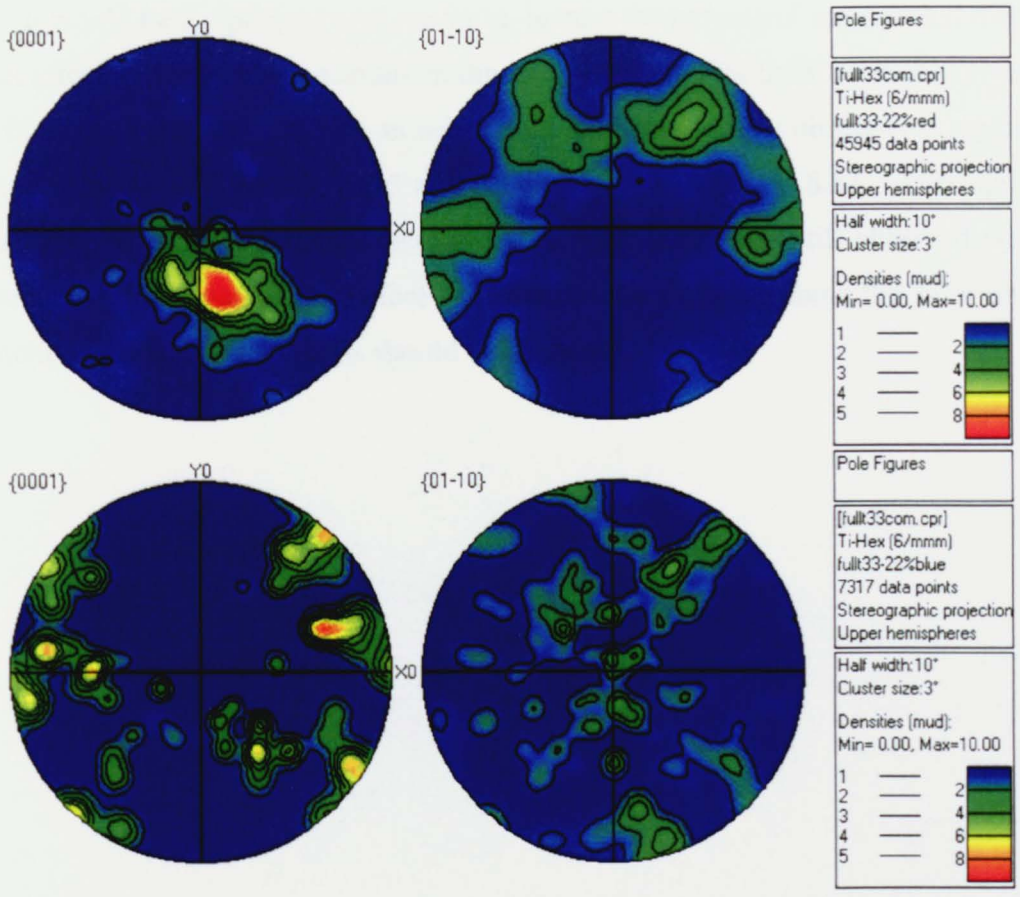

Figure 8.55 {0002} and {01 $\bar{1}$ 0} pole figures of clustered zone of similarly orientated grains.

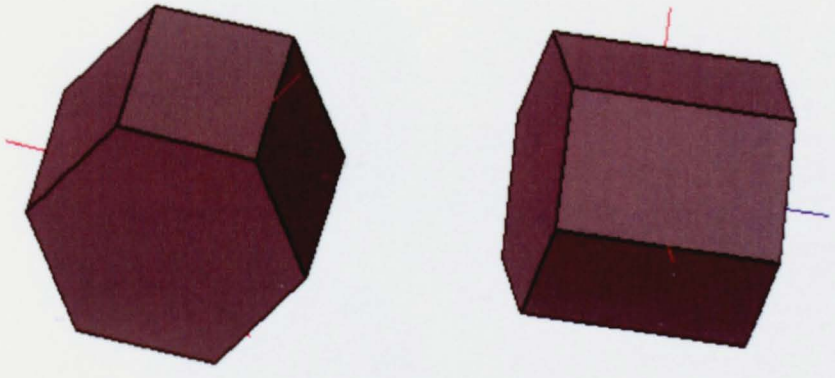

Figure 8.56 3-D crystal orientations of α_p clusters Figure 8.52(a) and (b).

Looking at the thermomechanically processed test samples it is evident that the similarly orientated clusters are retained through the process route. The clusters range in size from 400-1000μm and in most cases are grouped with clear boundaries. In all the α_p results there are strong textures (>5 MRD) displaying little or no rotation about the compression direction, fibres which would be expected from a compression sample in this plane.

It would be tempting to analyse the α_p texture evolution and suggest that there is a direct effect of the increasing strain on the α_p orientation. The basal orientation rotates away from the transverse towards an orientation almost parallel with the viewing plane after a critical strain between 0.175 and 0.375, as seen in Figure 8.57. Although the general trend would suggest this there are a number of clusters still observed with a transverse basal orientation and before any conclusions are made about the deformation behaviour of the α_p the α_s datasets should be analysed.

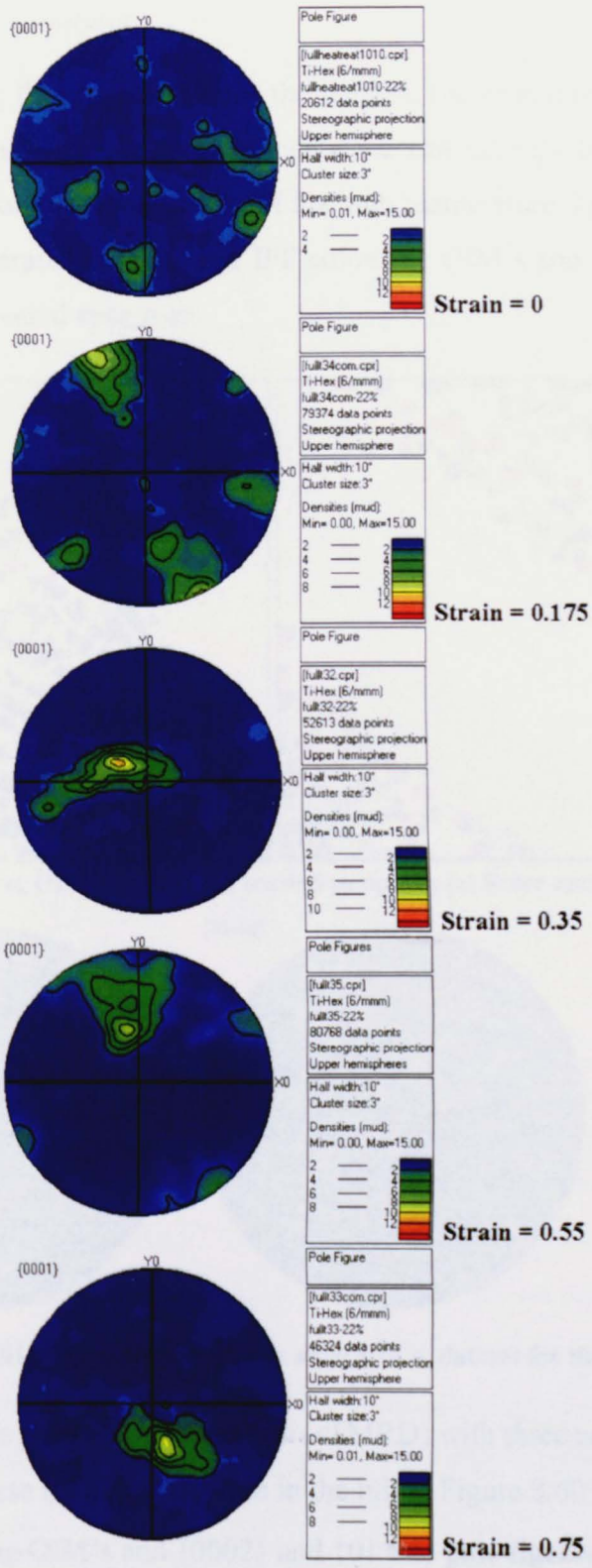

Figure 8.57 Schematic summary of {0002} orientations of α_p grains in the thermo-mechanically processed samples.

8.3.2.2 Secondary alpha analysis

After removing the α_p grains from the dataset, the remaining information will relate to the α_s morphology. Utilising this data we can attempt to analyse both the deformation and transformation behaviour of the high temperature β phase. Figures 8.58 and 8.59 show the separated α_s Euler and IPF colouring OIM's and the associated pole figures from the heat treated specimen.

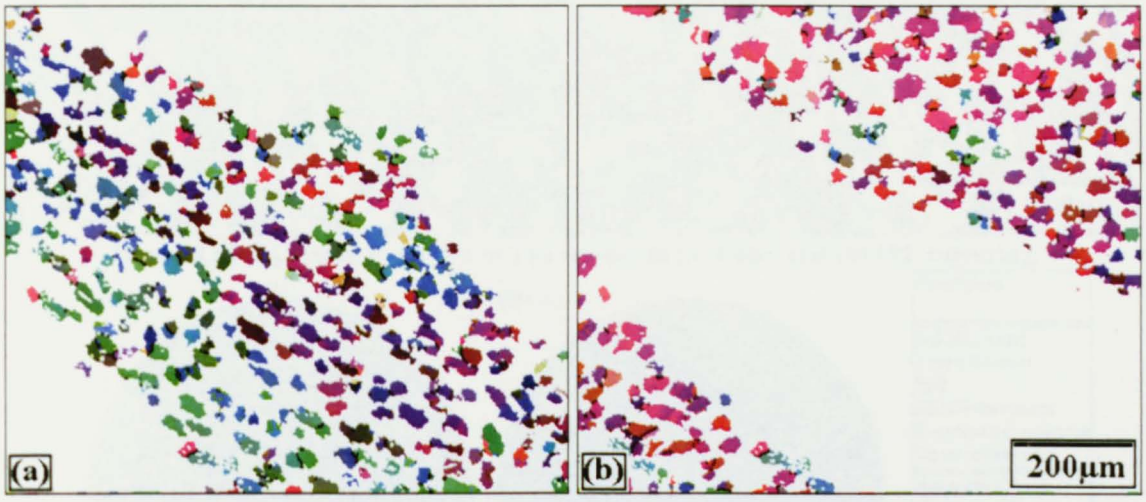

Figure 8.58 Separated α_s OIM's of the heat treated sample in (a) Euler and (b) IPF colouring.

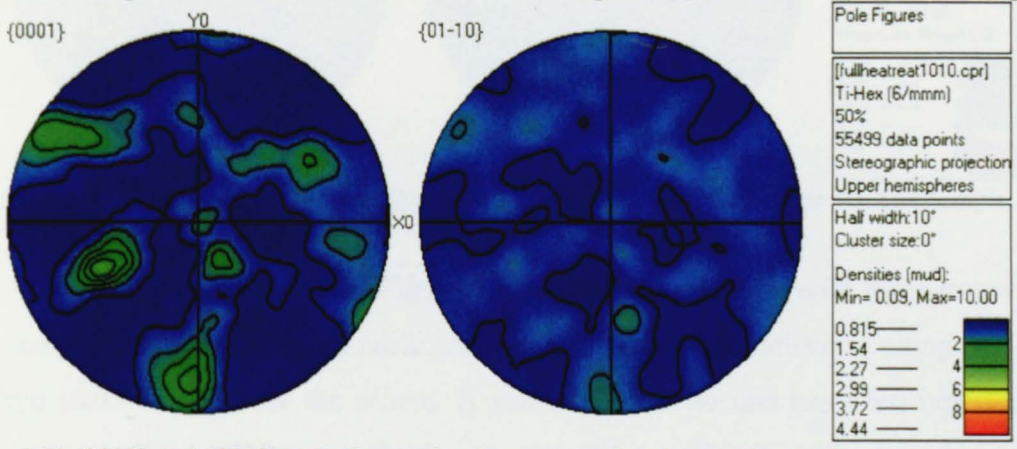

Figure 8.59 {0002} and {0110} pole figures for the separated α_s dataset for the heat treated sample

This pole figure shows a weak texture (<5MRD) with three components rotated away from the transverse basal texture seen in the billet. Figure 8.60 and 8.61 show the Euler and IPF colouring OIM's and {0002} and $\{01\bar{1}0\}$ pole figures for the α_s dataset for sample T16, having received a strain of 0.175.

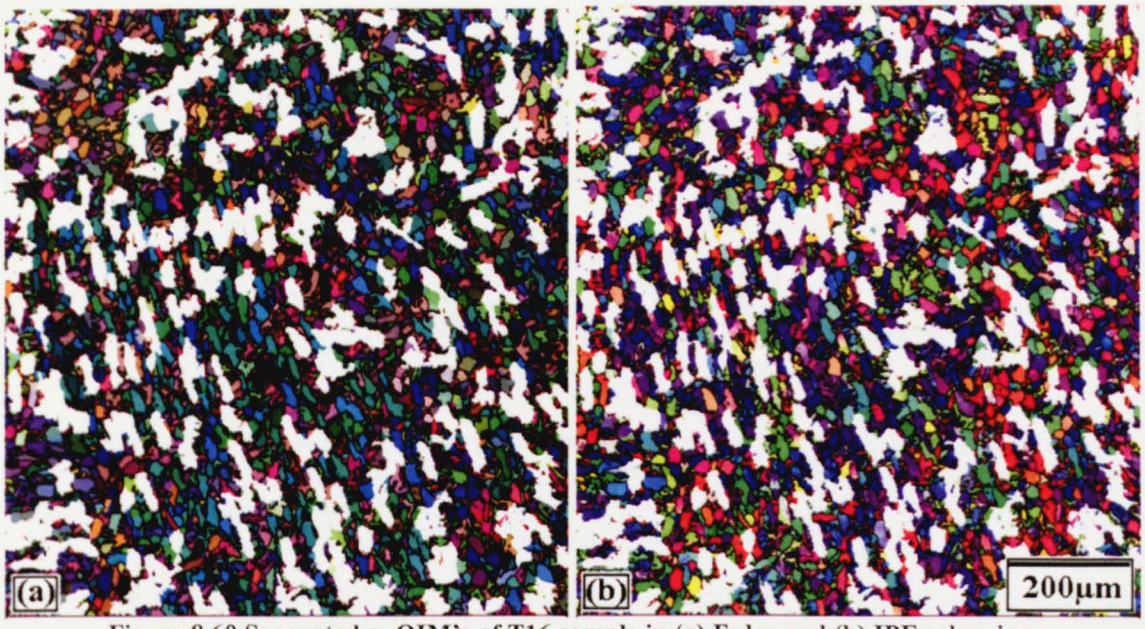

Figure 8.60 Separated α_s OIM's of T16 sample in (a) Euler and (b) IPF colouring.

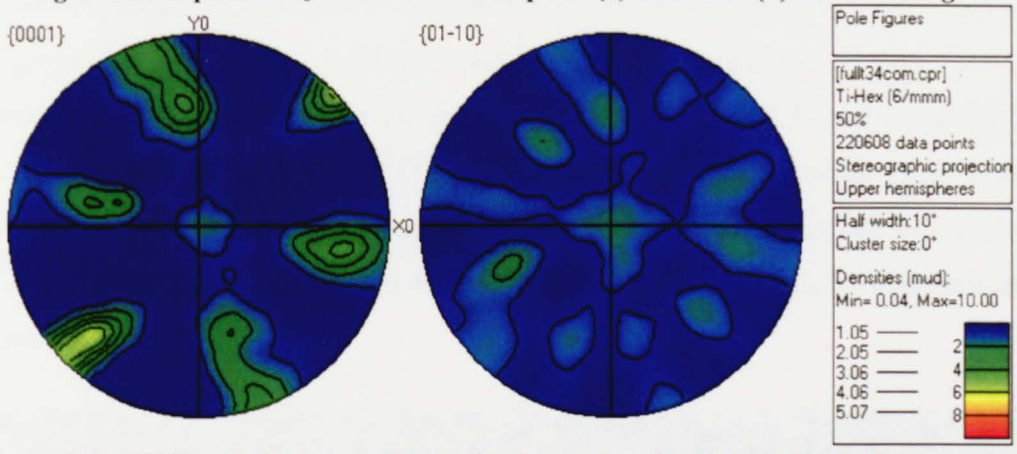

Figure 8.61 {0002} and {0110} pole figures for the separated α_s dataset for the T16 sample.

The {0002} pole figure in Figure 8.61 illustrates a texture with three transverse basal components and a parallel basal component, one of the transverse components is preferred (6.05 MRD) over the others. A similar texture to this has been reported by Stanford and Bate (2004) as being commonly associated with transformed β microstructures of rolled Ti6Al-4V, and their results are seen in Figure 8.62(a). Figure 8.62(b) shows the transformation texture calculated through the burgers relationship with no variant selection.

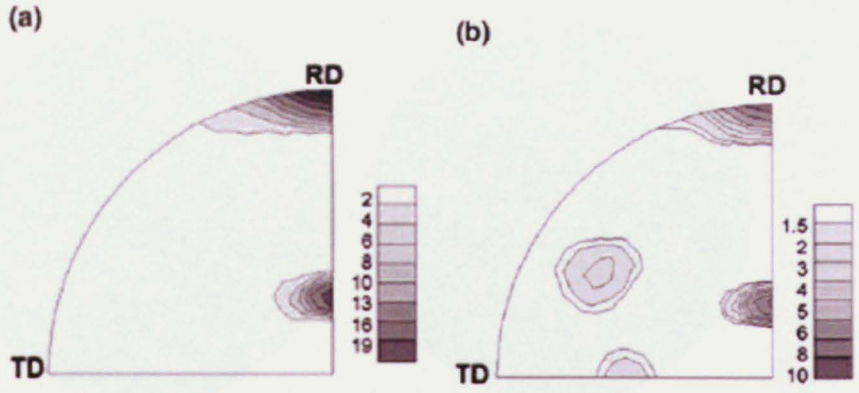

Figure 8.62 Adapted from Stanford and Bate 2004, (a) Measured α_s transformation texture of the furnace cooled sample measured using EBSD shown as {0 0 0 2} pole figure and (b) the calculated α_s transformation texture assuming transformation of the β texture in the same sample without variant selection shown as {0 0 0 1} pole figure.

As the strain increases the texture is maintained, however, its intensity decreases. Figures 8.63-8.66 show the Euler and IPF colouring OIM's and associated pole figures for T14, having received a strain of 0.375. Figures 8.67 and 8.68 were produced from the T17 data set, having received a strain of 0.55. Finally, Figures 8.69 and 8.70 show the results from the T15 data set, having received a strain of 0.75. In all the {0002} pole figures there are strong transverse basal components and in most cases there is also an off-basal component relating to the corresponding α_p texture seen in the previous section.

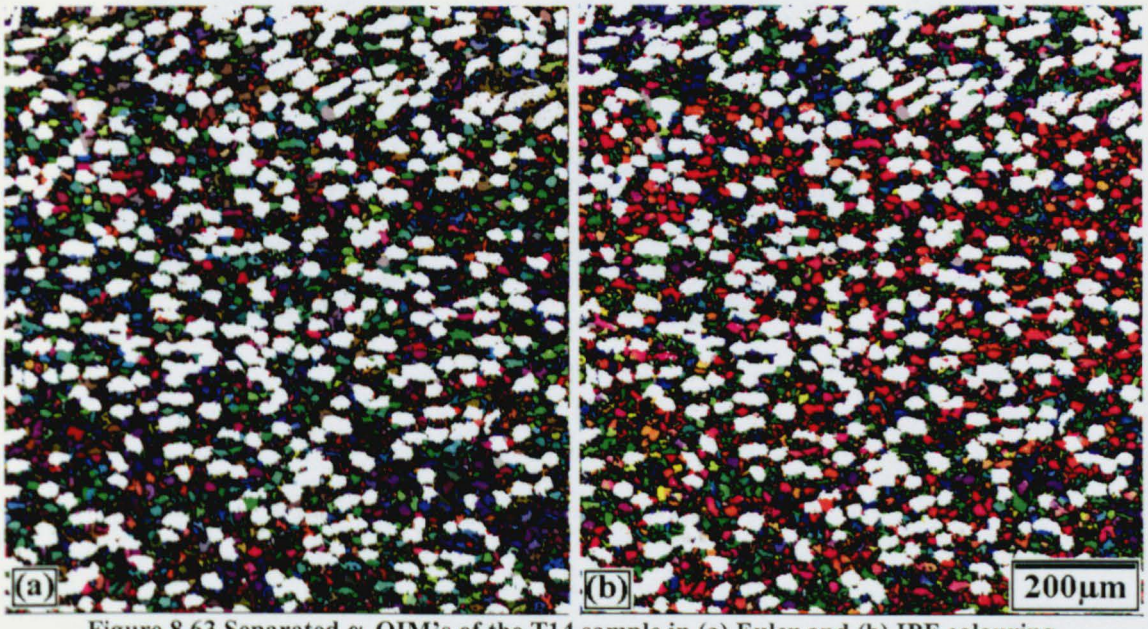

Figure 8.63 Separated α_s OIM's of the T14 sample in (a) Euler and (b) IPF colouring.

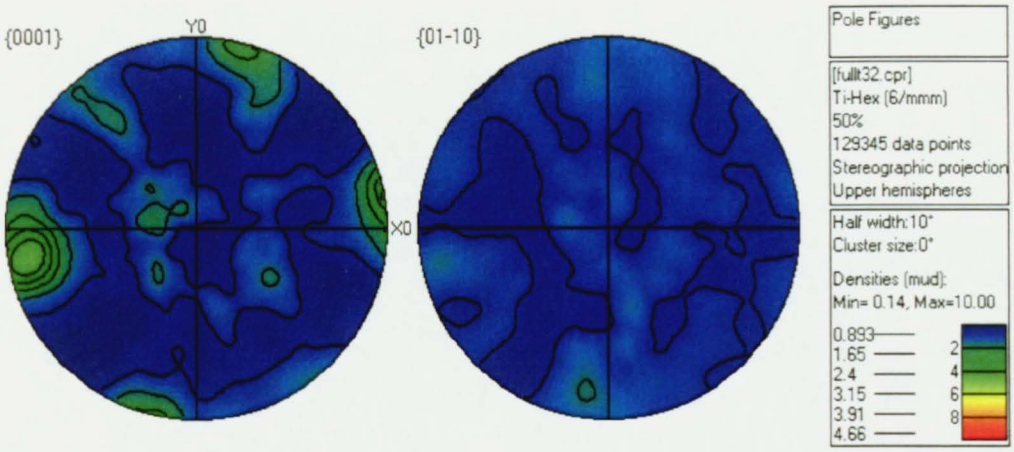

Figure 8.64 {0002} and {0110} pole figures for the separated α_s dataset for the T14 sample

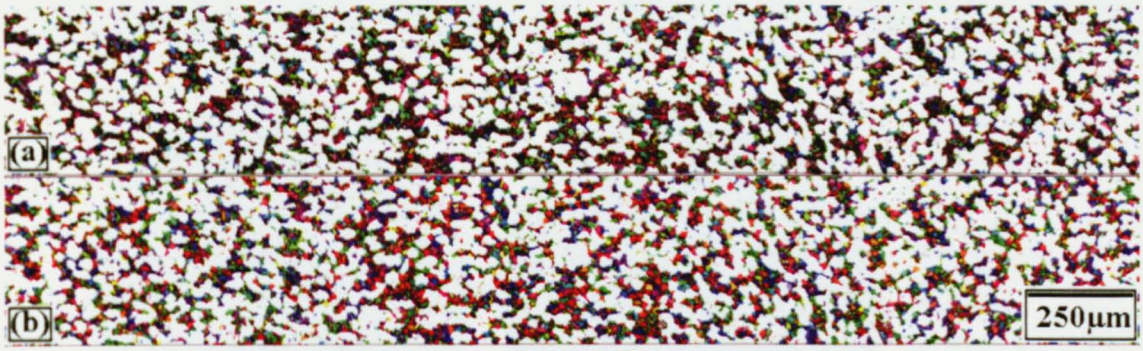

Figure 8.65

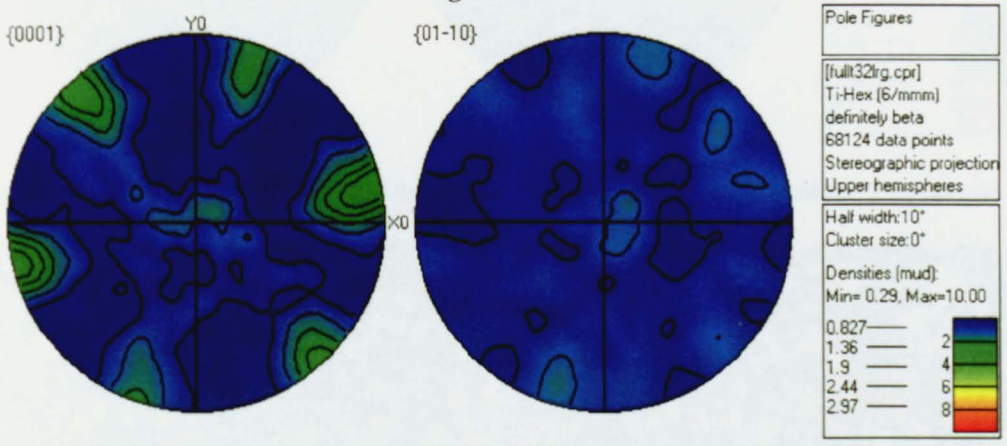

Figure 8.66

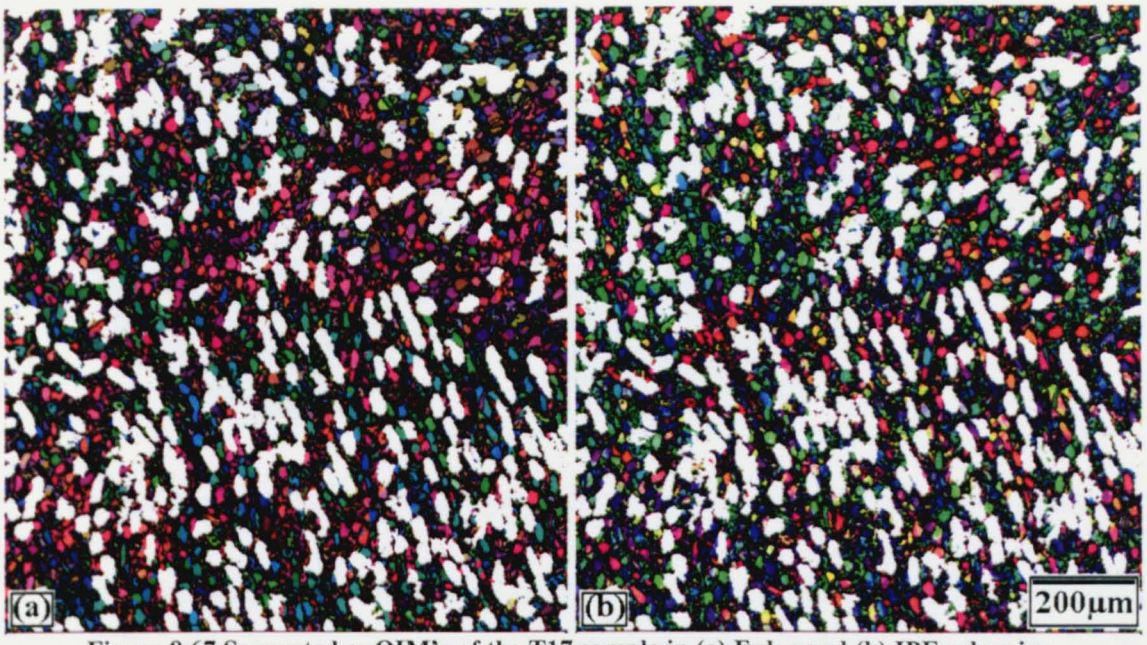

Figure 8.67 Separated α_s OIM's of the T17 sample in (a) Euler and (b) IPF colouring.

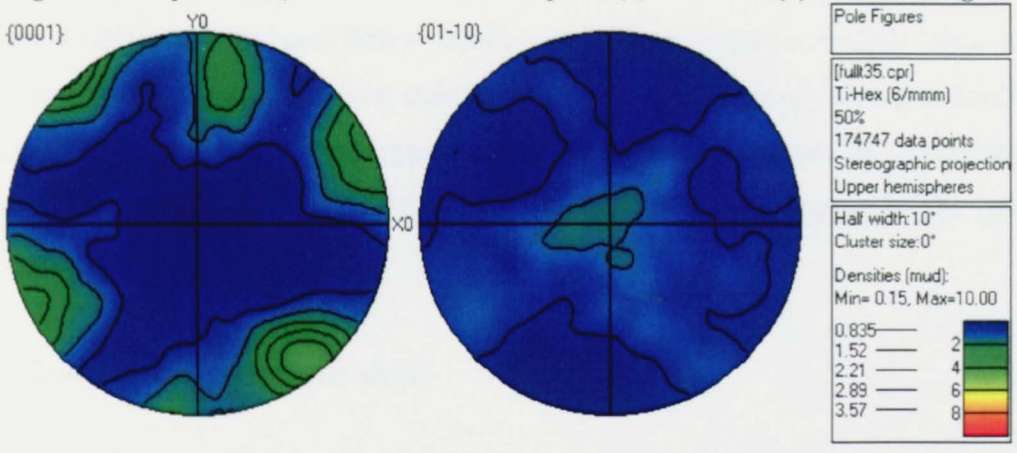

Figure 8.68 {0002} and {0110} pole figures for the separated α_s dataset of the T17 sample

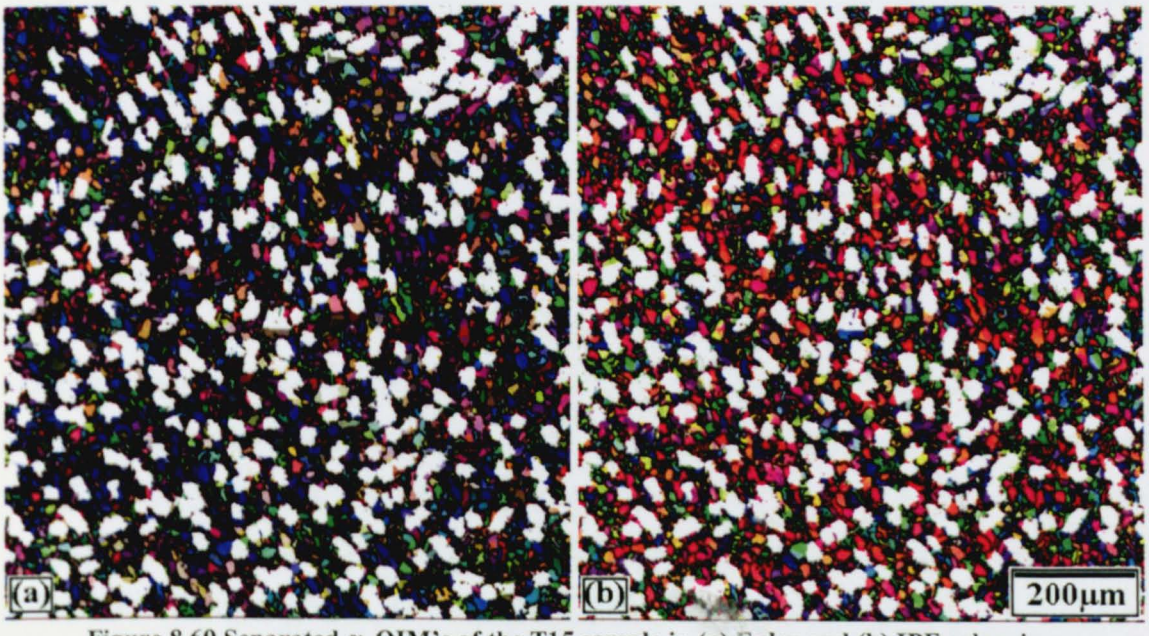

Figure 8.69 Separated α_s OIM's of the T15 sample in (a) Euler and (b) IPF colouring.

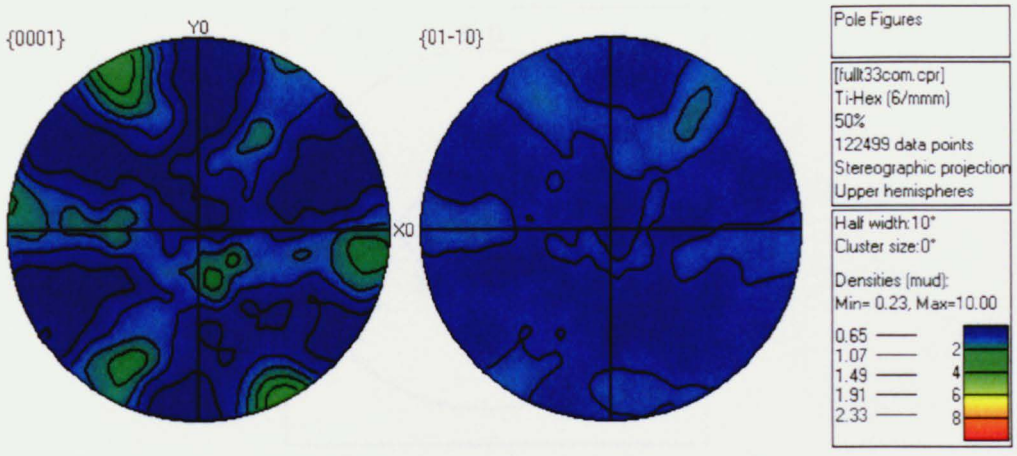

Figure 8.70 {0002} and {0110} pole figures for the separated α_s dataset for the T15 sample

All the transformation textures seen in Figures 8.58 to 8.70 are comparable with the transformation textures reported by Stanford and Bate (2004) in Ti-6AL-4V shown in Figure 8.62(a). Stanford and Bates (2004) texture measurements revealed that the α_s texture was markedly sharper than calculated on a basis of equal variant probability (Figure 8.62(b)), indicating that significant variant selection occurs. It would appear also that a single component in all the results analysed previously dominates the {0002} pole figures.

8.3.2.3 Summary of separated analysis

The hot deformation textures of Ti alloys have been documented previously and were reviewed in Chapter 2, with Moril et al (1986) and Lutjering (2003) offering detailed reviews. As discussed in Chapter 2, α_p textures developed during hot deformation in dual phase Ti alloys depend strongly on the volume fraction and geometrical arrangement of each phase during deformation (Moril et al, 1986, Lebensohn, 1997). Moril et al, studying Ti6Al-4V distinguished three separate regimes for deformation based on the temperatures at which deformation was completed;

Firstly, at low temperatures where the α_p volume fraction is high ($\approx$85%) the material can be regarded as a single phase as the α_p grains are contiguous separated only in some regions by small pinned β grains. In the Moril et al's work this temperature was 800°C, where as in this work that regime would be in the < 950°C temperature range. In single phase α-Ti-Al alloys a basal type {0001}<0110> texture, see Figure 8.71, forms during rolling in the single phase (Kocks, Wenk, Tome, 2003).

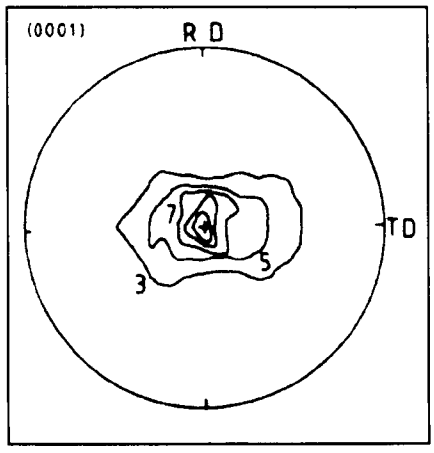

Figure 8.71 Common rolling texture in α titanium plate (Kocks, Wenk and Tome).

Secondly, at higher temperatures, where the microstructure consists of α_p and β in similar proportions, for Ti-6Al-4V this was 900°C and for Timetal 834 this would be at temperatures between 980-1000°C, deformation of the α_p is severely affected by the surrounding β. In this case the α_p grains are completely separated by the β phase and as such do not suffer the same constraints as in single phase material and as such it is concluded in Ti-6Al-4V that favourably orientated grains (weak orientation) deform by single slip on <a> systems and α_p grains with a hard orientation remain unreformed but may rotate by flow of the β phase around them.

Finally, at very high temperatures, where the β volume fraction exceeds the α_p, the deformation behaviour of the BCC β phase controls the deformation behaviour. Lutjering (2003), Williams & Peters (1983) all conclude the textures seen in Figure 8.72(a) are imposed on Ti alloys during hot working, further detailed in Kocks, Wenk and Tome (2003) with respect to c/a ratio, which in the case of Titanium will be 1.587.

For this work, the hot deformed textures observed are compiled in Figure 8.73, showing the {0002} pole figures of the α_p, α_s and the complete data sets separately.

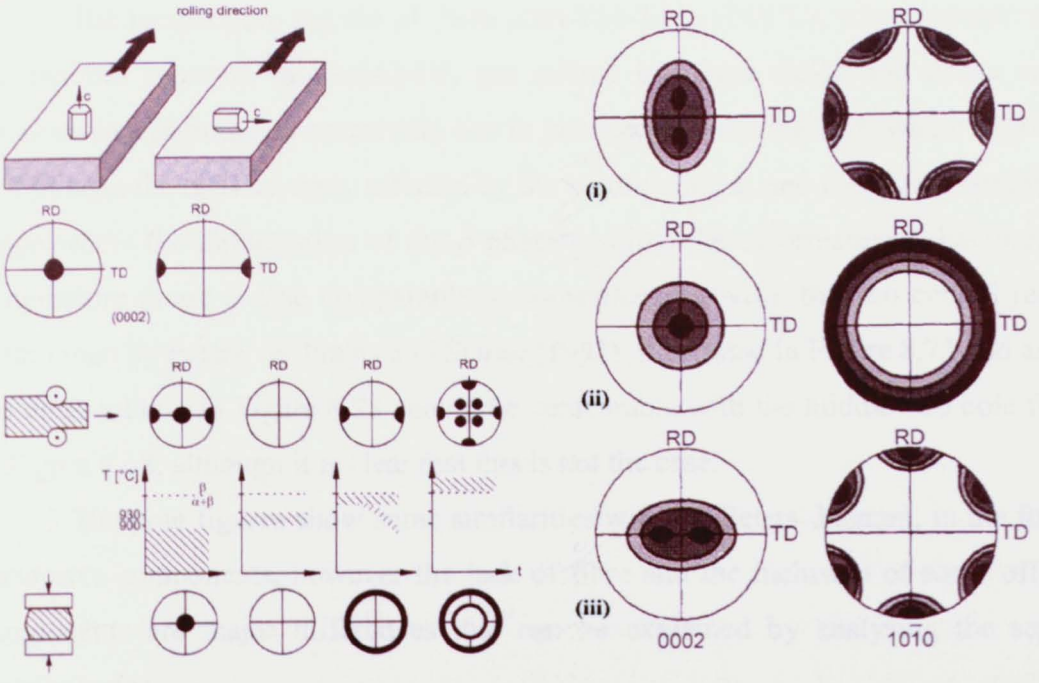

Figure 8.72 (a) Schematic showing common alpha textures associated with rolling and compression and (b) effect of c/a ratio on texture (i) greater than 1.633, (ii) approximately equal to 1.633 or (iii) less than 1.633.

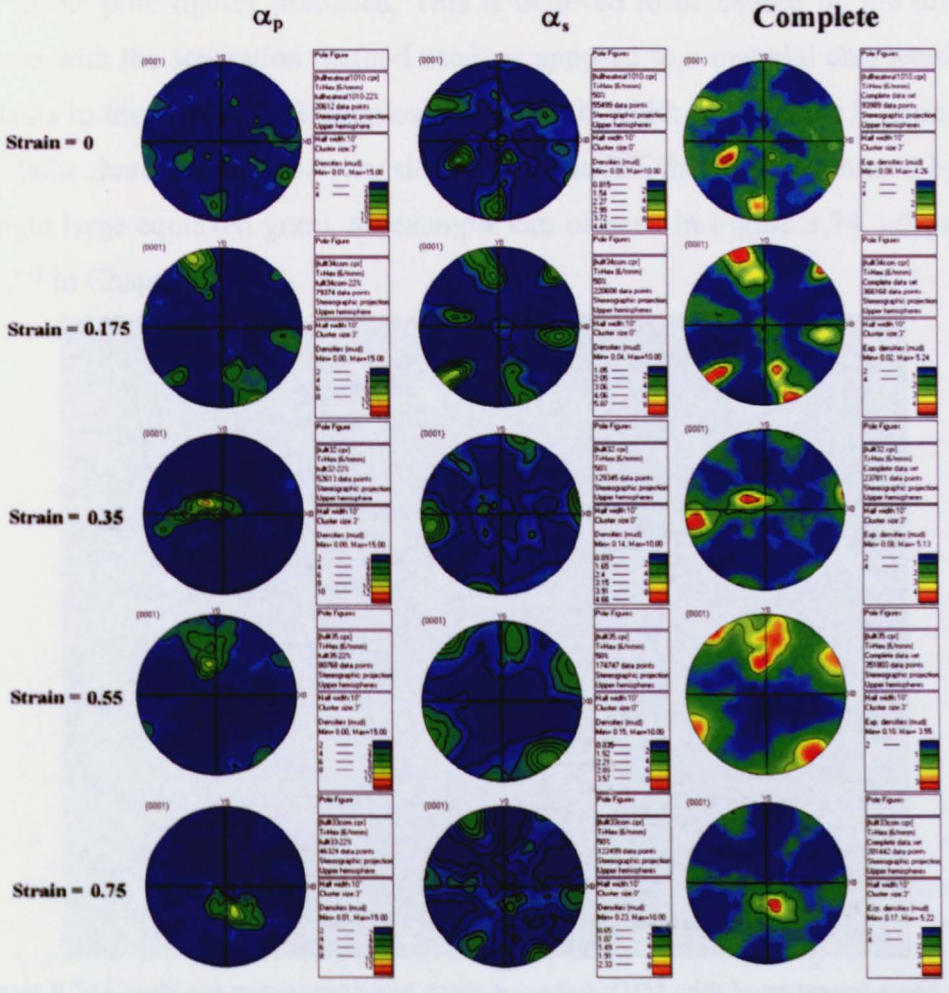

Figure 8.73 Schematic summary of α_p, α_s and complete data sets from axisymmetric compression testing.

The temperature regime of these tests T14-T17 (1010°C), when compared with the regimes reported in Ti-6Al-4V, are related by phase fields and phase volume fractions to a regime that essentially lies in between the intermediate, where Moril et al (1986) state the α_p is severely affected by the surrounding β, and the higher temperature range where the deformation of the β phase controls the deformation behaviour. This temperature range is also comparable to somewhere between the two central regimes determined by Peters, Williams and Starke (1983), illustrated in Figure 8.72 and as such the third column in Figure 8.73 should be comparable with the middle two pole figures in Figure 8.68, although it is clear that this is not the case.

The pole figures show some similarities with the Peters diagram, in the form of transverse components, however the lack of fibre and the inclusion of some off-basal components are major differences that can be explained by analysing the separate morphologies.

Initially, separating the α_p and α_s in the non-deformed samples leads to little change in the pole figures produced. This is believed to be caused by the difficulties associated with the separation method used, as apposed to a material characteristic. As the α_s laths in the heat treated samples span the full width of the prior β grain, and all parallel laths share the same or very similar orientations, they are determined by EBSD as a single large equiaxed grain, an example can be seen in Figure 8.74, adapted from Figure 7.7 in Chapter 7.

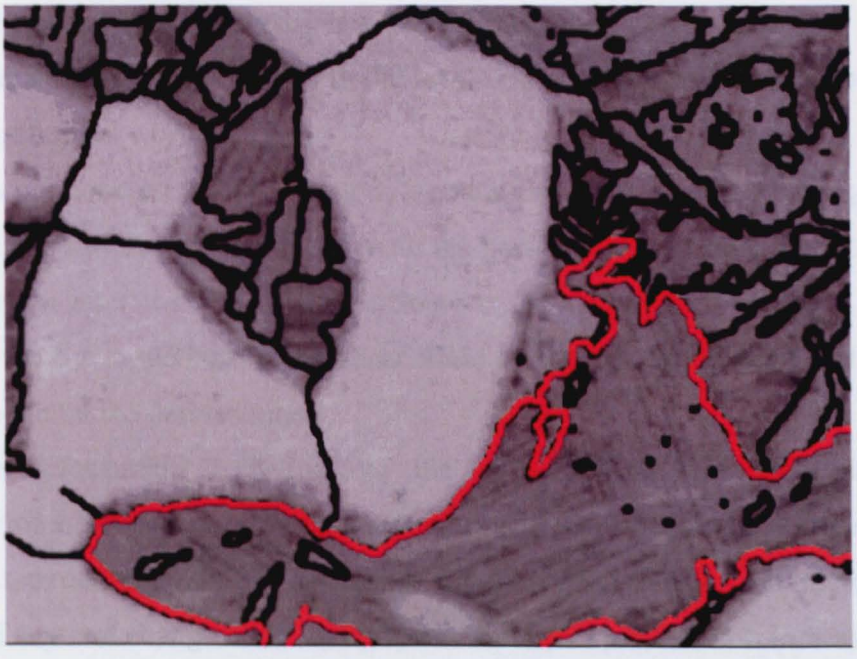

Figure 8.74 Combined micrograph and grain boundary OIM with large transformed grain illustrated in red.

Comparison of both the α_p and α_s textures in the deformed samples show very distinct differences. In the α_p results, (left hand column Figure 8.73) there are initial transverse textures, in the heat treated and T16 samples, associated with the inherent textures seen in the billet rotating towards strong almost parallel basal textures, in sample T14, T15 and T17. The strong {0002) orientations show no fibre about the Z-axis which would be expected from a compression test and sample of this type. The cluster size is seen to increase due to the pancaking of the cluster with increased deformation.

The α_s texture also shows a strong non-fibred texture, however the α_s texture is a tranverse/basal texture and in each {0002} pole figure there appears to be 4 texture components, 3 located transversally and 1 located off-basal. In all cases, one of the transverse components possesses a stronger texture than the others. The work of Germain et al, (2005) also concludes "A pronounced β-α_s variant selection takes place in sharp textured regions of a bimodal Timetal 834 billet containing 30% α_p grains surrounded by secondary α_s colonies. In each observed macrozone, the β-α_s phase transformation has favoured α_s variants having in average their c-axes in the same macroscopic direction as the α_p grains. Consequently, at room temperature, the sharp local texture of a macrozone is due to the overlapping of the α_p single component and the main α_s component. A detailed local analysis of neighbouring α_p/α_s variants clearly shows that locally the favoured variants align their c-axes with those of a neighbouring α_p grain. The sharpness of this variant selection mechanism varies from one macrozone to the other, as it is strongly related to the local orientation distribution of neighbouring α_p/β grains after hot working.

It is our conclusion that during deformation at 1010°C most of the α_p grains are forced to rotate towards an orientation with the basal plane perpendicular to the applied strain direction after a strain of 0.175. Some α_p grains remain transverse and this is believed to be due to the lack of any shear stress on the <a> slip systems, believed to be active, throughout the deformation.

The deformation behaviour of the β is difficult to assess due to the transformation of the hot worked microstructure and its effect on the texture. It is clear that the texture determined from the α_s is as expected from transformed microstructures. The lack of any real change in the α_s texture components present with increased strain is due to the possible 12 variant orientations obtained from one single beta orientation through the burgers relationship. However, more telling is the dilution of the

transformed texture component with increasing strain suggesting one of two possibilities;

- The orientations of the high temperature β has become more diffuse, or
- Variant selection within the transformation has decreased.

8.3.2.4 Further parameter analysis

Having addressed the material behaviour at industrial forging conditions, in order to address the effects of strain rate and temperature on the deformation behaviour, further analysis was completed on samples D6, D8, D9 and D10. Samples D6, T14 and D9 are comparable in order to determine the effect of temperature on the deformation behaviour and samples D8, D9 and D10 are comparable on order to determine any effects of strain rate.

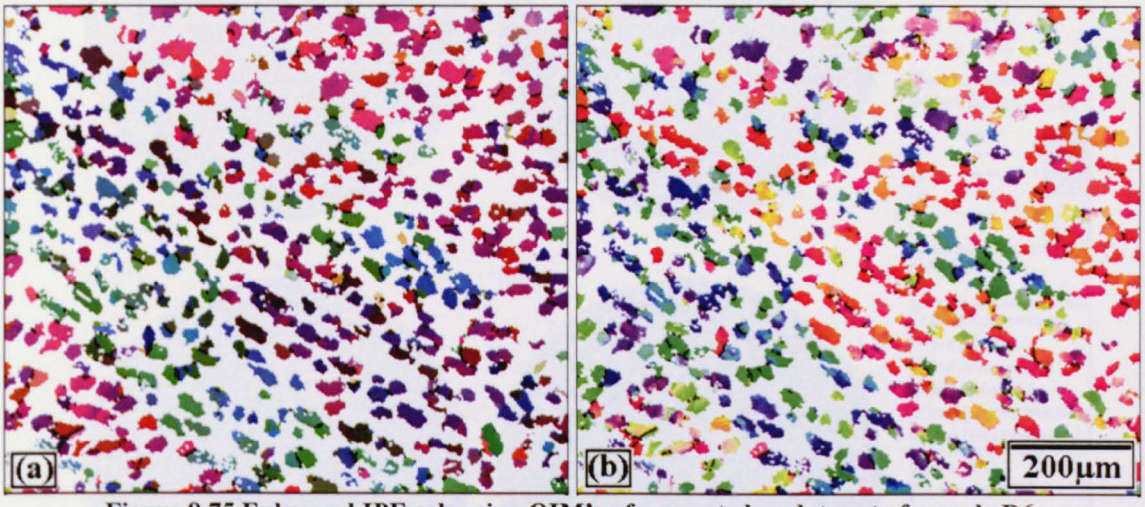

Figure 8.75 Euler and IPF colouring OIM's of separated α_p data set of sample D6.

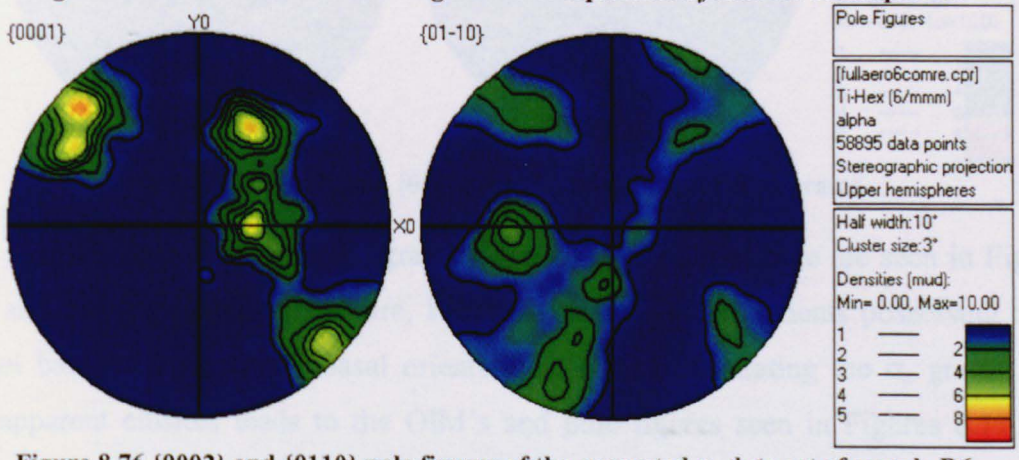

Figure 8.76 {0002} and {0110} pole figures of the separated α_p data set of sample D6.

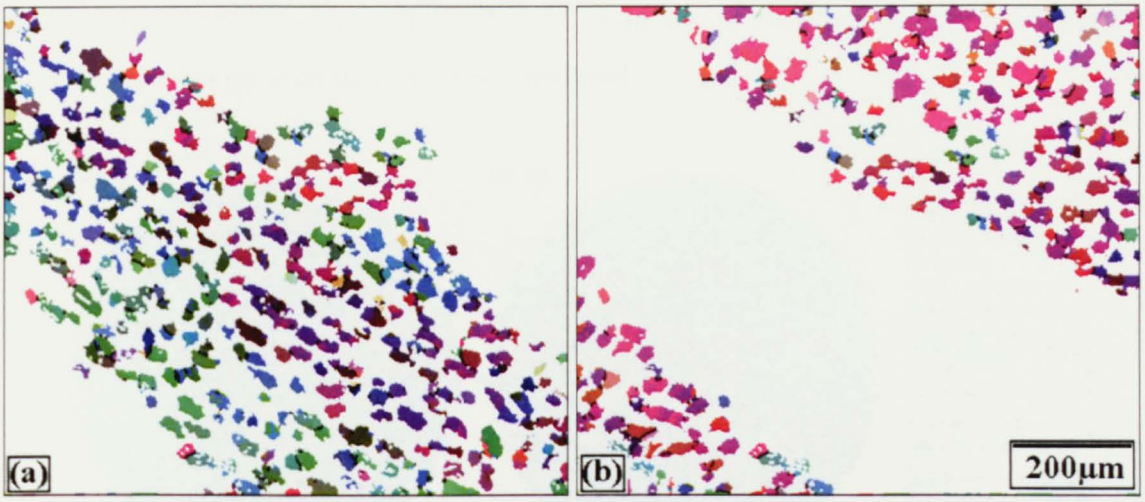

Figure 8.77 Clustered α_p grains isolated from the D6 sample.

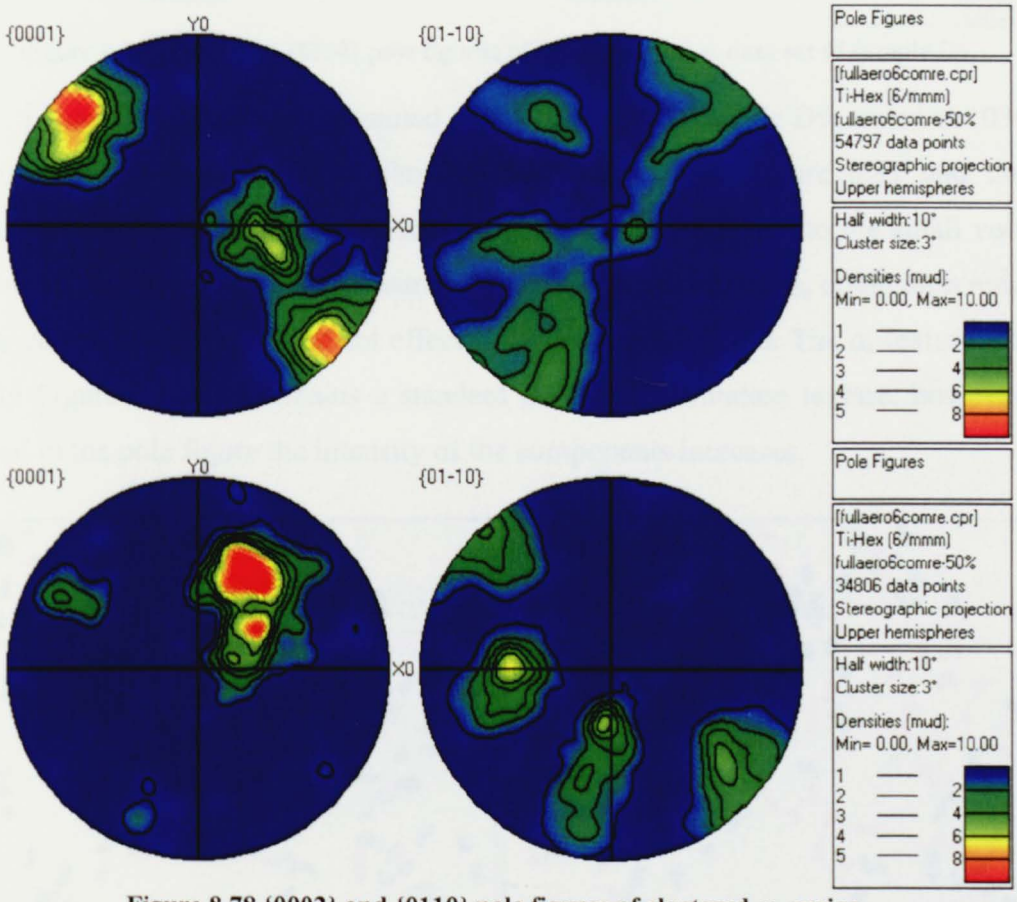

Figure 8.78 {0002} and {0110} pole figures of clustered α_p grains.

Initial separation of the α_p grains ($\approx$45%) in the D6 sample are seen in Figure 8.75, and the associated pole figure, Figure 8.76, shows components possessing both parallel basal and transverse basal orientations. Further separating the α_p grains into their apparent clusters leads to the OIM's and pole figures seen in Figures 8.77 and 8.78. Clusters greater than 1mm in diameter are visible and the dominant cluster possesses an off-basal orientation with very little rotation about the Z direction. The

results are as seen previously in the 1010°C tests, the α_s transformation texture (Figure 8.79) is the weakest seen in all samples analysed.

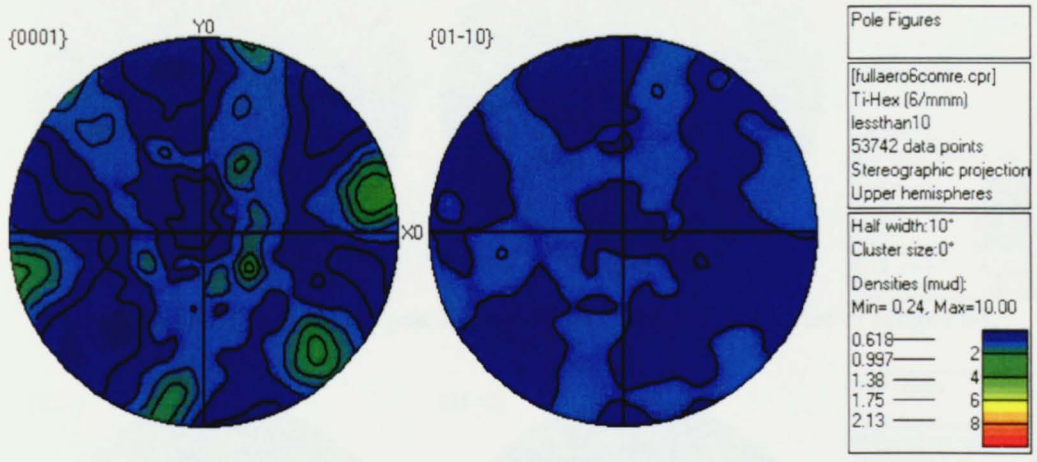

Figure 8.79 {0002} and {0110} pole figures of the separated α_s data set of sample D6.

Figure 8.80 shows the separated ≈10% α_p grains of sample D9, tested at 1030°C, the pole figures produced from the data set can be seen Figure 8.81 and the α_p orientation is seen to remain transverse basal. It is clear, that due to the small volume fraction of hard α_p grains in the β matrix at high temperatures, the α_p orientation remains unchanged as the α_p grains are not effected by the applied strain. The α_s texture can be seen in Figure 8.82 and remains a standard $\beta \rightarrow \alpha$ transformation texture, however, as detailed in the pole figure the intensity of the components increases.

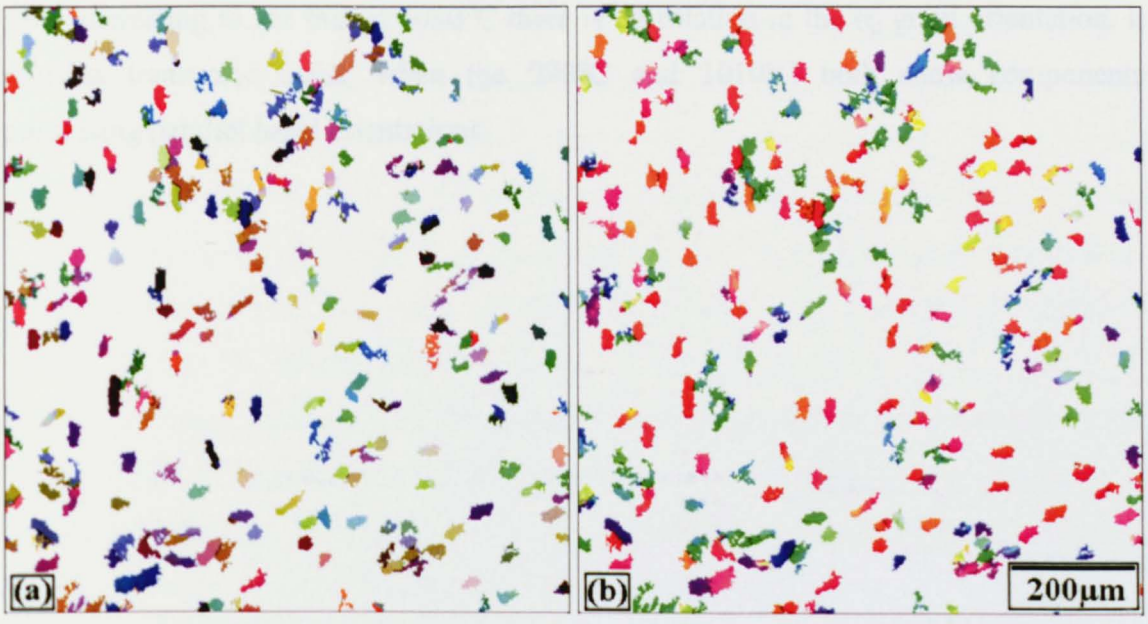

Figure 8.80 α_p OIM's of the D9 sample in (a) Euler and (b) IPF colouring

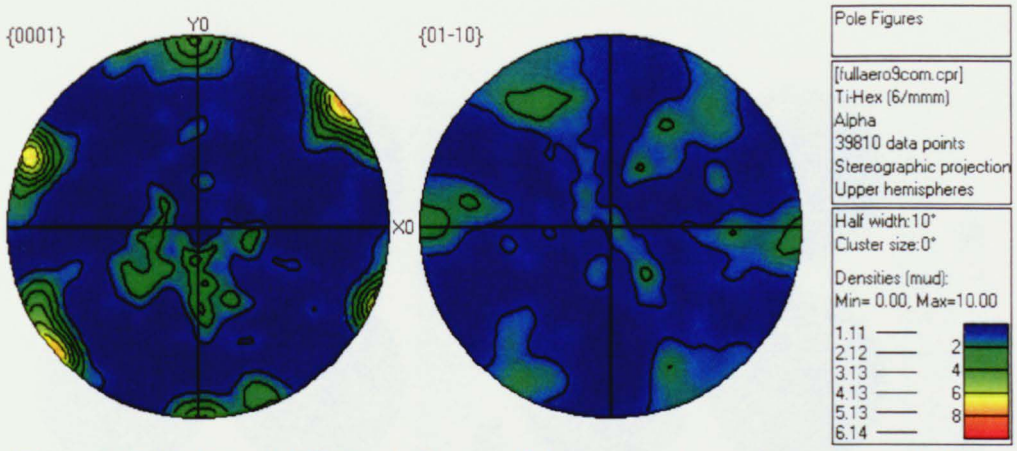

Figure 8.81 {0002} and {0110} pole figures of the separated α_p data set of sample D9.

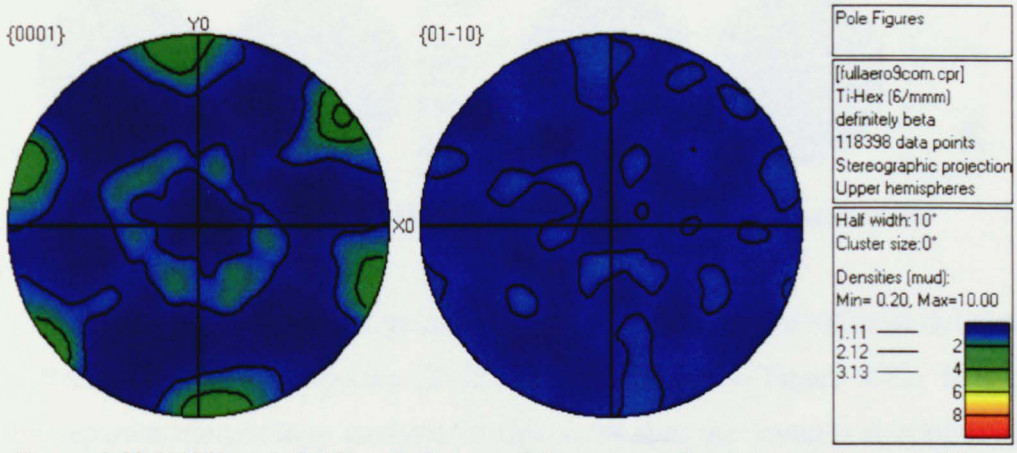

Figure 8.82 {0002} and {0110} pole figures of the separated α_s data set of sample D9.

The results detailed in this section have been summarised in Figure 8.83. It is very interesting to see that at 1030°C there is no rotation in the α_p grain orientation, it remains transverse basal, when the 990°C and 1010°C both show components possessing parallel basal orientations.

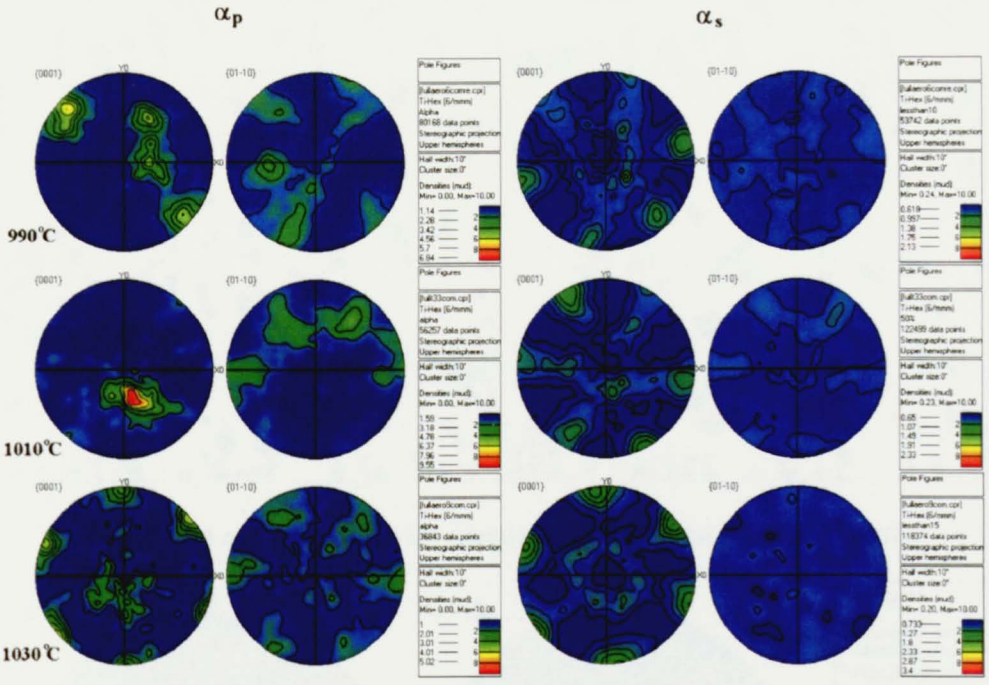

Figure 8.83 Summary of the effect of temperature on the α_p and α_s datasets.

With the following results gained we can elucidate on the textures detailed by Leyens, Peters (2003) and Lutjering (2003) seen previously in Figure 8.72. It is clear from the separate morphology analysis in this work that the textures described are a function of the dominant phase at the hot working temperatures analysed. At low temperatures the expected texture is a parallel basal texture, which has been determined in this work as an α_p deformation texture, which is the dominant phase at these temperatures. At temperatures approaching the transus, the texture detailed in Figure 8.72 is fully transverse, this has also been seen in the D9 sample in this work, and is due to the transformation texture of the dominant β phase at theses temperatures combined with the transverse nature of the ≈10% α_p grains. It is interesting that at intermediate temperatures no texture is seen, possibly due to the equal measure of α_p and α_s components cancelling each other out.

The effect of strain rate was assessed by analysing samples D8 (Figures 8.84 and 8.85) and D10 (Figures 8.86 and 8.87) and comparing them with D9 seen previously in Figures 8.80-8.82.

Figure 8.84 α_p OIM's of the D8 sample in (a) Euler and (b) IPF colouring

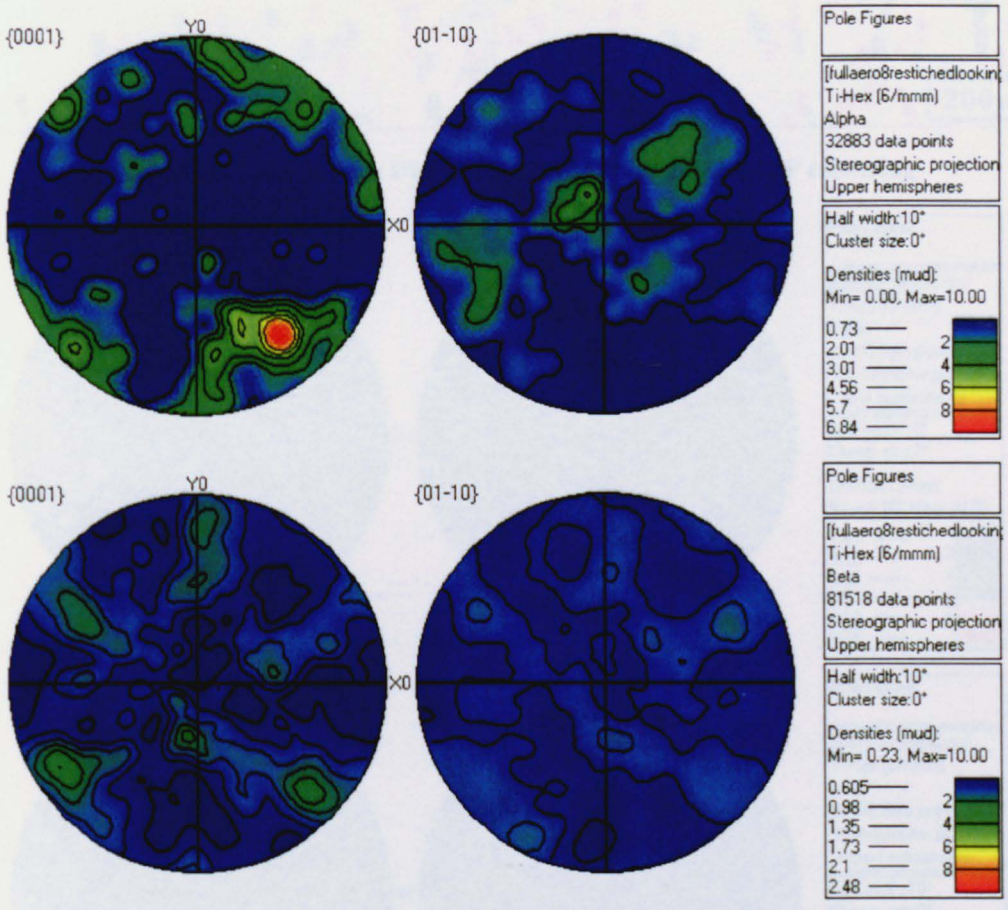

Figure 8.85 (a) {0002} and {0110} pole figures of the separated α_p data set of sample D8 and (b) {0002} and {0110} pole figures of the separated α_s data set of sample D8.

The results seen here for sample D8, deformed to a strain of 0.7 at a temperature of 1030° C with a strain rate of $20s^{-1}$, show a transverse basal orientation in the α_p grains (>7MRD). The α_s texture is the most random seen in this work and it is difficult to draw any conclusions from the contoured peaks.

Figures 8.86 and 8.87 show the α_p OIM and associated {0002} and {01-10} pole figures of the α_p and α_s data sets of sample D10, having received a strain of 0.7, at a temperature of 1030°C with a strain rate of $0.2s^{-1}$.

Figure 8.86 α_p OIM's of the D10 sample in (a) Euler and (b) IPF colouring

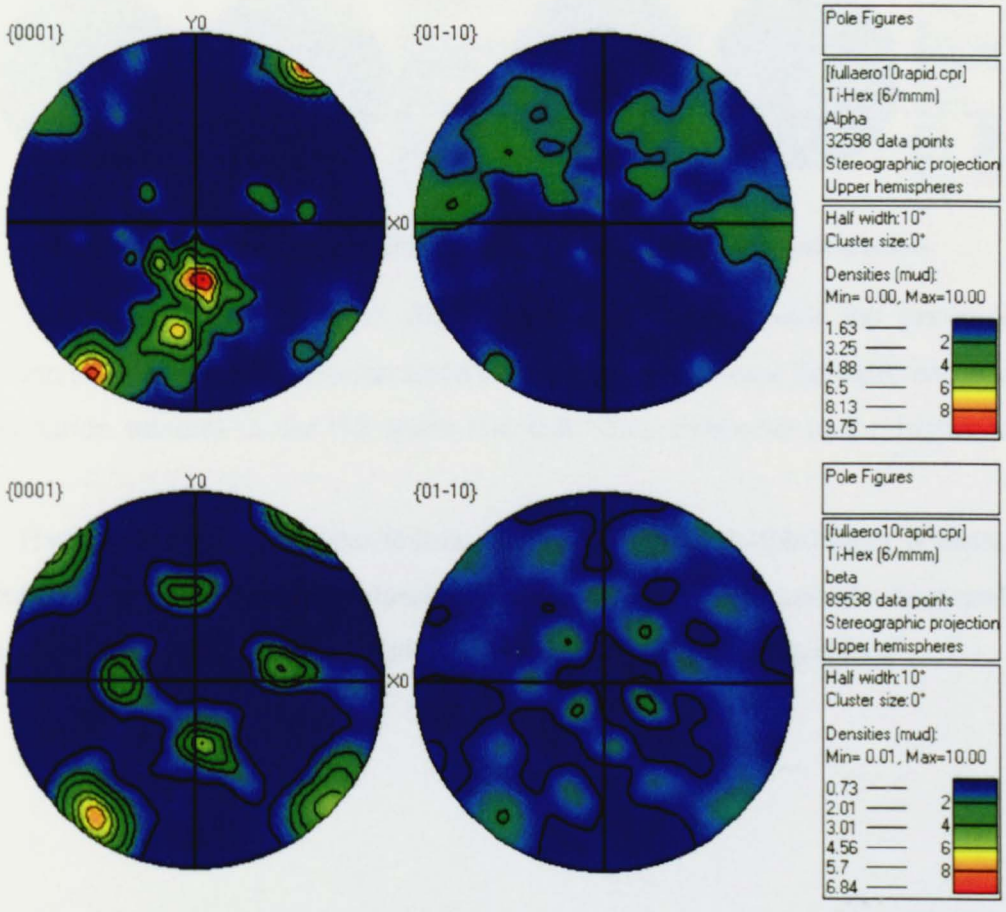

Figure 8.87 (a) {0002} and {0110} pole figures of the separated α_p data set of sample D8 and (b) {0002} and {0110} pole figures of the separated α_s data set of sample D8.

Again, there is a strong transverse basal orientation in the α_p but there is also a strong almost parallel basal orientation. The α_s texture seen in Figure 8.87(b) is a strong non-transformation texture which has not previously been encountered in this work. A summary of the effect of strain rate on the textures produced can be seen in Figure 8.88.

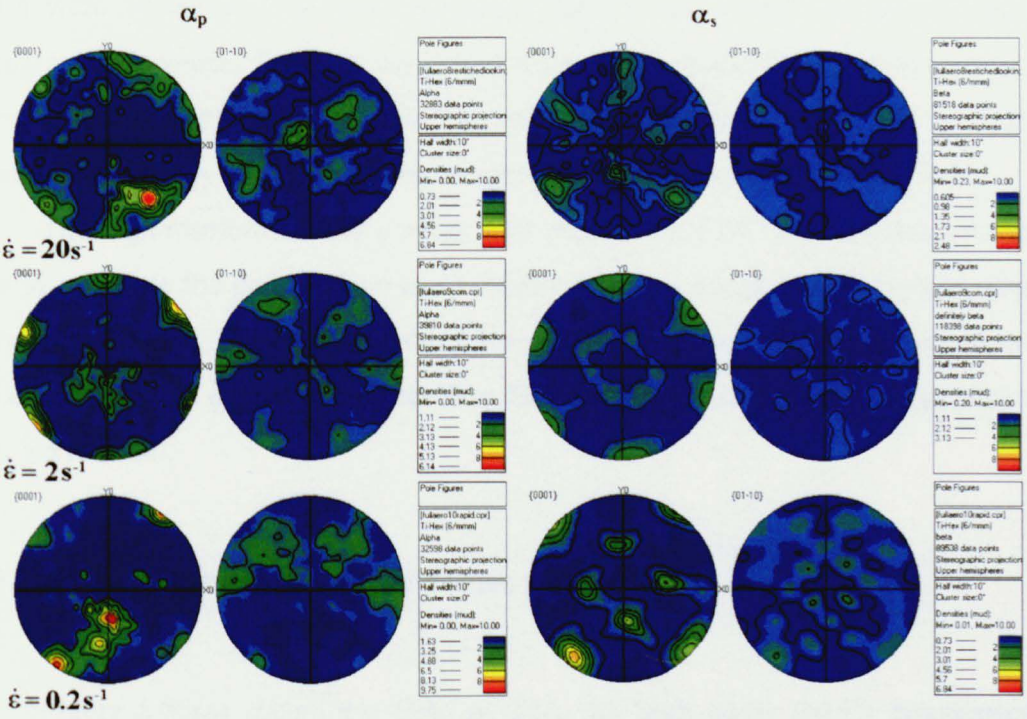

Figure 8.88 Summary of the effect of strain rate on the α_p and α_s orientations.

The highest strain rate of $20s^{-1}$ appears to disperse both the preferred α_p orientation and the α_s transformation texture. It is interesting to see the differences in the transformation textures in the 0.2 strain rate test when compared to the higher strain rates.

Having assessed the global texture evolution of both morphologies present, it is also required that the microstructural evolution and local textural development are analysed in order to fully comprehend the materials deformation behaviour.

8.3.3 Microstructural analysis through EBSD

8.3.3.1 Introduction.

Using the EBSD data sets where smaller step sizes were used, high resolution OIM's were produced. The high resolution OIM's can effectively be viewed as a micrograph. However, the high resolution OIM offers much more, as the orientation information for each pixel in the 'micrograph' is available and can be used to investigate sub-grain misorientations, twinning boundaries and crystal rotations.

The high resolution OIM's of the heat treated and T14-17 have been analysed in order to elucidate the deformation mechanisms active in the α_p grains during industrial forging operations. The results from this section will help determine whether the rotation of the α_p is due to slip or because the deformation of the high temperature β is forcing a rotation.

8.3.3.2 Analysis of microstructure at a strain equal to 0.175

Figure 8.89(a) shows the OIM of T16, the high angle (>15°) boundaries are identified by a thick black line and the low angle (1-15°) misorientations are identified by thin black lines. Four α_p grains have been identified for further examination and labelled A, B, C and D. The sub-grain misorientations and crystal rotations within each grain have been investigated and are detailed in the following section (Figures 8.90-8.94). The black speckled areas seen in parts of this OIM are due to the mis-indexing of HCP α crystal as a BCC β crystal creating a high angle misorientation which doesn't actually exist, Figure 8.89(b).

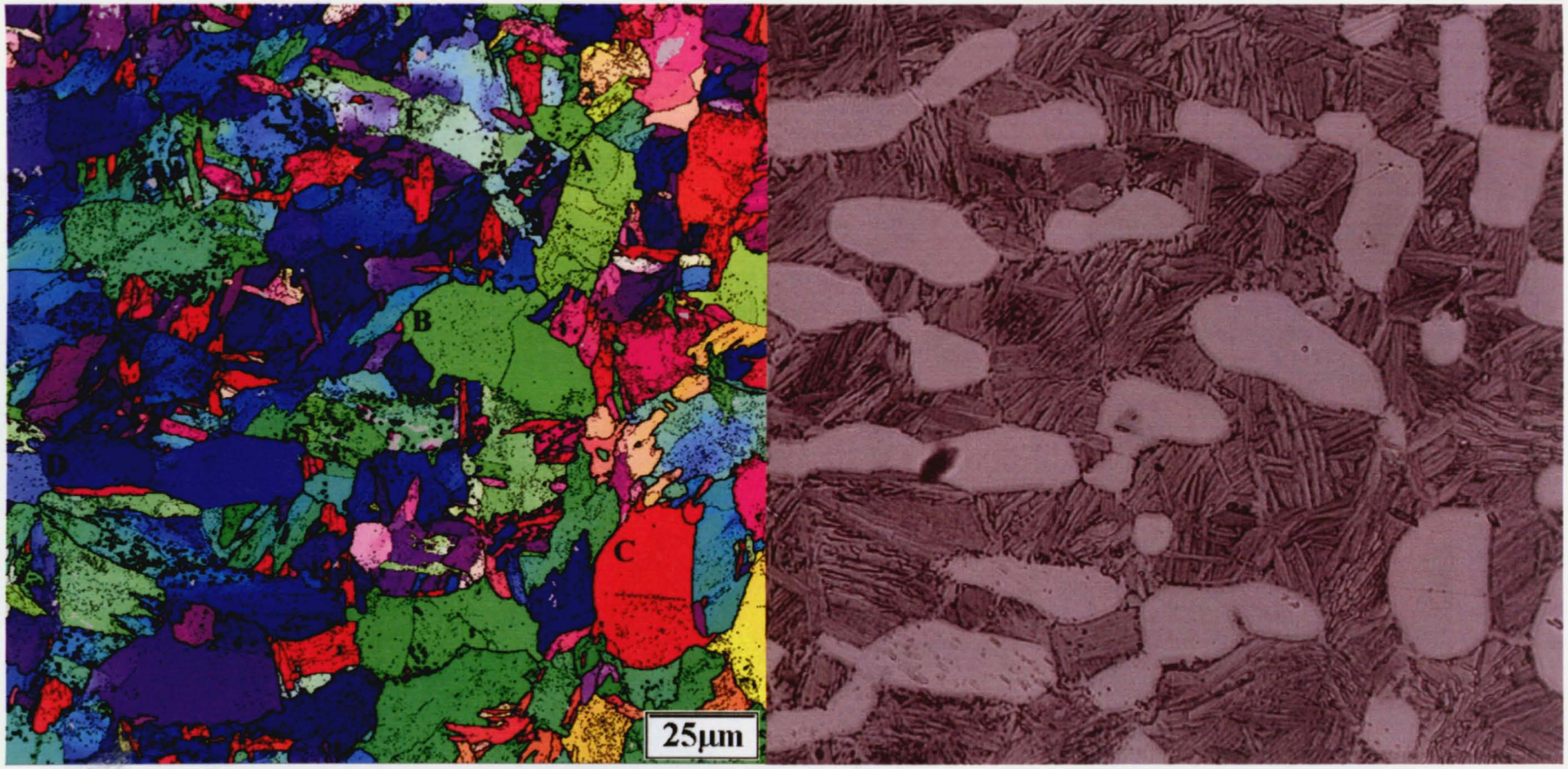

Figure 8.89 (a) IPF colouring OIM of T15 sample showing misorientations between 1-15° as a thin black line and misorientations >15° as a thick black line, Grains A-E are labelled. (b) an optical micrograph of the same area.

Initially grain A has been examined and can be seen in Figure 8.90's IPF OIM (a) and micrograph (b), the accumulated sub-grain misorienations were measured along the lines A and B and can be seen in Figure 8.90(d) and (c).

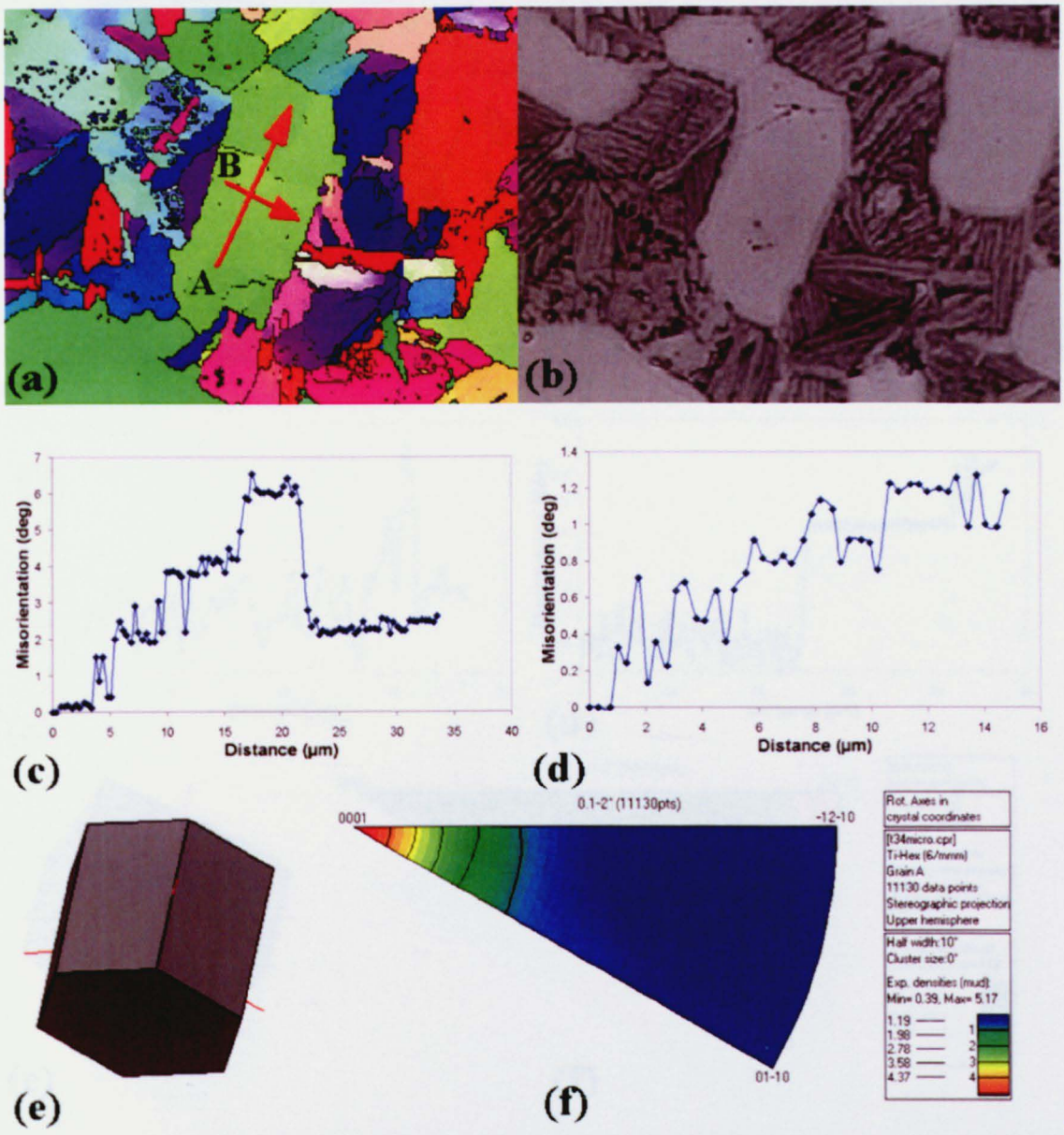

Figure 8.90 Single grain analysis of Grain A from Figure 8.85, (a) misorientation anlysis was completed along lines A and B, (b) optical micrograph of same grain, (c) misorientation profile along line A, (d) misorientation profile along line B, (e) grain orientation and (f) crystal rotation axis.

It can be seen that the misorientations in this grain accumulate along line A to a maximum curvature of approximately 7° before returning approximately 4° then gradually increasing again. Line B, also shows an accumulation along its length but with very small increases to a maximum of 1.2°. The crystal orientation of grain A is

illustrated in Figure 8.90(e) and the rotation was determined by crystal rotation axis analysis to be about the <0002> direction.

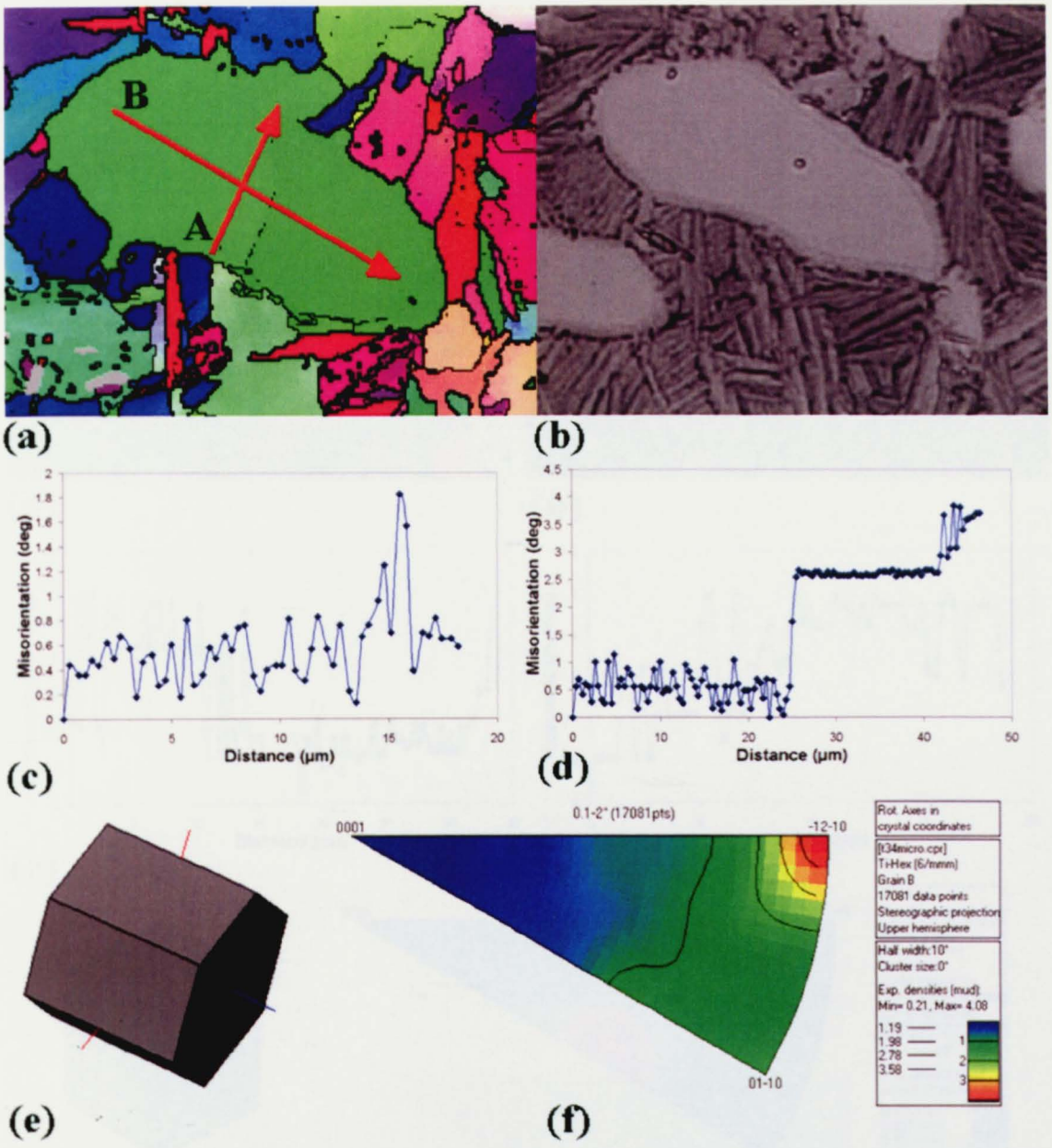

Figure 8.91 Single grain analysis of Grain B from Figure 8.85, (a) misorientation analysis was completed along lines A and B, (b) optical micrograph of same grain, (c) misorientation profile along line A, (d) misorientation profile along line B, (e) grain orientation and (f) crystal rotation axis.

Grain B, shown in Figure 8.91 has a similar basal orientation to grain A with respect to the deformation axis, however the grain rotation is different. The misorientations along line A (Figure 8.91(c)) are quite small in magnitude and oscillate between an accumulation and degradation of the grain rotation. Line B (Figure 8.91(d)) follows a similar trend before a large misorientation of approximately 3° 25μm along

the line. The crystal orientation of this grain is illustrated if Figure 8.91(e) and the rotation is about the <-12-10> directions as illustrated in Figure 8.91(f).

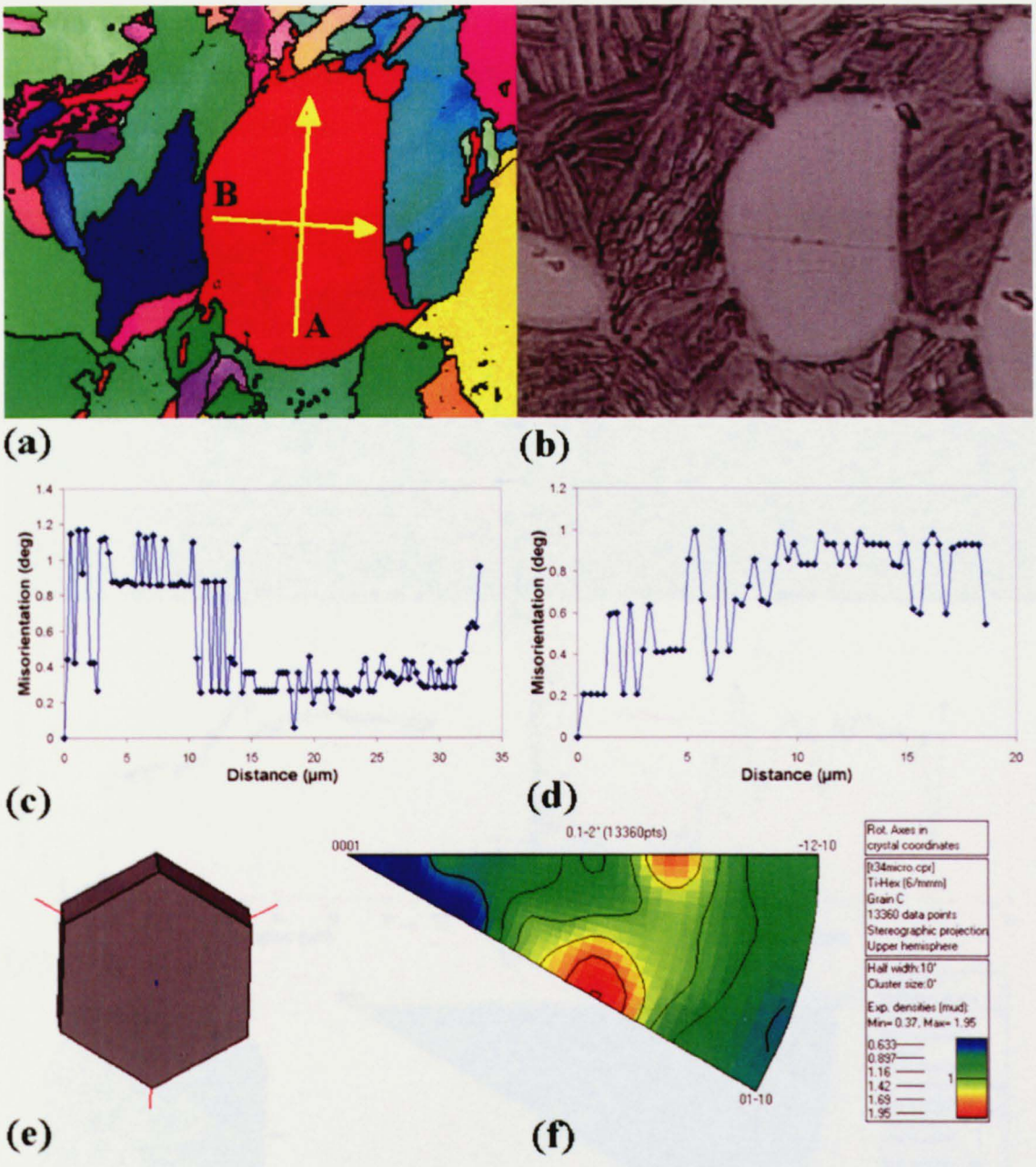

Figure 8.92 Single grain analysis of Grain C from Figure 8.85, (a) misorientation analysis was completed along lines A and B, (b) optical micrograph of same grain, (c) misorientation profile along line A, (d) misorientation profile along line B, (e) grain orientation and (f) crystal rotation axis.

Grain C is illustrated in Figure 8.92, the grain has an almost parallel basal orientation and there is very little sub-grain misorientation, never accumulating more

than a 1.2° rotation. The crystal rotation axis is less defined than in the other grains seen, but small intensities of 1.95 MRD are observed about the <10-11> directions.

Grain D is analysed in Figure 8.93, the initial orientation is illustrated in figure 8.93(e) and has an almost perfectly transverse basal orientation. There is a general accumulation in the sub-grain misorientation with a single 5° misorientaion noticeable in the misorientation profile.

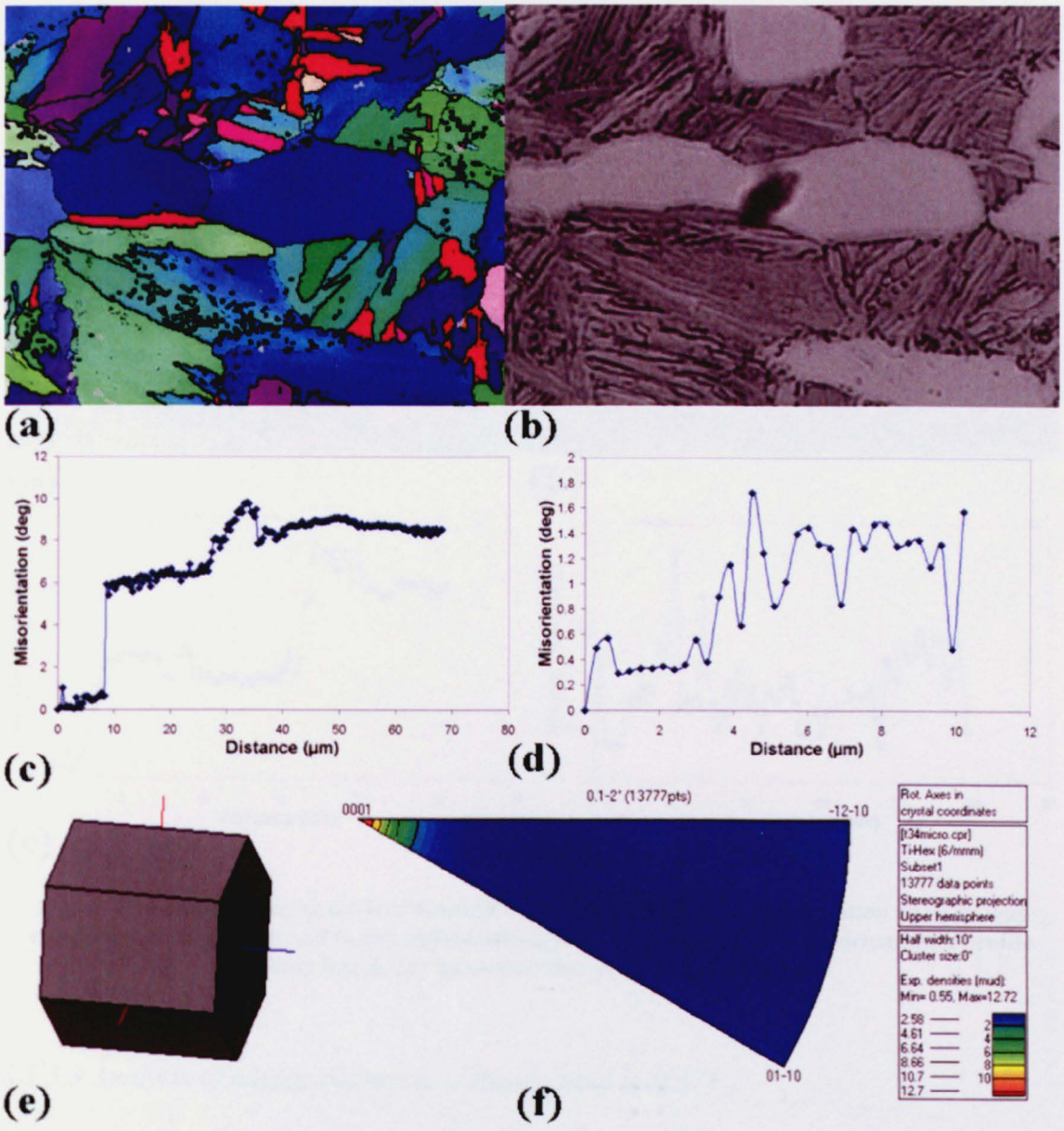

Figure 8.93 Single grain analysis of Grain D from Figure 8.85, (a) misorientation analysis was completed along lines A and B, (b) optical micrograph of same grain, (c) misorientation profile along line A, (d) misorientation profile along line B, (e) grain orientation and (f) crystal rotation axis.

The crystal rotation axis is well defined (> 12MRD) around the <0002> direction.

There is evidence within the micrograph and OIM that some α_s grains share their orientation with neighbouring α_p grains as in the case of Grain E, seen in Figure 8.94. The sub-grain misorientations were measured within this grain along lines A and B and the accumulated graphs seen in Figures 8.94(c) and (d). This may also explain to some extent the lack of radial fibre in the This may indicate that the α_p is acting as a nucleation site for the formation of α_s laths. There is also a possibility that these neighbouring grains may explain the lack of a radial fibre in the α_s texture.

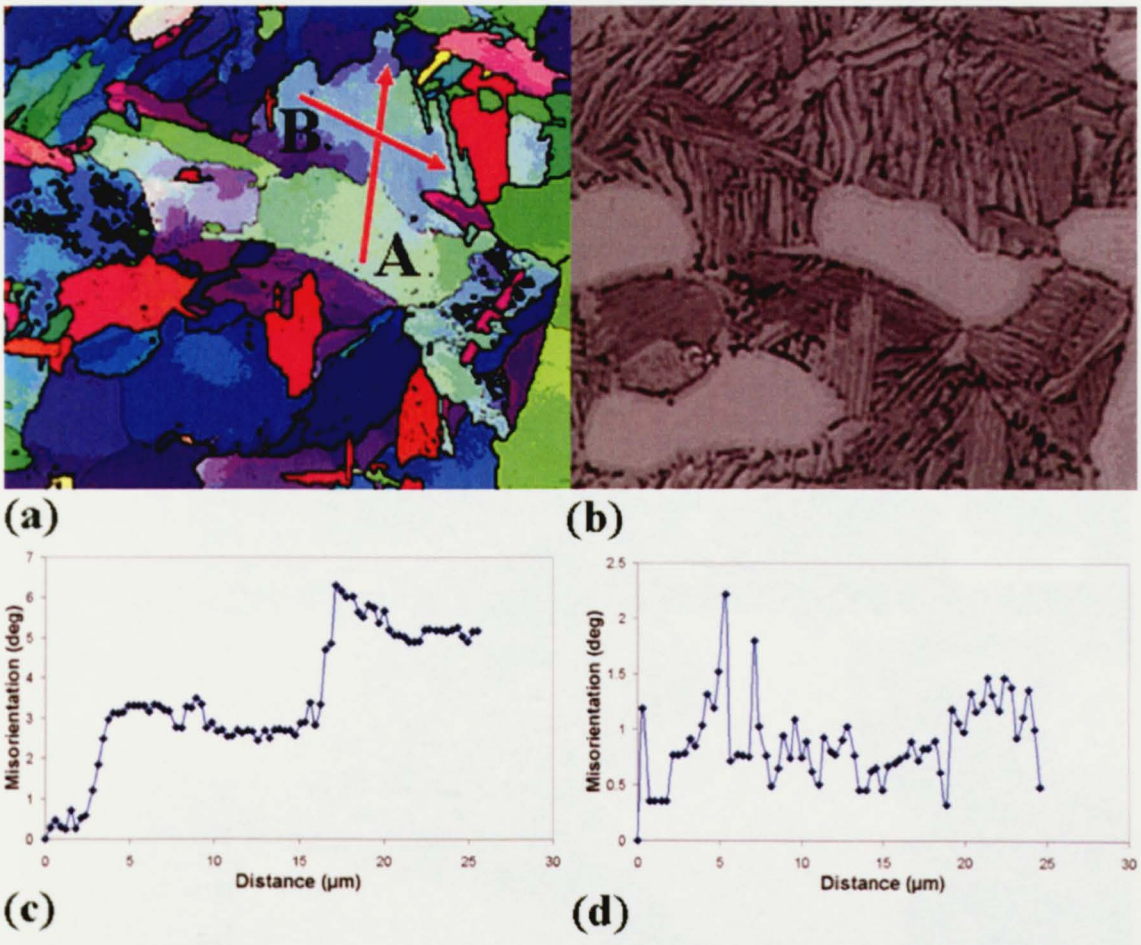

Figure 8.94 Single grain analysis of Grain E from Figure 8.85, (a) misorientation analysis was completed along lines A and B, (b) optical micrograph of same grain, (c) misorientation profile along line A, (d) misorientation profile along line B.

8.3.3.3 Analysis of microstructure at a strain equal to 0.375

For this particular condition we have again focussed on 4 α_p grains which are labelled [A] through to [D], seen in Figure 8.95(a). All 4 grains exhibit a deformation substructure that has grain interiors displaying relatively sparse linear boundaries whilst the grain boundary regions have a higher density of sub-boundaries producing a more

equiaxed structure. The optical micrograph of the same area can be seen in Figure 8.95(b) and again illustrates the mis-indexing responsible for the black areas in the OIM. As in Section 8.4.2, to gauge the level of deformation within these grains misorientation profiles were carried out across complete grains [C] and [D] which are also shown in Figure 8.96 and labelled (a-d).

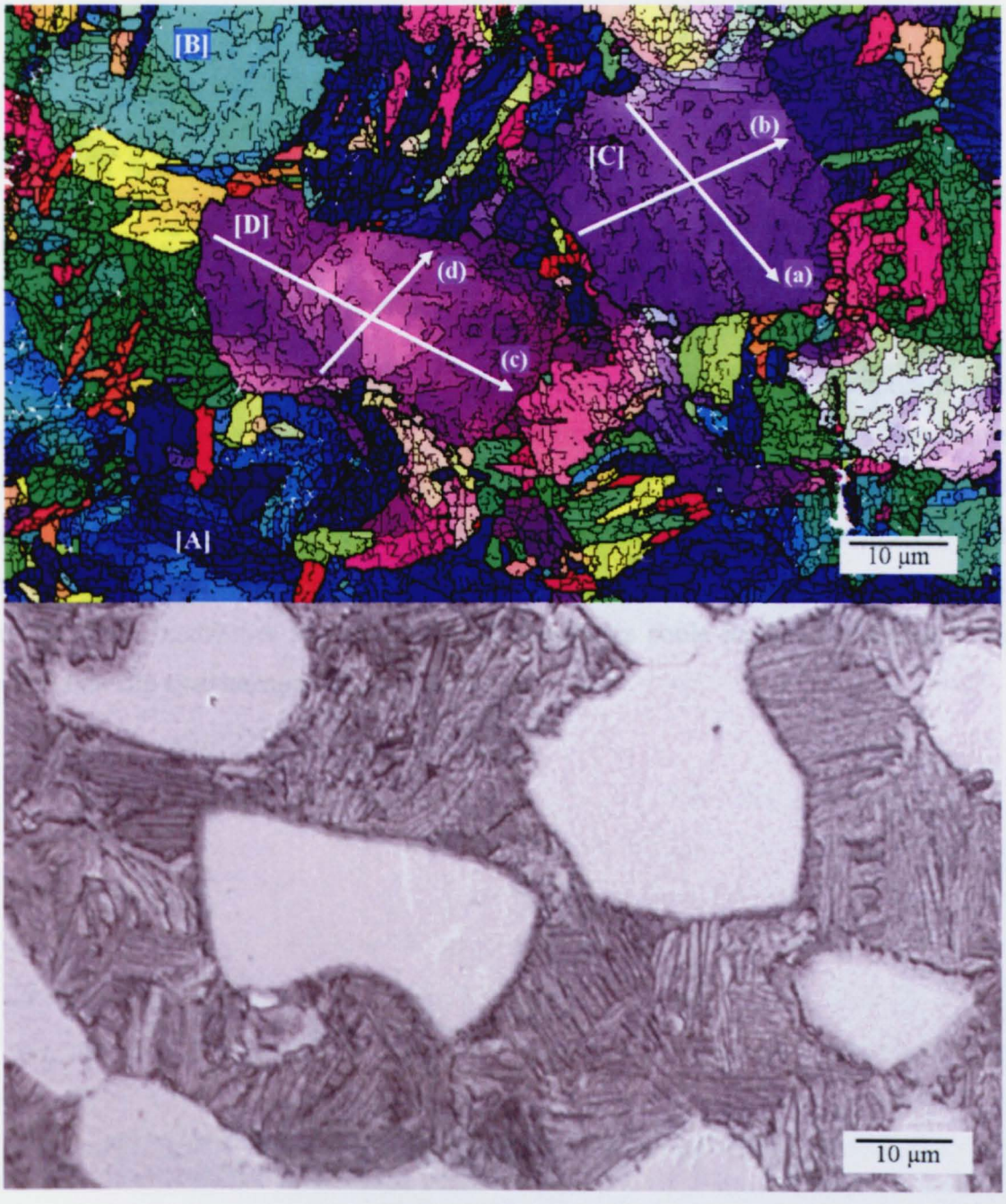

Figure 8.95 (a) IPF colouring OIM of T15 sample showing misorientations between 1-15° as a thin black line and misorientations >15° as a thick black line, Grains A-E are labelled. (b) an optical micrograph of the same area.

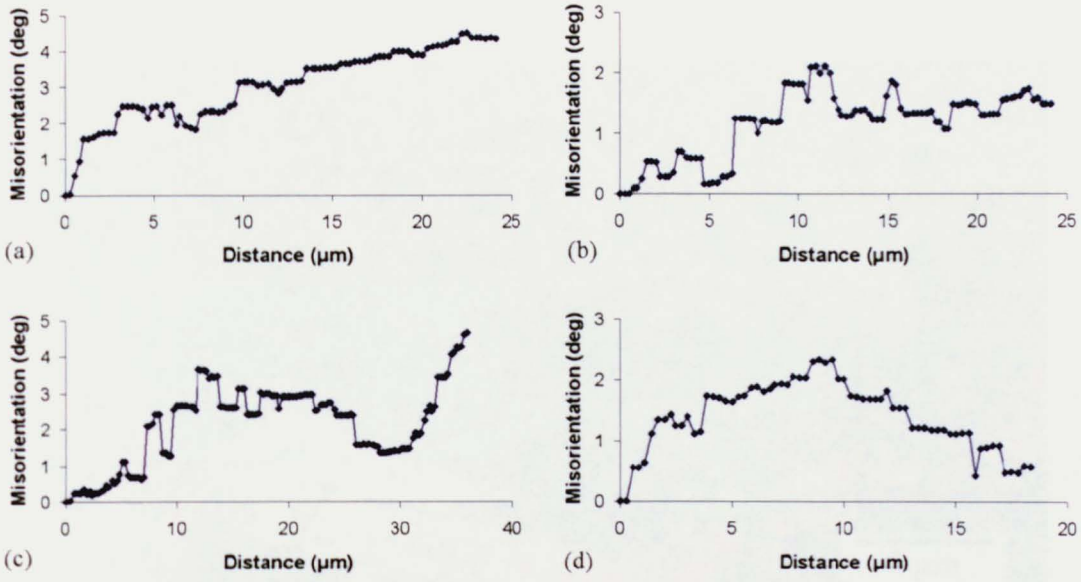

Figure 8.96 Misorientation profiles for grains C and D along lines (a), (b), (c) and (d).

For grain [C] there is a gradual misorientation accumulation of approximately 5° across the grain, whereas, for grain [D] the misorientation builds up to a maximum in the centre of the grain with the most significant misorientation gradient near the grain boundaries. However, in all cases the accumulated misorientation is less than 5° with no single misorientation greater than 1°. This low level of misorientation and the linear nature of the boundaries suggest that these boundaries could be directly related to the individual slip systems operating within the α_p.

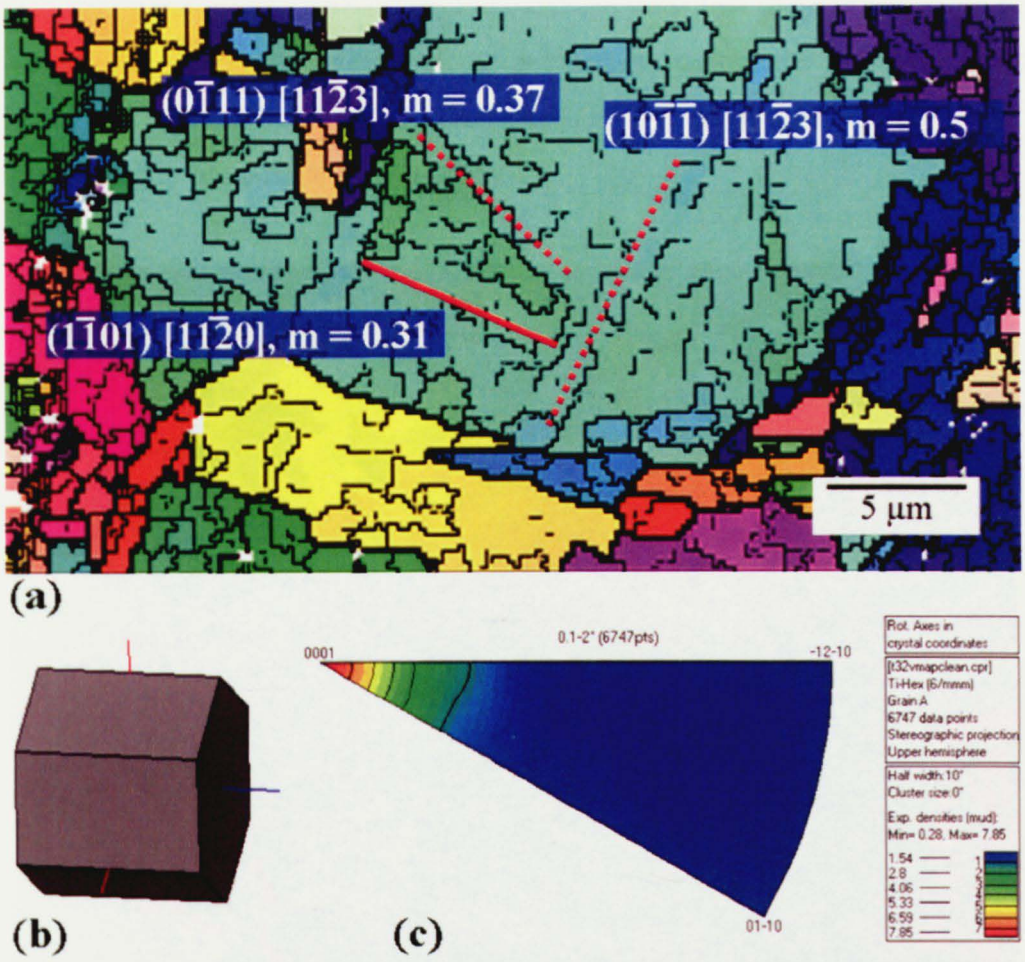

Figure 8.97 Single grain analysis of Grain B from Figure 8.91, (a) trace analysis was completed against linear substructure, (b) grain orientation and (c) crystal rotation axis.

Figures 8.97 to 8.99 show grains [B] to [D] with corresponding traces of possible slip systems. In most cases the most well defined linear boundaries have a slip trace with a relatively high Schmid factor (>0.2) corresponding to it, suggesting that these linear boundaries correspond directly to active slip systems, a technique that was utilised in the literature (Bridier, 2005). The crystal orientation of grain B can be seen in Figure 8.93(b) and the crystal rotation axis can be seen in Figure 8.93(c), again showing a rotation about the <0002> directions.

Looking at grain [D] (Figure 8.99) as a further example it can be seen that there are at least five slip systems virtually parallel with the linear substructure (1 <a>Pr, 2 <a>Py, 1<c+a>Py, and 1<c+a>Py2) suggesting that these are active slip systems. In most cases where there were both <a> and <c+a> type slip systems potentially active on the same plane, i.e. the prismatic plane, there was a difference in Schmid factor of at

least 0.1 between the possible active slip systems making it relatively simple to establish the operating slip system . In turn, this suggests that there is a mixture of <a> and <c+a> slip operating within the α_p under these deformation conditions as has previously been stated by Paton. & Backofen (1970) and Williams et al. (2002) for commercial purity titanium and Ti-Al alloys.

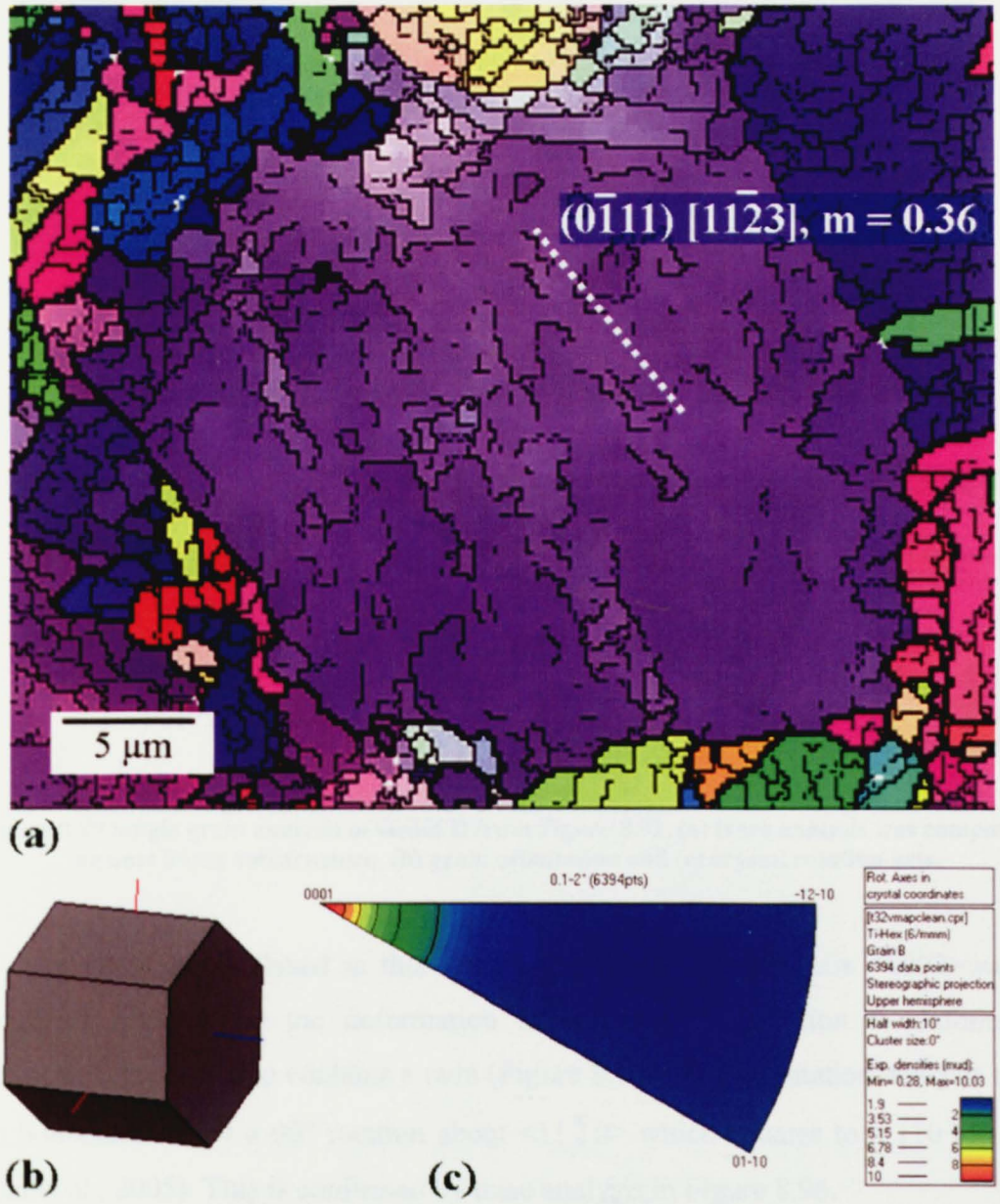

Figure 8.98 Single grain analysis of Grain C from Figure 8.91, (a) trace analysis was completed against linear substructure, (b) grain orientation and (c) crystal rotation axis.

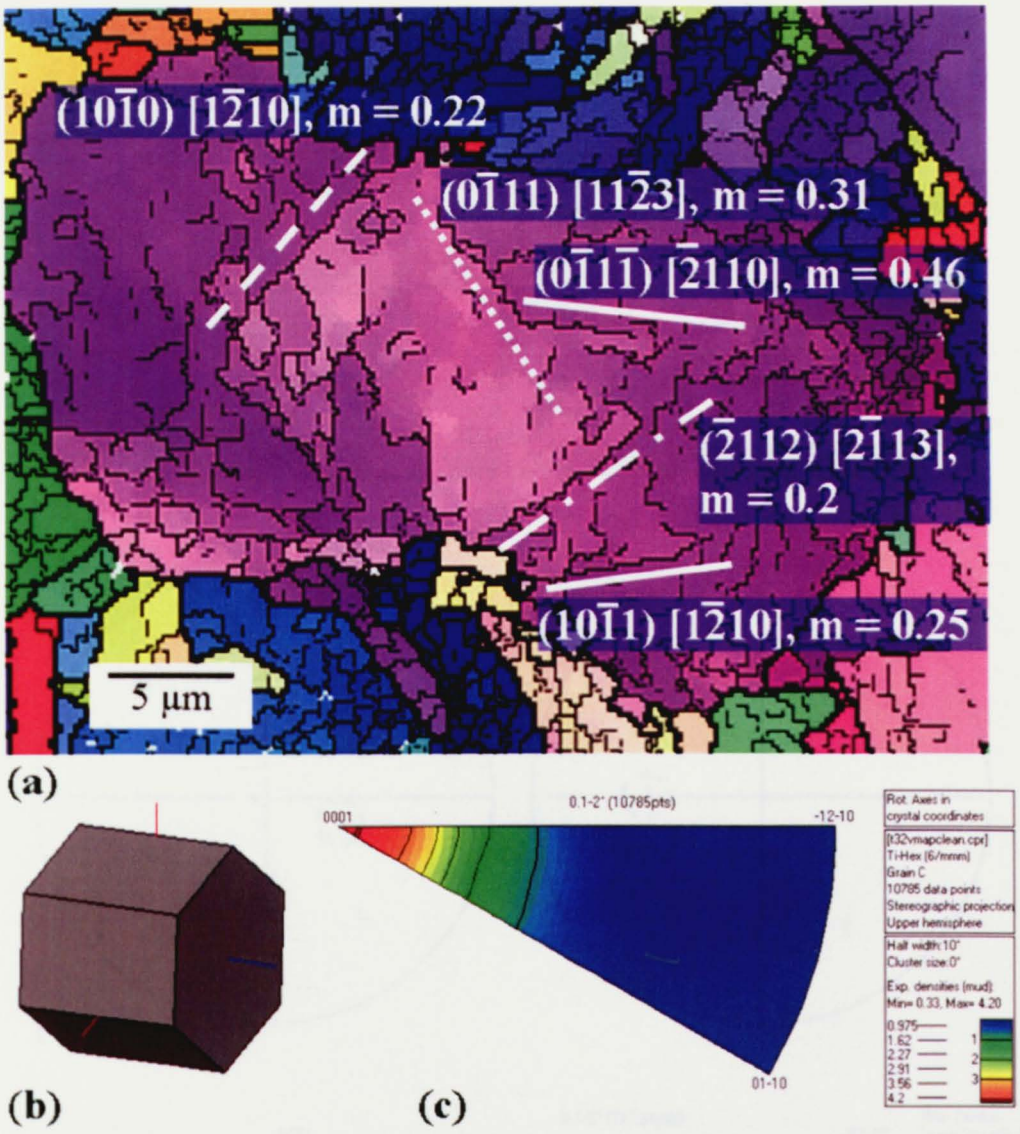

Figure 8.99 Single grain analysis of Grain D from Figure 8.91, (a) trace analysis was completed against linear substructure, (b) grain orientation and (c) crystal rotation axis.

In all grains analysed in this sample the crystal rotation axis <0002>was the determined rotation for the deformation substructure. In addition to deformation substructure, grain A also contains a twin (Figure 8.100). Misorientation analysis of the twin boundaries show a 90° rotation about <11$\bar{2}$0> which equates to a {10$\bar{1}$2} twin (Chun et al., 2005). This is confirmed by trace analysis in Figure 8.96.

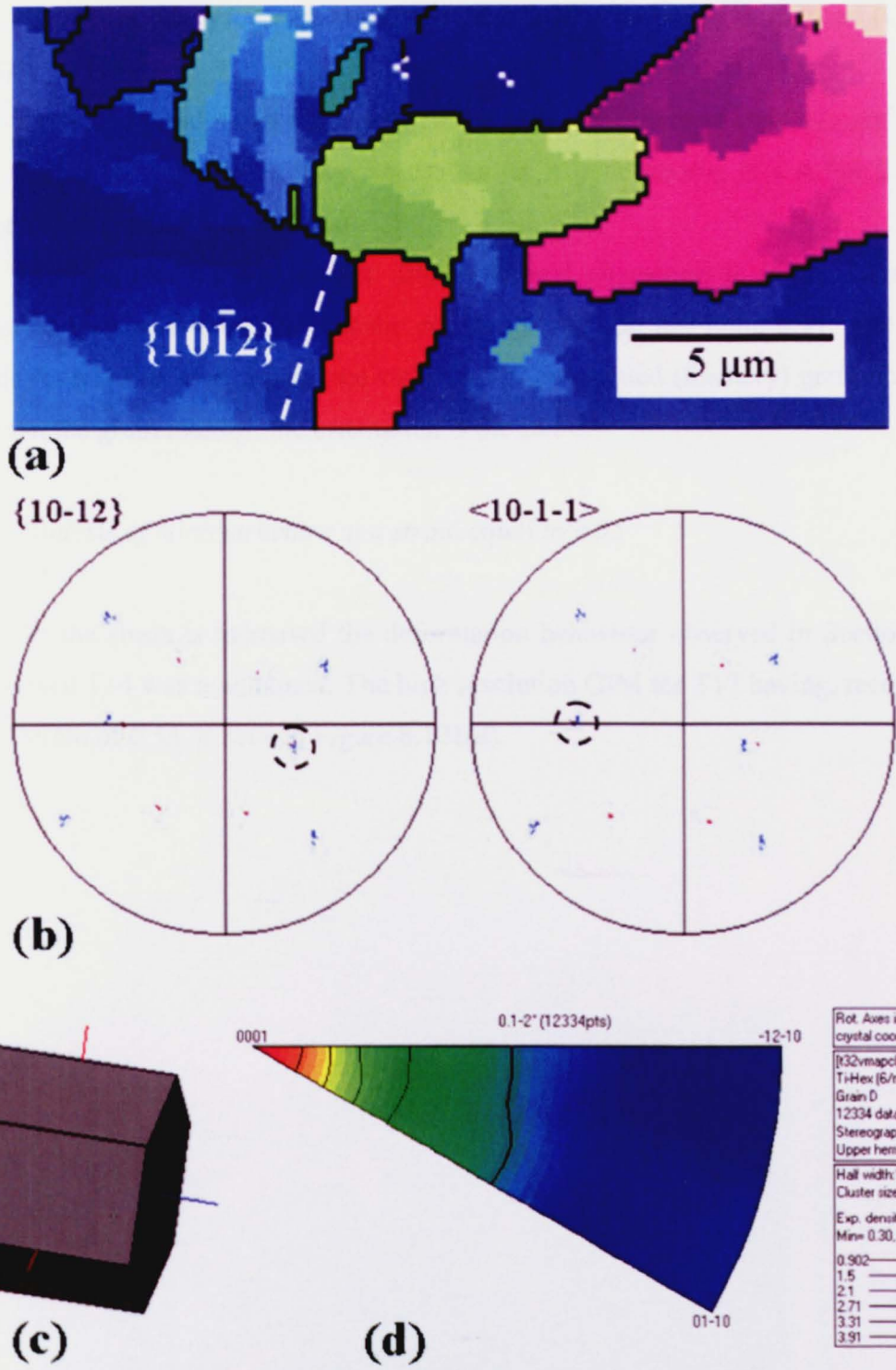

Figure 8.100 Single grain analysis of Grain A from Figure 8.91, (a) Trace analysis was completed along the twin boundary, (b) {10-12} and <10-1-1> show shared twin planes and directions, (c) orientation and (d) crystal rotation axis.

It should be noted that for this condition very few twins were even observed in low magnification optical analysis. This would suggest that for this material at this strain level and temperature and strain rate twinning is not a major deformation mechanism. Three possible reasons for the absence of twinning are;

1. With a relatively high strain the likelihood of twinning is reduced (Chun et al., 2005)

2. The aluminium content suppresses twinning (Williams et al, 2002), and

3. The α_p may not be fully constrained as it is deforming in a softer β matrix leading to less requirement for twinning.

Furthermore, another notable microstructural characteristic is the serrated α_p boundaries visible on the OIM and the optical micrograph in Figure 8.91. The EBSD analysis reveals that even though the etch attacks the serrated (feathery) grain boundary more than the grain interior, the orientation is the same.

8.3.3.4 Analysis of microstructure at a strain equal to 0.55

As the strain is increased the deformation behaviour observed in Section 8.4.3 on specimen T14 was maintained. The high resolution OIM for T17 having, received an applied strain of 0.55, is seen in Figure 8.101(a).

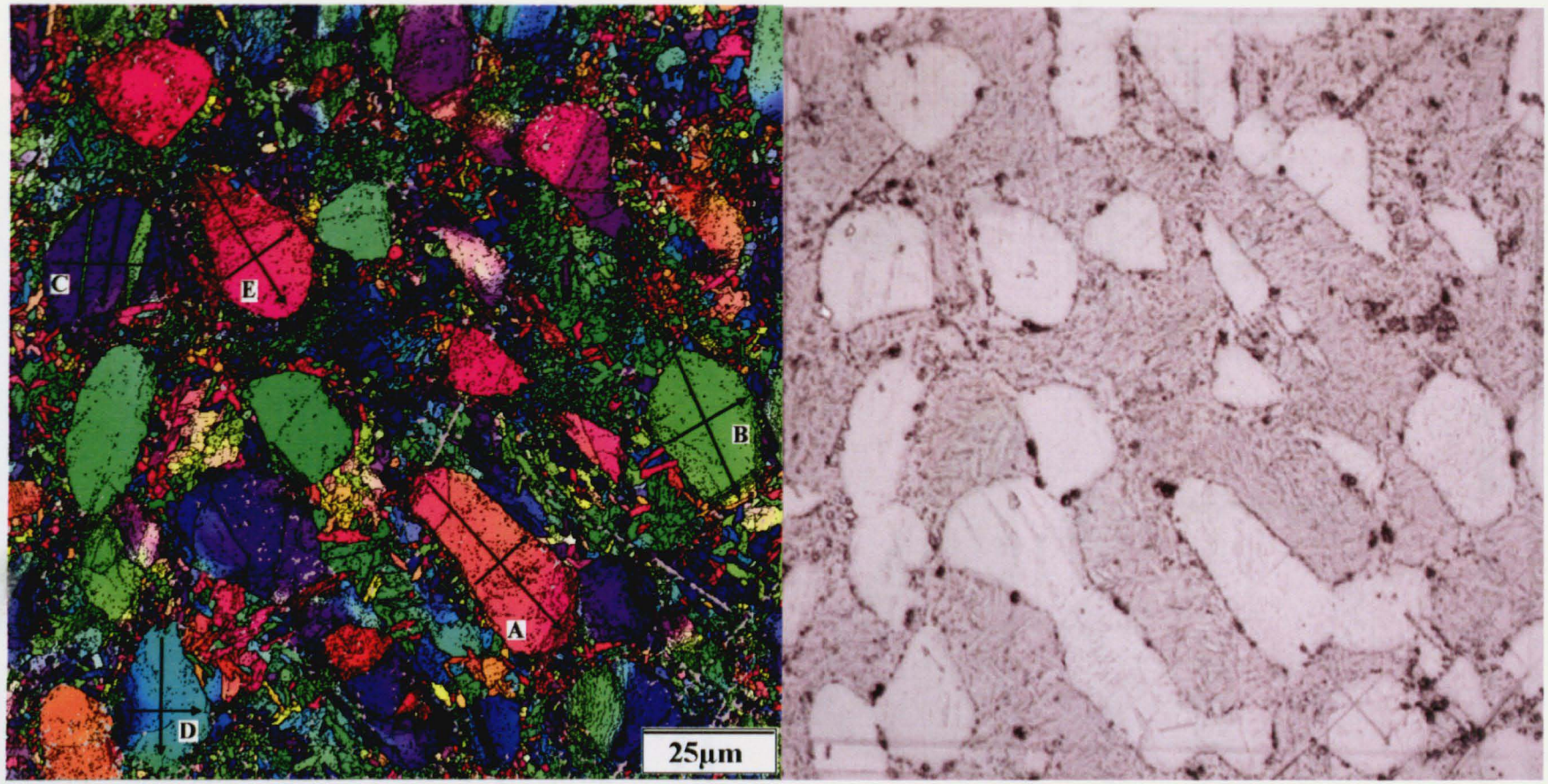

Figure 8.101 (a) IPF colouring OIM of T15 sample showing misorientations between 1-15° as a thin black line and misorientations >15° as a thick black line, Grains A-E are labelled. (b) an optical micrograph of the same area.

Again a number of grains were analysed, labelled [A] to [E] in Figure 8.101(a), and the micrograph of the same area can be seen in Figure 8.101(b). Once more there is evidence of feathery alpha, as the α_p grain boundaries are serrated and effected differently by the etch.

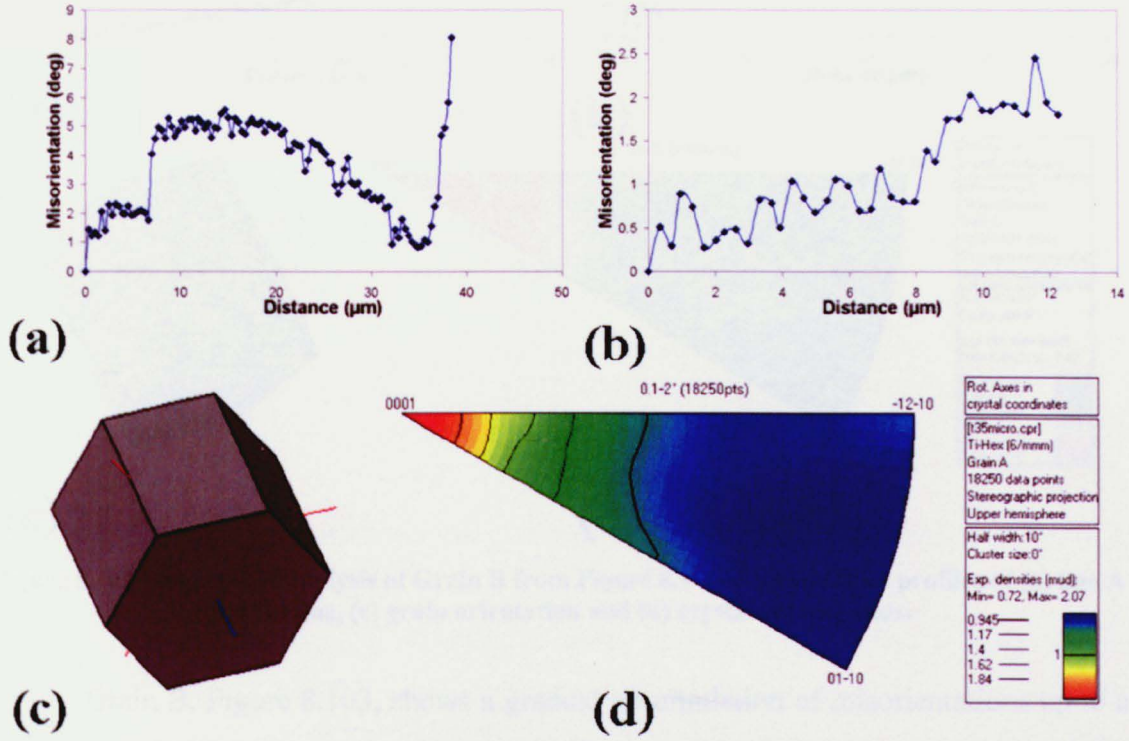

Figure 8.102 Single grain analysis of Grain A from Figure 8.97, Misorientation profiles of (a) line A and (b) line, (c) grain orientation and (d) crystal rotation axis.

Grain A exhibits an accumulation of misorientations along line A to a maximum of approximately 6° the rotating back before a steep rise is misorientation of approximately 8°. This profile can be seen in the Figure 8.102(a) and the misorientation profile for line B can be seen in Figure 8.102(b), the grain orientation is illustrated in Figure 8.102(c) and the crystal rotation axis is again <0002>.

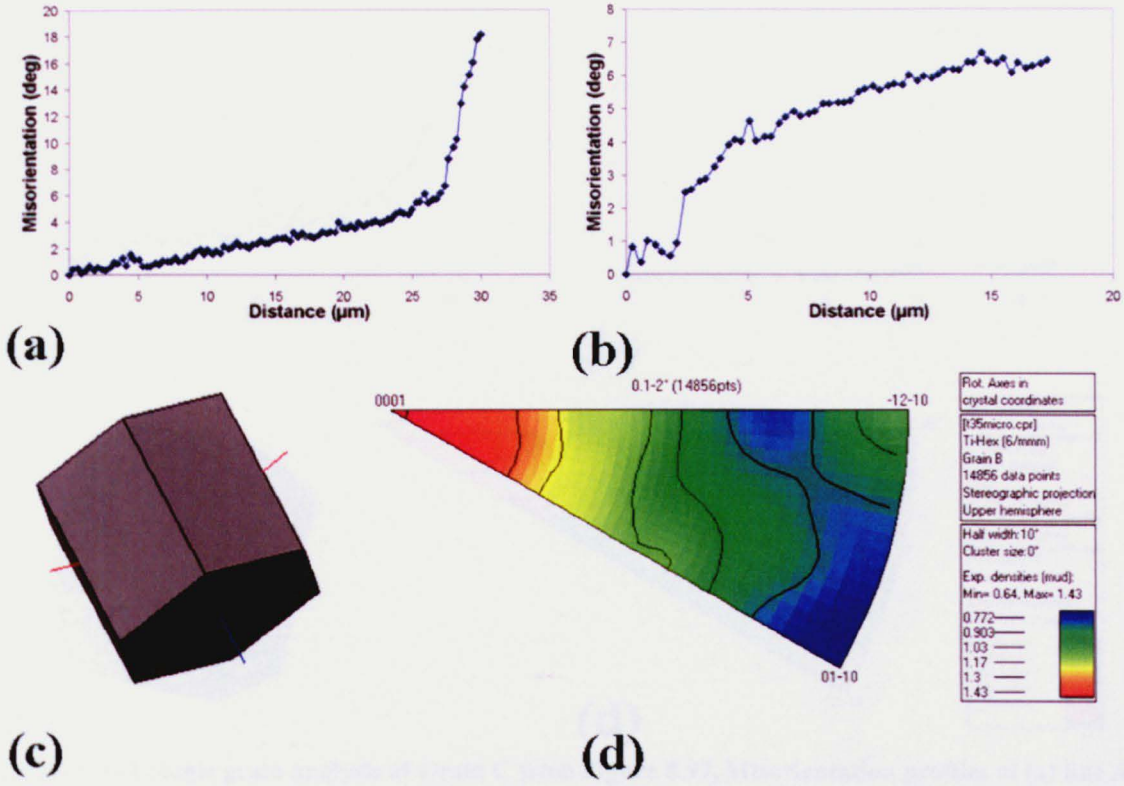

Figure 8.103 Single grain analysis of Grain B from Figure 8.97, Misorientation profiles of (a) line A and (b) line, (c) grain orientation and (d) crystal rotation axis.

Grain B, Figure 8.103, shows a gradual accumulation of misorientations up to a maximum of 18° and again the most significant misorientation gradient occurs near the grain boundaries. A rotation about the <0002> crystal axis is observed.

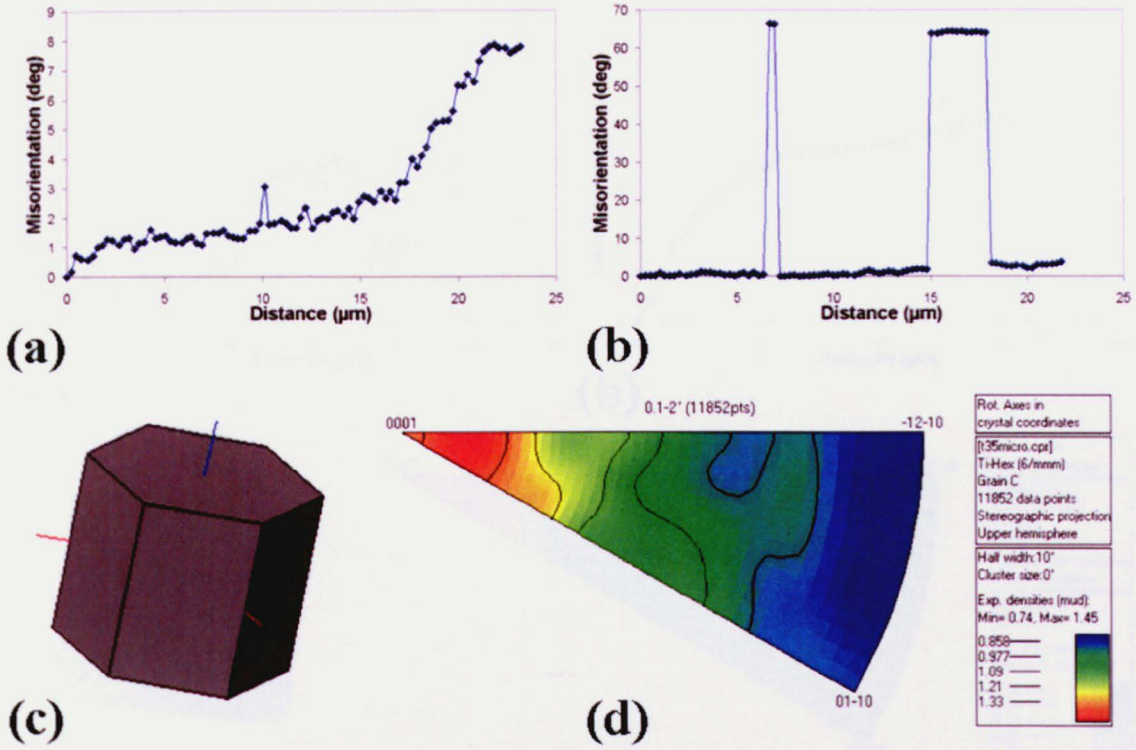

Figure 8.104 Single grain analysis of Grain C from Figure 8.97, Misorientation profiles of (a) line A and (b) line, (c) grain orientation and (d) crystal rotation axis.

It is interesting that in an OIM of this size there is little evidence of twinning as was the case with Grain A from T14, however, Figure 8.96 illustrates grain C, a twinned grain, and shows the extent of sub-grain misorientation (Figure 8.104(a) and (b)) and the grains orientation (Figure 8.104(c))and common rotation axis Figure 8.104(d). The twin was analysed as documented previously and was determined to be a $\{10\bar{1}1\}$ Twin.

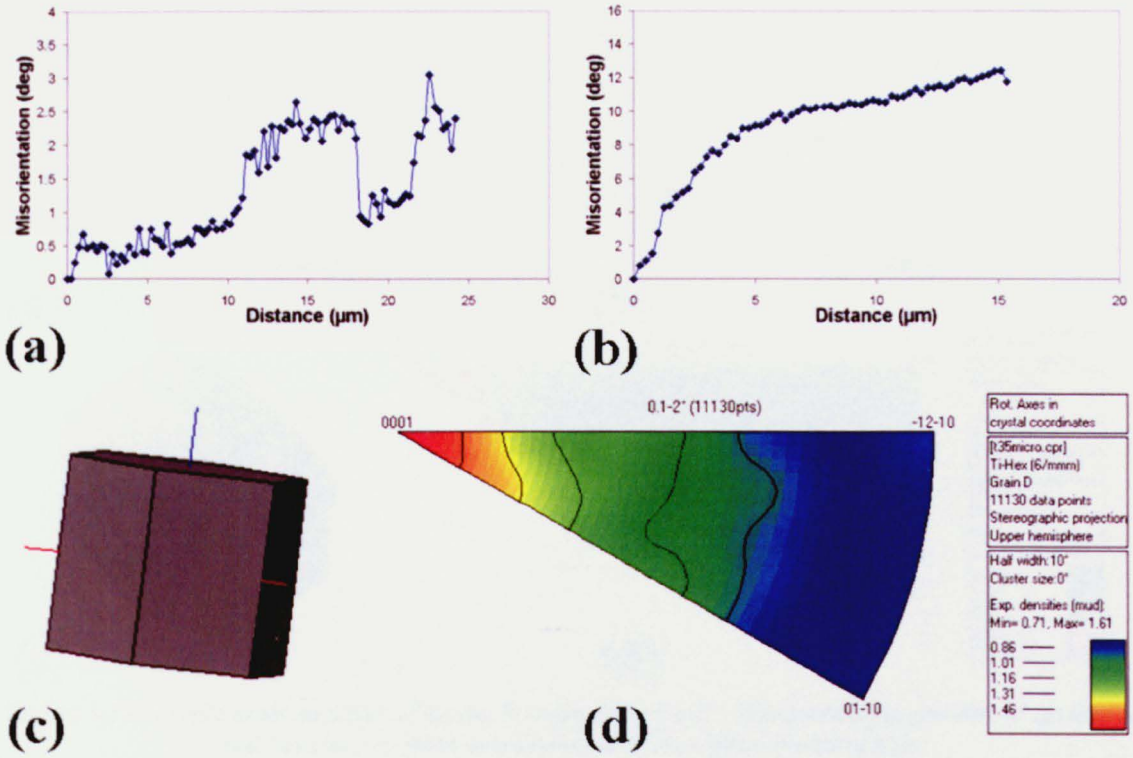

Figure 8.105 Single grain analysis of Grain D from Figure 8.97, Misorientation profiles of (a) line A and (b) line, (c) grain orientation and (d) crystal rotation axis.

Grain D (Figure 8.105), also exhibits a high accumulation of sub-grain misorientations (>12º) in the larger dimension with the major misorientation build up at grain boundaries. In the transverse plane only a small misorientation accumulation is recorded,< 3.5MRD. Figure 8.105(c) shows the crystal orientation of grain D, an almost perfectly transverse basal orientation. The crystal rotation axis is, again, about the <0002> direction.

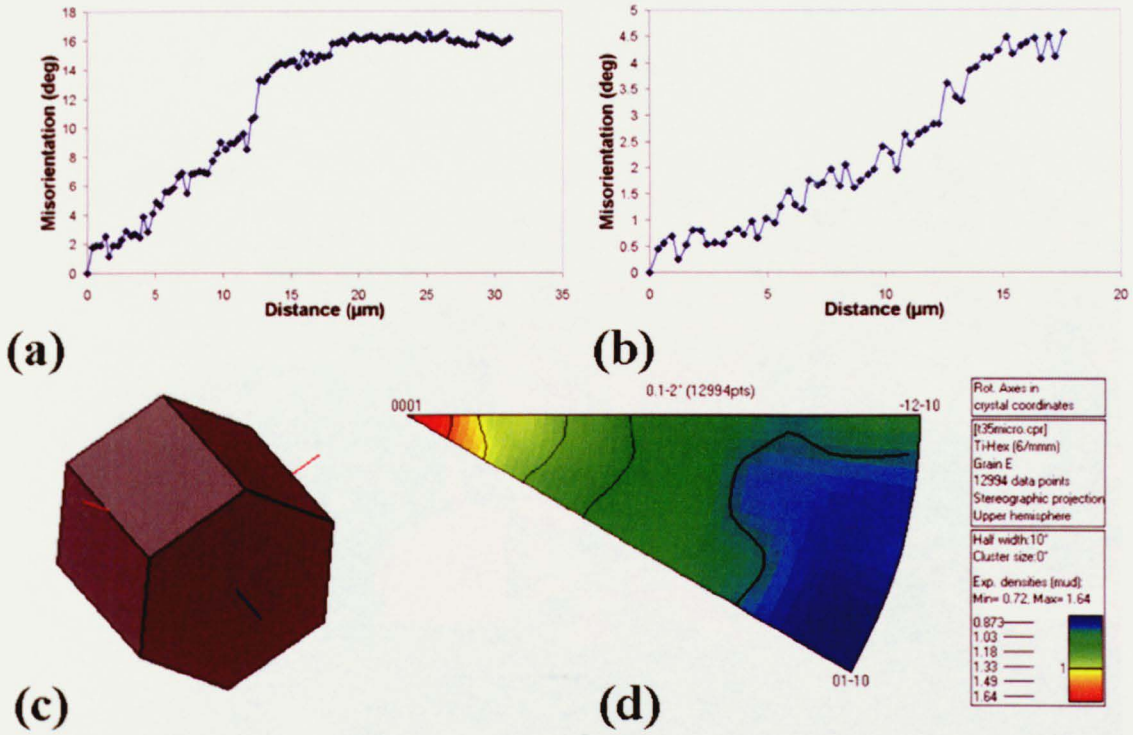

Figure 8.106 Single grain analysis of Grain E from Figure 8.97, Misorientation profiles of (a) line A and (b) line, (c) grain orientation and (d) crystal rotation axis.

The final grain analysed, Grain E, shown in Figure 8.106 possesses an accumulated misorientation of over 16° (Figure 8.106(a)) and the preferred crystal rotation axis is the <0002>. Interestingly, there is a again an increase in the occurrence of rotations about the <-12-10> crystal axis.

8.3.3.5 Analysis of microstructure at a strain equal to 0.75

Figure 8.107 shows the OIM of Sample T15, deformed to a strain of 0.75, again separate grains have been identified for further analysis and have been labelled A to F.

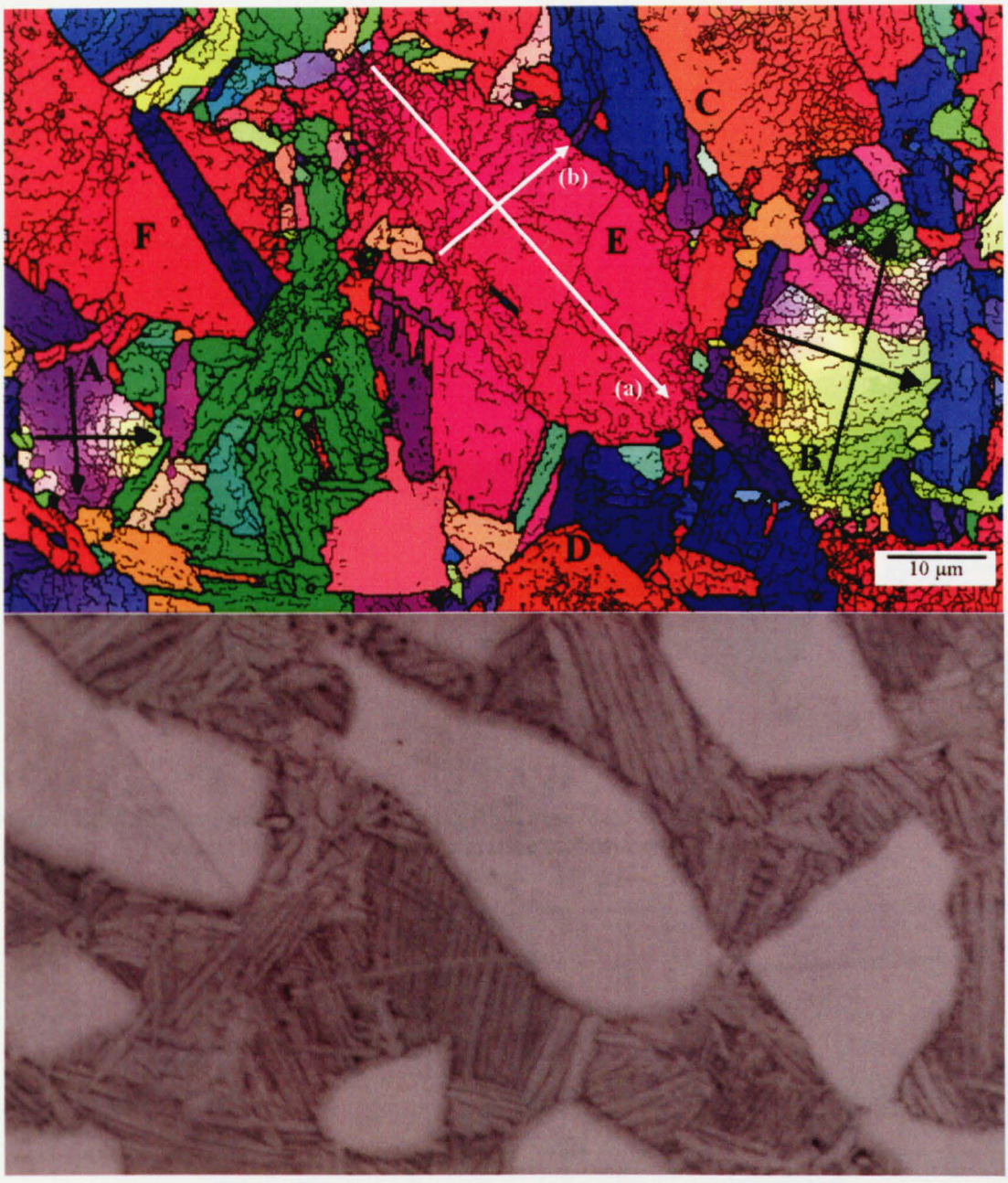

Figure 8.107 (a) IPF colouring OIM of T14 showing misorientations 1-15° as a thin black line and misorientations >15° as a thick black line. (b) an optical micrograph of the same area.

This micrograph shows the clearest evidence of feathery alpha seen in this work so far. The serrated boundaries noticeable on grains B and E are also seen clearly on the optical micrograph. The deformation substructure exhibited in the OIM is again linear within the grain interior and denser and equiaxed towards the grain boundaries. Grain A although relatively small exhibits a large amount of deformation substructure (>18°) over 14μm and, as is now becoming quite common, the misorientations are concentrated near the grain boundary.

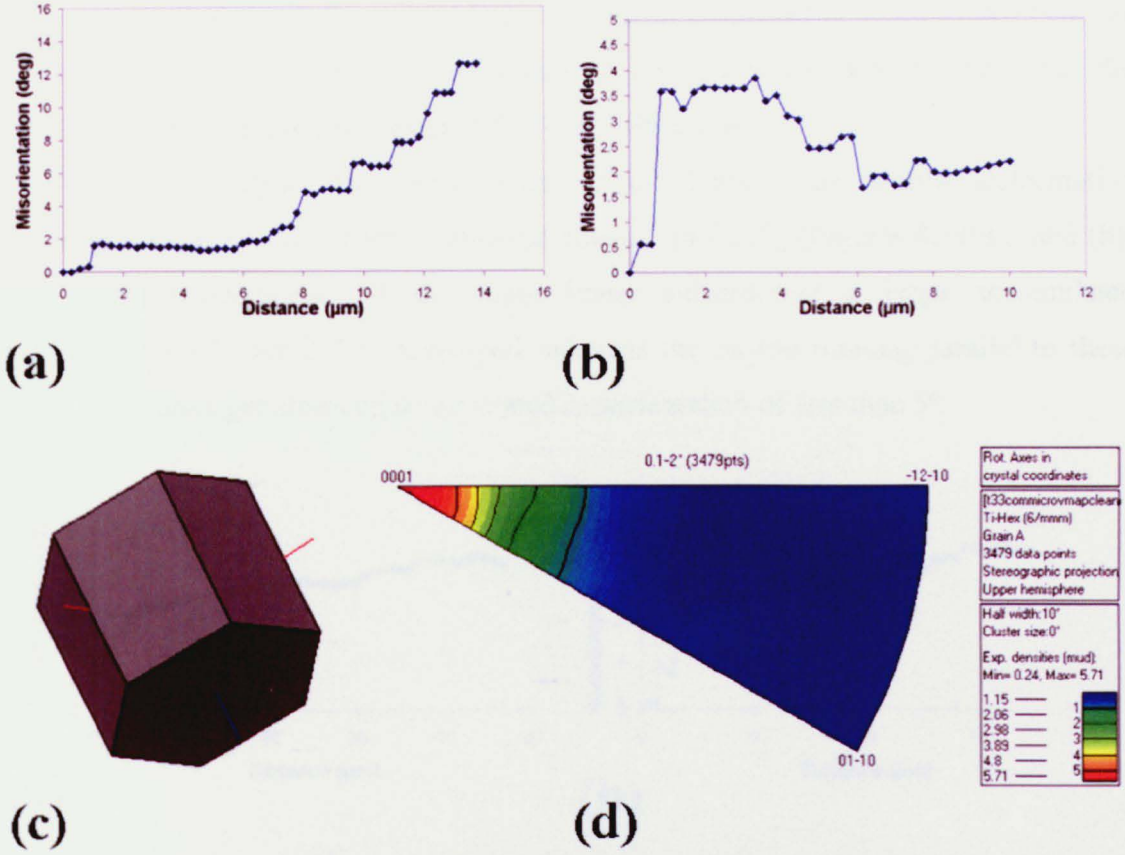

Figure 8.108 Single grain analysis of Grain A from Figure 8.103, Misorientation profiles of (a) line A and (b) line, (c) grain orientation and (d) crystal rotation axis.

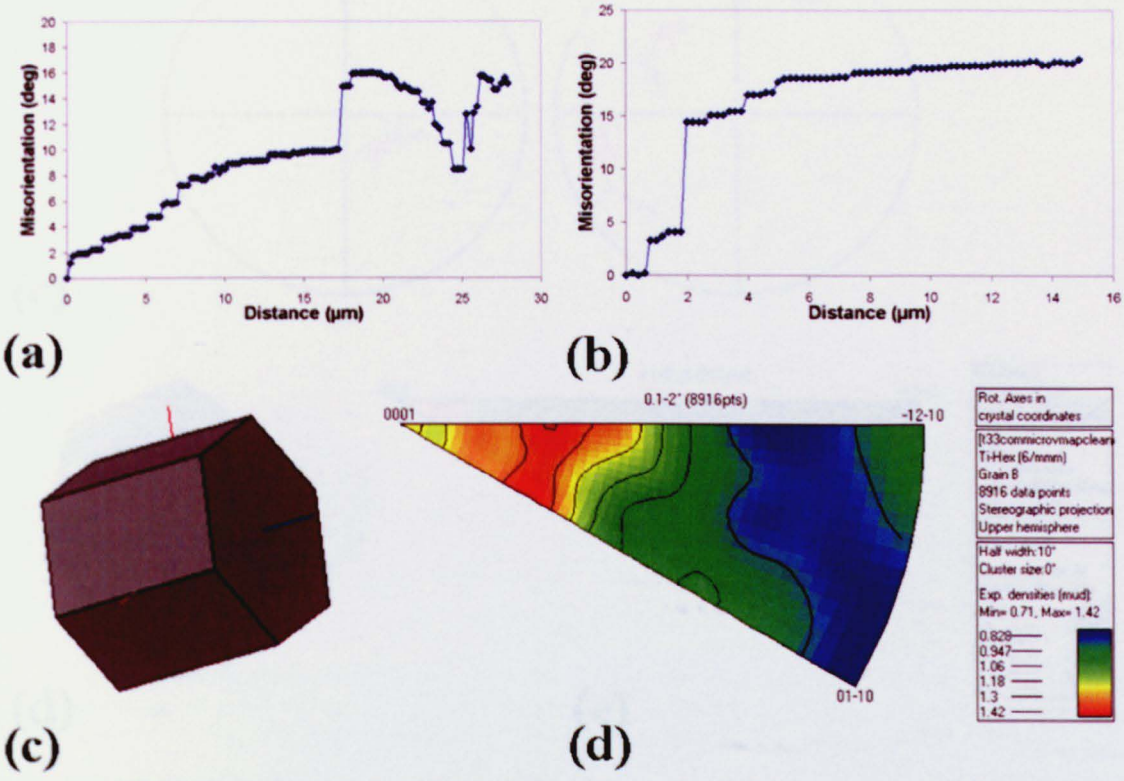

Figure 8.109 Single grain analysis of Grain B from Figure 8.103, Misorientation profiles of (a) line A and (b) line, (c) grain orientation and (d) crystal rotation axis.

Grain B also exhibits a very large amount of deformation concentrated near the grain boundaries. The crystal rotation axis in this grain has moved away from the <0002> direction and is now closer to the <???> direction.

Further analysis on grains C and D all display very similar deformation characteristics, however, misorientation profiles of grain [E] (Figures 8.110(a) and (b)) show that perpendicular to the main linear substructure a large accumulated misorientation of over 25° is developed, whereas the profile running parallel to these linear boundaries generates an accumulated misorientation of less than 5°.

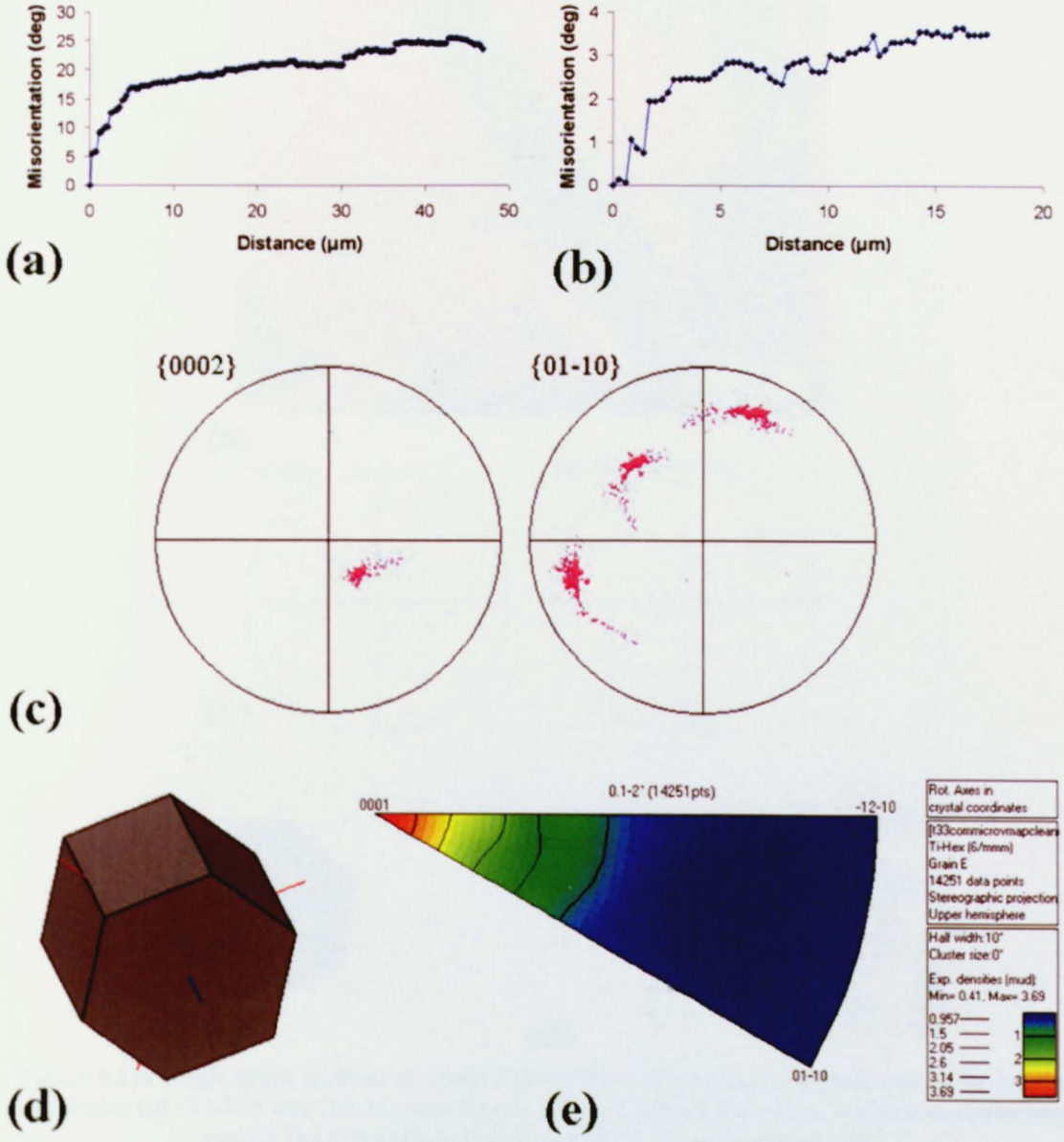

Figure 8.110 Single grain analysis of Grain E from Figure 8.103, Misorientation profiles of (a) line A and (b) line, and the (c) {0002} and {0110} pole figures of grain E with (d) the 3-D grain orientation and (e) crystal rotation axis.

Trace analysis in this grain also showed no correspondence of highly stressed slip systems with the deformation substructure. This was the case for all the grains analysed, suggesting the deformation microstructure has become complex making EBSD analysis of slip system activity virtually impossible. Like the OIM's in Figure 8.100 and 8.101 from sample T14 and T16, the OIM in Figure 8.111(a) also contains a twin in grain F. This twin, however, does not appear to satisfy any of those suggested in the literature, Chapter 2.

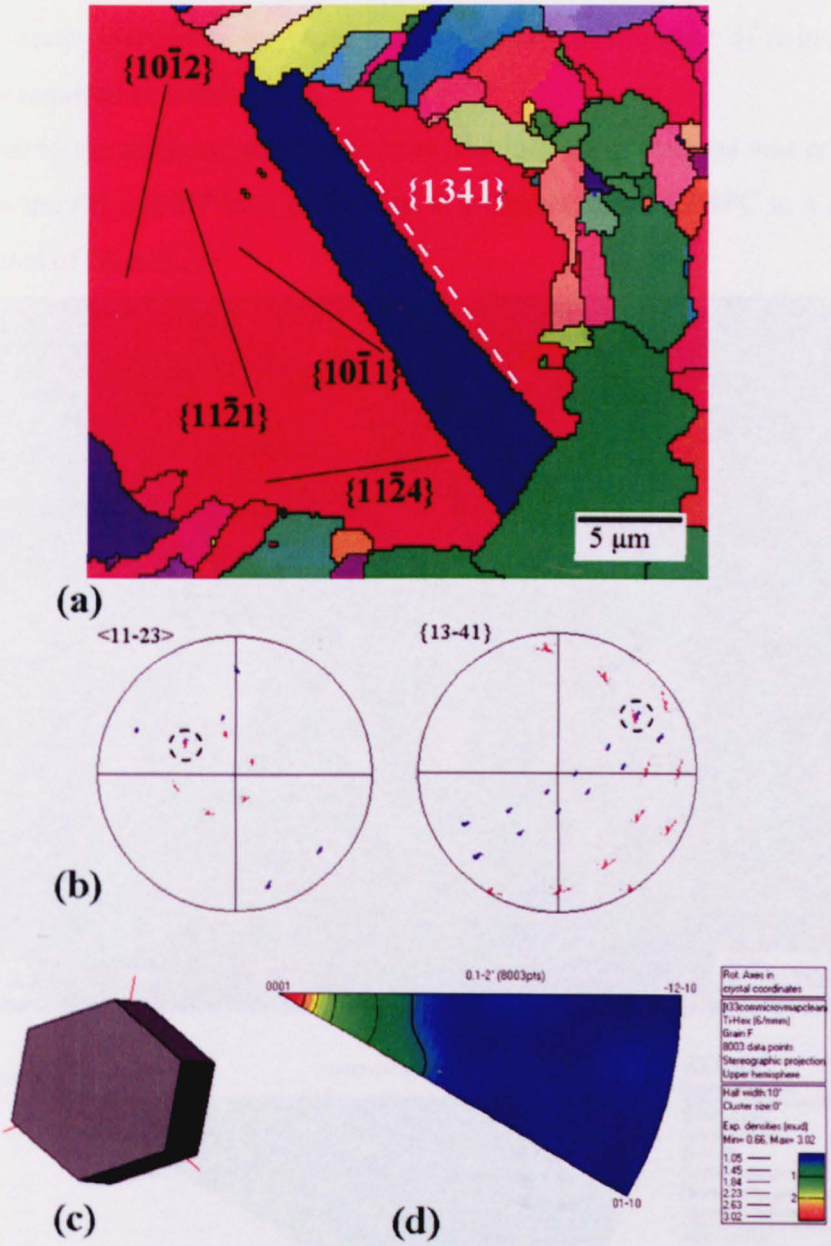

Figure 8.111 Single grain analysis of Grain F from Figure 8.103, (a) Trace analysis of the wtwin boundaries (b) <11-23> and {13-41} pole figures showing shared directions and planes of the twin and (c) the 3-D grain orientation and (d) crystal rotation axis.

Extensive analysis showed that twin parent and child had common $\{10\bar{1}2\}$, $\{10\bar{1}1\}$, $\{11\bar{2}1\}$, and $\{10\bar{2}4\}$ planes whose traces are shown in Figure 8.111. Clearly none of the traces in Figure 8.107(a) match, suggesting a relatively rare twin has been observed. There is also the possibility that the material has been further deformed after twinning, however, this seems unlikely as the twin boundaries are straight and parallel and had the same misorientation across the whole boundary. It is tempting to suggest from the data we have that the twin occurs on the $\{13\bar{4}1\}$ plane with a $<11\bar{2}3>$ shear direction, however, there is no evidence in the literature of this type of twin and as such more work is required to confirm this.

Further to the strain accumulation tests, the following analysis was completed on samples from the D5 and D7 tests completed at a temperature of 990°C to a strain of 0.7 with strain rates of 20 and $2s^{-1}$.

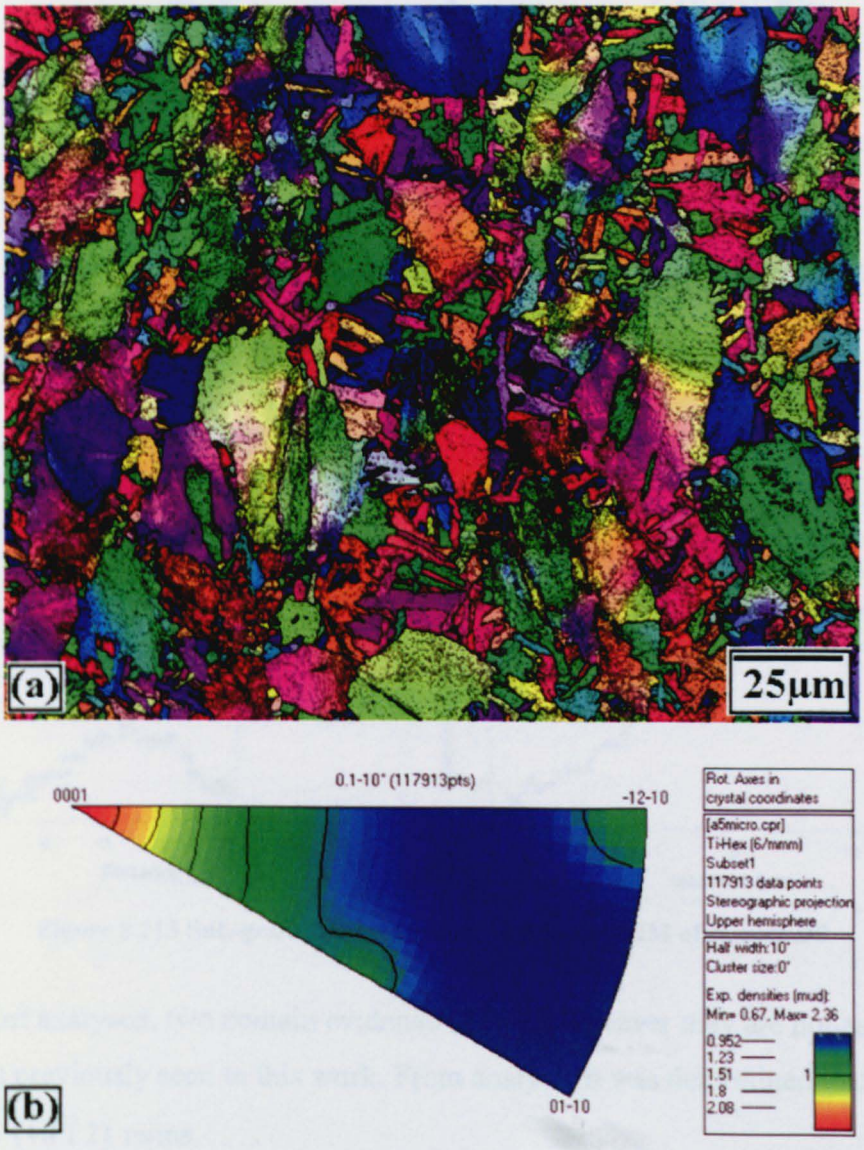

Figure 8.112 (a) IPF colouring OIM and (b) preferred crystal rotation axes of sample D5.

From the grains analysed within this OIM the misorientation profiles in Figure 8.113 were produced.

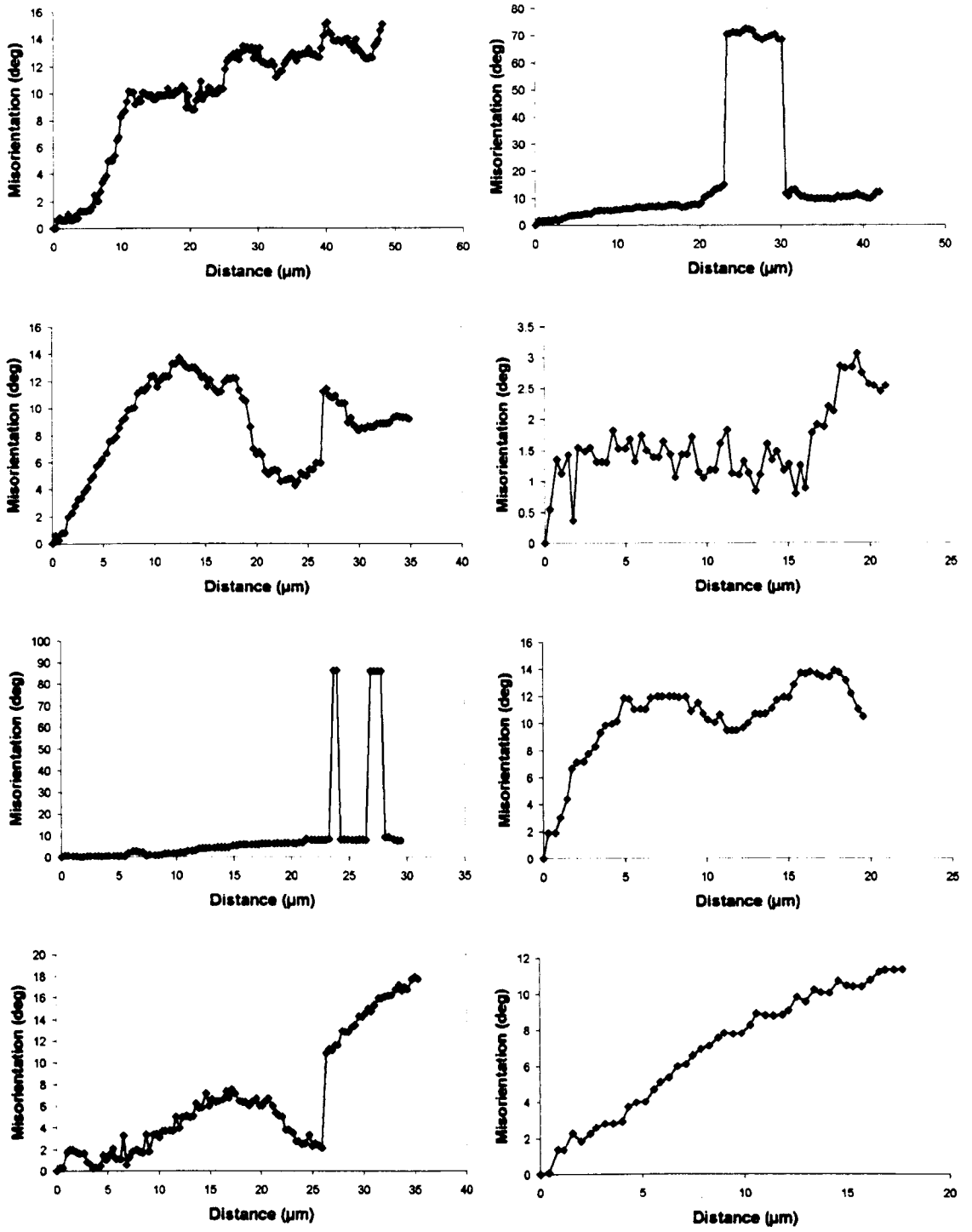

Figure 8.113 Sub-grain misorientations within the OIM of sample D5

Of the grains analysed, two contain evidence of twins however they are not as clear in the OIM as previously seen in this work. From analysis it was determined that both twins were $\{10\bar{1}2\}$ twins.

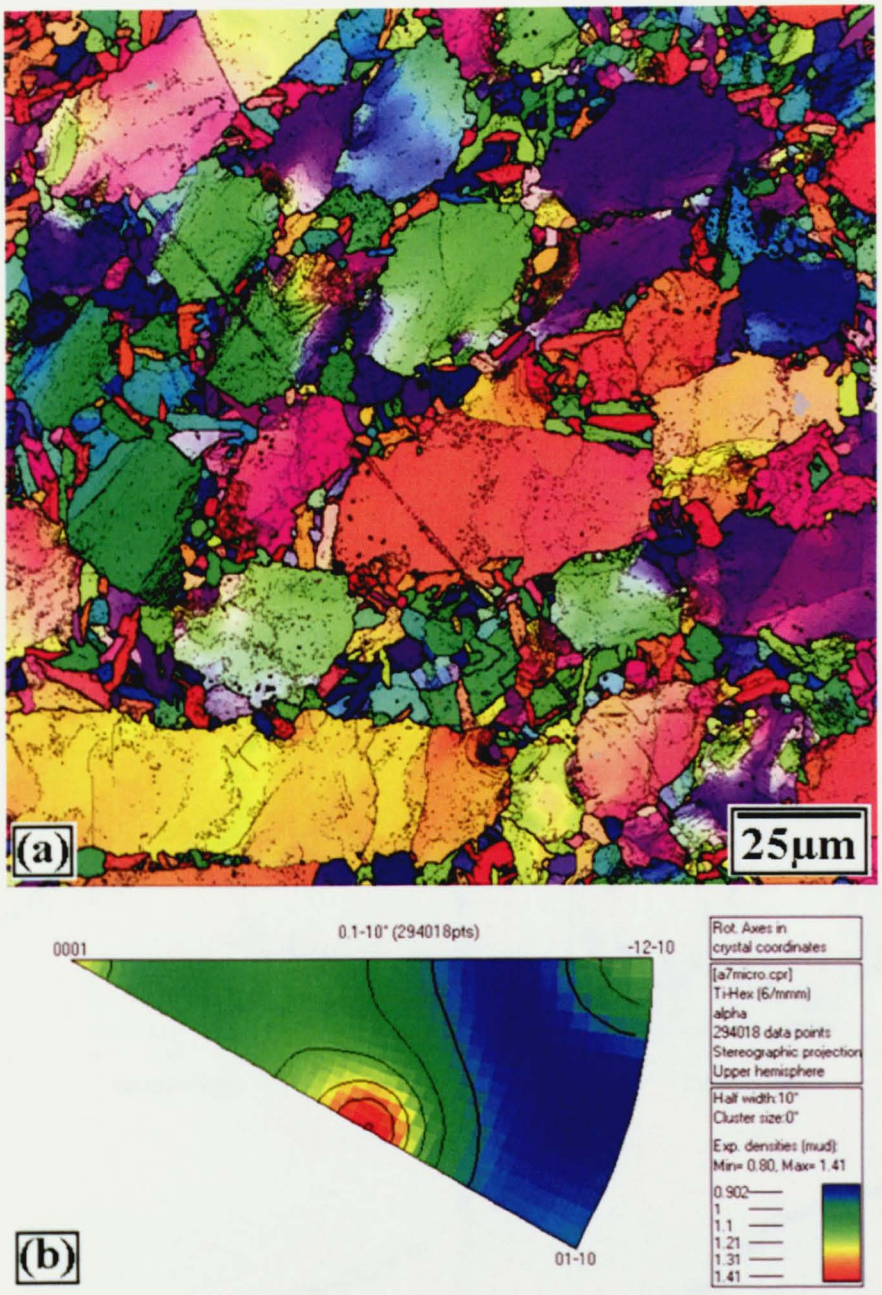

Figure 8.114 (a) IPF colouring OIM and (b) preferred crystal rotation axes of sample D7.

The grains analysed in Figure 8.114 produced the misorientation profiles in Figure 8.115, the grains show a maximum accumulated misorientation of approximately 12°. Within the OIM Figure 8.114(a) there is no evidence of twinning and the preferred sub-grain crystal rotation axis (Figure 8.114(b)) has moved away from the <0002> direction and is seen to be about the <10-11> direction with further evidence of the occurrence of rotation about the <-12-10> direction.

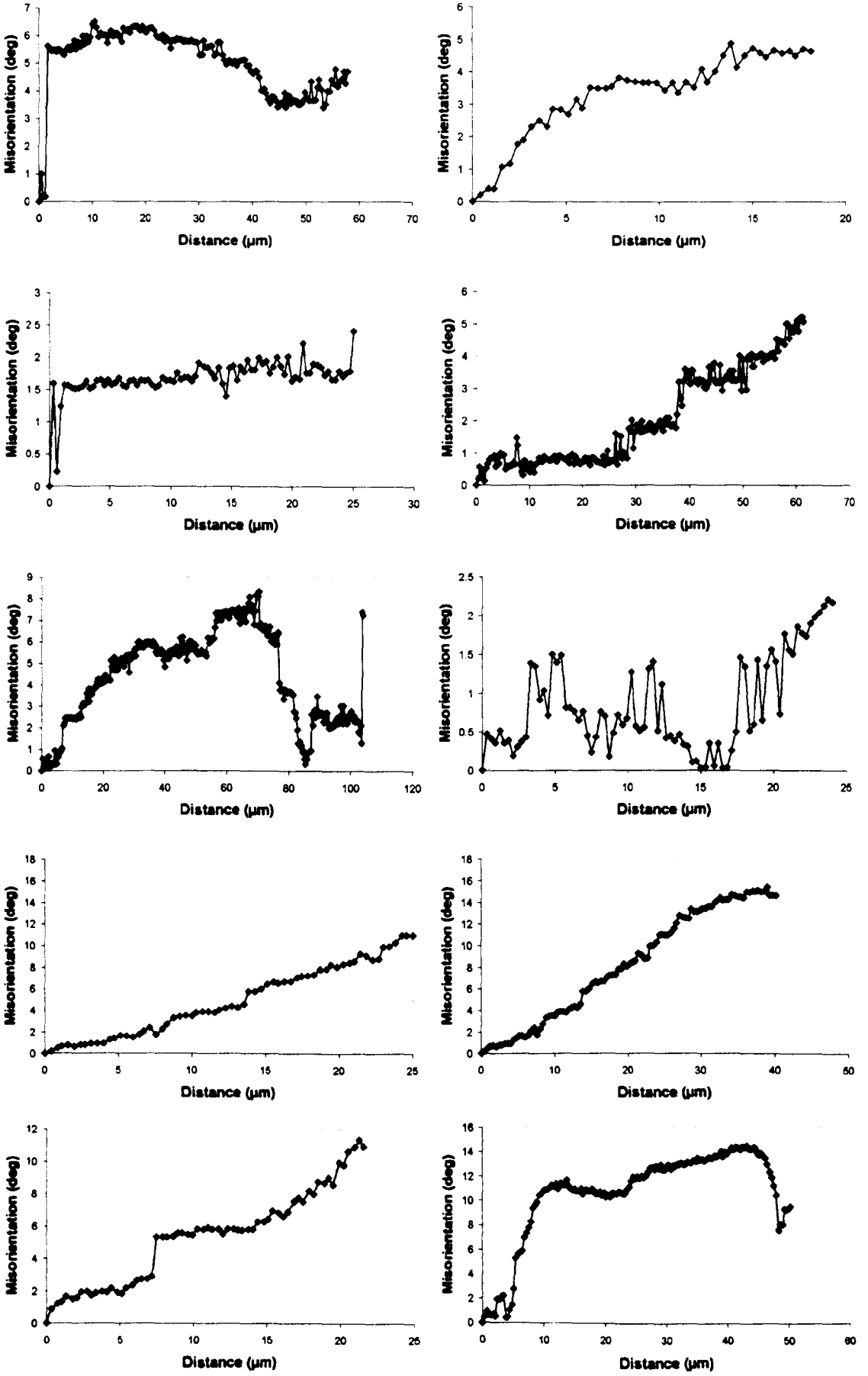

Figure 8.115 Sub-grain misorientations within the OIM of sample D7.

8.3.4 Summary of Microstructure Analysis

From the analysis of the high resolution OIM's the following conclusions can be made. As detailed throughout the investigation there is a very large amount of sub-grain misorientations rotated about the <0002> crystal axis. Figure 8.109 averages the crystal rotation axes and the sample rotation axes for all grains analysed in each deformed specimen.

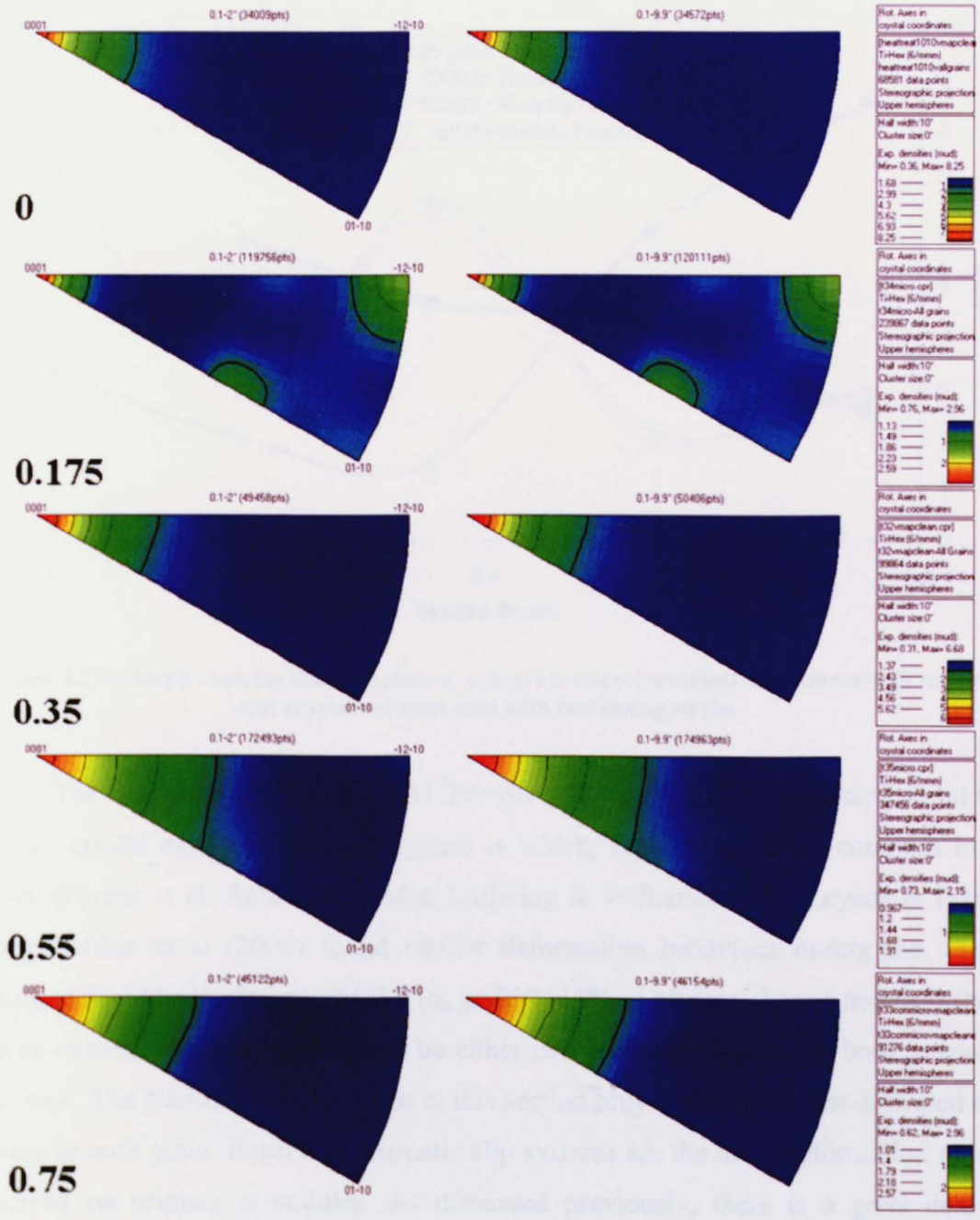

Figure 8.116 Summary of crystal rotation axes in the thermomechanically processed samples with increasing strain.

As the applied strain increases so does the sub-grain misorientation accumulation as illustrated by the sub-grain misorientation profiles. The highest measured accumulated misorientation in each sample can be seen in Figure 8.117. However, as the strain increases the dominance of the <0002> rotation is reduced suggesting further slip systems are activated as strain increases. A slight increase in sub-grain misorientation is also noted with an increase in strain rate, illustrated in both the OIM's and misorientation profiles in Figures 8.112-8.115.

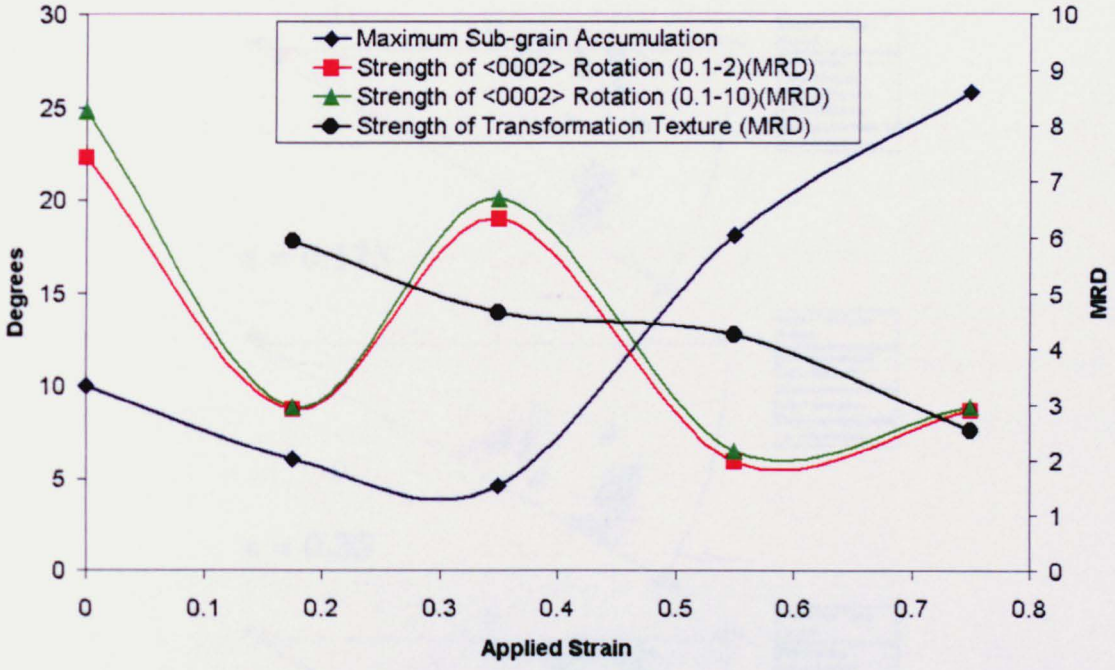

Figure 8.117 Graph showing the evolution of sub-grain mirorientations, transformation texture and crystal rotation axes with increasing strain.

The first order slip system, $<11\bar{2}0>\{01\bar{1}0\}$ would lead to a rotation about the <0002> crystal axis, and this slip system is widely reported as being common in Ti alloys. (Farenc et al, Acta Mat & Met, Lutjering & Williams, 2003, Leyens & Peters, 2003). Bridier et al (2005) found similar deformation behaviour during the tensile testing of Ti-6Al-4V, several nodules (α_p grains) (11% of all investigated nodules) show two co-existing slip systems that can be either two prismatic systems or both prismatic and basal. The statistical values given in this section only concern the first activated slip system in each grain. Basal and prismatic slip systems are the main deformation modes observed on primary α nodules. As discussed previously, there is a great deal of evidence suggesting that the <a>prismatic slip system dominates, however, it would not

be able to accommodate a rotation from a transverse basal orientation to a parallel basal orientation, which has been observed in the texture analysis.

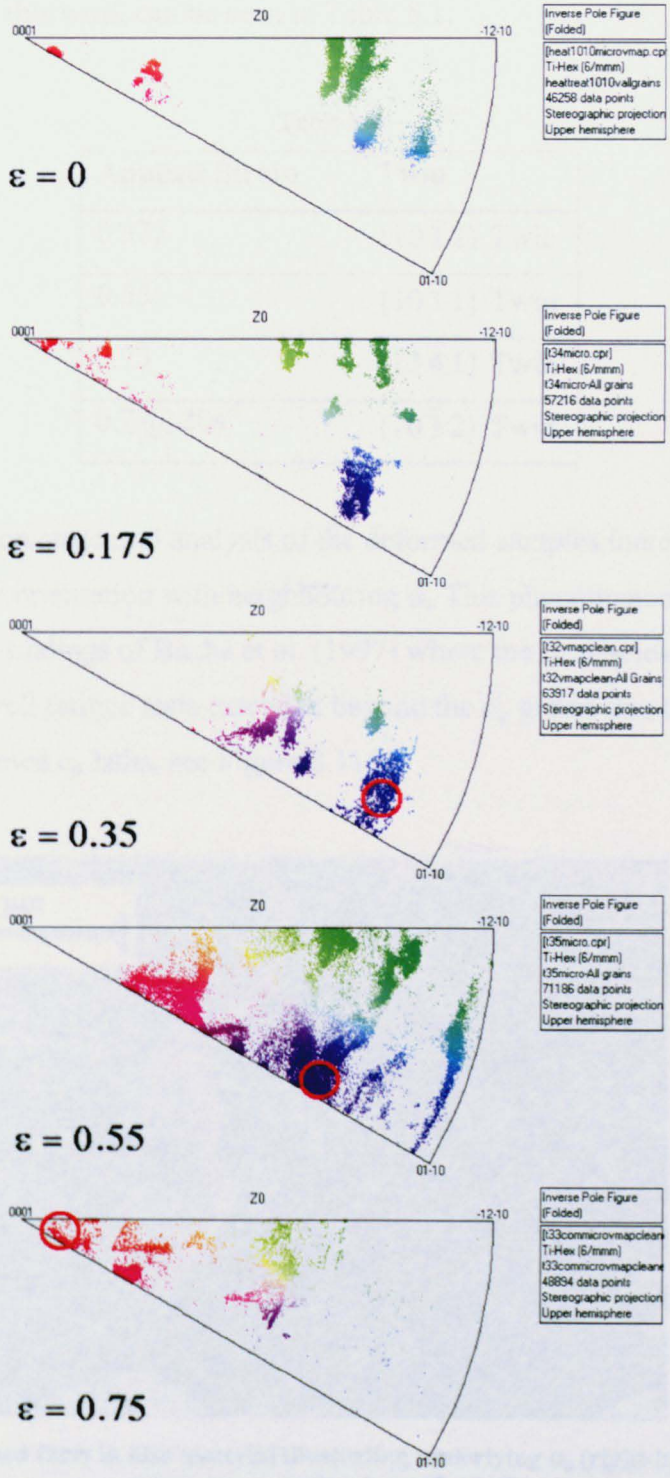

Figure 8.118 IPF of the analysed grains in each test sample, Twinned grains are highlighted by the red circles.

There is clear evidence of twinning in the deformed samples and the orientation of the twinned grains can be seen in Figure 8.118. Twinning occurs when grains possess

a hard orientation, where the basal plane is parallel with the compression direction or very close to transverse, this is due to the lack of shear stress on the active slip systems. Twins observed in this work can be seen in Table 8.1.

Table 8.1

Applied Strain	Twin
0.375	$\{10\bar{1}2\}$ Twin
0.55	$\{10\bar{1}1\}$ Twin
0.75	$\{13\bar{4}1\}$ Twin
0.7 @ $20s^{-1}$	$\{10\bar{1}2\}$ Twin

Throughout the microstructural analysis of the deformed samples there is evidence of α_p grains sharing their orientation with neighbouring α_s. This phenomenon is believed to be responsible for the findings of Bache et al. (1997) where the quasi-cleavage facets seen after fracture in dwell fatigue tests extended beyond the α_p grains into the neighbouring regions of transformed α_s laths, see Figure 8.119.

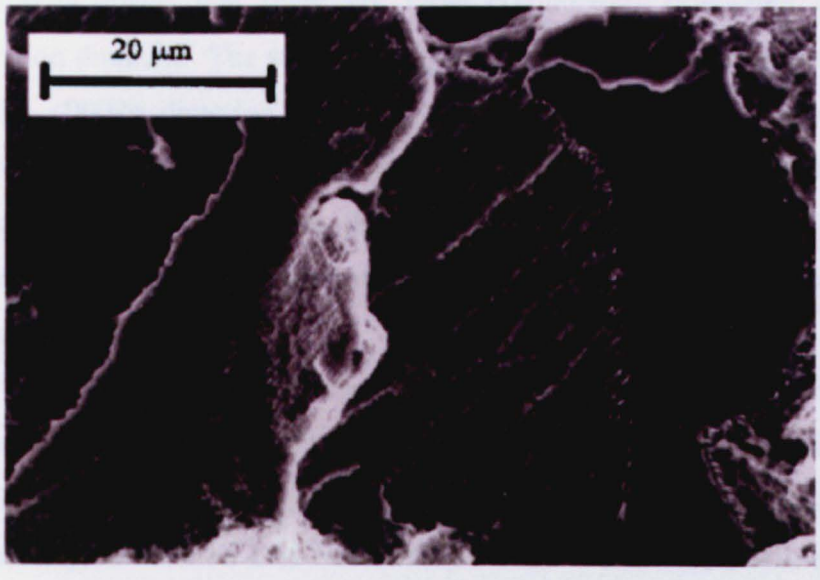

Figure 8.119 Etched facet in disc material illustrating underlying α_p (right-hand side) and α_s microstructure (Bache et al, 1997)

8.4 Texture evolution during industrial forging

As determined from Section 8.2.4 the starting material is heavily textured with a large transverse basal orientation.

At industrial deformation temperatures (1010°C) prior to deformation, the orientation of the 22% α_p remains clustered within a BCC β matrix, the α_p texture after cooling is as seen in the billet material. There is a reasonably high amount of sub-grain misorientation within the α_p prior to any applied strain, this is due to the shape chahange and movement associated with the volume change in the surrounding phase during transformation from BCC β to HCP α_s (Leyens & Peters, 2003). The common misorientation crystal rotation axis is about the <0002> direction, however there is evidence in the crystal rotation IPF of both <1210> rotation and <???>. The α_s orientation is a weak but is an expected transformation texture slightly rotated when compared with the α_p. It is difficult to determine the non-deformed β behaviour in this alloy due to the transformation after high temperature deformation.

After a strain of 0.175 there is little change in the α_p orientation, the major components remain transverse, and the clustering is maintained. It is clear from the {0002} pole figure that there are three components orientated evenly about the deformation direction. The sub-grain crystal rotation axis becomes further concentrated about the <0002> direction with only small traces of the rotation about the <1210> direction remaining. There is a similar amount of sub-grain misorientation in the α_p as in the heat treated sample again due to the transformation volume change. The α_s transformation texture becomes further defined with a single component more dominant than the others.

As the strain increases there is evidence of a rotation of the α_p grains from the transverse basal orientation to the parallel basal orientation. The dominant cluster of α_p grains is over 1mm in diameter and possesses an off-basal orientation. However, the dominant crystal rotation axis remains the <0002> direction, which is puzzling as this crystal rotation would not accommodate such a rotation of α_p. Therefore, there must be further slip systems in operation or an external rotation on the α_p causing the rotation. The α_s texture once again is a transformation texture standard in $\beta \rightarrow \alpha$ transformation {Stanford and Bate, 2003).

There is a large increase in sub-grain misorientation at an applied strain of 0.55 suggesting that the α_p is now being exposed to more strain. This is due to the

geometrical factors reported by Moril (1986) where the isolated α_p grains gather closer together and begin to infer constraint on each other.

Finally at a strain of 0.75, again, an off-parallel basal orientation is observed suggesting that this is a stable orientation and is now being maintained. Again, the <0002> direction is the crystal rotation axis is preferred, however, there is evidence of further crystal rotation about the -12-10. The sub-grain misorientation in this sample is the highest recorded as further strain has imparted further constraint.

9. CONCLUSIONS

During this work the effects of hot working on the microstructure and crystallographic texture evolution of Timetal®834 have been investigated using process parameters typical of the hot forging process route. Having assessed the industrial process parameters in Chapter 5, the effect of these parameters on the as-received material was analysed. As well as the main aims and objectives, a technique for the separate analysis of phase morphologies in titanium alloys has been developed and established. During the completion of this work a number of firsts were achieved at the University of Sheffield;

- Axisymmetric compression testing of Timetal®834.
- EBSD analysis of Timetal®834.
- Large (>5mm^2) EBSD maps running over 13 days.

Having now established these techniques at the University have already been impleted in subsequent work.

Further conclusion drawn from this study can be broken down into two main sections, flow behaviour analysis and microstructural and crystallographic texture analysis. Here the conclusions from Chapters 5, 6 and 7 are collated and will be considered later in Chapter 10 where further experiments are considered.

9.1 Flow Behaviour Analysis

- The peak stress of Timetal®834, when deformed at a strain rate of 2 s^{-1}, can be seen to decrease as the beta volume percentage increases, defined by the equation;

$$\sigma_p = 1416.3\beta_{\%}^{-0.5687}$$

- There is little indication of dynamic recrystallisation within this material, as the flow softening behaviour of the raw data is removed after temperature correction. Furthermore, there is clear evidence of a large degree of sub-grain boundaries within the α_p grains indicating no recrystallisation in the α_p as well as evidence of transformation to α_s from a substructured β microstructure.

- From the methodology described in section 3.2 it is only possible to determine an apparent activation energy (Q_{def}), further testing and analysis is needed to increase the accuracy of the activation energy. A value for Q_{def} of 958.70 kJ/mol has been determined.
- A friction coefficient of $\mu = 0.197$ was determined when deforming Timetal 834 using AML 1000 lubrication on M22 platens.
- Variations in flow behaviour with previous work where flow softening is observed is caused by the variation in the morphologies of the α phase in the dual phase field at deformation temperatures, due to different starting material conditions, thus making comparisons with other published works difficult.

9.2 Microstructural and Crystallographic Texture Analysis

- The billet material received possessed large clusters of similarly orientated α_p grains.
- EBSD Euler maps determined that these clusters ranged in size from approximately 200μm to 800μm, with an average diameter of 380μm in the plane perpendicular to the longitudinal direction.
- This suggests a very large prior beta grain size within the starting billet material, as each cluster could be inherited from a single beta grain or a sub-grain within a larger beta grain.
- The preferred orientation of these clusters has been described as a transverse basal texture, where the basal plane is aligned with the longitudinal direction of the billet, perpendicular to the billet plane.
- With an application of strain up to 0.75 at forging temperatures aligned with the longitudinal billet direction, the α_p clusters remain, increasing in diameter to over 1mm due to pancaking.
- At an applied strain between 0.175 and 0.35 the preferred orientation of the α_p grains rotates away from a transverse basal orientation towards an almost parallel basal orientation.
- There is evidence to suggest that some clustered regions with a transverse basal orientation remain in the high strain samples. This is believed to be due to the

cluster maintaining its hard orientation throughout deformation and as such avoiding any shear stress on its active slip planes.

- The sub-grain misorientation in the α_p increases with increasing strain.
- The preferred sub-grain rotation axis in the α_p is about the <0002> direction, however there is also evidence of rotation about the <10-11> and <-12-10> directions.
- Slip in the α_p is supplemented by deformation twinning when the basal plane is close to parallel or perpendicular to the compression direction.

10. FURTHER WORK

10.1 Introduction

In this chapter, the conclusions and overall findings of this work are considered and further work is suggested. The further work will be divided into thermomechanical processing and microstructural and crystallographic texture analysis

10.2 Thermomechanical Processing

Initially friction

The axisymmetric compression test is limited by geometry factors to a maximum applied strain of 0.75, after which the effects of friction becomes detrimental to the integrity of the test. It is clear from these results that as the applied strain increases, the dominant slip systems in the α_p grains change. It is therefore suggested that PSC testing is used to infer further levels of strain into the microstructure

Further analysis of the effect of the starting microstructure on the flow behaviour is needed. It is suggested that a schedule of tests deformed at the same temperature but after varying heat treatments be completed, an example of which can be seen in Table 10.1;

Table 10.1 Suggested further testing to investigate the effect on microstructure on the flow behaviour of Timetal®834.

Pre-treatment Temperature (°C)	Deformation Temperature (°C)	Phases present
950	990	50%α_p 50%β^*
970	990	50%α_p 50%β^*
990	990	50%α_p 50%β^*
1010	990	20%α_p, 30%α_s, 50%β
1030	990	10%α_p, 40%α_s, 50%β
1055	990	0%α_p, 50%α_s, 50%β

*Assuming α_s transforms to β first.

This testing schedule will show the influence of the kinking of the α_s on the flow behaviour. The deformation temperature can be varied in order to further the analysis.

10.3 Microstructural and Crystallographic Texture Analysis

Further work is needed to in order to define the effective structural unit size of the α_p, and as such, the ability to obtain larger EBSD data sets for statistically confident data analysis is needed. With the development of EBSD technologies in the past 5 years this should include the use of larger specimen holders and a faster cameras. An increase in step size will allow larger areas to be mapped and a better idea of the magnitude of the similarly orientated areas can be gained. One of the realisations in this work was although the α_p grains size in the as-received billet material was 25-30μm, the effective cluster size was 300-400μm and as such an EBSD mapping step size as large as 50μm could have been utilised in order to obtain huge maps enabling the assessment of the global billet texture.

11. REFERENCES

Abson, A. J. and J. J. Jonas *Hot Compression Behaviour of Thermomechanically Processed Alpha Zr* . Metals Technology. **4**, pp. 462-468. 1977.

Ahmed, T. and H. Rack *Phase transformations during cooling in α+β titanium alloys.* Materials Science and Engineering. **A243**, pp. 206-211. 1997.

Andres, C., G. Albrecht and G, Lutjering *Correlation between microstructure and creep behaviour of the high temperature Ti alloy IMI 834.* Zeitschrift Fur Metallkunde. **88**, pp. 1997.

Bache, M.R. *A review of dwell sensitive fatigue in titanium alloys: the role of microstructure, texture and operating conditions.* International Journal of Fatigue (UK).**25**, pp. 1079-1087. 2003.

Bache, M.R., M. Cope, H.M. Davies, W. J. Evans and G. Harrison *Dwell sensitive fatigue in a near alpha titanium alloy at ambient temperature.* International Journal of Fatigue (UK) **19**(Supplement 1), pp. S83-S88.1997.

Bache, M.R., W. J. Evans, V. Randle, R.J. Wilson. *Characterization of mechanical anisotropy in titanium alloys.* Materials Science and Engineering: A, **257**, pp. 139-144. 1998.

Bache, M R; Evans, W J; Davies, H M. *Electron back scattered diffraction (EBSD) analysis of quasi-cleavage and hydrogen induced fractures under cyclic and dwell loading in titanium alloys.* Journal of Materials Science (UK). **32**, pp. 3435-3442. 1997.

Bache, M. R., W. J. Evans, B. Suddell and F.R.M. Herrouin. *The effects of texture in titanium alloys for engineering components under fatigue.* International Journal of Fatigue (UK) **23**: S153-S159. 2001

Bate, P.S., P.L. Blackwell and J.W. Brooks In: P. Lacombe, R. Tricot and G. Beranger, Editors. *Thermo-mechanical processing of Titanium IMI 834. Sixth World Conference on Titanium*, France. 1988

Private communication with Professor Bate, The University of Sheffield, 2007.

Baxter, G.. *Fatigue Damage Accumulation in Titanium Alloy IMI 834.* Engineering Materials. Sheffield, University of Sheffield. 1994.

Baxter, G. J., W.M. Rainforth and L, Grabowski *TEM observations of fatigue damage accumulation at the surface of the near- alpha titanium alloy IMI 834.* Acta Materialia (USA).**44**, pp.3453-3463.1996

Bhattacharyya, D., G. Viswanathan, R, Denkenberger, D Furrer, H.L. Fraser *The role of crystallographic and geometrical relationships between α and β phases in an α/β titanium alloy.* Acta Materialia **51**, pp 4679-4691. 2003.

Bieler, T.R., M.G. Glavicic, S.L. Semiatin *Using OIM to investigate the microstructural evolution of Ti-6Al-4V.* JOM. **54**, pp31-36. 2002.

Bieler, T R; Semiatin, S L. *The origins of heterogeneous deformation during primary hot working of Ti-6Al-4V.* International Journal of Plasticity. **18**, pp1165-1189. 2002.

Blenkinsop, P. A. and D. F. Neal. *High temperature titanium alloys: the metallurgical understanding, development, and achievements of conventional alloys.* Conference Metallurgy and Technology of Practical Titanium Alloys, Chiba, Japan, 7-10 Dec. 1993. Minerals, Metals and Materials Society/AIME, Warrendale, PA 15086, USA. Published 1994.

Bowden F.P. and D. Tabor. *Friction and lubrication*, 2nd ed., Methuen and Co. Ltd., London, 1967.

Boyer, R. *An overview on the use of titanium in the aerospace industry.* Materials Science and Engineering **A213**: pp 103-114. 1996.

Bridier, F., P. Villechaise, J. Mendez *Analysis of the different slip systems activated by tension in a alpha/beta titanium alloy in relation with local crystallographic orientation.* Acta Materialia. **53**, pp. 555-567. 2005.

Brewer, W., R. Bird, T.A. Wallace. *Titanium alloys and processing for high speed aircraft.* Materials Science and Engineering **A243**: 299-304. 1998.

Burger, W G. *On the process of transition of the cubic-body-centered modification into the hexagonal-close-packed modification of zirconium* Physica, **1**, pp.561-586 1934.

Callister, W.D., *Materials science and engineering : an introduction*, 5th ed; New York; Chichester : Wiley, 2003.

Cahn RW, VCH Verlags gesellschaft mbH, *Materials Science and Technology: a Comprehensive Treatment.* Processing of Metals and Alloys (Germany) **15**, pp. 429-480, 1991.

Chambers, G J G; Scanlan, J V, *Forgings in titanium alloys (Ti alloy forgings for aircraft industry, utilizing high strength/weight ratio)*;Oxford Pergamon Press LTD., 1970

Cho, J., D. Dye, K.T. Conlon, M.R. Daymond, R.C. Reed. *Intergranular strain accumulation in near-alpha titanium alloy during plastic deformation.* Acta Materialia **50**: pp 4847-4864. 2002

Chun, Y.B. Yu, S.H., Semiatin, S.L., Hwang, S.K. *Effect of deformation twinning on microstructure and texture evolution during cold rolling of CP-titanium.* Materials Science and Eng. A **398**, pp 209–219. 2005.

Cullity, B. Stock, S R. *Elements of X-ray Diffraction*, Prentice Hall, Upper Saddle River, NJ. 2001

Daeubler, M., D. Helm, G Lutjering. *Influence of heat treatment on microstructure and mechanical properties of cast IMI 834.* Titanium '95: Science and Technology. 1995.

Daeubler, M. A., D. Helm, D.F. Neal. 1990. *Applications of IMI 834 in Aeroengines--a Collaborative IMI/MTU Programme.* Titanium Development Association: pp 78-87.

Davenport S.B, N.J Silk, C.N Sparks, C.M. Sellars(2000). *Development of constitutive equations for modelling of hot rolling.* Materials Science and Technology (UK) **16**: 539-546. 2000

Davenport, S., C. Sparks, C.M. Sellars. *Modelling hot rolling of C-Mn steel using constitutive equations.* Thermomechanical Processing in Theory, Modelling and Practice, ASM Stockholm, Sweden. pp249-258. 1996

Dieter, G. E. *Mechanical Metallurgy.* New York, McGraw-Hill.1988

Ding, R., Z. Guo, A, Wilson. *Microstructural evolution of a Ti-6Al-4V alloy during thermomechanical processing.* Materials Science and Engineering **A327**: 233-245. 2002

Donachie, M. J. *Titanium; A Technical Guide.* OH, ASM International. 1988

Es-souni, M. *Creep behaviour and creep microstructure of a high-temperature titanium alloy Ti-5.8Al-4.0Sn-3.5Zr-0.7Nb-0.35Si-0.06C (Timetal 834). Part I. Primary and steady-state creep.* Materials Characterization **46**: 365-379. 2001

Evans, R. W. and P. J. Scharning. *Axisymmetric compression test and hot working properties of alloys.* Materials Science and Technology (UK) **17**(8): 995-1004. 2001.

Evans, W. and M. R. Bache. *Hydrogen and fatigue behaviour in a near alpha titanium alloy.* Scripta Metallurgica et Materialia **32**(7): 1019-1024. 1995

Evans, W. J. *Stress Relaxation and Notch Fatigue in Ti-6Al-4V.* Scripta Metallurgica. **21**(9): 1223-1227.1987.

Evans, W. J. (1998). *Optimising mechanical properties in alpha + beta titanium alloys.* Conference Thermomechanical Processing and Metallurgy of Titanium Alloys, Wollongong, Australia, 7-11 July 1997, Switzerland.

Evans, W. J. and M. R. Bache *The Role of Hydrogen in the Fatigue Response of a Near Alpha Titanium Alloy.* Conference Strength of Materials. ICSMA 10, Sendai, Japan, 22-26 Aug. 1994.

Evans, W. J., M. R. Bache, P J Nicholas. *The prediction of fatigue life at notches in the near alpha titanium alloy Timetal 834.* International Journal of Fatigure (UK) 23, 103-109, 2001.

Filip, R., K. Kubiak, et al. *The effect of microstructure on the mechanical properties of two-phase titanium alloys.* Journal of Materials Processing Technology **133**: 84-89. 2003.

Flower, H. M. *Microstructural Development in Relation to Hot Working of Titanium Alloys*. Materials Science and Technology, **6**, pp 1082-1092, 1990.

Ford, H and J.M. Alexander *Rolling hard materials in thin gauges*, Journal of the Institute of Metals, **92**, 397, 1963.

Germain, L., Gey, N., Humbert, M., Hazotte, A., Bocher, P. & Jahazi, M. *An automated method to analyze separately the microtextures of primary α_p grains and the secondary α_s inherited colonies in bimodal titanium alloys.* Materials Characterization **54**, 216–222. 2005.

Germain, L., Gey, N., Humbert, M., Bocher, P. & Jahazi, M. *Analysis of sharp microtexture heterogeneities in a bimodal IMI 834 billet.* Acta Materialia. **53**, 3535-3543. 2005.

Germain, L., Gey, N., Humbert, M., Bocher, P. & Jahazi, M. *$\beta \rightarrow \alpha_s$ variant selection in sharp hcp textured regions of a bimodal IMI834 billet.* Materials Science Forum **495-497**, 663-668. 2005.

Gey, N. and M. Humbert. *Specific analysis of EBSD data to study the texture inheritance due to the β to α phasr transformation*. Journal of Materials Science **38**: 1289-1294. 2003.

Gey, N., M. Humbert, H, Moustahfid. *Study of the α to β phase transformation of a Ti-6Al-4V sheet by means of texture change*. Scripta Materialia **42**: 525-530. 2000.

Glavicic, M., P. Kobryn, T.R. Bieler, S.L. Semiatin. *A method to determine the orinetation of the high-temperature beta phase from measured EBSD data for the low temperature alpha phase in Ti-6Al-4V*. Materials Science and Engineering **A346**: 50-59. 2005

Glavicic, M G; Miller, J D; Semiatin, S L; *A method to measure the texture of secondary alpha in bimodal titanium-alloy microstructures*. Scripta Materialia. **54**, pp. 281-286. 2006

S. Guillard, M. Thirukkonda, P.K. Chaudhury, in: I. Weiss, R. Srinivasan, P. Bania, D. Eylon, S.L. Semiatin (Eds.), *Advances in the Science and Technology of Titanium Alloy Processing*, TMS, Warrendale, PA, 1997, pp. 93–100

Hatherly, F. J. H. a. M. *Recrystallization and related annealing phenomena*. Oxford, Elsevier Science Ltd. 2002.

Hatherley and Hutchinson, An introduction to textures in metals, (London) : (Institution of Metallurgists), (1979)

Higginson and Sellars, Worked Examples in Quantitative Metallography, 2003

Hinton, J. Laboratory Simulation of Microstructural Evolution in AISI 430 Ferritic Stainless Steel during the Steckel Mill Process. Engineering Materials, The University of Sheffield

Humbert, M; Gey, N; Germain, L, *Study and Modelling Of Some Variant Selections In BCC to HCP Phase Transformations.* Materials Science Forum. Vol. 495-497, pp. 1111-1120. 2005

Humphreys, F J. *Grain and subgrain characterisation by electron backscatter diffraction.* Journal of Materials Science. **36**, pp. 3833-3854. 2001

Private Communication with Professor Bevis Hutchinson, The University of Sheffield 2006.

Hyun, Y T. Kim, J W. Lee, J H. Kim, S E. Lee, Y T; *The influence of VAR Processing on Solidification Behaviour in Ti-6Al-4V Alloy.* Proceedings of the 10th World Conference on Titanium. Edited by Lutjering and Albrecht. Wiley-VCH 2003.

Jupp, S. *Fundamental Modelling of Friction During the Hot Rolling of Steel.* Engineering Materials. The University of Sheffield. 2005.

Kestler, H., H. Mughrabi, H, Renner. *Optimization of microstructure and mechanical properties of the hot-forged titanium alloy IMI 834 by heat treatment.* Titanium '95: Science and Technology. pp 1171-1179. 1995

Kocks, Argon, Ashby; *Thermodynamics and Kinetics of slip*, Pergamon Press,1975

Kocks, U F. Tome, C N. Wenk, H-R. *Texture and Anisotropy* (Paperback)" Cambridge University Press. 1998

Kunogi M. *A new method of cold extrusion.* J Sci Res Inst (Tokyo) **50**, pp 215-46, 1956.

Leyens and Peters, Titanium and titanium alloys : fundamentals and applications, Weinheim : Wiley-VCH, c2003

Lin, J. and Y. Liu. *A set of unified constitutive equations for modelling microstructure evolution in hot deformation.* Journal of Materials Processing Technology **143-144**: 281-285. 2003.

Lindeman, J. and L. Wagner. *Microtextural effects on mechanical properties of duplex microstructures in (α+β) titanium alloys.* Materials Science and Engineering **A263**: 137-141. 1999.

Lundberg, S. E. *Evaluation of friction in the hot rolling of steel bars by means of on line forward slip measurements*, Scandanavian Journal of Metallurgy, **33**, 129-145, 2004.

Lutjering, G. *Influence of processing on microstructure and mechanical properties of (α+β) titanium alloys.* Materials Science and Engineering **A243**, pp 32-45. 1998.

Lutjering, G., J. Albrecht, et al. *Influence of cooling rate and beta grain size on the tensile properties of (alpha + beta) Ti-alloys.* Conference Titanium '95. Birmingham, UK, 22-26 Oct. 1995.

Lutjering, G and J. C. Williams, *Titanium*. Ed: B.Derby. Publ: [14302] Berlin, Germany; Springer-Verlag; 2003

Maier, H. J., S. Hardt, et al. *High-temperature fatigue damage mechanisms in near-alpha titanium alloy IMI 834*. International Journal of Fatigue (UK) **21**, pp 779-789. 1999.

Male AT, Cockcroft MG. *A method for the determination of the coefficient of friction of metals under condition of bulk plastic deformation*. Journal of the Institute of Metals, pp 38-46, 1965.

Moril, K., H. Mecking, Y. Nakayama. G. Lutjering, *Stability of the texture of Ti-6Al-4V during rolling in the two phase field.* Scripta Metallurgica, **20**, pp 1795-1800, 1986.

Naka, S. *Advanced titanium-based alloys.* Current Opinion in Solid State & Materials Science (USA) **1**, pp 333-339. 1996.

Neal, D. F. *Development and Evaluation of High Temperature Titanium Alloy IMI 834.* Les Editions de Physique, pp 253-258. 1988.

Neal, D. F. *Development of Timetal-834.* Materials Design Approaches and Experiences, Indianapolis, USA, Minerals and Materials Society/AIME. 2001.

Nishikiori, S., H. Hattori, et al. *Dual-structure compressor disk of heat-resistant titanium alloy.* Conference Titanium '95. Vol. II, Birmingham, UK, 22-26 1995.

Pang, H T. Reed, P A S. *Effects of Temperature and Dwell on the Fatigure Crack Propagation of Nickel-Base Turbine Disc Superalloy RR1000.* Materials Research Group, university of Southampton, 2001.

Partridge, P.G. *The crystallography and deformation modes of hexagonal close packed metals*. Metallurgical Review. **118,** pp. 169-194. 1968.

Paton, N.E. & Backofen, W.A *Plastic Deformation of Titanium at Elevated Temperatures*. Metallurgical Transactions. **1**, 2839-2347. 1970.

Polmear, I. *Light alloys; Metallurgy of the light metals.* Oxford, Butterworth and Heinemann. 1995.

Qu, Jun; Blau, Peter J; Watkins, Thomas R; Cavin, Odis B; Kulkarni, Nagraj S. *Friction and wear of titanium alloys sliding against metal, polymer, and ceramic counterfaces,* Wear. **258**, pp. 1348-1356. 2005

Randle, V. *Crystallographic analysis of facets using electron backscatter diffraction.* Journal of Microscopy (UK) **195**(3), pp 226-232. 1999.

Randle, V. and O. Englar. *Introduction to Texture Analysis. Macrotexture, Microtexture and Orientation Mapping*. London, Taylor and Francis. 2000.

Ridley, N; Wang, Z C; Lorimer, G W, Titanium '95. Vol. I; Birmingham; UK; 22-26 Oct. 1995. pp. 604-611. 1996

Roebuck, B., Lord, J.D., Brooks, M., Loveday, M.S., Sellars, C.M. & Evans, R.W. *Measurement Good Practice Guide No. 3: Measuring Flow Stress in Hot Axisymmetric Compression Tests.* The National Physical Laboratory, UK. 2002.

Rollett, A D.
http://neon.mems.cmu.edu/rollett/27750.old.Spg05/Components_pt2_13Jan05_v2.ppt., 04/06/06).

S.L. Semiatin, J. O. B., T.M. Brown, D.P. DeLo, T.R. Bieler, J.H. Beynon. *Strain-path effects during hot working of Ti-6Al-4V with a colony-alpha microstructure.* Metallurgical and Materials Transactions **A32**,pp 1556-1559. 2001.

Semiatin, I. W. a. S. L. *Thermomechanical processing of alpha titanium alloys-an overview.* Materials Science and Engineering **A263**: 243-256. 1999.

Semiatin, S. L., V. Seetharaman, et al. *Hot workability of titanium and titanium aluminide alloys--an overview.* Conference Thermomechanical Processing and Metallurgy of Titanium Alloys, Wollongong, Australia, 7-11 July 1997.

Shih, D. S., F. S. Lin, et al. *The Effect of Microstructure and Texture on the Fatigue Crack Propagation of an alpha + beta Titanium Alloy.* Deutsche Gesellschaft fur Metallkunde, pp 2259-2266. 1985.

N.J. Silk and M.R. van der Winden; *Interpretation of hot plane strain compression testing of aluminium specimens*, Materials Science and Technology, 15, p295, 1999.

Smallman, R. and R. Bishop. *Metal and Materials; Science, Processes, Applications.* Oxford, Butterworth-Heinemann Ltd. 1995.

Stanford and Bate, Acta Materialia. Vol. 52, no. 17, pp. 5215-5224. 4 Oct. 2004

http://www.struers.com/modules/emetalog, 2004

Sufogulu et al, Tribology International 35(2002) 27-34

Thomas, M.J., Wynne, B.P. & Rainforth, W.M. (2005) *Texture Evaluation of Titanium Aerospace Alloy Ti 834 Using Hot Axisymmetric Compression Tests.* Materials Science Forum **495-497**, 693-698. 2005.

Thomas, M.J., Wynne, B.P. & Rainforth, W.M. (2005) *An alternative method to separate and analyse the microtextures and microstructures of primary alpha grains and transformed beta grains in near-α titanium alloy Timetal 834.* Materials Characterisation. **55**, pp388-394, 2005

Thomsen, M. L. and D. W. Hoeppner. "The effect of dwell loading on the strain accumulation behavior of titanium alloys." International Journal of Fatigue (UK) **20(4)**: 309-317. 1998.

Torster, F., A. Gysler, et al. *Effect of microstructure and test temperature on fatigue properties of IMI 834.* Conference Titanium '95. Vol. II, Birmingham, UK, 22-26 Oct. 1995.

Vaudin, M. *Crystallographic Texture in Ceramics and Metals.* Journal of Research of the National Institute of Standards and Technology **106**(6): 1063-1069. 2001.

Wanjara, P; Jahazi, M; Monajati, H; Yue, S; Immarigeon, J-P; *Hot working behavior of near-alpha alloy IMI834,* Materials Science and Engineering **A396**, pp. 50-60. 2005

H.R. Wenk and P. Van Houtte; *Texture and Anisotropy, Reports on Progress in Physics*, **67**, p1367. 2004.

Weiss, I. and S. L. Semiatin. *Thermomechanical processing of beta titanium alloys--an overview.* Conference Thermomechanical Processing and Metallurgy of Titanium Alloys, Wollongong, Australia, 7-11 July 1997.

Weiss, I. and S. L. Semiatin. *Thermomechanical processing of alpha titanium alloys--an overview.* Conference Metallurgy Technology and Applications of Titanium Alloys, Xian, Shaanxi, China, 15-18 Sept. 1998.

Williams, DB. *Practical Analytical Electron Microscopy in Materials Science.* deerfield Beach, FL: Verlag Chemie International; 1984.

Williams, J.C, Starke EA, Peters, M in *Deformation Processing and Structures*, 1982 Materials Science Seminar, ASM. 1982.

Williams, J C; Baggerly, R G; Paton, N E. *Deformation behavior of Hcp Ti-Al alloy single crystals*, Metallurgical and Materials Transactions A (USA). **33A** , pp. 837-850. 2002

Timet Data Sheets; http://www.timet.com/index_new.htm, 2004

Zhu, Z., J. Gu, et al. *Variant selection and its effect on phase transformation textures in cold rolled titanium sheet.* Materials Science and Engineering **A280**: 199-203. 2000.

(www.technologie-entwicklung.de /Gasturbines.html) 2005